Design and preparation of functional coordination compounds based on poly-β-diketone and polypyrazolyl ligands

Ivana Borilović

DESIGN AND PREPARATION OF FUNCTIONAL COORDINATION COMPOUNDS BASED ON POLY-β-DIKETONE AND POLYPYRAZOLYL LIGANDS

Universitat de Barcelona

Facultat de Química

Departament de Química Inorgànica i Orgànica

(Secció de Química Inorgànica)

Programa de Doctorat: Doctorat de Química Orgànica

Química supramolecular y materiales avanzados

Grup de Magnetisme i Molècules Funcionals

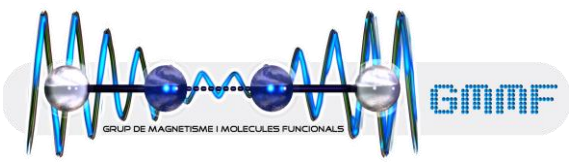

Ivana Borilović

Director y Tutor: Prof. Guillem Aromí Bedmar
Departament de Química Inorgànica i Orgànica

Guillem Aromí Bedmar, Professor del Departament de Química Inorgànica i Orgànica (Secció de Química Inorgànica) de la Facultat de Química de la Universitat de Barcelona,

CERTIFICA: que el treball titulat *DESIGN AND PREPARATION OF FUNCTIONAL COORDINATION COMPOUNDS BASED ON POLY-β-DIKETONE AND POLYPYRAZOLYL LIGANDS* que presenta la Ivana Borilović per optar al grau de Doctor per la Universitat de Barcelona, ha estat realitzat sota la seva dirección al Departament de Química Inorgànica i Orgànica (Seccio de Química Inorgànica) d'aquesta Facultat.

Barcelona, Setembre de 2018

Prof. Guillem Aromí Bedmar

Content

There is nothing more wonderful than being a scientist. A scientist in his laboratory is not just a mere technician: he is also a child confronting natural phenomena that impress him as though they were fairy tales. Nowhere I would rather be than in my lab, staining up my clothes and getting paid to play.

Marie Sklodowska Curie

Mojoj osobi...

CHAPTER I

INTRODUCTION

1.1. Introduction

The close relationship between the coordination chemistry and molecular magnetism has been established from the very beginning of the latter. Combining the versatile organic scaffolds and the diverse physico-chemical properties of transition and rare-earth metals, coordination chemistry illuminated the discovery of numerous molecular functional systems, ranging from the bi-stable single molecule magnets (SMMs) and spin crossover (SCO) materials, to the molecular prototypes of quantum bits (qubits) and logic gates (qugates). On the other hand, systematic studies of magnetic properties provided the meaningful insights into the electronic structure of coordination entities, resulting with many magneto-structural correlations and predictable models. Beyond the fundamental findings, successful integration of molecular magnets to surfaces emerged the evolution of nanoscale magnetic devices and the field of molecular spintronics. As a result, novel interest for the molecular systems was triggered since controlled structural variations among the plethora of building blocks could be exploited to tailor the specific functions. In that context, especially appealing has become the pursuit of systems which will allow the controlled manipulation of molecular spins and charges for the information storage and processing.

Combining the judiciously designed *bis*−β-diketone and polypyrazolyl scaffolds with the crystal field effects on the 3*d* metal ions, this manuscript exposes different methods of selective preparation of new heterometallic coordination compounds and the subtle modulation of their magnetic properties. Apart from their conventional magneto-structural relevance, special interest has been dedicated to develop the systems which exhibit strong ferromagnetic coupling and slow relaxation of the magnetization, even when incorporating exclusively isotropic metal ions. Moreover, synthetic strategy based on controlled transfer of the ligand asymmetry to its coordination compounds provided several entities which fulfil the necessary requirements to be exploited as the molecular prototypes of universal logic gates in quantum information processing.

1.2. General aspects of the molecular magnetism

Macroscopic magnetic properties of the molecular nanomagnets can be generally related to the laws of classical physics. Hence, a molecule exposed to the magnetic field *H* will acquire magnetization, *M*, determined by its molar magnetic susceptibility, χ_M:[1]

$$\chi_M = \frac{\partial M}{\partial H} \tag{1.1}$$

In the limit of the weak magnetic fields *H*, this expression becomes simplified into:

$$M = \chi_M \cdot H \tag{1.2}$$

Molar magnetic susceptibility consists of the omnipresent negative (diamagnetic) component which is generated by the closed-shell molecular moieties and positive (paramagnetic) component arising from the unpaired electrons in the molecule. In classical physics, magnetization of the substance is a direct measure of its energy variation in interaction with the applied field:

$$M = -\frac{\partial E}{\partial H} \tag{1.3}$$

Consequently, substances with the negative magnetic susceptibility and magnetization will be repelled by the magnetic field resulting with an increment of their energy, while the positively magnetised substances will align with the magnetic field and lower its energy. Applying the same principle on the quantum systems, magnetization of any molecule will be defined by the energy change upon the interaction of the applied magnetic field *H* with the angular momenta of its thermally populated states. Thus, a molecule with energy levels E_n (n=1, 2,…n) placed in the magnetic field *H* will acquire macroscopic magnetization *M* defined as:

$$M = \frac{N_A \sum_n (-\frac{\partial E_n}{\partial H}) \cdot e^{-\frac{E_n}{k_B T}}}{\sum_n e^{-\frac{E_n}{k_B T}}} \tag{1.4}$$

Hence, macroscopic magnetization is a cooperative phenomenon which includes the total sum of the microscopic magnetizations of every populated energy level ($\mu_n = -\frac{\partial E_n}{\partial H}$) weighted by their Boltzmann distribution ($\frac{e^{-\frac{E_n}{k_B T}}}{\sum_n e^{-\frac{E_n}{k_B T}}}$). The problematic side of the given formula is the determination of the $E_n = f(H)$ functions of all the populated states, which are required for its derivatives. Simplification of these functions was accomplished by Van Vleck's increasing powers of *H*:

$$E_n(H) = E_n^{(0)} + E_n^{(1)}H + E_n^{(2)}H^2 \ldots \quad (1.5)$$

with $E_n^{(0)}$ being the energy of *n* level in the zero field and $E_n^{(x)}$ being the Zeeman coefficients of x-order. Introducing the power function $E_n(H)$, microscopic magnetization can be written as:

$$\mu = -E_n^{(1)} - 2E_n^{(2)}H - \ldots \quad (1.6)$$

Additional approximations assuming the $H/\ k_BT << 1$ and nil magnetization in the zero field, allowed the extraction of the well-known Van Vleck's formula of the magnetic susceptibility:

$$\chi = \frac{N_A \sum_n (\frac{E_n^{(1)2}}{k_B T} - 2E_n^{(2)}) \cdot e^{-\frac{E_n^{(0)}}{k_B T}}}{\sum_n e^{-\frac{E_n^{(0)}}{k_B T}}} \quad (1.7)$$

Although the derived expression still retains the three unknown quantities $E_n^{(x)}$(x= 0, 1 and 2), Van Vleck's formula can be employed when the eigenvalues $E_n^{(0)}$ and eigenfunctions $|n\rangle$ of the molecular Hamiltonian in zero-field are familiar, since the $E_n^{(1)}$ and $E_n^{(2)}$ factors can be extracted from the perturbation theory. Therefore, an analytical expression of the temperature dependence of the molar magnetic susceptibility for a given spin *S* can be derived:

$$\chi_M = \frac{N_A g^2 \mu_B^2}{3k_B T} \frac{\sum_n S(S+1)(2S+1) \cdot e^{-\frac{E_n^{(0)}}{k_B T}}}{\sum_n (2S+1) e^{-\frac{E_n^{(0)}}{k_B T}}} \quad (1.8)$$

In the most simplified paramagnetic molecule, such as isolated isotropic spin centre *S*, equation (1.8) can be expressed as the Curie Law:

$$\chi_M = \frac{N_A g^2 {\mu_B}^2}{3k_B T} S \cdot (S+1) \quad (1.9)$$

When only one spin state *S* is populated, the temperature-dependent magnetic response of such system will yield a straight line parallel to the *x*-axis (*T*). Proportionally with χ_M, magnetization of the system will increase as the temperature is lowered. Thus, field dependence of the magnetization at the lowest temperature will progress towards the saturation limit (M_{sat}) where all spins are parallel to the magnetic field:

$$M_{sat} = g \cdot S \cdot \mu_B \cdot N_A \quad (1.10)$$

However, such simplicity is almost never encountered in the real systems which often exhibit the spin-orbit coupling, anisotropy and interactions between the spin carriers.

Moreover, even when the splitting of the energy levels by the magnetic field becomes comparable with the thermal energy k_BT (approximation $H/k_BT << 1$ is no longer valid), Curie Law has to be replaced by the Curie-Weiss Law which only slightly broadens its applicability (θ-paramagnetic Weiss temperature):

$$\chi_M = \frac{N_A g^2 \mu_B{}^2}{3k_B(T-\theta)} S \cdot (S+1) \tag{1.11}$$

On the other hand, the *bottom up* perspective of quantum mechanics offers the complete rationalisation of the macroscopic properties of any molecular system from its electronic structure. The latter is completely determined by the time independent Schrödinger equation:

$$\hat{H}\Psi = E\Psi \tag{1.12}$$

in which application of the Hamiltonian operator $\hat{H}$ on the molecular wavefunction Ψ determines the energy of the state *E*. Specifically, energy of a certain spin state can be determined by matrix diagonalization of the spin Hamiltonian, which for the coordination compounds can be constructed out of four major components: spin-orbit coupling, Zeeman splitting, crystal-field interaction and exchange interaction.[2, 3] The contribution of these components to the macroscopic magnetic properties is largely dependent on the nature of the involved metal ions. Thus, spin-obit coupling is particularly relevant for the compounds holding 4*f* metals, while the exchange interactions, crystal field effects and spin-orbit coupling shape variably of the electronic structure the magnetic response of the 3*d* compounds.

Microscopic magnetization (μ) of the free open-shell ion is defined by its total magnetic (angular) moment (*J*) which includes the contributions of the spin moment (*S*) and the orbital moment (*L*) as a consequence of the spin-orbit coupling:

$$J_{max} = L + S > J > J_{min} = L - S \tag{1.13}$$

According to the Hund's third rule, the maximum *J*, (J_{max}), is the lowest energy state for more than half-filled shells, while the minimum *J*, (J_{min}), is the lowest energy state for less than half-filled shells. Energy structure is determined by the ${}^{2S+1}L_J$ terms derived from the Russell-Saunders coupling scheme, while the Hamiltonian operator defining the spin-orbit coupling is written as:

$$\hat{H} = \lambda \cdot \hat{L} \cdot \hat{S} \tag{1.14}$$

with λ being the spin-orbit coupling constant of the metal ion. However, the latter equation holds true only for the transition metals which exhibit relatively small λ values, unlike heavier 4*f* ions for which spin-orbit coupling effects become larger and mixing of the terms should be taken into account.

Exposure to the magnetic field splits the 2*J*+1 degeneracy of the M_J states within the $^{2S+1}L_J$ energy term according to the Zeeman Hamiltonian:

$$\hat{H} = \mu_B \cdot B \cdot (\hat{L} + g_e\hat{S}) \tag{1.15}$$

where g_e=2.0023, as determined by relativistic effects. Thus, energy of each M_J state will be determined as:

$$E_{M_J} = g_J \cdot \mu_B \cdot B \cdot M_J \tag{1.16}$$

$$g_J = 1 + \frac{J(J+1)+S(S+1)-L(L+1)}{2J(J+1)} \tag{1.17}$$

with g_J being the Landé factor. Described effect stabilises the projections of the angular momentum parallel to the magnetic field and generates the observable magnetic response of the molecule. The corresponding magnetic moment of any *J* level and its projection to the z-axis will determined as:

$$\mu_J = g_J \cdot \mu_B\sqrt{J \cdot (J+1)} \qquad \mu_J^z = -g_J \cdot \mu_B \cdot M_J \tag{1.18}$$

By integrating the free ions into appropriate ligand field, the orbital moment can be supressed or even quenched, especially for the compounds incorporating 3*d* metal ions with high coordination number. In that case, equations (1.12) and (1.13) include additional orbital reduction parameter, σ:

$$\hat{H} = \lambda \cdot (\sigma\hat{L} \cdot \hat{S}) \tag{1.19}$$

$$\hat{H} = \mu_B \cdot B \cdot (\sigma\hat{L} + g_e\hat{S}) \tag{1.20}$$

Thus, in the case of completely quenched orbital moment (σ=0), only spin contribution will affect the magnetic moment of the coordination entity. Moreover, dressing the free metal ion with the ligands imposes the perturbation on the energy of the $^{2S+1}L_J$ multiplets. One of the first attempts of rationalising the magnetic properties and electronic structure of the coordination compounds was the crystal field model, based on the concept of purely electrostatic metal-ligand interaction. However, this qualitative description almost immediately evolved into the ligand field model in which the point charges of the spherical crystal field potential were replaced by the corresponding ligand orbitals and with the

potential expressed through the symmetry of the imposed coordination environment. For instance, incorporation of the 3*d* metal ion such as Fe(II) (*e.g.*) in certain ligand field breaks the degeneracy of the 3*d* orbitals into sublevels whose number and energies are determined by the nature of the ligands (π and σ bonding) and by the symmetry of the coordination environment around the metal ion (coordination number and geometry, Figure 1.1).

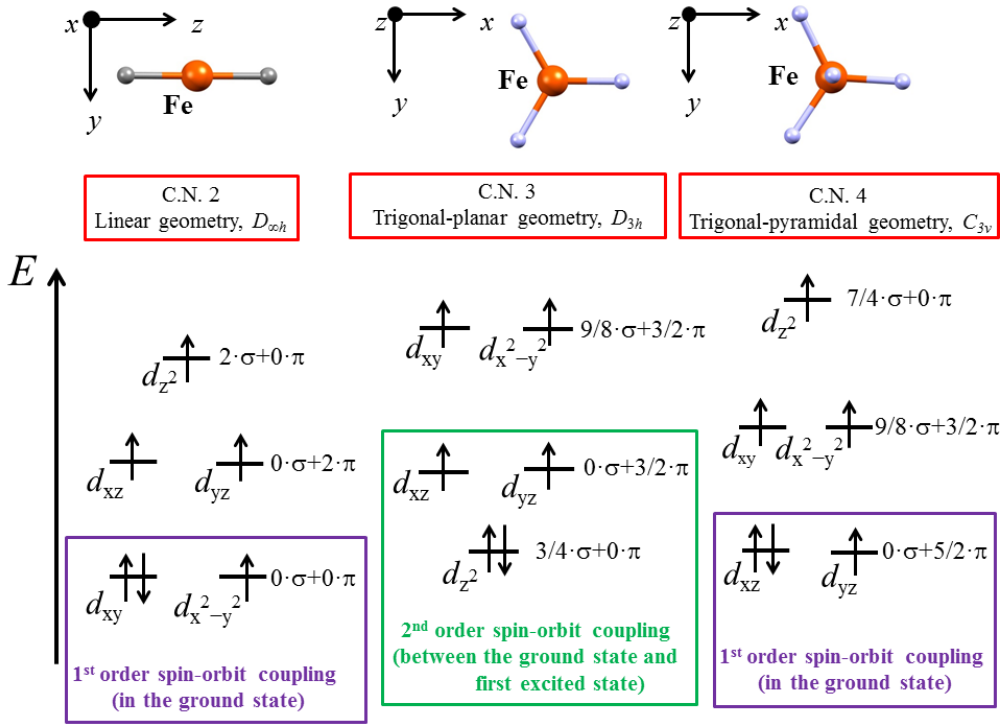

Figure 1.1: Coordination geometries, 3*d* energy levels and the spin-orbit coupling of the low-coordinate Fe(II) molecular magnets.

The imposed potential of the ligand field on the $|JM_J\rangle$ functions is often parametrised through the Stevens operator equivalents:[4, 5]

$$\hat{H} = \sum_{k=2,4,6..}^{\infty} \sum_{q=-k}^{k} B_k^q \langle r^k \rangle \beta_k \hat{O}_k^q \qquad (1.21)$$

In this equation, $B_k^q\langle r^k\rangle$ is the crystal field potential, β_k is the operator parameter while $\hat{B}_k^q$ is the Stevens operator equivalent (*k*-operator rank; *q*-operator order) composed of polynomials of the angular momentum operators. In the latter, only the operators with the even rank *k* (2, 4, 6,…, 2*S*) contribute to the crystal field splitting. Symmetry of the ligand field restricts the non-zero $A_k^q\langle r^k\rangle$ coefficients by transforming the crystal field Hamiltonian into totally symmetric representation of the point group determined by the molecular structure.[6]

As a direct consequence of the spin-orbit coupling in S>1/2 systems, certain molecular structures and related spin distributions result with the loss of degeneracy of the spin microstates even in the absence of magnetic field. This phenomenon, called the zero-field splitting effect (ZFS), generates the anisotropy of a molecular system. The *in-state* orbital angular momentum (orbital momentum generated in the ground state) generates the large ZFS due to the unequal occupation of the levels while the *out-of state* orbital angular momentum (spin-orbit mixing of certain excited states into the ground state) only combined with the structural distortions generates the ZFS (Figure 1.1). Additionally, the ZFS effect in radicals can be induced by direct interaction of the magnetic dipoles of unpaired electrons (spin-dipolar contributions). Hamiltonian describing the ZFS of the certain spin state S can be defined as:

$$\widehat{H} = \hat{S}\boldsymbol{D}\hat{S} \tag{1.22a}$$

or

$$\widehat{H} = D_{xx}\hat{S}_x^2 + D_{yy}\hat{S}_y^2 + D_{zz}\hat{S}_z^2 \tag{1.22b}$$

where $\boldsymbol{D}$ is a traceless, symmetric tensor whose components D_{xx}, D_{yy} and D_{zz} are related with the corresponding spin components operators $\hat{S}_i^2$(i=x,y,z) defining the axial and the rhombic zero-field splitting parameters D and E, respectively:

$$\widehat{H} = D\left[\hat{S}_z^2 - \frac{1}{3}S(S+1)\right] + E(\hat{S}_x^2 - \hat{S}_y^2) \tag{1.23a}$$

$$D = \frac{3\,D_{zz}}{2} \qquad E = \frac{|D_{xx} - D_{yy}|}{2} \tag{1.23b}$$

By convention, axial and rhombic parameters of the anisotropy are limited within the range $|E/D| \leq 1/3$. In perfectly axial symmetry (D_{xx}= D_{yy}), existence of only D parameter simplifies the ZFS spin Hamiltonian to:

$$\widehat{H} = D\hat{S}_z^2 \tag{1.24}$$

Axial anisotropy determines the energies of the M_s levels (E_{Ms}=$D\cdot$ M_s^2) such that the negative axial anisotropy stabilises the highest M_s states while the positive axial anisotropy stabilises the lowest M_s states as the ground ones. In the former case, electronic spin will be preferably oriented parallel to the field (z-axis, easy axis) while in the latter case it will be oriented perpendicularly to the field (easy-plane xy). Rhombic (transverse) anisotropy (E)

causes the mixing of the M_S states (ΔM_S=2) and variation of the characters of the microstates for integer S. In other words, in the presence of only axial anisotropy, any M_S=±S levels are degenerate, while upon appearance of rhombic anisotropy (E) their degeneracy becomes broken for integer S or remains intact for half-integer S (Kramers doublets). Described ZFS effects for the S=2 spin state (high-spin Fe(II) ion for example) are shown in Figure 1.2.

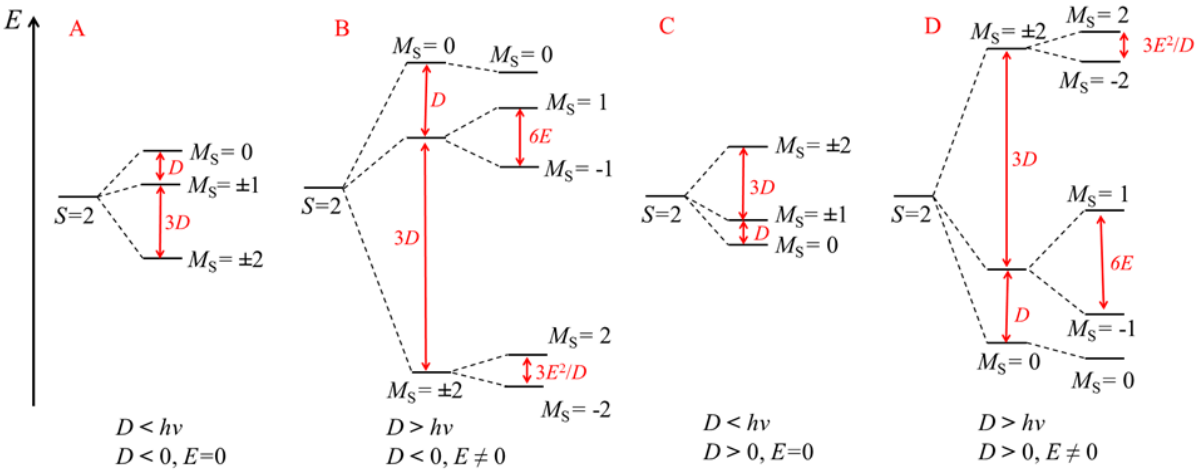

Figure 1.2: Zero-field splitting for the S=2 spin state: A (small) and B (large) negative axial anisotropy; C (small) and D (large) positive axial anisotropy.

The ZFS parameters can be fully determined (sign and magnitude) from the anisotropy of the g factor (EPR spectroscopy; λ=spin-orbit coupling constant):

$$D = \frac{\lambda}{2}\left[g_z - \frac{g_x+g_y}{2}\right] \qquad E = \frac{\lambda}{4}(g_x - g_y) \tag{1.25}$$

where

$$g^2 = \frac{g_x^2+g_y^2+g_z^2}{3} \tag{1.26}$$

As mention earlier, orbital momentum of the metal ions within the coordination compounds can be significantly quenched by the applied ligand field, thus, ZFS parameters should exhibit the similar dependence. Moreover, axial and rhombic anisotropy can be directly estimated from the second-order Stevens operators:

$$D = 3B_2^0\beta_2 \qquad E = B_2^2\beta_2 \tag{1.27}$$

Finally, multinuclear coordination compounds usually exhibit interactions between the incorporated metal centres which impose additional perturbation on their magnetic

moments. In the simplest case of two neighbouring spin carriers (S_1 and S_2), the sign and the strength of their interaction can be quantified by the isotropic exchange coupling constant (J) from the phenomenological Heisenberg-Dirac-Van Vleck Hamiltonian:

$$\hat{H} = -2J\hat{S}_1\hat{S}_2 \tag{1.28}$$

The magnitude and the sign of exchange constant are determined by the overall sum of ferromagnetic and antiferromagnetic interactions between the individual spin carriers. Thus, for $J > 0$, prevailing ferromagnetic interactions increase the individual magnetic moments of spin carriers, while for $J< 0$, antiferromagnetic interactions dominantly anneal those moments, yielding the ground state S of the coupled dimer defined as $S=S_1+S_2$ or $S=|S_1-S_2|$, respectively. In heterometallic compounds where $S_1\neq S_2$, antiferromagnetic interaction resulting with the non-zero spin S is often characterised as ferrimagnetic. Independently of the dominant nature of the coupling, the available spin states of any strongly coupled dimer ($|J|>>0$) belong to the range of $|S_1-S_2|\leq S \leq S_1+S_2$ with the energy of S being determined by the magnitude of J:

$$E(\mathrm{S}) = J \cdot [S \cdot (S+1)] \tag{1.29}$$

Consequently, energy separation between the S levels will be also determined by the magnitude of J, while its population will be limited by the available thermal energy k_BT. Hence, temperature-dependent study of the molar magnetic susceptibility can easily provide insights into the nature and the magnitude of magnetic interactions within coordination compounds. Same is valid for the weak coupling ($|J|\neq 0$), which only implies additional component of the overall spin Hamiltonian of the system, where single-ion contributions such as ZFS, spin-orbit coupling, *etc.* should be also taken into account.

Most common ways of establishing the interaction between the metal centres are the dipolar and the exchange interaction. Long range interactions between the dipolar magnetic moments of the spin carriers are weaker ($J\sim\frac{1}{r^3}$; r-distance between the metals), providing the accountable contributions in the multinuclear 4*f*-systems or in systems with the exchange-correlated spin domains. On the other hand, stronger exchange interactions between the singly occupied orbitals (magnetic orbitals) of closely positioned spin carriers can be established by the direct overlap (*direct exchange*) or by the ligand-assisted overlap

(*superexchange).* In the latter case, spin of the open-shell metal centres polarises the paired electrons in the molecular orbitals of the ligands, allowing them to act as the mediators of the interactions. Related with the superexchange, mixed-valent systems often exhibit the double-exchange interaction based on the electron delocalization between the bridged spin carriers (dominantly ferromagnetic interaction). Regardless of the interaction pathway, overlap between the magnetic orbitals (their type) is the key factor which determines the nature of the coupling. Thus, systems with maximised spatial overlap between the orbitals of their spin carriers will exhibit antiferromagnetic interaction. Likewise, systems with the total zero overlap resulted from the non-zero positive and negative regions will exhibit the ferromagnetic coupling, while the total zero overlap with absence of any non-zero contribution will characterise the non-interacting spin carriers. Interestingly, molecular systems meet the conditions for the antiferromagnetic interactions much more frequently than for the ferromagnetic. The latter can be strictly directed in the heterometallic systems by employing the Kahn's principle of orthogonality between the magnetic orbitals of spin carriers (Figure 1.3A).[7-9] Thus, by combining the metal centres with the magnetic orbitals of π-symmetry (d_{xy}, d_{xz} or d_{yz}) and σ-symmetry ($d_{x^2-y^2}$ or d_{z^2}), ferromagnetic interaction arises due to the fact that their overlap integral sums to zero (any antiferromagnetic contribution vanishes). Similarly, ferromagnetic interaction in the homometallic compounds can be arranged through the prudent design of the mediator ligands, capable of either imposing topologically the zero overlap between the symmetry-related magnetic orbitals (orthogonality between the coordination sites, Figure 1.3B)[10, 11] or participating in the spin polarisation coupling (*m*-phenylene linkers between the coordination sites, Figure 1.3C).[12-18] Alternatively, ferrimagnetic interactions in heterometallic systems can also generate the non-zero magnetic moment of the ground state.

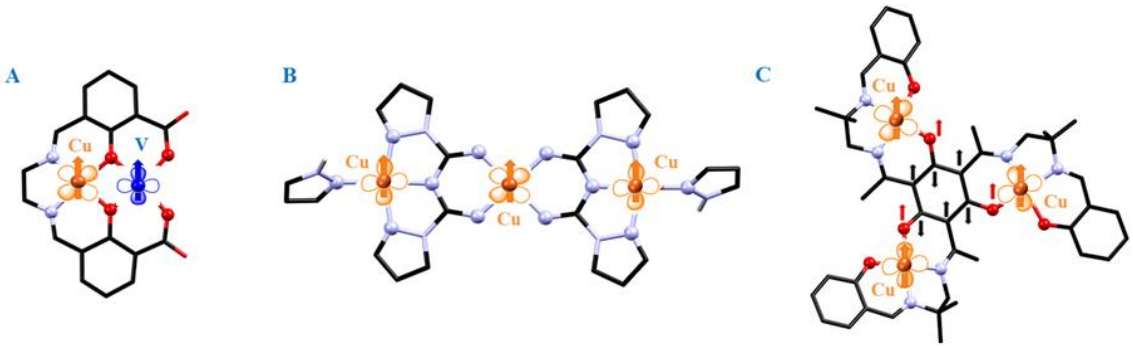

Figure 1.3: Designed ferromagnetic interactions in molecular magnets. A) Strict orthogonality between the magnetic orbitals in Kahn's heterometallic dimer [$CuVO(fsa)_2en(CH_3OH)$], Refcode: BIGFAY.[8, 9] B) Accidental, topological orthogonality between the symmetry-related magnetic orbitals in homometallic [$Cu_3(dcadpz)_2(pz)_2(ClO_4)_2$]$(ClO_4)_2$ (Refcode: KACMEH).[11] C) Ferromagnetic coupling in homometallic [(talen)Cu_3]cluster induced by spin polarization of 1,3,5-functionalised aromatic core[17] (Refcode: YADNOH).

1.3. Physics of the single molecule (ion) magnets

Single-molecule magnets (SMMs) are the metallo-organic compounds which exhibit the slow relaxation of the magnetisation and hysteresis of purely molecular origin.[19, 20] The latter establishes the major difference between the SMMs and the classical, bulk magnets (magnetic nanoparticles): although the exhibited magnetic phenomena are essentially the same, in the case of the SMMs those features are entirely molecular characteristic and do not require existence of any intermolecular interaction or long-range ordering which in turn are crucial for the bulk magnets. Hence, molecular nanomagnets can be dissolved or incorporated to surfaces and still retain their properties. Furthermore, benefiting features of the molecular materials are the uniform size, chemical flexibility and high purity.

The slow relaxation of magnetisation mostly originates from the non-zero spin ground state (S, large number of unpaired electrons) combined with the presence of negative Ising type of magnetic anisotropy (easy axis, D<0). The ZFS effects on the spin state S can be represented with a potential energy double well holding degenerate and equally occupied M_S and $-M_S$ levels in absence of any magnetic field (D<0, E=0; Figure 1.4A). Applying the external magnetic field, the M_S levels containing the spins aligned with the field will fall in energy while the remaining levels will rise (Zeeman effect, $\Delta E = M_S \cdot g \cdot H_Z \cdot \mu_B$, Figure 1.4B). As a

consequence, the spin population will fall in one side of the double well (energy level $M_S = -S$, Figure 1.3B) meaning that the system becomes magnetized. If the external magnetic field is then switched off, the energy levels recover its initial equilibrium (Figure 1.4C), by reducing the population of spins from the level $M_S = -S$ to the level $M_S = S$. This process of magnetic relaxation can be achieved in two possible ways: as a thermal process (Figure 1.4C) or as a quantum tunnelling process in the ground or excited state (Figure 1.4D). The detectable slow relaxation of the magnetization takes place only when both processes (thermal and quantum tunneling) are slow enough to generate the measurable magnetic response. Thermal relaxation process (known also as a phonon-assisted Orbach relaxation) can be understood as a spin rotation: spin is rotating from $M_S = -S$ through the position where S is perpendicular to the field direction ($M_S = 0$) to the $M_S = S$. However, this process requires the absorption of energy and generates the energy barrier towards thermal inversion of the magnetic moment which in total amounts to the gap between $M_S = -S$ and $M_S = 0$ levels (the height between two compartments of the double well). The effective barrier to the relaxation of magnetisation, U_{eff}, can be defined as the energy needed to transform the SMM into a simple paramagnet and is directly proportional to the spin state and the axial anisotropy of the system:

$$U_{eff} = S^2|D| \qquad U_{eff} = (S^2 - 1/4)|D| \qquad (1.30)$$

Integer spin	Non-integer spin

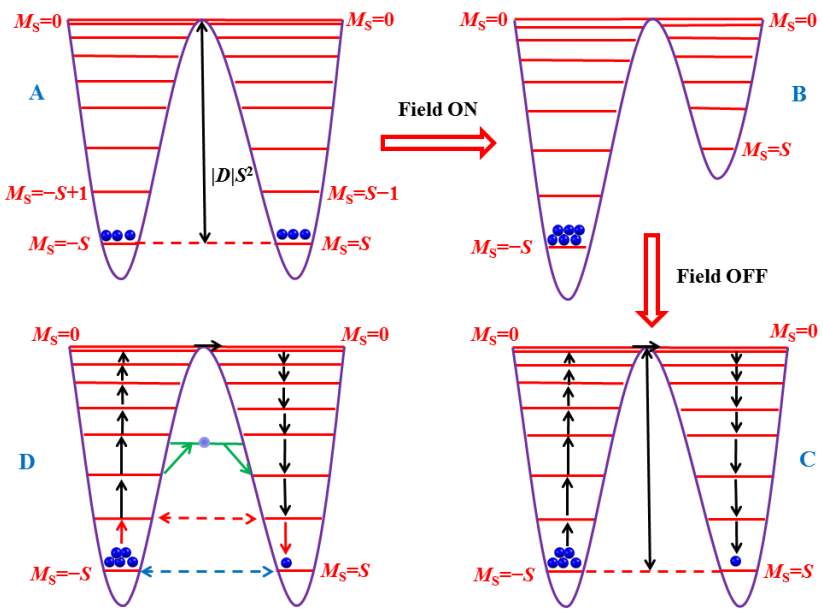

Figure 1.4: Schematic diagram representing the processes of magnetization and magnetic relaxation in SMMs. A) Zero-field splitting effects (ZFS) on a spin state *S* with two equally populated wells. B) Zeeman effect on the magnetization favors the population of the left well; C) Ideal Orbach (thermal) relaxation of the magnetization over the anisotropy barrier after removing the external magnetic field (black arrows); D) Different relaxation pathways which accelerate the spin reversal. Quantum tunneling through the anisotropy barrier in the ground state (blue arrow) or between thermally activated degenerated states (thermally assisted tunneling, red arrows). Two-phonon processes over the relaxation barrier: Orbach relaxation (black arrows) through real M_S states and Raman process (green arrows) through virtual excited state. Figure inspired by Konar *et al.*[21]

Lattice vibrations liberate the thermal energy packages know as phonons which interact with spin inducing only ΔM_S=1 transition between the microstates (Orbach process): initial absorption of the phonon to the excited state is followed by the relaxation with the phonon emission (black arrows Figure 1.4C). Thus, the relaxation process has to go slowly over the thermal barrier, as in classical physics. However, the laws of quantum mechanics allow the existence of alternative quantum tunnelling pathway, which accelerates the spin reversal by direct relaxation from $-M_S$ level to M_S level through the energy barrier. This process can occur directly between the ground ± M_S levels (quantum tunnelling in the ground state, Figure 1.4D) or it can be characterised as thermally assisted tunnelling (electron absorbs energy package and then tunnels through the barrier, Figure 1.4D). The origin of the tunneling relaxation process is the non-zero transverse/rhombic anisotropy (*E*) which arises from the structural distortions and lower symmetry of the system and mixes the M_S levels.

In the zero magnetic field, in the absence of transverse anisotropy, the degenerate $\pm M_S$ levels represent the energy eigenstates of the system which are not allowed to mix, thus, quantum tunneling is forbidden. Upon appearance of the transverse anisotropy, the M_S levels are no longer the energy eigenstates: the eigenstates are now the superpositions of the M_S levels from the left and the right side of the well, meaning that the quantum tunneling becomes allowed. At higher energy, the second order transverse anisotropy mixes the M_S levels with $\Delta M_S=2$ while the fourth order transverse anisotropy mixes the M_S levels with $\Delta M_S=4$. Apart from described processes, interactions between spins and lattice vibrations enable additional relaxation pathways which accelerate the spin reversal. The Raman relaxation mechanism is very similar to the thermal relaxation (two phonon processes), differing only in the nature of the excited state which now includes the virtual state (Figure 1.4D).[20] On the other hand, the relaxation in the lowest temperature region is often governed by the direct mechanism which reorients the spin between the $-M_S$ and $+M_S$ levels with an emission of one lattice phonon.

The first evidence for slow magnetic relaxation in SMMs usually comes from alternate-current (ac) susceptibility measurements at low temperatures, although some other techniques such as Mössbauer spectroscopy, inelastic neutron scattering, *etc.* can be employed. The ac measurements investigate the dynamic susceptibility of a sample over a range of temperatures by applying a small magnetic field (usually 1-5 Oe) that oscillates at frequencies between 1 and 10000 Hz. Additionally, zero or non-zero direct-current field (dc field) can be applied. Since any molecule exhibiting the SMM behaviour has to overcome the relaxation barrier and possess the preferable alignment with the field due to anisotropy, this experimental setup results in the delayed (relaxation time τ) and detectable dynamic susceptibility signals. The dynamic susceptibility is a complex quantity, dependent of the angular frequency (ω) of the oscillating ac field, which includes two components: real, χ', in-phase with the AC oscillating field (dispersion) and imaginary, χ'', out-of-phase with the oscillating field (absorption):

$$\chi(\omega) = \chi'(\omega) - i\chi''(\omega) \tag{1.31}$$

The appearance of the out-of-phase maxima that are frequency-dependent is the most reliable signature of the SMM behaviour. Dynamics of the magnetization relaxation can be

investigated using the Cole-Cole (Argand) plots in which χ'' is plotted against χ' for various frequencies at a constant temperature. Relaxation time and the width of its distribution can be quantified by fitting the χ'_M and χ''_M data to the generalised Debye model[22]:

$$\chi_{ac}(\omega) = \chi_S + \frac{\chi_T - \chi_S}{1+(i\omega\tau)^{(1-\alpha)}} \quad (1.32)$$

$$\chi'(\omega) = \chi_S + (\chi_T - \chi_S)\frac{1+(\omega\tau)^{1-\alpha}\sin\left(\frac{\pi\alpha}{2}\right)}{1+2(\omega\tau)^{1-\alpha}\sin\left(\frac{\pi\alpha}{2}\right)+(\omega\tau)^{2-2\alpha}} \quad (1.33)$$

$$\chi''(\omega) = (\chi_T - \chi_S)\frac{\left((\omega\tau)^{1-\alpha}\cos\left(\frac{\pi\alpha}{2}\right)\right)}{1+2(\omega\tau)^{1-\alpha}\sin\left(\frac{\pi\alpha}{2}\right)+(\omega\tau)^{2-2\alpha}} \quad (1.34)$$

In this equation, α is the Cole-Cole parameter (0< α <1), τ is the Cole-Cole relaxation time, χ_T and χ_S are the isothermal and the adiabatic susceptibility, respectively, while ω is the angular frequency (ω=2πν). χ_T is the differential susceptibility in the limit of the lowest field frequencies for which thermal equilibrium between the spin and the lattice is obtained. Adiabatic susceptibility, χ_S, is revealed for the highest field frequencies for which the oscillations of the magnetic field are faster than the time constant τ (the spin is uncoupled to the lattice). The relaxation time τ is defined by the angular frequency (ω) at which the Cole-Cole plot reaches the maximum ($\tau = \omega^{-1}$), while the parameter α directly describes the width of distribution of the relaxation times where 0 value corresponds to the relaxation with one time constant while larger α values correspond to the flatter distribution of the time constants around τ. Debye theory predicts that if whole magnetization relaxes with a single characteristic time, the Cole-Cole plot describes a regular semicircle positioned on the χ' axis. More complex behaviour reflected as the existence of more semicircles or partially merged semicircles in the Cole-Cole plot indicates the existence of two or more different processes of the relaxation. The relaxation of magnetisation of a SMM follows the Arrhenius law for a thermally activated process to overcome the energy barrier: $\tau = \tau_0 \cdot \exp(U_{eff}/k_B T)$. Hence, both the energy barrier (U_{eff}/k_B) and the specific relaxation time (τ_0) can be determined from a simple plot of ln(τ) versus (1/T). Usually, the linearity between ln(τ) and (1/T) can be observed at the highest temperatures indicating the dominance of the thermal relaxation process (Orbach process). On the other hand, temperature-independent region in this plot is characteristic signature of the relaxation involving quantum tunneling mechanism, while the plot curvature indicates the coexistence of different mechanisms.

Another evidence of the magnetic bistability of the SMMs is the isothermal magnetisation versus field hysteresis loop below the characteristic blocking temperature (T_B), which often reveals the characteristic steps indicative of the quantum tunnelling of magnetization. The blocking temperature of the hysteresis loop defines the limit below which magnetic information can be maintained for a certain period of time, while the coercive field of the loop corresponds to the magnetic field required to reduce the remnant magnetization. Hysteresis loops can be measured in the SQUID magnetometer down to 1.8 K, or using micro-SQUID or micro-Hall probe with suitable sweep rates for the field in the mK range. Blocking temperatures and anisotropy barriers can be obtained from magnetisation decay measurements, also performed using a micro-SQUID. Another useful technique is element-sensitive X-ray magnetic circular dichroism (XMCD) which can be used to probe the magnetism of each metal in the heterometallic complexes or to probe the magnetic properties of the SMMs deposited to the surface.

As indicated earlier, negative axial anisotropy was postulated as a necessary feature of any molecular spin system to exhibit the SMM properties. However, over the last few years this classic definition has slightly altered since the field-induced slow relaxation of the magnetization was observed for the systems with either positive axial anisotropy (mostly Co(II) compounds) or no anisotropy at all (pure S=1/2 ground state systems). First evidence of this exceptional behaviour was reported by Long *et al.* for the pseudotetrahedral Co(II) compound [(3G)CoCl](CF_3SO_3) (3G=1,1,1-tris-[2*N*-(1,1,3,3-tetramethylguanidino)methyl]ethane) possessing the easy plane anisotropy (D = 12.7 cm^{-1}) as determined from the high-field EPR studies.[23] Spin-lattice relaxation between the M_S=±1/2 states was observed under the applied dc field of 1500 Oe with a barrier of 24 cm^{-1}. Offered rationalisation of this phenomena was that phonon bottleneck effect slows down the direct process between the M_S=±1/2 states, while the non-zero transverse anisotropy activates the Orbach process through the excited M_S=±3/2 Kramers doublet, by mixing the states with the opposite sign. Similar observations were later established for several other Co(II) systems in different coordination geometries ranging from the tetrahedral to the distorted octahedral and exhibiting the relaxation barriers up to 59.6 cm^{-1}.[24-28] Among the alternative explanations, transverse anisotropy controlled barrier of Orbach process and Raman relaxation were considered.[25, 28] However, the most elaborated

study, aiming at origin of this phenomena, was carried out by Ruiz and Luis on the model octahedral Co(II) compound $Co(acac)_2(H_2O)_2$, an effective S=1/2 system below 30 K due to the large axial anisotropy D≈57 cm^{-1}.[29] The dynamic ac susceptibility under an applied field revealed the spin lattice relaxation rate which could be fitted considering the contributions of direct relaxation mechanism (below 3K) and Raman process. However, higher temperature range was also adjustable to the Arrhenius plot for the meaningless thermally activated Orbach process with derived barriers of 14-17 cm^{-1}, substantially reduced from the expected order of D. Moreover, since the Van Vleck cancellation mechanism forbids the direct relaxation mechanism between the M_S=±1/2 states in the zero-field (Figure 1.5A)[30, 31] and the energy barrier for the Orbach process is hardly reachable by phonons at the lowest temperatures, Raman relaxation mechanism seemed as the only viable option in agreement with the experimental ac data. However, detection of the direct processes below 3 K inspired the evolution of a model based on the hyperfine interactions (electronuclear spin entanglement, Figure 1.5B). Thus, coupling between the Co nuclear spin I=7/2 and the electronic spin S=1/2 converts the M_S=±1/2 Kramers doublet into the manifold of 16 electronuclear spin states which provide a feasible relaxation pathway ($\Delta m_S \neq 0$, $\Delta m_I = 0$) after being submitted to Zeeman splitting (dc field, Figure 1.5C). Furthermore, interactions between the nuclear spin and the lattice weaken the selection rule $\Delta m_I = 0$, providing the pathway for all the possible transitions between the electronuclear states ($\Delta m_S \neq 0$, $\Delta m_I \neq 0$, Figure 1.5D). Recently afterwards, similar relaxation dynamics was reported by Sessoli *et al*. for the mononuclear vanadyl compound $VO(dpm)_2$ (pure S=1/2 system; I(V)=7/2), confirming the validity of the given model.[32]

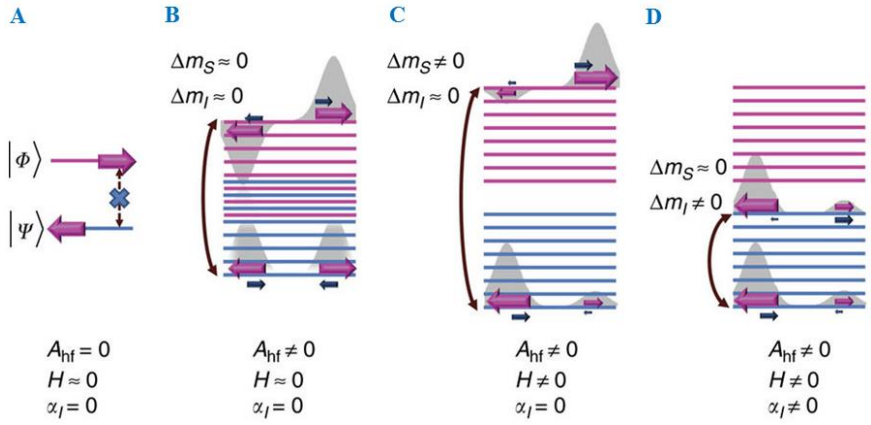

Figure 1.5: A) Symmetry forbidden spin reversal within the M_s=±1/2 Kramers doublet due to the Van Vleck cancellation mechanism.[30] B) Electronuclear spin entanglement ($A_{hf} \neq 0$) between the Co nuclei

(I=7/2) and M_s=±1/2 Kramers doublet. C) Zeeman splitting (H≠0) of the two electronuclear spin states manifolds triggers the spin reversal between the states with the same m_I. D) Interactions between the nuclear spin and phonons (α_I≠0) allow the transitions between all electronuclear spin states (Δm_S≠0, Δm_I≠0).[29]

1.4. Chemistry behind the single-molecule magnets evolution

The SMM behaviour was reported for the first time in the early 1990s for the mixed-valent Mn(III/IV) compound $[Mn_{12}O_{12}(O_2CMe)_{16}(H_2O)_4]$ (Mn_{12}) in which oxide and acetate ligands promote the overall ferromagnetic coupling between the manganese ions.[33, 34] The S=10 ground state of the cluster, combined with the small axial anisotropy (D = −0.5 cm^{-1}), defines the relaxation energy barrier U_{eff} = 49.0 cm^{-1}. Moreover, magnetic bistability of the system is evidenced in the appearance of the magnetization hysteresis loop below a blocking temperature T_B=3.5 K.[35] Since this revolutionary discovery, considerable efforts were devoted to development of many different classes of SMMs with an intention to enhance both the T_B and U_{eff}. The first period of the SMM evolution ascended as the legacy of the Mn_{12}, involving mostly serendipitous preparation of polymetallic 3*d* clusters with the predominant ferrimagnetic or ferromagnetic interactions (high spin ground states, S>>0). In the first review (2006), Aromí and Brechin reported 91 SMMs of which majority were manganese clusters (mainly Mn(III) and mixed-valent systems) with a small contributions of iron [9 Fe(III) + 2 Fe(II)], nickel [8 SMMs], cobalt [2 SMMs] and vanadium [2 V(III)] SMMs.[36] Besides the homometallic compounds, 13 heterometallic 3*d* and 3 heterometallic 3*d*-4*f* systems were reported. One of the few significant achievements from those early days of molecular magnetism was the preparation of the $[Mn^{III}_6]$ cluster (S=12 ground state; D=−0.43 cm^{-1}) which exhibited the record energy barrier at the time (U_{eff}= 60.05 cm^{-1}; T_B=4.5 K).[37] Additionally, Christou *et al.* reported the supramolecular dimer of mixed-valent $[Mn_4]$ nanomagnets which evidenced for the first time the property of quantum entanglement (superposition of the spin wave functions) and promoted the SMM molecules as a potential molecular hardware for the quantum computing.[38, 39] Recently afterwards, the same group published the $[Mn_{84}]$ torus molecule (S=6, T_B=1.5 K), the largest molecular nanomagnet up to date with a diameter of 4.2 nm which is comparable in size with magnetic nanoparticles and defines the interface between the quantum and classical

physics.[40] However, despite of many chemically impressive systems, in more than fifteen years of extensive research no significant improvement was found in comparison with the firstly discovered Mn_{12} SMM. Likewise, the fact that clusters such as $[Mn_{17}]$[41] and $[Mn_{19}]$[42] with the highest recorded spin ground states (S=37; D=−0.009 cm^{-1} and S=83/2, respectively) exhibit very fast or no observable relaxation at all was very indicative that the SMM design strategy solely based on increasing the spin state was not successful. Moreover, in a theoretical follow up of the experimental findings, Waldmann, Ruiz and Neese demonstrated that there is an inherent limitation in this approach since the large spin ground states correlate with the smaller anisotropy ($|D|$~$1/S^2$).[43-45] Therefore, rational design of molecular magnets by increasing the total spin ground state is not as effective as expected since the relaxation barrier U_{eff} doesn't improve by the power factor ~ S^2 (equation 1.29), but more probably by S^0. Waldmann's mathematical rationale of this conclusion emphasizes that overall zero-field tensor D of the cluster with N spin carriers is limited by the spin-dependent projection coefficients (d_i) of the local single ion tensors D_i[45]

$$D = \sum_{i=1}^{N} d_i \, D_i \tag{1.35}$$

$$d_i \sim \frac{S_i \cdot (2S_i - 1)}{S \cdot (2S - 1)} \tag{1.36}$$

Consequently, focus of investigation shifted to mononuclear 3d compounds, especially those integrating low-coordinate Fe(I)/(II) and Co(II) ions, which embody moderately high spin state (S=3/2 or S=2) with a large anisotropy originating from partially or completely unquenched orbital momentum (Figure 1.2).[46, 47] Earliest reports by Reiff *et al.* revealed the completely unquenched orbital momentum of the free Fe(II) ion for the linear iron(II) compounds $Fe[C(SiMe_3)_3]_2$ and $Fe[N(t\text{-}Bu)_2]_2$ and partially quenched momentum upon bending of linear geometry in case of $Fe\{N(H)Ar\}_2$ compound ($Ar=C_6H_3$-2,6-(C_6H_2-2,4,6-Me_3)$_2$.[48-50] Recently after these findings, Long *et al.* reported the trigonal-pyramidal iron(II) compound $K[(tpa^{Mes})Fe]$ as a first example of a mononuclear transition metal-based single molecule magnet.[51] Variable-field magnetization studies revealed the large axial anisotropy D= −39.6 cm^{-1} originating from the first-order orbital momentum, as well as the small contribution of the transverse anisotropy E= −0.4 cm^{-1}, related with the deviations from the ideal C_{3v} symmetry. Set of frequency dependent out-of-phase χ_m'' peaks was observed under an applied field of 1500 Oe. Posteriorly, slow relaxation of the magnetization was confirmed

for the extended families of trigonal bipyramidal and linear Fe(II) compounds.[52, 53] Especially impressive was the great improvement of the SMM performance when Fe(II) compound $Fe[C(SiMe_3)_3]_2$ was reduced to its Fe(I) analogue $[K(crypt\text{-}222)][Fe\{C(SiMe_3)_3\}_2]$.[53, 54] Although both systems present the metal centre in a perfectly linear coordination environment (C–Fe–C angle is 180°-Fe(II) and 179.2°-Fe(I)), the Fe(II) complex exhibits the SMM behaviour only under an applied dc magnetic field of 500 Oe (U_{eff} =146 cm^{-1}) while the Fe(I) compound behaves as a SMM under zero dc field with an enhanced barrier U_{eff} =226 cm^{-1} and magnetic blocking (hysteresis) below 4.5 K (Figure 1.9). Root of this improvement can be found in the different electronic structure of the constituent ions, where simple one-electron reduction alters the non-Kramers *S*=2 to Kramers *S*=3/2 ion and, consequently, reduces the effects of the quantum tunneling of magnetization.[55] The relevance of this simple iron(I) system goes beyond the record-breaking SMM since its magnetic behaviour clearly evidences how simple 3*d*-based SMM can compete in performance with the 4*f*-systems.

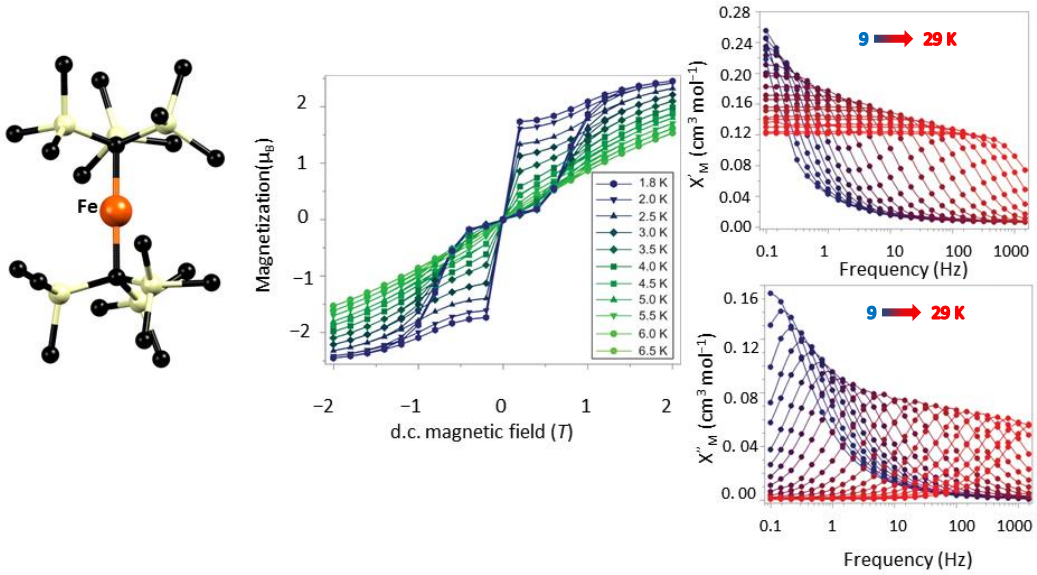

Figure 1.9: Crystal structure and slow relaxation of magnetization of two coordinate mononuclear Fe(I) SMM $[K(crypt\text{-}222)][Fe\{C(SiMe_3)_2\}_2]$ (U_{eff}=226 cm^{-1}: T_B=4.5 K: sweep rate: 5 mT/s).[54]

Further interest for this class of SMMs was encouraged by the predictive qualitative model of the magnetic anisotropy by Ruiz *et al.*, who related the sign and magnitude of *D* with the electronic structure of 3*d* metals and their coordination geometry.[56] Broadening of scope to

other 3*d* ions such as axially elongated Mn(III), Ni(I)/(II) and Cr(II) or 5*d* Rh(IV) centre led to discovery of over one hundred mononuclear single-ion magnets in less than a decade.[46, 47] The most impressive relaxation dynamics was reported by Gao *et al*. for two-coordinate Co(II) imido compound [(IPr)CoNdmp] (dmp = 2,6-dimesitylphenyl) which in zero dc field exhibits the record relaxation barrier for any transition metal based SMM (U_{eff}=413 cm^{-1}) and hysteresis loops below the T_B=9.5 K.[57] Apart from the linear coordination geometry which preserves the first-order orbital momentum, presence of the covalently bound $[Co{=}N]^+$ core contributes to the inherently large magnetic anisotropy of the ground $|M_J = \pm 7/2\rangle$ Kramers doublet. Finally, photoactive mononuclear iron(II) systems exhibiting the spin-crossover behaviour are especially interesting class of molecular nanomagnets, possessing the magnetic tristability related with the field-induced slow relaxation of magnetization in photoinduced high-spin state (LIESST-SMM). Clérac *et al*. reported this behaviour for octahedral $[Fe(1\text{-propyltetrazole})_6](BF_4)_2$ and trigonal-pyramidal $PhB(MesIm)_3Fe{-}N{=}PPh_3$ compounds (U_{eff}=15 cm^{-1} and 15.3 cm^{-1}, respectively), evidencing the potential of such systems for ternary information storage.[58, 59]

Long before the discovery of mononuclear 3*d* SMMs, Ishikawa *et al*. reported the Tb^{3+} and Dy^{3+} double-deckers with the phtalocyanine ligands as the first two SMMs holding only one paramagnetic centre and first two lanthanide-based SMMs,[60] with the record-breaking relaxation barrier of 230 cm^{-1} (Tb^{3+}; T_B=1.7 K).[60, 61] Ishikawa's revolutionary discovery turned the attention of researchers towards the coordination compounds containing 4*f*-ions, igniting a new strategy in the SMM design aiming at increasing the anisotropy (*D*) in 4f *single-ion magnets* (SIMs). Initially, extensive phtalocyanine family of compounds was evolved, exploiting the ligand-field strength as a tailoring tool for M_J splitting and magnetization relaxation barrier (up to 652 cm^{-1}).[62, 63] However, blocking temperatures of those system remained trapped within few kelvin degrees (T_B≈2 K), highlighting the problematics of effective spin reversal via quantum tunnelling between the ground or first-excited Kramers doublet.[64, 65] In attempt to extinguish this phenomena, strategies aiming at exchange-coupled polynuclear systems were followed, incorporating either 3*d* metals (hybrid *d-f* systems)[66] or organic radicals as ligands (hybrid *p-f* systems)[67]. Hybrid *d-f* systems evolved as an ideal combination of large single-ion anisotropies (*f*-centres) and significant magnetic interactions promoted by the 3*d* ions. Despite the fact that hybrid *d-f* systems

clusters were known since the earliest days of the molecular magnetism, studies of the magnetization dynamics remained unreported until 2004, when ferromagnetically coupled $[Cu\text{-}Ln]_2$ squares (Ln=Tb, U_{eff}=14.6 cm^{-1}; Dy) and mixed-valent $[Dy_6Mn^{III}_4Mn^{IV}_2]$ cluster were published.[68, 69] Posterior research was chiefly based on the serendipitous self-assembly of structurally versatile complexes incorporating anisotropic 3*d* ions such as Mn(III), Co(II) and Ni(II) together with 4*f*-ions Dy^{3+} and Tb^{3+} as the most common building blocks.[66] Initially, evolution of the heterometallic *d-f* systems continued with exploitation of the mixed valent manganese(III/IV) systems. Among the most exciting results, one should emphasize the $[Mn^{IV}_3Mn^{III}_{18}Ln]$ (Ln-Dy, Gd) complexes, reported by Christou *et al.* in 2011.[70] The unique structure of these clusters involves the central $[Mn^{IV}_3LnO_4]$ cubane decorated through oxide bridges with the dissimilar Mn^{III}_7 and Mn^{III}_8 loops. The SMM properties were exhibited by both derivatives (U_{eff} =19.2 (Gd) and 51.4 cm^{-1} (Dy)), while magnetic blocking was only observable for the Dy analogue below 3 K. In the same year, Dehnen *et al.* reported two self-assembled $[Ln_2Mn^{III}_6]$ (Ln-Tb^{3+}, La^{3+}) clusters with the wheel topology of the peripheral, axially elongated, manganese(III) ions which surround the Ln^{3+} core.[71] Slow relaxation of the magnetization was observed for both compounds in zero dc field, with the energy barriers in thermally activated regime of 22.8 cm^{-1} (Ln=La^{3+}) and 71.6 cm^{-1} (Ln=Tb^{3+}). Slower relaxation of terbium derivative resulted from the simultaneous increment of the magnetic anisotropy and the spin state of the cluster, as witnessed from the dc studies where dominant ferromagnetic interactions between the metal centres were established. Additionally, magnetic bistability of the $[Tb_2Mn^{III}_6]$ cluster was evidenced in appearance of the field-dependent magnetization hysteresis loops up to 4 K. However, the highest relaxation barriers for this class of SMMs are usually found within the family of $[Co^{III}_2Dy_2]$ compounds with the defective dicubane (butterfly) topology. Rentschler *et al*. reported the existence of two thermally activated magnetization relaxation pathways for $[Co_2Dy_2(OMe)_2(teaH)_2(piv)_6]$ complex with the corresponding barriers U_{eff} =35 cm^{-1} (4.5-7.5 K) and U_{eff} =88 cm^{-1} (7.5 K-9.5 K).[72] Briefly after, Murray *et al.* reported akin family of compounds for which relaxation dynamics was subtly tuned by changes in the coordination sphere around the antiferromagnetically coupled Dy^{3+} sites (55 cm^{-1}< U_{eff} < 80 cm^{-1}).[73] Systematic magneto-structural correlations of the same group extracted several synthetic strategies for increasing the relaxation barrier and for quenching the quantum tunneling of the magnetization. The latter was effectively demonstrated on structurally related systems

when diamagnetic Co^{III} ions were replaced by the paramagnetic Cr^{III} ions (S=3/2), which provided the strong antiferromagnetic interactions within the (3*d*-4*f*)$_2$ core. Consequently, ac studies revealed the anisotropy barriers up to 55 cm^{-1}, accompanied with detectable magnetization versus field hysteresis loops below T_B=3.5 K.[74-78] Surprisingly, in majority of studied systems, weak exchange interactions between the paramagnetic 3*d* and 4*f* metals (several cm^{-1}) usually reduce the SMM performance through additional magnetization relaxation pathways which diminish the U_{eff}.[66, 79] Alternatively, relaxation barrier of the [$Co^{III}_2Dy_2$] compounds was successfully enhanced by introducing the electron-withdrawing substituents on the carboxylate ligands bonded to Dy^{3+} sites (76.9 cm^{-1}< U_{eff} < 95.6 cm^{-1}), while the theoretical calculations emphasized the importance of the diamagnetic 3*d* and 4*s* ions in supressing the quantum tunnelling of the magnetization.[76, 80] Such combined studies are of vital importance for further improvement of the prolific family of 3*d*-4*f* SMMs, which at the moment rise moderately above the performance of 3*d* clusters. More promising results come from few known examples of 3*d*-5*f* SMMs, starting from the beautiful $Mn^{II}_6(UO_2)_{12}$ wheel reported by Mazzanti *et al.* in 2012. Mentioned compound was assembled by the cation-cation interactions between the uranyl 5*f*^{1} $[U^VO_2]^+$ moieties from the [UO_2(salen)(py)][Cp*$_2$Co] metalloligand and Mn(II) ions in pyridine. Magnetic bistability of the system was evidenced by the staircase magnetization versus field hysteresis loops (T_B=4K) which showed the characteristic quantum tunneling steps below 2.5 K. Additionally, ac studies revealed the sets of frequency dependent χ' and χ'' curves whose relaxation times could be fitted to the Arrhenius law, giving the relaxation barrier U_{eff}=98.7 cm^{-1}. Same group extended their work to other uranyl-based systems, including the discrete M^{II}–O=U=O–M^{II} compounds (M=Mn^{II}, Fe^{II}, Co^{II}, Ni^{II}; $J_{M\text{-}U}$>0 ; M=Mn^{II}: T_B=3 K, U_{eff} =56.3 cm^{-1})[81-83] where SMM behavior originates from the exchange interactions between the metal centers, evidenced by the poor, field-induced, performance of the derivative incorporating diamagnetic Cd^{2+} ion. Moreover, same structural motifs were successfully employed in a construction of the single-chain magnets featuring either linear [Mn^{II}(py)$_4$–O=U=O–]$_n$ (T_B=6 K; U_{eff}=93.1 cm^{-1})[84] or zig-zag [[Mn^{II}(py)$_2$(NO_3)–O=U=O–]$_n$ (T_B=3 K; U_{eff} =84.9 cm^{-1})[85] conformation of the metallic core.

SMM design strategy based on hybrid *p-f* systems proved to be even more effective in lifting the degeneracy of M_J pairs, increasing the T_B up to 13.9 K for the isostructural complex

anions $[Ln_2\{N(SiMe_3)_2\}_4(THF)_2(N_2)]^-$ (Ln-Gd, Tb, Dy, Ho, Er), (Figure 1.7).[86, 87] Core or those complexes includes pseudotetrahedral Ln centres which are strongly coupled to the radical μ, η^2:η^2-$[N_2]^{3-}$ bridge (S=1/2), generated by the consecutive reductions of N_2. Zero-field slow relaxation of the magnetization was observed for Tb, Dy and Ho derivatives (U_{eff}=227.0; 123 and 73 cm^{-1}, respectively), while field-induced (H=1000 Oe) SMM behaviour was observed for the Er derivative (U_{eff}=36 cm^{-1}). Impressively, largest relaxation barriers were followed up with the largest reported blocking temperatures T_B=13.9 K (Tb) and T_B=8.3 K (Dy), as a result of the effective exchange bias.

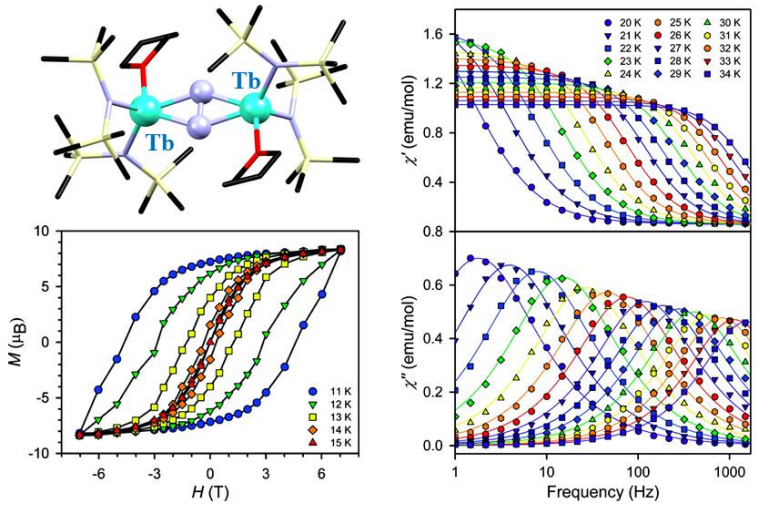

Figure 1.7: Crystal structure and the SMM behaviour of the $[K(18\text{-crown-6})(THF)_2][\{[(Me_3Si)_2N]_2(THF)Tb\}_2(\mu\text{-}\eta^2\text{:}\eta^2\text{-}N_2)]$ (U_{eff}=227 cm^{-1}: T_B=13.9 K: sweep rate: 0.9mT/s).[86]

Subsequently, Long *et al.* expanded this SMM design principle to lanthanocene compounds, by incorporating the bipyrimidyl and 2,3,5,6-tetra(2-pyridyl)pyrazinyl radical anions into cationic $[(Cp)_2Ln\text{-}(\mu\text{-radical})\text{-}Ln(Cp)_2]^+$ systems, as well as hexaazatrinaphthylene radical anion, $[HAN]^{\bullet-}$, into triangular $[(Cp)_6Ln_3(\mu^3\text{-HAN})]$ compounds (Ln-Tb, Dy).[88-90] Despite the modest relaxation barriers of these systems (35.9-87.8 cm^{-1}), high blocking temperatures were again successfully reached for $[Dy_2]^+$ (T_B=6.5 K)[89] and $[Dy_3]$ clusters (T_B=3.5 K).[88]

Alternative approach of quenching the quantum tunnelling in mononuclear 4*f*-nanomagnets requires strict control of the ligand field symmetry and electrostatic potential to promote the coordination geometries with strong anisotropy. Ideally, symmetry of the imposed ligand field should stabilise the largest M_J sublevels as the doubly degenerate ground state, while its potential should provide the large separation between the ground and excited

states. In that sense, highly symmetric systems are especially desirable in order to cancel out any transverse anisotropy which deteriorates the SMM performance. Considering the angular dependence of the 4*f* magnetic orbitals and distribution of its electron density, Long and Rinehart coined the simple qualitative model of oblate and prolate 4*f*-ions which can exhibit strong anisotropy in axial and equatorial ligand fields, respectively.[91] For instance, large energy barrier of terbium phtalocyanine is easily understandable taking into account the concept of an oblate ion in an axial ligand field. On the other hand, prolate Er(III) ion has been established as an excellent SMM building block within the equatorial ligand field, such as π-electron cloud of cyclooctatetraene dianion $(COT)^{2-}$, delivering the relaxation energy barriers up to 150 cm^{-1} and blocking temperatures up to T_B=10 K ($[Er(\eta^8\text{-}COT)_2]^-$.[92] Among the several theoretical models investigating the design criteria for strongly axial *f*-based SMM, low coordinated complexes $[Dy{-}O]^+$ and L−Dy−L were considered by Chibotaru/Ungur and Chilton, respectively, with a prediction of relaxation barriers U_{eff} > 2000 cm^{-1} and T_B>77 K for a perfectly linear geometries.[93-95] Chilton, Layfield *et al*. reported very recently an experimental study of organometallic compounds based on metallocenium cation $[(Cp^{ttt})_2Dy]^+$ which exemplifies how clever ligand design and manipulation of experimental conditions can produce the closest molecular approximations of such models.[96, 97] Bent linear geometry around the oblate Dy^{3+} site (Cp^{ttt}–Dy–Cp^{ttt} angle of 152.845(2)°) resulted with the impressive display of magnetic bistability, including the record-holding anisotropy barrier U_{eff}=1277 cm^{-1} and truly remarkable blocking temperature T_B=60 K (coercive field *H*=0.06 T; sweep rate 3.9 mT/s).[96] *Ab initio* consideration of the electronic structure indicated the high axiality of the system which suppresses the quantum tunneling of the magnetization in the ground and first two excited doublets, allowing the dominant thermal relaxation mechanism via sixth Kramers doublet. Highlighted synergy between the experimental findings and theoretical predictions evidences the possibility of reaching the long-standing dream of applicable molecular nanomagnets at high working temperatures. Looking beyond the scope of organometallic systems, probability of reaching such coordinatively unsaturated *f*-compounds is very small, but the general idea of imposing strong axial and weak (non-existent) equatorial ligand fields inspired the significant progress in SMM design and performance. For instance, Tong's SMM-tailoring strategy based on use of pentagonal-bipyramidal Dy^{3+} building blocks (D_{5h} symmetry) has proven to be extremely fruitful, generating the highest relaxation barriers ($U_{eff} \leq 1261$ cm^{-1}) and operable blocking

temperatures (T_B≈20 K).[98-101] In initial study, desorption of terminal methanol ligand from the structure of linear [Zn−Dy−Zn] complex triggered the single-crystal to single-crystal transformation which changed the coordination geometry around the Dy(III) site from pentagonal-bipyramidal to octahedral. Interestingly, minor structural modification was accompanied with a remarkable switch of the magnetic anisotropy and SMM properties, from impressive U_{eff}=305 cm^{-1}and T_B=11 K to practically negligible value (no χ_m'' peak in zero dc field). As confirmed by the *ab initio* calculations, observed magnetic behavior originates from the perfectly axial or isotropic M_J=±15/2 Kramers doublets, respectively.[98] Later work of the group focused on achieving the ideal D_{5h} symmetry of the Dy^{3+} sites by combining the strong axial field of phosphine oxide ligands and weak equatorial field of solvent ligands in $[Dy(Cy_3PO)_2(H_2O)_5]X_3\cdot(Cy_3PO)$ compounds. As a result, Orbach relaxation over large energy barriers U_{eff}=328.1 cm^{-1} (X=Cl) and U_{eff}=377.4 cm^{-1} (X=Br) was accompanied with the high blocking temperatures T_B=11 K and T_B=20 K (X=Cl, Br, respectively; 0.02 T/s) and large coercive field of 12.5 kOe at 2 K (X=Br; Figure 1.8A).[99] The *ab initio* calculations showed that the main anisotropy axes of the ground doublet are almost collinear with the axial Dy−O bonds, while better SMM performance of Br derivative was related to the higher axiality ($g_z/g_{x,y}$) of its ground state. Interestingly, this approach worked also on related non-Kramers holmium(III) analogue, where large spin reversal barrier of 237 cm^{-1} was generated by the effective suppression of the quantum tunneling through the crystal-field effects and hyperfine coupling (J=8 and I(^{165}Ho=7/2)).[102] Changing the first coordination sphere around the Dy(III) to heteroleptic N_4X (X-Cl, Br) ligand field and introducing the negatively charged phenoxide as axial ligands, relaxation barrier energies were raised up to 492.1 cm^{-1} (X-Cl; via second excited Kramers doublet) and 712.4 cm^{-1} (X-Br; via third excited Kramers doublet), accompanied with the open hysteresis loops below 8 K and 14 K, respectively (Figure 1.8B).[100] Recently, similar strategy was employed by Zheng and Winpenny in a construction of $[Dy(O^tBu)_2(py)_5](BPh_4)$ complex which displayed the record-breaking effective energy barrier (U_{eff}=1261.5 cm^{-1}; T_B=14 K) and the χ_m'' maxima visible above 100 K.[101]

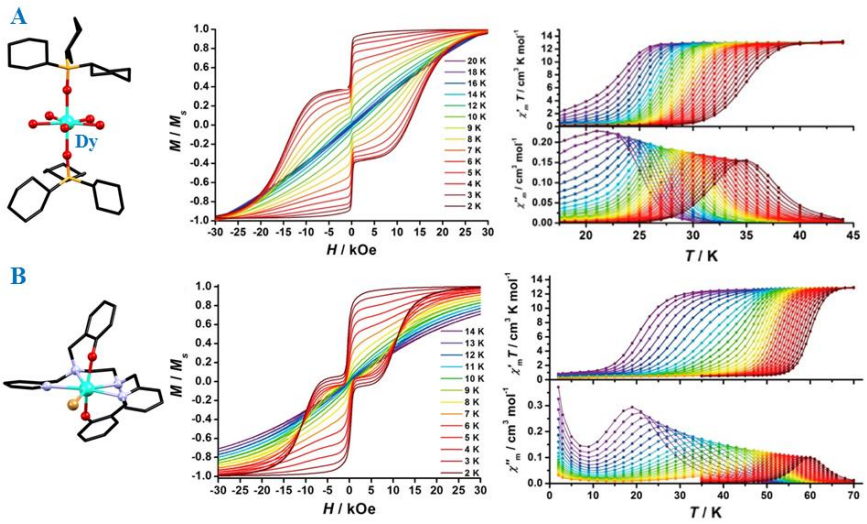

Figure 1.8: Crystal structure and the SMM behaviour of the pentagonal-bipyramidal dysprosium(III) SMMs: A) $[Dy(Cy_3PO)_2(H_2O)_5]Br_3$ (U_{eff}=377.4 cm^{-1}: T_B=20 K: sweep rate: 0.02 T/s);[99] B) [Dy(bbpen)Br] (H_2bbpen=*N*,*N*′-bis(2-hydroxybenzyl)-*N*,*N*′-bis(2-methylpyridyl)ethylenediamine) (U_{eff}=712.4cm^{-1}: T_B=14 K: sweep rate: 0.02 T/s).[100]

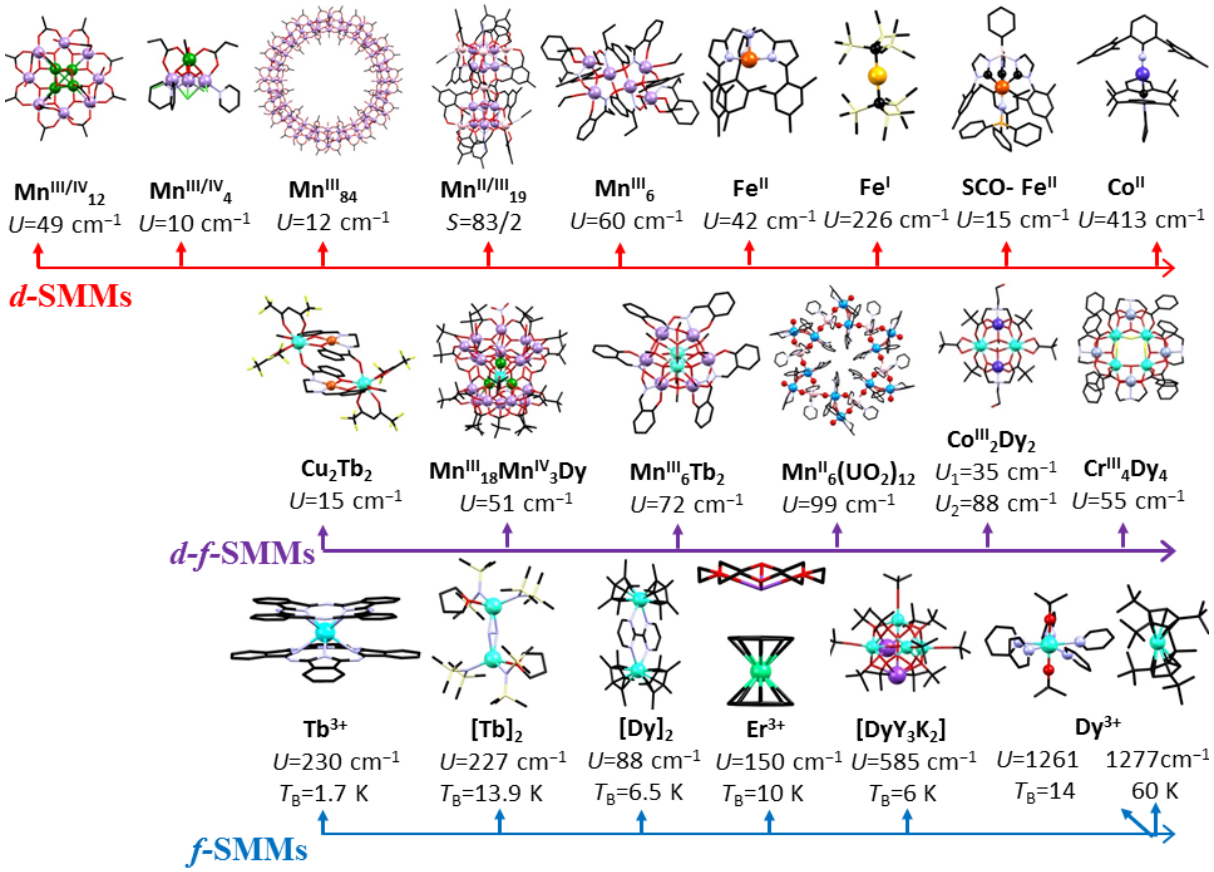

Figure 1.6: Evolution timeline of different classes of molecular nanomagnets discussed in the text.

1.5. General aspects of quantum computing

Among the potential applications of molecular magnets, the manipulation of their electronic spins to perform the quantum computing tasks is by far the most appealing one. In the classical computation, information is encoded as the binary bit (0 or 1) and manipulated by the operations of the logic gates. The state of each bit (0 or 1) is physically embodied in the voltage-gated macrostates of the transistor components in microprocessors. With the technological revolution and fast advancement of the computing power, the miniaturization and increased complexity of the memory storage devices were mandatory, adopting these days the high-density nanoscale features. Below the certain limit, physical description of such system will start to deviate from the laws of classical physics and enter to the quantum mechanics regime. Alternatively, by embracing the bottom up approach, quantum properties of molecules could be exploited for the quantum information processing (QIP).[103-106] A basic element of information in quantum computing is a quantum bit (qubit), which is physically embodied in the microstates of two-level (|1> and |0>) quantum system. Unlike classical bit which adopts either 0 or 1 state, qubit can exist as the |0>, |1> or any possible linear combination of these two orthogonal states (quantum superposition of the wavefunction):

$$|\Psi\rangle = \alpha|1\rangle + \beta|0\rangle \qquad (1.37)$$

where α and β represent the complex coefficients which fulfil the condition $\alpha\cdot\alpha^{*}+\beta\cdot\beta^{*}=1$. The superpositioned state represents a pure quantum state that can easily evolve into the statistical mixture of |1> and |0> states in the decoherence process, arising from the interactions of the qubit with its environment.[107] The entire set of possible states of qubit can be presented by the surface of unitary Bloch sphere in the polar coordination system (Figure 1.10).

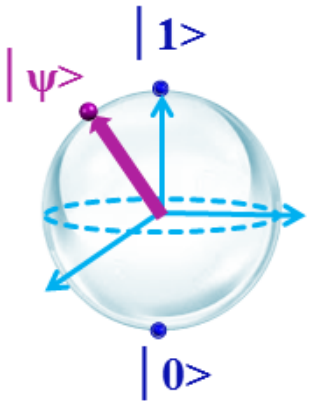

Figure 1.10: Schematic representation of the Bloch sphere of qubit highlighting the two basic states |0> and |1> (blue balls) and their quantum superposition $|\Psi\rangle = \alpha|1\rangle + \beta|0\rangle$ (violet arrow+ball).

Logic operations that covert initial state of qubits (input) into final state (output) are performed by the quantum logic gates, qugates, composed of one or an ensemble of qubits. Any quantum operation can be described by the matrix of unitary transformation or represented as the trajectory on the Bloch sphere between the initial and final state of the qubit. Especially interesting are the universal quantum gates, since they represent a set of elementary operations which can be combined to execute any complex logic operations. The most important 2-qubit quantum gates are the controlled-not (C-NOT) qugate, which changes the state of the target qubit only if the control qubit is initialised in a given state (|1> in Figure 1.11., Table 1.1), and the √SWAP qugate which switches the states of the qubits only if they are inverted (|1> and |0>, Figure 1.11, Table 1.1), generating the superposition of the initial and the final state.[108] Similarly, more complex 3-qubit CC-NOT (TOFFOLI) qugate flips the state of the third, target, qubit only if the first two control qubits are in a given state (|1,1>, Figure 1.11, Table 1.1), while C-√SWAP (FREDKIN) qugate switches the states of the inverted second and the third qubit (target qubits) only if the first one (control qubit) is in a determined state (|1>, Figure 1.11, Table 1.1), generating again the superposition of the initial and the final state. Most importantly, the output state of the quantum logic operations cannot be expressed as the simple product of the individual qubit states, meaning that full description of any qubit in such entangled state of the system requires the consideration of the remaining qubits. Consequently, projection of one qubit to its eigenstates allows the precise determination of the other qubits state. Taking this into account, any physical realisation of the multi-qubit qugates can be found only in quantum

systems exhibiting a weak interaction between their component qubits. Additionally, dissimilarity between the target and control qubits is important requirement in development of prototypes for controlled logic gates (C-NOT and CC-NOT).

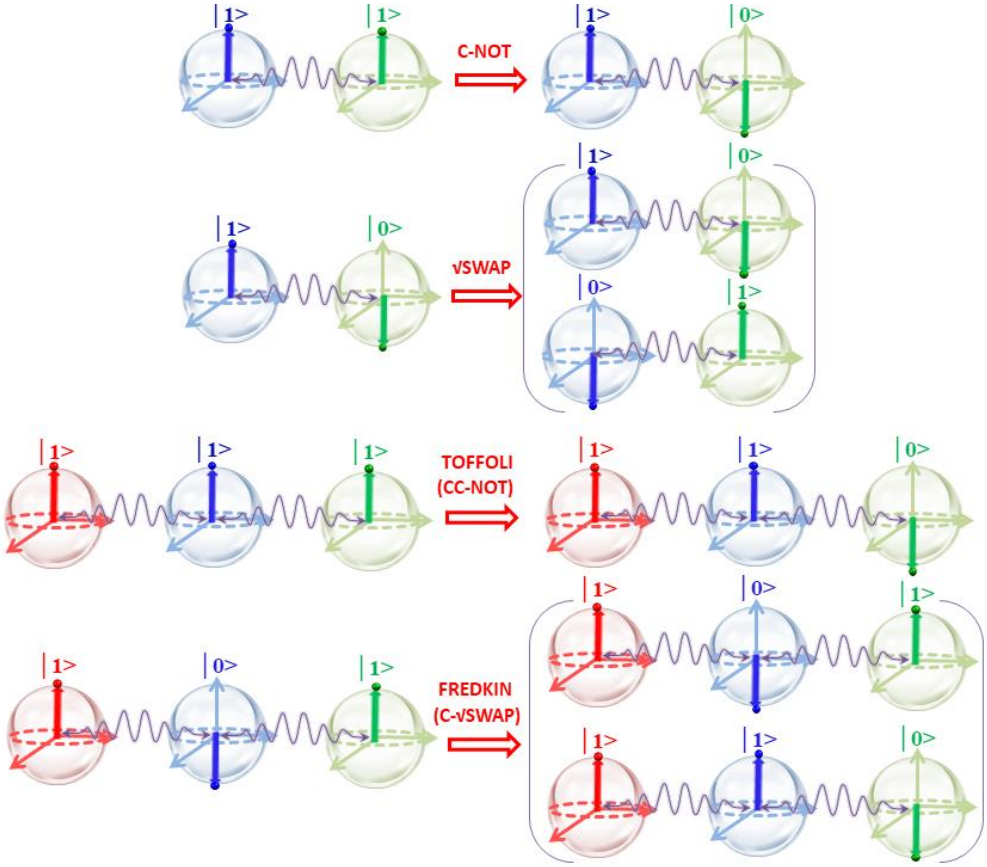

Figure 1.11: Schematic representation of the multi-qubit qugates and related C-NOT, √SWAP, CC-NOT and C-√SWAP operations. For simplicity, only $|1,1\rangle \rightarrow |1,0\rangle$ for C-NOT, $|1,0\rangle \rightarrow \{|1,0\rangle + |0,1\rangle\}$ for √SWAP, $|1,1,1\rangle \rightarrow |1,1,0\rangle$ for CC-NOT and $|1,0,1\rangle \rightarrow \{|1,0,1\rangle + |1,1,0\rangle\}$ for C-√SWAP operations are shown.

Table 1.1: Truth table of the multi-qubit qugates and related C-NOT, √SWAP, CC-NOT and C-√SWAP operations.[109]

Qugate	Input	Output	**Qugate**	Input	Output
C-NOT	0 0	0 0	**√-SWAP**	0 0	0 0
	0 1	0 1		0 1	1 0
Q_CQ_T	1 0	1 1	**Q_1Q_2**	1 0	0 1
	1 1	1 0		1 1	1 1
CC-NOT	0 0 0	0 0 0	**C-√SWAP**	0 0 0	0 0 0
(TOFFOLI)	0 0 1	0 0 1	(FREDKIN)	0 0 1	0 0 1
	0 1 0	0 1 0		0 1 0	0 1 0
	0 1 1	0 1 1		0 1 1	0 1 1
$Q_CQ_CQ_T$	1 0 0	1 0 0	**$Q_1Q_2Q_3$**	1 0 0	1 0 0
	1 0 1	1 0 1		1 0 1	1 1 0
	1 1 0	1 1 1		1 1 0	1 0 1
	1 1 1	1 1 0		1 1 1	1 1 0

Properties of the quantum entanglement and superposition ensure the great advantages of the quantum information processing over its classical analogue. Quantum register of *N*-qubits will attain a state defined as a superposition of the 2^N products states of the individual qubits (|1> and |0>), while the state of classical register will include only a sequence of the 0/1 states. This difference ensures the quantum parallelism which could be used in Shor's factoring algorithm and in parallel processing of multiple operations in one single step. On the other hand, use of the superimposed control qubit in the C-NOT logic gates provides the entangled output state, ensuring the safer information processing without the possibility of using COPY operations.[107]

The proposed prototypes of the qubits include the trapped atoms/ions,[110-112] nuclear spins,[113] photons[114, 115], quantum dots,[116] nitrogen-vacancy in diamond,[117] superconductors[118, 119] and electronic spin.[120] Among the most astonishing results of the implemented systems to this date, one should emphasize the long-lived superpositioned state of an ensemble of charged $^{31}P^+$ donors integrated in the isotopically purified ^{28}Si.[121] The measured coherence time exceeds 39 min at the room temperature and over 3 h at the cryogenic 4.2 K, which brings the dream of storing qubits at ambient conditions closer to reality. However, down point of such system is the need for cryogenic encoding and reading-out the information, where only 37% of the qubit ensemble survives the manipulation process. Pioneering the Mn_{12} and Fe_8 SMMs as the appealing qubit hardware,

Loss and Leuenberger inspired the coordination chemists to exploit the electronic spin of paramagnetic molecules in quantum information processing.[120] Recently after their theoretical proof of concept, Christou *et al.* demonstrated experimentally existence of the quantum entanglement between the pair of Mn_4 clusters, illuminating new horizons of molecular magnetism.[38]

Regardless of the nature of implemented qubits, requirements which any physical system needs to fulfil to be implemented in the quantum computing are known as the DiVincenzo criteria.[122] Primarily, each qubit has to be *a scalable well-defined two level system* to ensure the possibility of encoding the information as$|1\rangle$ and $|0\rangle$. For this purpose, any radical or open-shell coordination complex possessing the ground spin state S=1/2 (pure or effective) represents a true two-level quantum system defined with the spin orientations ($\pm M_S$=1/2 as $|1\rangle$ and $|0\rangle$) which can be easily manipulated by the microwave frequency of the standard EPR spectrometer. Scalability of such system aims at the inclusion of increased number of identical qubits in a construction of the operable quantum computer. This delivers a great advantage to the uniform molecular-based qubits over other proposed systems since flexible functionalisation of the organic scaffold in the coordination complexes can be exploited to deposit them homogeneously on surfaces and to construct the appropriate devices. Secondly, *initialization of the qubits* has to be an easy and efficient procedure which will define properly the state of the qubit at any moment. For coordination compounds, this task is easily achievable by application of external magnetic field and by lowering the temperature to concentrate the Boltzmann distribution in the ground spin state. Thirdly, *long coherence (decoherence) time of qubits* is essential to ensure the possibility of performing the operations of quantum computing. Decoherence time (τ_d) of a qubit defines the timescale at which the encoded information is maintained in the superpositioned state (amplitudes and phases of α and β coefficients) and it can be optimised through the modulations of the molecular environment of the embedded spin. One of the most important mechanisms of decoherence includes the excitation relaxation between the different states of the molecule that heads into thermal equilibrium within the longitudinal relaxation time constant T_1. Faster mechanism includes the previously mentioned phase decoherence of the superpositioned state which leads to statistical mixture of states within the transverse relaxation time constant T_2 ($T_1 >> T_2$). Pulsed EPR measurements with Hahn-echo sequence are the most commonly used tool to determine the reliability of qubits,

which should exhibit 10^4-10^5 longer decoherence time (T_2) than the gating (clock) time τ_g, defined with a timescale at which employed experimental setup switches the state of the qubit from the initial input to the final output ($\tau_g \approx 10$ ns).[123] Alternately, this requirement is often expressed as the figure of merit, Q:

$$Q = \frac{\tau_g}{\tau_d} \leq 10^{-4} \qquad (1.38)$$

$$Q = \frac{\tau_g}{T_2} \leq 10^{-4}$$

One of the most common ways of increasing the coherence times of the paramagnetic qubits is based on the use of nuclear-spin free ligands where hyperfine interactions between the electronic spin of qubits and the nuclear bath of its environment are disabled. Secondly, endless combinations of spin carriers and imposed diamagnetic environments ensure the fundamental possibility of correlating the observed decoherence time with the molecular features of qubit and, consequently, refining the qubit design.

Furthermore, the individual qubits should be assembled into *universal quantum gates* such as C-NOT or √SWAP (two qubits) or TOFFOLI and FREDKIN (three qubits) which can be implemented for the quantum computing. To achieve this goal, the interaction between the component qubit should be weak enough to preserve the individual energy levels, but at the same time it should be strong enough to provide the entangled states of the whole ensemble. Moreover, the dissimilar component qubits of the C-NOT and TOFFOLI gate should exhibit different energy level schemes in order to be addressed separately. Finally, result of any quantum operation should be easily readable through the final state of the target qubit. In the case of the electronic spin based systems, exploiting the strategic functionalization of organic scaffolds, individual qubits can be easily assembled in an operable quantum gate, where their interactions can be subtly tuned by the length of diamagnetic linkers to generate the entangled states of an ensemble or to improve the coherent information processing. Likewise, by implementing stimuli responsive or asymmetric ligands, √SWAP or C-NOT quantum gates can be selectively constructed from the individual spin qubits.

1.6. Electronic spin based qubits and molecular prototypes of quantum gates

Despite great amount of work focused on understanding how to maximize the lifetime or quantum coherence of the qubit quantum states, very few reports address the challenge of making operative molecular quantum gates by engaging more than one qubit. One of the earliest examples of such system was vanadyl capped polyoxometalate $[PMo_{12}O_{40}(VO)2]^{n-}$ as molecular protype of √SWAP qugate.[124] Using electric potential to manipulate the charge of polyoxomolybdate core, weak antiferromagnetic interaction between localised *S*=1/2 vanadyl qubits was switched off and on. In this field of research, the most prolific studies were carried out using pairs of $[Cr_7Ni]$ ring clusters (S = ½ ground state).[125-127] Our group was addressing this challenge by exploiting rich coordination chemistry of β-diketone ligands with lanthanides and transition metals to generate different heterometallic clusters prototypes of C-NOT and √SWAP quantum gates. As the most valuable outcome for the latter, $[CuZn]_2$ and $[NiCu]_2$ spin qubits were connected by a photo-switchable *bis*-β–diketone incorporating dithienylethene photochromic spacer.[128] Magnetic studies confirmed that both heterometallic dimers possess true or effective *S*=1/2 ground state and exhibit weak interaction within [CuM···MCu] topology of clusters, fulfilling all the requirements to be considered as spin qubits. Moreover, quantum coherence studies by pulsed Q-band EPR spectroscopy revealed that both systems exhibit very good phase memory times (T_m) of 3.59 and 6.03 μs at 7 K, while solution studies of photo switching process showed its reversibility, ensuring means of controllable modification of the magnetic interaction between qubits. However, limitation of uncomplete conversion in solid state hinders the possibility of exploiting those compounds as prototypes of √SWAP qugates since light modulated inter-qubit interaction can't be properly validated.

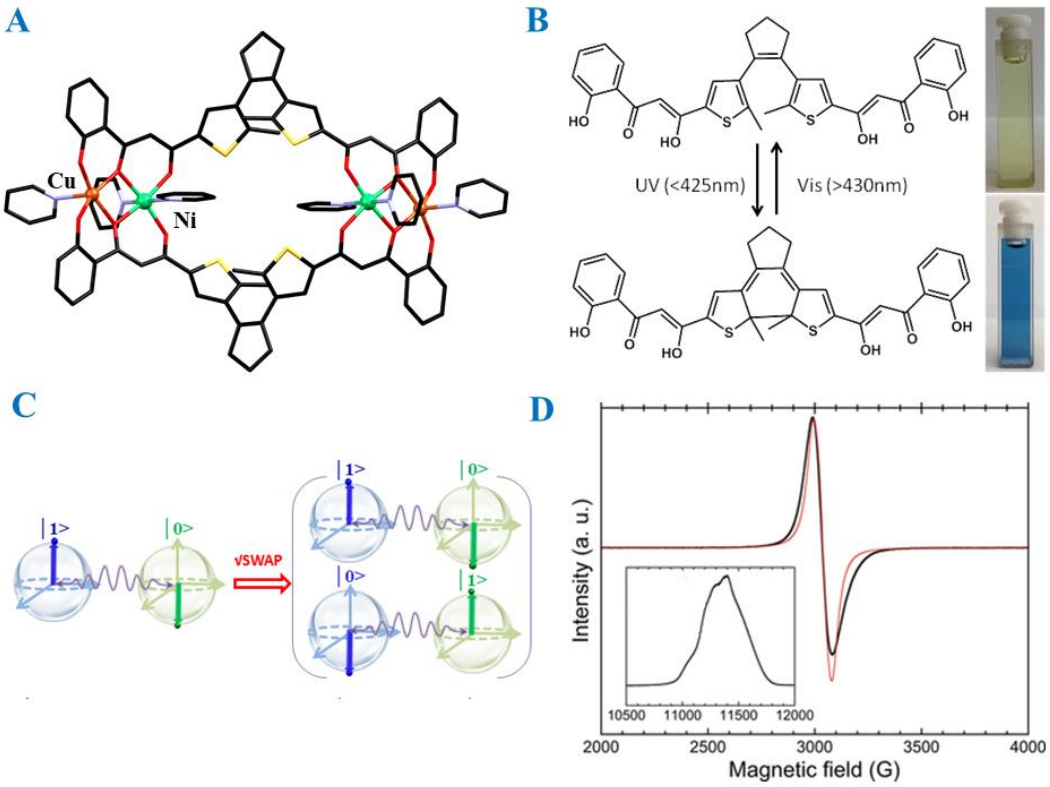

Figure 1.12. Molecular structure (A), powder X-Band EPR spectrum (B) and corresponding frozen solution electron spin echo detected Q-band EPR spectrum of potential √SWAP qugate (C) $[(CuNi)_2(L)_2(Py)_6]$ constructed from light responsive *bis*-β-diketone H_4L (B) (H_4L-1,2-bis{5-[3-oxo-3-(2-hydroxyphenyl)propanoyl]-2-methyl-thio-phen-3-yl}cyclopentene, B).[128]

Another research line included engineered assembly of heterometallic [4*f*,4*f*'] dimers within asymmetric ligand with carboxylate-β-diketonate functionalities. Different sizes of coordination pockets in ligand enabled very selective formation of bimetallic 4*f*-dimers of Kramer's ions where doubly degenerate ground state can be addressed individually for the realization of C-NOT quantum logic gates.[129-131] Of all possible combinations, [CeEr] dimers proved to ideal candidate for such applications since both metals exhibit different magnetic configurations (J_{Ce}=5/2, g_{Ce}=6/7; J_{Ce}=15/2, g_{Ce}=6/5) and possess reduced content of nuclear spins which might deteriorate coherence. Using EPR spectroscopy and magnetic susceptibility measurements, ground state doublet for each metal at its site was extracted from structurally related compounds involving smaller or larger diamagnetic partner ([CeY] and [LaEr]). Comparing the analogous measurements on [CeEr] derivative, strength of magnetic interaction between tilted spin moments (70°) was successfully extracted, giving insights into low-energy level structure and its magnetic field dependence. Echo detected

EPR spectrum revealed coherence for |01> ↔ |00> transition (T_2=410 ns) which corresponds to C-NOT gate operation where the first qubit (0) acts as control. Such discovery highlighted the great potential of implementing electronic spin-based qubits for quantum information processing.

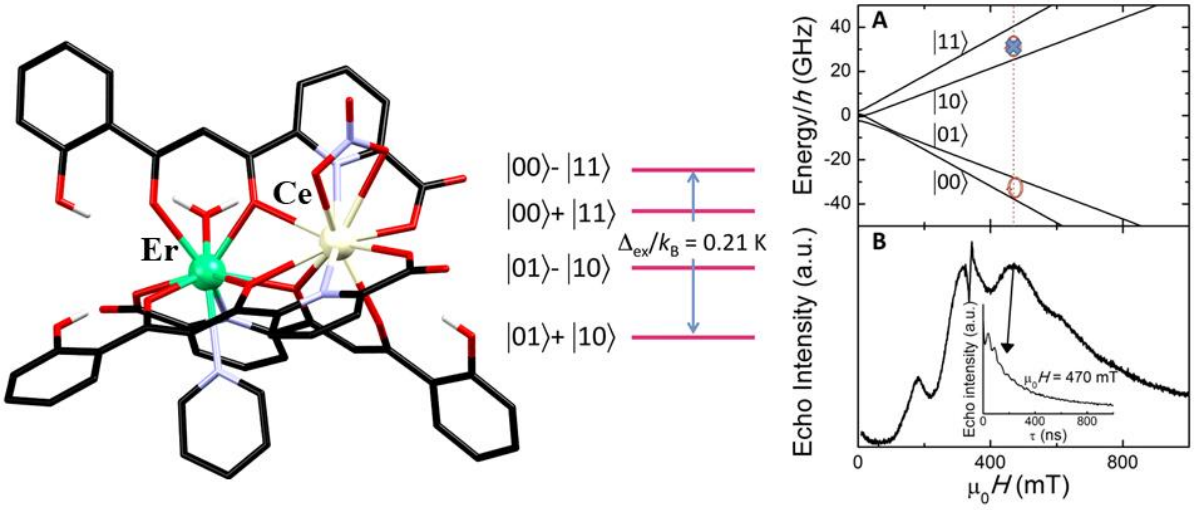

Figure 1.13. *Left to* right: Molecular structure of [CeEr] dimer, low-energy level structure and corresponding frozen solution electron spin echo detected X-band EPR spectrum for C-NOT (|01> ↔ |00>) operation between qubits.[129]

1.7. Overview and objectives of thesis

The work presented in this thesis aims at rational design of functional molecular magnets by developing diverse synthetic approaches for selective preparation of the heterometallic assemblies. This challenging pursuit relies on the implementation of sophisticatedly engineered *bis*-β-diketone and related *bis*-pyrazole ligands, where number, size and distribution of the coordination pockets can be easily tuned by the plethora of possible building blocks.[132, 133] Versatile functionalities and topologies in the designed scaffolds provide a fruitful playground for selective alignment of dissimilar 3*d* metal ions into (weakly) coupled cluster pairs, linear arrays, square platforms and metallamacrocycles.

Chapter II discloses the preparation of new ligand **H_4L1** holding two fused phenol-β-diketone coordination pockets, capable of assembling the clusters with a rare topology of oxo-hydroxido coupled pair of dimers (Scheme 1.1). Interestingly, preparation of those entities required only one equivalent of chelating ligand which even then ensured the high

selectivity in formation of heterometallic systems, based on the crystal field effects between the inner octahedral metallic site and the peripheral square-pyramidal site. Nonetheless, established pair-impair ratio between the constituent metal ions and ligand, as well as the strong antiferromagnetic coupling within the highly selective [CuNi] pair of dimers, inspired the evolution of more promising systems elaborated in the Chapter III.

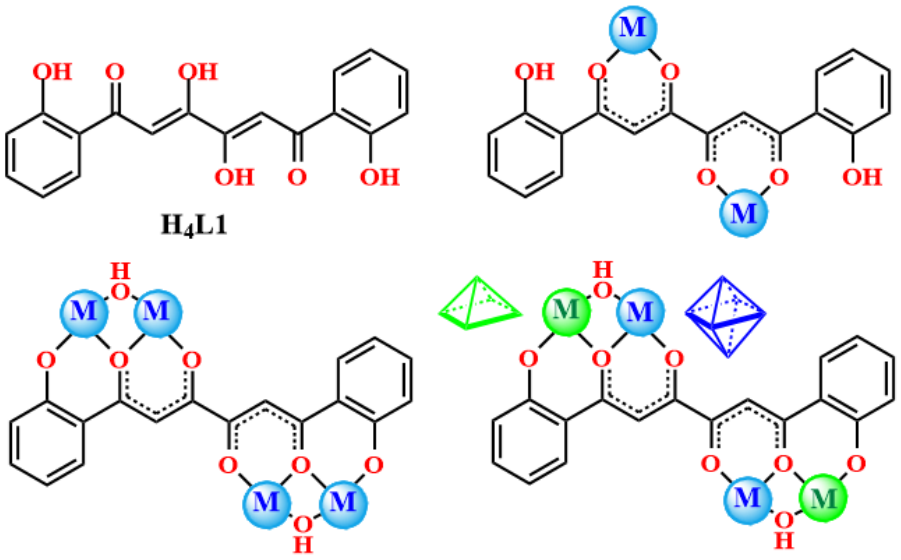

Scheme 1.1: The structure of **H_4L1** and observed coordination modes of its deprotonated forms in prepared homometallic and heterometallic coordination compounds.

Chapter III discusses the line of research dedicated to preparation of molecular prototypes of multiqubit quantum logic gates, incorporating either vanadyl ions (true *S*=1/2) or antiferromagentically coupled [CuNi] dimers (effective *S*=1/2). To fulfil all necessary requirements for such systems, four novel *bis*-β-diketone ligands were designed and synthesised, embodying either asymmetric backbone or bearing different functionalities, such as chelating 1,10-phenanthroline or 2,2'-bipyridine moieties (Scheme 1.4). Those characteristics of prepared ligands assign them as some of the most complex members of this extensive family, since only several asymmetric *bis*-β-diketone are known,[134] while complex functionalities of chelating *N*-donors have never been incorporated. Relying on the successful strategy presented in Chapter II, controlled reaction stoichiometry with pair-impair metal to ligand ratio enabled the preparation of three novel coordination entities embedding the non-equivalent effective spins *S*=1/2 (asymmetric [CuNi] dimers), as witnessed from the structural and magnetic studies. The unique electronic structure of those systems assigns them as the suitable molecular prototypes for the C-NOT and CC-NOT

quantum gates. Apart from this appealing accomplishment, some of the most complex vanadium metallamacrocycles were obtained, but their higher symmetry hampered any promising application in quantum computing.

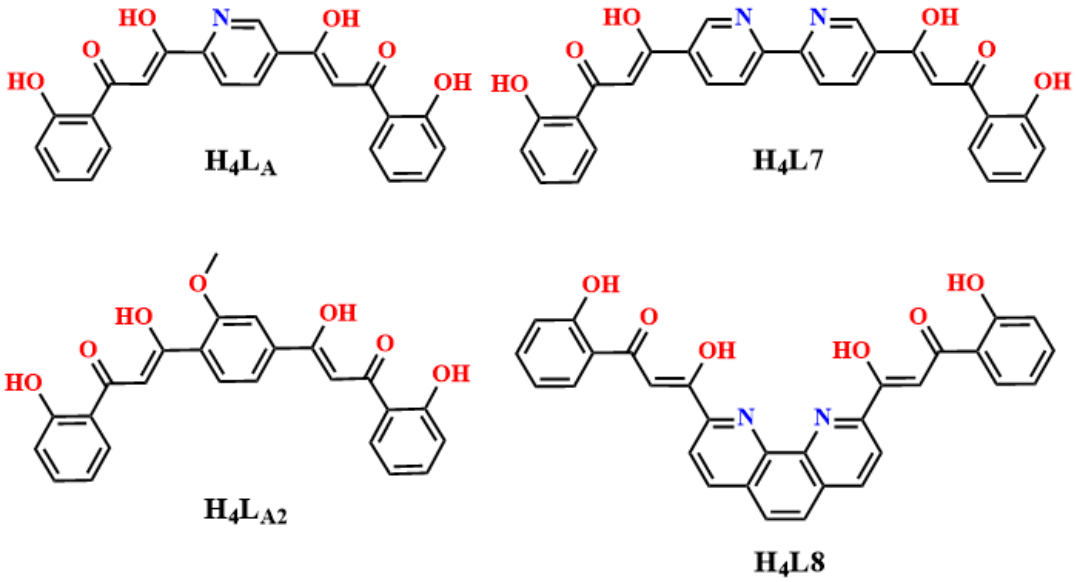

Scheme 1.4: Structures of the asymmetric (**H_4LA** and **H_4L_{A2}**, *left*) and multifunctional ligands (**H_4L7** and **H_4L8**, *right*) enriched with different sets of donor atoms.

Chapter IV elaborates the coordination chemistry of the new phenolic pyrazole ligand **H_4L4**, designed with an idea to selectively chelate different 3*d* metals into linear arrays based on their preference towards (-*N*,*N*) or (-*O*,*N*) coordination environment. Testing that assumption on homometallic compounds indicated that only vanadyl cation (VO^{2+}) discriminates between the different ligating donor sets and resides exclusively in the (-*O,N*) coordination pocket, while maintaining the central -N_4 chelating site partially protonated and metal-free (Scheme 1.2). The latter feature promoted this system as a tailored metalloligand for encapsulation of additional metal ions, facilitating the selective preparation of novel, unprecedented heterobimetallic and heterotrimetallic architectures. Moreover, obtained results indicate that employing this synthetic approach with the principles of Kahn's orbital symmetry model opens up the possibility of designing the heterometallic assemblies with predictable magnetic properties, including even the slow relaxation of the magnetization.[7]

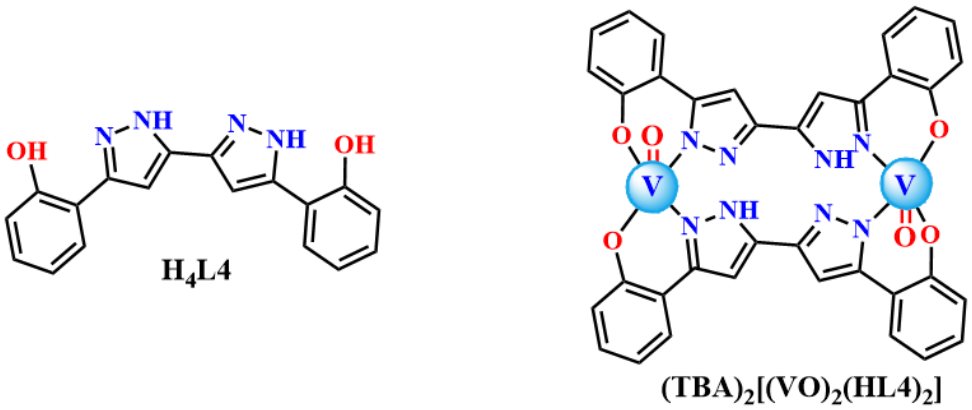

Scheme 1.3: Structures of the ligand **H_4L4** and derived metalloligand $(TBA)_2[(VO)_2(HL4)_2]$.

1.8. Literature

1. O. Kahn, *Molecular magnetism*, VCH, 1993.
2. C. Benelli and D. Gatteschi, in *Introduction to Molecular Magnetism*, Wiley-VCH Verlag GmbH & Co. KGaA, 2015, DOI: 10.1002/9783527690541.ch2, pp. 25-32.
3. C. Benelli and D. Gatteschi, in *Introduction to Molecular Magnetism*, Wiley-VCH Verlag GmbH & Co. KGaA, 2015, DOI: 10.1002/9783527690541.ch3, pp. 33-50.
4. B. Bleaney and K. W. H. Stevens, *Reports on Progress in Physics*, 1953, **16**, 108.
5. K. W. H. Stevens, *Proceedings of the Physical Society. Section A*, 1952, **65**, 209.
6. A. Abragam and B. Bleaney, *Electron Paramagnetic Resonance of Transition Ions*, OUP Oxford, 2012.
7. O. Kahn, *Angewandte Chemie International Edition in English*, 1985, **24**, 834-850.
8. O. Kahn, J. Galy, Y. Journaux, J. Jaud and I. Morgenstern-Badarau, *Journal of the American Chemical Society*, 1982, **104**, 2165-2176.
9. O. Kahn, P. Tola, J. Galy and H. Coudanne, *Journal of the American Chemical Society*, 1978, **100**, 3931-3933.
10. T. Glaser, H. Theil, I. Liratzis, T. Weyhermüller and E. Bill, *Inorganic Chemistry*, 2006, **45**, 4889-4891.
11. M.-L. Tong, Y.-M. Wu, Y.-X. Tong, X.-M. Chen, H.-C. Chang and S. Kitagawa, *European Journal of Inorganic Chemistry*, 2003, **2003**, 2385-2388.
12. J. A. McCleverty and M. D. Ward, *Accounts of Chemical Research*, 1998, **31**, 842-851.
13. T. Glaser, *Chemical Communications*, 2011, **47**, 116-130.
14. Z.-P. Ni and M.-L. Tong, in *Molecular Magnetic Materials*, Wiley-VCH Verlag GmbH & Co. KGaA, 2017, DOI: 10.1002/9783527694228.ch3, pp. 53-77.
15. T. Glaser, *Coordination Chemistry Reviews*, 2013, **257**, 140-152.
16. I. Fernández, R. Ruiz, J. Faus, M. Julve, F. Lloret, J. Cano, X. Ottenwaelder, Y. Journaux and M. C. Muñoz, *Angewandte Chemie International Edition*, 2001, **40**, 3039-3042.
17. T. Glaser, M. Heidemeier, S. Grimme and E. Bill, *Inorganic Chemistry*, 2004, **43**, 5192-5194.
18. B. Feldscher, A. Stammler, H. Bogge and T. Glaser, *Dalton Transactions*, 2010, **39**, 11675-11685.
19. C. Benelli and D. Gatteschi, in *Introduction to Molecular Magnetism*, Wiley-VCH Verlag GmbH & Co. KGaA, 2015, DOI: 10.1002/9783527690541.ch11, pp. 179-193.
20. D. Gatteschi, R. Sessoli and J. Villain, *Molecular nanomagnets*, Oxford University Press on Demand, 2006.
21. S. Goswami, A. K. Mondal and S. Konar, *Inorganic Chemistry Frontiers*, 2015, **2**, 687-712.
22. K. S. Cole and R. H. Cole, *The Journal of Chemical Physics*, 1941, **9**, 341-351.
23. J. M. Zadrozny, J. Liu, N. A. Piro, C. J. Chang, S. Hill and J. R. Long, *Chemical Communications*, 2012, **48**, 3927-3929.
24. C. Rajnák, J. Titiš, O. Fuhr, M. Ruben and R. Boča, *Inorganic Chemistry*, 2014, **53**, 8200-8202.
25. J. Vallejo, I. Castro, R. Ruiz-García, J. Cano, M. Julve, F. Lloret, G. De Munno, W. Wernsdorfer and E. Pardo, *Journal of the American Chemical Society*, 2012, **134**, 15704-15707.
26. W. Huang, T. Liu, D. Wu, J. Cheng, Z. W. Ouyang and C. Duan, *Dalton Transactions*, 2013, **42**, 15326-15331.
27. R. Herchel, L. Váhovská, I. Potočňák and Z. Trávníček, *Inorganic Chemistry*, 2014, **53**, 5896-5898.
28. E. Colacio, J. Ruiz, E. Ruiz, E. Cremades, J. Krzystek, S. Carretta, J. Cano, T. Guidi, W. Wernsdorfer and E. K. Brechin, *Angewandte Chemie International Edition*, 2013, **52**, 9130-9134.
29. S. Gómez-Coca, A. Urtizberea, E. Cremades, P. J. Alonso, A. Camón, E. Ruiz and F. Luis, *Nature Communications*, 2014, **5**, 4300.
30. J. H. Van Vleck, *Physical Review*, 1940, **57**, 426-447.

31. R. Orbach, *Proceedings of the Royal Society of London. Series A. Mathematical and Physical Sciences*, 1961, **264**, 458-484.
32. L. Tesi, E. Lucaccini, I. Cimatti, M. Perfetti, M. Mannini, M. Atzori, E. Morra, M. Chiesa, A. Caneschi, L. Sorace and R. Sessoli, *Chemical Science*, 2016, **7**, 2074-2083.
33. T. Lis, *Acta Crystallographica Section B*, 1980, **36**, 2042-2046.
34. R. Sessoli, H. L. Tsai, A. R. Schake, S. Wang, J. B. Vincent, K. Folting, D. Gatteschi, G. Christou and D. N. Hendrickson, *Journal of the American Chemical Society*, 1993, **115**, 1804-1816.
35. R. Sessoli, D. Gatteschi, A. Caneschi and M. A. Novak, *Nature*, 1993, **365**, 141-143.
36. G. Aromí and E. K. Brechin, in *Single-Molecule Magnets and Related Phenomena*, ed. R. Winpenny, Springer Berlin Heidelberg, Berlin, Heidelberg, 2006, DOI: 10.1007/430_022, pp. 1-67.
37. C. J. Milios, A. Vinslava, W. Wernsdorfer, S. Moggach, S. Parsons, S. P. Perlepes, G. Christou and E. K. Brechin, *Journal of the American Chemical Society*, 2007, **129**, 2754-2755.
38. S. Hill, R. S. Edwards, N. Aliaga-Alcalde and G. Christou, *Science*, 2003, **302**, 1015-1018.
39. W. Wernsdorfer, N. Aliaga-Alcalde, D. N. Hendrickson and G. Christou, *Nature*, 2002, **416**, 406-409.
40. A. J. Tasiopoulos, A. Vinslava, W. Wernsdorfer, K. A. Abboud and G. Christou, *Angewandte Chemie International Edition*, 2004, **43**, 2117-2121.
41. E. E. Moushi, T. C. Stamatatos, W. Wernsdorfer, V. Nastopoulos, G. Christou and A. J. Tasiopoulos, *Inorganic Chemistry*, 2009, **48**, 5049-5051.
42. A. M. Ako, I. J. Hewitt, V. Mereacre, R. Clérac, W. Wernsdorfer, C. E. Anson and A. K. Powell, *Angewandte Chemie International Edition*, 2006, **45**, 4926-4929.
43. E. Ruiz, J. Cirera, J. Cano, S. Alvarez, C. Loose and J. Kortus, *Chemical Communications*, 2008, DOI: 10.1039/B714715E, 52-54.
44. F. Neese and D. A. Pantazis, *Faraday Discussions*, 2011, **148**, 229-238.
45. O. Waldmann, *Inorganic Chemistry*, 2007, **46**, 10035-10037.
46. G. A. Craig and M. Murrie, *Chemical Society Reviews*, 2015, **44**, 2135-2147.
47. J. M. Frost, K. L. M. Harriman and M. Murugesu, *Chemical Science*, 2016, **7**, 2470-2491.
48. W. M. Reiff, A. M. LaPointe and E. H. Witten, *Journal of the American Chemical Society*, 2004, **126**, 10206-10207.
49. W. M. Reiff, C. E. Schulz, M.-H. Whangbo, J. I. Seo, Y. S. Lee, G. R. Potratz, C. W. Spicer and G. S. Girolami, *Journal of the American Chemical Society*, 2009, **131**, 404-405.
50. W. Alexander Merrill, T. A. Stich, M. Brynda, G. J. Yeagle, J. C. Fettinger, R. D. Hont, W. M. Reiff, C. E. Schulz, R. D. Britt and P. P. Power, *Journal of the American Chemical Society*, 2009, **131**, 12693-12702.
51. D. E. Freedman, W. H. Harman, T. D. Harris, G. J. Long, C. J. Chang and J. R. Long, *Journal of the American Chemical Society*, 2010, **132**, 1224-1225.
52. W. H. Harman, T. D. Harris, D. E. Freedman, H. Fong, A. Chang, J. D. Rinehart, A. Ozarowski, M. T. Sougrati, F. Grandjean, G. J. Long, J. R. Long and C. J. Chang, *Journal of the American Chemical Society*, 2010, **132**, 18115-18126.
53. J. M. Zadrozny, M. Atanasov, A. M. Bryan, C.-Y. Lin, B. D. Rekken, P. P. Power, F. Neese and J. R. Long, *Chemical Science*, 2013, **4**, 125-138.
54. J. M. Zadrozny, D. J. Xiao, M. Atanasov, G. J. Long, F. Grandjean, F. Neese and J. R. Long, *Nat Chem*, 2013, **5**, 577-581.
55. D. Gatteschi and R. Sessoli, *Angewandte Chemie International Edition*, 2003, **42**, 268-297.
56. S. Gomez-Coca, E. Cremades, N. Aliaga-Alcalde and E. Ruiz, *Journal of the American Chemical Society*, 2013, **135**, 7010-7018.
57. X.-N. Yao, J.-Z. Du, Y.-Q. Zhang, X.-B. Leng, M.-W. Yang, S.-D. Jiang, Z.-X. Wang, Z.-W. Ouyang, L. Deng, B.-W. Wang and S. Gao, *Journal of the American Chemical Society*, 2017, **139**, 373-380.

58. C. Mathonière, H.-J. Lin, D. Siretanu, R. Clérac and J. M. Smith, *Journal of the American Chemical Society*, 2013, **135**, 19083-19086.
59. X. Feng, C. Mathonière, I.-R. Jeon, M. Rouzières, A. Ozarowski, M. L. Aubrey, M. I. Gonzalez, R. Clérac and J. R. Long, *Journal of the American Chemical Society*, 2013, **135**, 15880-15884.
60. N. Ishikawa, M. Sugita, T. Ishikawa, S.-y. Koshihara and Y. Kaizu, *Journal of the American Chemical Society*, 2003, **125**, 8694-8695.
61. N. Ishikawa, M. Sugita, T. Ishikawa, S.-y. Koshihara and Y. Kaizu, *The Journal of Physical Chemistry B*, 2004, **108**, 11265-11271.
62. C. R. Ganivet, B. Ballesteros, G. de la Torre, J. M. Clemente-Juan, E. Coronado and T. Torres, *Chemistry – A European Journal*, 2013, **19**, 1457-1465.
63. N. Ishikawa, Y. Mizuno, S. Takamatsu, T. Ishikawa and S.-y. Koshihara, *Inorganic Chemistry*, 2008, **47**, 10217-10219.
64. N. Ishikawa, M. Sugita and W. Wernsdorfer, *Angewandte Chemie International Edition*, 2005, **44**, 2931-2935.
65. N. Ishikawa, M. Sugita and W. Wernsdorfer, *Journal of the American Chemical Society*, 2005, **127**, 3650-3651.
66. L. Rosado Piquer and E. C. Sanudo, *Dalton Transactions*, 2015, **44**, 8771-8780.
67. S. Demir, I.-R. Jeon, J. R. Long and T. D. Harris, *Coordination Chemistry Reviews*, 2015, **289–290**, 149-176.
68. S. Osa, T. Kido, N. Matsumoto, N. Re, A. Pochaba and J. Mrozinski, *Journal of the American Chemical Society*, 2004, **126**, 420-421.
69. C. M. Zaleski, E. C. Depperman, J. W. Kampf, M. L. Kirk and V. L. Pecoraro, *Angewandte Chemie International Edition*, 2004, **43**, 3912-3914.
70. C. Papatriantafyllopoulou, W. Wernsdorfer, K. A. Abboud and G. Christou, *Inorganic Chemistry*, 2011, **50**, 421-423.
71. M. Hołyńska, D. Premužić, I.-R. Jeon, W. Wernsdorfer, R. Clérac and S. Dehnen, *Chemistry – A European Journal*, 2011, **17**, 9605-9610.
72. A. V. Funes, L. Carrella, E. Rentschler and P. Albores, *Dalton Transactions*, 2014, **43**, 2361-2364.
73. S. K. Langley, L. Ungur, N. F. Chilton, B. Moubaraki, L. F. Chibotaru and K. S. Murray, *Inorganic Chemistry*, 2014, **53**, 4303-4315.
74. S. K. Langley, D. P. Wielechowski, V. Vieru, N. F. Chilton, B. Moubaraki, L. F. Chibotaru and K. S. Murray, *Chemical Science*, 2014, **5**, 3246-3256.
75. S. K. Langley, D. P. Wielechowski, V. Vieru, N. F. Chilton, B. Moubaraki, B. F. Abrahams, L. F. Chibotaru and K. S. Murray, *Angewandte Chemie International Edition*, 2013, **52**, 12014-12019.
76. S. K. Langley, C. Le, L. Ungur, B. Moubaraki, B. F. Abrahams, L. F. Chibotaru and K. S. Murray, *Inorganic Chemistry*, 2015, **54**, 3631-3642.
77. K. R. Vignesh, S. K. Langley, K. S. Murray and G. Rajaraman, *Chemistry – A European Journal*, 2017, **23**, 1654-1666.
78. S. K. Langley, C. M. Forsyth, B. Moubaraki and K. S. Murray, *Dalton Transactions*, 2015, **44**, 912-915.
79. E. Moreno Pineda, N. F. Chilton, F. Tuna, R. E. P. Winpenny and E. J. L. McInnes, *Inorganic Chemistry*, 2015, **54**, 5930-5941.
80. K. R. Vignesh, S. K. Langley, K. S. Murray and G. Rajaraman, *Inorganic Chemistry*, 2017, **56**, 2518-2532.
81. L. Chatelain, J. P. S. Walsh, J. Pécaut, F. Tuna and M. Mazzanti, *Angewandte Chemie International Edition*, 2014, **53**, 13434-13438.
82. L. Chatelain, J. Pécaut, F. Tuna and M. Mazzanti, *Chemistry – A European Journal*, 2015, **21**, 18038-18042.
83. L. Chatelain, F. Tuna, J. Pecaut and M. Mazzanti, *Dalton Transactions*, 2017, **46**, 5498-5502.

84. V. Mougel, L. Chatelain, J. Hermle, R. Caciuffo, E. Colineau, F. Tuna, N. Magnani, A. de Geyer, J. Pécaut and M. Mazzanti, *Angewandte Chemie International Edition*, 2014, **53**, 819-823.
85. L. Chatelain, F. Tuna, J. Pecaut and M. Mazzanti, *Chemical Communications*, 2015, **51**, 11309-11312.
86. J. D. Rinehart, M. Fang, W. J. Evans and J. R. Long, *Journal of the American Chemical Society*, 2011, **133**, 14236-14239.
87. J. D. Rinehart, M. Fang, W. J. Evans and J. R. Long, *Nat Chem*, 2011, **3**, 538-542.
88. C. A. Gould, L. E. Darago, M. I. Gonzalez, S. Demir and J. R. Long, *Angewandte Chemie*, 2017, DOI: 10.1002/ange.201612271, n/a-n/a.
89. S. Demir, J. M. Zadrozny, M. Nippe and J. R. Long, *Journal of the American Chemical Society*, 2012, **134**, 18546-18549.
90. S. Demir, M. Nippe, M. I. Gonzalez and J. R. Long, *Chemical Science*, 2014, **5**, 4701-4711.
91. J. D. Rinehart and J. R. Long, *Chemical Science*, 2011, **2**, 2078-2085.
92. K. R. Meihaus and J. R. Long, *Journal of the American Chemical Society*, 2013, **135**, 17952-17957.
93. L. Ungur and L. F. Chibotaru, *Physical Chemistry Chemical Physics*, 2011, **13**, 20086-20090.
94. N. F. Chilton, *Inorganic Chemistry*, 2015, **54**, 2097-2099.
95. N. F. Chilton, C. A. P. Goodwin, D. P. Mills and R. E. P. Winpenny, *Chemical Communications*, 2015, **51**, 101-103.
96. R. Layfield, F.-S. Guo, B. Day, Y.-C. Chen, M.-L. Tong and A. Mansikamäkki, *Angewandte Chemie International Edition*, DOI: 10.1002/anie.201705426, n/a-n/a.
97. C. A. P. Goodwin, F. Ortu, D. Reta, N. F. Chilton and D. P. Mills, *Nature*, 2017, **548**, 439.
98. J.-L. Liu, Y.-C. Chen, Y.-Z. Zheng, W.-Q. Lin, L. Ungur, W. Wernsdorfer, L. F. Chibotaru and M.-L. Tong, *Chemical Science*, 2013, **4**, 3310-3316.
99. Y.-C. Chen, J.-L. Liu, L. Ungur, J. Liu, Q.-W. Li, L.-F. Wang, Z.-P. Ni, L. F. Chibotaru, X.-M. Chen and M.-L. Tong, *Journal of the American Chemical Society*, 2016, **138**, 2829-2837.
100. J. Liu, Y.-C. Chen, J.-L. Liu, V. Vieru, L. Ungur, J.-H. Jia, L. F. Chibotaru, Y. Lan, W. Wernsdorfer, S. Gao, X.-M. Chen and M.-L. Tong, *Journal of the American Chemical Society*, 2016, **138**, 5441-5450.
101. Y.-S. Ding, N. F. Chilton, R. E. P. Winpenny and Y.-Z. Zheng, *Angewandte Chemie International Edition*, 2016, **55**, 16071-16074.
102. Y.-C. Chen, J.-L. Liu, W. Wernsdorfer, D. Liu, L. F. Chibotaru, X.-M. Chen and M.-L. Tong, *Angewandte Chemie*, 2017, **129**, 5078-5082.
103. R. P. Feynman, *Foundations of Physics*, 1986, **16**, 507-531.
104. T. D. Ladd, F. Jelezko, R. Laflamme, Y. Nakamura, C. Monroe and J. L. O/'Brien, *Nature*, 2010, **464**, 45-53.
105. C. H. Bennett and D. P. DiVincenzo, *Nature*, 2000, **404**, 247-255.
106. M. Nielsen and I. Chuang, *Quantum Computation and Quantum Information (Cambridge Series on Information and the Natural Sciences)*, Cambridge University Press, 2004.
107. F. Troiani and M. Affronte, *Chemical Society Reviews*, 2011, **40**, 3119-3129.
108. G. Aromi, D. Aguila, P. Gamez, F. Luis and O. Roubeau, *Chemical Society Reviews*, 2012, **41**, 537-546.
109. C. P. Williams, *Explorations in Quantum Computing*, Springer Publishing Company, Incorporated, 2008.
110. J. I. Cirac and P. Zoller, *Physical Review Letters*, 1995, **74**, 4091-4094.
111. C. Monroe, D. M. Meekhof, B. E. King, W. M. Itano and D. J. Wineland, *Physical Review Letters*, 1995, **75**, 4714-4717.
112. T. Monz, K. Kim, W. Hänsel, M. Riebe, A. S. Villar, P. Schindler, M. Chwalla, M. Hennrich and R. Blatt, *Physical Review Letters*, 2009, **102**, 040501.
113. N. A. Gershenfeld and I. L. Chuang, *Science*, 1997, **275**, 350-356.
114. E. Knill, R. Laflamme and G. J. Milburn, *Nature*, 2001, **409**, 46-52.

115. A. Politi, J. C. F. Matthews and J. L. O'Brien, *Science*, 2009, **325**, 1221-1221.
116. D. Loss and D. P. DiVincenzo, *Physical Review A*, 1998, **57**, 120-126.
117. M. V. G. Dutt, L. Childress, L. Jiang, E. Togan, J. Maze, F. Jelezko, A. S. Zibrov, P. R. Hemmer and M. D. Lukin, *Science*, 2007, **316**, 1312-1316.
118. M. Ansmann, H. Wang, R. C. Bialczak, M. Hofheinz, E. Lucero, M. Neeley, A. D. O'Connell, D. Sank, M. Weides, J. Wenner, A. N. Cleland and J. M. Martinis, *Nature*, 2009, **461**, 504-506.
119. L. DiCarlo, J. M. Chow, J. M. Gambetta, L. S. Bishop, B. R. Johnson, D. I. Schuster, J. Majer, A. Blais, L. Frunzio, S. M. Girvin and R. J. Schoelkopf, *Nature*, 2009, **460**, 240-244.
120. M. N. Leuenberger and D. Loss, *Nature*, 2001, **410**, 789-793.
121. K. Saeedi, S. Simmons, J. Z. Salvail, P. Dluhy, H. Riemann, N. V. Abrosimov, P. Becker, H.-J. Pohl, J. J. L. Morton and M. L. W. Thewalt, *Science*, 2013, **342**, 830-833.
122. D. P. DiVincenzo, *Fortschritte der Physik*, 2000, **48**, 771-783.
123. M. Affronte, *Journal of Materials Chemistry*, 2009, **19**, 1731-1737.
124. J. Lehmann, A. Gaita-Ariño, E. Coronado and D. Loss, *Nature Nanotechnology*, 2007, **2**, 312.
125. J. Ferrando-Soria, *Magnetochemistry*, 2016, **2**, 36.
126. E. J. L. McInnes, G. A. Timco, G. F. S. Whitehead and R. E. P. Winpenny, *Angewandte Chemie International Edition*, 2015, **54**, 14244-14269.
127. G. A. Timco, T. B. Faust, F. Tuna and R. E. P. Winpenny, *Chemical Society Reviews*, 2011, **40**, 3067-3075.
128. J. S. Uber, M. Estrader, J. Garcia, P. Lloyd-Williams, A. Sadurní, D. Dengler, J. van Slageren, N. F. Chilton, O. Roubeau, S. J. Teat, J. Ribas-Ariño and G. Aromí, *Chemistry – A European Journal*, 2017, **23**, 13648-13659.
129. D. Aguilà, L. A. Barrios, V. Velasco, O. Roubeau, A. Repollés, P. J. Alonso, J. Sesé, S. J. Teat, F. Luis and G. Aromí, *Journal of the American Chemical Society*, 2014, **136**, 14215-14222.
130. F. Luis, A. Repolles, M. J. Martinez-Perez, D. Aguila, O. Roubeau, D. Zueco, P. J. Alonso, M. Evangelisti, A. Camon, J. Sese, L. A. Barrios and G. Aromi, *Phys. Rev. Lett.*, 2011, **107**.
131. Y. H. Lan, S. Klyatskaya, M. Ruben, O. Fuhr, W. Wernsdorfer, A. Candini, V. Corradini, A. L. Rizzini, U. del Pennino, F. Troiani, L. Joly, D. Klar, H. Wende and M. Affronte, *J. Mater. Chem. C*, 2015, **3**, 9794-9801.
132. E. D. Doidge, J. W. Roebuck, M. R. Healy and P. A. Tasker, *Coordination Chemistry Reviews*, 2015, **288**, 98-117.
133. G. Aromí, P. Gamez and J. Reedijk, *Coordination Chemistry Reviews*, 2008, **252**, 964-989.
134. T. D. Roberts, M. A. Little, L. J. Kershaw Cook and M. A. Halcrow, *Dalton Transactions*, 2014, **43**, 7577-7588.

CHAPTER II

TOPOLOGY AND SITE SELECTIVITY IN HYDROXO-β-DIKETONATO COUPLED PAIRS OF 3*d* DIMERS

2.1. Introduction

In the pursuit of novel multifunctional materials, inexhaustible spring of tools is the field of coordination chemistry, a judicious matrimony between versatile organic scaffolds and diverse physico-chemical properties of transition and rare-earth metals. One of the modern challenges within this field of research consists of finding ways how to implement sophisticatedly engineered ligands in design of metal-organic assemblies with predetermined functions and topologies. Our group is successfully addressing this challenge with design of polydentate ligands from *n*-β-diketone family which can be easily prepared by Claisen condensation between organic compounds bearing ester and ketone functional groups (1≤n≤ 3, Scheme 2.1).[1-3]

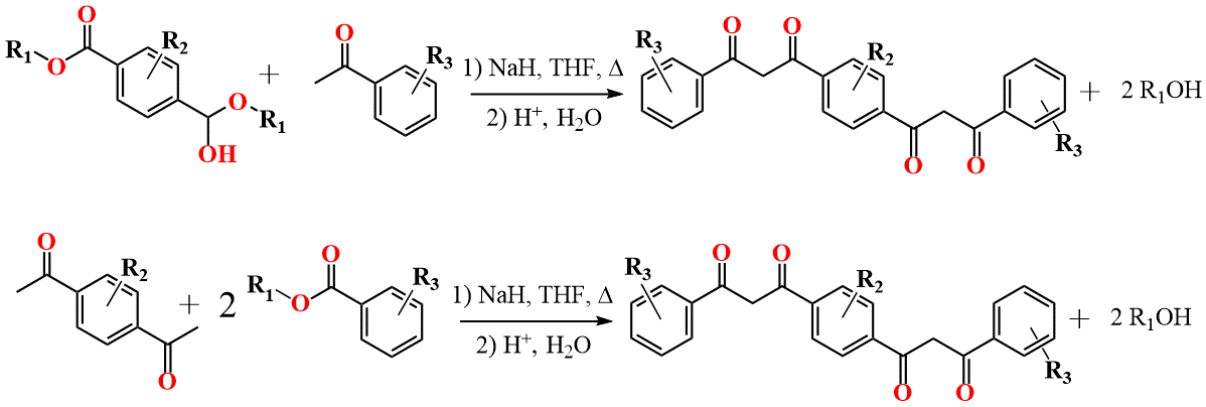

Scheme 2.1. General preparation of *bis*-β-diketone ligands (*n*=2) by Claisen condensation from its precursors.

Such ease of functionalization from unlimited source of possible building blocks secures direct means of tuning rigidity, electronic and steric nature of β-diketone derivatives, as well as the possibility of shaping the number, size, separation and distribution of coordination pockets within them. Hence, heterocyclic ketone or ester precursors enhance the chelating ability of resulting β-diketone ligands towards transition metals and lanthanides by generating additional ketonato-heteroatom binding sites and enabling formation of linear arrays of metal ions.[1, 4, 5] Similarly, by varying the length and substitution at spacer moiety between two β-diketone pockets, topology of formed metal-organic assemblies can be tuned between weakly coupled molecular cluster pairs[6-8], metallohelicates[9, 10], metallomacrocycles[11-14] or cage clusters.[1, 3, 15, 16] Moreover, prudent choice of bifunctional building blocks with additional groups such as acidic -OH and -COOH will affect the charge of

resulting β-diketone ligands in deprotonated form and expand its possible coordination modes, topologies and charges of formed clusters. Use of aromatic building blocks ensures significant rigidity to the structure of ligands due to extended conjugation with 1,3-diketone moieties which spans over entire organic framework. Since β-diketone ligands can coexist in solution in keto and enol form (tautomery), such conjugation can often shift the equilibrium towards more stable enol tautomer, both in solution and solid state (Scheme 2.2).

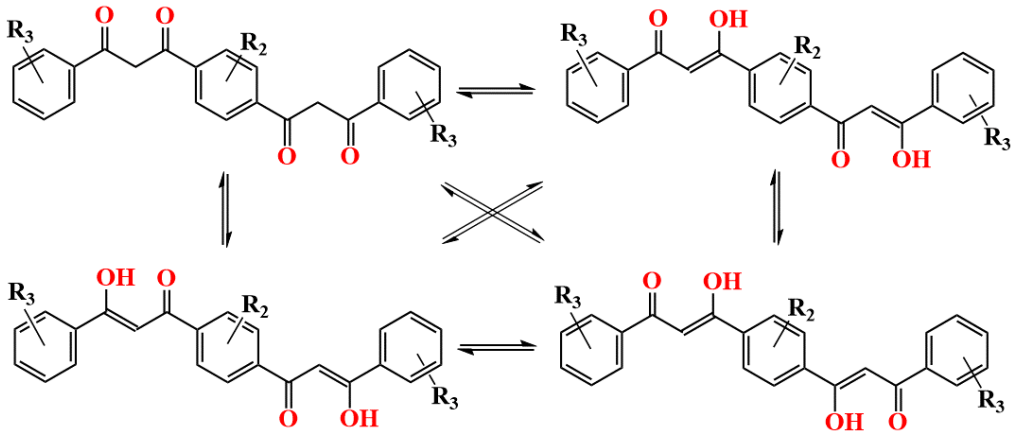

Scheme 2.2. Keto-enol equilibrium in *bis*-β-diketone ligands.

Of numerous derivatives, *bis*-β-diketone ligands functionalised with phenol spacer or wing moieties contain groups of acidic hydrogen atoms with different p*K*a values which can be selectively removed by addition of adequately strong base or different equivalents of very strong bases. By this virtue, this class of ligands was used to generate different *bis*-chelated dinuclear and tetranuclear clusters with predesigned topology and very selective site distribution imposed by ligand-based geometric constraints (Scheme 2.3).[6, 7] More precise, wider β-diketone coordination pockets chelate perfectly six-coordinate metal ions, while narrower phenolato-ketonato coordination pockets cause pyramidalization of coordination geometry towards distorted square-pyramidal or trigonal-bipyramidal (Scheme 2.3). Subsequently, described site preference was successfully employed in selective construction of heterometallic compounds with unique distribution of metal ions within the clusters due to crystal field energy effects.[6, 7]

Continuing this line of research, new flexible β-diketone ligand, 1,6-di(2-hydroxyphenyl)-1,3,4,6-hexanetetrone (H_4L1), was designed to hold two directly connected β-diketone-phenol moieties. Idea behind such design was to exploit this ligand in assembly of coupled homometallic and heterometallic pairs of 3*d* dimers. Additionally, we decided to study

potential site selectivity imposed by only one chelating ligand, enforcing the *trans* disposition of its coordination pockets with appropriate metal-ligand stoichiometry. Following sections of this chapter will report coordination abilities of H_4L1 towards late 3*d* transition metals (Co^{II}, Ni^{II}, Cu^{II}, Zn^{II}) as well as the structures and magnetic properties of generated homometallic dinuclear $[M_2(H_2L1)(py)_8](ClO_4)_2$ and tetranuclear $([M_4(L)(OH)_2(py)_{8\text{-}10}](ClO_4)_2$ clusters, together with derived heterometallic analogues $[(M1M2)_2(L1)(OH)_2(py)_{10}](ClO_4)_2$.

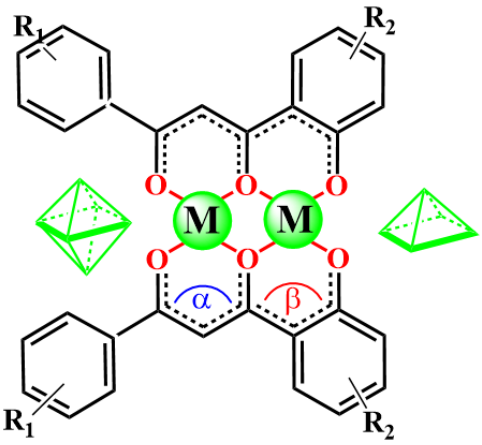

Scheme 2.3. Two types of coordination pockets within homometallic [MM] dimer chelated by two β-diketone ligands enriched with phenolic wings. C–C–C angles α, β (α>β) reflect different size of corresponding chelating sites and imposed coordination geometry within them.

2.2. Design, synthesis and characterisation of 1,6-di(2-hydroxyphenyl)-1,3,4,6-hexanetetrone, H_4L1

New β-diketone ligand H_4L1, designed to embody two connected phenol-β-diketone coordination pockets, was prepared by Claisen condensation between dimethyl oxalate and 2-hydroxyacetophenone (Scheme 2.4).

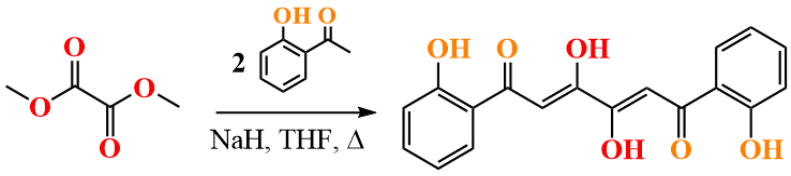

Scheme 2.4. Preparation of the *bis*-β-diketone ligand H_4L1 from its precursors.

Purity and composition of isolated ligand were confirmed by ^1H NMR spectroscopy, mass spectrometry and elemental analysis (Appendix II, Figs. II.A1 and II.A2). ^1H NMR

spectroscopy confirmed existence of enolic form of the ligand in deuterated chloroform solution which was also found to be dominant also in the solid state structure. Single crystal diffraction revealed that H_4L1 crystallises in monoclinic $P2_1/c$ space group with one half of the molecule in the asymmetric unit (Table II.A1, A2). Remaining half of the structure is generated from the crystallographically independent atoms by the symmetry operation over an inversion centre, while two molecules define the unit cell content. Apart from the enolic form, solid state structure of H_4L1 features *trans* conformation, with two phenol-β-diketone moieties facing opposite directions (Figure 2.1).

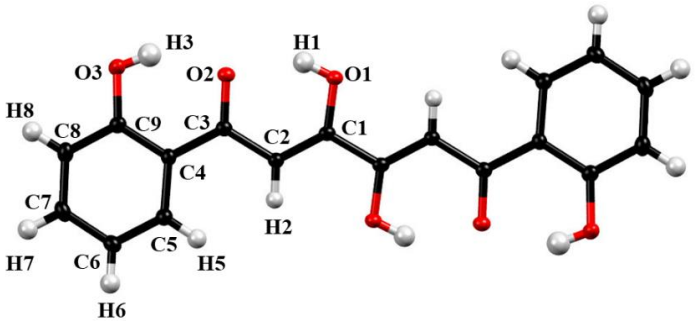

Figure 2.1: Molecular structure of **H_4L1** emphasizing the *trans*-orientation of its connected phenol-β-diketone coordination moieties. Only crystallographically independent atoms are labelled while the other half of molecule is generated by the symmetry operation over an inversion centre. All displacement ellipsoids are drawn at 50% probability.

Described orientation maximises the rich network of intra- and intermolecular hydrogen bonding interactions and increases stability of crystal structure (Figure 2.2). In four intramolecular hydrogen bonds, carbonyl oxygen atoms (O2) interact as hydrogen acceptors with the neighbouring enol (O1) and phenol (O3) OH groups (purple contacts, Figure 2.2, Table II.A3). Additionally, each carbonyl oxygen atom of H_4L1 interacts in the same way with two enol OH groups from the neighbouring molecules in the lattice, generating eight intermolecular hydrogen bonding interactions per ligand (blue contacts, Figure 2.2-A). Such supramolecular arrangement is additionally supported with π···π interactions between the aromatic backbone of H_4L1 which are ordering hydrogen bonded sheets of the molecules into stacked layers (Figure 2.2-B).

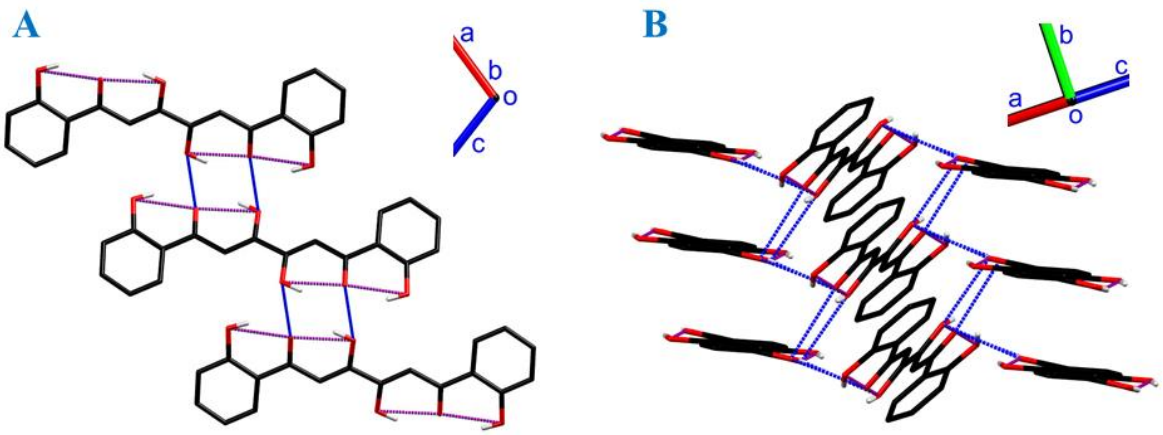

Figure 2.2: Crystal packing of H_4L1 featuring the intra- and intermolecular hydrogen bonding interactions (A, purple and blue contacts, respectively) and π···π stacked layers of molecules. Hydrogen atoms taking part in the interactions are shown, the rest is omitted for clarity.

Rigidity of solid state structure of this ligand is reduced in a solution where free rotation around the single bond connecting two identical ligating sets permits two different conformations and related coordination modes. In *trans* conformation, two coordination pockets are facing opposite directions and define ideal environment to generate a pair of discrete 3*d* monomers or dimers using partially or fully deprotonated ligand (Scheme 2.5, A and A1, respectively). On the other hand, *cis* conformation of the ligand maximises its chelating ability and can be used to generate molecular arrays of ions (Scheme 2.5, B) or discrete trimers of 3*d* monomers or dimers which can encapsulate additionally larger ions (Na^+, 4*f*-Ln^{3+}) into central crown-ether like O_6 cavity (Scheme 2.5, C and C1). Ideally, strict metal-ligand ratio of the reaction mixture should control desired ligand conformation and determine corresponding topology of formed cluster. Following sections of this chapter will exploit this premise through designed construction of homometallic and heterometallic coupled pairs of discrete 3*d* dimers.

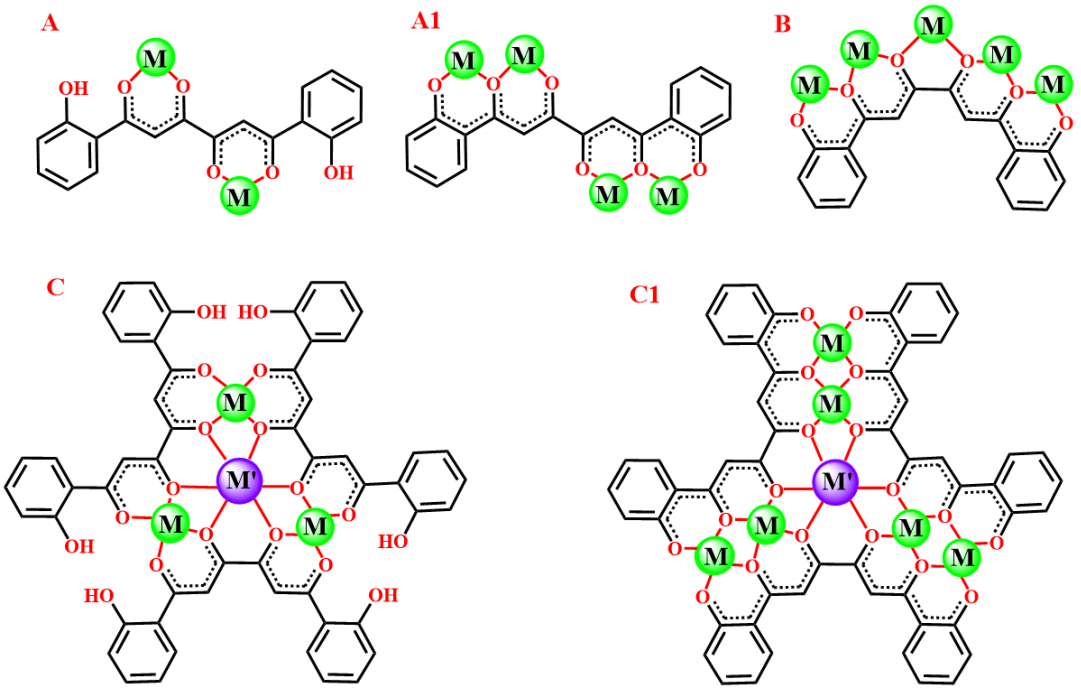

Scheme 2.5. Possible coordination modes and conformations of partially ($[H_2L1]^{2-}$, A and C) and fully deprotonated ($[L1]^{4-}$, A1, B and C1) ligand H_4L1.

2.3. Homometallic $[M_2(H_2L1)(py)_8](ClO_4)_2$ and $[(MM)_2(OH)_2(L1)(py)_x](ClO_4)_2$ coordination compounds

2.3.1. Design, synthesis and structure of $[M_2(H_2L1)(py)_8](ClO_4)_2$ ($M=Co^{II}$, Ni^{II}, Zn^{II})

To force *trans* conformation of H_4L1 and overcome its full chelating capacity, initial set of reactions was tried out in pyridine with pair-impair metal-ligand ratio (2:1) involving partially deprotonated $(H_2L1)^{2-}$ and perchlorate salts of heavier 3*d* metal ions (Co^{II}, Ni^{II}, Cu^{II}, Zn^{II}). Idea behind such approach was that deprotonated β-diketonato coordination pocket will chelate two divalent 3*d* ions, while pyridine as solvent will prevent possible polymerisation of this building block to 1-D polymer. Perchlorate salts were used because of the relatively large anion size which can nicely compensate the double positive charge of formed complex cation and match with its size to improve the crystallisation. Additionally, relatively inert coordination abilities of perchlorate anions secure the possibility of generating isostructural series of compounds, regardless the nature of employed metal ions.[17]

This approach proved to be very successful for Co^{II}, Ni^{II} and Zn^{II}, while in case of Cu^{II} different pyridine complexes of $Cu(ClO_4)_2$ were found less soluble species in equilibrium with desired compound:

$$2\ M(ClO_4)_2 + H_4L1 + 2\ TBAOH + 8\ py \longrightarrow [M_2(H_2L1)(py)_8](ClO_4)_2 + 2\ TBAClO_4 + 2\ H_2O$$

M=Co^{II} (**1**), Ni^{II} (**2**) and Zn^{II} (**3**)

Single crystal X-ray diffraction confirmed the existence of predicted, isostructural $[M_2(H_2L1)(py)_8]^{2+}$ complexes (M=Co^{II} (**1**), Ni^{II} (**2**), Zn^{II} (**3**)) which crystallize in triclinic *P*-1 space group with two pyridine molecules as lattice solvent (Tables II.A4, II.A7, II.A8, II.A9). Defined content of asymmetric unit corresponds to whole unit cell for compound **2**, while unit cells of compounds **1** and **3** include two asymmetric units. Looking at the structure of $[M_2(H_2L1)(py)_8]^{2+}$ cations, two hexacoordinate M^{II} centers are chelated equatorially by two *trans* orientated β-diketonato coordination pockets of partially deprotonated $[H_2L1]^{2-}$ (μ_2-$[H_2L1]^{2-}$, Figure 2.3). Remaining coordination sphere around M^{II} is completed by four pyridine co-ligands, two in equatorial plane and remaining two at the axial positions. Hence, both crystallographically independent M^{II} ions are located within octahedral O_2N_4 crystal field (equatorial O_2N_2). Intramolecular distance between the M^{II} sites alters in order 7.217(1) Å (**1**), 7.154 Å (**2**) and 7.254 Å (**3**), reflecting nicely small deviations from coplanarity of equatorial planes around the perfectly embedded (d<0.03 Å) Co^{II}, Ni^{II} and Zn^{II} ions (intersecting angles 1.94° (**1**), 1.00° (**2**) and 2.06°(**3**)). Detailed insights into M^{II} coordination environment reveals average axial M−N bond of 2.179 Å (**1**), 2.110 Å (**2**) and 2.198 Å (**3**), which are slightly elongated in comparison with equatorial bonds averaged at 2.114 Å (**1**), 2.081 Å (**2**) and 2.141 Å (**3**) (Tables II.A7-A9). In both cases, bond lengths increase in order Ni<Co<Zn, following similar trend as Shannon-Prewitt crystal radii of six-coordinate M^{II} (Figure 2.4).[18] Same conclusion can be extracted analysing the average bond distances of all six bonds around M^{II} ions (2.136 Å (**1**), 2.091 Å (**2**) and 2.160 Å (**3**)). Hydrogen bonding between protonated phenol wings (C–H···O dimers) of complex cations $[M_2(H_2L1)(py)_8]^{2+}$ organizes 1-D chains of parallel molecules which extend into 2-D layers through C–H···O and anion···π interactions with perchlorate. Finally, third dimension of the crystal structure is generated via C–H···π contacts between axial and equatorial pyridine ligands or axial pyridine ligands and $[H_2L1]^{2-}$. Such supramolecular arrangement leaves only small voids for

lattice pyridine molecules, stabilized in the structure by C–H···N, C–H···O and C–H···π contacts with the $[M_2(H_2L1)(py)_8](ClO_4)_2$ core.

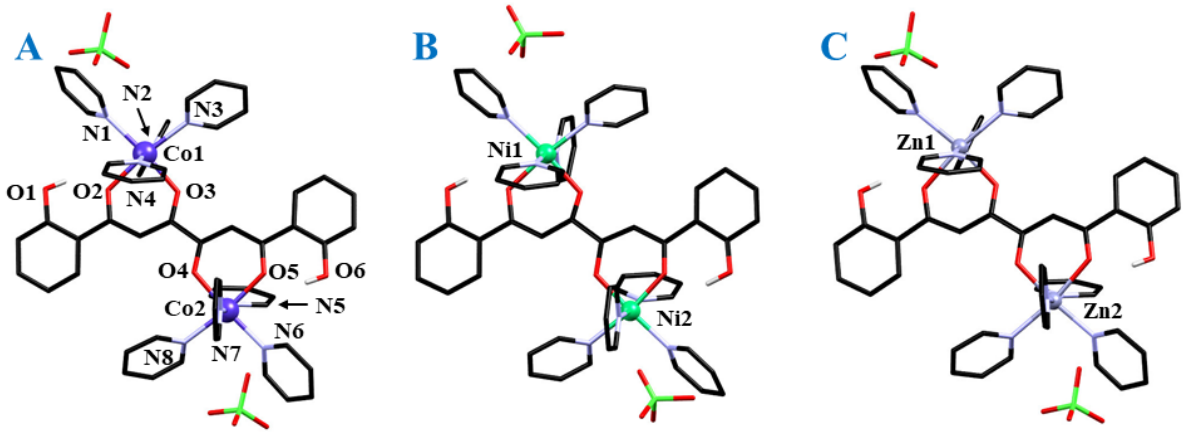

Figure 2.3: Molecular structures and labelling scheme of $[Co_2(H_2L1)(py)_8](ClO_4)_2$ (**1**, A), $[Ni_2(H_2L1)(py)_8](ClO_4)_2$ (**2**, B), and $[Zn_2(H_2L1)(py)_8](ClO_4)_2$ (**3**, C). Labelling scheme of crystallographically independent heteroatoms indicated for the structure of **1** is identical for all compounds. Hydrogen atoms affecting the charge of cluster are shown, the rest is omitted for clarity.

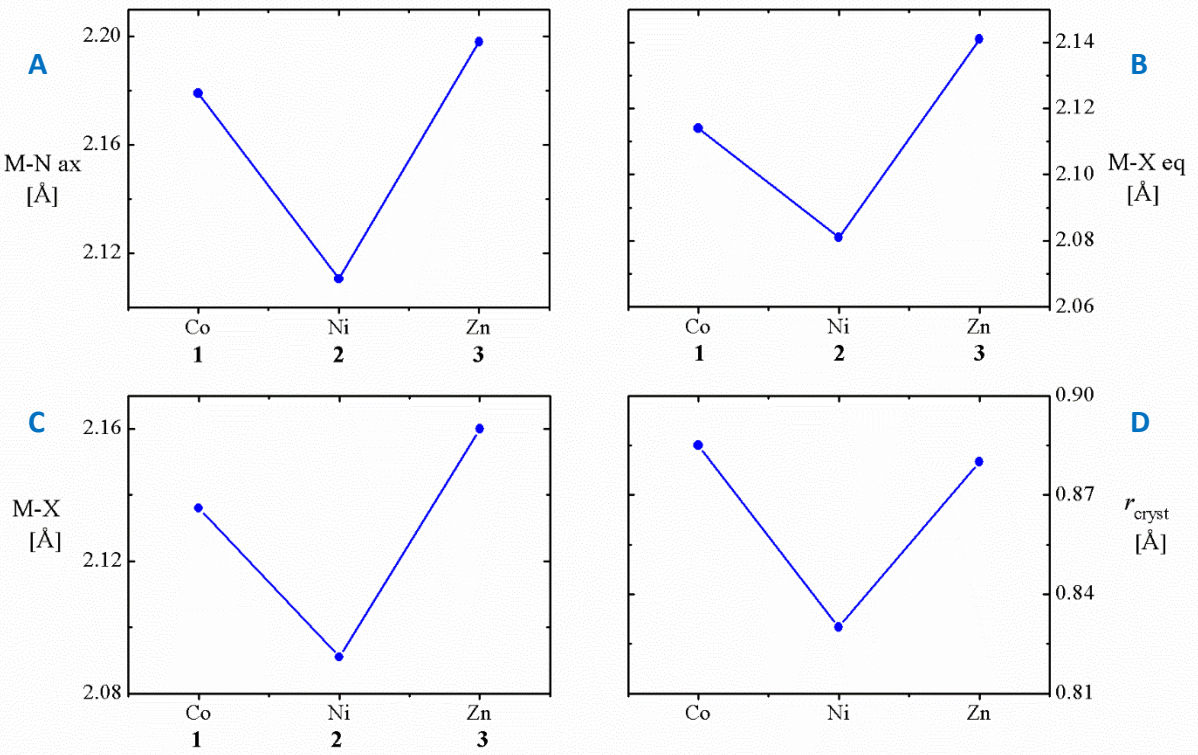

Figure 2.4: Bonding geometry of hexacoordinate M^{II} centres in compounds **1**-**3**. A) Average axial M–N bond distances. B) Average equatorial M–X bond distances. C) Average distance of all M–X bonds. D) Shannon-Prewitt crystal and ionic radii of elements.

2.3.2. Design, synthesis and structure of homometallic $[(MM)_2(OH)_2(L1)(py)_n](ClO_4)_2$ (M=Co^{II}, Ni^{II}, Cu^{II}, Zn^{II})

Following the success of designed pair-impair strategy in a construction of simple dimeric $[M_2(H_2L1)(py)_8](ClO_4)_2$ species, complexity of homometallic clusters was additionally increased by reacting fully deprotonated ligand $[L1]^{4-}$ and two equivalents of hydroxide co-ligand with four equivalents of metal ions in pyridine. Idea behind this approach was to saturate four chelating coordination pockets of $[L1]^{4-}$ with four divalent M^{2+} ions, generating two pairs of bridged [MM] dimers in $[M_4(L1)]^{4+}$ (Scheme 2.5-B). Furthermore, two additional hydroxide co-ligands were added with an intention to increase the stability of such assembly by reducing its positive charge and by offering additional bridging node within each dimer which should increase the strength of intradimer coupling between the spin carriers. Such approach proved to be successful, allowing the preparation of four homometallic clusters formulated as $[(MM)_2(L1)(OH)_2(py)_n](ClO_4)_2$ (**4**-**7**, M=Co^{II}, Ni^{II}, Cu^{II} and Zn^{II}, respectively):

$$4\ M(ClO_4)_2 + H_4L1 + 6\ TBAOH + n\ py \longrightarrow [(MM)_2(L1)(OH)_2(py)_n](ClO_4)_2 + 6\ TBAClO_4 + 4\ H_2O$$

M=Co^{II} (**4**), Ni^{II} (**5**) and Zn^{II} (**7**) n=10

M=Cu^{II} (**6**) n=8

Single crystal X-ray diffraction confirmed that those compounds are not isostructural due to variable composition and symmetry of complex cation $[(MM)_2(L1)(OH)_2(py)_n]^{2+}$ and variable lattice solvent content (Tables II.A4-5). Unit cells of compounds **4** (M=Co^{II}) and **5** (M=Ni^{II}) belong to monoclinic *I*2/*a* and $P2_1/n$ space groups, respectively, and include four equivalents of ionic compound $[(MM)_2(L1)(OH)_2(py)_{10}](ClO_4)_2$ accompanied with four or three pyridine molecules as lattice solvents, respectively. On the other hand, unit cell of compounds **6** (M=Cu^{II}) and **7** (M=Zn^{II}) belongs to triclinic *P*-1 space group. Unit cell of compound **6** includes two formulae units of ionic compound $[(CuCu)_2(L1)(OH)_2(py)_8](ClO_4)_2$, four lattice pyridine molecules and two water molecules, while unit cell of compound **7** is defined only by one formula unit of ionic compound $[(ZnZn)_2(L1)(OH)_2(py)_{10}](ClO_4)_2$. Topology of $[(MM)_2(L1)(OH)_2(py)_n]^{2+}$ complexes include two pairs of [MM] dimers chelated within completely deprotonated and *trans* orientated phenolato-β-diketonato coordination pocket (μ_4-$[L1]^{4-}$ coordination mode) and bridged additionally by one hydroxide co-ligand (Figure 2.5). Structural differences between the complex cations arise from different number of

pyridine ligands which complete the first coordination sphere around metals. Hence, structure of homometallic $[(MM)_2(L1)(OH)_2(py)_{10}]^{2+}$ (M=Co^{II}, Ni^{II}, Zn^{II}) holds two five-coordinate peripheral M^{II} ion within square-pyramidal O_3N_2 crystal field, while two inner M^{II} ions reside in octahedral O_3N_3 crystal field within the β-diketonato pocket (Figure 2.5). Both metal centres of [MM] dimers are surrounded equatorially by O_3N crystal field, meaning that axial bonds include one or two pyridine ligands for pentacoordinate or hexacoordinate site, respectively. In contrast, structure of homometallic $[(CuCu)_2(L1)(OH)_2(py)_8]^{2+}$ complex holds four pentacoordinate Cu^{II} centres which reside within square-pyramidal O_3N_2 crystal field (equatorial O_3N crystal field). Two [MM] pairs in structures of **5** and **6** are crystallographycally inequivalent, while identical pairs of [CoCo] and [ZnZn] in structures of **4** and **8**, respectively, are related by symmetry operation over an inversion centre. Intradimer distance between the adjacent M^{II} sites alters in order 3.1608(9) Å (**4**), 3.089 Å (**5**), 3.0181 Å (**6**), 3.1763(4) Å (**7**), while the intramolecular distance between the inner M^{II} sites of dimers measures 7.266(1) Å (**4**), 7.217(1) Å (**5**), 7.069(2) Å (**6**) and 7.3534(9) Å (**7**). Bonding details around the inner M^{2+} centre reveal that average axial M−N bond (2.191 Å (**4**), 2.133 Å (**5**), 2.294 Å (**6**), 2.2393 Å (**7**)) are slightly elongated in comparison with equatorial bonds which are averaged at 2.069 Å (**4**), 2.052 Å (**5**) 1.956 Å (**6**) and 2.0834 Å (**7**) (Tables II.A10-13). Such distribution indicates that axial M–N bond distances decrease in order Ni<Co<Zn<Cu, while equatorial bonds decrease in order Cu<Ni<Co<Zn, similarly as Irving-Williams stability trend for M^{II} complexes and Shannon-Prewitt crystal radii of six-coordinate M^{II} (Figure II.A3, Table II.A20).[18] The latter can be also found analysing the average bond distances at the inner M^{II} sites which are averaged at 2.109 Å (**4**), 2.079 Å (**5**) 2.023 Å (**6**) and 2.135 Å (**7**). Shorter distances and more pronounced differences in bonding are observed at peripheral pentacoordinate M(II) site. Axial M−N bonds measure 2.115 Å (**4**), 2.017 Å (**5**), 2.221 Å (**6**) and 2.093 Å (**7**), following the trend Ni<Zn<Co<Cu. On the other hand, average equatorial bond distance (2.038 Å (**4**), 2.011 Å (**5**) 1.958 Å (**6**) and 2.046 Å (**7**)) and average of all bonds (2.053 Å (**4**), 2.012 Å (**5**) 2.011 Å (**6**) and 2.056 Å (**7**)) increase in order Cu<Ni<Co≈Zn (Figure II.A3). Such differences in bonding indicate large distortion of square-pyramidal geometry around peripheral M^{II} which can be quantified by angular parameter τ≈0.55 (**4**), 0.10 (**5**), 0.14 (**6**), 0.27 (**7**), emphasizing that Co^{II} and Zn^{II} site deviate the most from ideal geometry (τ=0).[19, 20] Looking at the positioning of metal centres within the equatorial donor sets, octahedral Co^{II}, Ni^{II} and Zn^{II} ions are almost perfectly embedded in ligand plane (d<0.05 Å),

while square-pyramidal inner Cu^{II} (d≈0.16 Å) and peripheral M^{II} ions (d≈0.49 Å (Co^{II}), 0.35 Å (Ni^{II}), 0.32 Å (Cu^{II}), 0.47 Å (Zn^{II})) are pulled outside the respective plane towards the axial pyridine ligand (Figure II.A4). Equatorial planes of inner M^{II} sites are parallel in compounds **4**, **7** (symmetry related atoms) and **6** (Θ=0.49°), while in **5** they intersect under angle of 17.7° (Table II.A20). Similarly, equatorial planes of adjacent peripheral and inner M^{II} sites are intersecting under angle of 20.8° (**4**), 4.6 and 19.1° (**5**), 20.2 and 22.1° (**6**) and 12.2° (**7**). Crystal packing of homometallic $[(MM)_2(L1)(OH)_2(py)_n]^{2+}$ complexes is mostly organized through perchlorate anions which act as hydrogen acceptors in numerous O–H···O and C–H···O interactions with bridging hydroxide, pyridine co-ligands and lattice solvents. Additionally, C–H···O, C–H···N, C–H···π and π···π contacts between the aromatic moieties of complex cations provide additional stability to densely packed crystal structure, generating only few voids in which lattice pyridine and/or water molecules reside.

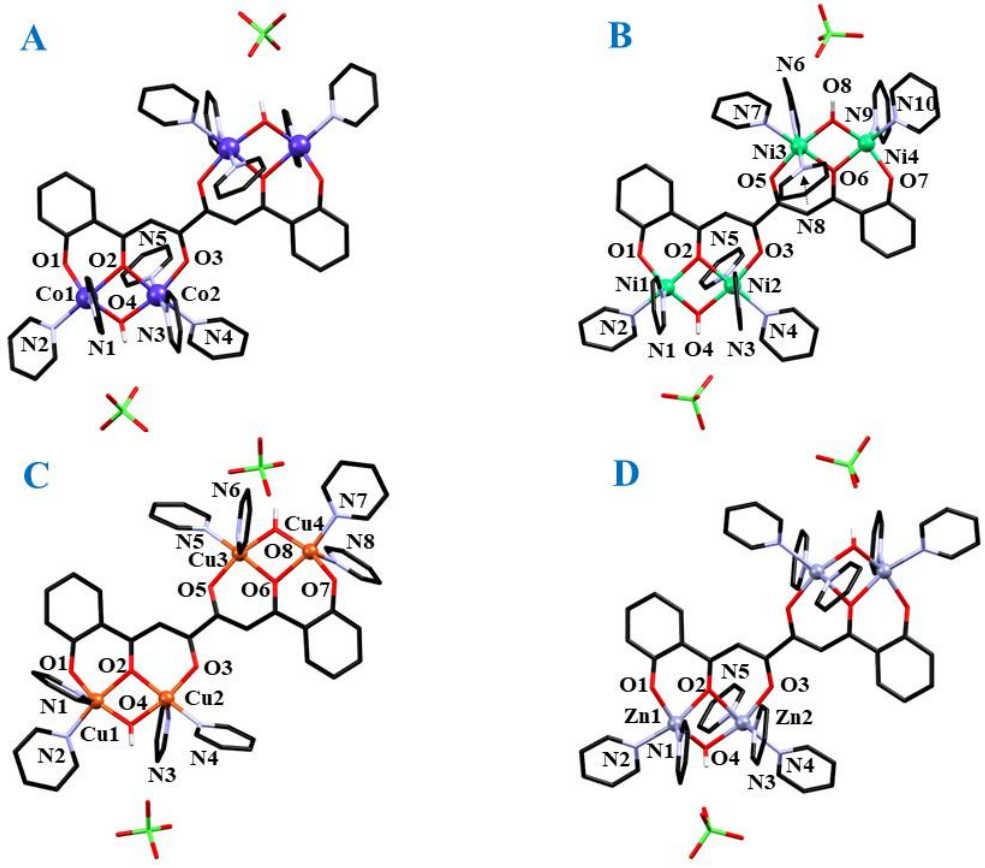

Figure 2.5: Molecular structure and labelling scheme of $[(CoCo)_2(L1)(OH)_2(py)_{10}](ClO_4)_2$ (**4**, A), $[(NiNi)_2(L1)(OH)_2(py)_{10}](ClO_4)_2$ (**5**, B), $[(CuCu)_2(L1)(OH)_2(py)_8](ClO_4)_2$ (**6**, C) and $[(ZnZn)_2(L1)(OH)_2(py)_{10}](ClO_4)_2$ (**7**, D). Only crystallographically independent heteroatoms are labelled. Hydrogen atoms affecting the charge of cluster are shown, the rest is omitted for clarity.

2.4. Heterometallic $[(M1M2)_2(L1)(OH)_2(py)_{10}](ClO_4)_2$ coordination compounds

2.4.1. Design, synthesis and structure of heterometallic $[(CuM2)_2(OH)_2(L1)(py)_{10}](ClO_4)_2$ (M2=Co^{II}, Ni^{II}, Zn^{II})

As indicated from the homometallic $[(MM)_2(L1)(OH)_2(py)_n](ClO_4)_2$ series, geometrical restraints of two coordination pockets within single $[L1]^{4-}$ ligand are enough to impose different crystal field environment around chelated metals within them. Hence, narrower biting angle of external phenolato-ketonato binding site dictates presence of five-coordinate metal ions while inner and wider β-diketonato site chelates six-coordinate M^{II} centre. An exception from this rule can be found only in the case of homometallic [CuCu···CuCu] cluster, where both metallic sites are five-coordinate with square-pyramidal geometry. Such exceptional preference of Cu^{II} for lower coordination number suggested possible high selectivity in constructing heterometallic $[(CuM2)_2(L1)(OH)_2(py)_n](ClO_4)_2$ series (M=Co^{II}, Ni^{II}, Zn^{II}). To test this assumption, bimetallic mixture of perchlorate salts was allowed to react with $[L1]^{4-}$ in pyridine, mimicking the exact conditions and stoichiometry used in preparation of homometallic $[(MM)_2(L1)(OH)_2(py)_n](ClO_4)_2$ series:

$$2\ M2(ClO_4)_2 + 2\ Cu(ClO_4)_2 + H_4L1 + 6\ TBAOH + 10\ py \longrightarrow [(CuM2)_2(L1)(OH)_2(py)_{10}](ClO_4)_2 + 6\ TBAClO_4 + 4\ H_2O$$

M2=Co^{II} (**8**), Ni^{II} (**9**) and Zn^{II} (**10**)

Success of proposed strategy was verified using the single crystal X-ray diffraction, proving that pure $[(CuM2)_2(L1)(OH)_2(py)_{10}](ClO_4)_2$ complexes were formed in all three cases. Unit cells of compounds **8** (M2=Co^{II}) and **9** (M2=Ni^{II}) belong to monoclinic $P2_1/n$ space group while compound **10** (M2=Zn^{II}) crystallizes in triclinic P-1 space group (Table II.A5-6). Moreover, differences can be found in the unit cell content which for compounds **8** and **9** counts four equivalents of ionic compound $[(CuM2)_2(L1)(OH)_2(py)_{10}](ClO_4)_2$ accompanied with sixteen (**8**) or eight (**9**) pyridine molecules as lattice solvents, while in case of compound **10**, two formulae unit of $[(CuZn)_2(L1)(OH)_2(py)_{10}](ClO_4)_2$ crystallise with two water molecules. Topology of all three $[(CuM)_2(L1)(OH)_2(py)_n]^{2+}$ complexes are identical to previously described homometallic analogues, thus, two pairs of hydroxo-bridged [CuM] dimers are chelated within completely deprotonated and *trans* orientated phenolato-β-diketonato coordination pockets (μ_4-$[L1]^{4-}$ coordination mode), while the rest of their

coordination sphere is filled with pyridine co-ligands (Figure 2.6). Peripheral phenolato-ketonato binding sites of the ligand chelate five-coordinate Cu^{II} ion within square-pyramidal O_3N_2 crystal field (equatorial O_3N crystal field), while inner β-diketonato sites hold M^{II} ions reside in octahedral O_3N_3 crystal field within the β-diketonato pocket (equatorial O_3N crystal field). In all three compounds, two [MM] dimers are crystallographycally inequivalent and separated at distance of 7.274(2) Å (**8**), 7.1466(9) Å (**9**) and 7.180(2) Å (**10**), while intermetallic distances within dimers average at 3.076 Å (**8**), 3.051 Å (**9**) and 3.107 Å (**10**). Coordination environment around the peripheral Cu^{II} sites is almost identical in all three compounds and almost identical to the one found in homometallic $[(CuCu)_2(L1)(OH)_2(py)_8](ClO_4)_2$ complex (**6**). To be precise, elongated axial Cu−N bonds measure 2.239 Å (**8**), 2.227 Å (**9**) and 2.225 Å (**10**), whilst irrelevant differences can be also found comparing the average equatorial bond distances (1.965 Å (**8**), 1.970 Å (**9**) and 1.980 Å (**10**)) and the averages of all bonds (2.019 Å (**8**), 2.022 Å (**9**) and 2.029 Å (**10**), tables II.A14-16, Figure II.A7). Moreover, average distortion of square-pyramidal geometry around Cu^{II} (τ≈0.13 (**8**), 0.14 (**9**), 0.15 (**10**)) and its distance from corresponding equatorial planes (d≈0.29 Å (**8**), 0.29 Å (**9**) and 0.34 Å (**10**)) reflect nicely great similarity between those sites (Table II.A20, Figure II.A5). On the other hand, bonding details around the inner M^{2+} centres show significant differences between the compounds following the same pattern as reported for their homometallic analogues. Average axial M−N bonds (2.193 Å (**8**), 2.144 Å (**9**), 2.260 Å (**10**)) are again longer than average equatorial bonds (averaged at 2.063 Å (**8**), 2.037 Å (**9**) and 2.064 Å (**10**)) and averages of all six bonds (2.107 Å (**8**), 2.073 Å (**9**) and 2.129 Å (**10**)), increasing in order Ni<Co≤Zn (Figure II.A7). Again, octahedral Co^{II}, Ni^{II} and Zn^{II} ions are almost perfectly positioned in equatorial ligand plane (d<0.07 Å), as expected from their homometallic structures, highlighting additionally high site selectivity in formation of these heterometallic assemblies. Equatorial planes of inner M^{II} sites intersect under angles of 17.5° (**8**), 19.0° (**9**) and 22.2° (**10**), while same angles for adjacent peripheral and inner M^{II} sites measure 4.0/19.7° (**8**), 8.5/12.0 (**9**), 10.5/21.5° (**10**). Crystal structure stability in heterometallic $[(CuM)_2(L1)(OH)_2(py)_n]^{2+}$ complexes originates from electrostatic interactions between the complex cations and perchlorate anions, which also mediate as hydrogen acceptors in up to twelve O−H···O and C−H···O hydrogen bonding interactions with bridging hydroxide and pyridine co-ligands from complex cations, as well as with the lattice solvents.

Additionally, densely packed crystal structure is organized through large number of short π···π and C–H···π contacts between the aromatic moieties of complexes.

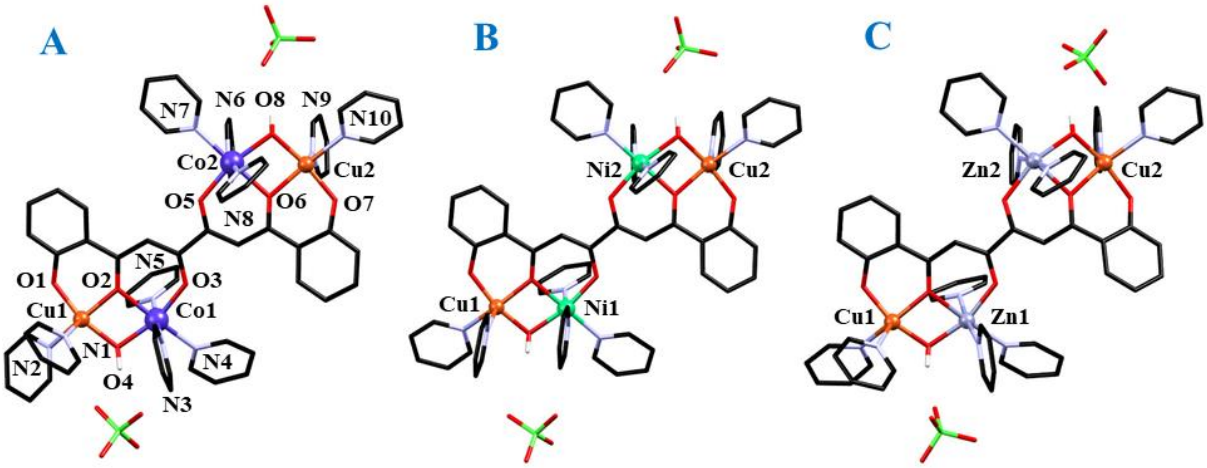

Figure 2.6: Molecular structure and labelling scheme of $[(CoCu)_2(L1)(OH)_2(py)_{10}](ClO_4)_2$ (**8**, A), $[(CuNi)_2(L1)(OH)_2(py)_{10}](ClO_4)_2$ (**9**, B) and $[(CuZn)_2(L1)(OH)_2(py)_8](ClO_4)_2$ (**10**, C). Labelling scheme of crystallographically independent heteroatoms indicated for the structure of **8** is identical for all compounds. Hydrogen atoms affecting the charge of clusters are shown, the rest is omitted for clarity.

2.4.2. Design, synthesis and structure of heterometallic $[(M1M2)_2(OH)_2(L1)(py)_{10}](ClO_4)_2$ (M1,M2=Co^{II}, Ni^{II}, Zn^{II})

Homometallic $[(MM)_2(OH)_2(L1)(py)_{10}](ClO_4)_2$ complexes (M= Co^{II}, Ni^{II}, Zn^{II}) indicate that remaining heavier 3*d* metal ions don't seem to exhibit strict electivity towards octahedral or square-pyramidal coordination geometry since they easily adopt both depending on the size of chelating pocket where they are located. This would mean that degree of selectivity in construction of heterometallic compound from these building blocks would be purely determined by the difference in crystal field stabilisation energy between at least four possible distribution of bimetallic mixture in isostructural clusters (Scheme 2.6). From that point of view, compounds holding Ni^{II} ions in octahedral β-diketonato site should be thermodynamically more stable than any other configuration, since crystal field theory predicts the largest stabilisation energy for $3d^8$ ion in such environment. Similar rationale can be used to predict higher selectivity for Co^{II} ions in comparison with Zn^{II} for octahedral site, since latter $3d^{10}$ metal ion should not contribute with any stabilisation energy upon

coordination. In addition, same concept can be expanded to square-pyramidal site too, suggesting homometallic [Co_4] (**4**) and [Ni_4] (**5**) structures to be the most stable products.

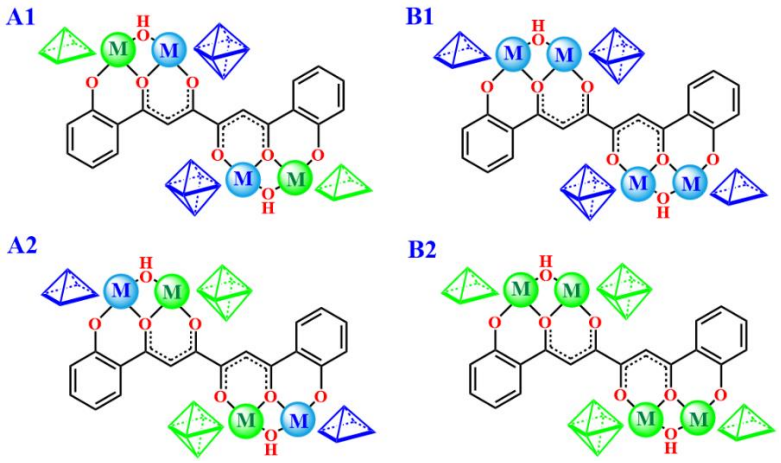

Scheme 2.6. Possible distributions and topologies of bimetallic mixture (red and blue balls) in isostructural heterometallic (A1 and A2) and homometallic (B1 and B2) clusters.

In order to test the selectivity in formation of heterometallic $[(M1M2)_2(OH)_2(L1)(py)_{10}](ClO_4)_2$ complexes (M1,2 =Co^{II}, Ni^{II}, Zn^{II}), bimetallic mixtures of perchlorate salts were mixed with $[L1]^{4-}$ in pyridine, mimicking same conditions and correct stoichiometry as in previously $[(CuM)_2(L1)(OH)_2(py)_{10}](ClO_4)_2$ series:

$$2\ M1(ClO_4)_2 + 2\ M2(ClO_4)_2 + H_4L1 + 6\ TBAOH + 10\ py \longrightarrow [(M1M2)_2(L1)(OH)_2(py)_{10}](ClO_4)_2 + 6\ TBAClO_4 + 4\ H_2O$$

M1, M2=Co^{II}, Ni^{II} (**11**), Ni^{II}, Zn^{II} (**12**) and Co^{II}, Zn^{II} (**13**)

Probed reactions yielded substantial amounts of single crystals, allowing us to obtain accurate structural insights and to validate the success of proposed strategy. Unit cells of compounds **11** ($[Co^{II}Ni^{II}]_2$), **12** ($[Zn^{II}Ni^{II}]$) and **13** ($[Zn^{II}Co^{II}]$) correspond to monoclinic $P2_1/n$ space group, similarly as previously described heterometallic compounds **8** ($[Cu^{II}Co^{II}]_2$) and **9** ($[Cu^{II}Ni^{II}]$) and homometallic compound **5** ($[Ni^{II}Ni^{II}]$, Table II.A6). Apart from expect cluster $[(M1M2)_2(L1)(OH)_2(py)_{10}](ClO_4)_2$, asymmetric unit contains three (**13**) or four (**11**, **12**) lattice pyridine molecules, while the unit cell includes two (**11**) or four (**12**, **13**) asymmetric units. Main structural features of three $[(MM')_2(L1)(OH)_2(py)_{10}]^{2+}$ complexes are identical to previously described homo- and heterometallic analogues so detailed description will be omitted here for the sake of brevity (Figure 2.7). In compounds **12** and **13**, two [M1M2] dimers are crystallographycally inequivalent and separated at distance of 7.2191(9) Å (**12**) and 7.2082(9) Å (**13**), while compound **11** holds two symmetry-related [M1M2] dimers (inversion centre) separated at distance of 7.2037(7) Å (**11**). Respective intermetallic

intradimer distances measure 3.1633 (8) Å (**11**), 3.137 Å (**12**) and 3.153 Å (**13**). Equatorial planes of inner $M2^{II}$ sites intersect under angles of 0° (**11**), 20.6° (**12**) and 24.2° (**13**), while same angles for adjacent peripheral and inner $M1^{II}/M2^{II}$ sites measure 16.8° (**11**), 3.6/18.6 (**12**), 6.4/19.4° (**13**). Detailed inspection of coordination environment around inner octahedral site in compounds **11** and **12** unveiled great similarity with corresponding Ni^{II} site in homometallic $[(NiNi)_2]$ compound **5** and heterometallic $[(NiCu)_2]$ compound **9**. More specifically, axial M−N bond lengths average at 2.146 Å (**11**) and 2.134 Å (**12**), while average equatorial bond lengths are 2.052 Å (**11**) and 2.043 Å (**12**). Resemblance in coordination geometry can be also found looking at the overall average of all bonds (2.083 Å (**11**) and 2.074 Å (**12**), Table II.A20, A17, Figure II.A8). On the other hand, analysis of coordination geometry around the peripheral five-coordinate $M1^{II}$ site shows great similarity of **11** to homometallic $[(CoCo)_2]$ compound **4** and **12** to homometallic $[(ZnZn)_2]$ compound **7**. In **11**, axial M−N bond measures 2.072(3) Å while average equatorial bond length and average length of all bonds are 2.041 Å and 2.047 Å, respectively. Similar values can be found at the same site in **12**, where axial M−N bond, average equatorial bond and average length of all bonds measure 2.070 Å, 2.049 Å and 2.053 Å, respectively (Table II.A18, A20, Figure II.A8). The latter case is within experimental error identical to corresponding site in homometallic $[(ZnZn)_2]$ compound **7**, while great similarity between coordination environment for Zn^{II} and Co^{II} was also already established (*vide supra*). Additional similarities with the homometallic analogues can be extracted from average distortion of square-pyramidal geometry around $M1^{II}$ (τ≈0.61 (**11**), 0.19 (**12**)) and its distance from corresponding equatorial planes (d≈0.41 Å (**11**), 0.48 Å (**12**)**,** Figure II.A6).

Almost identical geometry around the peripheral M1 site can be found in compound **13**: axial M−N bond, average equatorial bond and average length of all bonds measure 2.077 Å, 2.046 Å and 2.052 Å, respectively, while distortion parameter τ and M1 distance from equatorial plane are 0.175/0.448 and 0.485/0.487 Å, respectively (Table A.II19-20). Since these sites are almost identical in homometallic Zn^{II} and Co^{II} analogue, no direct conclusion about metal disposition can be extracted. However, geometry around inner octahedral site in **13** suggest the presence of Co^{II}, as expected from the initial concept. More precise, axial M−N bond lengths, average equatorial bond lengths and average length of all bonds measure 2.198 Å, 2.066 Å and 2.110 Å, respectively. Additionally, refinement of metallic composition in compounds **8**-**13** as heterometallic reduces the final R_1 value for 0.2-0.5%.

As described earlier, crystal structure of heterometallic $[(M1M2)_2(L1)(OH)_2(py)_{10}]^{2+}$ complexes is stabilised by electrostatic interactions with perchlorate anions, which participate also in anion···π interactions, as well as hydrogen acceptors in up to 10 twelve O–H···O and C–H···O hydrogen bonding interactions with bridging hydroxide, pyridine co-ligands from complex cations and lattice pyridine molecules. Through such network of interactions, chains of parallel $[(M1M2)_2(L1)(OH)_2(py)_{10}]^{2+}$ complexes are assembled. Additionally, numerous short π···π, C–H···π and C–H···N contacts can be found between the aromatic fragments of complex cations and/or lattice pyridine molecules.

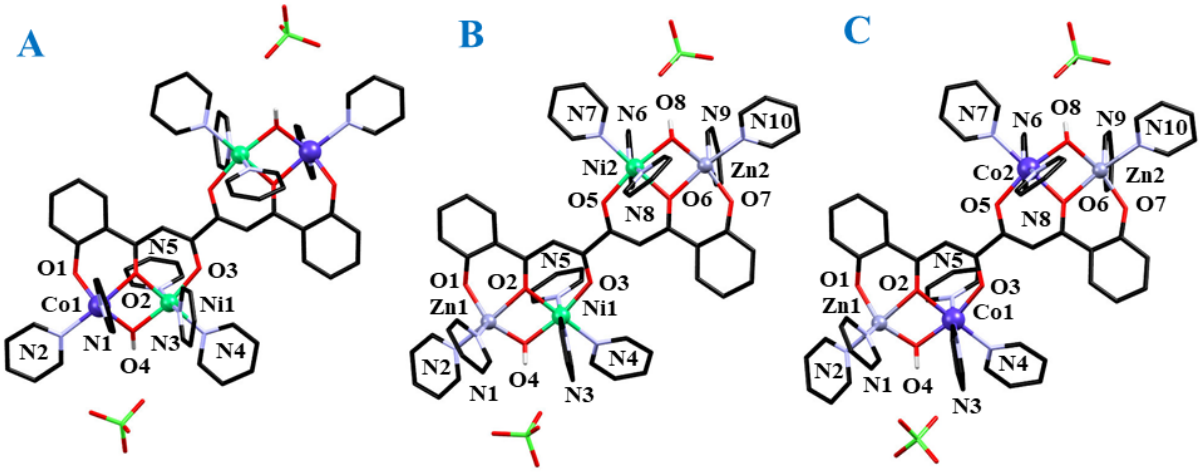

Figure 2.7: Molecular structure and labelling scheme of $[(CoNi)_2(L1)(OH)_2(py)_{10}](ClO_4)_2$ (**11**, A), $[(ZnNi)_2(L1)(OH)_2(py)_8](ClO_4)_2$ (**12**, B) and $[(ZnCo)_2(L1)(OH)_2(py)_{10}](ClO_4)_2$ (**13**, B) and Only crystallographically independent heteroatoms are labelled. Hydrogen atoms affecting the charge of clusters are shown, the rest is omitted for clarity.

2.4.3. Magnetic properties of homometallic and heterometallic coordination compound with H_4L1

Magnetic properties of compounds **1**-**13** (except diamagnetic compounds **3** and **7**) were studied through variable temperature (2-300 K) magnetization measurements performed on their powdered microcrystalline samples under the constant magnetic field of 0.3 (**11**), 0.5 or 1 T (**6**). In addition, this study was complemented with magnetization measurements at 2 K in the field range of 0–5 T.

In compound **1**, detected room temperature (300 K) $\chi_M T$ product for two high-spin Co^{II} ions (S=3/2) of 5.602 cm^3Kmol^{-1} (g_{calc}=2.44) was substantially higher than the theoretically predicted one (g=2.0, $\chi_M T$=3.75 cm^3Kmol^{-1}). Upon cooling, this value drops steadily down to

80 K ($\chi_M T$=4.632 cm^{3}Kmol^{-1}), followed by abrupt decline ending with $\chi_M T$=0.156 cm^{3}Kmol^{-1} (2K). Field-dependent magnetization measurement at 2K revealed *S*-shaped magnetization curve with plateau until 1 T which in higher fields grows up to 3.066 μ_B (5 T), well below the expected 6 μ_B (Figure 2.8). Detected magnetic properties reveal unquenched first-order spin-orbit coupling of Co^{II} ions ($^4T_{1g}$ ground term, *S*=3/2, *L*=1) and potential weak antiferromagnetic coupling between them by superexchange mechanism across oxalate core of $[H_2L1]^{2-}$. To establish those contributions, experimental data ($\chi_M T$ *vs T* and $M/N\mu_B$ *vs H*) were modelled simultaneously by matrix diagonalization of the spin Hamiltonians in PHI[21] (Scheme 2.7):

$$\hat{H} = \mu_B B \sum_i g_i \hat{S}_i + D_{Co}\left(\hat{S}^2_{z_{Co1}} - \frac{\hat{S}^2_{Co1}}{3} + \hat{S}^2_{z_{Co2}} - \frac{\hat{S}^2_{Co2}}{3}\right) - 2J_{Co-Co}\left(\hat{S}_{Co1}\hat{S}_{Co2}\right)$$

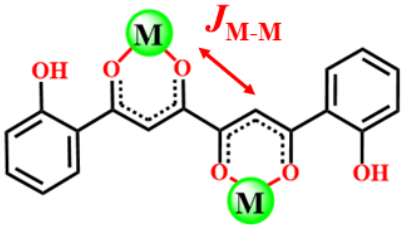

Scheme 2.7: Coupling scheme for compounds **1** and **2**.

Components of this spin Hamiltonian in order of their appearance are Zeeman effect, zero-field splitting (axial ZFS parameter *D*) and exchange coupling between Co^{II} ions, as indicated at Scheme 2.7. Good models were built by fixing the g_{Co}=2.44, while fitted parameters converged to $J_{Co\text{-}Co}$= –1.35 cm^{-1} and D_{Co}=61.67 cm^{-1} . Change in D_{Co} sing yielded good fit for $\chi_M T$ *vs T* curve with $J_{Co\text{-}Co}$= –0.76 cm^{-1} and D_{Co}=–80.14 cm^{-1} but failed to reproduce the shape and values of $M/N\mu_B$ *vs H* curve. Slightly more complicated model, considering spin-orbit coupling of octahedral Co^{II} ions was constructed from spin Hamiltonian:

$$\hat{H} = \mu_B B \sum_i (g_i \hat{S}_i + \sigma_i \hat{L}_i) - 2J_{Co-Co}\left(\hat{S}_{Co1}\hat{S}_{Co2}\right) + \sum_i \lambda_i (\sigma_i \hat{L}_i \cdot \hat{S}_i)$$

In this equation, first component of the sum defines the Zeeman effect, second one corresponds to the exchange coupling between Co^{II} ions, while third contribution comes from spin-orbit coupling. The parameters λ_i and σ_i are the spin-orbit coupling constant (–171.5 cm^{-1}) and the orbital reduction parameter (ideally, σ_i =-3/2), respectively, *J* is the exchange constant, $\hat{S}_i$ (*S*=3/2) is the total spin operator of the individual Co(II) ions, $\hat{L}_i$ (*L*=1) is their orbital angular momentum, *B* is the magnetic induction and μ_B is the Bohr

magneton. To avoid the overparametrisation of spin Hamiltonian, g_{Co} was fixed at 2.00, while fitted parameters converged to σ_i=–1.040, λ_i=–139.84 cm^{-1} and $J_{Co\text{-}Co}$=-1.397 cm^{-1} (Figure 2.8). Obtained $J_{Co\text{-}Co}$ value agrees nicely with the one extracted from crystal-field spin Hamiltonian, while values of σ_i and λ_i are in reasonable agreement with the theoretically expected one, bearing in mind that orbital contributions in octahedral Co^{II} ions are partially quenched by the ligand field.

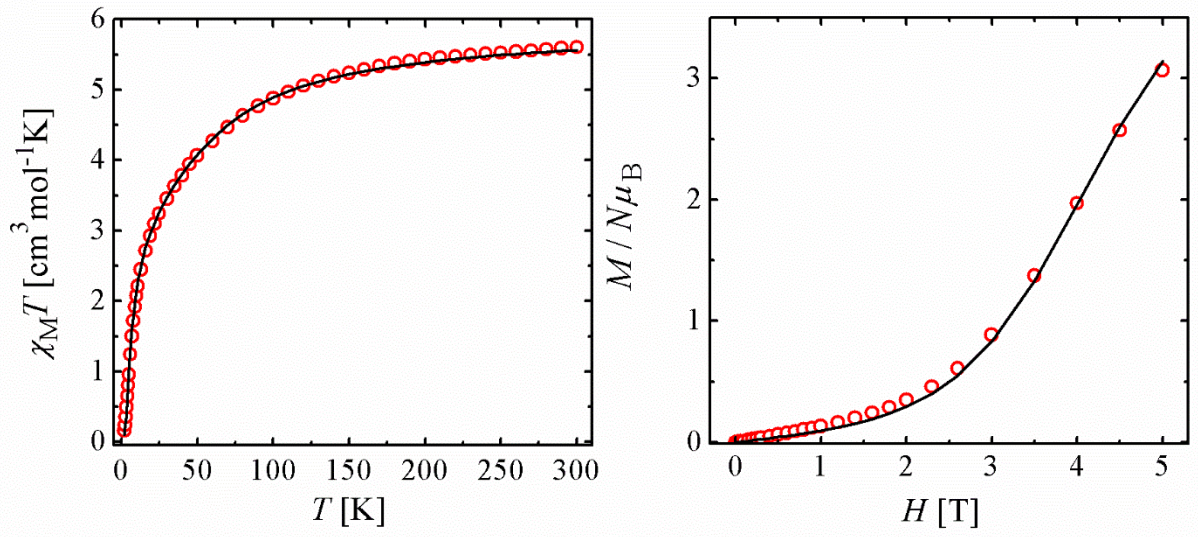

Figure 2.8. $\chi_M T$ vs T and $M/N\mu_B$ vs H curves for compound **1** with the best fit (solid line). Measurement setup: cooling mode (300→2 K), B = 0.5 T; T_{mag} = 2 K.

Measured room temperature (300 K) value of $\chi_M T$ product for compound **2** was 2.285 cm^3Kmol^{-1} (g_{calc}=2.14, Figure 2.X), as expected from its solid state structure holding two Ni^{II} ions (g=2.0, $\chi_M T$=2.00 cm^3Kmol^{-1}). Upon cooling, the $\chi_M T$ product drops steadily down to 60 K ($\chi_M T$=1.880 cm^3Kmol^{-1}), followed by abrupt decline down to 2 K which ends at 0.016 cm^3Kmol^{-1}. Described behaviour is indicative of weak antiferromagnetic coupling between two Ni^{II} centres bridged through oxalate core of $[H_2L1]^{2-}$ which leads to S=0 ground state of the cluster **2**. This conclusion is supported also with field-dependent magnetization measurement at 2K, where highest measured value at 5 T was 0.094 μ_B, significantly below the expected 4 μ_B for two S=1 ions (g=2, Figure 2.9). Strength of magnetic coupling, as well as possible anisotropy of Ni^{II} ions were estimated by modelling the experimental data ($\chi_M T$ *vs* T and $M/N\mu_B$ *vs* H) through matrix diagonalization of the spin Hamiltonians in PHI[21] :

$$\widehat{H} = \mu_B B \sum_i g_i \hat{S}_i + D_{Ni}\left(\hat{S}^2_{z_{Ni1}} - \frac{\hat{S}^2_{Ni1}}{3} + \hat{S}^2_{z_{Ni2}} - \frac{\hat{S}^2_{Ni2}}{3}\right) - 2J_{Ni-Ni}\left(\hat{S}_{Ni1}\hat{S}_{Ni2}\right)$$

$$\hat{H} = \mu_B B \sum_i g_i \hat{S}_i - 2J_{\mathrm{Ni-Ni}}(\hat{S}_{\mathrm{Ni1}}\hat{S}_{\mathrm{Ni2}})$$

The best model of $\chi_M T$ *vs* T and $M/N\mu_B$ *vs* H was constructed by fixing the isotropic g values of Ni(II) to 2.12, while fitted parameters converged to $J_{\mathrm{Ni\text{-}Ni}}$= –5.11 cm^{-1} and D_{Ni}=–7.09 cm^{-1} or $J_{\mathrm{Ni\text{-}Ni}}$= –5.13 cm^{-1} and D_{Ni}=5.57 cm^{-1} (Figure 2.9). Apart from those, simpler models considering only $J_{\mathrm{Ni\text{-}Ni}}$ contributions (fixed g_{Ni}=2.13, $J_{\mathrm{Ni\text{-}Ni}}$=–5.16 cm^{-1}), with or without intermolecular interactions, managed to reproduce well the $\chi_M T$ *vs* T curve, but failed to replicate the $M/N\mu_B$ *vs* H curve. Observed antiferromagnetic coupling between Ni^{II} sites in **2** occurs between almost coplanar $d_{x^2-y^2}$ magnetic orbitals by superexchange mechanism mediated by oxalate core of $[H_2L1]^{2-}$.

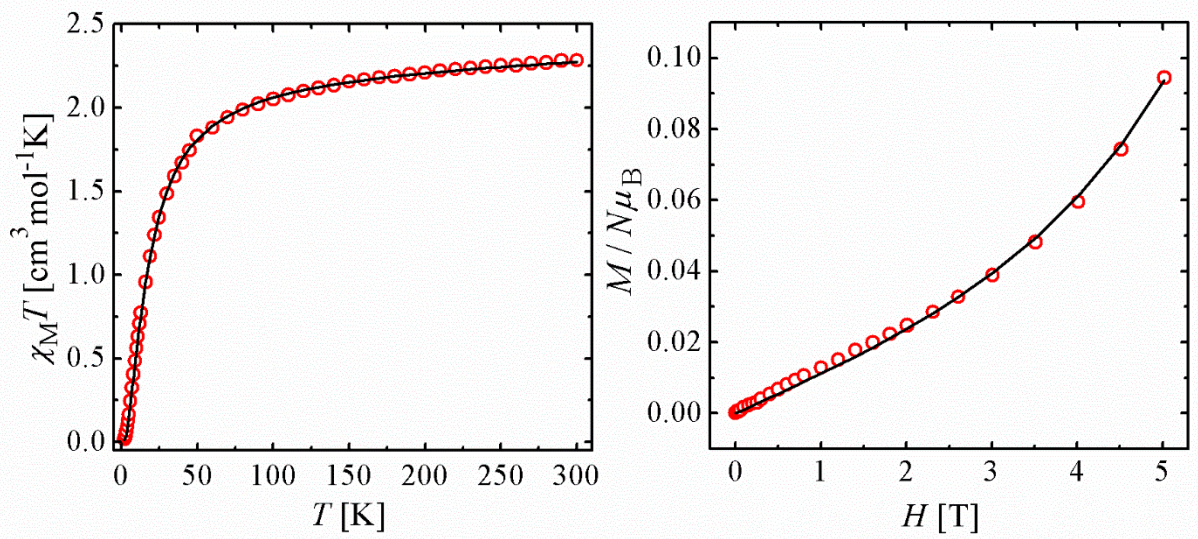

Figure 2.9. $\chi_M T$ vs T and $M/N\mu_B$ vs H curves for compound **2** with the best fit (solid line). Measurement setup: cooling mode (300→2 K), B = 0.5 T; T_{mag} = 2 K.

Magnetic response of homometallic [Co_4] cluster **4** of 10.506 cm^{3}Kmol^{-1} (g_{calc}=2.37) is well above the expected 7.5 cm^{3}Kmol^{-1} for four high-spin Co^{II} ions (S=3/2, g=2.00), similarly as it was the case in dinuclear precursor **1**. Upon cooling, the $\chi_M T$ product is decreasing almost linearly down to 100 K ($\chi_M T$=8.891 cm^{3}Kmol^{-1}), followed by faster decline ending at 1.306 cm^{3}Kmol^{-1} at 2 K. Field-dependent magnetization measurement (2K) produced almost linearly increasing curve which ends at 4.033 μ_B (5 T), well below the expected 12 μ_B for four uncoupled Co^{II} ions (S=3/2, Figure 2.10). Such behaviour indicates possible antiferromagnetic interactions between metal ions, as well as possible zero-field splitting effects arising from unquenched spin-orbit coupling. Due to high complexity of such

systems, experimental data ($\chi_M T$ *vs T* and $M/N\mu_B$ *vs H*) were fitted simultaneously by matrix diagonalization of the spin Hamiltonian (Scheme 2.8):

$$\hat{H} = \mu_B B \sum_i g_i \hat{S}_i + D_{Co}\left(\hat{S}^2_{z_{Co2}} - \frac{\hat{S}^2_{Co2}}{3} + \hat{S}^2_{z_{Co3}} - \frac{\hat{S}^2_{Co3}}{3}\right) - 2J_{Co2-Co3}\left(\hat{S}_{Co2}\hat{S}_{Co3}\right) -$$
$$-2J_{Co1-Co2}\left(\hat{S}_{Co1}\hat{S}_{Co2} + \hat{S}_{Co3}\hat{S}_{Co4}\right)$$

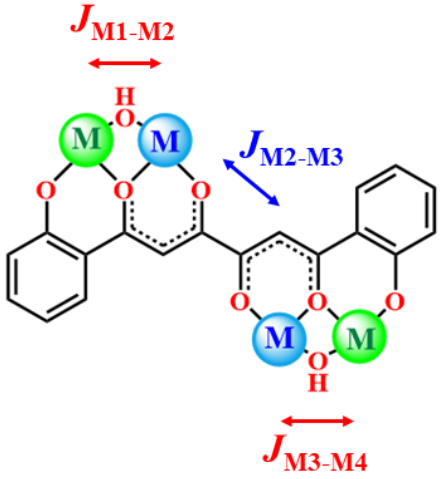

Scheme 2.8: Applied coupling scheme for compounds **4**-**13**.

To avoid the overparametrisation of spin Hamiltonian, g_{Co1}=g_{Co4}, g_{Co2}=g_{Co3} and $J_{Co2\text{-}Co3}$ were fixed to 2.25, 2.48 and –1.400 cm^{-1}, as extracted previously from dinuclear Co^{II} compound **1**. Fitted parameters, $J_{Co1\text{-}Co2}$ and D_{Co2}=D_{Co3}, converged to –2.36 cm^{-1} and 65.51 cm^{-1}, providing very good agreement of proposed model with experimental $\chi_M T$ *vs T* and $M/N\mu_B$ *vs H* curves (Figure 2.10). Similar attempts were made with negative D_{Co2}=D_{Co3} (–80.01 cm^{-1}), which led to $J_{Co1\text{-}Co2}$=–1.75 cm^{-1}, but agreement between that model and $M/N\mu_B$ *vs H* curve was worse than in previous case, although $\chi_M T$ *vs T* curve was nicely reproduced. Possible anisotropy of peripheral, five-coordinate, Co1 and Co4 sites was neglected to simplify the model and avoid overparametrisation. Obtained D_{Co2}=D_{Co3} values correspond nicely with the equivalent parameters extracted in compound **2**.

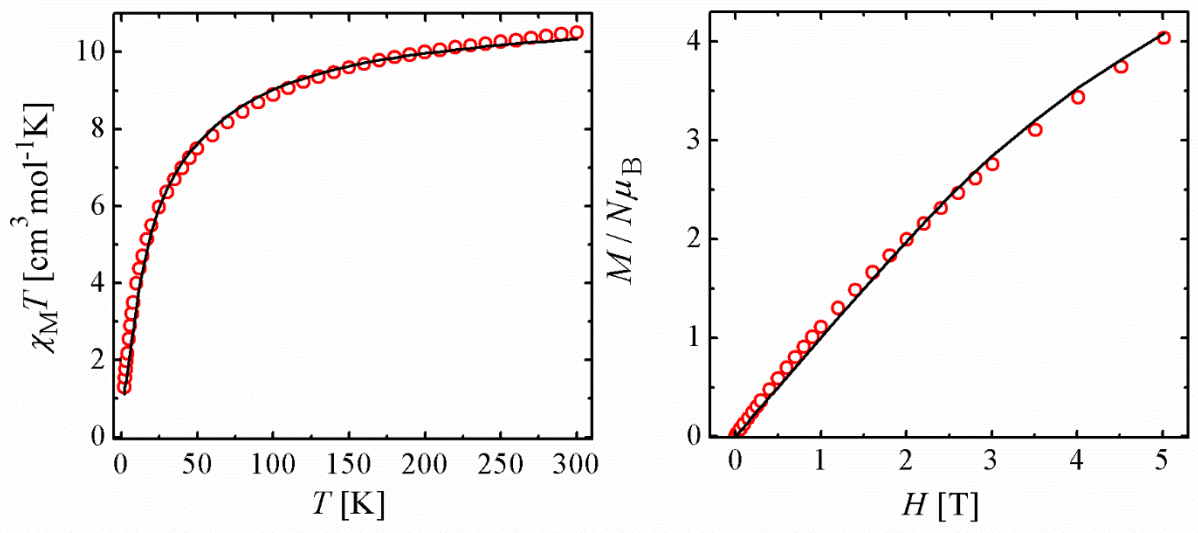

Figure 2.10. $\chi_M T$ vs T and $M/N\mu_B$ vs H curves for compound **3** with the best fit (solid line). Measurement setup: cooling mode (300→2 K), B = 0.5 T; T_{mag} = 2 K.

Room temperature $\chi_M T$ value of tetranuclear Ni^{II} compound **5** was 4.589 cm^{3}Kmol^{-1}, slightly above the theoretically predicted 4.00 cm^{3}Kmol^{-1} (S=1, g=2.00). Upon cooling, this value drops slowly down to 50 K (3.136 cm^{3}Kmol^{-1}), followed by sharp decay down to 0.248 cm^{3}Kmol^{-1} at 2 K. Described behaviour is indicative of weak antiferromagnetic coupling within the cluster with S=0 ground state. Support to this claim comes from $M/N\mu_B$ vs H curve where highest measured value of 0.652 μ_B (5T) is well below calculated 8 μ_B for four S=1 ions (g=2, Figure 2.11). Collected experimental data ($\chi_M T$ *vs* T and $M/N\mu_B$ *vs* H) were modelled through matrix diagonalization of the spin Hamiltonian:

$$\hat{H} = \mu_B B \sum_i g_i \hat{S}_i - 2J_{\mathrm{Ni2-Ni3}}\left(\hat{S}_{\mathrm{Ni2}}\hat{S}_{\mathrm{Ni3}}\right) - 2J_{\mathrm{Ni1-Ni2}}\left(\hat{S}_{\mathrm{Ni1}}\hat{S}_{\mathrm{Ni2}} + \hat{S}_{\mathrm{Ni3}}\hat{S}_{\mathrm{Ni4}}\right)$$

Fixing g_{Ni}=2.16 and $J_{Ni2\text{-}Ni3}$ to -5.50 cm^{-1}, as extracted from compound **2**, $J_{Ni1\text{-}Ni2}$ converged to –6.22 cm^{-1}, reproducing nicely experimental $\chi_M T$ *vs* T data. However, very poor agreement was achieved with field-dependent magnetization curve which couldn't be improved even with addition of paramagnetic impurity. Therefore, initial model was expanded with single-ion anisotropy contributions:

$$\hat{H} = \mu_B B \sum_i g_i \hat{S}_i + D_{\mathrm{Ni}}\left(\hat{S}^2_{z_{\mathrm{Ni1}}} - \frac{\hat{S}^2_{\mathrm{Ni1}}}{3} + \hat{S}^2_{z_{\mathrm{Ni2}}} - \frac{\hat{S}^2_{\mathrm{Ni2}}}{3} + \hat{S}^2_{z_{\mathrm{Ni3}}} - \frac{\hat{S}^2_{\mathrm{Ni3}}}{3} + \hat{S}^2_{z_{\mathrm{Ni4}}} - \frac{\hat{S}^2_{\mathrm{Ni4}}}{3}\right) -$$
$$-2J_{\mathrm{Ni2-Ni3}}\left(\hat{S}_{\mathrm{Ni2}}\hat{S}_{\mathrm{Ni3}}\right) - 2J_{\mathrm{Ni1-Ni2}}\left(\hat{S}_{\mathrm{Ni1}}\hat{S}_{\mathrm{Ni2}} + \hat{S}_{\mathrm{Ni3}}\hat{S}_{\mathrm{Ni4}}\right)$$

In the latter case, applying the same set of fixed parameters, D_{Ni}=3.54 cm^{-1} and $J_{Ni1\text{-}Ni2}$=–6.20 cm^{-1} were obtained as fitted parameters. Proposed model showed again excellent

agreement with susceptibility values but failed to do the same with magnetization (Figure 2.11). Negative D_{Ni} converged always to positive, while the only model which successfully reproduced the whole dataset included overestimated $|D_{Ni}|$ values higher than 20 cm^{-1} and was therefore neglected. Intradimer [NiNi] magnetic interaction in **5** ($J_{Ni1\text{-}Ni2}$≈–6.2 cm^{-1}) seems to be comparable or slightly weaker than reported for structurally related {μ-$(O)_2$-[NiNi]} clusters (Refcodes LEHBUY and QOYPEA, $J_{Ni1\text{-}Ni2}$≈–12 and 5 cm^{-1}, respectively).[7, 22]

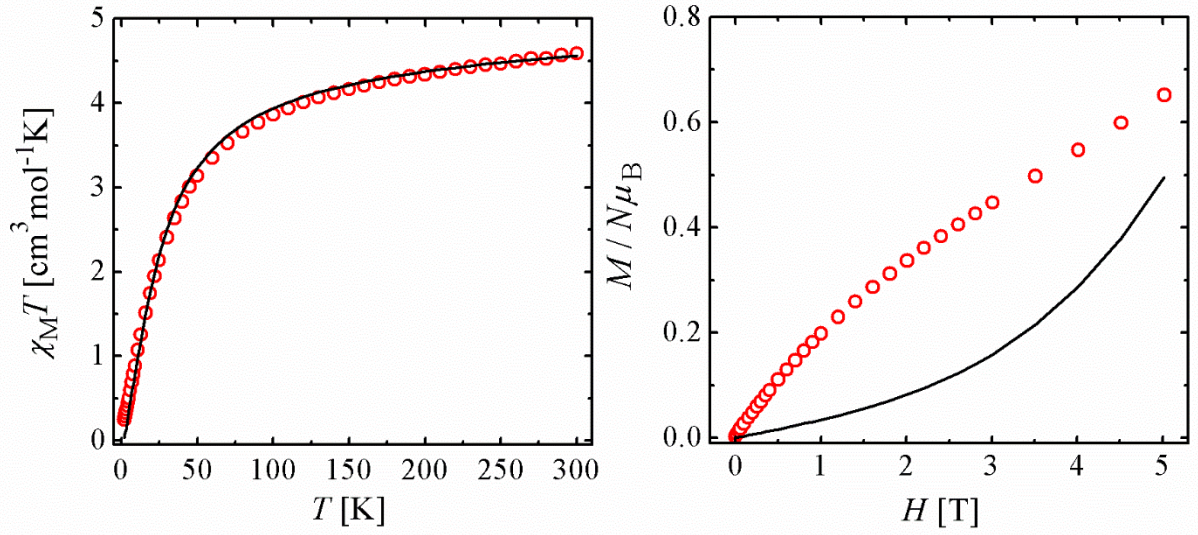

Figure 2.11. $\chi_M T$ vs T and $M/N\mu_B$ vs H curves for compound **5** with the best fit (solid line). Measurement setup: cooling mode (300→2 K), B = 0.5 T; T_{mag} = 2 K.

Magnetic properties of homometallic [Cu_4] cluster **6** unveiled strong antiferromagnetic interactions between spin carriers, as expected from the structure holding two {μ-(O), μ-(OH)-[CuCu]} dimers. Measured room temperature value of $\chi_M T$ product (0.365 cm^3Kmol^{-1} at 300 K) is well below the expected $\chi_M T$=1.50 cm^3Kmol^{-1} (g=2.0) for four isolated Cu^{II} ions. Upon lowering the temperature, the $\chi_M T$ product is decreasing linearly down to 120 K ($\chi_M T$=0.01 cm^3Kmol^{-1}) and then vanishes completely (Figure 2.12). Such temperature dependence suggests that below 120 K only S=0 ground state of **6** is populated and well isolated from excited states due to very strong antiferromagnetic coupling between magnetic $d_{x^2-y^2}$ orbitals of Cu^{II} ions. To validate the strength of this interaction, experimental data ($\chi_M T$ vs T) were modelled by matrix diagonalization of following spin Hamiltonians:

$$\hat{H} = \mu_B B \sum_i g_i \hat{S}_i - 2J_{Cu1-Cu2}\left(\hat{S}_{Cu1}\hat{S}_{Cu2} + \hat{S}_{Cu3}\hat{S}_{Cu4}\right)$$

$$\hat{H} = \mu_B B \sum_i g_i \hat{S}_i - 2J_{Cu1-Cu2}\left(\hat{S}_{Cu1}\hat{S}_{Cu2} + \hat{S}_{Cu3}\hat{S}_{Cu4}\right) - 2J_{Cu2-Cu3}\left(\hat{S}_{Cu2}\hat{S}_{Cu3}\right)$$

In the first case, only intradimer interaction between adjacent Cu^{II} sites is considered ($J_{Cu1\text{-}Cu2}$), while in the latter case this model was expanded with additional interaction between the inner Cu^{II} sites through oxalate core ($J_{Cu2\text{-}Cu3}$). Starting with the simpler model, experimental data were reproduced nicely with $J_{Cu1\text{-}Cu2}$= –271.37 cm^{-1} and fixed g_{Cu}=2.00 (Figure 2.12). Inclusion of additional coupling interaction between inner Cu^{II} ions didn't improve significantly the quality of the fitting, moreover, extracted $J_{Cu2\text{-}Cu3}$ values were not reliable since their magnitude and sign were fluctuating continually. Considering bond angles within {μ-(O), μ-(OH)-[CuCu]} dimers of 103.4° (μ-(OH)) and 98.8° (μ-(O)) strong antiferromagnetic coupling is expected to occur.[23, 24] However reported $J_{Cu1\text{-}Cu2}$ probably overestimates the strength of coupling since antiferromagnetic coupling is also expected to occur between the inner sites chelated by oxalate spacer. Additionally, magnitudes of reported $J_{Cu1\text{-}Cu2}$ for structurally related {μ-$(O)_2$-[CuCu]} clusters are smaller (Refcodes LEHBIY and MUKJAE, $J_{Cu1\text{-}Cu2}$≈–262 and –238 cm^{-1}, respectively).[6, 7]

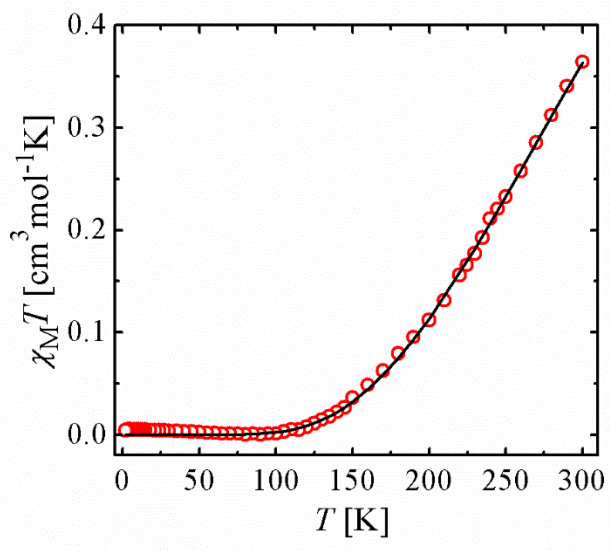

Figure 2.12. $\chi_M T$ vs T and $M/N\mu_B$ vs H curves for compound **6** with the best fit (solid line). Measurement setup: cooling mode (300→2 K), B = 1 T; T_{mag} = 2 K.

DC studies of heterometallic $[CuCo]_2$ compound **8** confirmed that bulk samples represent faithfully proposed composition and topology from the single crystal structure. Measured $\chi_M T$ product at room temperature (300 K) of 5.38 cm^3Kmol^{-1} is above the calculated 4.50 cm^3Kmol^{-1} (g=2.0) for a heterometallic system incorporating two uncoupled S=1/2 and S=3/2 metal ions (high-spin Co^{II}). Reduction of temperature results with almost linear

decline of $\chi_M T$ values down to 100 K (3.69 cm^3Kmol^{-1}) which is succeeded by even sharper decay down to 2 K (0.24 cm^3Kmol^{-1}). Field dependent magnetization measurements at the latter temperature showed almost linear $M/N\mu_B$ *vs* H dependence with the highest measured value of 0.84 μ_B (5 T), significantly below the calculated 8 μ_B for uncoupled $[CuCo]_2$ cluster (g=2.00, Figure 2.13). Hence, collected experimental data suggest intradimer antiferromagnetic coupling between S=3/2 and S=1/2 metal ions, accompanied with interdimer interaction between inner S=3/2 spin carries and S=0 ground state of the cluster. To estimate the strength of magnetic interaction, together with anisotropy of Co^{II} centres, experimental data ($\chi_M T$ *vs* T and $M/N\mu_B$ *vs* H) were fitted simultaneously to spin Hamiltonian:

$$\widehat{H} = \mu_B B \sum_i g_i \hat{S}_i + D_{\mathrm{Co}} \left(\hat{S}^2_{z_{\mathrm{Co2}}} - \frac{\hat{S}^2_{\mathrm{Co2}}}{3} + \hat{S}^2_{z_{\mathrm{Co3}}} - \frac{\hat{S}^2_{\mathrm{Co3}}}{3} \right) - 2J_{\mathrm{Co2-Co3}} \left(\hat{S}_{\mathrm{Co2}} \hat{S}_{\mathrm{Co3}} \right) -$$

$$-2J_{\mathrm{Cu1-Co2}} \left(\hat{S}_{\mathrm{Cu1}} \hat{S}_{\mathrm{Co2}} + \hat{S}_{\mathrm{Co3}} \hat{S}_{\mathrm{Cu4}} \right)$$

To avoid the excessive parametrisation, g_{Co}=2.40, g_{Cu}=2.00 and $J_{Co2\text{-}Co3}$=–1.40 cm^{-1} were kept constant, while fitted parameters were D_{Co} and $J_{Cu1\text{-}Co2}$. The best model portraying whole set of experimental data yielded D_{Co}=22.52 cm^{-1} and $J_{Cu1\text{-}Co2}$=–39.89 cm^{-1}. However, minor deviations were found at the lowest temperature region of $\chi_M T$ *vs* T curve, which were improved by fitting only susceptibility data to the spin Hamiltonian. In that case, fits converged to D_{Co}=30.46 cm^{-1} and $J_{Cu1\text{-}Co2}$=–39.07 cm^{-1} which also simulate well the shape of $M/N\mu_B$ *vs* H curve, but underestimate its values (Fgure 2.13). Similar quality in fitting $\chi_M T$ *vs* T curve was obtained with negative D_{Co}=–36.25 cm^{-1} and $J_{Cu1\text{-}Co2}$=–39.41 cm^{-1}, but such models fails to follow the field dependent magnetization curve.

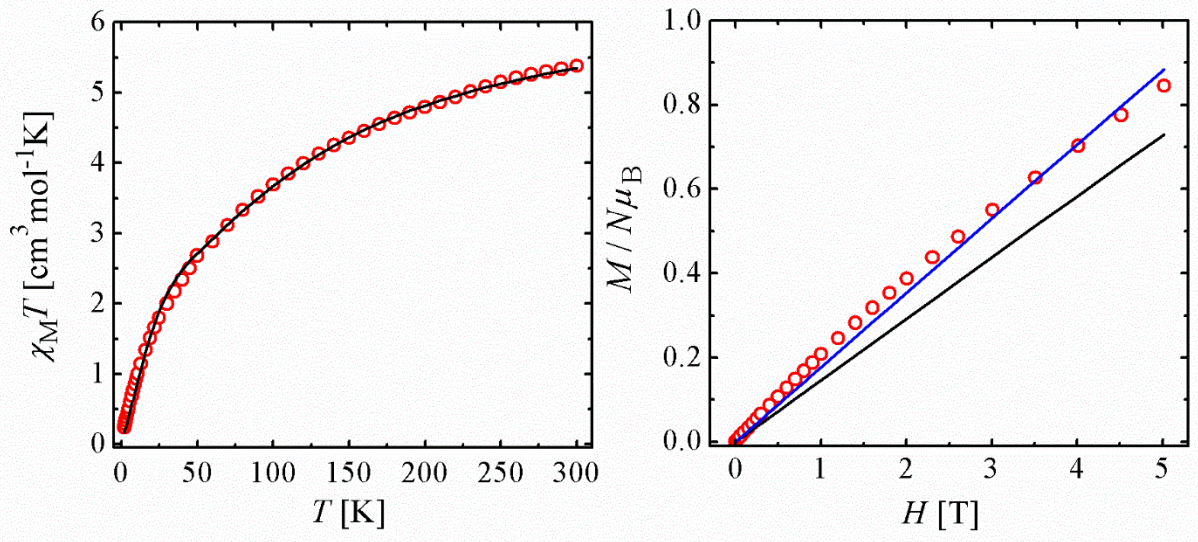

Figure 2.13. $\chi_M T$ vs T and $M/N\mu_B$ vs H curves for compound **8** with the best fit (solid black line, D_{Co}=30.46 cm^{-1} and $J_{Cu1\text{-}Co2}$=–39.07 cm^{-1}). Blue line at $M/N\mu_B$ vs H curve shows simulation of corresponding spin Hamiltonian with D_{Co}=22.52 cm^{-1} and $J_{Cu1\text{-}Co2}$=–39.89 cm^{-1}. Measurement setup: cooling mode (300→2 K), B = 0.5 T; T_{mag} = 2 K.

Measured room temperature (300 K) value of $\chi_M T$ product in heterometallic [CuNi]$_2$ compounds **9** of 2.62 cm^{3}Kmol^{-1} is slightly below the expected 2.750 cm^{3}Kmol^{-1} for a heterometallic system incorporating two uncoupled S=1/2 and S=1 spin carriers (g=2.0). Upon cooling, this value drops continuously down to 40 K, followed by small plateau in 25-40 K range (≈0.87 cm^{3}Kmol^{-1}) and posterior sharp decay down to 2 K, ending with $\chi_M T$=0.07 cm^{3}Kmol^{-1}. Such variation of molar magnetic susceptibility with temperature indicates that moderate antiferromagnetic coupling occurs within {μ-(O), μ-(OH)-[CuNi]} core, together with antiferromagnetic interaction between formed S=1/2 dimers. Ground state S=0 is also suggested by field-dependent magnetization measurements at 2K, where highest measured value of 0.17 μ_B (5 T) falls well below the calculated 2 μ_B for two S=1/2 dimers or 6 μ_B for uncoupled [CuNi]$_2$ cluster (g=2.00, Figure 2.14). Strength of magnetic interaction was validated from experimental $\chi_M T$ *vs* T and $M/N\mu_B$ *vs* H data using the matrix diagonalization of spin Hamiltonian:

$$\hat{H} = \mu_B B \sum_i g_i \hat{S}_i - 2J_{Cu1-Ni2}\left(\hat{S}_{Cu1}\hat{S}_{Ni2} + \hat{S}_{Ni3}\hat{S}_{Cu4}\right) - 2J_{Ni2-Ni3}\left(\hat{S}_{Ni2}\hat{S}_{Ni3}\right)$$

Very good agreement with experimental data was obtained by fixing parameters g_{Ni}=2.15 and g_{Cu}=2.00, while refined $J_{Cu1\text{-}Ni2}$ and $J_{Ni2\text{-}Ni3}$ converged to –46. 75 cm^{-1} and –2. 77 cm^{-1}, respectively (Figure 2.X). However, such model deviates from shape and magnitude of

$M/N\mu_B$ *vs H* curve. Good improvement with the latter an be achieved if contribution of small paramagnetic impurity (≤ 5 %, *S*=1) is considered, yielding slightly modified $J_{Cu1\text{-}Ni2}$ and $J_{Ni2\text{-}Ni3}$ of –45. 39 cm^{-1} and –2. 80 cm^{-1} (Figure 2.14). Further expansion of spin Hamiltonian with ZFS component at Ni^{II} site:

$$\hat{H} = \mu_B B \sum_i g_i \hat{S}_i + D_{Ni}\left(\hat{S}^2_{z_{Ni2}} - \frac{\hat{S}^2_{Ni2}}{3} + \hat{S}^2_{z_{Ni3}} - \frac{\hat{S}^2_{Ni3}}{3}\right) - 2J_{Ni2-Ni3}\left(\hat{S}_{Ni2}\hat{S}_{Ni3}\right) -$$

$$-2J_{Cu1-Ni2}\left(\hat{S}_{Cu1}\hat{S}_{Ni2} + \hat{S}_{Ni3}\hat{S}_{Cu4}\right)$$

showed only minor improvement of $\chi_M T$ *vs T* fit but doesn't raise quality of predicted magnetization curves. Best extracted parameters correspond to $J_{Cu1\text{-}Ni2}$= –46. 75 cm^{-1}, $J_{Ni2\text{-}Ni3}$= –2.76 cm^{-1} and D_{Ni}=1.10 or –1.50 cm^{-1}. Obtained $J_{Cu\text{-}Ni}$ values for {μ-(O), μ-(OH)-[CuNi]} dimers in **9** are lower than reported ones for structurally related compounds holding μ-$(O)^2$-[CuNi] dimers (refcodes: MUKJEI and LEHCEJ) with $J_{Ni\text{-}Cu}$= −65.8 cm^{-1}/$J_{Ni\text{-}Cu}$=−72.9 cm^{-1}, respectively.[6, 7]

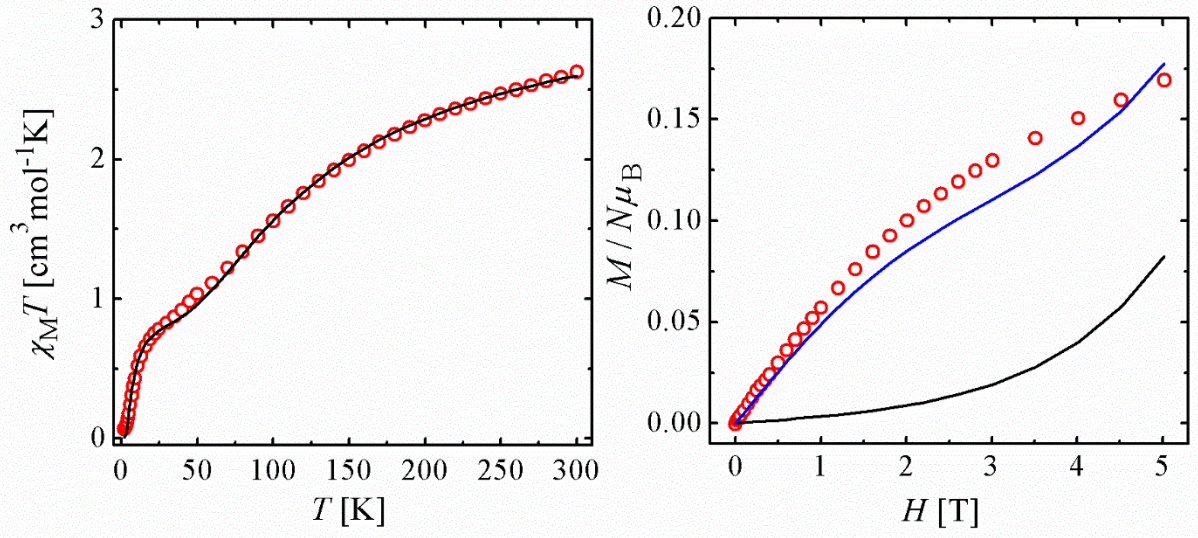

Figure 2.14. $\chi_M T$ vs *T* and $M/N\mu_B$ vs *H* curves for compound **9** with the best fit (solid black line). Blue line fitting $M/N\mu_B$ vs *H* curve includes contribution of small paramagnetic impurity (*S*=1, x=0.05). Measurement setup: cooling mode (300→2 K), *B* = 0.5 T; T_{mag} = 2 K.

Bulk magnetization measurement of **9** were reinforced by the variable-temperature EPR spectroscopy of powdered sample (Figure 2.15). At the room temperature this sample is EPR silent, as expected for moderately antiferromagnetically coupled [CuNi] dimer. Below 80 K, very broad resonance related with ΔM_s=1 transition in *S*=1/2 state starts to appear at *g*=2.222. Spectroscopically determined average *g* value of the ground doublet ($^2A_1$) state of

the [CuNi] dimers in **9** agrees nicely with the average $g_{1/2}$ (2.20) calculated from weighted single-ion *g* values extracted from bulk magnetization measurements:[25]

$$g_{1/2} = \frac{4g_{\mathrm{Ni}} - g_{\mathrm{Cu}}}{3}$$

As the temperature continues to decline to 50 K, observed resonance becomes sharper and another spectral feature at g≈5.00 starts to evolve. Upon cooling down to 30 K, the latter transition starts to be more probable and its intensity increases, while g=2.222 resonance is declining. Below 20 K, central resonance splits to characteristic half-field transitions (g=2.22 and g=2.14), arising from triplet state (axial S=1 spectrum, ΔM_s=1) which becomes populated only in the lowest temperature range due to weak intradimer coupling between effective S=1/2 [CuNi] dimers ($J_{\mathrm{Ni2\text{-}Ni3}} \approx -2.8$ cm^{-1}).

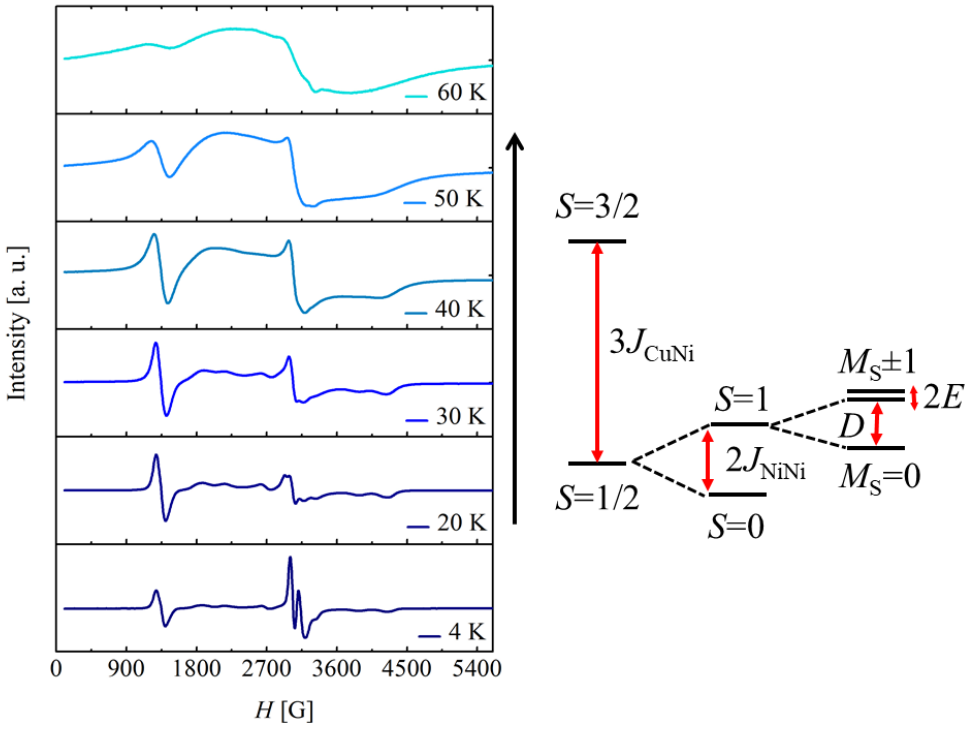

Figure 2.15. *Left*: Variable temperature (4-60 K) X-band EPR spectra (f = 9.418 GHz) of a powdered sample of compound **9**. *Right*: Proposed coupling scheme and corresponding distribution of energy levels for [CuNi] dimers in **9**.

Measured room temperature (300 K) value of $\chi_M T$ product for heterometallic $[CoNi]_2$ compound **11** of 6.51 cm^{3}Kmol^{-1} is only slightly elevated from expected 5.75 cm^{3}Kmol^{-1} for a structure holding two Ni^{II} ions (g=2.0, $\chi_M T$=2.00 cm^{3}Kmol^{-1}) and two high-spin Co^{II} ions (g=2.0, $\chi_M T$=3.75 cm^{3}Kmol^{-1}). Upon cooling, the $\chi_M T$ product drops steadily down to 60 K ($\chi_M T$=5.26 cm^{3}Kmol^{-1}), followed by abrupt decline down to 2 K which ends at 1.10

cm^3Kmol^{-1} (Figure 2.16). Described behaviour might reflect weak antiferromagnetic coupling between spin carriers of possible single-ion zero-field splitting effects. Similar conclusion can be extracted from field-dependent magnetization measurement at 2K, where magnetization slowly saturates with increasing field reaching 3.29 μ_B at 5 T. This value is significantly below the expected 10 μ_B for pairs of uncoupled S=1 and S=3/2 ions (g=2, Figure 2.X). Attempts of validating strength of magnetic coupling and possible anisotropy of Ni^{II} and Co^{II} ions were carried out by modelling the experimental data ($\chi_M T$ *vs* T and $M/N\mu_B$ *vs* H) through matrix diagonalization of spin Hamiltonians:

$$\hat{H} = \mu_B B \sum_i g_i \hat{S}_i + D_{\mathrm{Ni}} \left(\hat{S}^2_{z_{\mathrm{Ni2}}} - \frac{\hat{S}^2_{\mathrm{Ni2}}}{3} + \hat{S}^2_{z_{\mathrm{Ni3}}} - \frac{\hat{S}^2_{\mathrm{Ni3}}}{3} \right) - 2J_{\mathrm{Ni2-Ni3}} \left(\hat{S}_{\mathrm{Ni2}} \hat{S}_{\mathrm{Ni3}} \right) -$$

$$-2J_{\mathrm{Co1-Ni2}} \left(\hat{S}_{\mathrm{Co1}} \hat{S}_{\mathrm{Ni2}} + \hat{S}_{\mathrm{Ni3}} \hat{S}_{\mathrm{Co4}} \right)$$

$$\hat{H} = \mu_B B \sum_i g_i \hat{S}_i + D_{\mathrm{Ni}} \left(\hat{S}^2_{z_{\mathrm{Ni2}}} - \frac{\hat{S}^2_{\mathrm{Ni2}}}{3} + \hat{S}^2_{z_{\mathrm{Ni3}}} - \frac{\hat{S}^2_{\mathrm{Ni3}}}{3} \right) - D_{\mathrm{Co}} \left(\hat{S}^2_{z_{\mathrm{Co1}}} - \frac{\hat{S}^2_{\mathrm{Co1}}}{3} + \hat{S}^2_{z_{\mathrm{Co4}}} - \frac{\hat{S}^2_{\mathrm{Co4}}}{3} \right) -$$

$$-2J_{\mathrm{Ni2-Ni3}} \left(\hat{S}_{\mathrm{Ni2}} \hat{S}_{\mathrm{Ni3}} \right) - 2J_{\mathrm{Co1-Ni2}} \left(\hat{S}_{\mathrm{Co1}} \hat{S}_{\mathrm{Ni2}} + \hat{S}_{\mathrm{Ni3}} \hat{S}_{\mathrm{Co4}} \right)$$

Unfortunately, even by fixing $J_{\mathrm{Ni2\text{-}Ni3}}$ to –5.1 cm^{-1} or –2.8 cm^{-1} (compounds **2** and **9**) and g_{Co}=g_{Ni}=2.15 reasonable model couldn't be obtained. Attempts of swapping the positions of spin carriers were also tried, but both cases led to unreasonably high D_{Ni} parameters and low $J_{\mathrm{Co\text{-}Ni}}$ values. Contributions of possible paramagnetic impurities were not considered although such scenario shouldn't be neglected.

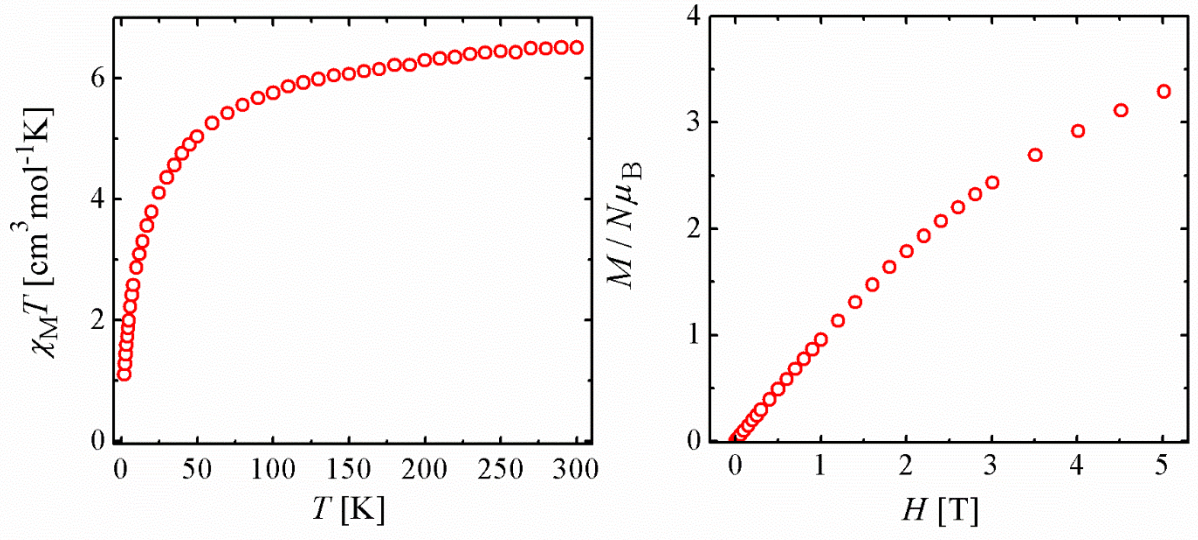

Figure 2.16. $\chi_M T$ vs T and $M/N\mu_B$ vs H curves for compound **11**. Measurement setup: cooling mode (300→2 K), B = 0.3 T; T_{mag} = 2 K.

In heterometallic $[NiZn]_2$ compound **12**, measured room temperature (300 K) value of $\chi_M T$ product of 2.374 cm^3Kmol^{-1} (g_{calc}=2.18) was consistent with proposed heterometallic nature of compound being only slightly above the expected 2.00 cm^3Kmol^{-1} for two paramagnetic Ni^{II} ions (g=2.0) and two diamagnetic Zn^{II} ions. Decrease in temperature is followed by steady reduction of the $\chi_M T$ product down to 50 K ($\chi_M T$=2.042 cm^3Kmol^{-1}). Below the latter temperature, sharp decline of $\chi_M T$ occurs, ending at 0.175 cm^3Kmol^{-1}(2 K), indicative of weak antiferromagnetic interactions between two spin carriers. Field-dependent magnetization measurement at 2K increases linearly with increasing magnetic field reaching the highest value of only 0.733 μ_B, well below the expected 4 μ_B for two S=1 ions (g=2, Figure 2.17). Possible anisotropy of Ni^{II} ions, as well as their interaction, were estimated by modelling the experimental data ($\chi_M T$ *vs* T and $M/N\mu_B$ *vs* H) through matrix diagonalization of spin Hamiltonians:

$$\widehat{H} = \mu_B B \sum_i g_i \hat{S}_i - 2J_{\mathrm{Ni-Ni}}\left(\hat{S}_{\mathrm{Ni2}}\hat{S}_{\mathrm{Ni3}}\right)$$

$$\widehat{H} = \mu_B B \sum_i g_i \hat{S}_i + D_{\mathrm{Ni}}\left(\hat{S}^2_{z_{\mathrm{Ni2}}} - \frac{\hat{S}^2_{\mathrm{Ni2}}}{3} + \hat{S}^2_{z_{\mathrm{Ni3}}} - \frac{\hat{S}^2_{\mathrm{Ni3}}}{3}\right) - 2J_{\mathrm{Ni-Ni}}\left(\hat{S}_{\mathrm{Ni2}}\hat{S}_{\mathrm{Ni3}}\right)$$

Model considering only magnetic interaction between Ni^{II} centres reproduced nicely $\chi_M T$ *vs* T data with fixed g_{Ni}=2.16 and J_{Ni2Ni3}= –3.24 cm^{-1} but it underestimated $M/N\mu_B$ *vs* H values at intermediate fields. These deviations can't be fixed even with contribution of impurities in the model so anisotropy of Ni^{II} was considered. The best replication of experimental data was achieved by fixing g_{Ni}=2.16 and D_{Ni}=12.50 cm^{-1} and refining J_{Ni2Ni3} to –2.94 cm^{-1} (Figure 2.17). Switching the sign of D_{Ni} to –9.16 cm^{-1} reproduced nicely temperature dependence of $\chi_M T$ product, but showed weaker agreement with magnetization data. Smaller J_{Ni2Ni3} values for **12** than those obtained for homometallic derivatives **2** and **5** could possibly originate form larger angle between equatorial planes of two Ni^{II} centres which decreases the degree of overlap between $d_{x^2-y^2}$ magnetic orbitals.

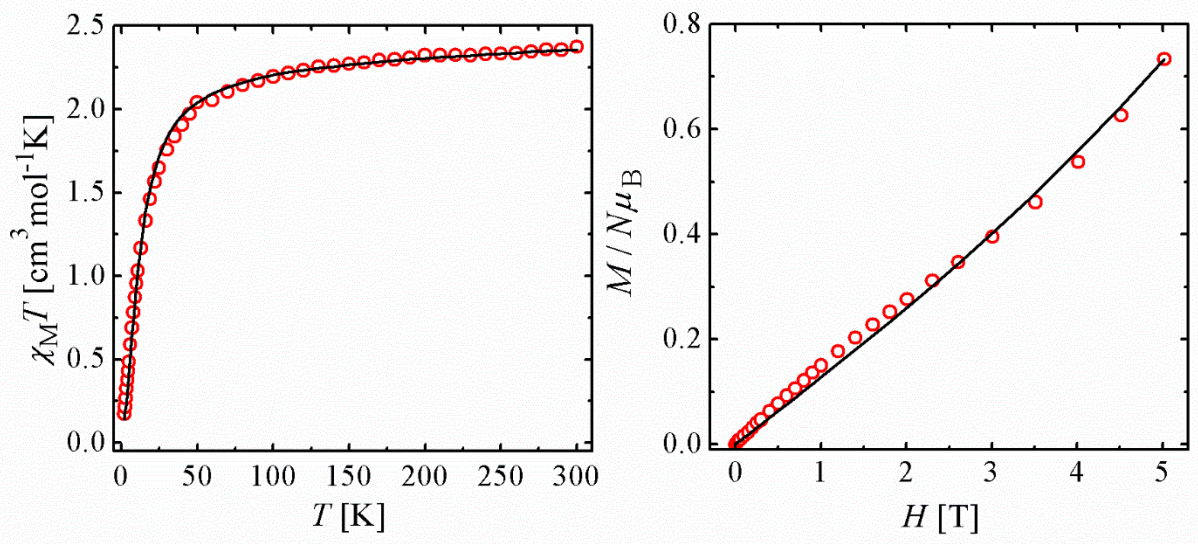

Figure 2.17. $\chi_M T$ vs T and $M/N\mu_B$ vs H curves for compound **12** with the best fit (solid line). Measurement setup: cooling mode (300→2 K), B = 0.5 T; T_{mag} = 2 K.

Finally, dc studies of heterometallic $[CoZn]_2$ compound **13** showed great similarity with dinuclear $[Co_2]$ compound **1**, as expected from the proposed disposition of metals in solid state structure. Observed room temperature (300 K) $\chi_M T$ product of 6.122 cm^{3}Kmol^{-1} (g_{calc}=2.55) exceeds significantly expected 3.75 cm^{3}Kmol^{-1} (g=2.00) for two high-spin Co^{II} ions (S=3/2). Upon cooling, this value decays slowly down to 70 K (5.081 cm^{3}Kmol^{-1}), followed by sharp drop to $\chi_M T$=0.585 cm^{3}Kmol^{-1} at 2 K. Similarly with behaviour of compound **2**, field-dependent magnetization measurement at 2K showed *S*-shaped magnetization curve with the highest value of 3.115 μ_B (5 T), well below the expected 6 μ_B (Figure 2.18). Such behaviour reflects potential antiferromagnetic interaction between high-spin Co^{II} ions with probable orbital contributions to magnetic moment and related zero-field splitting effects. These were validated from experimental $\chi_M T$ *vs* T and $M/N\mu_B$ *vs* H data by matrix diagonalization of spin Hamiltonian:

$$\hat{H} = \mu_B B \sum_i g_i \hat{S}_i + D_{Co}\left(\hat{S}^2_{z_{Co2}} - \frac{\hat{S}^2_{Co2}}{3} + \hat{S}^2_{z_{Co3}} - \frac{\hat{S}^2_{Co3}}{3}\right) - 2J_{Co-Co}\left(\hat{S}_{Co2}\hat{S}_{Co3}\right)$$

By fixing the g_{Co}=2.55, fitted parameters yielded $J_{Co\text{-}Co}$= –1.29 cm^{-1} and D_{Co}=49.90 cm^{-1} or D_{Co}=–66.47 cm^{-1} and $J_{Co\text{-}Co}$= –0.74 cm^{-1}. Both models reproduce nicely $\chi_M T$ *vs* T curve and shape of $M/N\mu_B$ *vs* H curve but underestimate its values at lower fields and overestimate it at higher fields (Figure 2.18). This issue couldn't be solved even by inclusion of spin-orbit coupling in spin Hamiltonian:

$$\hat{H} = \mu_B B \sum_i (g_i \hat{S}_i + \sigma_i \hat{L}_i) - 2J_{\mathrm{Co-Co}}(\hat{S}_{\mathrm{Co2}}\hat{S}_{\mathrm{Co3}}) + \sum_i \lambda_i (\sigma_i \hat{L}_i \cdot \hat{S}_i)$$

From this model, σ_i=–1.21, λ_i=–100.63 cm^{-1} and $J_{\mathrm{Co\text{-}Co}}$=-1.29 cm^{-1} were extracted as fitted parameters, with fixed g_{Co}=2.00. Nevertheless, here obtained $J_{\mathrm{Co\text{-}Co}}$ coupling constants agree nicely with the previously reported ones for compound **1**.

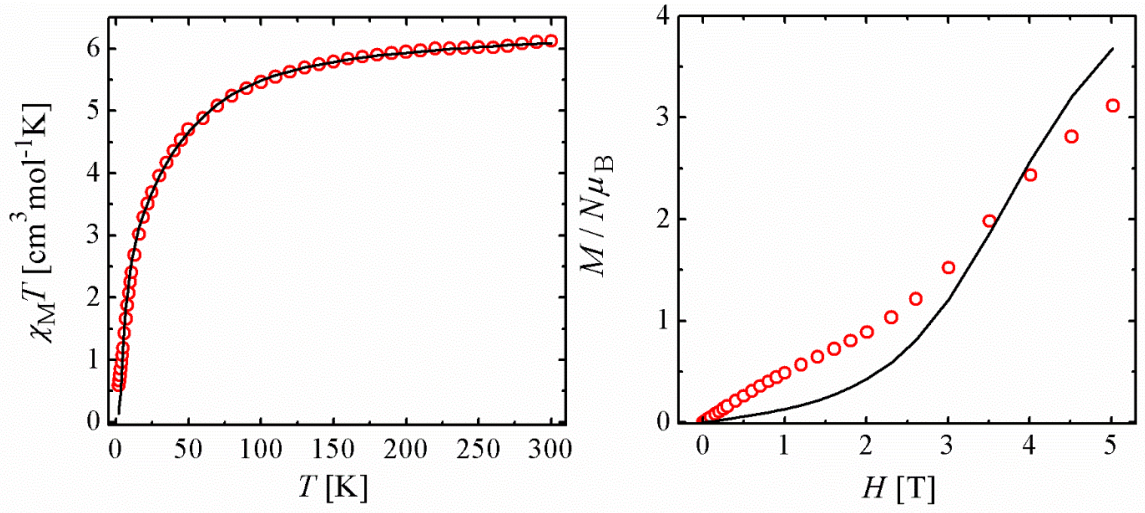

Figure 2.18. $\chi_M T$ vs T and $M/N\mu_B$ vs H curves for compound **13** with the best fit (solid line). Measurement setup: cooling mode (300→2 K), B = 0.5 T; T_{mag} = 2 K.

2.4.4. Experimental

Solvents and reagents were used as received from commercial suppliers in preparations of ligands and compounds. An exception was made only for Claisen condensations, where anhydrous THF (PureSolv Micro Solvent Purification Systems) was used as solvent to avoid any hydrolysis as possible side reaction. Sodium hydride was applied as a suspension in mineral oil (60% w/w), which was purified by washing with hexanes under nitrogen and posterior extraction of solvent by filter cannula (*vide infra*). Tetrabutylammonium hydroxide was employed as a solution in methanol (c=1 mol/dm^3), while cobalt(II), nickel(II), copper(II) and zinc(II) perchlorates were used as hexahydrated salts.

H_4L1: Sodium hydride (4.47 g, 111.8 mmol) was suspended under nitrogen atmosphere in 80 mL of hexanes. Mixture was stirred at room temperature for 10 min, followed by extraction of solvent by filter cannula. Described procedure was repeated once again and to the resulting white solid was subsequently added dry THF (100 mL). In a separate Schlenk flask, 2-hydroxyacetophenone (6.92 g, 50.8 mmol) was dissolved under nitrogen in 50 mL of dry THF and then added dropwise to the suspension of NaH in THF. Described procedure was accompanied with yellow-green colouring of the reaction mixture and evolution of hydrogen. Upon complete addition, obtained suspension was stirred for 15 min at room temperature, ending with addition of THF solution (50 mL) of dimethyl oxalate (3.00 g, 25.4 mmol). Reaction was then carefully brought to reflux since abrupt hydrogen evolution occurs when the temperature hits 50 °C, followed by sudden orange colouring of reaction mixture. After 12 h of reflux, orange suspension was cooled down to room temperature and THF was removed under reduced pressure. Obtained orange-red solid was then dissolved in water and acidified with HCl(aq) to the pH=3. Precipitated yellow-brown solid was collected by filtration and purified by recrystallisation from acetone (average yield 2.60 g, 31%).
^{1}H NMR (400 MHz, $CDCl_3$), δ(ppm): 6.97 (t, 2H, -Ar-*H*), 7.03 (d, 2H, -Ar-*H*), 7.15 (s, 2H, -COC*H*COH), 7.53 (t, 2H, -Ar-*H*), 7.84 (d, 2H, -Ar-*H*), 11.92 (s, 2H, Ar-O*H*), 14.17 (s, 2H, -OH_{enol}). ESI MS: m/z $[H_3L1]^-$= 325.07. IR (KBr pellet) v/cm^{-1}: 3420 b, 3114 s, 3049 b, 1625 s, 1598 s, 1575 s, 1489 s, 1442 s, 1404 b, 1334 s, 1301 s, 1265 s, 1205 s, 1163 s, 1130 s, 1106 s, 1034 s, 848 s, 832 s, 812 s, 760 s, 741 s, 704 s, 684 b, 602 s, 531 w, 507 s, 477 w, 425 w. Single crystals of ligand **H_4L1** were obtained by dissolving the solid **H_4L1** in hot chloroform

and slowly cooling down the solution. EA (%); Calc. (Found for $C_{18}H_{14}O_6 \cdot 0.2\ H_2O$): C 65.53 (65.68), H 4.40 (4.56), N 0.00 (0.00).

$[Co_2(H_2L1)(C_5H_5N)_8](ClO_4)_2$ (1): Tetrabutylammonium hydroxide (185 µL, 0.185 mmol) was added to light yellow solution of ligand **H_4L1** (30.0 mg, 0.092 mmol) in pyridine (10 mL) causing its immediate change of color to orange. Obtained mixture was stirred at room temperature for 10 min and then was added dropwise to a pyridine solution (10 mL) of $Co(ClO_4)_2 \cdot 6H_2O$ (67.3 mg, 0.184 mmol), changing its appearance from pink to dark orange. Resulting solution was covered and stirred at room temperature for 60 min before filtration (no precipitate was observed). Isolated filtrate was divided in two parts which were then layered with hexanes or Et_2O to produce orange-red blocks by liquid-liquid diffusion over a period of three weeks (average yield 45.0 mg, 38%). IR (KBr pellet) ν/cm^{-1}: 3430 vb, 3074 b, 1601 s, 1583 s, 1554 s, 1487 s, 1456 vs, 1405 s, 1336 s, 1298 s, 1240 s, 1213 s, 1104 sb, 1069 vs, 1041 s, 1011 s, 939 w, 812 s, 763 s, 700 s, 625 s, 432 s.

$[Ni_2(H_2L1)(C_5H_5N)_8](ClO_4)_2$ (2): Synthetic procedure was done in the same way as previously described for **1**, starting from 30.0 mg (0.092 mmol) of **H_4L1** and 67.2 mg (0.184 mmol) of $Ni(ClO_4)_2 \cdot 6H_2O$. After 60 min of stirring at room temperature, obtained orange solution was filtered to remove small crop of insoluble precipitate (less than 5 mg) and divided in two equal parts which were layered with Et_2O or hexanes. After a period of three weeks, liquid-liquid diffusion completed the formation of orange blocks (average yield 42 mg, 36%). IR (KBr pellet) ν/cm^{-1}: 3428 b, 3070 b, 1603 s, 1586 s, 1552 s, 1486 s, 1456 s, 1444 s, 1404 s, 1334 s, 1298 s, 1240 s, 1210 s, 1103 s, 1069 s, 1039 s, 1010 w, 813 w, 761 s, 700 s, 624 s, 567 w, 543 w, 431 s. EA (%); Calc. (Found for $C_{58}H_{52}N_8O_{14}Ni_2Cl_2 \cdot 1.7\ C_5H_5N$): C 56.73 (56.89), H 4.33 (4.40), N 9.65 (9.46).

$[Zn_2(H_2L1)(C_5H_5N)_8](ClO_4)_2$ (3): Synthetic procedure was done in the same way as previously described for **1**, starting from 30.0 mg (0.092 mmol) of **H_4L1** and 68.5 mg (0.184 mmol) of $Zn(ClO_4)_2 \cdot 6H_2O$. After 60 min of stirring at room temperature, obtained yellow solution was filtered to remove small crop of insoluble precipitate (less than 5 mg) and divided in two equal parts which were layered with Et_2O or hexanes. After a period of three weeks, liquid-liquid diffusion completed the formation of light yellow blocks (average yield 29 mg, 25%). IR (KBr pellet) $\nu/cm^{-}1$: 3430 vb, 3074 b, 1601 s, 1583 s, 1554 s, 1487 s, 1456 vs, 1405 s, 1336 s, 1298 s, 1240 s, 1213 s, 1104 sb, 1069 vs, 1041 s, 1011 s, 939 w, 812 s, 763 s, 700 s, 625 s, 432 s.

$[Co_4(L1)(OH)_2(C_5H_5N)_{10}](ClO_4)_2$ (4): Tetrabutylammonium hydroxide (550 μL, 0.550 mmol) was added to the light yellow solution of ligand **H_4L1** (30.0 mg, 0.092 mmol) in pyridine (10 mL) causing its immediate change of color to orange. Obtained mixture was stirred at room temperature for 10 min and then was added dropwise to a pyridine solution (10 mL) of $Co(ClO_4)_2{\cdot}6H_2O$ (134.6 mg, 0.368 mmol), changing its appearance from pink to dark red. Resulting solution was covered and stirred at room temperature for 60 min before filtration. No precipitate was observed, while isolated filtrate was divided in two parts which were then layered with hexanes and Et_2O to produce dark red needles by liquid-liquid diffusion over a period of three weeks (average yield 57 mg, 39%). Larger crystals were grown using vapour-liquid diffusion of the same solvent-antisolvent systems. IR (KBr pellet) ν/cm^{-1}: 3447 vb, 3067 b, 1602 s, 1557 s, 1524 s, 1486 s, 1435 vs, 1377 s, 1308 s, 1249 s, 1200 s, 1138 s, 1096 sb, 1064 vs, 1037 vs, 931 s, 855 sw, 805 s, 754 s, 698 s, 624 s, 591 s, 545 s, 426 s.

$[Ni_4(L1)(OH)_2(C_5H_5N)_{10}](ClO_4)_2$ (5): Synthetic procedure was done in the same way as previously described for **4**, starting from 30 mg of **H_4L1** and $Ni(ClO_4)_2{\cdot}6H_2O$ (134.5 mg, 0.368 mmol). After 60 min of stirring at room temperature, obtained dark orange solution was filtered and filtrate was divided in two equal parts which were layered with Et_2O or hexanes. After a period of three weeks, liquid-liquid diffusion completed the formation of orange-brown needles (average yield 62 mg, 43%). Larger crystals were grown using vapour-liquid diffusion of the same solvent-antisolvent systems. IR (KBr pellet) ν/cm^{-1}: 3430 vb, 3069 b, 1602 s, 1555 s, 1522 s, 1484 s, 1431 s, 1374 s, 1335 s, 1294 s, 1247 s, 1214 s, 1198 s, 1151 s, 1087 s, 1066 s, 1040 s, 1011 s, 929 s, 851 w, 866 w, 753 s, 695 s, 629 s, 558 s, 429 s.

$[Cu_4(L1)(OH)_2(C_5H_5N)_8](ClO_4)_2$ (6): Synthetic procedure was done in the same way as previously described for **4**, starting from 30 mg of **H_4L1** and $Cu(ClO_4)_2{\cdot}6H_2O$ (136.3 mg, 0.368 mmol). After 60 min of stirring at room temperature, obtained dark brown solution was filtered to remove small amount of insoluble precipitate. Obtained filtrate was then layered with Et_2O or hexanes. After a period of three weeks, liquid-liquid diffusion completed the formation of yellow-green blocks (average yield 45 mg, 34%). IR (KBr pellet) ν/cm^{-1}: 3450 vb, 3067 b, 1601 s, 1558 s, 1524 s, 1488 s, 1435 vs, 1377 s, 1308 s, 1249 s, 1200 s, 1138 s, 1098 sb, 1064 vs, 1037 vs, 931 s, 855 sw, 805 s, 755 s, 698 s, 624 s, 591 s, 545 s, 423 s.

. EA (%); Calc. (Found for $C_{58}H_{52}N_8O_{16}Cu_4Cl_2{\cdot}0.9\ H_2O{\cdot}C_5H_5N$): C 49.22 (49.22), H 3.85 (3.89), N 8.20 (8.23).

$[Zn_4(L1)(OH)_2(C_5H_5N)_{10}](ClO_4)_2$ (7): Synthetic procedure was done in the same way as previously described for **4**, starting from 30 mg of **H_4L1** and $Zn(ClO_4)_2{\cdot}6H_2O$ (137.0 mg, 0.368 mmol). After 60 min of stirring at room temperature, obtained orange solution was filtered and filtrate was divided in two equal parts which were layered with Et_2O or hexanes. After a period of three weeks, liquid-liquid diffusion completed the formation of orange needles (average yield 39 mg, 26%). Larger crystals were grown using vapour-liquid diffusion of the same solvent-antisolvent systems. IR (KBr pellet) ν/cm^{-1}: 3447 vb, 3067 b, 1602 s, 1557 s, 1524 s, 1486 s, 1435 vs, 1377 s, 1308 s, 1249 s, 1200 s, 1138 s, 1096 sb, 1064 vs, 1037 vs, 931 s, 855 sw, 805 s, 754 s, 698 s, 624 s, 591 s, 545 s, 426 s. EA (%); Calc. (Found for $C_{68}H_{62}N_{10}O_{16}Zn_4Cl_2{\cdot}3.1\ H_2O$): C 49.10 (48.91), H 4.13 (3.93), N 8.42 (8.27).

$[(CuCo)_4(L1)(OH)_2(C_5H_5N)_{10}](ClO_4)_2$ (8): Tetrabutylammonium hydroxide (550 µL, 0.550 mmol) was added to the light yellow solution of ligand H_4L1 (30.0 mg, 0.092 mmol) in pyridine (10 mL) causing its immediate change of color to orange. Obtained mixture was stirred at room temperature for 10 min and then was added dropwise to a pyridine solution (10 mL) of $Co(ClO_4)_2{\cdot}6H_2O$ (67.3 mg, 0.184 mmol) and $Cu(ClO_4)_2{\cdot}6H_2O$ (68.1 mg, 0.184 mmol), changing its appearance from pink suspension to red-brown solution. Resulting mixture was covered and stirred at room temperature for 90 min before filtration. No precipitate was observed, while isolated filtrate was divided in two parts which were then layered with hexanes and Et_2O to produce orange-red needles by liquid-liquid diffusion over a period of three weeks (average yield 42 mg, 29%). Larger crystals were grown using vapour-liquid diffusion of the same solvent-antisolvent systems. IR (KBr pellet) ν/cm^{-1}: 3450 vb, 3069 b, 1601 s, 1555 s, 1523 s, 1487 s, 1433 vs, 1376 s, 1310 s, 1248 s, 1199 s, 1136 s, 1097 sb, 1064 vs, 1037 vs, 931 s, 855 sw, 805 s, 754 s, 698 s, 624 s, 591 s, 543 s, 428 s.
EA (%); Calc. (Found for $C_{68}H_{62}N_{10}O_{16}Co_2Cu_2Cl_2$): C 51.33 (51.10), H 3.93 (4.04), N 8.80 (9.15).

$[(CuNi)_2(L1)(OH)_2(C_5H_5N)_{10}](ClO_4)_2$ (9): Synthetic procedure was done in the same way as previously described for **8**, starting from 30 mg of H_4L1 and bimetallic mixture containing $Cu(ClO_4)_2{\cdot}6H_2O$ (68.1 mg, 0.184 mmol) and $Ni(ClO_4)_2{\cdot}6H_2O$ (67.2 mg, 0.184 mmol). After 90 min of stirring at room temperature, obtained yellow-brown solution was filtered. Obtained filtrate was then layered with Et_2O or hexanes. After a period of three weeks, liquid-liquid diffusion completed the formation of yellow-brown needles (average yield 61 mg, 42%). Larger crystals were grown using vapour-liquid diffusion of the same solvent-antisolvent systems. IR (KBr pellet) ν/cm^{-1}: 3450 b, 3070 b, 1601 s, 1555 s, 1526 s, 1483 s, 1426 b, 1362

s, 1349 s, 1319 s, 1249 s, 1203 s, 1140 s, 1091 s, 1067 s, 1040 b, 931 s, 853 s, 805 s, 751 s, 696 s, 630 s, 559 s, 431 w. EA (%); Calc. (Found for $C_{68}H_{62}N_{10}O_{16}Cu_2Ni_2Cl_2{\cdot}2.15\ H_2O$): C 50.12 (49.96), H 4.10 (3.92), N 8.60 (8.63).

$[(CuZn)_2(L1)(OH)_2(C_5H_5N)_{10}](ClO_4)_2$ (10): Synthetic procedure was done in the same way as previously described for **8**, starting from 30 mg of H_4L1 and bimetallic mixture containing $Cu(ClO_4)_2{\cdot}6H_2O$ (68.1 mg, 0.184 mmol) and $Zn(ClO_4)_2{\cdot}6H_2O$ (68.5 mg, 0.184 mmol). After 90 min of stirring at room temperature, obtained yellow-brown solution was filtered to remove significant amount of insoluble precipitate (average 23 mg). Obtained filtrate was then layered with hexanes. After a period of three weeks, liquid-liquid diffusion completed the formation of yellow-brown needles (average yield 12 mg, 8 %). IR (KBr pellet) ν/cm^{-1}: 3450 vb, 3069 b, 1601 s, 1555 s, 1523 s, 1487 s, 1433 vs, 1376 s, 1310 s, 1248 s, 1199 s, 1136 s, 1097 sb, 1064 vs, 1037 vs, 931 s, 855 sw, 805 s, 754 s, 698 s, 624 s, 591 s, 543 s, 428 s.

$[(CoNi)_2(L1)(OH)_2(C_5H_5N)_{10}](ClO_4)_2$ (11): Synthetic procedure was done in the same way as previously described for **8**, starting from 30 mg of H_4L1 and bimetallic mixture containing $Co(ClO_4)_2{\cdot}6H_2O$ (67.3 mg, 0.184 mmol) and $Ni(ClO_4)_2{\cdot}6H_2O$ (67.2 mg, 0.184 mmol). After 90 min of stirring at room temperature, obtained orange-red solution was filtered. Obtained filtrate was then layered with Et_2O or hexanes. After a period of three weeks, liquid-liquid diffusion completed the formation of dark orange needles (average yield 56 mg, 39%). Larger crystals were grown using vapour-liquid diffusion of the same solvent-antisolvent systems. IR (KBr pellet) ν/cm^{-1}: 3450 vb, 3068 b, 1599 s, 1555 s, 1526 s, 1483 s, 1443 s, 1430 s, 1370 s, 1349 b, 1311 b, 1249 s, 1202 s, 1138 s, 1091 vs, 1066 vs, 1032 vs, 1026 b, 1009 s, 930 s, 852 s, 807 s, 752 s, 695 s, 625 s, 549 s, 426 s. EA (%); Calc. (Found for $C_{68}H_{62}N_{10}O_{16}Co_2Ni_2Cl_2{\cdot}4.70\ H_2O$): C 49.02 (48.78), H 4.32 (3.96), N 8.41 (8.05).

$[(ZnNi)_2(L1)(OH)_2(C_5H_5N)_{10}](ClO_4)_2$ (12): Synthetic procedure was done in the same way as previously described for **8**, starting from 30 mg of H_4L1 and bimetallic mixture containing $Ni(ClO_4)_2{\cdot}6H_2O$ (67.2 mg, 0.184 mmol) and $Zn(ClO_4)_2{\cdot}6H_2O$ (68.5 mg, 0.184 mmol). After 90 min of stirring at room temperature, obtained orange solution was filtered and filtrate was then layered with Et_2O or hexanes. After a period of three weeks, liquid-liquid diffusion completed the formation of orange needles (average yield 52 mg, 35%). Larger crystals were grown using vapour-liquid diffusion of the same solvent-antisolvent systems. IR (KBr pellet) ν/cm^{-1}: 3451 vb, 3069 b, 1598 s, 1554 s, 1523 s, 1482 s, 1431 s, 1371 s, 1351 s, 1250 s, 1214 s, 1201 s, 1138 s, 1088 s, 1066 s, 1037 vs, 1008 s, 928 w, 853 s, 809 s, 752 s, 695 s, 623 s, 548

s, 424 s. EA (%); Calc. (Found for $C_{68}H_{62}N_{10}O_{16}Zn_2Ni_2Cl_2 \cdot 1.60\ H_2O$): C 50.32 (50.32), H 4.05 (4.09), N 8.63 (8.67).

$[(ZnCo)_2(L1)(OH)_2(C_5H_5N)_{10}](ClO_4)_2$ (13): Synthetic procedure was done in the same way as previously described for **8**, starting from 30 mg of H_4L1 and bimetallic mixture containing $Co(ClO_4)_2 \cdot 6H_2O$ (67.3 mg, 0.184 mmol) and $Zn(ClO_4)_2 \cdot 6H_2O$ (68.5 mg, 0.184 mmol). After 90 min of stirring at room temperature, obtained red solution was filtered and filtrate was then layered with Et_2O or hexanes. After a period of three weeks, liquid-liquid diffusion completed the formation of red needles (average yield 44 mg, 30%). Larger crystals were grown using vapour-liquid diffusion of the same solvent-antisolvent systems.IR (KBr pellet) ν/cm^{-1}: 3448 vb, 3069 b, 1603 s, 1584 s, 1547 s, 1480 s, 1444 vs, 1406 s, 1333 s, 1280 s, 1235 s, 1214 s, 1094 s, 1066 s, 1030 s, 928 s, 853 s, 809 s, 753 vs, 697 s, 625 s, 546 s, 427 s. EA (%); Calc. (Found for $C_{68}H_{62}N_{10}O_{16}Zn_2Co_2Cl_2 \cdot 4.85\ H_2O$): C 48.55 (48.15), H 4.30 (3.88), N 8.33 (8.35).

2.4.5. Literature

1. G. Aromí, P. Gamez and J. Reedijk, *Coordination Chemistry Reviews*, 2008, **252**, 964-989.
2. P. A. Vigato, V. Peruzzo and S. Tamburini, *Coordination Chemistry Reviews*, 2009, **253**, 1099-1201.
3. A. J. Brock, J. K. Clegg, F. Li and L. F. Lindoy, *Coordination Chemistry Reviews*, 2018, **375**, 106-133.
4. D. Aguilà, L. A. Barrios, O. Roubeau, S. J. Teat and G. Aromí, *Chemical Communications*, 2011, **47**, 707-709.
5. G. Aromí, *Comments on Inorganic Chemistry*, 2011, **32**, 163-194.
6. L. A. Barrios, D. Aguilà, O. Roubeau, P. Gamez, J. Ribas-Ariño, S. J. Teat and G. Aromí, *Chemistry – A European Journal*, 2009, **15**, 11235-11243.
7. J. S. Uber, M. Estrader, J. Garcia, P. Lloyd-Williams, A. Sadurní, D. Dengler, J. van Slageren, N. F. Chilton, O. Roubeau, S. J. Teat, J. Ribas-Ariño and G. Aromí, *Chemistry – A European Journal*, 2017, **23**, 13648-13659.
8. F. Li, J. K. Clegg, P. Jensen, K. Fisher, L. F. Lindoy, G. V. Meehan, B. Moubaraki and K. S. Murray, *Angewandte Chemie International Edition*, 2009, **48**, 7059-7063.
9. V. A. Grillo, E. J. Seddon, C. M. Grant, G. Aromí, J. C. Bollinger, K. Folting and G. Christou, *Chemical Communications*, 1997, DOI: 10.1039/A702971C, 1561-1562.
10. H.-F. Li, P.-F. Yan, P. Chen, Y. Wang, H. Xu and G.-M. Li, *Dalton Transactions*, 2012, **41**, 900-907.
11. J. K. Cherutoi, J. D. Sandifer, U. R. Pokharel, F. R. Fronczek, S. Pakhomova and A. W. Maverick, *Inorganic Chemistry*, 2015, **54**, 7791-7802.
12. P. J. Bonitatebus Jr and S. K. Mandal, *Chemical Communications*, 1998, DOI: 10.1039/A708693H, 939-940.
13. R. W. Saalfrank, N. Löw, S. Kareth, V. Seitz, F. Hampel, D. Stalke and M. Teichert, *Angewandte Chemie International Edition*, 1998, **37**, 172-175.
14. Y. Zhang, S. Wang, G. D. Enright and S. R. Breeze, *Journal of the American Chemical Society*, 1998, **120**, 9398-9399.
15. J. Salinas-Uber, L. A. Barrios, O. Roubeau and G. Aromí, *Polyhedron*, 2013, **54**, 8-12.
16. V. Velasco, D. Aguilà, L. A. Barrios, I. Borilovic, O. Roubeau, J. Ribas-Ariño, M. Fumanal, S. J. Teat and G. Aromí, *Chemical Science*, 2015, **6**, 123-131.
17. R. Díaz-Torres and S. Alvarez, *Dalton Transactions*, 2011, **40**, 10742-10750.
18. R. Shannon, *Acta Crystallographica Section A*, 1976, **32**, 751-767.
19. A. W. Addison, T. N. Rao, J. Reedijk, J. van Rijn and G. C. Verschoor, *Journal of the Chemical Society, Dalton Transactions*, 1984, DOI: 10.1039/DT9840001349, 1349-1356.
20. S. Alvarez and M. Llunell, *Journal of the Chemical Society, Dalton Transactions*, 2000, DOI: 10.1039/B004878J, 3288-3303.
21. N. F. Chilton, R. P. Anderson, L. D. Turner, A. Soncini and K. S. Murray, *Journal of Computational Chemistry*, 2013, **34**, 1164-1175.
22. L. A. Barrios, D. Aguilà, S. Méllat, O. Roubeau, S. J. Teat, P. Gamez and G. Aromí, *Comptes Rendus Chimie*, 2008, **11**, 1117-1120.
23. V. H. Crawford, H. W. Richardson, J. R. Wasson, D. J. Hodgson and W. E. Hatfield, *Inorganic Chemistry*, 1976, **15**, 2107-2110.
24. E. Ruiz, P. Alemany, S. Alvarez and J. Cano, *Inorganic Chemistry*, 1997, **36**, 3683-3688.
25. A. Bencini, C. Benelli, A. Dei and D. Gatteschi, *Inorganic Chemistry*, 1985, **24**, 695-699.

CHAPTER III

DESIGN AND PREPARATION OF COORDINATION COMPOUNDS AS MOLECULAR PROTOTYPES OF QUANTUM GATES

3.1. Introduction

As elaborated in the introducing chapter, one of the greatest potentials of the molecular magnetism is to deliver a molecular spin-based system for quantum information processing.[1] To reach that milestone, optimised electronic spin based qubits such as single metal ions or their clusters should be assembled into quantum gates in a controllable manner. This means that each qubit within the qugate has to be behave as the well isolated two-levels system to facilitate the encoding of information, but at the same time the whole ensemble should remain weakly coupled to exhibit the property of the quantum entanglement between the spin wave functions.[2] Additionally, molecular prototypes for the universal C-NOT quantum gates should incorporate a certain degree of asymmetry between their component qubits in order to address and initialise them individually.

In the context of molecular building blocks for quantum computing, the coordination compounds of vanadium(IV) have shown an immense potential. To start, one of the first complexes exhibiting the long quantum coherence evidenced in appearance of Rabi oscillations was a polyoxometalate cluster with the S=1/2 ground state.[3] Following this study, Loss and Coronado showed how electrically gated antiferromagnetic interaction between the vanadyl centres (S=1/2) in the redox-active polyoxometallate $[PMo_{12}O_{40}(VO)_2]^{n-}$ can be considered as a realisation of a molecular prototype for the √SWAP quantum gate.[4, 5] In addition, quantum coherence studies by Freedman *et al.* of a single vanadium(IV) qubits in the nuclear-spin free environments provided the record phase memory times for molecular systems,[6-8] while extension of this work by Sessoli showed that vanadyl oxocation (VO^{2+}) can outperform the free V^{4+} qubits by slowing down the T_1 decay, giving evidence of the quantum coherence even at the room temperature, regardless the spin nature of the ligands.[9, 10]

On the other hand, previous work of our group highlighted how predesigned β-diketone scaffold can be easily employed in the construction of quantum logic gates. Firstly, asymmetric environment of the carboxylate-β-diketone ligand H_3L was used to selectively embed [4*f*-4*f*'] dimers among which [CeEr] pair fulfilled all the necessary requirements to be employed as the C-NOT-2-qubit quantum gate.[11] Recently, symmetric ligand field of the photoswitchable *bis*-β-diketone was used to prepare the family of clusters containing weakly coupled [3*d*-3*d*'] pairs.[12] Combination of the photochromic dithienylethene spacer

between the two-level M_S=±1/2 [CuZn] or [CuNi] qubits with their microsecond phase memory times evidenced the possibility of using those entities as the light-modulated √SWAP quantum gates.

Continuing this legacy in this chapter, different approaches of connecting the 3*d*-based effective *S*=1/2 qubits into *n*-quantum gates (n=2, 3) will be presented. First strategy deals with the incorporation of individual vanadyl ions into the symmetric *bis*-β-diketone scaffold, while the second one focuses on the rational integration of the antiferromagnetically coupled [$Cu^{II}Ni^{II}$] dimers within the asymmetric and multifunctional *b*is-β-diketone ligands. While the rich redox chemistry of the vanadyl ions disabled the possibility of directing the formation of its assemblies, well defined oxo-hydroxo bridged [CuNi] building block allowed the controlled transmission of the imposed asymmetry of the ligating systems to the coordination entity. In that sense, prudent design and rational use of the new asymmetric ligands H_4L_A and H_4L_{A2} ensured the preparation of two molecular prototypes for the C-NOT-2-qubit quantum gates and one possible prototype of the rare TOFFOLI-3-qubit quantum gate, which until now has only been proposed by Luis *et al*. for certain coherent oscillations between the eight spin states in the magnetically diluted $K_{12}[Gd(H_2O)_5P_5W_{30}O_{110}]$.[13]

3.2. Vanadium assemblies with the *bis*-β-diketone ligands

3.2.1. Synthesis and structural study of the vanadium metallacyclophanes

Inspired by the growing importance of vanadium in emerging areas of molecular magnetism we've decided to explore the coordination chemistry of vanadium with the *bis*-β-diketone ligands, with the long-term view of exploiting its potential in the context of quantum computing. Since this chemistry was rather poorly explored and presented a new line of research for our group[14], choice of the starting ligands included the structurally versatile 1,3-*bis*-(3-oxo-3-(2-hydroxyphenyl)-propionyl)-benzene (**H_4L5**) and 1,3-*bis*-(3-oxo-3-(2-hydroxyphenyl)-propionyl)-pyridine (**H_4L6**, Scheme 3.1) whose reactivity with the late first row transition metals was already established. Prior to this work, two separated phenolato-diketonato coordination pockets within the ligand **H_4L5** were employed in a controlled preparation of weakly coupled dinuclear and tetranuclear (homo- and heterometallic) assemblies of the 3*d* metals.[15, 16] On the other hand, additional dipicolinato chelating site in the ligand **H_4L6** led to the discovery of some unexpected

structural features. Employment of this ligand under weakly basic conditions allowed the deprotonation of only β-diketone moiety leading to the octanuclear cluster $[Co_8O(OH)(H_2L2)_6]NO_3$, which encapsulates a very rare [μ_3-O···H···μ_3-O] structural motif.[17] Similarly, use of a strong base (TBAOH, NaH) and a coordinating solvent (pyridine) directed the outcome of aerobic analogous reactions towards the unusual tetranuclear $[Co_4(L2)_2(OH)(py)_7]NO_3$ and octanuclear $[Co_8Na_4(L2)_4(OH)_2(CO_3)_2(py)_{10}](BF_4)_2$ coordination compounds.[18] The exceptionality of these structures lies in the existence of a very rare bridging "crevice" pyridine ligand within the former, or two trapped carbonate anions, within the latter, forced to stay at the shortest non-covalent distance ever observed. Interestingly, all the studied compounds integrate the ligands in a linear conformation, with both coordination pockets facing the same direction (*syn*, *syn* conformation, Scheme 3.1).

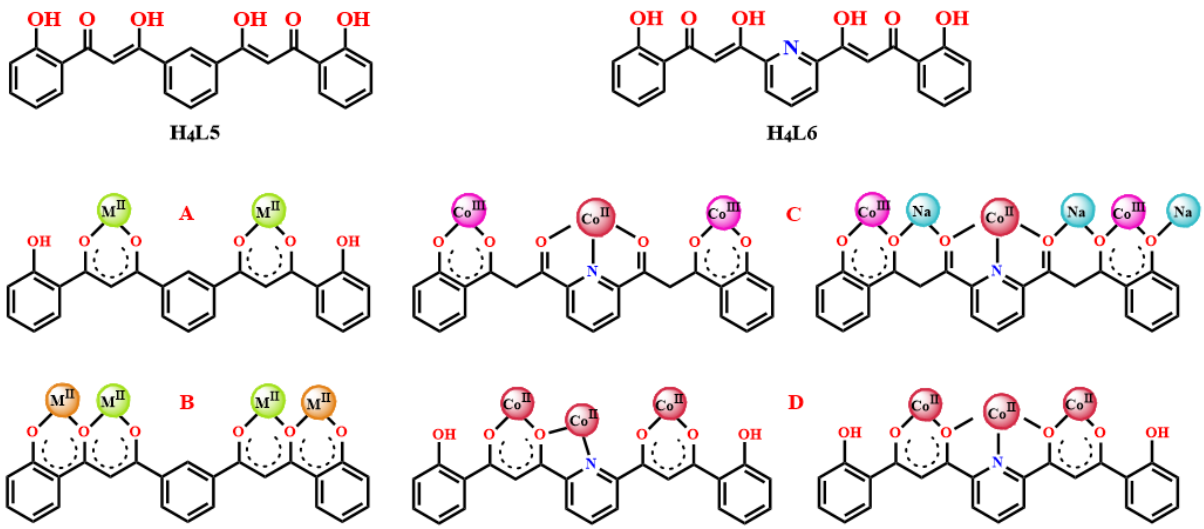

Scheme 3.1: Ligands **H_4L5** and **H_4L6**, together with their known coordination modes and conformations. (**A**) $[M_2(H_2L5)_2]$[15]; (**B**) $[M_4(L5)_2]$ and $[M_2M'_2(L5)_2]$[16]; (**c**) $[Co_4(L6)_2(OH)(py)_7]NO_3$ (*left*) and $[Co_8Na_4(L6)_4(OH)_2(CO_3)_2(py)_{10}](BF_4)_2$ (*right*)[18]; (**E**) $[Co_8O(OH)(H_2L6)_6]NO_3$[17]

Surprisingly, replacing the late 3*d* metals with vanadyl ions and mimicking the same reaction conditions yielded the completely different reactivity patterns. Thus, aerobic reaction between hydrated vanadyl sulfate and **$L5^{4-}$** (deprotonated using the NaH) in pyridine produced the tetranuclear cluster $[(VO)_4(H_2L5)_4(py)_4]$ (**14**). Yield of this reaction was greatly dependent of the employed stoichiometry which in the end was optimised with metal-ligand ratio of 2:1. Attempts to replicate the reaction outcome using the exact stoichiometry with the same or a different base (Et_3N, TBAOH) were unsuccessful, which could indicate the

existence of side reactions and a potential templating role of Na^+. Nevertheless, formation of this compound may be described with a balanced chemical equation:

$$4\ VOSO_4{\cdot}H_2O + 4\ H_4L5 + 8NaH + 4py \longrightarrow [(VO)_4(H_2L5)_4(py)_4] + 8H_2 + 4Na_2SO_4 + 4H_2O$$

Compound **14** crystallizes in the monoclinic space group $P2_1/c$ as a neutral metallacyclophane $[(VO)_4(H_2L1)_4(py)_4]$ accompanied with the six pyridine molecules (Table III.A1). The asymmetric unit is defined by one half of the molecular components, whereas the unit cell is composed of two clusters. Molecular structure of **14** consists of four vanadyl $(V^{IV}O)^{2+}$ ions held together by two pairs of conformational isomers of partially deprotonated $\mathbf{H_2L5^{2-}}$ ligands (Figure 3.1A). Additionally, each metallic site coordinates to one pyridine molecule which completes the distorted octahedral O_5N coordination environment around them. Each $\mathbf{H_2L5^{2-}}$ ligand chelates two vanadyl ions with its two β-diketonato coordination pockets while the phenolic protons remain intact. The topology of the metallic core can be described as rhomboidal, resulting from the linear and bent (V-shaped) conformations of the $\mathbf{H_2L5^{2-}}$ ligands, obtained by differing degrees of rotation around the single bonds between the central *m*-phenylene spacer and the β-diketone groups (with both planes either near 0° or near 180°). Thus, the short side of the parallelogram (V···V distance of 7.514(3) Å) spans the ligand in a linear conformation where both chelating pockets are orientated in the same direction. The longer side (V···V distance of 10.892(4) Å) is defined by bent (V-shape) $\mathbf{H_2L5^{2-}}$ ligands with both coordination pockets pointing to opposite directions. The latter pair of ligands exhibits a nearly flat conformation and lie parallel to each other, establishing mutual intramolecular π···π interactions and leaving no voids for the inclusion of the guest molecules. Consequently, diagonals of the $[V_4]$ parallelogram include one short and one long V···V distance, measuring 6.508(3) Å and 17.546(5) Å), respectively. As mentioned before, asymmetric unit is defined by one half of the cluster, meaning that two vanadyl sites are crystallographically independent. Octahedral ligand field around the metals consists of axial oxo and *O*-diketonato donors while the equatorial plane is defined by the NO_3 ligand field. *Trans* effect along the axis of the V=O bond (average 1.595 Å) leads to two very disparate V–O bond distances, with axial V−O being the longest (average 2.142 Å, Table III.A3). The equatorial plane around vanadium atoms is not fully homogeneous either, with three V–O bonds lengths in the range of 1.944(8) to 2.011(8) Å, and one V–N bond of 2.149(10) and 2.142(10) Å for V1 and V2 respectively, while the metals

are situated approximately 0.3 Å outside this O_3N plane towards the oxo donor. Similar vanadyl preference to stronger bonding with oxygen donors in comparison with the nitrogen has already been established in the previous chapter. Moreover, described distortions agree with the reported parameters for other vanadium compounds with the same coordination environment.[19-24]

Stabilization of the crystal structure of this cluster is achieved through intramolecular hydrogen bonding between the phenolic –OH groups and the oxygen atoms from the adjacent coordinated β-diketonato moiety (Table III.A5). Additionally, one V=O···C supramolecular contact (V1=O13···C51; O···C dist., 3.12(2) Å and V–O–C angle of 173.5(5)°) links individual clusters into chains within the lattice (Table III.A2).[25] Apart from described, rich aromatic core of the cluster ensures the abundance of the π···π stacking contacts, C–H···O and C–H···π hydrogen bonding interactions (Table III.A5). The latter open the voids between the molecular sheets which constitute the channels occupied by pyridine molecules (Figure 3.1B).

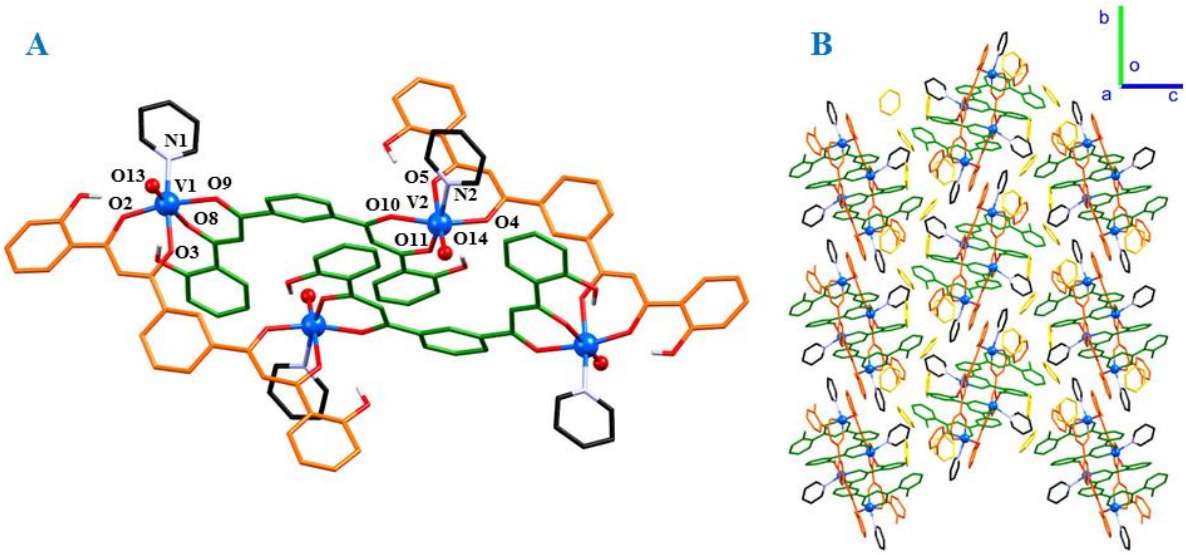

Figure 3.1: A) Molecular structure of $[(VO)_4(H_2L5)_4(py)_4]$ (**14**) with crystallographically-independent heteroatoms labeled. Only phenolic hydrogen atoms affecting the charge of the cluster are shown for clarity. Carbon atoms of each ligand conformation are orange (linear) and green (bent), while these of pyridine are black. B) Crystal packing of the compound **14** emphasizing the pyridine channels (yellow) between the antiparallel sheets of clusters within the structure.

Interestingly, replication of the identical reaction conditions with the ligand **H_4L6** introduced dramatic differences to obtained product, here consisting of a mixed valent $V^{V}V^{IV}$ neutral cluster identified as $[(V^{V}O)_4(V^{IV}O)_2O_4(L6)_2(py)_6]$ (**15**):

$$6\ VOSO_4{\cdot}H_2O + 2\ H_4L6 + 12\ NaH + 6\ py + O_2 \longrightarrow [(V^{V}O)_4(V^{IV}O)_2O_4(L2)_2(py)_6] + 12\ H_2 + 6\ Na_2SO_4 + 4\ H_2O$$

Partial one-electron oxidation of V(IV) ions in this aerobic reaction in basic medium suggests that the incorporated oxide O^{2-} co-ligands could originate from atmospheric oxygen or, eventually, from the molecules of H_2O present in the reaction system. Likewise, reported reactions of the ligand **H_4L6** with Co(II) also proceeded with the partial oxidation of the metal, yielding the Co^{III}/Co^{II} coordination systems.[18] Besides this, the major difference in the formation of the hexanuclear cluster **15** from previously described compound **14** is the increased metal to ligand ratio and presence of fully deprotonated ligands. In analogy with the preparation of compound **14**, low yield implies again the possible occurrence of side reactions, while the essential role of the sodium base indicates its possible templating effects in the formation of metallamacrocycle **15**, such as the stabilization of the unusual bent conformation of the ligand.

Crystallographic analysis showed that the unit-cell of a mixed-valent coordination cluster $[(V^{V}O)_4(V^{IV}O)_2O_4(L6)_2(py)_6]$ belongs to the triclinic *P*-1 space group and includes additionally 3.44 pyridine molecules as the crystallization solvent (Table III.A1). On the other hand, half of the given content defined the asymmetric unit. Molecular structure of **15** can be described as the cyclic coordination cage in which two fully deprotonated *bis*-β-diketone ligands (**$L6^{4-}$**) connect two well-separated mixed metal $V^{V}_2V^{IV}$ aggregates. Interestingly, the **$L6^{4-}$** scaffold exhibits a very rare bent conformation which allows the asymmetric coordination mode where each ligand binds two metals of the separated trinuclear metallic core (Scheme 3.2). More specific, first phenoxido-diketonato moiety of **$L6^{4-}$** in *syn*, *syn*-conformation is chelating and bridging two V(V) metals (monoatomic *O* bridge), whereas its equivalent in *syn*, *anti*-conformation chelates vanadium(IV) ion with the β-diketonate pocket and binds to the V(V) centre through the phenolate moiety as a terminal ligand. The coordination environment around the metal centres is completed with the three terminal pyridine molecules and two μ-O^{2-} groups (edges of the $[V_3]$ triangle),

ranging from distorted octahedral O_4N_2 V3(IV) and O_5N V1(V) to O_5 square-pyramidal V2(V). The shortest side of the metallic triangle is defined by two V^V atoms (*d*(V1···V2) = 3.125(1) Å), allocated within the hydroxyphenyl-β-diketonate pocket, while the longest one corresponds to a V^{IV}–V^V pair of atoms (*d*(V1···V3) = 5.644(1) Å), with no direct link between them. The remaining side of the triangle measures 3.560(1) Å and spans a V^{IV} (V3) and V^V (V2) ion through the μ-O^{2-} bridge. Observed topology of the metallic core is enabled by the high flexibility of the ligand, where distribution and orientation of oxygen and nitrogen atoms towards the cavity of the coordination cage indicate that the formation of this entity could be templated (probably by sodium ions). Moreover, gathered assembly of two vanadium triangles has no precedents for this family of *bis*-β-diketonate ligands.

Looking at bonding details in the metallic core, vanadium(IV) site (V3) exhibits an almost identical distortion as seen in for compound **14**, with noticeable *trans* effect which pulls the metal 0.237 Å away from the equatorial plane where differing V−O (average 1.958 Å) and V−N bonds (average 2.144 Å) are encountered (Table III.A4). Consequently, axial V−O distance (2.124(3) Å) is significantly more elongated. Square pyramidal V(V) site (V2) also exhibits severe distortion at the equatorial plane (V–O bonds ranging 1.689(3) to 2.064(3)Å). Interestingly, the V2–O bond of the V^{IV}–V^V bridge is shorter (1.689(3) Å) than that involved in the V^V–V^V bridge (1.923(4) Å). The octahedral vanadium(V) site (V1) is also much distorted, partially because of the heteroleptic O_5N ligand field, with the equatorial V−O bond distances ranging from 1.735(3)-1.992(3) Å, axial V−O of 2.221(4) Å and equatorial V−N of 2.195(4) Å. Similarly to the compounds presented in Chapter 2 and previously reported pairs of dimers[16], coordination numbers of the V^V sites located within the hydroxyphenyl-β-diketonate pocket are five and six, respectively, due to the restricted biting angle of the former.

Supramolecular organization of clusters in polymeric layers is established through V=O···C close contacts at V3 site, supported by the π···π stacking contacts and V=O···C–H contacts at V2 (Table III.A6). The latter interactions also organize the neighboring layers into three-dimensional network. Dense network of the intermolecular interactions assembles ten neighboring molecules per cluster, opening the voids in crystal structure for the accommodation of crystallization pyridine molecules.

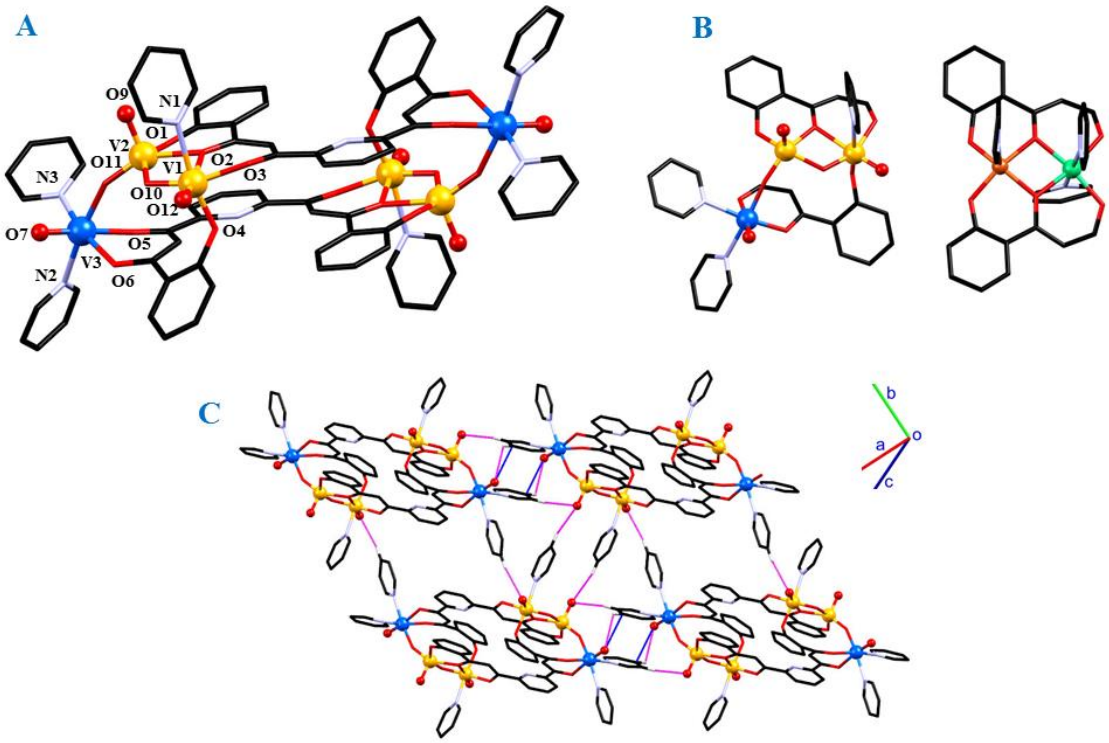

Figure 3.2: A) Molecular structure of $[(V^{V}O)_4(V^{IV}O)_2O_4(L6)_2(py)_6]$ (**15**) with crystallographically-independent heteroatoms labeled. B) *Left*: Topology of the metallic core in **15** and comparison of its coordination modes of the phenolato-ketonato coordination pockets in with those in molecular structure of the $[Ni_2Cu_2(L5)_2(py)_6]$[16] (*right*). C) Vanadyl intermolecular interactions in the crystal structure: *Left to right*: Polymerization of molecular entities into chains through V═O···C interactions (purple lines) and the V═O···H−C contacts (magenta lines) at the V3 (V^{IV}) and V2 metal sites (central V^{V}). *Top to bottom*: Interaction between the chains through V═O···H−C contacts at the V1 metal site (external V^{V}) with the coordinated pyridine at the V3 site of the neighbouring layer. On all figures, only hydrogen atoms taking part in the interactions are shown for clarity.

Interestingly, the structural disparity of **H_4L5** versus **H_4L6** products seen previously in chemistry of the late 3*d* metals is also maintained here (Schemes 3.1). However, neither of the presented vanadium clusters is comparable with any other known compound containing these ligands (Scheme 3.2).

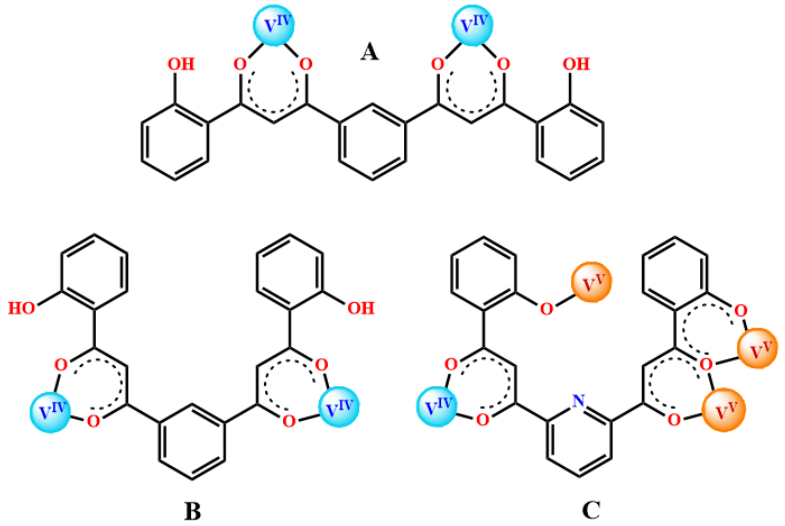

Scheme 3.2: Coordination modes and conformations of $\mathbf{H_2L5^{2-}}$ and $\mathbf{L6^{4-}}$ in the structures of the compounds **14** (A and B) and **15** (C). Oxidation states of vanadium ions are indicated in the superscripts.

As mentioned earlier, coordination chemistry of extended β-diketone ligands with vanadium remains relatively scarce. In fact, very few known systems include dinuclear V^{III} helicate[26] and a collection of dinuclear metallamacrocyclic compounds of V(II), V(III), and V(IV),[27-29] meaning that here reported compounds **14** and **15** represented the most complex metallamacrocycles up to date. Although control of the rich redox chemistry of vanadium might seem problematic, this field of research definitively encourages more exploration, especially when considering the relevance of vanadium compounds in the evolving field of quantum computing.

3.2.2. Solution stability of the vanadium metallacyclophanes

Slight solubility of metallacyclophanes **14** and **15** in THF, MeOH, and DMF allowed the assessment of their stability in solution through mass spectrometry. Thus, positive mode MALDI-TOF spectra of **14** (Figures III.A1-A3) confirmed the existence of the tetranuclear $[(VO)_4(H_2L5)_4]$ core in THF solution, as well as some of its fragments like $[(VO)_4(L5)_2]^+$, $[V(VO)_3(L5)_2]^+$ and $[V_2(VO)_2(HL5)_3(CH_3OH)]^+$. Similarly, fragments lacking one or two of the metal ions and ligands were also observed (e.g., $[(VO)_3(HL5)_2]^+$, $[(VO)_3(HL5)(H_2L5)]^+$, $[(VO)_3(HL5)_2(H_2L5)]^+$, $[(VO)_2(H_2L5)_2]^+$, $[(VO)_2(H_2L5)_2] + Na^+$ (K^+), and $[V(VO)(H_2L5)_2]^+$), as well as those including dihydroxybenzoic acid (DHB) in their composition (e.g.,

$[(VO)_3(H_2L5)_4(C_6H_3(OH)_2COOH]^+$, $[(VO)_3(H_2L5)_3(C_6H_3(OH)_2COO)_3]^+$, $[(VO)_3(H_2L1)_3(C_6H_3(OH)_2COO)_2]^+$, *etc.*) inherent to the technique employing DHB matrix (Figure III.A3). Significant fragmentation of this compound is evident also from the existence of many monometallic fragments such as $[V(H_2L5)]^+$, $[(VO)(H_3L5)]^+$, $[(VO_2)(H_4L5)]^+$ where the oxidation state of vanadium varies from +3 to +5. In the negative mode of detection (Figure III.A4), polynuclear molecular fragments with different metal to ligand ratios were found (e.g., $[(VO)_3(VO_2)(L5)_2]^-$, $[(VO)_3(HL5)(L5)]^-$ and $[(VO)(VO_2)L5]^-$) along with mononuclear entities, such as $[V(L5)]^-$ and $[(VO)(HL5)]^-$. On the other hand, existence of the hexanuclear core $[(VO)_6(L6)_2]$ was not observed through MALDI-TOF spectra of compound **15** (neither in positive nor negative mode) due to the significant fragmentation of the molecule (Figures III.A5-A6). This fact is understandable bearing in mind that the stability of this cluster decreases significantly with the loss of axial pyridine ligands as well as oxide co-ligands. In the positive mode of detection (Figure III.A6), polynuclear entities such as $[(VO)_2(H_2L6)_2] + Na^+$ and $[(VO)_3(HL6)_2] + Na^+$ are the most abundant along with sodium and potassium salts of free ligand ($H_4L6 + Na^+$ and $H_4L6 + K^+$). Related to this, mononuclear $[V(L6)]^-$ and $[(VO)(HL6)]^-$ moieties are dominating the negative mode MALDI-TOF spectra of this compound (as previously seen also in the case of the compound **14**) together with the appearance of dinuclear and trinuclear species (e.g., $[(VO)_3(HL6)(L6)]^-$, $[V(VO)(HL6)_2]^-$, Figure III.A5).

3.2.3. Study of the magnetic behaviour

Considering the paramagnetic nature of the compounds **14** and **15**, variable temperature (2-300 K) magnetization measurements were performed on their powdered microcrystalline samples under the constant magnetic fields of 1 T and 0.5 T, respectively. In addition, this study was complemented with magnetization measurements at 2 K in the field range of 0–5 T.

In the case of tetranuclear vanadyl macrocycle **14**, measured room temperature (300 K) value of the $\chi_M T$ product was 1.58 cm^3Kmol^{-1}, only slightly above the expected 1.500 cm^3Kmol^{-1} for four uncoupled S = 1/2 spin centers with g=2.0 (Figure 3.3). Hence, the postulated V(IV) oxidation state of the metal centres was correctly assigned. Upon lowering the temperature, the $\chi_M T$ product remains constant, following the Curie Law down to 18 K

after which a slight increase leads to the maximum value of 1.60 cm^3Kmol^{-1} at 10 K. Below the latter temperature, sharper decline of the $\chi_M T$ product occurs ending at 1.48 cm^3Kmol^{-1} at 2 K. Described behaviour indicates that the vanadyl centres within the **42** are very weakly coupled. Consistent with this, the highest measured value of $M/N\mu_B$ *vs* H curve (3.91 μ_B at 5 T) lies only slightly below the expected 4 μ_B for four S=1/2 centres (g=2, Figure 3.3).

Experimental data ($\chi_M T$ *vs* T and $M/N\mu_B$ *vs* H) were modelled (PHI[30]) using the matrix diagonalization of the spin Hamiltonian constructed from the coupling scheme 3.3:

$$\hat{H} = \mu_B B \sum_i g_i \hat{S}_i - 2J_1(\hat{S}_1\hat{S}_2 + \hat{S}_3\hat{S}_4) - 2J_2(\hat{S}_2\hat{S}_3 + \hat{S}_1\hat{S}_4)$$

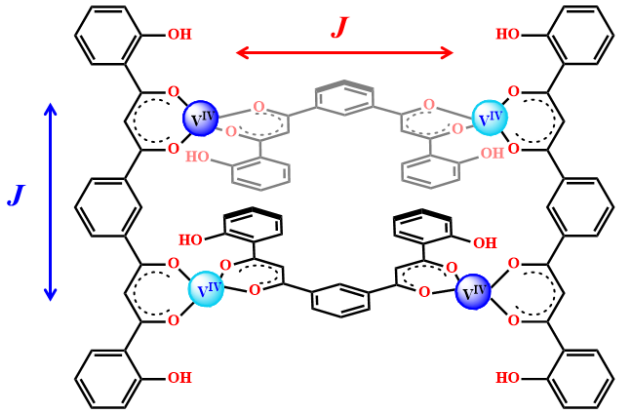

Scheme 3.3: Coupling scheme for the compound **14**. Different coloring emphasizes the distribution of the crystallographically inequivalent V1 and V2 sites.

Two possible pathways of interaction between the crystallographically inequivalent vanadyl centres, across the linear and bent conformation of the ligands, are shown as blue and red arrow in the scheme 3.3. By fixing the isotropic g value for all vanadyl centres at g=2.04, optimised model yielded the small coupling constants J_1=0.51 cm^{-1} and J_2=−0.31 cm^{-1} together with additional contribution from intermolecular interactions zJ=0.02 cm^{-1}. Opposite sign of coupling constants disables their direct correlation with the possible pathways of interaction, especially when taking into account that such small values can be strongly affected by errors. In fact, almost equally good model can be obtained by fixing the g=2.04 and by considering only the intra(inter)molecular interaction zJ=0.022 cm^{-1}. In agreement with the Curie behaviour from the magnetization measurements, variable temperature EPR spectroscopy (5-298 K) revealed the increasing intensity of the isotropic spectral feature centred at g=1.989 upon cooling (Figure 3.3). The smaller g value than the

theoretical one of the free electron (g=2.0023) is in excellent agreement with the literature reported studies of the vanadyl-based systems.[24, 31, 32] Unfortunately, broadness of the detected resonance hindered the possibility of observing any hyperfine structure arising from the presence of the ^{51}V nuclei (I=7/2).

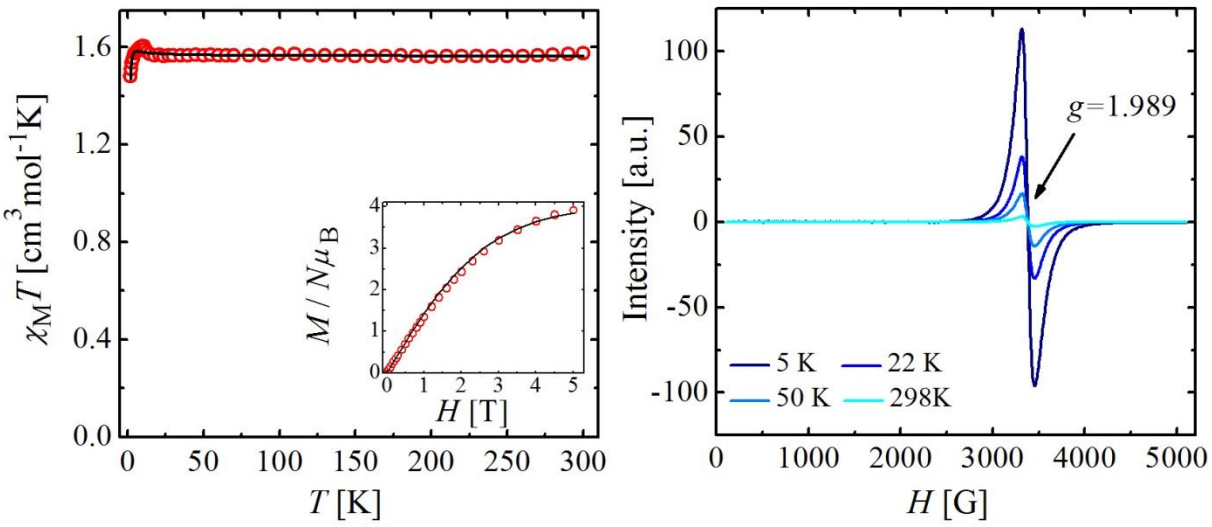

Figure 3.3. *Left:* $\chi_M T$ *vs* T and $M/N\mu_B$ *vs* H (inset) curves for compound **14** with the best fit (solid line). Measurement setup: cooling mode (300→2 K), B = 1 T; T_{mag} = 2 K. *Right:* Variable temperature (5-298 K) X-band EPR spectra (f = 9.418 GHz) of a powdered sample of complex **14**.

On the other hand, hexanuclear cluster **15** contains two distant V^{IV} paramagnetic metal centres (S = 1/2) while the remaining four metal ions are diamagnetic vanadium(V) (S = 0). Intramolecular separation of the spin carrier metals at 14.679(1) Å indicates that no meaningful coupling between them should be observed. Detected magnetic behaviour confirmed the ascribed oxidation states since the $\chi_M T$ product at 300 K (0.730 cm^{3}Kmol^{-1}) is only slightly below the expected value for two uncoupled (S=1/2) vanadium(IV) centers (0.750 cm^{3}Kmol^{-1}; g=2.0, Figure 3.4). Upon cooling, the typical Curie behaviour is observed in almost entire thermal range, confirming the absence of any meaningful interaction between the spin carriers. Consistently, the highest measured value of the $M/N\mu_B$ *vs* H curve (1.78 μ_B at 5 T) lies slightly below the expected 2 μ_B for two S=1/2 centres (g=2, Figure 3.4).

Simultaneous fit of the experimental $\chi_M T$ vs. T and $M/N\mu_B$ vs. H curves (PHI[30]) was successful employing the fixed g value of 1.94 and weak intermolecular interactions (zJ=0.03 cm^{-1}). The latter could be established through V=O···C contacts between the neighbouring molecules which connect two V^{IV} centres across their coordinated pyridine molecules

(intermolecular V3···V3 distance of 7.314(1) Å). Similarly, temperature variable X-band EPR spectra reveal only one broad isotropic resonance centred at *g*=1.991 which gains on the intensity upon cooling, as expected from the observed Curie behaviour (Figure 3.4).

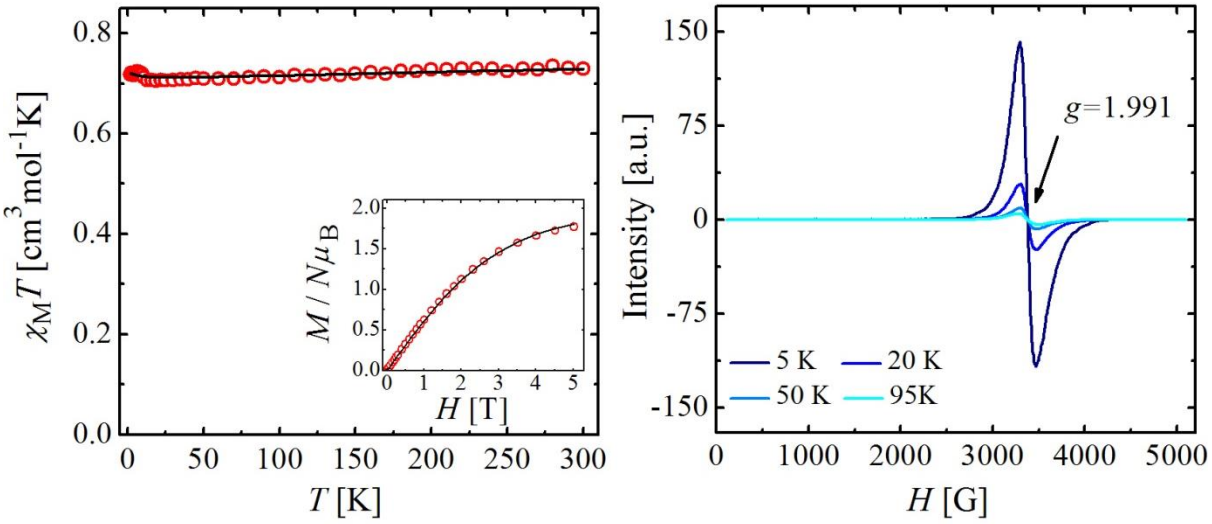

Figure 3.4. *Left:* $\chi_M T$ *vs T* and $M/N\mu_B$ *vs H* (inset) curves for compound **15** with the best fit (solid line). Measurement setup: cooling mode (300→2 K), *B* = 0.5 T; T_{mag} = 2 K. *Right:* Variable temperature (5-95K) X-band EPR spectra (*f* = 9.418 GHz) of a powdered sample of complex **15**.

Small discrepancies between the spectroscopically detected values and those obtained from fitting the magnetization data origin from the fact that the latter are obtained using a collective bulk thermodynamic quantity, subject to experimental errors, such as the accuracy on the molecular mass. Similarly, applied corrections for diamagnetism or temperature-independent paramagnetism alter also the *g* values extracted from the magnetization studies.

3.3. Asymmetric and symmetric coordination compounds incorporating the *S*=1/2 [CuNi] dimers

3.3.1. Design, synthesis and characterisation of 2,5-*bis*-(3-oxo-3-(2-hydroxyphenyl)propionyl)pyridine, H_4L_A

As mentioned earlier, topology and symmetry of the poly-β-diketone ligands can be easily designed by choosing selectively its building blocks based on the functionalised ketones and esters. Hence, by introducing the asymmetry in any of the starting materials it is possible to transfer the same asymmetry to the final ligand and, consequently, to its coordination compounds. Following this idea, new ligand H_4L_A was designed from the asymmetric central

spacer based on the 2,5-pyridinedicarboxylic acid and 2-hydroxyacetophenone as the wing functionality. Preparation of the final ligand required two steps of synthesis with the first one being the esterification of the carboxylic acid to its methyl-diester. After isolation and purification, prepared diester was then employed as starting material in the Claisen condensation with 2-hydroxacetophenone in the second synthetic procedure (Scheme 3.4).

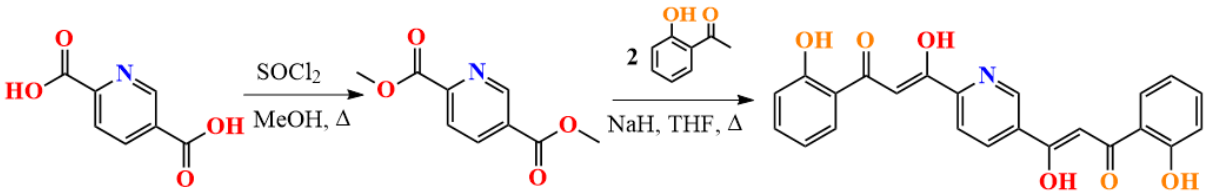

Scheme 3.4. Preparation of the asymmetric *bis*-β-diketone ligand $\mathbf{H_4L_A}$ from its precursors.

As it can be seen from the structure of this ligand, the presence of the central pyridine ring functionalised at its 2,5-carbon sites separates linearly (*para* substitution) two sets of the dissimilar phenol-β-diketone coordination pockets. Thus, 3-oxo-3-(2-hydroxyphenyl)propionyl substituent in *ortho* position (C2) aligns the set of three different chelating sites: pyridine-ketone ('*NO*'), β-diketone ('*OO*') and phenol-ketone ('*OO*'). On the other hand, same functionality in the *meta* position (C5) maintains only a pair of β-diketone ('*OO*') and phenol-ketone ('*OO*') chelating sites (Scheme 3.5).

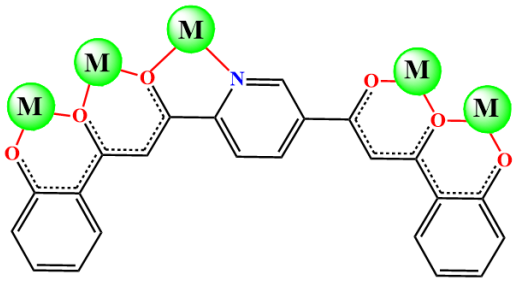

Scheme 3.5: Possible coordination mode of the μ_5-$[L_A]^{4-}$.

Obtained ligand was characterised by usual techniques such as ^{1}H NMR spectroscopy, mass spectrometry and elemental analysis (Appendix III, Figs. III.A7 and III.A11). However, only ^{1}H NMR spectroscopy undoubtedly confirms the asymmetry of the ligand and its existence in the enolic form in solution. The former is clear from the appearance of two sets of the characteristic O*H* protons from the phenolic and the enolic moiety. Similarly, every other hydrogen atom from the molecule can be detected separately, as expected for the asymmetric structure. Moreover, detailed insights in the molecular structure of the $\mathbf{H_4L_A}$

were obtained from the analysis of its single crystals (obtained from the DMF solution). Interestingly, this molecule crystallises alone in the monoclinic $P2_1/c$ space group, where one half of the molecule defines the asymmetric unit (2 molecules in the unit cell), while the other half is generated by the symmetry operation over an inversion centre. In other words, symmetry of the crystal structure is higher than the symmetry of the molecule itself. Consequently, there is a positional disorder of the central pyridine ring between the N1 atom and the C11−H11 moiety. Since the crystallography gives an average of the molecular structure, this means that the real image involves two different orientations of the molecule within the lattice, each one with the occupancy of the 50 %. Additionally, **H_4L_A** molecules exist exclusively in the enolic form in the solid state (as seen previously from ^{1}H NMR studies), with *trans*-oriented phenol-β-diketone coordination pockets. (Figure 3.5, Table III.A7 and III.A8). Interestingly, pyridine donor site is also *trans*-oriented in respect with its nearest functional substituent.

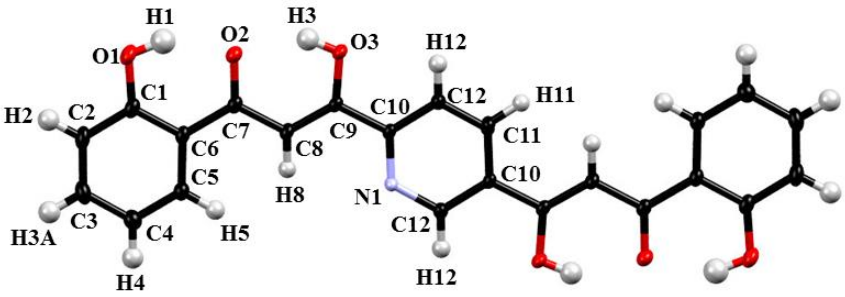

Figure 3.5: Molecular structure of **H_4L_A** emphasizing the *trans*-orientation of its dissimilar phenol-β-diketone coordination pockets. Only crystallographically independent atoms are labelled while the other half of the molecule is generated by the symmetry operation over an inversion centre. For clarity, only one positional disorder of the central pyridine ring is shown. All displacement ellipsoids are drawn at 50% probability.

Trans-conformation of the **H_4L_A** molecules maximises the rich network of twelve intra- and intermolecular hydrogen bonding interactions (six at each phenol-β-diketone moiety, Figure 3.6). Four of them are intramolecular, in which oxygen atoms from the carbonyl moieties (O2) act as hydrogen acceptors from the enol and phenol OH groups (purple contacts, Figure 3.6). Remaining intermolecular interactions are established between the dissimilar phenol-β-diketone functionalities, in which phenol oxygen atoms (O1) act as the hydrogen acceptors from the enolic-OH groups (O3), while the oxygen atoms from the carbonyl

groups interacts with phenolic –OH moiety from the neighbouring molecule (blue contacts, Figure 3.6). Additionally, planarity of the π-conjugated system enables the effective π···π interactions which arrange the hydrogen bonded sheets of the molecules into stacked layers (Figure 3.6, red contacts).

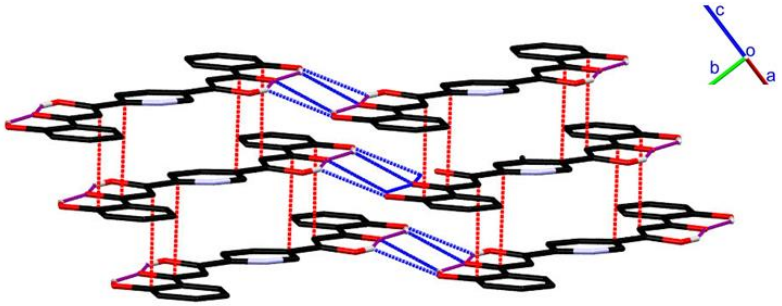

Figure 3.6: Crystal packing of $\mathbf{H_4L_A}$ featuring the intra- and intermolecular hydrogen bonding interactions (purple and blue contacts, respectively) and π···π contacts (red). Only hydrogen atoms taking part in the interactions are shown, the rest is omitted for clarity.

3.3.2. Design, synthesis and structure of the asymmetric compound $[(CuNi)_2L_A(OH)_2(py)_{10}](ClO_4)_2$

In order to transfer directly the asymmetry of $\mathbf{H_4L_A}$ to its coordination compounds, synthetic strategy was based on pair-impair stoichiometry between the metals and the ligand, respectively, as presented in the Chapter II for the family of homo- and heterometallic compounds $[(M1M2)_2(L1)(OH)_2(py)_{10}](ClO_4)_2$. Moreover, choice of the metals was now limited to the Cu^{II}-Ni^{II} pair, since previously discussed crystallographic and magnetic studies have shown that this combination offers the highest selectivity in formation of the heterometallic system and, additionally, presents the strongest antiferromagnetic coupling between the component spin carriers. The latter is extremely important to secure the isolated two-level (M_S=±1/2) ground state of the qubits. Following the proposed μ_5-$[L_A]^{4-}$ coordination mode (Scheme 3.5), initial topology of the compound was designed as weakly coupled effective spins S=1/2 originating from the $[Ni_2Cu]$ and [NiCu] clusters. However, reaction setup including right amounts of the building blocks and hydroxide co-ligands in pyridine failed to produce the targeted pentanuclear compound, giving instead a complex with weakly coupled pair of dissimilar [CuNi] dimers. Obtained $[(CuNi)_2L_A(OH)_2(py)_{10}](ClO_4)_2$ (**16**) compound was also prepared using the correct stoichiometry of the components, as confirmed by the structural analysis of obtained crystals:

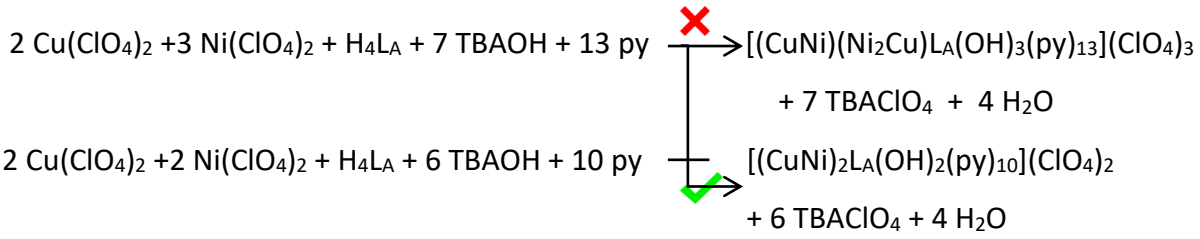

Structure of the ionic compound **16** (monoclinic $P2_1/c$ space group) is composed of the complex cation $[(CuNi)_2L_A(OH)_2(py)_{10}]^{2+}$, whose charge is compensated by two perchlorate anions, and six lattice pyridine molecules (Figure 3.7A). Two formulae units of the given composition define the unit cell, while only half of it determines the asymmetric unit, identically as in the starting ligand H_4L_A. Moreover, centre of the inversion in the middle of complex cation imposes higher symmetry of the average crystal structure than the real molecular symmetry, meaning that a positional disorder of two different orientations of the cation is presented within the lattice, each one with the occupancy of the 50 %. Identically to compounds presented in Chapter II, complex cation consists of two separated [CuNi] dimers, chelated within each pair by the completely deprotonated phenolato-β-diketonato coordination pocket (μ_4-$[L_A]^{4-}$ coordination mode) and bridged by one hydroxide co-ligand. Dissimilarity between the metallic pairs is determined by their proximity to the nitrogen donor from the central pyridine spacer, with one pair being located within the *ortho* positioned pocket and the second one within the opposed *meta* chelating site. First coordination sphere around the metals is completed by ten pyridine ligands, three at each Ni^{II} site within the β-diketonato pocket and two per each peripheral Cu^{II} site. Hence, Ni(II) ions reside in the octahedral O_3N_3 coordination environment, while the copper(II) ions are placed in distorted square-pyramidal O_3N_2 ligand field. Distance between the adjacent Ni^{II} and Cu^{II} sites measures 3.0482(8) Å, while the intramolecular distance between the closest Ni^{II} sites of pairs measures 11.122(1) Å. Bonding details around the Ni^{2+} centre reveal slightly elongated axial Ni–N bond (average 2.115 Å) in comparison with the equatorial coordination where Ni–N and Ni–O measure 2.088(4) Å and 2.034 Å (average), respectively. More pronounced differences are observed at the Cu(II) site, where axial Cu–N bond (2.229(4) Å) is significantly weaker than the equatorial Cu–N (2.076(3) Å) and Cu–O (average 1.943) bonds. Similarly, distortion of the square-pyramidal geometry is easily observed from the bonding angles between the axial and equatorial donors which fall within the wide range of

91.8(1)°-110.7(1)°. Perchlorate anions interact with the complex cation as acceptors in the hydrogen bonding O–H···O and C–H···O interactions with bridging hydroxide and axial pyridine ligands of the CuNi dimer, respectively (Figure 3.7B). Moreover, each perchlorate anion takes part in nine C–H···O interactions which four different $[(CuNi)_2L_A(OH)_2(py)_{10}]^{2+}$cations and one molecule of the lattice pyridine, dictating the supramolecular arrangement of this compound. Additionally, C–H···π and π···π contacts between the aromatic moieties surrounding the peripheral Cu^{II} sites contribute to dense crystal packing of the complex cations into chains and stabilisation of the structure (Figure 3.7B). Generated voids between the molecular chains are filled with the lattice pyridine molecules and perchlorate anions.

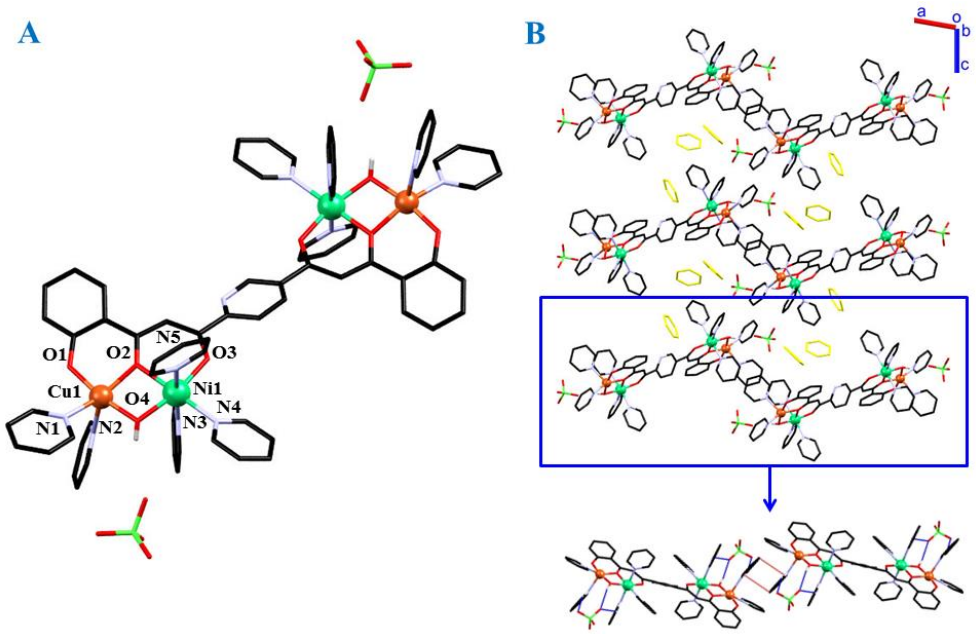

Figure 3.7: A) Molecular structure and labelling scheme of $[(CuNi)_2L_A(OH)_2(py)_{10}](ClO_4)_2$ (**16**). Only crystallographically independent heteroatoms are labelled. B) Crystal structure of the compound **16** emphasizing organisation of parallel chains of cations which generate voids for the lattice pyridine molecules (yellow). Hydrogen bonding (blue) and π···π stacking contacts (red) within the molecular chains are emphasised at the bottom. Hydrogen atoms affecting the charge of the cluster or taking part in the interactions are shown, the rest is omitted for clarity.

3.3.3. Design, synthesis and characterisation of 2-methoxy-1,4-bis-(3-oxo-3-(2-hydroxyphenyl)propionyl)benzene, H_4L_{A2}

After successfully achieved ligand to complex asymmetry transfer with the **H_4L_A**, new asymmetric ligands were designed with in attempt to increment the differences between their [CuNi] qubits. First in this line is the analogous ligand **H_4L_{A2},** prepared from the asymmetric central spacer based on 2-methoxy-1,4-benzenedicarboxylic acid and 2-hydroxyacetophenone as the wing functionality. In this case, the synthesis of the ligand involved three steps since 2-methoxy-terephtalic acid is not affordably available. Instead, 2,5-dimethylanisole was employed as the starting material since it can be easily oxidised to the corresponding carboxylic acid using the basic aqueous $KMnO_4$ solution.[33, 34] Acidification of the reaction mixture yields 2-methoxy-1,4-benzenedicarboxylic acid which was then easily converted to its methyl ester as the starting material in the Claisen condensation with 2-hydroxacetophenone (Scheme 3.6).

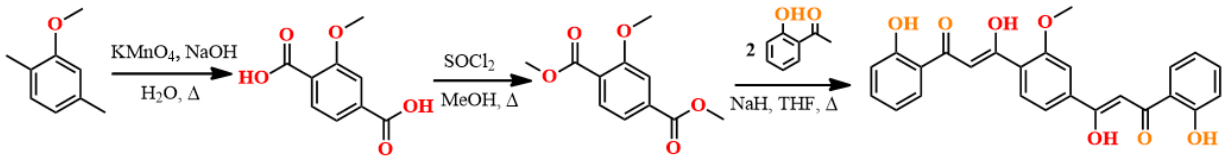

Scheme 3.6. Preparation of the asymmetric *bis*-β-diketone ligand **H_4L_{A2}** from its precursors.

Similarly to H_4L_A, functionalisation of the anisole spacer at its 2,5-carbon sites separates linearly (*para* substitution) two sets of the dissimilar phenol-β-diketone coordination pockets. Thus, *ortho* positioned (C2) phenol-ketone substituent aligns the set of three different ('*OO*') chelating sites: methoxy-ketone, β-diketone and phenol-ketone. On the other hand, same functionality in the *meta* position (C5) holds a pair of ('*OO*') coordination pockets (Scheme 3.7).

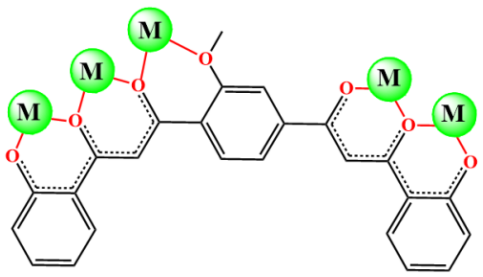

Scheme 3.7. Possible coordination mode of the μ_5-$[L_{A2}]^{4-}$.

Mass spectrometry and elemental analysis confirmed purity and the given composition of the ligand (Appendix III, Fig. III.A8). Similarly, ^{1}H NMR spectroscopy verified the asymmetry of the ligand since two sets of the characteristic O*H* protons from the phenolic and the enolic moiety were detected. Additionally, existence of the solution keto-enolic equilibrium was established with the latter form being the dominant one (Figure III.A). Single crystals of the **H_4L_{A2}** were grown from DMF solution and successfully analysed with X-Ray diffraction. As expected from the previous findings, solid state structure features enolic form of the ligand with *trans*-positioned phenol-β-diketone functionalities (Figure 3.8). Similarly to the nitrogen donor from pyridine ring in the H_4L_A, methoxy group is also *trans*-oriented in respect to the nearest β-diketone substituent, however, its position is well localised (no positional disorder).

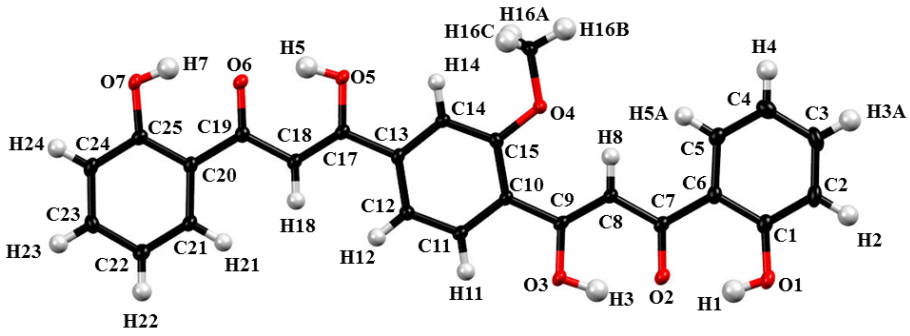

Figure 3.8: Molecular structure of **H_4L_{As}** emphasizing the *trans*-orientation of its dissimilar phenol-β-diketone coordination pockets. Crystallographically independent atoms are labelled and all displacement ellipsoids are drawn at 50% probability.

Reason why position of the methoxy group is well defined is the existence of intramolecular hydrogen bonding interaction with C−H moiety of the nearer β-diketone (C8). Additionally, intramolecular hydrogen bonds are established in the same pattern as observed in the structure of the H_4L_A, with central carbonyl oxygen atoms (O2 and O6) as the acceptors of the hydrogen bridges from the phenol and enol OH group. However, the pattern of the intermolecular hydrogen bonding is slightly altered. Thus, enol oxygen atoms (O5 and O3) act as the acceptors of hydrogen bonding interactions with the phenol wings, while the carbonyl oxygen atoms (O2 and O6) act as the hydrogen acceptors in interaction with the enolic OH-group. On the other hand, phenol oxygen atom O7 takes part in additional hydrogen bonding interaction with C24−H24 bond from the phenol moiety of the

neighbouring molecules which slightly shifts molecules and reduces the stacking interactions. Nevertheless, π···π contacts between the phenol wings and β-diketone pockets are firmly established, stacking the hydrogen bonded sheets of molecules in the 3-D assembly (Figure 3.9).

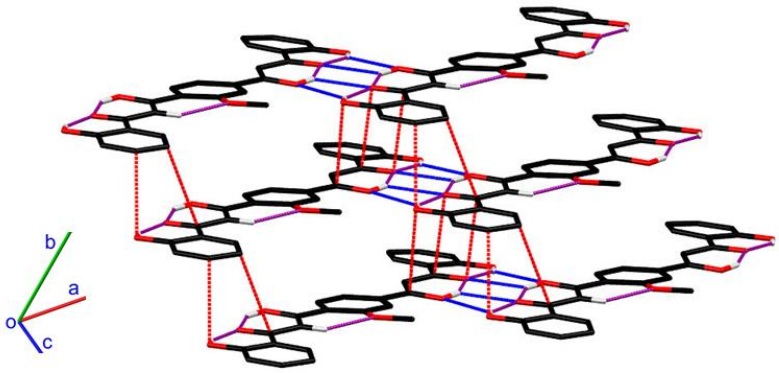

Figure 3.9: Crystal packing of the $\mathbf{H_4L_{A2}}$ featuring intra- and intermolecular hydrogen bonding interactions (purple and blue contacts, respectively) and π···π contacts (red). Hydrogen atoms taking part in the interactions are shown, the rest is omitted for clarity.

3.3.4. Design, synthesis and structures of asymmetric compounds based on H_4L_{A2}

Asymmetry transfer from $\mathbf{H_4L_{A2}}$ to its [CuNi]-based coordination compounds was carried out in the same way as with ligand $\mathbf{H_4L_A}$, employing the pair-impair stoichiometry between the components of the reaction. Thus, two reaction setups employing variable amounts of metallic building blocks and hydroxide co-ligands were evaluated, aiming at the preparation of dissimilar *S*=1/2 moieties in form of antiferromagnetically coupled [(CuNi)···(CuNiNi)] and [(CuNi)···(CuNi)] clusters. Again, both approaches resulted with the latter outcome (compound **17**), with no experimental evidence of pentanuclear entity.

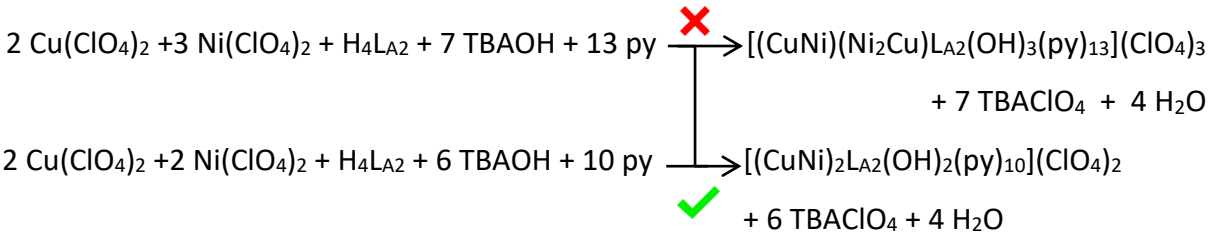

Plausible explanation of observed reactivity could be found in competition for coordination between the solvent pyridine molecules and donor groups (-***O***Me and –***N***) from the central

spacers of $\mathbf{H_4L_A}$ and $\mathbf{H_4L_{A2}}$. Observed equatorial coordination of pyridine molecules to the Ni^{2+} sites also impedes the further expansion of the cluster, while alternative engaging of the diketone-heteroatom coordination pocket would increase the steric hindrance of the [CuNiNi] cluster, imposing more rigid coordination geometry for the central Ni^{II} site. Additionally, higher positive charge of targeted $[(CuNi)\cdots(CuNiNi)]^{3+}$ cation could also disfavour its formation.

In any case, crystal structure of the ionic compound **17** is essentially identical to the compound **16** (monoclinic $P2_1/c$ space group), composed of the complex cation $[(CuNi)_2L_{A2}(OH)_2(py)_{10}]^{2+}$, two perchlorate anions, and five lattice pyridine molecules (Figure 3.10A). Two formulae units of the given composition define the unit cell, while only half of it determines the asymmetric unit, with the other half being generated by symmetry over an inversion centre. Hence, complex cations of the compound **17** are disordered over two opposite orientations, generating the higher symmetry of the average crystallographic structure than the real molecular symmetry. In the structure of the cation $[(CuNi)_2L_{A2}(OH)_2(py)_{10}]^{2+}$, deprotonated phenolato-β-diketonato moieties of the ligand chelate two hydroxide bridged [CuNi] dimers (μ_4-$[L_{A2}]^{4-}$ coordination mode), which differ among themselves by their proximity to methoxy substituent on asymmetric core of the ligand. Ni^{II} ions are located within the inner, β-diketonato pocket, in a octahedral O_3N_3 coordination environment, while Cu^{II} ions are found at the periphery of the structure, in a distorted square-pyramidal O_3N_2 ligand field. Distance between the adjacent Ni^{II} and Cu^{II} sites measures 3.0520(8) Å, while the intramolecular distance between the closest Ni^{II} sites of pairs measures 11.199(2) Å. Bonding details around both metals are almost identical as in compound **16**. The hexacoordinated Ni^{2+} centre features slightly elongated axial bonding with pyridine (average Ni−N 2.118 Å), while stronger bonding with heteroleptic equatorial O_3N ligand field is reflected in shorter Ni−N (2.089(3) Å) and Ni−O (average 2.036 Å) bonds. Similarly, axial Cu−N bond (2.218(3) Å) is significantly weaker than the equatorial Cu−N (2.075(3) Å) and Cu−O (average 1.945) bonds. Distortions of the square-pyramidal geometry are reflected through the wide range (of 91.0(1)°-112.2(1)°) of bonding angles between the axial and equatorial donors. Each perchlorate anion acts as a hydrogen acceptor in eleven O−H···O and C−H···O hydrogen bonding interactions, with three contacts involving the hydroxide co-ligand and axially bonded pyridine molecules at the corresponding [CuNi] dimer of the complex cation (Figure 3.10B). Remaining hydrogen bridges are established

with four neighbouring $[(CuNi)_2L_{A2}(OH)_2(py)_{10}]^{2+}$cations and two lattice pyridine molecules. Moreover, additional stabilisation of the complex cation arises from the intramolecular hydrogen bonding between the methoxy substituent of aromatic spacer and central C–H fragment within the closest β-diketone moiety (Figure 3.10B). Furthermore, π···π contacts between the axially bonded pyridine ligands at peripheral Cu^{II} sites determine the supramolecular chain arrangement of cations, leaving the voids in between filled with lattice pyridine molecules and anions (Figure 3.10B).

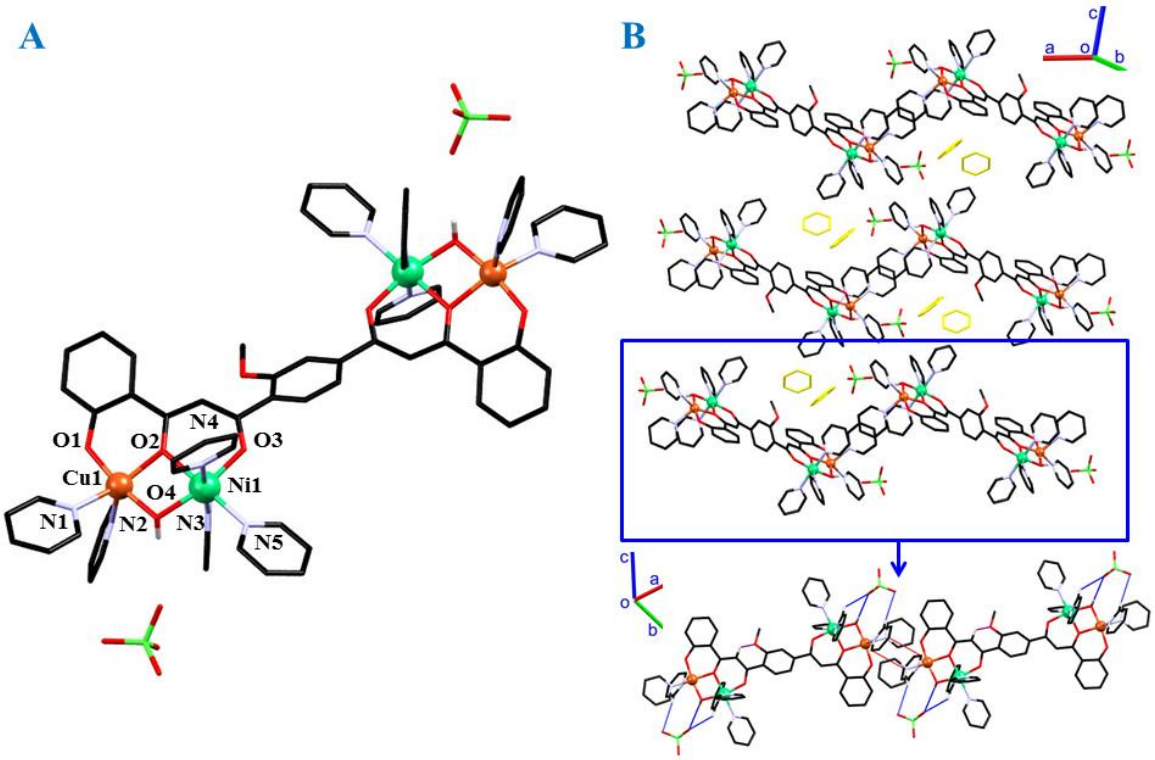

Figure 3.10: A) Molecular structure and labelling scheme of $[(CuNi)_2L_{A2}(OH)_2(py)_{10}](ClO_4)_2$ (**17**). Only crystallographically independent heteroatoms are labelled. B) Crystal structure of the compound **17** emphasizing the organisation of antiparallel chains of cations which generate voids for the lattice pyridine molecules (yellow). Intra- and intermolecular hydrogen bonding (violet and blue, respectively) and the π···π stacking contacts (red) within the molecular chains are emphasised at the bottom. Hydrogen atoms affecting the charge of the cluster or taking part in interactions are shown, the rest is omitted for clarity.

Interestingly, use of the same building blocks in decreased metal-ligand stoichiometry from pair-impair 2:2:1 to triply impaired 1:1:1 ratio allowed the preparation of another asymmetric cluster based on $\mathbf{H_4L_{A2}}$, formulated as $[(CuNi)_3(L_{A2})_3(py)_9]$ (**18**):

$$3\ Cu(ClO_4)_2 + 3\ Ni(ClO_4)_2 + 3\ H_4L_{A2} + 12\ TBAOH + 9\ py \longrightarrow [(CuNi)_3(L_{A2})_3(py)_9] + 12\ TBAClO_4 + 12\ H_2O$$

Crystal structure of this compound (triclinic *P*−1 space group) reveals the presence of three lattice pyridine molecule in the central cavity of peculiar $[(CuNi)_3(L_{A2})_3(py)_9]$ metallacoronand assembly with a three dissimilar [CuNi] nodes (Figure 3.11A). Given composition defines the asymmetric unit of the crystal structure, while the unit cell includes two such ensembles. Molecular structure of the $[(CuNi)_3(L_{A2})_3(py)_9]$ complex can be presented as a pseudo-equilateral triangle whose edges are defined by three fully deprotonated and face to face oriented $(L_{A2})^{4-}$ ligands chelating three [CuNi] vertices (trimer of dimers topology, Figure 3.11A). In concrete, two β-diketonato coordination pockets define equatorial ligand field around the inner Ni(II) ions, while phenolato-diketonato donors chelate the peripheral Cu(II) ions, as seen previously for compounds **16** and **17**. Axial sites of the hexacoordinated Ni^{II} centres are filled with two pyridine molecules (octahedral N_2O_4 ligand field, while square-pyramidal Cu(II) centres complete its coordination sphere with one pyridine molecule (NO_4 ligand field). As mentioned earlier, all three [CuNi] pairs are different among themselves, due to highly asymmetric disposition of the methoxy substituents on central spacer. Hence, local geometries of aromatic cores in vicinity of each [CuNi] pair include dissimilar combinations of molecular fragments: 2 OMe/2 C_{Ar}–H ([Cu1Ni1]), 1 OMe/3 C_{Ar}–H ([Cu2Ni2]) and 4 C_{Ar}–H [Cu3Ni3]). Asymmetry of the [CuNi] dimers affects the geometrical parameters of the complex **18**, where intradimer Cu···Ni distances vary from 3.032(1)-3.054(1) Å, while interdimer Ni···Ni distances and Ni···Ni···Ni angles fall between 10.157(2)-10.325(3) Å and 59.24(1)-60.87(1)° ranges, respectively. Local coordination geometries around the metal centres reflect similar differences, which are detailed in the table III.A21 (Appendix III). For the sake of brevity, it's enough to emphasize that average equatorial M−O bond distances measure 1.992 Å (Ni) and 1.940 Å (Cu), while the axial M−N bond distances average at 2.147 Å (Ni) and 2.217 Å (Cu). Intramolecular stabilisation of the structure arises from hydrogen bonding contacts between the methoxy substituents of the central spacer and C−H moieties of the nearest 1,3-diketonato pockets, as seen previously in the structures of free ligand and compound **17**. Similarly, peripheral phenolate aromatic cores from the ligands take part in the intermolecular C−H···O hydrogen bonding interactions, establishing different patterns and numbers of contacts which amplify

the established differences in the environment around the [CuNi] dimers. For instance, phenolate rings in the vicinity of the [Cu1Ni1] and [Cu3Ni3] pairs take part in three contacts, while the same moiety around the [Cu2Ni2] collaborates in only two such contacts. In this way, individual $[(CuNi)_3(L_{A2})_3(py)_9]$ molecules are arranged in a supramolecular 2-D sheet with fascinating hexagonal hydrogen bonding motifs. Third dimension of the crystal structure is also generated via C–H···O hydrogen bonding between the antiparallel molecular sheets, in which axial pyridine ligands from [Cu1Ni1] dimer and Ni2 centre act as hydrogen donors to phenolate acceptors from three neighbouring molecules. This three-dimensional arrangement, combined with large cavity in the heart of the complex, leaves plenty of voids for lattice pyridine channels within the structure (Figure 3.11C).

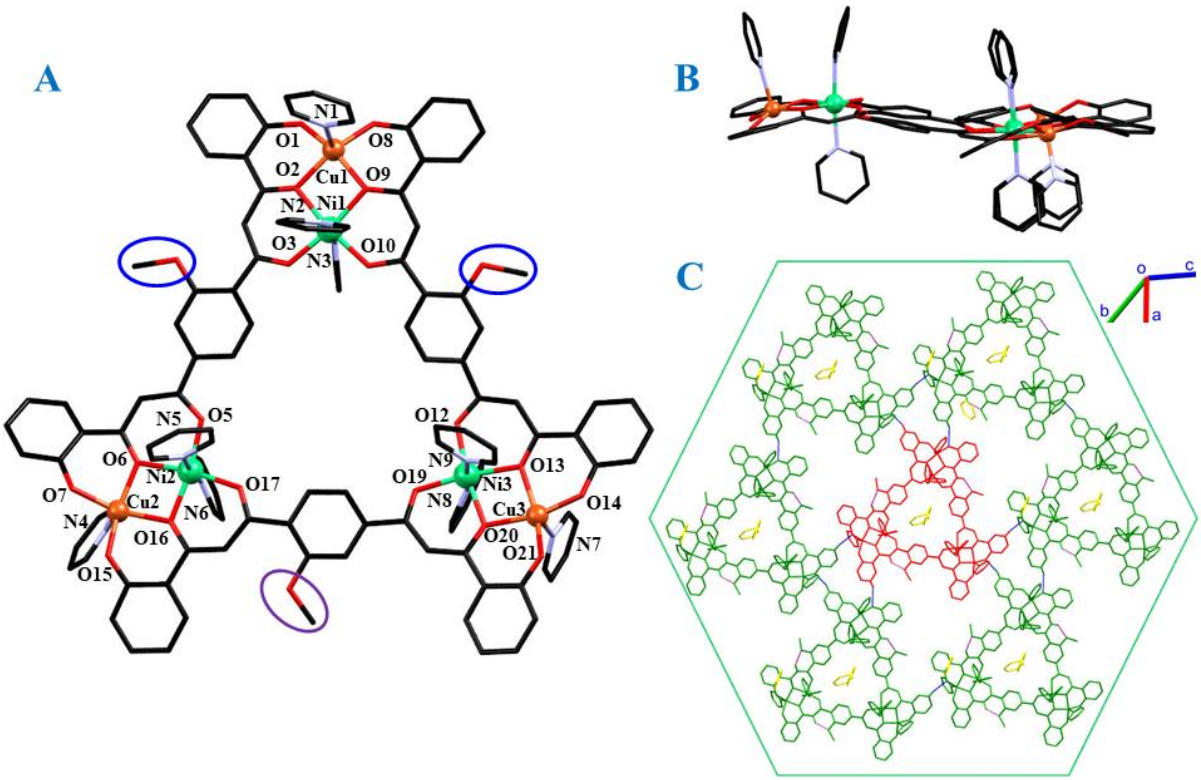

Figure 3.11: A) Molecular structure and labelling scheme of $[(CuNi)_3(L_{A2})_3(py)_9]$ (**18**). Blue and violet circles highlight the distribution of the methoxy substituents on aromatic spacer which affects the symmetry of the cluster. B) Side view of the molecular structure of the compound **18**, emphasizing position of the axial ligands and the non-planarity of the metallacoronand. C) Supramolecular arrangement of the complex **18** in a 2-D hydrogen bonded sheets. Hexagonal structural motifs around the central molecule (red) are emphasized along with the pyridine channels (yellow) in the core of the complex (green hexagon serves only as a guide to an eye). Intra- and intermolecular

hydrogen bonding interactions are indicated as violet and blue contacts, respectively. Hydrogen atoms taking part in the interactions are shown, while the rest is omitted for clarity.

The triangular metallacoronand structural motif with triple bimetallic vertices has been reported previously by Murray *et al.* for $[Cu_2]_3$ and $[CuNi]_3$ clusters, assembled from symmetric 1,4-*bis*-β,δ-triketone ligand with phenyl spacer between the coordination pockets.[35] Despite the general structural similarity between the compound **18** and reported systems, distribution of metal ions within the cluster is completely opposite since Murray's $[CuNi]_3$ complex features hexacoordinated Ni(II) ions within the peripheral coordination pocket, while pentacorodinated Cu(II) centre was found at inner metallic site (Figure 3.12B). Reason for this probably arises from peculiar differences in ligand structures, involving biting angles of chelating pockets as the most important parameter. Average biting angle of the inner β-diketonato coordination pocket in the structure of **18** is α=127.0° (range 126.04-128.44°), matching nicely with an average angle of α=127.5° for peripheral 3,5-triketonato site in Murray's [CuNi] trimer (range 125.11-132.63°). Interestingly more pronounced differences were found for pentaccordinated Cu(II) site, where compound **18** exhibits the average angle of β=122.3° (range 121.52-122.67°) while reported trimer gives an average of β=125.1° (range 122.40-127.37°). Additionally, wider biting angle ranges and higher flexibility of Murray's 1,4- *bis*(β,δ-triketone) can be related with the presence of isopropyl wings which don't participate in delocalization of electronic density in deprotonated ligand. On the other hand, presence of aromatic hydroxyphenyl moieties in the structure of $(L_{A2})^{4-}$ extends the π-conjugation over the entire molecule, contributing to its rigidity.

Additionally, use of the simplified 1,4-*bis*-β-diketone ligands holding only one chelating functionality (H_2L) allowed the preparation of family of compounds with triangular $[M_3L_3(X)_n$ $0<n<6]$ metallacoronand structure ($M=Co^{II}$, Ni^{II}, Cu^{II}, Zn^{II}).[36-39] Assembly assisted by simple donor ligands (X) such as pyridine or DMF led to isolation of discrete molecular assemblies,[36-38] while engagement of bitopic, linker ligands such as pyrazine, 4,4'-bipyridine, dabco *etc*. favoured 1-D polymerisation of the triangular platforms.[40] Expansion of ligand backbone with biphenylene spacer generated large central void of 118 $Å^2$ within the discrete [M_3; M=Co, Cu] metallocyclic tectone (15 Å edge of triangle) which was posteriorly converted into highly porous (56% of the unit cell volume) 3-D MOF, implementing hexamethylenetetramine as a trigonal linker.[41] Apart from presenting beautiful molecular

architectures, Clegg *et al*. showed the possible application of these electrically neutral systems in liquid-liquid extraction of 3*d*-metals by functionalising the ligands with lipophilic alkyl wings.[38]

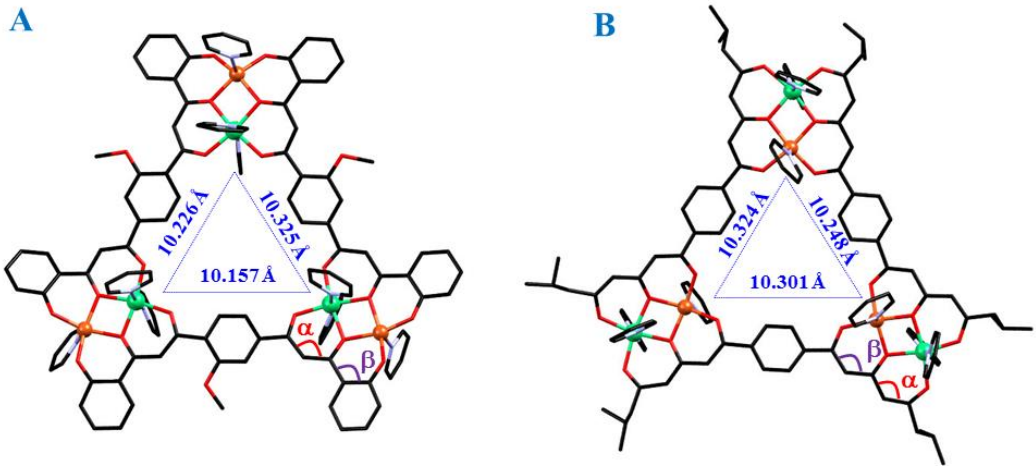

Figure 3.12: Comparison of the molecular structures of compound **18** (A) and $[(CuNi)_3L_3(py)_9]$ compound (B) reported by Murray *et al*. (Refcode: TUDFUU).[35] Intramolecular distances of inner metallic centres are indicated in the central cavities of the clusters.

3.3.5. Design, synthesis and characterisation of 5,5'-*bis*-(3-oxo-3-(2-hydroxyphenyl)propionyl)-2,2'-dipyridil, H_4L7

Another idea of tailoring the dissimilarities and interaction between the qubit components was to construct the organic scaffold with different functionalities which can bind selectively weakly coupled metallic assemblies of different nuclearity. In this way, the asymmetry of the qubits would be related with their nuclearity (topology) and with the local crystal field. First ligand designed for this purpose (**H_4L7**) embodies previously explored phenol-β-diketone functional group (oxygen donors) with the chelating 2,2'-bipy (nitrogen donors) as the central spacer. In order to maximise the distance between the qubits and weaken their interaction, substitution at the C5 carbon atoms of the 2,2'-dipyridil spacer seemed as the most reasonable choice since at the same time allows the linear alignment of the chelating sites and maximises their separation. Thus, starting from the commercially available 5,5'-dimethyl-2,2'-dipyrdile, akin synthetic procedure was employed as seen previously for the ligand H_4L_{A2} (Scheme 3.8).[42, 43] Hence, oxidation with the potassium permanganate in basic

aqueous medium yielded the 2,2'-bipyridine-5,5'-dicarboxylic acid which was easily converted to its methyl ester upon addition of thionyl chloride in MeOH. Claisen condensation of the obtained ester with 2-hydroxyacetophenone in dry THF successfully provided the aimed ligand **H_4L7**.

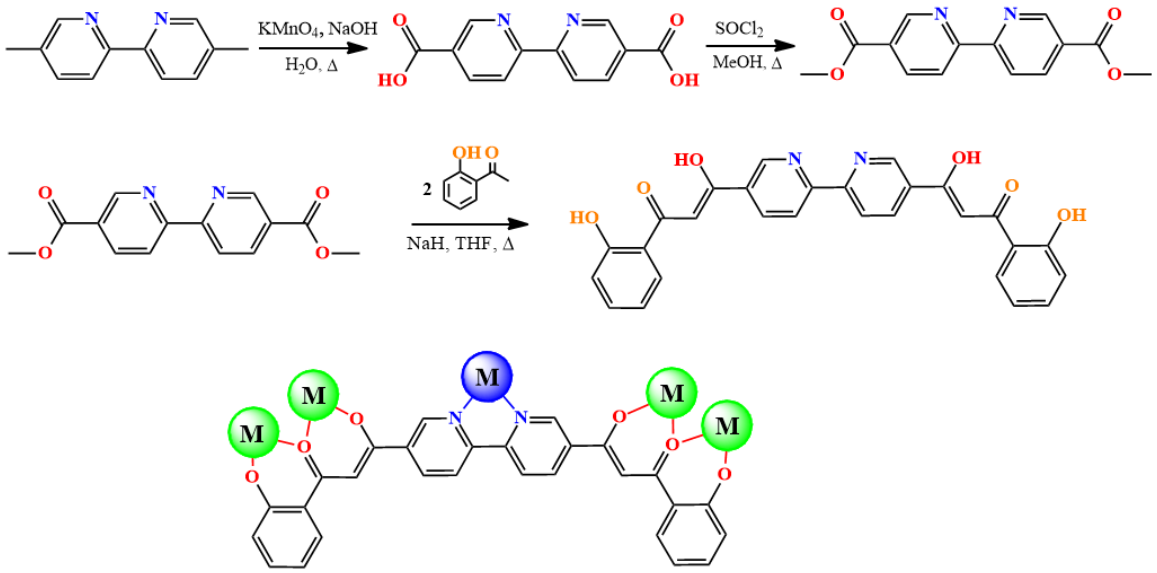

Scheme 3.8. Preparation of the multifunctional *bis*-β-diketone ligand **H_4L7** and its possible coordination mode μ_5-$[L7]^{4-}$.

Ligand characterisation by ^{1}H NMR spectroscopy, mass spectrometry and elemental analysis confirmed its purity and the given composition (Appendix III, Fig. III.A8). Moreover, single crystals analysis of **H_4L7** (grown from the DMF) provided detailed insights in its solid state structure. Similarly to the previously described systems, enolic form of the ligand is accompanied with the *trans*-positioning of the phenol-β-diketone functionalities. Additionally, these coordination pockets maintain the *trans*-orientation in respect to the adjacent pyridine rings of the 2,2'-bipy spacer whose donor atoms are also oppositely directed (Figure 3.13). Described conformation preserves the established pattern of the intramolecular hydrogen bonding interactions with carbonyl O2 atom acting as acceptor of hydrogen bridges from the phenol and enol OH group.

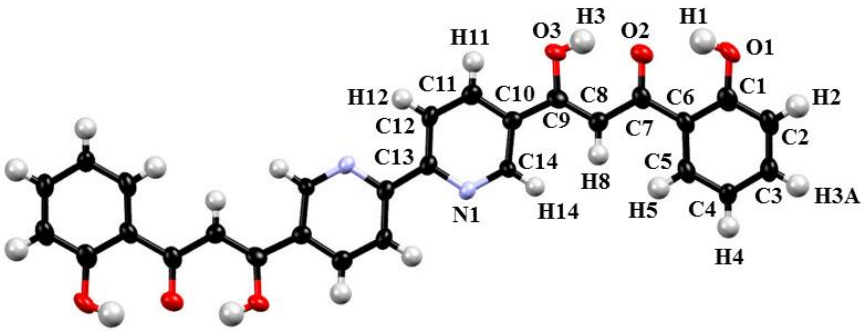

Figure 3.13: Molecular structure of **H_4L7** emphasizing the *trans*-orientation of its phenol-β-diketone and 2,2'-bipyridyl coordination pockets. Crystallographically independent atoms are labelled and all displacement ellipsoids are drawn at 50% probability.

On the other hand, intermolecular hydrogen bonds are established between the *trans*-oriented nitrogen donors from the central pyridine rings and the phenol wings (C2−H2, Figure 3.14A). Specifically, each molecule participates in four interactions, acting as hydrogen donor through phenol wings and as hydrogen acceptor through its central 2,2'-bipy spacer. Consequently, layers of the *quasi*-perpendicular molecules are intercalated in polymeric 2-D sheets. Moreover, planarity of this supramolecular arrangement supports the effective π···π interactions which determine the third dimension of the structure (Figure 3.14B).

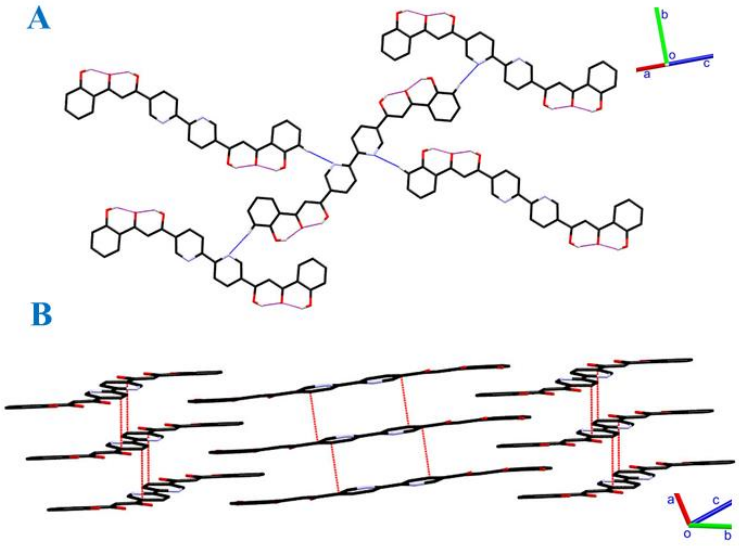

Figure 3.14: Supramolecular motifs in the crystal structure of **H_4L7**. A) Intra-(purple) and intermolecular (blue) hydrogen bonding interactions. B) π···π contacts (red) between the hydrogen bonded layers of the molecules. Only hydrogen atoms taking part in the interactions are shown for clarity.

3.3.6. Design, synthesis and structure of symmetric compound $[(CuNi)_2(L7)(OH)_2(py)_{10}](ClO_4)_2$

Following the proposed μ_5-$[L7]^{4-}$ coordination mode (Scheme 3.8), initial topology of corresponding coordination compound was designed as array of weakly coupled effective spins S=1/2, distributed within the molecule as [NiCu]···Cu···[NiCu] clusters. According to this idea, [CuNi] dimers would be placed again in deprotonated phenolato-diketonato pockets, while central Cu^{II} centre would occupy the chelating 2,2'-bipy site of the spacer, completing its coordination sphere by solvent pyridine donors. Hence, adequate reaction setup included 2:3:1:6 stoichiometry between perchlorate salts of metals (Ni and Cu, respectively), **H_4L7** and hydroxide co-ligand. Unfortunately, this setup failed to produce desired product, giving instead a symmetrical complex $[(CuNi)_2L7(OH)_2(py)_{10}](ClO_4)_2$ (**19**), holding solely pair of distant [CuNi] dimers. Applying the correct 2:2:1:6 stoichiometry, this compound was also prepared in more rational manner.

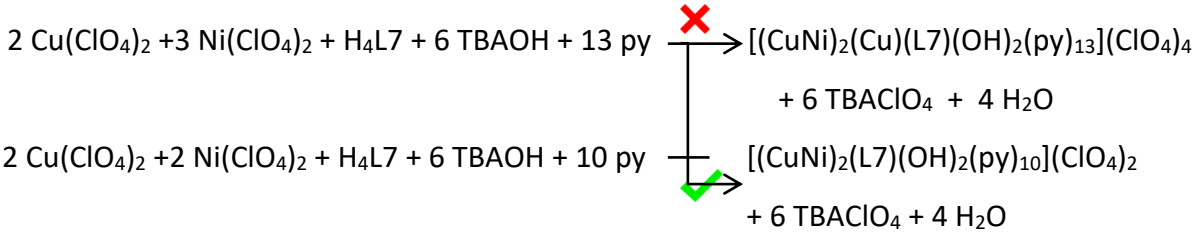

Understanding the causes which leave the central 2,2'-bipy spacer metal-free could again involve the coordinatively competitive pyridine solvent, although chelating effects of the ligand should be thermodynamically more favoured. However, bearing in mind the conformational flexibility of 2,2'-bipy moiety and its preference for *trans* oriented pyridine rings (*vide supra*), the chelating effects could be reduced and compensated by intermolecular hydrogen bonding. Additionally, high charge of designed $[(CuNi)\cdots Cu\cdots(NiCu)]^{4+}$ cation could also contribute to its destabilisation and boost the dissociation of the central Cu^{2+} ion from its structure. To overcome this problem, different reaction setups were conducted with mixed sources of metal ions combining the perchlorate salts, which provide the suitable inert anion for the complex cation, and negatively charged chelating anions such as acetylacetonate, chloride and acetate which could compensate the charge of additional Cu^{II} ion:

$2\ Cu(ClO_4)_2 + 2\ Ni(ClO_4)_2 + 2\ CuX_2 + H_4L7 + 6\ TBAOH + 10\ py \longrightarrow$

$\longrightarrow \{[CuNi(py)_5(OH)]_2[Cu(X)_2](L7)](ClO_4)_2 + 6\ TBAClO_4 + 4\ H_2O \quad X= Cl^-; (acac)^-; CH_3COO^-$

Unfortunately, these conditions led to extensive precipitation of products from the solution, obstructing the further structural characterisation. Nevertheless, limited characterisation of obtained precipitates indicates the success of the latter strategy, motivating the ongoing optimisation of the reaction and crystallisation conditions.

Structure of the ionic compound **19** (monoclinic $P2_1/c$ space group) includes the complex cation $[(CuNi)_2L7(OH)_2(py)_{10}]^{2+}$, two perchlorate counter ions, and lattice solvent mixture (1.14:0.43) of Et_2O and pyridine (Figure 3.7A). Two formulae units of the given composition define the unit cell, while only half of it determines the asymmetric unit, in analogy with the structure of starting ligand H_4L7. Connectivity features of complex $[(CuNi)_2L7(OH)_2(py)_{10}]^{2+}$ are identical to its structural analogues in compounds **16** and **17**. Hence, two distant [CuNi] dimers are chelated within the completely deprotonated phenolato-β-diketonato moiety of the ligand (μ_4-$[L7]^{4-}$ coordination mode) and bridged additionally by one hydroxide co-ligand. Octahedral Ni(II) ions reside in the inner, β-diketonato, coordination pocket and adopt octahedral geometry defined by O_3N_3 ligand field, with nitrogen donors coming from three coordinated pyridine molecule. Peripheral copper(II) ion are located within the smaller phenolato-β-diketonato coordination pocket, surrounded by distorted square-pyramidal O_3N_2 ligand field (2 py donors). Distance between the adjacent Ni^{II} and Cu^{II} sites measures 3.0972(6) Å, while the intramolecular distance between the symmetry related [CuNi] pairs measures 15.278(1) Å. Axial Ni−N bonds are slightly elongated (average 2.122 Å) in comparison with the equatorial bonding where Ni−N and Ni−O measure 2.095(3) Å and 2.041 Å, respectively. Similar tendency is observed at the Cu(II) site, where axial Cu−N bond (2.308(4) Å) is significantly longer than the equatorial Cu−N (2.020(3) Å) and Cu−O (average 1.945) bonds, while bonding angles between the axial and equatorial donors (range 91.8(1)°-110.7(1)°) emphasize the significant distortion of coordination sphere. Perchlorate anions participate in four hydrogen bonding O−H···O and C−H···O interactions with bridging hydroxide and pyridine ligands of the corresponding [CuNi] moiety within the complex cation (Figure 3.7B). Additional five intermolecular C−H···O interactions surround each anion with five different $[(CuNi)_2L7(OH)_2(py)_{10}]^{2+}$ cations and one molecule of lattice Et_2O/pyridine (positional disorder). The latter contributes even more to the stabilization of

crystal structure by participating in C–H···O/ C–H···N hydrogen bridge with the 2,2'-bipy spacer of the ligand. On the other hand, each nitrogen donor of the spacer acts as a double acceptor of C–H···N hydrogen bridges from the axial pyridine ligands of neighbouring cations. Additionally, two C–H···π contacts between the equatorial pyridine ligands around the peripheral Cu^{II} site and Ni-bonded pyridine ligands from the neighboring cations contribute to the supramolecular arrangement of the clusters.

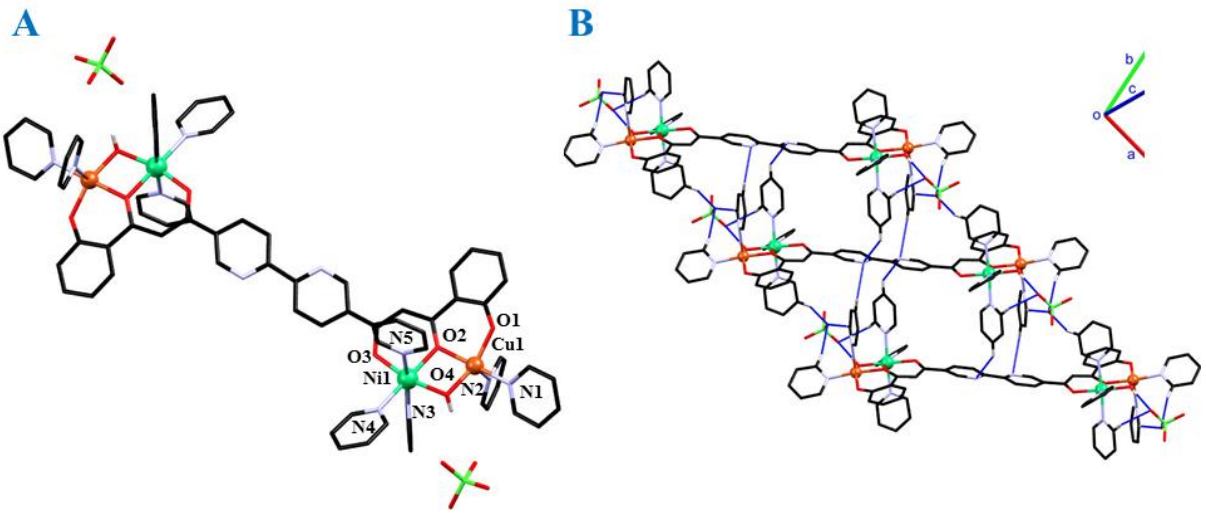

Figure 3.15: A) Molecular structure and labelling scheme of $[(CuNi)_2(L7)(OH)_2(py)_{10}](ClO_4)_2$ (**19**). Only crystallographically independent heteroatoms are labelled. B) Crystal structure of the compound **19** emphasizing the supramolecular chain structure of hydrogen bonded (blue contacts) ionic pairs. Hydrogen atoms affecting the charge of the cluster or taking part in the interactions are shown, the rest is omitted for clarity.

3.3.7. Design, synthesis and characterisation of 2,9-*bis*-(3-oxo-3-(2-hydroxyphenyl)propionyl)-1,10-phenanthroline, H_4L8

Further design of the multifunctional *bis*−β-diketone ligands involved the incorporation of the chelating 1,10-phenathroline moiety as the central spacer between the two phenol-β-diketone functionalities. Preparation of described **H_4L8** molecule started with the free-radical halogenation of the commercially available 2,9-dimethyl-1,10-phenanthroline (necuproine). In this reaction, benzoyl peroxide was employed as the initiator of the free-chlorine radicals originated from the *N*-chlorosuccinimide. Obtained 2,9-*bis*-trichloromethyl-1,10-phenanthroline was then hydrolysed using the concentrated sulfuric acid into

corresponding carboxylic diacid, which was converted *in situ* with the addition of EtOH to the ethyl diester.[44, 45] Finally, ligand **H_4L8** was easily prepared by the Claisen condensation of the obtained diester with two equivalents of 2-hydroxyacetophenone in the dry THF as solvent (Scheme 3.9).

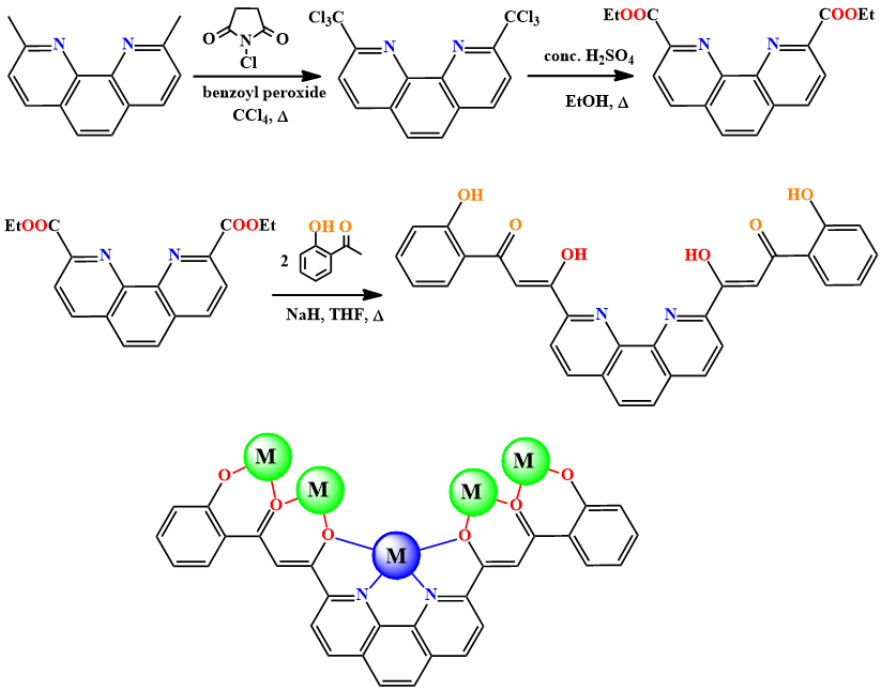

Scheme 3.9. Preparation of the multifunctional *bis*-β-diketone ligand **H_4L8** and its possible coordination mode μ_5-$[L8]^{4-}$.

Characterisation of the obtained ligand by ^{1}H NMR spectroscopy, mass spectrometry and elemental analysis confirmed its purity and the given composition (Appendix III, Fig. III.A9). Low solubility of the ligand in common solvents limited its crystallisation, since the most successful attempts (DMF as a solvent) resulted with the chemical conversion of the *bis*-β-diketone **H_4L8** to its flavone-β-diketone analogue **H_2L8**. The mechanism of this modification involves the nucleophilic attack of the distant carbonyl from the β-diketone moiety by the hydroxyl group from the adjacent phenol, resulting with the thermodynamically favoured six-membered ring closure. In the following step, heating of the intermediate hemiacetal eliminates the water molecule from its structure, resulting with the formation of flavone **H_2L8** (Scheme 3.10).

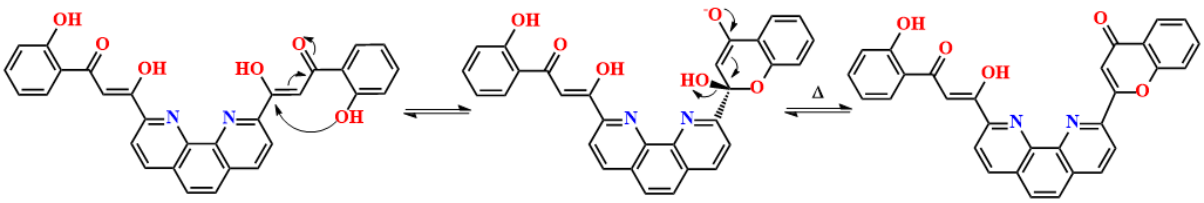

Scheme 3.10. Mechanism of the dehydrative cyclization of *bis*-β-diketone ligand **H_4L8** to its flavone-β-diketone analogue **H_2L8**.

Upon crystallisation, the same reaction batch provided two polymorphs of the **H_2L8** molecule (**H_2L8a** and **H_2L8b)**, differing structurally by orientation of the phenol wing and disposition of acidic protons (Figure 3.16). On the other hand, common features of both molecular forms are their existence as enolic tautomer and the bent, U-shaped conformation in which 1,10-phenanthroline spacer is perpendicular and *trans*-oriented with respect to the phenol-β-diketone functionality. The latter moiety is *cis*-oriented in the polymorph **H_2L8a**, exhibiting the established pattern of the intramolecular hydrogen bonding interactions, with carbonyl O2 atom acting as the acceptor of hydrogen bridges from the phenol and enol OH group. Additionally, flavone carbonyl group takes part in the intramolecular and intermolecular interactions with phenol and with the phenanthroline backbone of the closest neighbour, respectively. In contrast, *trans*-oriented phenol with respect to the β-diketone maximises the intramolecular hydrogen bonding (five contacts) in the structure of the **H_2L8b** (Figure 3.17). The flavone-phenol interactions in the core of structure are dominant (three contacts), with further contribution from the phenol-β-diketone and the β-diketone hydrogen bonding. The latter moiety, positioned at the periphery of the molecule, takes part also in the intermolecular interactions with the aromatic backbone of phenanthroline and flavone moieties. In the crystal structure of both polymorphs, stacking of the hydrogen bonded molecular chains is enabled by π···π contacts between their aromatic cores, with additional expansion in the structure of **H_2L8a** coming from the C–H···π interactions.

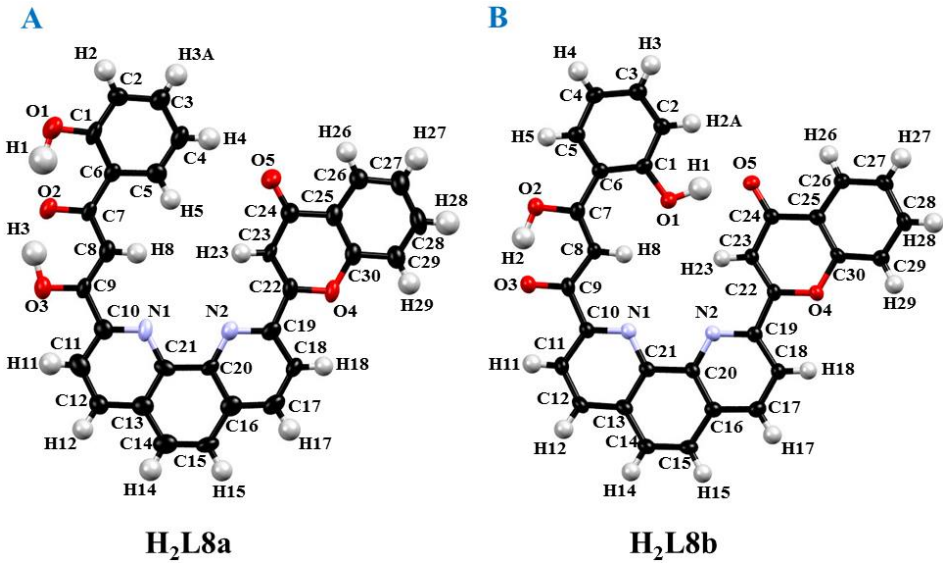

Figure 3.16: Molecular structure of the **H_2L8** polymorphs emphasizing the orientations of its phenol-β-diketone coordination pocket and disposition of acidic protons. Crystallographically independent atoms are labelled and all displacement ellipsoids are drawn at 50% probability.

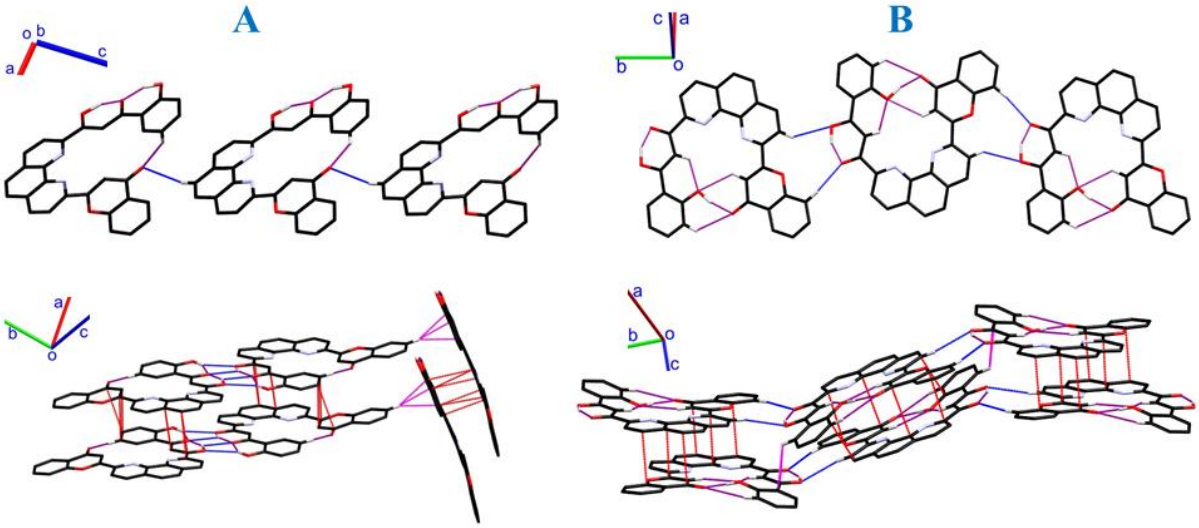

Figure 3.17: Supramolecular motifs in the crystal structure of **H_2L8** polymorphs (A- **H_2L8a**; B-**H_2L8b**). *Top*: Intra-(purple) and intermolecular (blue) hydrogen bonding interactions. *Bottom*: π···π contacts (red) and C–H···π contacts (magenta) between the hydrogen bonded layers of the molecules (violet and blue). Only hydrogen atoms taking part in the interactions are shown for clarity.

3.3.8. Design, synthesis and structure of the symmetric compound $[(CuNi)_2(L8)(OH)_2(py)_{10}](ClO_4)_2$

As seen previously, multitopic and asymmetric *bis*-β-diketone can be easily employed in formation of complex $[(CuNi)_2L(OH)_2(py)_{10}](ClO_4)_2$, holding a pair of distant [CuNi] dimers.

Hence, this system was targeted as an initial probe of reactivity and conformational flexibility of ligand H_4L8. Applying the correct 2:2:1:6 stoichiometry, aimed $[(CuNi)_2(L8)(OH)_2(py)_{10}](ClO_4)_2$ (**20**) compound was easily obtained.

$$2\ Cu(ClO_4)_2 + 2\ Ni(ClO_4)_2 + H_4L8 + 6\ TBAOH + 10\ py \longrightarrow [(CuNi)_2(L8)(OH)_2(py)_{10}](ClO_4)_2 + 6\ TBAClO_4 + 4\ H_2O$$

Single-crystal X-ray diffraction experiment confirmed the expected molecular structure of **20** (triclinic *P*−1 space group) which crystallises with 2.5 molecules of lattice pyridine. Given composition defines the asymmetric unit of the compound, while the unit cell is twice larger. General connectivity features of complex $[(CuNi)_2(L8)(OH)_2(py)_{10}]^{2+}$ are identical to previously described cations, so detailed description will be omitted here. However, striking difference between the compound **20** and its analogues arises from the U-shaped, bent, conformation of the $[L8]^{4-}$ backbone which contrasts to previously seen linear conformations (Figure 3.18A). Although this molecular shape of the ligand is comparable to its flavone-β-diketone derivative, the degree of planarity in former is significantly reduced, since closely-spaced phenolato-β-diketonato moieties are oriented to the opposite sides with respect to the central phenanthroline spacer. However, bearing in mind that those fragments are electrically charged in complex **20** and electrically neutral in **H_4L8**/**H_2L8**, loss of planarity in the former can be attributed to repulsive electric interactions. Moreover, low-symmetry of the observed ligand conformation breaks the equivalence between the coordinated [CuNi] dimers, as detectable from their geometrical parameters. Intradimer distances between the metallic sites measure 3.0502(8) Å and 3.0703(9) Å, while the intramolecular [Ni···Ni] and [Cu···Cu] distance between the dimers measure 11.477(1) Å and 10.637(1) Å, respectively. Comparison of the latter values underlines nicely the structural difference between the bent compound **20** and its linear analogues, where peripheral Cu^{II} sites are significantly more distant than the inner Ni^{II} centres. On the other hand, usual bonding tendencies are perfectly maintained with weaker axial Ni−N bonds (average 2.137 Å) in comparison with the equatorial Ni−N and Ni−O bonds which average at 2.062 Å and 2.032 Å, respectively. Similar situation is observed at the square-pyramidal Cu(II) site, where axial Cu−N bond (average 2.248 Å) is significantly weaker than the equatorial Cu−N (2.036 Å) and Cu−O (average 1.935) bonds. Two perchlorate anions participate as hydrogen acceptors in twelve hydrogen bonding O−H···O and C−H···O interactions with the corresponding [CuNi]

moiety of complex cation (bridging hydroxide co-ligand and pyridine) and with four neighbouring cations (pyridine ligands and phenanthroline spacer, Figure 3.18B). Additionally, intercation C–H···O interactions are established between the phenoxide oxygen atoms and axial (Ni) or equatorial (Cu) pyridine ligands, organising the ionic pairs in supramolecular sheets of antiparallel chains. In addition to existent cavities in the core of complex cations, such arrangement generates voids between the chains where crystallisation pyridine molecules can be found.

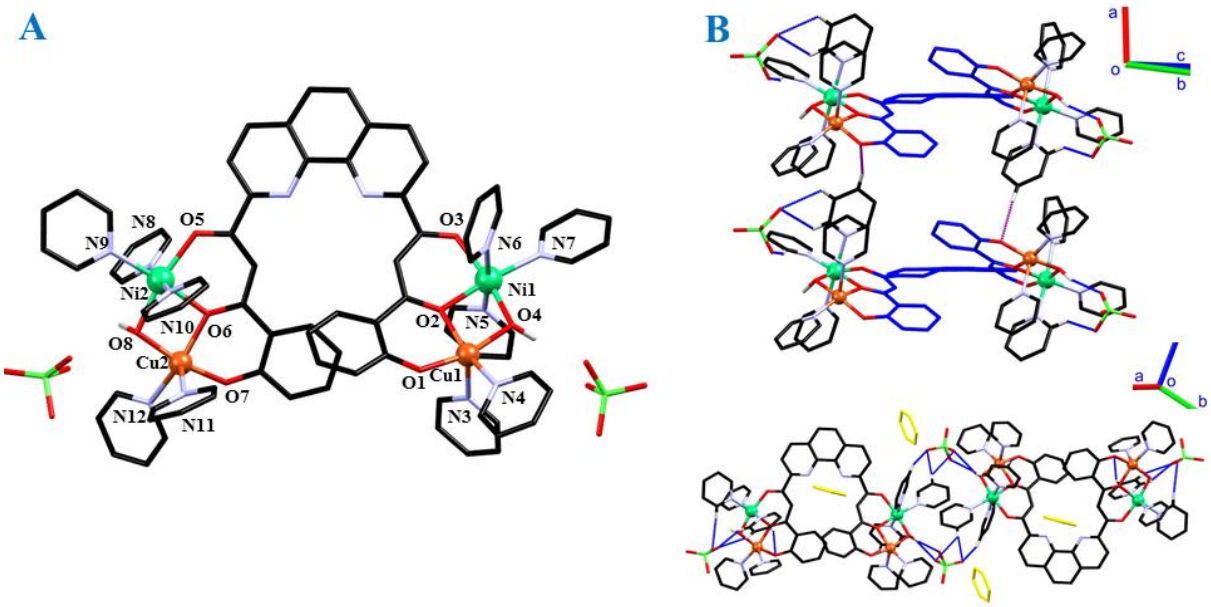

Figure 3.18: A) Molecular structure and labelling scheme of the $[(CuNi)_2(L8)(OH)_2(py)_{10}](ClO_4)_2$ (**20**). B) *Top*: Crystal structure of the compound **20** emphasizing the supramolecular chain structure of hydrogen bonded (purple contacts) complex cations and their interactions with corresponding perchlorate anions (blue contacts). Ligand backbone is shown in blue to emphasize its conformation within the complex **20**. *Bottom*: Top-down view along the supramolecular chains emphasizing pyridine voids (yellow) and antiparallel alignment of chains directed by cyclic network of hydrogen bonding interactions with perchlorate anions (blue contacts). Hydrogen atoms affecting the charge of the cluster or taking part in the interactions are shown, the rest is omitted for clarity.

3.3.9. Solution studies

The stability of clusters **16**-**20** in solution was tested by mass spectrometry (ESI and MALDI-TOF) and ^{1}H NMR spectroscopy. Unfortunately, adequate conditions were not established to detect the complex species $[(CuNi)_2L(OH)_2(py)_{10}]^{2+}$ in a THF solution. ESI(+) technique

revealed the existence of complex cations $[Ni(H_3L)]^+$ (*m*/*z*=460.03, 489.05, 537.06 and 561.06 for L=L_A, L_{A2}, L7 and L8, respectively) and $[Ni_2(HL)]^+$ (*m*/*z*=515.95, 544.97, 592.98 and 616.98 for L=L_A, L_{A2}, L7 and L8, respectively), while ESI(-) spectrograms were saturated with the perchlorate anion (*m*/*z*=98.95). Additionally, MALDI-TOF(+) spectrograms revealed the $[Cu(DCTB)_2]^+$ (*m*/*z*=563.1), and $[Ni(H_3L)]^+$ fragments as the most abundant species. Presumably, positive modes of ionization needed to detect the complex cations affect the bridging hydroxide ligands and convert them into non-bridging water molecules upon protonation, resulting with fragmentation of cluster and release of free copper(II) ions. Nevertheless, obtained information indicates that assigned heterometallic composition of clusters is truthful. Similar results were also obtained analysing the solutions of respective compounds in acetonitrile and methanol.

On the other hand, integrity and composition of the neutral hexanuclear cluster **18** were successfully established using the MALDI-TOF(+) technique. In THF solution of compound, the most intense signal corresponds to the cation $\{[(CuNi)(L_{A2})]^3\}^+$ (*m*/*z*=1651.0), which includes the central core of cluster **18** without the axial pyridine ligands (Figure III.A15). Similar observations will be exposed in the Chapter IV and can be rationalised with relatively weaker axial M—N bonds which are susceptible to dissociation or exchange with solvent molecules. Nevertheless, position of the observed peak and its isotopic distribution are nicely consistent with the theoretically expected ones from the solid state structure, thus confirming undoubtedly the assigned heterometallic composition of the compound (Figure III.A16). Additionally, higher assemblies are also found and identified as $\{[(CuNi)(L_{A2})]_3+Cu\}^+$ (*m*/*z*=1714.0), $\{[(CuNiL_{A2})_3]_2\}^+$ (*m*/*z*=3303.9) and $\{[(CuNiL_{A2})_3]_2 + Cu\}^+$ (*m*/*z*=3367.8). In an attempt of establishing the triple asymmetry between the [CuNi] dimers in **18**, its solution structure (d_6-DMSO) was investigated by paramagnetic ^{1}H NMR spectroscopy (Figure 3.19). Observed spectral window includes at least 11 detectable signals distributed over wide range of chemical shifts, starting from δ=-2.46 ppm and ending with δ=36.98 ppm. Unfortunately, release of the lattice pyridine molecules (δ=7.39, 7.79 and 8.58 ppm) hindered completely the region from 7-10 ppm in which aromatic hydrogen atoms of the $\mathbf{L_{A2}^{4-}}$ appear, visible only by shoulder on 6.95 ppm and by asymmetry in intensity between the peripheral pyridine signals. Similarly, solvent and water peaks (d_6-DMSO, δ=2.50 ppm, H_2O, δ=3.33 ppm) overlap with the resonances of hydrogen atoms from methoxy groups, disabling the possibility of establishing the asymmetry of cluster. However, very large

chemical shifts in the spectral window indicate that the paramagnetic $[CuNiL_{A2}]_3$ core of cluster **18** is preserved. Moreover, observed line broadenings of signals directly correlate faster nuclear relaxation with slower spin relaxation of the unpaired electrons from [CuNi] dimers.[46-48]

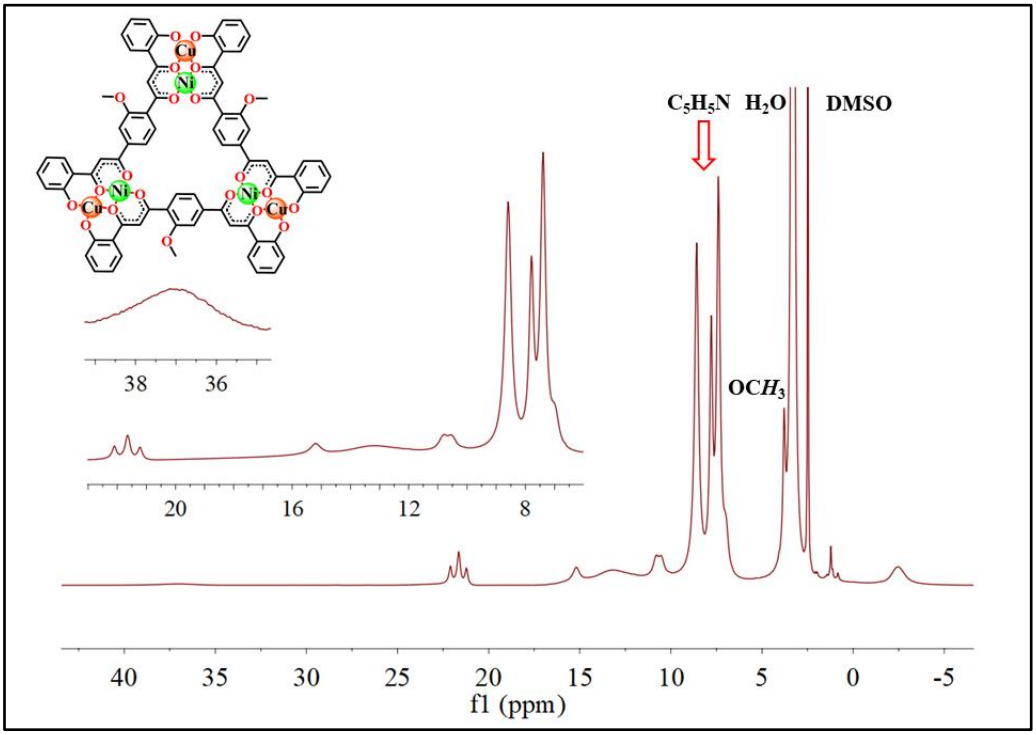

Figure 3.19: ^{1}H NMR spectrum of compound **18** in d_6-DMSO.

3.3.10. Comparison of bonding details in heterometallic [CuNi] clusters

Obtained family of structurally related [CuNi] compounds allows the analysis of their bonding details and tendencies. Looking at the peripheral Cu^{II} site, average axial Cu−N bond distances remain almost identical, varying from 2.229 Å (**16**), 2.218 Å (**17**), 2.308 Å (**19**), 2.248 Å (**20**), 2.217 Å (**18**). Slight elongation in compound **19** occurs since those pyridine molecules take part in π···π interactions, which is not the case for the other members of the series. Even smaller deviations, limiting with experimental error, can be found in average equatorial bond lengths which measure 1.976 Å (**16**), 1.977 Å (**17**), 1.964 Å (**19**), 1.960 Å (**20**) and 1.940 Å (**18**, Figure 3.20). Consequently, this tendency can be directly transmitted to averages of all bonds, 2.027 Å (**16**), 2.025 Å (**17**), 2.032 Å (**19**), 2.017 Å (**20**) and 1.995 Å (**18**), and distances from equatorial planes, 0.289 Å (**16**), 0.296 Å (**17**), 0.270 Å (**19**), 0.305 Å (**20**)

and 0.312 Å (**18**). On the other hand, evolution of distortion parameter of square-pyramidal geometry τ≈0.278 (**16**), 0.302 (**17**), 0.327 (**19**), 0.102 (**20**) and 0.054 (**18**) indicates that coordination geometry of Cu^{II} ions in oxo-hydroxo-bridged $[CuNi]_2$ compounds is more distorted from ideal square-pyramidal geometry than the one in asymmetric $(\mu\text{-O})_2$ $[CuNi]_3$ cluster **18**.

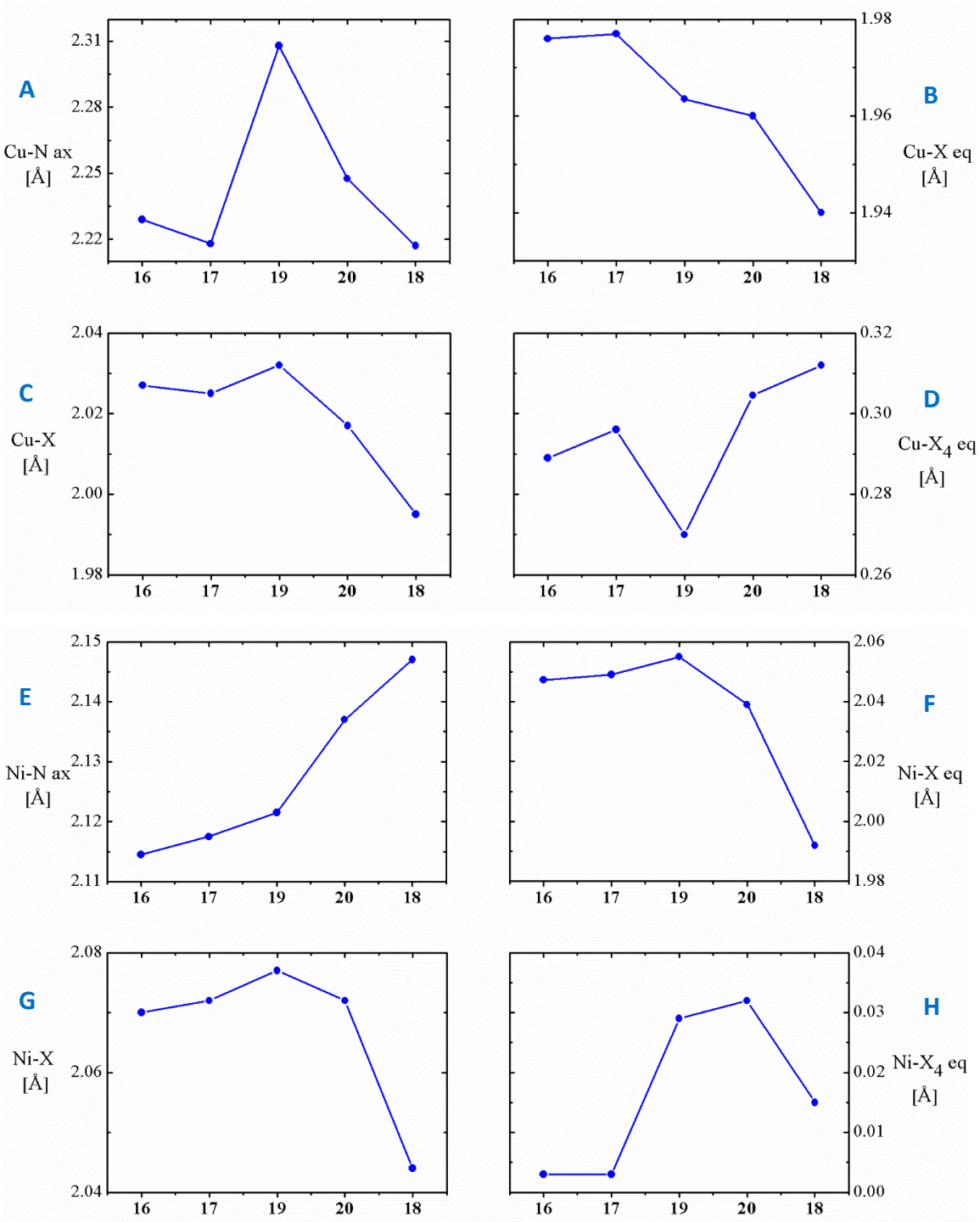

Figure 3.20: Bonding geometry of pentacoordinate Cu^{II} and hexacoordinate Ni^{II} centres in compounds **16**-**20**. Average axial M–N bond distances (A and E), average equatorial M–X bond

distances (B and F), average distance of all M–X bonds (C and G) and distances from equatorial plane.

Similar conclusions can be drawn for Ni^{II} sites which differ from Cu^{II} sites with almost identical axial Ni−N and equatorial Ni−X bond distances. Bonds with axial pyridine ligands change in very reduced range of 2.115 Å (**16**)-2.147 Å (**18**), similarly as equatorial bonds 2.055 Å (**19**)-1.992 Å (**18**). Hence, average bond lengths of all six bonds also remain locked within narrow range of 2.077 Å (**19**)-2.044 Å (**18**), together with the distances from equatorial planes ($0.003 \leq d \leq 0.032$ Å) which indicate perfectly embedded Ni^{II} ions. Biggest differences in these structures can be found when looking at the mutual positioning of metal ions and the angles between their equatorial planes. In compounds **16**, **17** and **19**, two inner Ni^{II} ions are coplanar (Θ=0 °), while for compounds **18** and **20** they intersect under angles of 7.24° (average) and 41.59°, respectively. Large angle in the latter is caused by unusual U-shaped, bent, conformation of the $[L8]^{4-}$ backbone which contrasts to other ligands which demonstrate high degree of rigidity and conjugation in linear conformations. Similar differences can be found in angles between neighboring equatorial planes in [CuNi] dimers, 8.23°(**16**), 8.40° (**17**), 16.11° Å (**19**), 12.59/16.40°(**20**) and 19.53-23.84° (**18**), which could alter the interaction between the magnetic $d_{x^2-y^2}$ orbitals at Cu^{II} and Ni^{II} sites.

3.3.11. Magnetic studies

Magnetic properties of the compounds **16**-**20** were studies through variable temperature (2-300 K) magnetization measurements performed on their powdered microcrystalline samples under the constant magnetic field of 0.5 T. In addition, this study was complemented with magnetization measurements at 2 K in the field range of 0–5 T. Due to simplicity and great similarity of their electronic structure, oxo-hydroxo-bridged $[CuNi]_2$ compounds will be described together firstly, followed by the characterisation of triple asymmetric $(\mu\text{-O})_2$ $[CuNi]_3$ cluster **18**.

Measured room temperature (300 K) values of the $\chi_M T$ product were 2.53, 2.62, 2.39 and 2.85 cm^3Kmol^{-1} for **16**, **17**, **19** and **20**, respectively, which differ slightly from the expected 2.750 cm^3Kmol^{-1} for a heterometallic system incorporating two uncoupled S=1/2 and S=1 spin centres (g=2.0, Figure 3.21). Upon lowering the temperature, the $\chi_M T$ product drops steadily down to 150 K, followed by the abrupt decline down to 30 K which ends with a

plateau in the lowest temperature range (0.94, 0.98, 0.85 and 1.00 cm^3Kmol^{-1} for **16**, **17**, **19** and **20**). Below 7 K, small decline of the $\chi_M T$ product occurs upon cooling ending at 0.82, 0.91, 0.80 and 0.94 cm^3Kmol^{-1} for **16**, **17**, **19** and **120**, respectively, at 2 K. Described behaviour is indicative of moderate antiferromagnetic coupling within the μ-(O), μ-(OH)-[CuNi] dimers which defines the effective S=1/2 ground state of the cluster. Consistent with this are also field-dependent magnetization measurements at 2K, where the highest measured values at 5 T (2.32, 2.19, 2.02 and 2.20 μ_B for **16**, **17**, **19** and **20**, respectively) correlate nicely with the expected 2 μ_B for two S=1/2 centres (g=2, Figure 3.21). In order to estimate the strength of magnetic coupling, experimental data ($\chi_M T$ *vs* T and $M/N\mu_B$ *vs* H) were modelled (PHI[30]) using the matrix diagonalization of the spin Hamiltonian (Figure 3.20):

$$\hat{H} = \mu_B B \sum_i g_i \hat{S}_i - 2J_{Cu-Ni}\left(\hat{S}_{\mathrm{Cu1}}\hat{S}_{\mathrm{Ni1}} + \hat{S}_{\mathrm{Cu2}}\hat{S}_{\mathrm{Ni2}}\right) - zJ$$

Extracted parameters of these fits are collected in the table 3.1, together with the parameters of expanded spin Hamiltonians where the interaction between the dimers ($J_{Ni\text{-}Ni}$) or the single-ion anisotropy of the Ni(II) sites ($\pm D_{Ni}$) were taken into account.

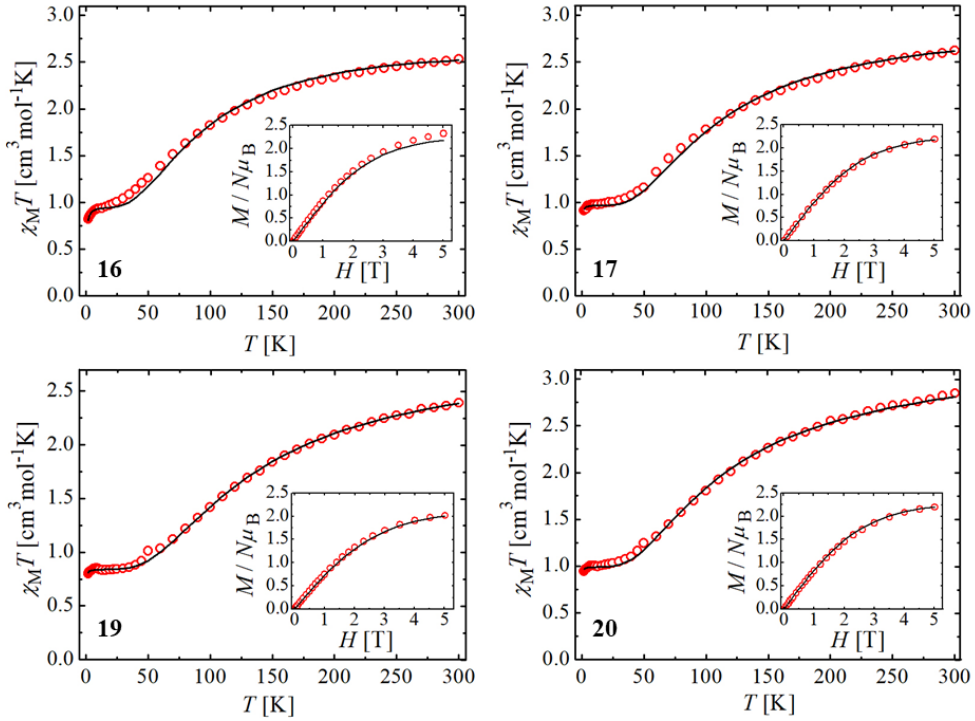

Figure 3.21. $\chi_M T$ *vs* T and $M/N\mu_B$ *vs* H (inset) curves for compounds **16, 17, 19** and **20** with the best fit (solid line). Measurement setup: cooling mode (300→2 K), B = 0.5 T; T_{mag} = 2 K.

Table 3.1. Fitting parameters for the dc studies of $[(CuNi)_2(L)(OH)_2(py)_{10}](ClO_4)_2$ compounds.

Compound	Fixed parameters	Fitted parameters
	$\hat{H} = \mu_B B \sum_i g_i \hat{S}_i - 2J_{\mathrm{Cu-Ni}}(\hat{S}_{\mathrm{Cu1}}\hat{S}_{\mathrm{Ni1}} + \hat{S}_{\mathrm{Cu2}}\hat{S}_{\mathrm{Ni2}}) - zJ$	
16	g_{Cu}=2.00, g_{Ni}=2.21, TIP=−6.0·10^{-4} cm^{3}mol^{-1}	J_{Cu-Ni}= −37.48 cm^{-1},zJ= −0.10 cm^{-1}
17	g_{Cu}=2.00, g_{Ni}=2.21, TIP=−3.0·10^{-4} cm^{3}mol^{-1}	J_{Cu-Ni}= −42.23 cm^{-1},zJ= −0.024 cm^{-1}
19	g_{Cu}=2.00, g_{Ni}=2.09	J_{Cu-Ni}= −50.42 cm^{-1},zJ= −0.018 cm^{-1}
20	g_{Cu}=2.00, g_{Ni}=2.22, TIP=2.5·10^{-4} cm^{3}mol^{-1}	J_{Cu-Ni}= −42.01 cm^{-1},zJ= −0.005 cm^{-1}
	$\hat{H} = \mu_B B \sum_i g_i \hat{S}_i - 2J_{\mathrm{Cu-Ni}}(\hat{S}_{\mathrm{Cu1}}\hat{S}_{\mathrm{Ni1}} + \hat{S}_{\mathrm{Cu2}}\hat{S}_{\mathrm{Ni2}}) - 2J_{\mathrm{Ni-Ni}}(\hat{S}_{\mathrm{Ni1}}\hat{S}_{\mathrm{Ni2}})$	
16	g_{Cu}=2.00, g_{Ni}=2.21, TIP=−6.0·10^{-4} cm^{3}mol^{-1}	J_{Cu-Ni}= −37.92 cm^{-1}, J_{Cu-Ni}= −0.12 cm^{-1}
17	g_{Cu}=2.00, g_{Ni}=2.21, TIP=−3.0·10^{-4} cm^{3}mol^{-1}	J_{Cu-Ni}= −42.32 cm^{-1}, J_{Cu-Ni}= −0.048 cm^{-1}
19	g_{Cu}=2.00, g_{Ni}=2.09	J_{Cu-Ni}= −49.42 cm^{-1}, J_{Cu-Ni}= −0.056 cm^{-1}
20	g_{Cu}=2.00, g_{Ni}=2.22, TIP=3.0·10^{-4} cm^{3}mol^{-1}	J_{Cu-Ni}= −42.37 cm^{-1}, J_{Cu-Ni}= −0.059 cm^{-1}
	$\hat{H} = \mu_B B \sum_i g_i \hat{S}_i + D_{\mathrm{Ni}}\left(\hat{S}^2_{z_{\mathrm{Ni1}}} - \frac{\hat{S}^2_{\mathrm{Ni1}}}{3} + \hat{S}^2_{z_{\mathrm{Ni2}}} - \frac{\hat{S}^2_{\mathrm{Ni2}}}{3}\right)$ $-2J_{\mathrm{Cu-Ni}}(\hat{S}_{\mathrm{Cu1}}\hat{S}_{\mathrm{Ni1}} + \hat{S}_{\mathrm{Cu2}}\hat{S}_{\mathrm{Ni2}}) - zJ$	
16	g_{Cu}=2.00, g_{Ni}=2.21, TIP=−6.0·10^{-4} cm^{3}mol^{-1}	J_{Cu-Ni}= −37.50 cm^{-1},zJ= −0.10 cm^{-1} D_{Ni} = 4.80 or −4.10 cm^{-1}
17	g_{Cu}=2.00, g_{Ni}=2.21, TIP=−3.0·10^{-4} cm^{3}mol^{-1}	J_{Cu-Ni}= −42.22 cm^{-1},zJ= −0.023 cm^{-1} D_{Ni} = 4.46 or −5.20 cm^{-1}
19	g_{Cu}=2.00, g_{Ni}=2.09	J_{Cu-Ni}= −50.51 cm^{-1} D_{Ni} = 0.99 or −1.10 cm^{-1}
20	g_{Cu}=2.00, g_{Ni}=2.22, TIP=2.5·10^{-4} cm^{3}mol^{-1}	J_{Cu-Ni}= −42.00 cm^{-1},zJ= −0.04 cm^{-1} D_{Ni} = 4.15 or −4.95 cm^{-1}

As can be seen from the reported results, expansion of the simple Heisenberg-Dirac-van Vleck spin Hamiltonian with the single-ion anisotropy contributions ($\pm D_{Ni}$) or intradimer coupling ($J_{Ni\text{-}Ni}$) doesn't alter significantly the value of $J_{Ni\text{-}Cu}$ which covers the range between −37.5 cm^{-1} (**16**) and −50.5 cm^{-1} (**19**). Moderate antiferromagnetic coupling within the [CuNi] dimers defines the effective S=1/2 ground state of the cluster and the small single-ion anisotropy of the octahedrally coordinate Ni(II) ion shouldn't contribute significantly to the $\chi_M T$ product in the lowest temperature range. Similarly, crystal structures of the $[(CuNi)_2(L)(OH)_2(py)_{10}](ClO_4)_2$ compounds indicate that the intermolecular distances between the pairs of [CuNi] dimers are in fact shorter than their intramolecular distances, justifying the more reasonable use of zJ than the intradimer coupling ($J_{Ni\text{-}Ni}$). Observed antiferromagnetic coupling within the [CuNi] dimers is expected since equatorially bridging oxygen donor atoms allow the effective superexchange interaction between the magnetic $d_{x^2-y^2}$ orbitals of metal ions. However, no correlation could be established between the value of $J_{Ni\text{-}Cu}$ and metal-metal distance (3.048(1)-3.097(1) Å) or bridging angles of the μ-(O), μ-(OH)-[CuNi] metallic core (97.6(1)-98.2(1)° for Cu−O−Ni and 100.0(1)-103.6(1)° for Cu−OH−Ni). Slightly stronger coupling in **19** could possibly correlate with the larger angle between the equatorial planes of Cu(II) and Ni(II) sites (16.05° for **19**, 8.23°, 8.38° and 12.49° for **16**, **17** and **20**) which reduces the orthogonality between the magnetic $d_{x^2-y^2}$ (Cu) and d_{z^2} (Ni) orbitals and, consequently, the ferromagnetic component of the interaction.

Findings from the bulk magnetization measurements were confirmed by EPR spectroscopy in the solid state and in frozen solution. Variable temperature EPR spectroscopy (4-298 K) on powdered samples revealed that all compounds are silent at the room temperature and become detectable only below 100 K. Upon cooling, isotropic spectral feature centred at g=2.215, 2.213, 2.212 and 2.229 for **16**, **17**, **19** and **20**, respectively, gains on intensity and becomes sharper (Figure 3.22, top). Such behaviour is expected for the antiferromagnetically coupled heterometallic [CuNi] dimers where effective S=1/2 ground state becomes dominantly populated only in the low temperature range. Similar findings were also confirmed studying the frozen THF solutions of the samples (c≈1mM) below 80 K. Very broad, isotropic resonances centred at g=2.203, 2.212, 2.205 and 2.218 become sharper upon cooling as the probability of the ΔM_S=1 transitions within the S=1/2 ground state increases (Figure 3.22, bottom). Excellent agreement between the spectral features of

the solid state and solution spectra indicates that the $[(CuNi)_2(L)(OH)_2(py)_{10}](ClO_4)_2$ clusters retain its structure when dissolved in THF. In all spectra, no hyperfine interaction with the $^{65}Cu(II)$ nuclei (I=3/2) was observed.

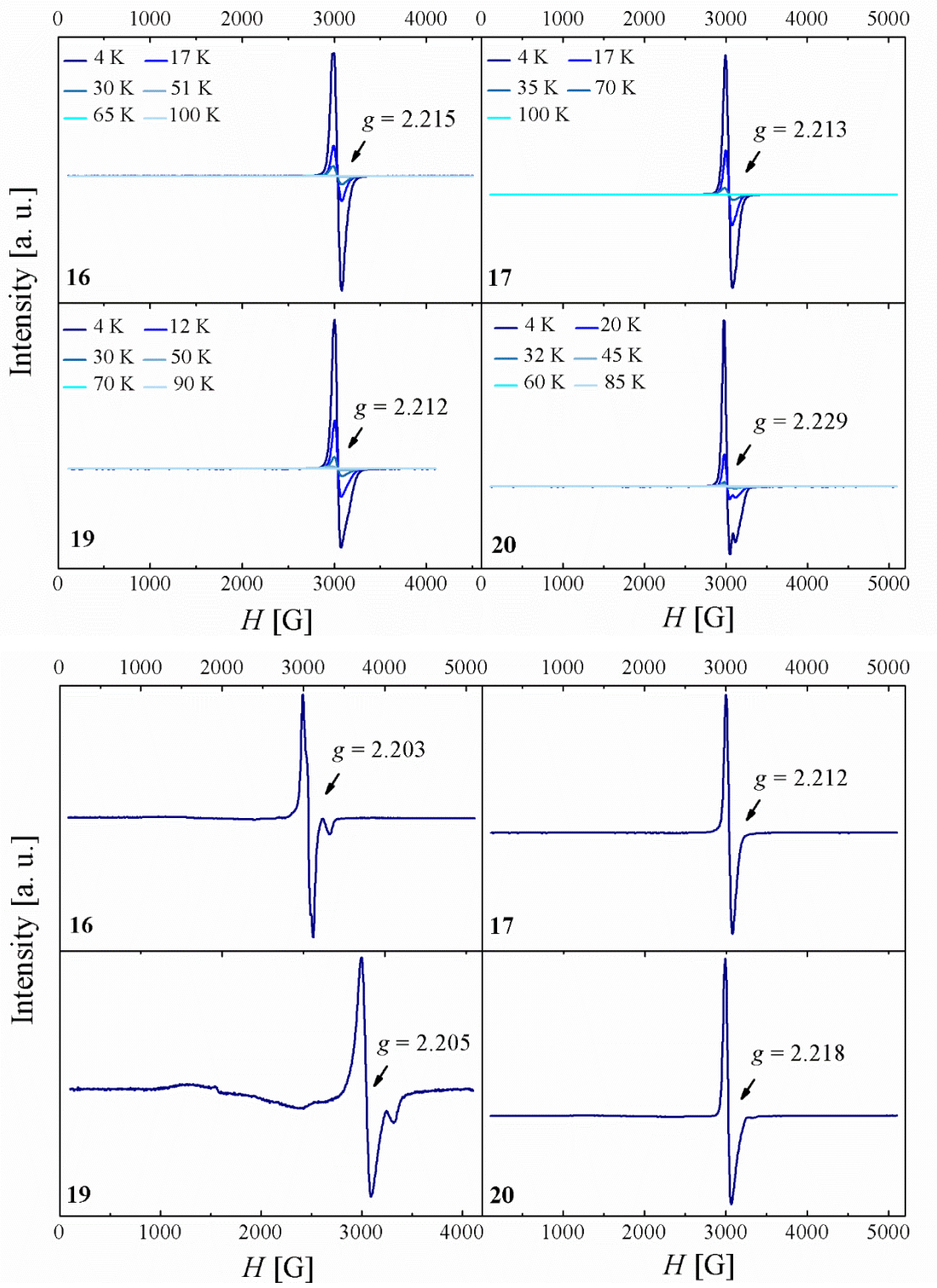

Figure 3.22. *Top*: Variable temperature (4-100 K) X-band EPR spectra (f = 9.418 GHz) of a powdered samples of compounds **16, 17, 19** and **20**. *Bottom*: EPR spectra of frozen THF solutions of compounds **16, 17, 19** and **20** at 4 K (c≈1mM).

Under the conditions of strong exchange, spectroscopically determined average *g* value of the ground doublet ($^2A_1$) state of the [CuNi] dimers can be related with the weighted single-ion *g* values:[49]

$$g_{1/2} = \frac{4g_{\mathrm{Ni}} - g_{\mathrm{Cu}}}{3}$$

Bearing in mind all the uncertainties of the method, the average $g_{1/2}$ calculated from the bulk magnetization measurements of 2.28, 2.28, 2.12 and 2.29 for **16**, **17**, **19** and **20**, respectively, agree nicely with the spectroscopically determined ones (2.215, 2.213, 2.212 and 2.229, respectively).

SQUID magnetometry measurements on compound **18** yielded similar result as previously described for the $[(CuNi)_2(L)(OH)_2(py)_{10}](ClO_4)_2$ family. Measured room temperature (300 K) value of the $\chi_M T$ product of 3.51 cm^3Kmol^{-1} is slightly below the expected 4.125 cm^3Kmol^{-1} for a heterometallic system incorporating three uncoupled *S*=1/2 and *S*=1 spin centres (*g*=2.0, Figure 3.23). Upon lowering the temperature, the $\chi_M T$ product drops continuously down to 50 K, followed by the plateau in the lowest temperature range (1.40 cm^3Kmol^{-1}). Below 7 K, small decline of the $\chi_M T$ product occurs upon cooling ending at 1.25 cm^3Kmol^{-1} at 2 K. Field-dependent magnetization measurements at 2K confirms the antiferromagnetic coupling within the μ-$(O)_2$-[CuNi] dimers since the highest measured value at 5 T (2.93 μ_B) agrees nicely with the expected 3 μ_B for three effective *S*=1/2 centres (*g*=2, Figure 3.22). In order to estimate the strength of magnetic coupling, experimental data ($\chi_M T$ *vs T* and $M/N\mu_B$ *vs H*) were modelled (PHI[30]) using the matrix diagonalization of the spin Hamiltonian (Figure 3.23):

$$\widehat{H} = \mu_B B \sum_i g_i \hat{S}_i - 2J_{Cu-Ni}\left(\hat{S}_{\mathrm{Cu1}}\hat{S}_{\mathrm{Ni1}} + \hat{S}_{\mathrm{Cu2}}\hat{S}_{\mathrm{Ni2}} + \hat{S}_{\mathrm{Cu3}}\hat{S}_{\mathrm{Ni3}}\right) - zJ$$

Best model was constructed by fixing g_{Ni}=2.18, g_{Cu}=2.00 and TIP=$-5.0\cdot10^{-4}$ cm^3mol^{-1}, yielding the *zJ*=−0.038 cm^{-1} and $J_{Ni\text{-}Cu}$= −60.49 cm^{-1}. Expanded spin Hamiltonians involving the single-ion anisotropy contributions (D_{Ni}=2.65 or −3.26 cm^{-1}) or intradimer coupling ($J_{Ni\text{-}Ni}$=−0.075 cm^{-1}) produced models of identical quality with $J_{Ni\text{-}Cu}$= −60.49 and −60.62 cm^{-1}, respectively.

Similarly, variable temperature EPR spectroscopy (15-150 K) on powdered sample revealed that **18** is EPR silent at the room temperature and becomes detectable only below 200 K when broad resonance centred at *g*=2.205 appears. Upon cooling, the intensity of this spectral feature increases and it becomes highly axial as the probability of ΔM_s=1 transitions

within the S=1/2 ground state increases (Figure 3.23, top). Detected average $g_{1/2}$ value agrees nicely with the calculated one from the bulk magnetization measurements ($g_{1/2}$=2.24). Similar findings were also confirmed in the spectrum of the frozen DMF solutions of the sample (c≈1mM) where single resonances centred at g=2.200 was found below 100 K, indicating that structure of cluster is preserved (Figure 3.23, bottom).

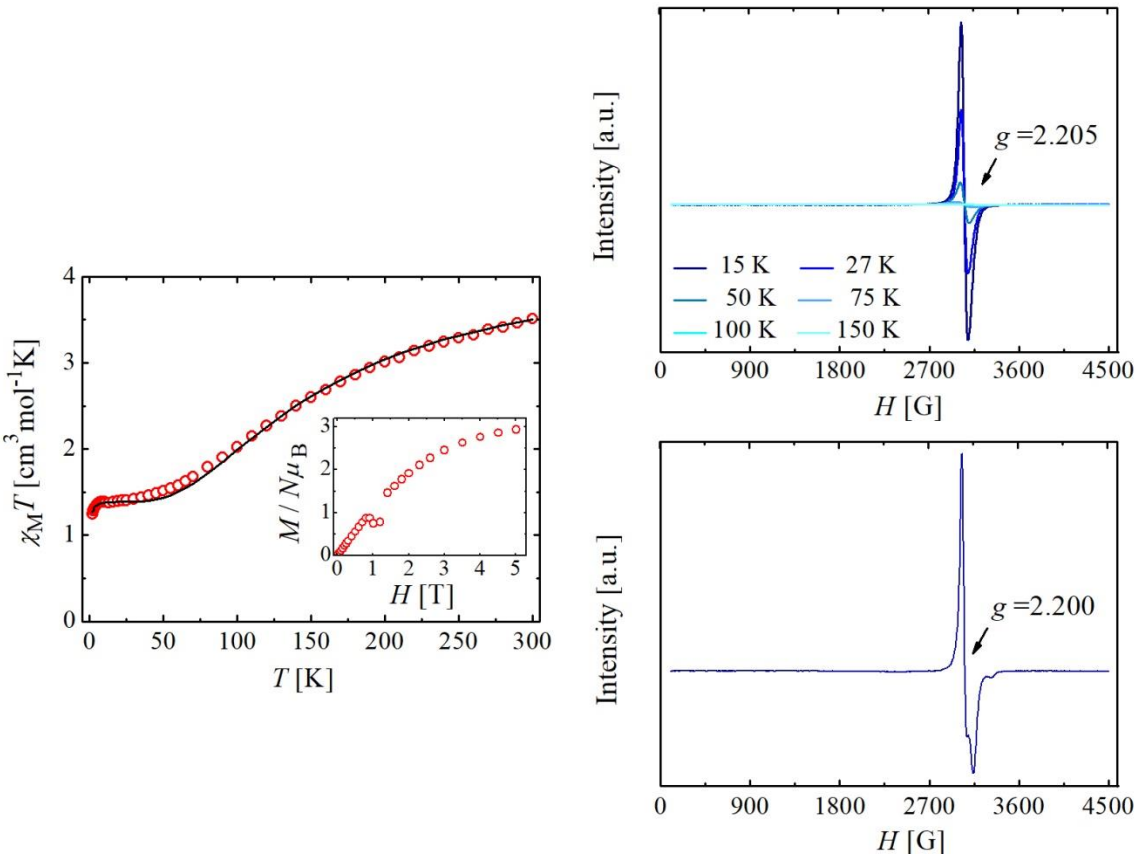

Figure 3.23. *Left*: $\chi_M T$ *vs* T and $M/N\mu_B$ *vs* H (inset) curves for compound **18** with the best fit (solid line). Measurement setup: cooling mode (300→2 K), B=0.5 T; T_{mag}=2 K. *Right top*: Variable temperature (15-150 K) X-band EPR spectra (f = 9.418 GHz) of a powdered sample of compound **18**. *Right bottom*: EPR spectra of frozen DMF solution of compound **18** at 4 K (c≈1 mM).

Obtained $J_{Ni\text{-}Cu}$= −60.49 cm^{-1} for **18** belongs to the middle range of the previously reported coupling constants (−11.8 cm^{-1} to −130.0 cm^{-1}) for the compounds containing the (μ-O)$_2$ [CuNi] metallic core (Table III.A23).[12, 50-60] Correlation of these values with the structural parameters seems to be fairly independent of the metal-metal distance, as well as the bridging Cu−O−Ni angles, but are rather influenced by the planarity of the (μ-O)$_2$ [CuNi] core. Hence, dimers with the largest O−Cu−O−Ni torsion angles and with the largest angle between the equatorial planes of the metals exhibit the weakest coupling coupling since the

superexchange mechanism between the magnetic $d_{x^2-y^2}$ orbitals becomes less effective (Table III.A23, refcodes DEWPAW[51] J_{Ni-Cu}= −11.8 cm^{-1} and UDUWEV[60] J_{Ni-Cu}= −12.0 cm^{-1}). Similarly tendency can be observed with the compounds KAHVAQ[54], KAJFEG[54] and LINWIO[55] which exhibit almost identical bond lengths and angles, but almost perfectly planar metallic core in the first two (torsion angles 4.25° and 3.70°; angles between the equatorial planes 5.08° and 4.60°, respectively) leads to the largest reported J_{Ni-Cu}= −114.9 and −130.0 $cm^{-1,}$ respectively, while the bent core in the third compound reduces the coupling to J_{Ni-Cu}= −47.0 cm^{-1}. Following the same logic, determined J_{Ni-Cu}= −60.49 cm^{-1} for **18** (average torsion angle 6.70, average angle between the equatorial planes 20.85°) agrees nicely with the recently reported photoswitchable $[CuNi]_2$ compound LEHCEJ[12] (torsion angle 6.70, angle between the equatorial planes 20.60°, J_{Ni-Cu}= −65.8 cm^{-1}). Likewise, slightly stronger coupling (J_{Ni-Cu}=−72.9 cm^{-1}) in structurally equivalent $[(CuNi)_2(L3)_2(py)_6]$ cluster (refcode MUKJEI)[16] can be correlated with more planar metallic core (torsion angle 2.49, angle between the equatorial planes 16.20°).

As mentioned in Chapter II, no literature resources were found about the compounds featuring discrete μ-(O), μ-(OH)-[CuNi] metallic core. Comparing the extracted coupling constants for the $[(CuNi)_2(L)(OH)_2(py)_{10}](ClO_4)_2$ family with the compound **18** and its analogues, it can be concluded that replacement of one oxo bridge with its protonated hydroxide equivalent results in a reduced capacity to moderate the interaction within the [CuNi] dimers by roughly 30%. Similar findings are extensively reported for the protonation, alkylation and metalation of μ-(O) bridges in iron(III) and manganese(IV) dimers. [61-63]

3.3.12. Pulsed EPR measurements

In order to evaluate the coupled [CuNi] pairs as potential molecular qubits, electron spin dynamics of compound **18** was investigated by pulsed Q-band (35 GHz) electron paramagnetic resonance (EPR) spectroscopy in a collaboration with Dr Joris Van Slageren (Univeristät Stuttgart). Electron spin echo detected Q-band EPR spectrum of frozen THF solution of **18** (1 mM) at 3.2 K complements nicely the previously described X-band spectrum, showing a single Δm_S=1 resonance with $g_\perp$=2.213 and $g_\parallel$=2.065 (Figure 3.24, top inset). Spin-lattice (T_1) and phase-memory (T_m) relaxation times of the most intense

resonance line (*H*=11302 G) were measured by inversion recovery and Hahn-echo decay experiments, respectively. Both decay datasets were fitted to biexponential functions:

$$I(\tau) = y_0 + A_s \cdot e^{-\frac{\tau}{T_{1,s}}} + A_f \cdot e^{-\frac{\tau}{T_{1,f}}} \quad 3.1$$

$$I(2\tau) = y_0 + A_s \cdot e^{-\frac{2\tau}{T_{m,s}}} + A_f \cdot e^{-\frac{2\tau}{T_{m,f}}} \quad 3.2$$

where τ represents the interpulse delay time, while two components weighed with *A*s and *A*f represent the contributions of fast and slow processes of relaxation. Inversion recovery fits yielded the set of parameters A_s=0.7, $T_{1,s}$=11 ms, A_f=1.3 and $T_{1,f}$=0.8 ms, while Hahn-echo decay fits to A_s=0.8, $T_{m,s}$=2.1 μs, A_f=0.9 and $T_{m,f}$=0.4 μs. Obtained values for slower process are slightly lower than those recently reported for analogous photoswitchable $[CuNi]_2$ compound (T_1=0.99 ms, T_m=3.59 μs at 7 K).[12] Moreover, decay of quantum coherence in the latter was found to be monoexponential. Appearance of the faster component of the relaxation in **18** is indicative of spectral diffusion of the spin which might originate from rotations of unrestrained methoxy substituents on the β-diketonate linkers between qubits or from use of nondeuterated solvent in the experiment (nuclear spin diffusion).[64, 65] Alternatively, use of the coordinating THF as solvent and the possibility of intermolecular hydrogen bonding through methoxy substituents might generate altered solution molecular forms from the solid state structure of **18**, as well as their assemblies, which will exhibit different relaxation rates. Similar biexponential or stretched monoexponential functions of coherence decay were found in solution studies of mononuclear bis-(β-diketonato)Cu^{II} complexes,[64] 3*d* phthalocyanine complexes (M=VO^{2+}, Cu^{2+}, Co^{2+}, Mn^{2+})[66], Cr_7Ni[65] and Fe_8 clusters.[67] In comparison of **18** with other exchange-coupled molecular qubits, phase memory time of the slower process compares with the $[(CuL)_3(OH)](ClO_4)_2$ (HL=(*E*)-2-((3-(methylamino)propylimino)methyl)phenol; T_m =1.29 μs at 5 K) and with the protonated and deuterated forms of Cr_7Ni wheels (0.340 μs ≤ T_m ≤ 0.929 μs at 5 K).[65, 68]

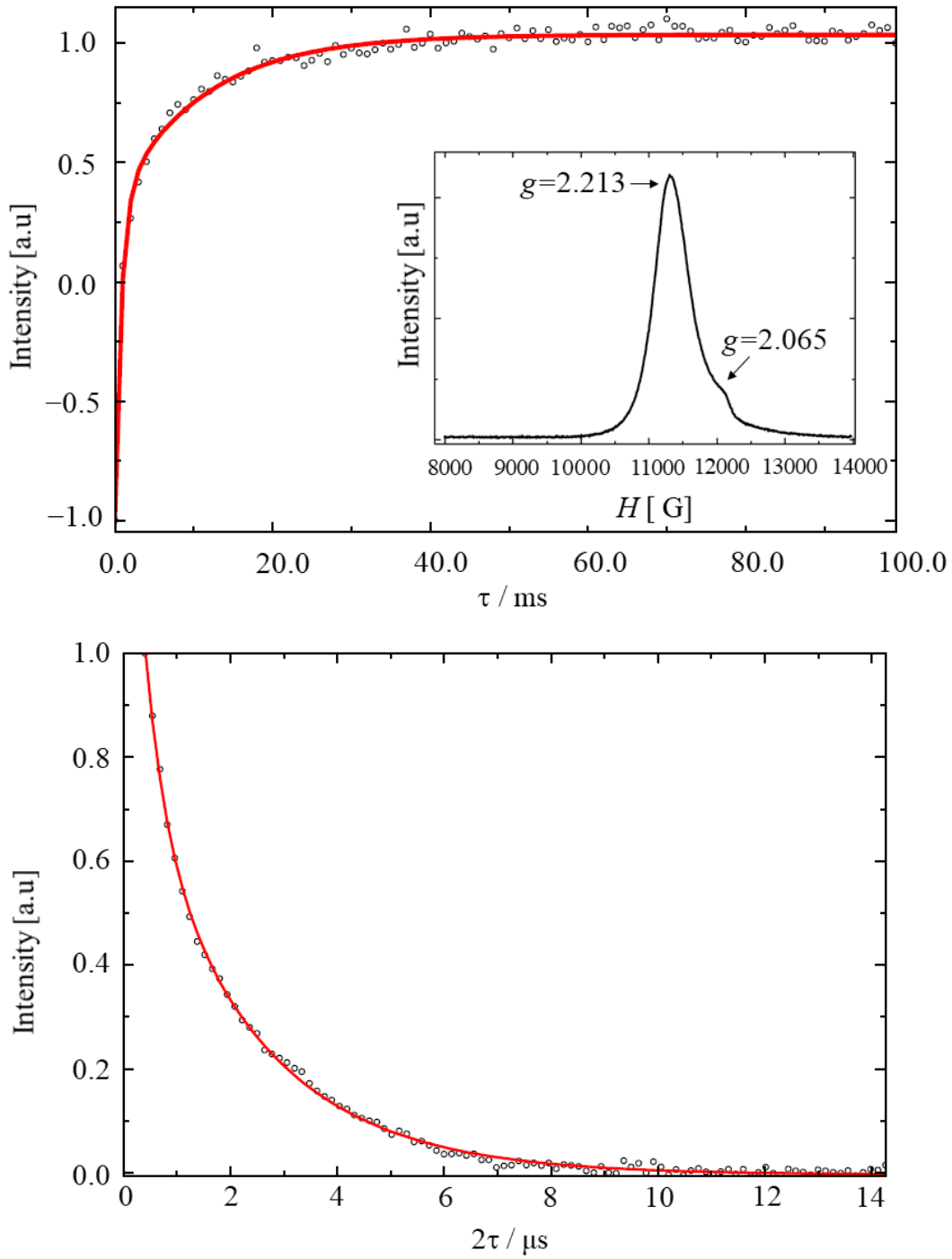

Figure 3.24: Pulsed Q-band (f=35 GHz) EPR spectroscopy of THF solution of **18** (1 mM) at 3.2 K. *Top inset*: Electron spin echo detected spectrum. *Top*: Inversion recovery relaxation of the most intense resonance line (*H*=11302 G, *g*=2.213). Full red line represents the biexponential fits to equation 3.1. *Bottom*: Hahn-echo decays relaxation of the most intense resonance line (*H*=11302 G, *g*=2.213). Full red line represents the biexponential fits to equation 3.2.

3.3.13. Experimental

Solvents and reagents were used as received from commercial suppliers in preparation of ligands and compounds An exception was only made for Claisen condensations, where anhydrous THF (PureSolv Micro Solvent Purification Systems) was used as solvent to avoid any hydrolysis as possible side reaction. Sodium hydride was applied as a suspension in mineral oil (60% w/w) which was purified by washing with hexanes under nitrogen and posterior extraction of solvent by filter cannula (*vide infra*). Tetrabutylammonium hydroxide was employed as a solution in methanol (c=1 mol/dm^3), while vanadyl sulfate was used as hydrated salt ($VOSO_4 \cdot xH_2O$), similarly as hexahydrated copper(II) and nickel(II) perchlorates. 2,5-dimethyl anisole[33, 34], 5,5'-dimethyl-2,2'-dipyridyl[42, 43] and 2,9-dimethyl-1,10-phenanthroline[44, 45] were converted to the corresponding carboxylic diacid or ester following reported procedures. Similarly, ligands 1,3-bis-(3-oxo-3-(2-hydroxyphenyl)-propionyl)-benzene (**H_4L5**)[15] and 1,3-bis-(3-oxo-3-(2-hydroxyphenyl)-propionyl)-pyridine (**H_4L6**)[69] were prepared according to a slightly modified procedure published by our group in which solvent of the reaction was changed from DME to dry THF.

Dimethyl 2,5-pyridinedicarboxylate: 2,5-pyridinedicarboxylic acid (3.00 g, 0.018 mol) was suspended at the room temperature in 100 mL of MeOH followed by dropwise addition of thionyl chloride (2.90 mL, 0.040 mol) After several minutes of stirring, initial suspension was converted to solution which was then refluxed overnight (12 h). Solution was then cooled down to the room temperature, followed by the removal of solvent on the rotavap. Obtained white-off solid was then dissolved in ethyl acetate with a subsequent dropwise addition of saturated aqueous solution of Na_2CO_3 (pH 10) to remove the traces of unreacted diacid and formed HCl. Obtained mixture was stirred vigorously for 30 min at the room temperature and then was transferred to the separation funnel. Isolated organic layer was dried over Na_2SO_4 and filtered, followed by the removal of solvent under reduced pressure and isolation of colourless crystals (average yield 3.05 g, 87 %).^{1}H NMR (400 MHz, $CDCl_3$), δ(ppm): 3.99 (s, 3H, -COOCH_3), 4.04 (s, 3H,-COOCH_3), 8.22 (d, 1H,-Ar-*H*), 8.45 (d, 1H, -Ar-*H*), 9.31 (s, 1H, -Ar-*H*). IR (KBr pellet) ν/cm^{-1}: 3017 b, 2963 b, 1712 sb, 1596 s, 1477 s, 1433 s, 1383 s, 1313 s, 1284 s, 1270 s, 1249 s, 1197 s, 1127 s, 1109 s, 1018 s, 953 s, 876 s, 819 s, 740 s, 692 s.

H_4L_A: Sodium hydride (2.71 g, 67.8 mol) was suspended under nitrogen atmosphere in 80 mL of hexanes. Mixture was stirred at the room temperature for 10 min, followed by the extraction of solvent by filter cannula. Described procedure was repeated once again and to the resulting white solid was subsequently added dry THF (100 mL). In a separate Schlenk flask, 2-hydroxyacetophenone (4.19 g, 30.8 mmol) was dissolved under nitrogen in 30 mL of dry THF and then added dropwise to the suspension of NaH in THF. Described procedure was accompanied with the yellow-green colouring of the reaction mixture and evolution of hydrogen. Upon complete addition, mixture was stirred for 15 min at the room temperature, ending with an addition of the THF solution (70 mL) of dimethyl 2,5-pyridinedicarboxylate (3.00 g, 15.4 mmol). Reaction was then brought to reflux and maintained like this overnight. After 14 h, orange suspension was cooled down to the room temperature and THF was removed under reduced pressure. Obtained orange solid was then dissolved in water and acidified with HCl(aq) to the pH=3. Precipitated yellow solid was collected by filtration and purified by recrystallisation from acetone (average yield 3.50 g, 56%). Single crystals of the ligand **H_4L_A** were obtained by dissolving the solid in boiling DMF and slowly cooling down the solution. ^{1}H NMR (400 MHz, $CDCl_3$), δ(ppm): 6.93 (s, 1H, -COC*H*COH), 6.97 (t, 2H, -Ar-*H*), 7.04 (t, 2H, -Ar-*H*), 7.52 (m, 2H, -Ar-*H*), 7.68 (s, 1H, -COC*H*COH), 7.80 (d, 1H, -Ar-*H*), 7.96 (d, 1H, -Ar-*H*), 8.20 (d, 1H, -Ar-*H*), 8.37 (d, 1H, -Ar-*H*), 9.20 (s, 1H, -Ar-*H*), 11.94 (s, 1H, Ar-O*H*), 12.08 (s, 1H, Ar-O*H*), 15.03 (s, 1H, -OH_{enol}), 15.33 (s, 1H, -OH_{enol}). ESI MS: *m/z* $[H_4L_A+H]^+$= 404.10, $[H_4L_A+Na]^+$= 426.10, $[H_3L_A]^-$= 402.10. IR (KBr pellet) *v*/cm^{-1}: 3420 b, 3042 b, 1685 b, 1617 s, 1579 s, 1543 s, 1482 s, 1420 s, 1348 s, 1333 s, 1277 s, 1239 s, 1198 s, 1161 s, 1086 s, 1032 s, 1019 s, 944 s, 889 b, 851 s, 805 s, 740 s, 657 s, 562 s, 522 s, 412 s. EA (%); Calc. (Found for **H_4L_A**·0.25 H_2O): C 67.73 (67.55), H 4.32 (4.32), N 3.43 (3.76).

Dimethyl 2-methoxy-1,4-benzenedicarboxylate: 2-methoxy-1,4-benzendicarboxylic acid (3.00 g, 0.015 mol) was suspended at the room temperature in 120 mL of MeOH, followed by dropwise addition of thionyl chloride (2.50 mL, 0.035 mol). After several minutes of stirring, initial suspension was converted to solution which was then refluxed overnight (12 h). Solution was then cooled down to the room temperature, followed by the removal of solvent on the rotavap. Obtained white-off solid was then dissolved in chloroform with a subsequent dropwise addition of saturated aqueous solution of Na_2CO_3 (pH 10) to remove

the traces of unreacted diacid and formed HCl. Obtained mixture was stirred vigorously for 30 min at the room temperature and then was transferred to the separation funnel. Isolated organic layer was dried over Na_2SO_4 and filtered, followed by the removal of solvent on the rotavap and isolation of colourless crystals (average yield 2.95 g, 86 %).^{1}H NMR (400 MHz, $CDCl_3$), δ(ppm): 3.91 (s, 3H, -OC*H*$_3$), 3.94 (s, 3H, -COOC*H*$_3$), 3.96 (s, 3H,-COOC*H*$_3$), 7.63-7.65 (m, 2H,-Ar-*H*), 7.80 (s, 1H, -Ar-*H*). IR (KBr pellet) ν/cm^{-1}: 2958 s, 2934 b, 1702 s, 1613 s, 1574 s, 1492 s, 1464 s, 1449 s, 1436 s, 1401 s, 1284 s, 1258 s, 1226 s, 1194 s, 1121 s, 1085 s, 1029 s, 982 s, 961 s, 891 s, 873 s, 821 s, 787 s, 749 s, 683 s, 693 s.

H_4L_{A2}: Sodium hydride (2.36 g, 59.0 mol) was suspended under nitrogen atmosphere in 80 mL of hexanes. Mixture was stirred at the room temperature for 10 min, followed by the extraction of solvent by filter cannula. Described procedure was repeated once again and to the resulting white solid was subsequently added dry THF (100 mL). In a separate Schlenk flask, 2-hydroxyacetophenone (3.65 g, 26.8 mmol) was dissolved under nitrogen in 30 mL of dry THF and added dropwise to the suspension of NaH in THF. Described procedure was accompanied with the yellow-green colouring of the reaction mixture and evolution of hydrogen. Upon complete addition, mixture was stirred for 15 min at the room temperature, ending with an addition of THF solution (70 mL) of dimethyl 2-methoxy-1,4-benzenedicarboxylate: (3.00 g, 13.4 mmol). Reaction was then brought to reflux and maintained like this overnight. After 14 h, orange suspension was cooled down to the room temperature and THF was removed under reduced pressure. Obtained orange solid was then dissolved in water and acidified with HCl(aq) to the pH=3. Precipitated yellow solid was collected by filtration and purified by recrystallisation from acetone (average yield 3.40 g, 59%). Single crystals of the ligand **H_4L_{A2}** were obtained by dissolving the solid in boiling DMF and slowly cooling down the solution. ^{1}H NMR (400 MHz, $CDCl_3$), δ(ppm): 4.11 (s, 3H, -OC*H*$_3$), 4.66 and 4.68 (s, 0.5H,-COC*H*$_2$CO), 6.90 (s, 1H, -COC*H*COH), 6.95 (t, 2H, -Ar-*H*), 7.02 (t, 2H, -Ar-*H*), 7.35 (s, 1H, -COC*H*COH), 7.49 (dd, 2H, -Ar-*H*), 7.60 (d+s, 2H, -Ar-*H*), 7.78 (dd, 2H, -Ar-*H*), 8.09 (d, 1H, Ar-*H*), 12.00 (s, 1H, Ar-O*H*), 12.11 (s, 1H, Ar-O*H*), 15.48 (s, 0.75H, -OH_{enol}), 15.50 (s, 0.75H, -OH_{enol}). ESI MS: *m/z* $[H_3L_{A2}]^-$= 431.12. IR (KBr pellet) ν/cm^{-1}: 3410 b, 3068 b, 1623 w, 1570 s, 1544 s, 1484 s, 1440 w, 1421 w, 1335 s, 1310 s, 1280 s, 1241 s, 1192 s, 1155 s, 1114 s, 1094 w, 1081 s, 1047 s, 1030 s, 906 s, 884 s, 864 s, 841 s, 814 s, 808 s, 767 s, 748 s,

729 s, 696 s, 620 s, 563 s, 524 s, 487 s, 429 s. EA (%); Calc. (Found for **H_4L_{A2}**·0.05 C_3H_7NO): C 69.27 (69.45), H 4.70 (4.98), N 0.16 (0.10).

Diethyl 2,2'-bipyridine-5,5'-dicarboxylate: 2,2'-bipyridine-5,5'-dicarboxylic acid (3.00 g, 0.012 mol) was suspended at the room temperature in 100 mL of EtOH, followed by dropwise addition of thionyl chloride (2.00 mL, 0.028 mol). After several minutes of stirring, initial suspension was converted to solution which was then refluxed overnight (12 h). Solution was then cooled down to the room temperature, followed by the removal of solvent on the rotavap. Obtained white-off solid was then dissolved in chloroform with a subsequent dropwise addition of saturated aqueous solution of Na_2CO_3 (pH 10) to remove the traces of unreacted diacid and formed HCl. Obtained mixture was stirred vigorously for 30 min at the room temperature and then was transferred to the separation funnel. Isolated organic layer was dried over Na_2SO_4 and filtered, followed by the removal of solvent on the rotavap and isolation of colourless crystals. (average yield 3.10 g, 84 %).^{1}H NMR (400 MHz, $CDCl_3$), δ(ppm): 1.44 (t, 3H, -OCH_2CH_3), 4.45 (q, 2H, -OCH_2CH_3), 8.44 (d, 1H, Ar-*H*), 8.57 (d, 1H, -Ar-*H*), 9.29 (s, 1H, -Ar-*H*). IR (KBr pellet) ν/cm^{-1}: 3010 b, 2964 s, 1716 s, 1591 s, 1449 s, 1365 s, 1260 s, 1170 s, 1091 s, 1019 s, 854 s, 796 s, 761 s, 722 s, 696 s.

H_4L7: Sodium hydride (1.76 g, 44.0 mol) was suspended under nitrogen atmosphere in 80 mL of hexanes. Mixture was stirred at the room temperature for 10 min, followed by the extraction of solvent by filter cannula. Described procedure was repeated once again and to the resulting white solid was subsequently added dry THF (70 mL). In a separate Schlenk flask, 2-hydroxyacetophenone (2.72 g, 20.0 mmol) was dissolved under nitrogen in 30 mL of dry THF and added dropwise to the suspension of NaH in THF. Described procedure was accompanied with the yellow-green colouring of the reaction mixture and evolution of hydrogen. Upon complete addition, mixture was stirred for 15 min at the room temperature, ending with an addition of THF solution (70 mL) of diethyl 2,2'-bipyridine-5,5'-dicarboxylate (3.00 g, 10.0 mmol). Reaction was then brought to reflux and maintained like this overnight. After 14 h, mixture was cooled to the room temperature and THF was removed under reduced pressure. Obtained orange solid was then dissolved in water and acidified with HCl(aq) to the pH=3. Precipitated yellow solid was collected by filtration and purified by recrystallisation from acetone (average yield 2.80 g, 58%). Single crystals of the

ligand **H_4L7** were obtained by dissolving the solid in boiling DMF and slowly cooling down the solution. ^{1}H NMR (400 MHz, d_6-DMSO), δ(ppm): 4.91 (s, 0.4H,-COC*H*$_2$CO), 7.03 (t, 2H,-Ar-*H*), 7.16 (m, 2H, -Ar-*H*), 7.51 (m, 2H, -Ar-*H*), 7.66 (t, 1H, -Ar-*H*), 7.81 (d, 1H, -Ar-*H*), 7.92 (dd, 1H, -Ar-*H*), 8.08 (d, 1H, -Ar-*H*), 8.25 (m, 1H, -Ar-*H*), 8.56 (m, 3H, -Ar-*H*), 9.02 (d, 1H, -Ar-*H*), 9.34 (d, 1H, -Ar-*H*), 11.31 (broad, Ar-O*H*). MALDI-TOF: *m*/*z* $[H_3L7]^-$= 479.2. IR (KBr pellet) *v*/cm^{-1}: 3430 b, 3030 b, 2921 s, 2856 s, 1615 s, 1580 s, 1555 s, 1484 s, 1474 s, 1428 s, 1324 b, 1302 s, 1240 s, 1205 s, 1163 s, 1090 s, 1039 s, 1021 s, 895 s, 842 s, 804 s, 775 s, 746 s, 676 s, 650 s, 630 s, 562 s, 523 s. EA (%); Calc. (Found for **H_4L7**·0.1 C_3H_7NO): C 69.68 (69.65), H 4.28 (4.49), N 6.03 (5.90).

Diethyl 1,10-phenanthroline-2,9-dicarboxylate: Compound was prepared following the reported procedure.[44, 45] Last step of the synthesis was slightly adapted from the original, with methanol being replaced with ethanol in order to increase the solubility of formed diester. Additional purification steps involved dissolution of diester in ethanol and drying over Na_2SO_4. ^{1}H NMR (400 MHz, $CDCl_3$), δ(ppm): 1.54 (t, 3H, -OCH$_2$C*H*$_3$), 4.57 (q, 2H, -OC*H*$_2$CH$_3$), 7.96 (s, 1H, -Ar-*H*), 8.45 (d, 1H, Ar-*H*), 8.46 (m, 2H, -Ar-*H*). IR (KBr pellet) *v*/cm^{-1}: 2982 s, 2941 w, 2897 b, 1710 s, 1610 s, 1598 s, 1554 s, 1500 s, 1474 s, 1446 w, 1370 s, 1274 s, 1259 s, 1210 s, 1164 s, 1133 s, 1092 s, 1015 s, 910 s, 880 s, 857 s, 823 s, 758 s, 719 s.

H_4L8: Sodium hydride (1.63 g, 40.7 mol) was suspended under nitrogen atmosphere in 80 mL of hexanes. Mixture was stirred at the room temperature for 10 min, followed by the extraction of solvent by filter cannula. Described procedure was repeated once again and to the resulting white solid was subsequently added dry THF (70 mL). In a separate Schlenk flask, 2-hydroxyacetophenone (2.52 g, 18.5 mmol) was dissolved under nitrogen in 30 mL of dry THF and added dropwise to the suspension of NaH in THF. Described procedure was accompanied with the yellow-green colouring of the reaction mixture and evolution of hydrogen. Upon complete addition, mixture was stirred for 15 min at the room temperature, ending with an addition of THF solution (70 mL) of diethyl 1,10-phenanthroline-2,9-dicarboxylate (3.00 g, 9.25 mmol). Reaction was then brought to reflux and maintained like this overnight. After 14 h, mixture was cooled to the room temperature and THF was removed under reduced pressure. Obtained orange solid was then dissolved in water and acidified with HCl(aq) to the pH=3. Precipitatated yellow solid was collected by filtration and purified by recrystallisation from acetone (average yield 2.20 g, 47%).

^{1}H NMR (400 MHz, $CDCl_3$), δ(ppm): 5.47 (s, 0.5H,-COC*H*$_2$CO), 6.97 (t, 2H, -Ar-*H*), 7.00 (t, 2H, -Ar-*H*), 7.81 (s, 1H, -COC*H*COH), 7.92 (s, 2H, -Ar-*H*), 7.97 (d, 2H, -Ar-*H*), 7.99 (d, 2H, -Ar-*H*), 8.08 (s, 1H, -COC*H*COH), 8.42 (m, 4H, -Ar-*H*), 12.08 (s, 2H, Ar-O*H*), 15.34 (s, 1.5H, -O*H*$_{enol}$). ESI MS: *m*/*z* [H_3L8]$^-$= 503.11. IR (KBr pellet) *v*/cm^{-1}: 3420 b, 3114 b, 3044 b, 1607 s, 1578 s, 1551 s, 1485 s, 1440 w, 1412 s, 1345 s, 1330 s, 1295 s, 1262 s, 1249 s, 1193 s, 1162 s, 1105 s, 1075 w, 1031 s, 867 s, 824 s, 799 s, 749 s, 706 w, 657 s, 632 s, 564 s, 521 s. Single crystals of the ligand **H_2L8** were obtained by dissolving the solid **H_4L8** in boiling DMF and slowly cooling down the solution. ^{1}H NMR (400 MHz, $CDCl_3$), δ(ppm): 7.37 (t, 1H, -Ar-*H*), 7.54 (m, 3H, -Ar-*H*), 7.72 (d, 1H, -Ar-*H*), 7.81 (t, 1H, -Ar-*H*), 7.93 (s, 2H, -Ar-*H*), 8.30 (d, 1H, -Ar-*H*), 8.38 (d, 2H, Ar-*H*), 8.43, 8.48, 8.51 (d,s,d 4H, Ar-*H*), 8.66 (s, 1H, -COC*H*COH), 11.70 (s, 1H, Ar-O*H*), 15.89 (s, 1H, -O*H*$_{enol}$). EA (%); Calc. (Found for **H_2L8**·0.5 H_2O): C 72.72 (72.63), H 3.87 (3.67), N 5.65 (5.87).

[(VO)$_4$(H_2L5)$_4$(py)$_4$] (**14**): Solid NaH (11.9 mg, 0.298 mmol) was added to the yellow solution of ligand **H_4L5** (30.0 mg, 0.075 mmol) in pyridine (10 mL) causing immediate hydrogen evolution and the change of color of the solution to light orange. The mixture was stirred at room temperature for 10 min and it was then added dropwise to a hot solution of $VOSO_4$·H_2O (27.0 mg, 0.149 mmol) in pyridine (10 mL) changing its color from blue to orange. The resulting reaction mixture was stirred at room temperature for 90 min and then filtered to remove a very small amount of brown precipitate (less than 3 mg). The remaining filtrate was layered with hexanes, diethyl ether, or toluene, producing very thin yellow-orange plates within a week with an average yield of 18.4 mg (37 %). Prior to any analysis, crystals were washed with water and toluene to remove traces of any residual salts (Na_2SO_4) and impurities. IR (KBr pellet) *v*/cm^{-1}:3440 b, 1620 s, 1518 s, 1338 s, 1299 s, 1198 s, 959 s, 760 s, 698 s. EA (%); Calc. (Found for **14**·2.65 H_2O·1.45 toluene): C 64.01 (64.04), H 4.30 (4.26), N 2.37 (2.33).

[(V^VO)$_4$(V^{IV}O)$_2$O$_4$(L6)$_2$(py)$_6$] (**15**): Solid NaH (11.9 mg, 0.298 mmol) was added to a yellow solution of ligand **H_4L6** (30.0 mg, 0.074 mmol) in pyridine (10 mL) causing immediate hydrogen evolution and the change of color of the solution to yellow-orange. The mixture was stirred at room temperature for 10 min and afterwards it was added dropwise to a hot solution of $VOSO_4$·H_2O (27.0 mg, 0.149 mmol) in pyridine (10 mL) changing its color from

blue to orange-brown. Resulting reaction mixture was stirred at room temperature for 90 min and then filtered. A very small amount of dark brown precipitate was removed (about 4 mg) by filtration. The filtrate was layered with toluene causing the formation of small dark orange plates within a week with an average yield of 21.6 mg (29 %). Prior to any analysis, crystals were washed with water and toluene to remove traces of any residual salts (Na_2SO_4) and impurities. IR (KBr pellet) v/cm^{-1}: 3424 vb, 1605 s, 1525 vs, 1444 s, 1345 s, 1251 s, 1215 s, 1070 s, 964 s, 952 s, 826 s, 765 s, 740 s, 694 s. EA (%); Calc. (Found for **15**·2H_2O·1.3toluene): C 53.94 (53.90), H 3.74 (3.60), N 5.91 (5.78).

[(CuNi)$_2$L$_A$(OH)$_2$(py)$_{10}$](ClO$_4$)$_2$ (**16**): Tetrabutylammonium hydroxide (375 µL, 0.375 mmol) was added to the yellow solution of ligand **H$_4$L$_A$** (25.0 mg, 0.062 mmol) in pyridine (10 mL) causing its immediate change of color to orange. Obtained mixture was stirred at room temperature for 10 min and then was added dropwise to a pyridine solution (10 mL) of $Cu(ClO_4)_2·6H_2O$ (45.9 mg, 0.124 mmol) and $Ni(ClO_4)_2·6H_2O$ (45.3 mg, 0.124 mmol), changing its appearance from blurry violet to clear orange-brown. Resulting solution was covered and stirred at room temperature for 90 min before filtration. Negligible amount of gelatinous precipitate (<1 mg) was removed, while isolated filtrate was layered with hexanes to produce orange-brown plates by liquid-liquid diffusion over a period of three weeks (average yield 67.5 mg, 65%). IR (KBr pellet) *v*/cm^{-1}: 3450 vb, 3050 vb, 1600 s, 1560 s, 1507 vs, 1437 vs, 1375 s, 1332 s, 1245 s, 1214 s, 1204 s, 1141 s, 1085 vs, 1064 vs, 1032 vs, 1012 s, 938 s, 864 s, 798 s. 752 vs, 696 vs. EA (%); Calc. (Found for **16**·3.3 H_2O): C 50.76 (50.62), H 4.18 (4.01), N 8.92 (8.89).

[(CuNi)$_2$L$_{A2}$(OH)$_2$(py)$_{10}$](ClO$_4$)$_2$ (**17**): Tetrabutylammonium hydroxide (350 µL, 0.350 mmol) was added to the yellow –green solution of ligand **H$_4$L$_{A2}$** (25.0 mg, 0.058 mmol) in pyridine (10 mL) causing its immediate change of color to orange. Obtained mixture was stirred at room temperature for 10 min and then was added dropwise to a pyridine solution (10 mL) of $Cu(ClO_4)_2·6H_2O$ (42.9 mg, 0.116 mmol) and $Ni(ClO_4)_2·6H_2O$ (42.3 mg, 0.116 mmol), changing its appearance from blurry violet to clear yellow-brown. Resulting solution was covered and stirred at room temperature for 90 min before filtration. Negligible amount of gelatinous precipitate (<1 mg) was removed, while isolated filtrate was layered with hexanes to produce yellow-brown plates by liquid-liquid diffusion over a period of three

weeks (average yield 57.8 mg, 59%). IR (KBr pellet) *v*/cm^{-1}:3450 vb, 3071 vb, 1600 s, 1560 s, 1507 s, 1483 s, 1434 vs, 1370 s, 1352 s, 1328 s, 1248 s, 1215 s, 1201 b, 1085 vs, 1064 vs, 1029 s, 955 b, 852 b, 798 s, 752 vs, 696 vs, 662 s. EA (%); Calc. (Found for **17**·1.55 H_2O): C 51.89 (51.73), H 4.18 (4.00), N 8.18 (8.16).

[(CuNi)$_3$(L$_{A2}$)$_3$(py)$_9$] (**18**): Tetrabutylammonium hydroxide (115 µL, 0.115 mmol) was added to the yellow –green solution of ligand **H$_4$L$_{A2}$** (12.0 mg, 0.028 mmol) in pyridine (8 mL) causing its immediate change of color to orange. Obtained mixture was stirred at room temperature for 10 min and then was added dropwise to a pyridine solution (8 mL) of $Cu(ClO_4)_2$·$6H_2O$ (10.3 mg, 0.028 mmol) and $Ni(ClO_4)_2$·$6H_2O$ (10.2 mg, 0.028 mmol), changing its appearance from blurry violet to clear yellow-brown. Resulting solution was covered and stirred at room temperature for 90 min before filtration. Depending on the humidity of used pyridine, variable amounts of gelatinous precipitate (0-5 mg) were observed, where precipitate-free reaction mixtures were obtained in completely dry solvent (stored over molecular sieves). Purified filtrate was layered with hexanes to produce orange-brown blocks by liquid-liquid diffusion over a period of one month (average yield 10.5-14.2 mg, 48-65 %). IR (KBr pellet) *v*/cm^{-1}: 3300 vb, 2927 w, 1597 s, 1547 s, 1498 vs, 1485 vs, 1438 vs, 1426 vs, 1375 s, 1351 w, 1321 s, 1246 s, 1195 s, 1135 w, 1095 w, 1068 w, 1023 s, 953 w, 937 w, 898 w, 848 s, 795 s, 745 vs, 695 vs. EA (%); Calc. (Found for **18**·5.55 H_2O): C 58.50 (58.25), H 4.26 (4.00), N 5.12 (4.88).

[(CuNi)$_2$(L7)(OH)$_2$(py)$_{10}$](ClO$_4$)$_2$ (**19**): Tetrabutylammonium hydroxide (250 µL, 0.250 mmol) was added to the blurry yellow–green solution of ligand **H$_4$L7** (20.0 mg, 0.042 mmol) in pyridine (10 mL) causing its immediate change of color to orange. Obtained mixture was stirred at room temperature for 10 min and then was added dropwise to a pyridine solution (10 mL) of $Cu(ClO_4)_2$·$6H_2O$ (30.9 mg, 0.083 mmol) and $Ni(ClO_4)_2$·$6H_2O$ (30.5 mg, 0.083 mmol), changing its appearance from blurry violet to clear orange-brown. Resulting solution was covered and stirred at room temperature for 90 min before filtration. No precipitate was observed, while isolated filtrate was layered with diethyl ether to produce yellow-brown blocks by liquid-liquid diffusion over a period of two weeks (average yield 38.4 mg, 53 %). IR (KBr pellet) *v*/cm^{-1}: 3450 vb, 1602 s, 1585 b, 1555 s, 1512 vs, 1441 vs, 1337 s, 1302 s, 1242 s,

1206 s, 1090 vs, 1065 vs, 940 s, 848 s, 791 s, 755 s, 698 vs, 606 s. EA (%); Calc. (Found for **19**·0.55 H_2O·0.85 C_5H_5N): C 54.22 (54.51), H 4.06 (4.35), N 9.88 (9.58).

[(CuNi)$_2$(L8)(OH)$_2$(py)$_{10}$](ClO$_4$)$_2$ (**20**): Tetrabutylammonium hydroxide (240 µL, 0.240 mmol) was added to the yellow –green solution of ligand **H_4L8** (20.0 mg, 0.040 mmol) in pyridine (10 mL) causing its immediate change of color to orange. Obtained mixture was stirred at room temperature for 10 min and then was added dropwise to a pyridine solution (10 mL) of $Cu(ClO_4)_2$·$6H_2O$ (29.4 mg, 0.080 mmol) and $Ni(ClO_4)_2$·$6H_2O$ (29.0 mg, 0.080), changing its appearance from blurry violet to clear orange-brown. Resulting solution was covered and stirred at room temperature for 90 min before filtration. No precipitate was observed, while isolated filtrate was layered with hexanes to produce yellow-brown blocks by liquid-liquid diffusion over a period of three weeks (average yield 41.6 mg, 59%). IR (KBr pellet) ν/cm^{-1}: 3450 vb, 3070 b, 1600 s, 1570 s, 1510 s, 1485 s, 1442 vs, 1376 s, 1329 s, 1246 s, 1214 s, 1081 vs, 1064 vs, 1034 vs, 1013 s, 939 s, 866 s, 802 w, 750 vs, 697 vs. EA (%); Calc. (Found for **20**·4.8 H_2O·3.4 C_5H_5N): C 54.84 (54.93), H 4.49 (4.57), N 10.15 (10.07).

3.3.14. Literature

1. M. N. Leuenberger and D. Loss, *Nature*, 2001, **410**, 789-793.
2. M. Affronte, *Journal of Materials Chemistry*, 2009, **19**, 1731-1737.
3. S. Bertaina, S. Gambarelli, T. Mitra, B. Tsukerblat, A. Muller and B. Barbara, *Nature*, 2008, **453**, 203-206.
4. Q. Chen and C. L. Hill, *Inorganic Chemistry*, 1996, **35**, 2403-2405.
5. J. Lehmann, A. Gaita-Arino, E. Coronado and D. Loss, *Nat Nano*, 2007, **2**, 312-317.
6. C.-J. Yu, M. J. Graham, J. M. Zadrozny, J. Niklas, M. D. Krzyaniak, M. R. Wasielewski, O. G. Poluektov and D. E. Freedman, *Journal of the American Chemical Society*, 2016, **138**, 14678-14685.
7. J. M. Zadrozny, J. Niklas, O. G. Poluektov and D. E. Freedman, *ACS Central Science*, 2015, **1**, 488-492.
8. J. M. Zadrozny, J. Niklas, O. G. Poluektov and D. E. Freedman, *Journal of the American Chemical Society*, 2014, **136**, 15841-15844.
9. M. Atzori, L. Tesi, E. Morra, M. Chiesa, L. Sorace and R. Sessoli, *J. Am. Chem. Soc.*, 2016, **138**, 2154-2157.
10. M. Atzori, E. Morra, L. Tesi, A. Albino, M. Chiesa, L. Sorace and R. Sessoli, *J. Am. Chem. Soc.*, 2016, **138**, 11234-11244.
11. D. Aguilà, L. A. Barrios, V. Velasco, O. Roubeau, A. Repollés, P. J. Alonso, J. Sesé, S. J. Teat, F. Luis and G. Aromí, *Journal of the American Chemical Society*, 2014, **136**, 14215-14222.
12. J. S. Uber, M. Estrader, J. Garcia, P. Lloyd-Williams, A. Sadurní, D. Dengler, J. v. Slageren, N. F. Chilton, O. Roubeau, S. J. Teat, J. Ribas-Ariño and G. Aromí, *Chemistry – A European Journal*, 2017, **23**, 13648-13659.
13. M. D. Jenkins, Y. Duan, B. Diosdado, J. J. García-Ripoll, A. Gaita-Ariño, C. Giménez-Saiz, P. J. Alonso, E. Coronado and F. Luis, *Physical Review B*, 2017, **95**, 064423.
14. I. Borilovic, O. Roubeau, I. Fernández Vidal, S. Teat and G. Aromí, *Magnetochemistry*, 2015, **1**, 45.
15. G. Aromi, C. Boldron, P. Gamez, O. Roubeau, H. Kooijman, A. L. Spek, H. Stoeckli-Evans, J. Ribas and J. Reedijk, *Dalton Transactions*, 2004, DOI: 10.1039/B410481A, 3586-3592.
16. L. A. Barrios, D. Aguilà, O. Roubeau, P. Gamez, J. Ribas-Ariño, S. J. Teat and G. Aromí, *Chemistry – A European Journal*, 2009, **15**, 11235-11243.
17. J. Salinas-Uber, L. A. Barrios, O. Roubeau and G. Aromí, *Polyhedron*, 2013, **66**, 274-278.
18. V. Velasco, D. Aguila, L. A. Barrios, I. Borilovic, O. Roubeau, J. Ribas-Arino, M. Fumanal, S. J. Teat and G. Aromi, *Chemical Science*, 2015, **6**, 123-131.
19. T. Carofiglio, E. Solari, C. Floriani, A. Chiesi-Villa and C. Rizzoli, *Polyhedron*, 1996, **15**, 4435-4440.
20. T. Ishida, S.-i. Mitsubori, T. Nogami, N. Takeda, M. Ishikawa and H. Iwamura, *Inorganic Chemistry*, 2001, **40**, 7059-7064.
21. Z. C. Kadirova, D. S. Rahmonova, S. A. Talipov, J. M. Ashurov and N. A. Parpiev, *Acta Crystallographica Section E*, 2009, **65**, m819.
22. Tarlok S. Lobana, I. Kinoshita, K. Kimura, T. Nishioka, D. Shiomi and K. Isobe, *European Journal of Inorganic Chemistry*, 2004, **2004**, 356-367.

23. E. Mestrovic, D.-K. Bucar, I. Halasz and V. Stilinovic, *Acta Crystallographica Section E*, 2004, **60**, m1920-m1922.
24. T. S. Smith, C. A. Root, J. W. Kampf, P. G. Rasmussen and V. L. Pecoraro, *Journal of the American Chemical Society*, 2000, **122**, 767-775.
25. V. Stilinovic, D.-K. Bucar, I. Halasz and E. Mestrovic, *New Journal of Chemistry*, 2013, **37**, 619-623.
26. V. A. Grillo, E. J. Seddon, C. M. Grant, G. Aromi, J. C. Bollinger, K. Folting and G. Christou, *Chemical Communications*, 1997, DOI: 10.1039/A702971C, 1561-1562.
27. P. J. Bonitatebus Jr and S. K. Mandal, *Chemical Communications*, 1998, DOI: 10.1039/A708693H, 939-940.
28. L. Chen, F.-L. Jiang, W.-P. Su, C.-Y. Yue, D.-Q. Yuan and M.-C. Hong, *Inorganica Chimica Acta*, 2009, **362**, 407-413.
29. J. K. Clegg, Y. Kim and L. F. Lindoy, *Journal of Inclusion Phenomena and Macrocyclic Chemistry*, 2015, **82**, 247-257.
30. N. F. Chilton, R. P. Anderson, L. D. Turner, A. Soncini and K. S. Murray, *Journal of Computational Chemistry*, 2013, **34**, 1164-1175.
31. T. S. Smith, R. LoBrutto and V. L. Pecoraro, *Coordination Chemistry Reviews*, 2002, **228**, 1-18.
32. J. Krzystek, A. Ozarowski, J. Telser and D. C. Crans, *Coordination Chemistry Reviews*, 2015, **301**, 123-133.
33. D. T.b. Hannah and D. C. Sherrington, *Journal of Materials Chemistry*, 1997, **7**, 1985-1991.
34. J. Yang, A. Grzech, F. M. Mulder and T. J. Dingemans, *European Journal of Inorganic Chemistry*, 2013, **2013**, 2336-2341.
35. F. Li, J. K. Clegg, P. Jensen, K. Fisher, L. F. Lindoy, G. V. Meehan, B. Moubaraki and K. S. Murray, *Angewandte Chemie International Edition*, 2009, **48**, 7059-7063.
36. D. V. Soldatov, A. S. Zanina, G. D. Enright, C. I. Ratcliffe and J. A. Ripmeester, *Crystal Growth & Design*, 2003, **3**, 1005-1013.
37. J. K. Clegg, L. F. Lindoy, B. Moubaraki, K. S. Murray and J. C. McMurtrie, *Dalton Transactions*, 2004, DOI: 10.1039/B403673E, 2417-2423.
38. J. K. Clegg, D. J. Bray, K. Gloe, K. Gloe, K. A. Jolliffe, G. A. Lawrance, L. F. Lindoy, G. V. Meehan and M. Wenzel, *Dalton Transactions*, 2008, DOI: 10.1039/B716653B, 1331-1340.
39. J. K. Clegg, F. Li and L. F. Lindoy, *Coordination Chemistry Reviews*, 2013, **257**, 2536-2550.
40. J. K. Clegg, L. F. Lindoy, J. C. McMurtrie and D. Schilter, *Dalton Transactions*, 2006, DOI: 10.1039/B517274H, 3114-3121.
41. J. K. Clegg, S. S. Iremonger, M. J. Hayter, P. D. Southon, R. B. Macquart, M. B. Duriska, P. Jensen, P. Turner, K. A. Jolliffe, C. J. Kepert, G. V. Meehan and L. F. Lindoy, *Angewandte Chemie International Edition*, 2010, **49**, 1075-1078.
42. I. Gamba, I. Salvadó, G. Rama, M. Bertazzon, M. I. Sánchez, V. M. Sánchez-Pedregal, J. Martínez-Costas, R. F. Brissos, P. Gamez, J. L. Mascareñas, M. V. López and M. E. Vázquez, *Chemistry – A European Journal*, 2013, **19**, 13369-13375.
43. M. V. López, S. V. Eliseeva, J. M. Blanco, G. Rama, M. R. Bermejo, M. E. Vázquez and J. C. G. Bünzli, *European Journal of Inorganic Chemistry*, 2010, **2010**, 4532-4545.
44. G. R. Newkome, G. E. Kiefer, W. E. Puckett and T. Vreeland, *The Journal of Organic Chemistry*, 1983, **48**, 5112-5114.

45. C. J. Chandler, L. W. Deady and J. A. Reiss, *Journal of Heterocyclic Chemistry*, 1981, **18**, 599-601.
46. F. H. Köhler, *Paramagnetic Complexes in Solution: The NMR Approach*, 2011.
47. I. Bertini, C. Luchinat, G. Parigi and E. Ravera, in *NMR of Paramagnetic Molecules (Second Edition)*, Elsevier, Boston, 2017, pp. 175-253.
48. I. Bertini, C. Luchinat, G. Parigi and E. Ravera, in *NMR of Paramagnetic Molecules (Second Edition)*, Elsevier, Boston, 2017, pp. 77-126.
49. A. Bencini and D. Gatteschi, *Electron Parametric Resonance of Exchange Coupled Systems*, 2011.
50. L. A. Barrios, D. Aguilà, O. Roubeau, P. Gamez, J. Ribas-Ariño, S. J. Teat and G. Aromí, *Chemistry – A European Journal*, 2009, **15**, 11235-11243.
51. Y. Journaux, O. Kahn, I. Morgenstern-Badarau, J. Galy, J. Jaud, A. Bencini and D. Gatteschi, *Journal of the American Chemical Society*, 1985, **107**, 6305-6312.
52. I. Morgenstern-Badarau, M. Rerat, O. Kahn, J. Jaud and J. Galy, *Inorganic Chemistry*, 1982, **21**, 3050-3059.
53. C. J. O'Connor, D. P. Freyberg and E. Sinn, *Inorganic Chemistry*, 1979, **18**, 1077-1088.
54. C. N. Verani, E. Rentschler, T. Weyhermuller, E. Bill and P. Chaudhuri, *Journal of the Chemical Society, Dalton Transactions*, 2000, DOI: 10.1039/A908426F, 251-258.
55. M. Yonemura, M. Ohba, K. Takahashi, H. Ōkawa and D. E. Fenton, *Inorganica Chimica Acta*, 1998, **283**, 72-79.
56. Z.-X. Zhu, L.-Z. Cai, X.-W. Deng, Y.-L. Zhou and M.-X. Yao, *New Journal of Chemistry*, 2017, **41**, 11097-11103.
57. T. Aono, H. Wada, Y.-I. Aratake, N. Matsumoto, H. Okawa and Y. Matsuda, *Journal of the Chemical Society, Dalton Transactions*, 1996, DOI: 10.1039/DT9960000025, 25-29.
58. A. Hori, Y. Mitsuka, M. Ohba and H. Ōkawa, *Inorganica Chimica Acta*, 2002, **337**, 113-121.
59. S. Yukinari, M. Toshihiro, N. Masaaki, K. Fumiaki, M. Naohide and T. Jean-Pierre, *Bulletin of the Chemical Society of Japan*, 1998, **71**, 2611-2619.
60. M. Yonemura, K. Arimura, K. Inoue, N. Usuki, M. Ohba and H. Ōkawa, *Inorganic Chemistry*, 2002, **41**, 582-589.
61. J. Jullien, G. Juhász, P. Mialane, E. Dumas, C. R. Mayer, J. Marrot, E. Rivière, E. L. Bominaar, E. Münck and F. Sécheresse, *Inorganic Chemistry*, 2006, **45**, 6922-6927.
62. M. J. Baldwin, T. L. Stemmler, P. J. Riggs-Gelasco, M. L. Kirk, J. E. Penner-Hahn and V. L. Pecoraro, *Journal of the American Chemical Society*, 1994, **116**, 11349-11356.
63. S. M. Gorun and S. J. Lippard, *Inorganic Chemistry*, 1991, **30**, 1625-1630.
64. S. Lenz, K. Bader, H. Bamberger and J. van Slageren, *Chemical Communications*, 2017, **53**, 4477-4480.
65. C. J. Wedge, G. A. Timco, E. T. Spielberg, R. E. George, F. Tuna, S. Rigby, E. J. L. McInnes, R. E. P. Winpenny, S. J. Blundell and A. Ardavan, *Physical Review Letters*, 2012, **108**, 107204.
66. K. Bader, M. Winkler and J. van Slageren, *Chemical Communications*, 2016, **52**, 3623-3626.
67. S. Takahashi, J. van Tol, C. C. Beedle, D. N. Hendrickson, L.-C. Brunel and M. S. Sherwin, *Physical Review Letters*, 2009, **102**, 087603.
68. P. Lutz, R. Marx, D. Dengler, A. Kromer and J. van Slageren, *Molecular Physics*, 2013, **111**, 2897-2902.

69. G. A. Craig, L. A. Barrios, J. S. Costa, O. Roubeau, E. Ruiz, S. J. Teat, C. C. Wilson, L. Thomas and G. Aromi, *Dalton Transactions*, 2010, **39**, 4874-4881.

CHAPTER IV

PYRAZOLE BASED COORDINATION COMPOUNDS: SERENDIPITOUS VERSUS TAILORED-METALLOLIGAND SYNTHETIC APPROACH

4.1. Introduction

One of the most appealing reasons in the pursuit of tailor-made molecules for particular applications is to find correlations between specific structural patterns and their properties. In terms of magneto-structural relationships, this task has been tackled since the earliest days of molecular magnetism and Kahn's orbital symmetry model.[1, 2] Although the first rationalisations were linking the nature of the coupling between metal centres with their electronic structure and bridging geometries, the attention has been shifted currently towards the prediction of the crystal field-single ion interaction and the resulting anisotropy.[3, 4] This evolution was motivated by the change of strategy in designing SMMs, moving from serendipitous preparation of large clusters (large *S*) to tailored mononuclear compounds with substantial anisotropy (*D*). An elegant way of benefiting from both approaches and the existing models could be the implementation of well-defined (metallo)ligands which are able to provide suitable crystal fields around single metal ions (shaping their anisotropy) while binding them into a cluster with a specific topology (thus, shaping the nature of their interaction in sign and magnitude).[5] This idea of tailoring the magnetic properties of coordination compounds was the main driving force behind the chemistry presented in this chapter.

The first part of Chapter IV overviews the coordination chemistry of the new pyrazole ligand **H_4L4**, designed here with an intention to selectively chelate different 3*d* metals ions into trinuclear heterometallic linear arrays using their preference for (-*N*,*N*) or (-*O*,*N*) coordination environment. In view of the lack of success in realizing this idea, the second part of the chapter focuses on the controllable use of the simple metalloligand $(TBA)_2[(VO)_2(HL4)_2]$ in a construction of complex molecular architectures with divalent 3*d* metals. Indeed, the presence of oxygen donors from VO^{2+} moieties together with porphyrin–like chelating site in the structure of the metalloligand shall provide high selectivity in the formation of heterotrimetallic assemblies along with the possibility of fine-tuning the magnetic properties with the nature of constituent metal centres. As a result, a supramolecular synthon V=O···M will be established as a strategic building block for generating fairly strong ferromagnetic interactions and large spin ground states. One of the most remarkable outcomes of this strategy was the observation of field-induced slow

relaxation of the magnetization in an impressive heterotrimetallic VO(IV)-Mn(II)-Cu(II) compound.

4.2. Serendipitous synthetic approach with ligand H_4L4

4.2.1. Synthesis and characterisation of 5,5'-(2-hydroxyphenyl)-3,3'-bi-1*H*-pyrazole, H_4L4

Starting from the tetraketone ligand **H_4L1** (Chapter II), in a standard ring closure reaction with hydrazine in refluxing methanol, the new phenolic pyrazole ligand **H_4L4** was prepared (Scheme 4.1). In this chemical modification, an excess of hydrazine converts two oxygen-rich 1,3-diketone moieties initially to *bis*-hydrazones (—C=N—NH_2) which then are transformed by heating into nitrogen-rich pyrazole rings. [6]

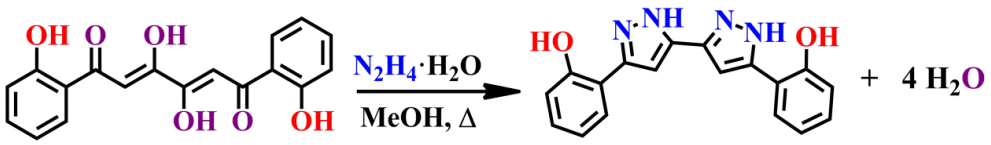

Scheme 4.1: Preparation of *bis*-pyrazole ligand **H_4L4** from its *bis*-β-diketone precursor **H_4L1**.

A crystalline product was obtained directly from the reaction mixture, which was characterised by ^{1}H NMR spectroscopy, mass spectrometry and elemental analysis (Appendix IV, Figs. IV.A1 and IV.A2). Detailed insights into the constitution of this ligand was acquired by the crystal structure determination, which revealed a unique *cis*-arrangement of two bonded phenol-pyrazole blocks in **H_4L4** together with a water of crystallisation (Figure 4.1, Table IV.A1 and IV.A2).

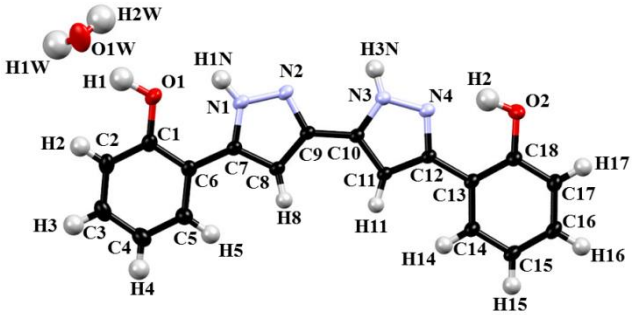

Figure 4.1: Molecular structure of **H_4L4** emphasizing the *cis*-orientation of its coordination sites. For simplicity, only one position of the disordered molecule of crystallisation water is shown. All displacement ellipsoids are drawn at 50% probability.

The geometry differs from the structure of the precursor ligand **H_4L1**, where two sets of coordination pockets are facing opposite directions (Chapter II). However, this is not unexpected since free rotation around the central C—C bond is enabled, therefore, both ligands can easily attain both conformations. The likely reason of the solid state *cis*-conformation of **H_4L4** is the existence of a cyclic network of 10 intra- and intermolecular hydrogen bonding interactions that assemble the molecular units into discrete dihydrated dimers (Figure 4.2 A, Table IV.A3). This supramolecular arrangement stabilises a very rare bipyrazole tautomer in which disposition of acidic protons (−NH and –OH) alternates between hydrogen donors and hydrogen acceptors. On the other hand, the aromatic core of the molecule facilitates a very effective crystal packing via π···π and C–H···π interactions (Figure 4.2, B and C), arranging the dimers into stacked zig-zag layers with a hydrophobic periphery and a hydrophilic interior.

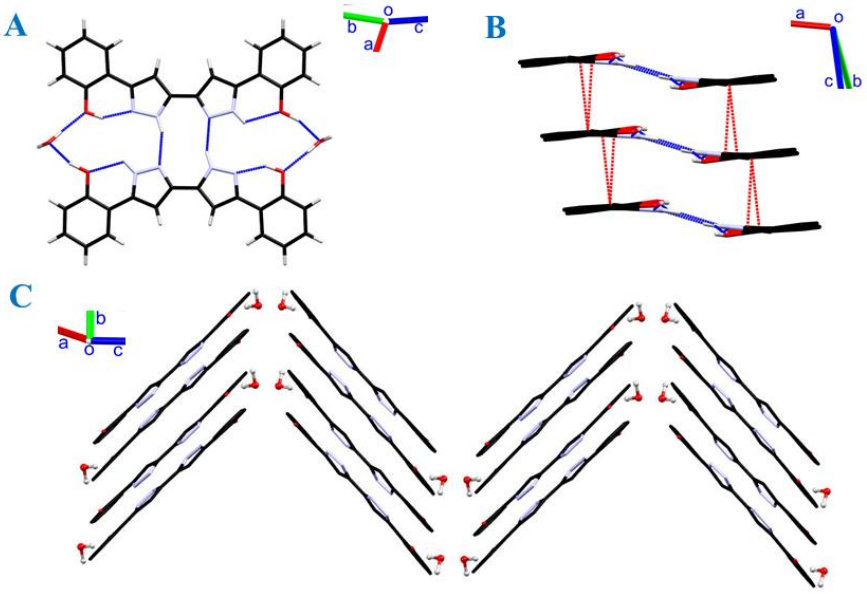

Figure 4.2: A) Intra- and intermolecular hydrogen bonding network within the dimeric arrangement of **H_4L4**. B) π···π stacking (red) between hydrogen bonded dimers (blue). C) Crystal packing of **H_4L4** emphasizing the structure of stacked zigzag layers with water channels.

Interestingly, this supramolecular motif is unique among the few structurally characterised 3,3'-bipyrazole molecules, which usually build their crystal structure *via* N–H···N, C–H···π and N–H···π interactions among perpendicularly oriented molecules. [7, 8]

4.2.2. Homometallic compounds of H_4L4 with 3*d* metals: Synthetic and structural insights

As witnessed from the crystallographic study, the topology of the dimeric assembly of **H_4L4** affords two different sets of connected coordination pockets: two peripheral 'O_2N_2' and the central 'N_4'. Hence, this organic scaffold can be easily employed to chelate three closely spaced metal ions into a linear array (Scheme 4.2). Moreover, the crystal field effects originating from the different size, composition and flexibility of the binding sites can induce distinct coordination geometries in homometallic clusters or direct the selective formation of heterometallic M_2M' assemblies.

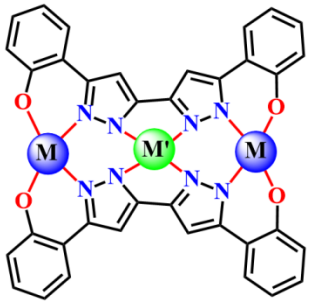

Scheme 4.2: Predesigned coordination mode of **H_4L4**.

In order to test these assumptions, reactivity patterns of **H_4L4** with divalent 3*d* metal ions (VO^{2+}, Mn^{2+}, Co^{2+}, Ni^{2+}, Cu^{2+}) were investigated. The strategy followed to obtain the homometallic compounds was to perform room temperature reactions of two equivalents of the fully deprotonated ligand (adding of TBAOH as base) with three equivalents of a metal salt (chloride, acetate or perchlorate) in pyridine. Layering the resulting solutions with antisolvents (Et_2O, hexanes, toluene) led to the formation of single crystals, which were analysed, providing the insights into the specific chemistry governed by the ingredient metal ion. As expected, the reaction of Cu^{2+} and Ni^{2+} with **$L4^{4-}$** allowed the isolation of the desired trinuclear compounds with general formulae $(TBA)_2[M_3L_2(py)_x]$:

$$3\ MCl_2 + 2\ H_4L4 + 8\ TBAOH + x\ py \longrightarrow \mathbf{(TBA)_2[M_3(L4)_2(py)_x]} + 6\ TBACl + 8\ H_2O$$

($M=Cu^{2+}$, x=0.5, **21**; $M=Ni^{2+}$, x=0, **22**)

The crystal structure of both compounds (monoclinic $P2_1/n$ space group, Table IV.A4) is assembled from the complex anion $[M_3(L4)_2(py)_x]^{2-}$ and two tetrabutylammonium cations. The presence of the latter indicates that the metal ions preserve their oxidation state, which

can only partially compensate the charge of the fully deprotonated ligating species. The asymmetric unit is defined with half of the molecular components, while the other half is generated by a symmetry operation over the centre of inversion. The structure of the complex anions confirms the expected linear topology of the cluster with two parallel ligands disposed at equatorial sites of the metallic core. In both compounds, the peripheral metal centres reside in square-planar 'N_2O_2' ligand fields while the remaining M^{2+} centre fills the central 'N_4' coordination pocket, as predicted in the Scheme 4.2. With the Ni(II) anion, all metal centres retain the square geometry, the peripheral sites being slightly distorted and having very short Ni—N and Ni—O distances, averaged at 1.902 and 1.862 Å, respectively (Table IV.A8, Figure 4.3). Even shorter Ni—N distances were found for the central Ni(II) ion (average 1.843 Å) which, surprisingly, is perfectly nested within the imposed 'N_4' ligand field (Figure 4.3).

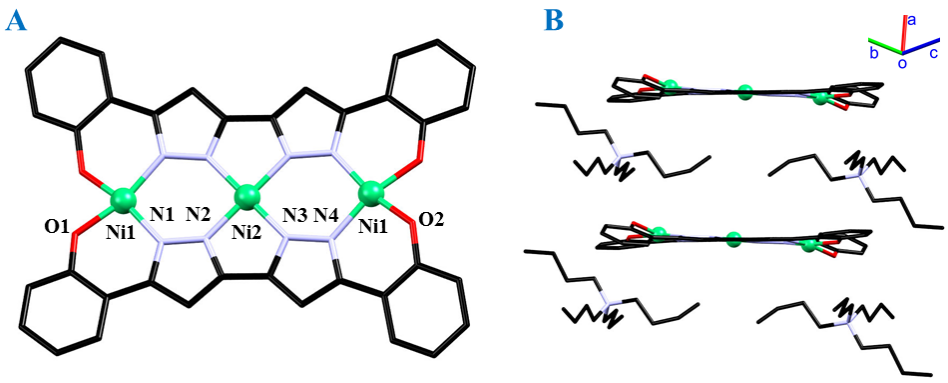

Figure 4.3: A) Molecular structure and labelling scheme of the $[Ni_3(L4)_2]^{2-}$ anion of **22**. Apart from nickel(II) ions (green balls), only crystallographically independent heteroatoms are labelled. B) Crystal packing of the $(TBA)_2[Ni_3(L4)_2]\cdot 2py$ (**22·2py**) highlighting the distribution of cationic-anionic layers. Solvate pyridine molecules and hydrogen atoms are omitted for clarity.

In contrast to the above, the Cu(II) analogue appears in form of two crystallographically independent complex anions, with half of the molecules having the square–planar geometry of the central metallic site while the other half holds a five-coordinated (square-pyramidal) Cu^{2+} centre with an axially coordinated pyridine molecule. Similarly to the $[Ni(II)]_3$ anion, the peripheral sites are slightly distorted with short Cu—N (average 1.967 Å) and Cu—O distances (average 1.916 Å). On the other hand, in both inequivalent anions, the central Cu(II) ion resides 0.340 Å outside the equatorial 'N_4' ligand field, showing an average Cu—N

distances of 1.954 Å (Figure 4.4, Table IV.A7). Some additional distortion emerges in the molecule with pentacoordinated Cu(II), as a result of the strongly elongated (2.45(6) Å) axial bond with pyridine.

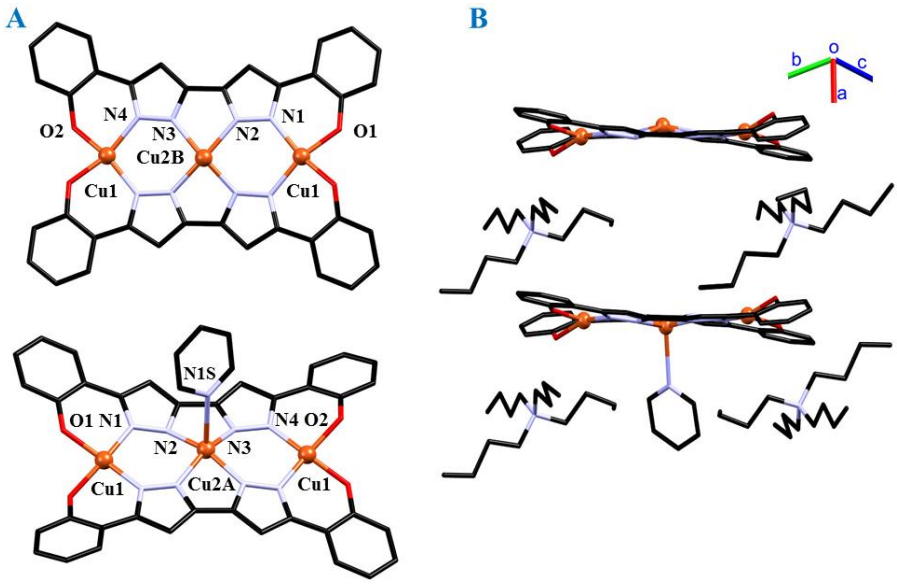

Figure 4.4: A) Molecular structure and labelling scheme of $[Cu_3(L4)_2(py)_x]^{2-}$ anions of **21**. Apart from the copper(II) ions (orange balls), only crystallographically independent heteroatoms are labelled. B) Crystal packing of the $(TBA)_2[Cu_3(L4)_2(py)_{0.5}]\cdot 1.5py$ (**21·1.5py**) highlighting the distribution of cationic-anionic layers. Solvate pyridine molecules and hydrogen atoms are omitted for clarity.

The greater planarity of the nickel(II) anion is nicely reflected in the shorter intramolecular metal-metal distance (3.843 Å) and the perfectly linear Ni—Ni—Ni angle of 180°, while the same parameters for Cu(II) amount to 3.87(6) Å and 170(2)°. In both compounds, the tetrabutylammonium cations are intercalated between the anionic clusters, stabilising the crystal structure with numerous C—H···π and C—H···O contacts with the organic scaffold of $\mathbf{L4}^{4-}$ and lattice pyridine molecules (Figs 4.3B and 4.4B).

During the course of this work, Oshio *et al.* published topologically almost identical $[Cu_3]$ and $[Ni_3]$ cationic clusters, assembled from the *bis*-pyridyl-bipyrazole analogue of $\mathbf{H_4L4}$.[9] Because of the larger cavity of the peripheral coordination pocket, bearing pyridyl instead of phenolic moiety, the terminal metal centres adopt square-pyramidal and octahedral coordination geometries for Cu(II) and Ni(II), respectively. On the other hand, the square-planar environment is preserved for central M^{2+} in both cases, as well as reported here (Figure 4.5). Consequently, the metallic core of the cationic $[M_3]^{2+}$ clusters is perfectly linear

(M—M—M angle of 180°), as all metal centres fit nicely with a better suited 'N_4' ligand field, allowing the greater planarity of the platform.

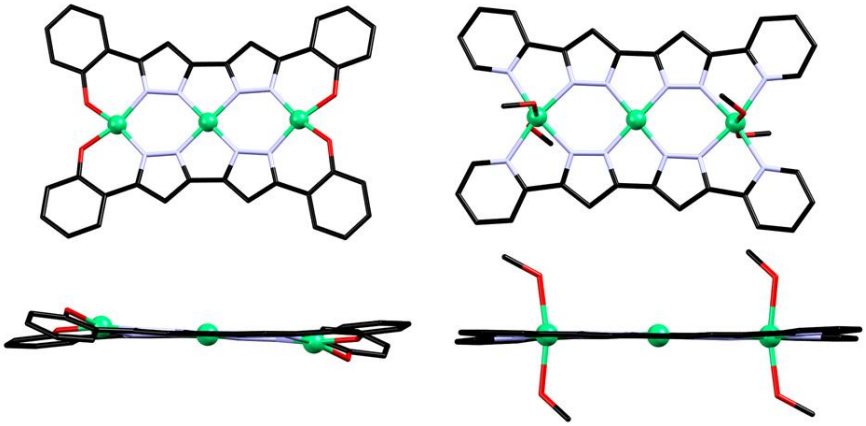

Figure 4.5: Comparison of the molecular structure and planarity of complex anion $[Ni_3(L4)_2]^{2-}$ from compound **22** (*left*) with these of the complex cation $[Ni_3(L)_2(MeOH)_4]^{2+}$ (*right*) reported by Oshio *et al.* (Refcode: LUBGAS; H_2L=5,5'-pyridyl-3,3'-bi-1*H*-pyrazole).[9] Hydrogen atoms, counter-ions and solvent molecules are omitted for clarity.

Moving to the early 3*d* metals, the chemistry of **H_4L4** with oxocation VO^{2+} was also investigated. Employing the previously discussed conditions and choosing vanadyl sulfate as a source of metal ions, the dinuclear compound $(TBA)_2[(VO)_2(HL4)_2]$ (**23**) was isolated and its structure was determined by single-crystal X-ray diffraction. Interestingly, this product was obtained in several reaction setups, varying the metal-ligand stoichiometry from 1:1 to 2:1. The only observable difference was the yield improvement upon increasing the quantity of vanadium. The reason is presumably the partial oxidation of vanadyl(IV) ions to V(V) in basic medium, especially when TBAOH is used as a base, since it stabilises the formation of negatively charged polyoxovanadates. Optimal reaction conditions were established for metal-ligand-base ratios 4:2:8 and 3:2:6. A general, balanced equation describing the formation of **23** can be written as:

$$2\ VOSO_4 + 2\ H_4L4 + 6\ TBAOH \longrightarrow (TBA)_2[(VO)_2(HL4)_2] + 2\ (TBA)_2SO_4 + 6\ H_2O$$

Compound **23** crystallises in the triclinic *P*-1 space group as a pyridine solvated ionic compound. Unlike the previously described copper(II) and nickel(II) complexes, vanadyl cations occupy the peripheral '*O,N*' coordination pockets, while the inner 'N_4' coordination site stays metal-free and partially protonated ($-N_2(NH)_2$). The resulting charge of the

$[(VO)_2(HL4)_2]^{2-}$ unit is compensated with two tetrabutylammonium cations (TBA^+), meaning that the vanadium centres maintain its oxidation state +IV. The unit cell of this compound is defined with two slightly different metallo-organic platforms, four TBA^+ cations and nine lattice pyridine molecules. On the other hand, the asymmetric unit is defined by half of each crystallographically inequivalent $[(VO)_2(HL4)_2]^{2-}$ anions, while the other half is generated by the symmetry operation over an inversion centre. Consequently, vanadyl centres of each crystallograpically independent molecule are equivalent and *trans*-oriented in respect to the equatorial ligand plane (Figure 4.6A). Average intramolecular distance among the metallic centres amounts to 8.267 Å. Additionally, positional disorder of the symmetrically inequivalent vanadyl cations (V1 and V2) over the two possible orientations was optimised in the refinement model in 92.8:7.2. For the sake of brevity, only major component of the disorder will be described here while the bonding details of the second component are given in the Table IV.A9. In any case, all metal centres are five-coordinated and reside in a very distorted square-pyramidal ligand field defined by the oxo ligand (axial V=O) and by the two terminal '*O*,*N*' coordination pockets of the **$[HL4]^{3-}$** ligands. As it can be expected, the axial V=O bonds (1.600-1.602 Å) are significantly shorter that the equatorial V—O (1.913-1.950 Å) and V—N (2.087-2.095 Å) bonds. These differences are reflected in the pyramidalisation of the coordination geometry around the vanadium(IV) centres, which are positioned 0.531 Å (V1) and 0.541 Å (V2) outside the equatorial 'O_2N_2' plane, towards the oxo ligand. Interestingly, while in clusters **21** and **22** the equatorial M—O bonds were comparable to the M—N bonds, in the case of vanadium(IV), the bonding with the pyrazolate core is significantly weaker in comparison with the phenolate. This affinity towards oxygen as well as the pyramidalisation of the coordination geometry due to the effect of the oxo ligand reduce the possibility of the placing the vanadyl ion into the central 'N_4' coordination pocket. Thus, not even double ratio of metal to ligand induces the formation of trinuclear cluster.

As seen earlier, tetrabutylammonium cations are positioned in the layers between the $[(VO)_2(HL4)_2]^{2-}$ clusters in a way that each anion interacts strongly with four TBA^+ cations *via* C—H···π and C—H···O(=V) contacts (Figure 4.6B). Lattice pyridine molecules fill the voids between the charged layers and interact weakly with their components.

Compound **23** joins the small family of pyrazole supported V(IV) clusters, of which the great majority involves mixed ligand systems with phosphonates, hydroxides, halides and carboxylates,[10-21] while only three complexes include solely a pyrazolate scaffold. [22, 23]

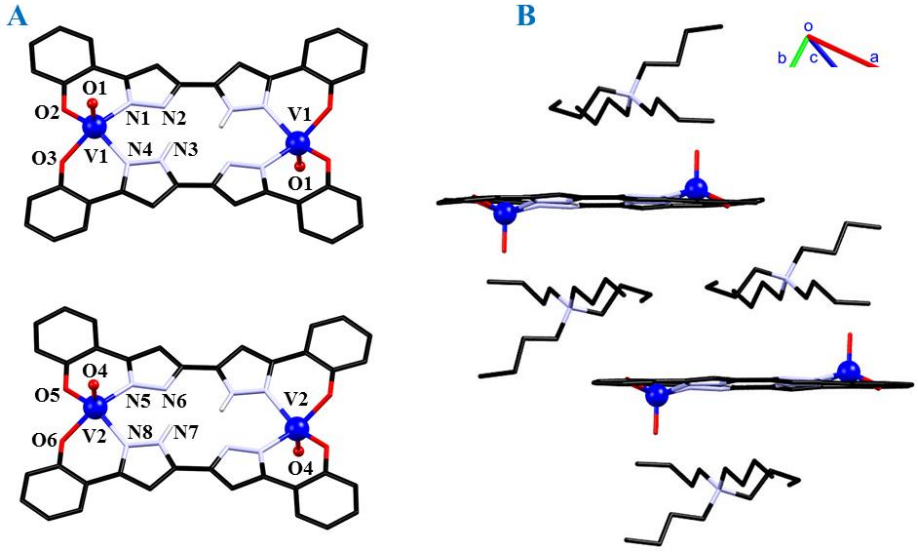

Figure 4.6: A) Molecular structure and labelling scheme of the crystallographically inequivalent $[(VO)_2(HL4)_2]^{2-}$ anions of **23**. Only acidic protons, affecting the charge of cluster, are shown for the clarity. Apart from vanadyl ions (blue and red balls), only crystallographically independent heteroatoms are labelled. B) Molecular structure of the $(TBA)_2[(VO)_2(HL4)_2]$ (**23**) highlighting the crystallographically inequivalent molecules and the distribution of the cationic-anionic layers. Solvate pyridine molecules and hydrogen atoms are omitted for the clarity.

A similar reactivity pattern was observed between Mn(II) and **H_4L4**, accompanied additionally with the one-electron oxidation of the metal ions under aerobic conditions. Therefore, as the main product of the already described reaction dinuclear neutral compound $[(Mn^{III})_2(HL4)_2]$ (**24a**) was isolated:

$$2\ MnCl_2 + 2\ H_4L4 + 4\ TBAOH + 1/2\ O_2 \longrightarrow [Mn_2(HL4)_2] + 4\ TBACl + 5\ H_2O$$

Similarly to the vanadyl analogue, compound **24a** crystallises in the triclinic *P*-1 space group, with the unit cell defined by two slightly different $[Mn_2(HL4)_2]$ molecules encapsulating one ionic pair of tetrabutylammonium chloride. The manganese(III) centres occupy only the peripheral '*O,N*' coordination pockets, while the inner 'N_4' coordination site stays partially protonated ($-N_2(NH)_2$). In contrast to the vanadyl complex, the coordination geometry around the Mn(III) centres is octahedral, shaped by a very distorted 'O_2N_4' ligand field

afforded by two equatorially disposed $[HL4]^{3-}$ ligands and two axially bounded pyridine molecules (Figure 4.7A). The presence of strong Jahn-Teller distortion is reflected in the bond distances, with axial Mn—N bonds reaching the average distance of 2.331 Å, while significantly shorter equatorial Mn—N and Mn—O bond distances amount to 2.022 Å and 1.873 Å, respectively. This axial elongation is commonly found in Mn(III) salen compounds, where the easy axis of magnetization (negative *D*) can be directly identified as the Jahn-Teller axis.[24] Both metallic sites in each crystallographically independent metallo-organic platforms are equivalent due to the existence of an inversion centre in the middle of each molecule. The average intramolecular distance between Mn(III) centres sums 8.110 Å, slightly shorter than in complex **23**, due to the comfortable positioning of Mn(III) ions into the equatorial N_2O_2 plane (atom-plane distance of 0.04 Å). Interestingly, no lattice solvents were found in the structure, as a result of the very dense crystal packing, where π···π interactions between the axial pyridine ligands organise neighbouring $[Mn_2(HL4)_2]$ molecules in chains. In this way, each platform interacts with two neighbouring platforms (above and below the equatorial plane, Figure 4.7C), while additional C–H···π contacts established at peripheral sites, arrange the molecules into linear arrays (Figure 4.7B). Small voids between the dense layers are filled with TBA^+Cl^- ionic pairs, which are stabilised and strongly attached to the metallic platforms with numerous hydrogen bonding interactions (Figure 4.7B and C).

Another molecular form of the $[Mn_2(HL4)_2]$ (**24b**) was obtained from the chemically reasonable synthesis starting from the $Mn(CH_3COO)_3$ and **H_4L4**:

$$2\ Mn(CH_3COO)_3 + 2\ H_4L4 + 6\ TBAOH \longrightarrow [Mn_2(HL4)_2] + 6\ TBA(CH_3COO) + 3\ H_2O$$

Compound **24b** crystallises in the monoclinic $P2_1/n$ space group, with the unit cell content defined by one $[Mn_2(HL4)_2]$ molecule and two pyridine molecules as the lattice solvent. Asymmetric unit is defined by the half of the unit cell, meaning that both Mn(III) are crystallographically equivalent over the inversion centre in the heart of the cluster. Within the O_2N_4 crystal field around the Mn(III), all bond distances are slightly longer than in **24a** with the equatorial Mn–O and Mn–N bonds measuring 1.892(3) Å and 2.041(3) Å, while axial Mn–N bonds with the pyridine ligands are 2.350(3) and 2.363(3) Å long, hinting the strong Jahn-Teller distortion. The intramolecular distance between Mn(III) centres of

8.136(6) Å is slightly longer than in complex **24a**, although Mn(III) ions are equally situated into the equatorial N_2O_2 plane (atom-plane distance of 0.042 Å). Crystal packing motif in **24b** is analogous to the structure of **24a**, enriched by additional C–H···O hydrogen bonding between the π-stacked chains which open up the voids for lattice pyridine molecules (interacting with the phenol wings via C–H···N and C–H···π contacts).

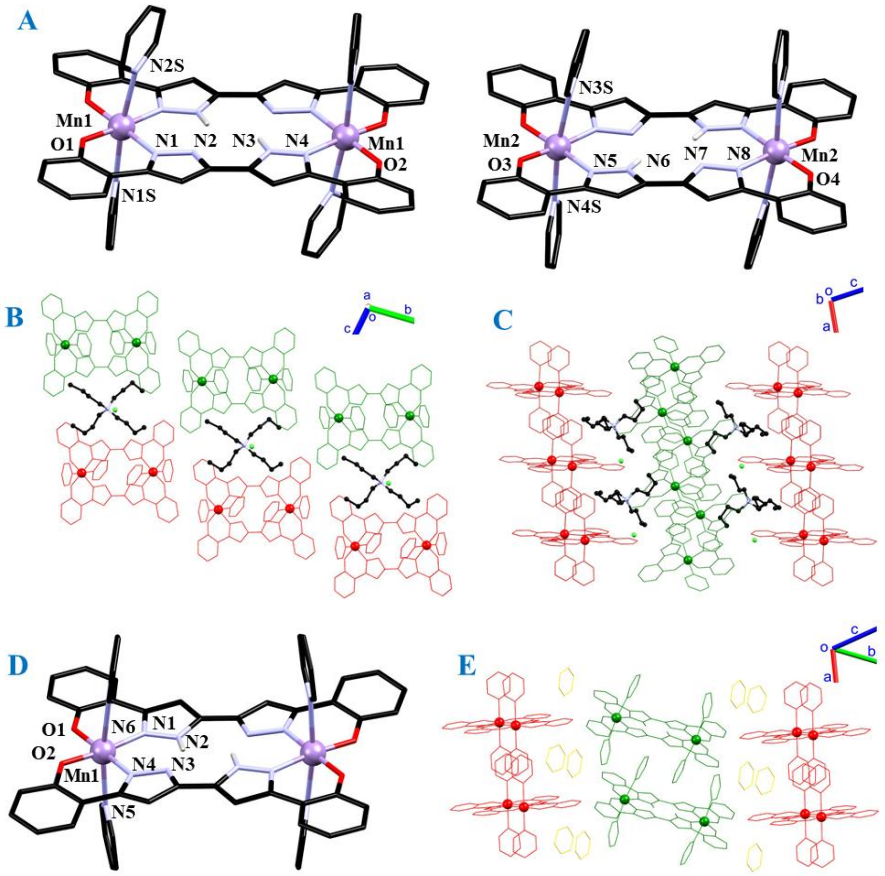

Figure 4.7: A) Molecular structure and labelling scheme of two crystallographically inequivalent $[Mn_2(HL4)_2]$ molecules of **24a**. Only acidic protons, affecting the charge of cluster, are shown for clarity. Apart from Mn(III) ions (violet balls), only crystallographically independent heteroatoms are labelled. B) Crystal structure of **24a** highlighting the layers of crystallographically inequivalent molecules (red and green) and the positioning of TBA^+Cl^- in the voids between them. C) π···π stacking and ordering of $[Mn_2(HL4)_2]$ molecules in chains (red). D) Molecular structure and labelling scheme of $[Mn_2(HL4)_2]$ molecules of **24b**. E) Crystal structure of **24b** highlighting the chain formation and pyridine voids between them (yellow). Hydrogen atoms are omitted for the clarity.

The reaction between Co^{2+} and **H_4L4**, led to the formation of the most intriguing product, a neutral complex $[(Co^{III})_3(L4)_2(OMe)(py)_5]$ (**25**). In similarity with manganese chemistry, three one electron oxidations in basic medium convert Co(II) to Co(III) ions, which are then

chelated with two fully deprotonated ligands $L4^{4-}$. The additional positive charge of the metallic core is compensated with the binding of a methoxide anion, which appears in the system on account of using the methanol solution of TBAOH. The balanced equation of these processes is:

$$6\ CoCl_2 + 4\ H_4L4 + 12\ TBAOH + 2\ MeOH + 10\ py + 3/2\ O_2 \longrightarrow 2\ [Co_3(L4)_2(OMe)(py)_5] + \\ +12\ TBACl + 15\ H_2O$$

Compound **25** crystallises in monoclinic $P2_1/c$ space group in form of two crystallographically inequivalent $[Co_2(L4)_2(py)_5(OMe)]$ platforms solvated with five pyridine molecules. Like in the Cu(II) and Ni(II) clusters, cobalt(III) cations occupy all three available coordination sites of the ligand, adopting the octahedral geometry with two equatorially disposed $[L4]^{3-}$ ligands. The axial ligands differ between the peripheral and the central Co(III) sites, given the fact that the former bind two molecules of pyridine each, while the latter fills its coordination sphere with one pyridine molecule and one methoxide anion (Figure 4.8A). Unlike the peripheral sites in Mn(III) dimer, the equatorial Co—N and Co—O bond distances (average 1.933 Å and 1.885 Å, respectively) are comparable to the axial $Co—N_{py}$ bonds (average 1.950 Å, Table IV.A11). A slightly different trend is observed for central Co(III) ions, with the equatorial Co—N bond distances being the shortest (average 1.882 Å), while the mean distances of the dissimilar axial $Co—N_{py}$ and $Co—O_{OMe}$ bonds are 1.995 Å and 1.900 Å, respectively. The metallic core of the cluster is almost perfectly linear (M—M—M angle of 179°), with an average distance between neighbouring Co(III) ions of 3.829 Å. However, the equatorial planes of adjacent sites are slightly tilted (the average angle between them is 11.36°) as a result of a slightly bent organic scaffold, which decreases the overall planarity of the system. The molecular units build the crystal structure with numerous C—H···π and C—H···O interactions, taking place mostly at the axial ligands and the peripheral phenoxide rings. Consequently, perpendicular layers of antiparallel molecules are formed with cyclic structural motifs assembled from four neighbouring molecules. This arrangement unlocks the voids in the structure in which lattice pyridine molecules reside (Figure 4.8B).

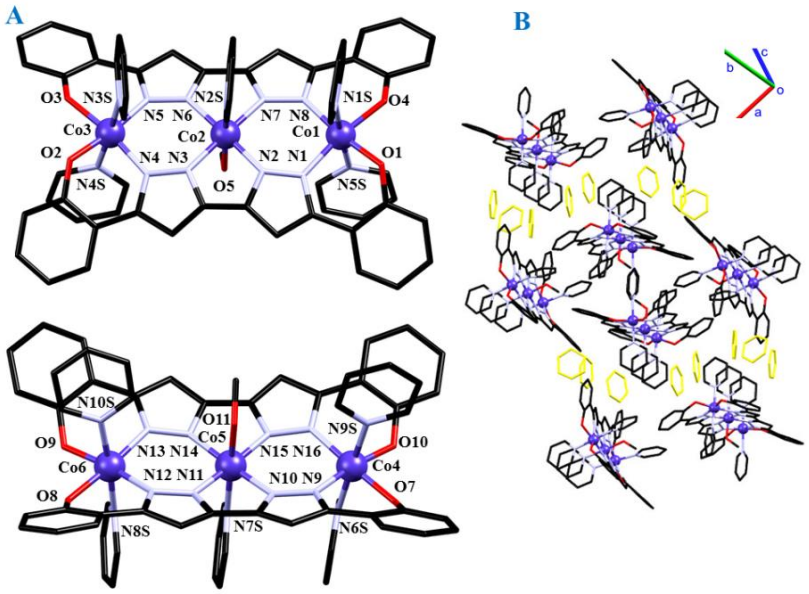

Figure 4.8: A) Molecular structure and labelling scheme of the crystallographically inequivalent $[Co_3(L4)_2(OMe)(py)_5]$ molecules. Co(II) ions (blue balls) and crystallographically independent heteroatoms are labelled. B) Crystal structure of **25** highlighting the cyclic molecular arrangement of perpendicular layers and related pyridine channels.

4.2.3. Homometallic compounds of H_4L4 with 3*d* metals: Solution studies

The stability of clusters **21**-**25** in solution was assessed by mass spectrometry and ^{1}H NMR (diamagnetic compounds **22**). Due to the moderate solubility of these complexes in common solvents, the employed technique was usually electrospray ionization (ESI), while MALDI-TOF was engaged for poorly soluble compounds **24** and **25**.

In the case of the anionic trinuclear compounds **21** and **22**, negative ion electrospray ionization, ESI(−), of acetonitrile solutions confirmed the integrity of the clusters since all detectable molecular peaks are nicely consistent with the solid state structure. For **21**, the molecular peak found at *m*/*z*=409.48 corresponds to the $[Cu_3(L4)_2]^{2-}$ anion, while an almost equally abundant protonated cluster, $\{[Cu_3(L4)_2]^{2-}+H^+\}$, is found at 819.96 (Figure IV.A3). Additionally, minor peaks of higher assemblies are also found and identified as $\{[Cu_3(L4)_2]^{2-}]_2+3H^+\}$ (*m*/*z*= 1636.92-1642.92). The isotopic distribution of the most abundant peaks coincides perfectly with the theoretically expected one, giving the definitive confirmation of the cluster integrity (Figure IV.A3). The only difference between the solid state and the solution structure is the lack of evidence for molecules with axially bounded

pyridine on the central Cu(II) ion. However, this is expected since the corresponding bond is very weak and prone to clevage in the solution. On the other hand, the ESI(+) spectrum confirms the presence of tetrabutylammonium cations, which compensate the charge of cluster as seen in the crystal structure. As expected, identical peaks in the positive mode were observed for the nickel analogue, while the negative mode, apart from the previously assigned peaks indicates the existence of the ligand anion $(H_3L4)^-$ (Figure IV.A4). The latter could be the consequence of fragmentation during the experiment or the harsher conditions applied to solubilise the compound (heating). Nevertheless, the isotopic distribution of the metal-containing molecular peaks undoubtedly confirms the stability of the $[Ni_3(L4)_2]^{2-}$ complex in solution (Figure IV.A4). Additional support to this claim was acquired by ^{1}H NMR of **22** in d_6-DMSO. As expected from the crystal structure, the diamagnetic nature of the compound allows the observation of five characteristic aromatic peaks, representing one quarter of the organic scaffold (Figure 4.9). Characteristic chemical shifts observed for **22** are systematically upfield shifted (0.34-0.57 ppm) in comparison with the free ligand (Figure IV.A8). Similarly, four characteristic peaks of the counter-ion TBA^+ were also identified and assigned to the *n*-butyl chain. As an ultimate confirmation of the solution stability of **22**, integration of all observable peaks agrees with the anticipated ratio from the crystal structure.

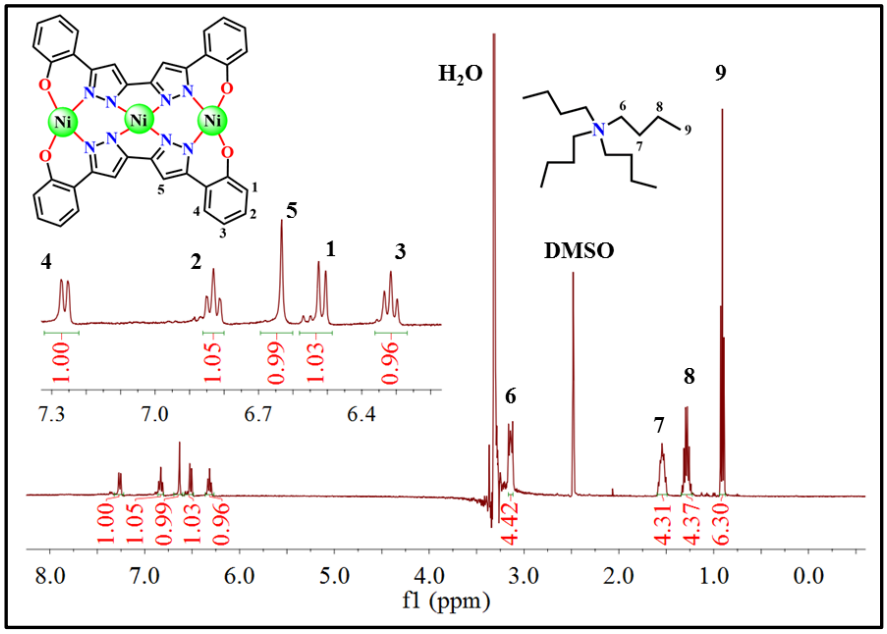

Figure 4.9: ^{1}H NMR of compound **22** in d^6-DMSO. Numbers indicated below the signals represent their integrals.

The negative ion ESI(−) spectrogram of compound **23** (methanol solution), follows the established trend with the most abundant peak identified as the $[(VO)_2(HL4)_2]^{2-}$ anion (*m*/*z*=382.03), along with the less intense contributions from $\{[(VO)_2(HL4)_2]^{2-}+H^+\}$, *m*/*z*=765.05, and $\{[(VO)_2(HL4)_2]^{2-}]_2+TBA^+\}$, found at *m*/*z*=1006.34 (Figure IV.A5). Positive ion ESI(+) spectrum reveals again the exclusive presence of TBA^+ ions with the expected isotopic distribution (Figure IV. A5). Solution studies of neutral compound **24a** by MALDI-TOF ascertained the integrity of the structure since great majority of detectable peaks corresponds to the $\{[Mn_2(HL4)_2]\}$ unit (Figure IV.A6). The only exceptions are assigned to $[(TBA)_2Cl]^+$ in (+) mode and a minor peak to $(H_3L4)^-$ in (−) mode. Looking at the metal-containing peaks, the spectrum in positive mode reveals the presence of cationic assemblies containing the $\{[Mn_2(L4)_2]\}^{2-}$ unit enriched with Mn^{3+} (*m*/*z*=865.6) or 3 TBA^+ cations (*m*/*z*=1538.8). Although the former species may also indicate the existence of $[Mn_3(L4)_2]^+$ complex as analogue of compound **24**, the appearance of this peak is probably result of *in situ* rearrnagement since all remaining signals correspond to the dinuclear entity. Support to this conclusion can be found in the (−) spectrum, where the $\{[Mn_2(HL4)_2]\}^-$ and $\{[Mn_2(L4)(HL4)]\}^-$ species dominate. The former results from electron ionisation of one Mn(III) centre to Mn(II) , while the latter is generated upon deprotonation of the initial cluster. The isotopic distribution of the most abundant peak, found at *m*/*z*=740.0, confirms the contribution of both forms to this signal (Figure IV.A6). Finally, fragmentation of metoxide anion from the structure of **25**, results in an ESI(+) spectrum dominanted by the cationic assembly $[Co_3(L4)_2]^+$, *m*/*z*=804.96, and its pyridine solvates $[Co_3(L4)_2(py)_n]^+$ (*m*/*z*=884.00 (n=1) and *m*/*z*=963.04 (n=2). Additionally, a minor fragment of the mixed valent $[Co^{II}Co^{III}(H_2L4)_2]^+$ cation was also detected at *m*/*z*=750.06 (Figure IV.A7). As expected, isotopic distribution of the observed signals undoubtedly confirms the assigned molecular composition (Figure IV.A7). Similarly, in (+) mode of MALDI-TOF, the $[Co_3(H_2L4)]^+$ fragment was found to be the most abundant molecular peak (*m*/*z*=374.2) with additional distribution involving previously described $[Co_3(L4)_2]^+$ and $[Co^{II}Co^{III}(H_2L4)_2]^+$ cations (Figure IV.A7).

4.2.4. Homometallic compounds of H_4L4 with 3*d* metals: Magnetic studies

The interaction between spin carriers in compounds **21**, **23** and **24b** was investigated by SQUID magnetometry and EPR spectroscopy. At ambient temperature (300 K), the $\chi_M T$

product for **21** is significantly lower than expected for three non-interacting copper(II) centres (measured 0.82 cm^3 K mol^{-1}, expected 1.125 cm^3 K mol^{-1} taking into account g = 2.0), indicative of strong antiferromagnetic interactions between them (Figure 4.11). This is additionally confirmed by the sharp decrease of $\chi_M T$ taking place upon lowering the temperature from 300 K to 70 K, after which a plateau at 0.40 cm^3 K mol^{-1} is reached. Below 5 K, a small drop of the $\chi_M T$ product is detectable ending at 0.37 cm^3 K mol^{-1} (2 K), which can be attributed to antiferromagnetic intermolecular interactions. Consistent with this, the highest measured value of $M/N\mu_B$ *vs* H curve (0.93 μ_B at 5 T) lies well below the expected 3 μ_B for three S=1/2 centres (g=2).

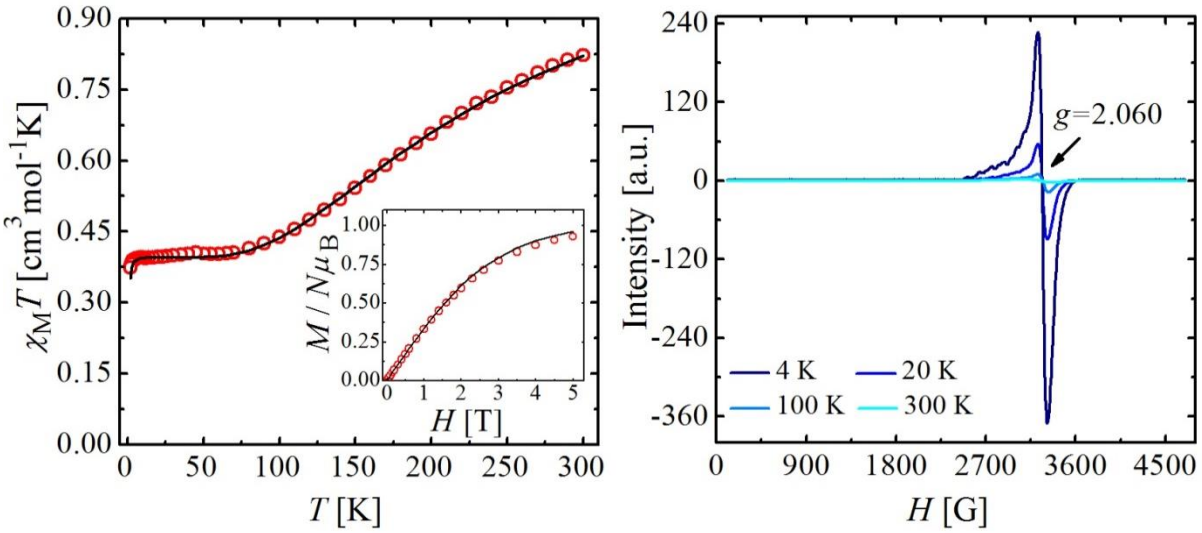

Figure 4.11: ***7*** *Left:* $\chi_M T$ *vs* T and $M/N\mu_B$ *vs* H (inset) curves for compound **21** with the best fit (solid line). Measurement setup: cooling mode (300→2 K), B = 1 T; T_{mag} = 2 K. *Right:* Variable temperature (4-300 K) X-band EPR spectra (f = 9.418 GHz) of a powdered sample of complex **21**.

In attempt to quantify the antiferromagnetic interactions between the Cu(II) centres, simultaneous fits of the experimental data ($\chi_M T$ *vs* T and $M/N\mu_B$ *vs* H) were completed using the program PHI[25] by matrix diagonalisation of the spin Hamiltonians defined in equations 4.1:

$$\hat{H} = \mu_B B \sum_i g_i \hat{S}_i - 2J\left(\hat{S}_1\hat{S}_2 + \hat{S}_2\hat{S}_3\right) \qquad (4.1a)$$

$$\hat{H} = \mu_B B \sum_i g_i \hat{S}_i - 2J\left(\hat{S}_1\hat{S}_2 + \hat{S}_2\hat{S}_3\right) - 2J_1\left(\hat{S}_1\hat{S}_3\right) \qquad (4.1b)$$

In both cases, J represents the coupling constant between the peripheral (S_1 and S_3) and central Cu(II) sites (S_2), while in the latter equation J_1 defines the possible interaction between two peripheral sites. Fixing the isotropic g factors at 2.07 (S_1 and S_3) and 2.12 (S_2), both models reproduced nicely the experimental data with either J=−100.05 cm^{-1} or J=−99.91 cm^{-1} and J_1=−0.30 cm^{-1} as the best parameters (Figure 4.11). The extracted exchange constants agree with the reported values for *bis*-pyrazolato bridged Cu(II) centres (−70< J< −268 cm^{-1}), where more effective exchange was found to be related with higher planarity of the [Cu(μ_2−N−N)$_2$Cu] core.[26-37] Interestingly, a ferromagnetically coupled Cu(II) dimer (J=16.3 cm^{-1}) was reported by Meyer *et al*., containing the flexible pyrazole-based porphyrin scaffold which facilitates Cu−N−N−Cu torsion angles of 80° and the consequent orbital orthogonality between both spin carriers.[38] Significantly reduced exchange constants for **21** in comparison with those reported by Oshio *et al.* for an analogous $[Cu_3(L)_2]^{2+}$ cluster (J=−194 cm^{-1} and J_1=−4.5 cm^{-1}),[9] can be rationalised by the higher distortion of the Cu(II) coordination environment, which decreases significantly the overlap between the magnetic orbitals (d_{x2-y2}). As seen from the structure of **21**, the central Cu(II) ion resides 0.340 Å outside the 'N_4' equatorial plane while in Oshio's compound, all three Cu(II) centres are positioned directly in the molecular plane of the ligand, with a negligible deviation of 0.030 Å at the peripheral sites.

Magnetometry findings were nicely complemented with variable temperature EPR spectroscopy (X-band), where an axial resonance centred at g=2.060 was detected with increasing intensity upon cooling (Figure 4.11). This spectral feature arises from Δm_S=1 transitions in the S=1/2 ground state of the antiferromagnetically coupled cluster which becomes more populated as the temperature is lowered (increasing intensity). Additionally, the spectroscopically detected g value of 2.060 agrees well with the plateau of 0.40 cm^3 K mol^{-1} observed in the $\chi_M T$ *vs* T curve.

On the other hand, the room temperature $\chi_M T$ product for **23** agrees with the expected value for two non-interacting S=1/2 vanadyl centres (measured 0.77 cm^3 K mol^{-1}, expected 0.75 cm^3 K mol^{-1} taking into account g = 2.0). Upon lowering the temperature, the Curie behaviour prevails until 5 K followed by a minor decline of $\chi_M T$ ending at 0.73 cm^3 K mol^{-1} (2 K, Figure 4.12). In addition, the highest measured value of the $M/N\mu_B$ *vs* H curve (1.90 μ_B at 5 T) remains slightly below the expected value of 2 μ_B for two S=1/2 (g=2).

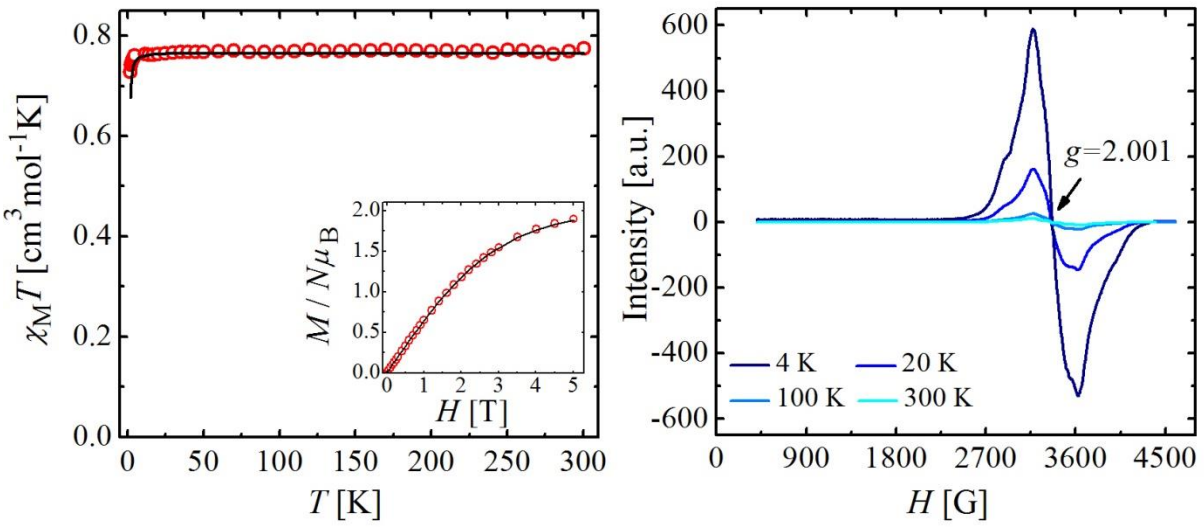

Figure 4.12: *Left:* $\chi_M T$ *vs T* and $M/N\mu_B$ *vs H* (inset) curves of compound **23** with the best fit (solid line). Measurement setup: warming mode (2→300 K), B = 1 T; T_{mag} = 2 K. *Right:* Variable temperature (4-300 K) X-band EPR spectra (f = 9.418 GHz) of a powdered sample of complex **23**.

The experimental data ($\chi_M T$ *vs T* and $M/N\mu_B$ *vs H*) were modelled taking into account weak antiferromagnetic interactions between spin carriers. Hence, the matrix diagonalization of the spin Hamiltonian:

$$\hat{H} = \mu_B B \sum_i g_i \hat{S}_i - 2J\left(\hat{S}_1 \hat{S}_2\right)$$

delivered g=2.02 and J=−0.042 cm^{-1} as optimal parameters. Weaker coupling between the vanadyl centres in comparison with peripheral copper(II) ions in **23** is consistent with their larger intramolecular separation (8.3 Å *vs* 7.7 Å). Magnetometry findings were confirmed with variable temperature EPR spectroscopy (X-band), which yielded isotropic spectra containing one broad resonance centred at g=2.001 (Figure 4.12). Intensity of the spectral features increases upon cooling (Curie behaviour) without revelling the hyperfine structure arising from the ^{51}V nuclei (I=7/2).

In addition, possible slow relaxation of magnetization of five-coordinated vanadyl centres was investigated by Dr Olivier Roubeau through temperature and frequency dependence of the alternate-current (ac) magnetic susceptibility. A first set of frequency dependent measurements (1-1420 Hz) formed under zero dc field and 4 Oe ac field at 1.8 K, showed no response of out-of-phase ac susceptibility (χ_M'', Figure IV.A9). However, application of a static field (range 250-5000 Oe) resulted in the appearance of frequency dependent in- and out-of-phase ac susceptibility signals, with the maximum value of χ_M'' corresponding to

approximately half of the $\chi_M^{'}$ value at low frequencies or half decrease of $\chi_M^{'}$, indicating that the relaxation of magnetization arises from all vanadyl spins of the sample. Consequently, the optimal applied dc field of 3000 Oe (highest $\chi_M^{''}$) was chosen for additional variable temperature measurements (1.8-20 K) in the frequency range 1-10000 Hz. Frequency dependent sets of the out-of-phase AC susceptibility ($\chi_M^{''}$) show that the maximum of the $\chi_M^{''}$ *vs* *v* curves is shifted towards higher frequency value as the temperature is increased accompanied with the decaying intensity (Figure IV. A10). The latter is clearly visible from the temperature dependence of the AC susceptibility data (Figure IV.A11) which also indicates that the maximum for the $\chi_M^{''}$ at the lowest temperature appears between 24.0 and 48.0 Hz. A representation of the results in the complex χ-plane (Argand plot, Figure 4.13), reveals a set of semicircles (indicative of single relaxation process) which lose their intensity upon heating.

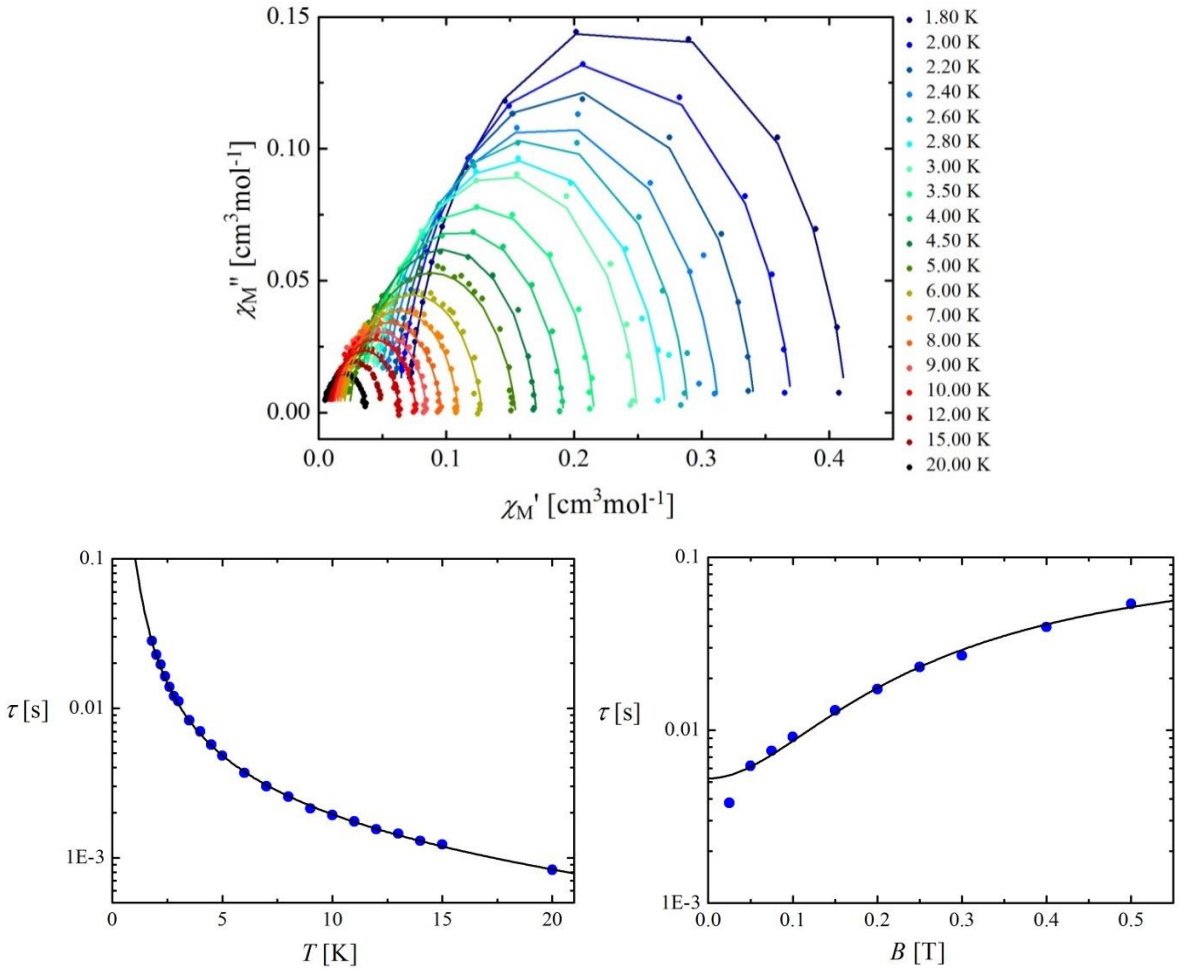

Figure 4.13: *Top:* Cole-Cole isotherms of the AC susceptibility for **23** under an applied DC field of 3000 Oe. The solid lines are fits to the experimental data. *Bottom*: Temperature and

field dependence (*T*= 1.8 K) of magnetization relaxation time (τ) for **23**. Solid lines are fits of experimental data (see text*)*.

In order to quantify the dynamics of the magnetization (relaxation time and the width of its distribution), the χ'_M and χ''_M data were fitted simultaneously to the generalised Debye model[39]:

$$\chi_{AC}(\omega) = \chi_S + \frac{\chi_T - \chi_S}{1+(i\omega\tau)^{(1-\alpha)}} \quad (4.2)$$

As seen in Figure 4.13, the fitted parameters are in good agreement with the experimental data, yielding a narrow distribution of α values for the entire temperature range taken into consideration ($0.09<\alpha<0.13$).

Exact pathway of the relaxation process was studied by fitting the temperature and field dependence (*T*= 1.8 K) of magnetization relaxation time (τ). Bearing in mind that the *S*=1/2 vanadyl ions don't possess any accessible state which can be thermally populated, the τ *vs T* data were first fit to a model including only direct and Raman processes. However, due to the poor reproducibility of the low temperature data, an additional Orbach term arising from weak antiferromagnetic coupling between vanadyl centres (*vide supra*) was taken into account. Thus, the model used to fit the relaxation time of **23** was:

$$\frac{1}{\tau} = aH^2T + bT^n + \frac{c\Delta^3}{[e^{\frac{\Delta}{T}}-1]} \quad (4.3)$$

The terms of this expression represent consecutively direct, Raman and Orbach relaxation mechanisms. In order to avoid the overparameterisation, the exponent of the Raman term was fixed to 3 while the Orbach gap Δ was optimised at 4 K. The obtained *a*, *b* and c parameters are 54 $s^{-1}K^{-1}$, 0.0123 $s^{-1}K^{-3}$ and 3.46 $s^{-1}K^{-3}$, respectively. Consequently, the low temperature relaxation dynamics is governed by a direct process while the contributions of Raman and Orbach relaxation mechanisms prevail at intermediate and higher temperatures. Similar relaxation dynamics was observed by Sessoli *et al.* for pentacoordinated vanadyl centers in $VO(dpm)_2$ (dpm-dipivaloylmethane), with the slight difference in Raman relaxation rate which is about four times slower for the here reported vanadyl dimer **23**.[40] On the other hand, field dependence of the relaxation time (τ) at 1.8 K shows a constant

increase up to 0.5 T which was simulated using the extended (direct mechanism) model proposed by van Vleck[41] (Raman mechanism):

$$\frac{1}{\tau} = cH^4 + d\frac{1+eH^2}{1+fH^2} \quad (4.4)$$

Optimising the zero field relaxation rate d to 190 s^{-1}, the derived parameters were $c \approx 0$ (direct mechanism), e=3.6 T^{-2} and f=70.3 T^{-2}.

Apart from the mentioned compound, Sessoli *et al.* reported the slow relaxation of the magnetization in three other vanadyl compounds, including the VO(phtalocyanine)[42], $[(Ph_4P)]_2[VO(dmit)_2]$ (dmit-1,3-dithiole-2-thione-4,5-dithiolate) [43] and $[VO(Et_2dtc)_2]$ (Et_2dtc-diethyldithiocarbamate).[44] Moreover, slow relaxation of the magnetization of a pure S=1/2 system was also reported for several mononuclear compounds containing other 3*d* metals, including two Ni(I),[45, 46] one low spin Mn(IV)[47] and one Cu(II)[48]. A rationalisation of this phenomena for the systems lacking the negative axial anisotropy was proposed by Ruiz and Luis based on their studies on the $Co^{II}(acac)_2(H_2O)_2$ complex, an effective-spin S=1/2 at the temperatures below 30 K due to the large easy-plane anisotropy.[49] According to their model mentioned in Chapter I, a combination of the hyperfine interactions (electronuclear spin entanglement) and coupling of the nuclear spins with the phonon bath leads to the relaxation pathways which are normally forbidden in the zero-field for pure S=1/2 ground state systems (van Vleck cancellation mechanism).[41, 49] In the case of the mononuclear vanadium compounds, interaction between the nuclear spin I=7/2 and the electronic spin S=1/2 converts the ground state Kramers doublet m_S=±1/2 into 16 sublevels which become separated under the applied magnetic field (Zeeeman splitting) into two states. Thus, eight phonon-induced transitions ($\Delta m_S \neq 0$, $\Delta m_I = 0$) become possible generating the non-zero changes in the magnetic moment and the slow relaxation of the magnetization.

The $\chi_M T$ product for **24b** at 300 K (5.83 cm^3 K mol^{-1}) agrees nicely with the expected one for two non-interacting high-spin manganese(III) centres (expected 6.00 cm^3 K mol^{-1} taking into account g = 2.0 and S=2). This value decreases steadily upon cooling down to 60 K (5.35 cm^3 K mol^{-1}) followed by the abrupt decline ending with 0.36 cm^3 K mol^{-1} at 2 K. Such behaviour indicates weak antiferromagnetic interactions between manganese(III) centres. Consistent with this, the highest measured value of $M/N\mu_B$ *vs* H curve (2.51 μ_B at 5 T) lies well below the expected 8 μ_B for two S=2 centres (g=2, Figure 4.14).

In attempt to quantify observed magnetic behaviour of **24b**, simultaneous fits of the experimental data ($\chi_M T$ *vs T* and $M/N\mu_B$ *vs H*) were completed using the program PHI[25] by matrix diagonalisation of the spin Hamiltonian:

$$\widehat{H} = \mu_B B \sum_i g_i \hat{S}_i + D\left(\hat{S}^2_{z_{Mn1}} - \frac{\hat{S}^2_{Mn1}}{3} + \hat{S}^2_{z_{Mn2}} - \frac{\hat{S}^2_{Mn2}}{3}\right) - 2J\left(\hat{S}_{Mn1}\hat{S}_{Mn2}\right)$$

The best model was constructed by fixing the isotropic *g* values of Mn(III) to 1.99, while fitted parameters converged to J= –0.96 cm^{-1} and D=–2.64 cm^{-1}.

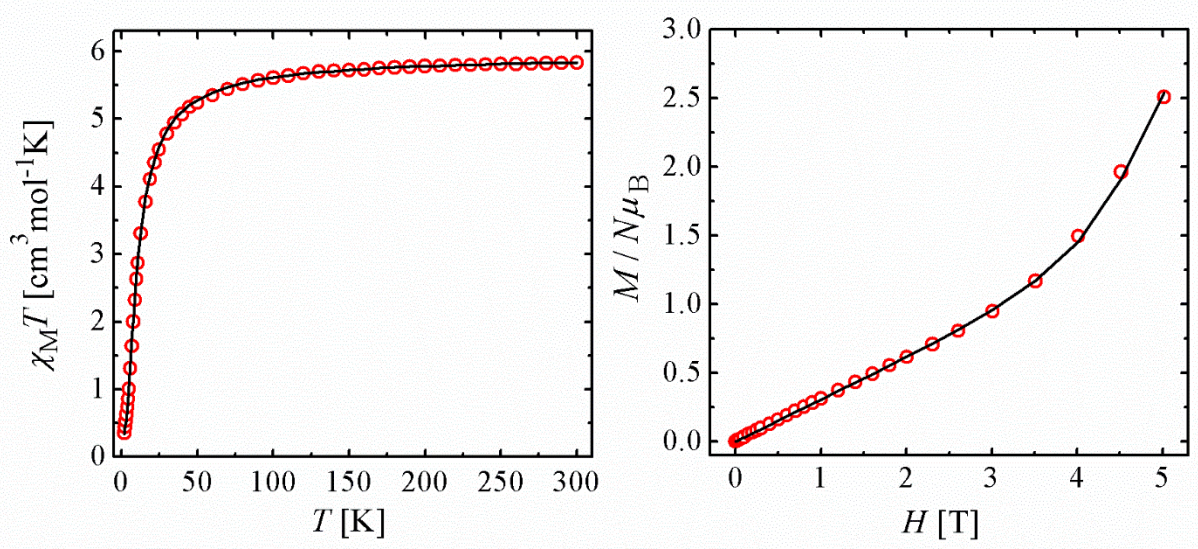

Figure 4.14: $\chi_M T$ *vs T* (left) and $M/N\mu_B$ *vs H* (right) curves of compound **24b** with the best fit (solid line). Measurement setup: warming mode (2→300 K), B = 0.3 T; T_{mag} = 2 K.

Attempt of changing the sign of axial anisotropy *D* failed to reproduce well the low temperature data, while exclusion of *J* from the model led to meaninglessly large and positive *D* parameter. Bearing in mind the presence of axially elongated crystal field around the Mn(III) centres in **24b**, $^5B_{1g}$ ground term and easy axis of magnetization are expected to occur.[24, 50] In addition, obtained *D* value agrees nicely with the reported ones for similar Mn(III) compounds ($|D| \leq 4.5$ cm^{-1}).[24] Observed antiferromagnetic coupling between the peripheral Mn(III) centres in **24b** (J=–0.96 cm^{-1}) is substantially stronger than the estimated interaction between the peripheral *S*=1/2 spin carriers in compounds **21** and **23** (J= –0.30 and –0.04 cm^{-1}, respectively) despite of similar metal-metal distances. Reason for this could be the highest planarity of metalloligand core where Mn(III) ions are perfectly embedded in two co-planar N_2O_2 coordination pockets of $(L4)^{4-}$enabling antiferromagnetic interaction through effective spin polarisation mechanism. Moreover, negative sign of *J* is characteristic for Mn(III) dimers having co-linear Jahn-Teller axis perpendicular to the bridging plane.[51, 52]

Unfortunately, almost zero magnetic moment at the lowest temperatures diminished any possibility of observing the slow relaxation of magnetization in zero or in the applied magnetic field.

4.2.5. Serendipitous efforts to generate the heterometallic compounds of H_4L4

Summarising the chemistry of the homometallic clusters incorporating H_4L4, diverse reactivity patterns were established, which unveiled a plethora of structural features, characteristic for the employed metal ion. Interestingly, only early 3*d* metal ions Mn(III) and VO(IV) showed the aimed selectivity towards the oxygen-abundant coordination environment, which could not be expanded even by increasing their molar ratio. In contrast, the late 3*d* metals (Cu^{2+}, Ni^{2+} and Co^{3+}) yielded the trinuclear coordination entities in which the coordination geometries of the metallic centres were unaffected by the differences in size and composition of the $[L4]^{4-}$ chelating sites. Encouraged by these observations, we decided to pursue the synthesis of heterometallic compounds, combining the vanadyl ion as an early 3*d* metal with copper(II) ions as its heavier partner. Application of the previously described one-pot reaction of $(L4)^{4-}$ on vanadyl-copper mixtures with the stoichiometries 1:2 and 2:1 resulted in both cases in the formation of complex mixtures of crystals. The differences in crystal forms and colours allowed their separation and individual analysis which showed that the described approach failed to produce the aimed heterometallic assemblies, since only the homometallic compounds **21** and **23** were identified (Figure 4.14). The only novelty was found in the reaction employing the VO^{2+}:Cu^{2+} stoichiometry 2:1, where a new homometallic copper(II) dimer, $(TBA)_2[Cu_2(HL4)_2]$ (**26**), was identified as a component of the mixture.

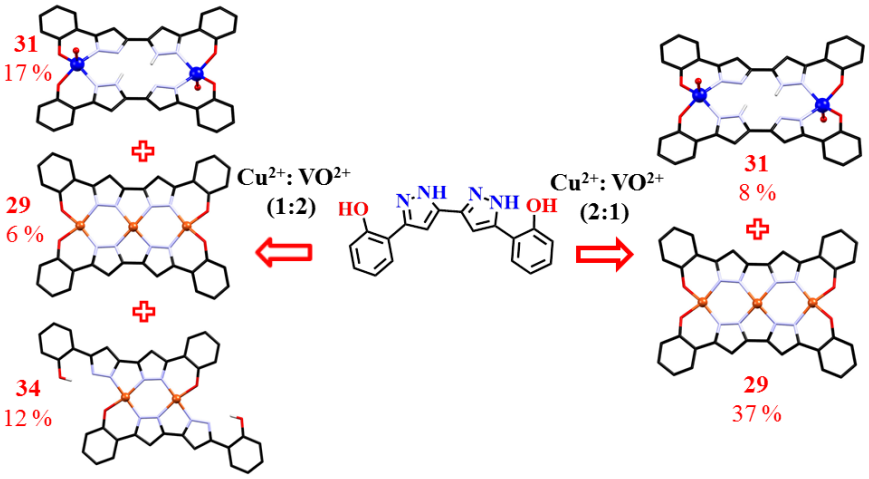

Figure 4.14: Summary of the serendipitous synthetic assays in attempts to construct the heterometallic VO-Cu assemblies. Hydrogen atoms, counter ions and solvent molecules are omitted for clarity. Percentages indicated next to the structures are the average yields of the corresponding products.

A balanced equation describing the formation of the compound **26** can be written as:

$$2\ CuCl_2 + 2\ H_4L4 + 6\ TBAOH \longrightarrow (TBA)_2[Cu_2(HL4)_2] + 4\ TBACl + 6\ H_2O$$

The crystal structure determination (monoclinic $P2_1/c$ space group, Table IV.A4) confirmed the existence of the complex anion $[Cu_2(HL4)_2]^{2-}$ and two tetrabutylammonium cations in the unit cell. Interestingly, the structure of the complex anion unveils a Cu(II) dimer coordinated equatorially by two shifted $[(HL4)^{-}]$ ligands where one terminal phenol moiety per ligand remains protonated (Figure 4.15A). Consequently, the square-planar coordination geometry around the Cu(II) centres is defined by the ON_3 ligand field, imposed by the phenolato-pyrazolato coordination pocket from one side and the bipyrazolato chelating site from the other ligand. This feature distinguishes the structure of compound **26** from the previously described homometallic entities (**21**-**25**) which hold two parallel ligands with or without a partially protonated bipyrazole moiety at the centre of the molecule (Figs. 4.14 and 4.15A). Moreover, the detected displacement of the ligating scaffold hints the possibility of using **H_4L4** to form tetranuclear linear clusters.

The Cu(II) centres of the molecule are symmetry equivalent over an inversion centre, separated by distance of 3.9145(7) Å. A slight distortion of their square-planar coordination geometry is reflected by the different Cu—N (average 1.956 Å) and Cu—O (1.894(2) Å, Table IV.A12) bond distances. Nevertheless, the metal centres are perfectly nested within the ON_3

ligand field (Cu atom to plane distance of 0.023 Å) affording the high planarity of the [Cu(μ_2–*N*–*N*)$_2$Cu] core (Cu–N–N–Cu torsion angle of 2.8(4)°). As seen previously in the structures **21**-**23**, tetrabutylammonium cations are sandwiched between the parallel anionic clusters, in the vicinity of the protonated phenol-pyrazole moiety. Apart from electrostatic interactions, each cation is connected with the neighbouring metallic platforms with four C—H···O and one C—H···N hydrogen bonding contacts. Similarly, additional stabilisation of the metallo-organic platform is achieved through the intramolecular hydrogen bonding interactions within the phenol-pyrazolato moiety (Fig. 4.15B).

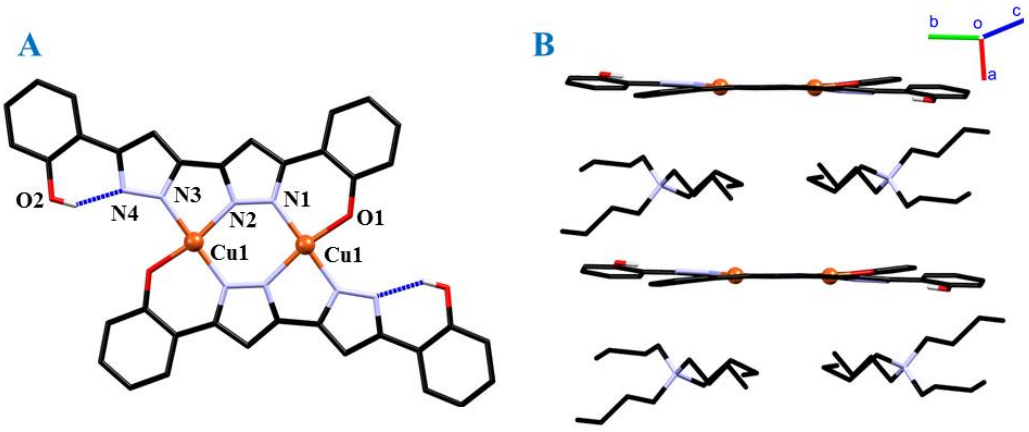

Figure 4.15: A) Molecular structure and labelling scheme of the $[Cu_2(HL4)_2]^{2-}$ anions of **26**. Only acidic protons, affecting the charge of cluster, are shown for clarity emphasizing the intramolecular hydrogen bonding interactions (blue). Apart from the copper(II) ions (orange balls), only crystallographically independent heteroatoms are labelled. B) Molecular structure of the $(TBA)_2[Cu_2(HL4)_2]$ (**26**) highlighting the distribution of the cationic-anionic layers. Hydrogen atoms are omitted for clarity.

All synthetic efforts to prepare pure compound **26** in a rational manner have been unsuccessful, limiting its characterisation. However, antiferromagnetic interaction between the Cu(II) centres was confirmed by the EPR spectroscopy on a powdered sample of crystals manually separated from the reaction mixture. The high temperature spectra (100-298 K) exhibit the characteristic half-field transitions (g=2.2 and g=1.9), which arise from the thermally populated triplet state (axial *S*=1 spectra, ΔM_s=1). Upon lowering the temperature to 50 K, the intensity of the spectral lines decreases while the new resonance centred at *g*=2.058 becomes detectable. This spectral feature corresponds to the small impurities of the compound **21** (see Fig. 4.11), attached to the crystals of **26.** Below 30 K, the resonances

of the Cu(II) dimer completely vanish since the ground state singlet becomes the only thermally available state. On the other hand, the population of the ground *S*=1/2 state of the Cu(II) trimer (**26)** grows with the increasing intensity of its resonance.

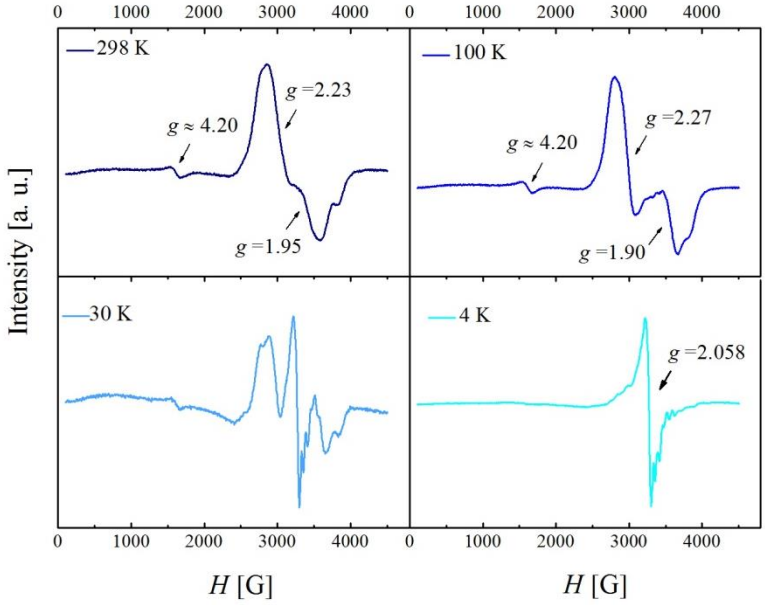

Figure 4.16: Variable temperature (4-298 K) X-band EPR spectra (*f* = 9.418 GHz) of a powdered sample of complex **26**. The intensity scale is optimised for every spectrum in order to emphasize its shape at the given temperature.

4.3. Tailored metalloligand synthetic approach with $(TBA)_2[(VO)_2(HL4)_2]$

4.3.1. Validation of the $(TBA)_2[(VO)_2(HL4)_2]$ as a potential metalloligand

The lack of success in the preparation of heterometallic compounds using the one-pot reactions led us to consider the possibility of using the dinuclear vanadyl compound $(TBA)_2[(VO)_2(HL4)_2]$ as a potential metalloligand. As mentioned before, only the vanadyl and Mn(III) compounds show the central *bis*-bipyrazole chelating pocket partially protonated and metal-free. The vanadyl compound **23** instead of the Mn(III) analogue (compound **24)** was a judicious choice because of its faster preparation (crystallisation within a week) and cleaner synthesis (the metal retains its oxidation state) with a high yield of crystalline material (>70%, Figure 4.17). Additional support for this choice was the good solubility and solution stability of this compound in a wide range of common organic solvents. A last, but equally important reason, is that vanadyl chemistry with pyrazole ligands has been poorly explored, especially on heterometallic systems, which still remain unreported.

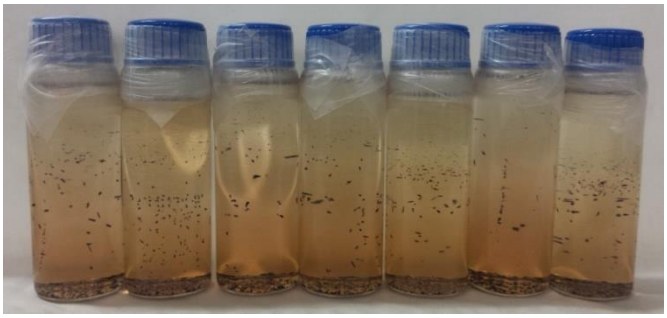

Figure 4.17: Typical crystallisation of the compound **23**.

An initial screening of compatibility between the size of the partially protonated [-*N*(*N*H)]$_2$ coordination pocket in **23** and the 3*d* metal ions was performed by analysing the crystal structures of the homometallic compounds (*vide supra*). Thus, the diagonal N−N distances within this pocket were evaluated as the best measure of the cavity size (Figure 4.18). This analysis showed that the metal-free coordination pocket in the vanadyl compound is perfectly suitable for the accommodation of Co^{3+} and Cu^{2+} ions, but remains slightly oversized for the Ni^{2+} ions. Identical tendency was found for the Mn(III) metalloligand, which holds exactly the same chelating pocket as the vanadyl dimer. Thus, no geometrical constraints prevent both bimetallic platforms to incorporate another 3*d* metal.

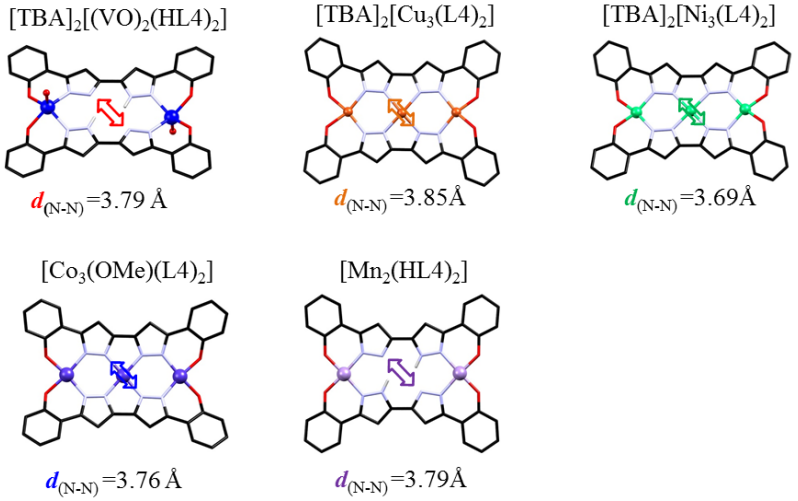

Figure 4.18: Comparison of the size of the central N_4 coordination pockets from the homometallic platforms **21**-**24**. Distances given below the structures are averaged values for all molecular forms of the compounds. Hydrogen atoms, counter ions, solvate molecules and axial ligands (except oxo atom from vanadyl ion) are omitted for clarity.

4.3.2. Heterometallic $[(VO)_2M(L4)_2]^{n-}$ assemblies: Synthetic and structural insights

In order to test the reactivity of the metalloligand **23**, different reaction setups were tried out, by varying systematically solvents, temperature of the reaction and order of addition of the reagents. Optimal conditions were found with the room temperature reaction of one equivalent of fully deprotonated metalloligand (by addition of TBAOH as base) with one equivalent of metal salt (chloride or perchlorate) in pyridine. Finally, vapour-liquid of liquid-liquid diffusion of Et_2O or hexanes into reaction mixture resulted in the formation of single crystals. In a benchmark reaction, addition of Cu^{2+} ions to deprotonated metalloligand **23** allowed the isolation of desired trinuclear compound $(TBA)_2[(VO)_2Cu(L4)_2(py)]$ (**27**):

$$CuCl_2 + (TBA)_2[(VO)_2(HL4)_2] + 2\ TBAOH + py \longrightarrow (TBA)_2[(VO)_2Cu(L4)_2(py)] + 2\ TBACl + 2\ H_2O$$

Interestingly, two slightly different crystal and molecular structures of this compound were obtained, depending on the antisolvent used in crystallisation process. The compound isolated using diethyl ether (**27**) will be described in detail since this batch was used for further measurements, while the structural features of the product obtained from hexanes layers (**27A**) will be briefly compared with the initial structure. Full crystallographic and structural details of both crystal forms are given in the tables IV.A5, IV.A13 and IV.A14 (Appendix IV).

The crystal structure of the compound **27** (monoclinic $P2_1/c$ space group) includes the complex anion $[(VO)_2Cu(L4)_2(py)]^{2-}$, two tetrabutylammonium cations and molecules of water (1) and pyridine (0.5) as crystallisation solvents. Two equivalents of the organic cations that compensate the charge of the metallo-organic platform indicate that all metal centres retain their oxidation state during the course of this reaction. The structure of the complex anion confirms the incorporation of the pentacoordinated Cu(II) ion within the equatorially disposed N_4 *bis*-bipyrazole pocket (Figure 4.19A). The square-pyramidal geometry of the metallic centre is completed with the axially bounded pyridine molecule. The peripheral vanadyl sites show the same coordination geometry which is identical in the free metalloligand, with two phenolato-pyrazolato coordination pockets in the equatorial plane and one oxo atom in the axial position. Interestingly, the $[V{=}O]^{2+}$ cations in **27** are *cis*-positioned, in the same direction as the pyridine ligand bonded to the central Cu(II) site. This is in contrast with *trans*-orientation of the metalloligand, indicating that one vanadyl centre

rotates to the other side of the organic platform during the integration of the copper(II) ion in the structure. The very distorted coordination geometry around vanadium(IV) centres is evident from short axial V=O bonds (1.602(3)-1.609(3) Å) and significantly longer equatorial V—O (average 1.930 Å) and V—N (average 2.073 Å) bonds (Table IV.A13). The strong bonding within the $[V=O]^{2+}$ oxocation causes the pyramidalisation of the coordination geometry around vanadium(IV) centres, which are positioned 0.524 Å (V2) and 0.547 Å (V1), respectively, outside the equatorial O_2N_2 plane, towards the oxo ligand (Figure 4.19B). Similarly, the distorted geometry around the copper(II) ion is mirrored by the significantly different axial and equatorial Cu−N bond lengths (2.227(3) Å and average 1.955 Å, respectively). The pyramidalisation of the ligating field expels the Cu(II) centre 0.413 Å above the equatorial plane in the direction of the pyridine ligand. Looking at the metallic core, the vanadium-copper distances are 3.9089(8) Å and 3.8609(8) Å, while the linear alignment of the centres is revealed through the V−Cu−V angle of 175.10(2)°. Because of the *cis* orientation, the distance between the peripheral vanadyl cations (7.763(1) Å) is shorter in comparison with the structure of the metalloligand. The alternation between the anionic $[(VO)_2Cu(L4)_2]^{2-}$ and the cationic TBA^+ layers shapes the crystal structure of this compound. The alkyl cations are hydrogen bonded *via* numerous C−H···π and C−H···O contacts with the oxocation $[V2=O]^{2+}$, the pyrazolate and the phenolate moieties of the metallic platform. Similarly, interactions between neighbouring platforms are established through the C−H···O contacts between the vanadyl groups (V1) and axially bounded pyridine molecules, strengthened additionally with the π···π stacking between the axial pyridine ligands. Crystallisation water molecules stabilise the crystal structure as mediators of a hydrogen bonded network between the *bis*-phenolato moieties (proximity of V1) and the pyrazole rings from the neighbouring complex anions. Consequently, perpendicular layers of π···π stacked anionic clusters are formed (Figure 4.19C). The remaining pyridine molecules fill the voids between the charged layers and interact weakly with their components.

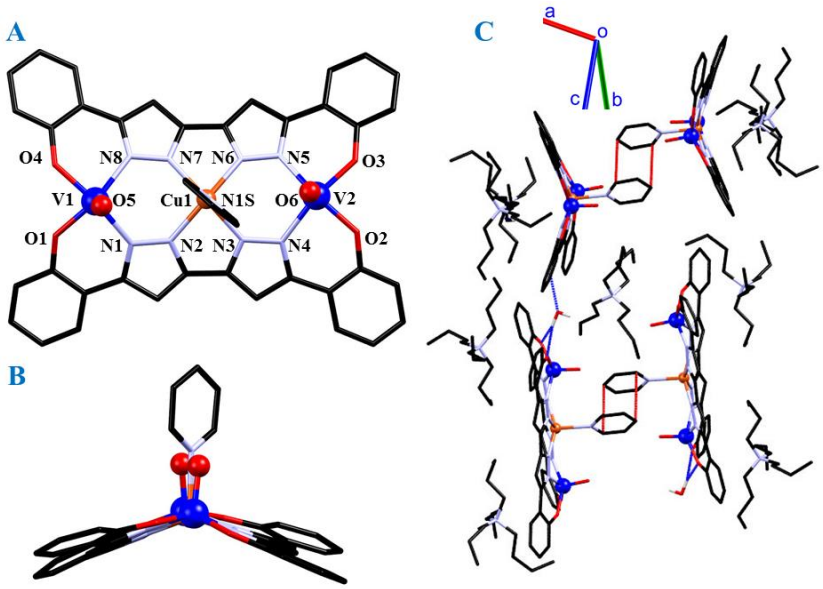

Figure 4.19: A) Molecular structure and labelling scheme of the $[(VO)_2Cu(L4)_2]^{2-}$ anions. Vanadyl centres are shown as blue (V) and red (O) balls, while the copper(II) ion is shown as orange ball. B) Side view of the $[(VO)_2Cu(L4)_2]^{2-}$ anions highlighting the *cis*-orientation of the axial ligands and the pyramidalisation of the metallic core. C) Crystal structure of the compound **23** emphasizing the distribution of cationic-anionic layers. π···π stacking between pyridine ligands from the neighbouring anionic clusters is shown with red lines, while the hydrogen bonding network mediated by the crystallisation water molecule is shown with blue lines. Hydrogen atoms (except from the water molecule) are omitted for clarity.

As mentioned earlier, another molecular form of this compound was obtained when hexanes were used as antisolvent. The crystal structure of **27A** (orthorhombic *Pbca* space group) exposes two crystallographically distinct $[(VO)_2Cu(L4)_2(py)]^{2-}$ anions, four TBA^+ counterions and a pyridine-water (2:1) mixture of crystallisation solvents. The coordination geometries in both anionic forms are essentially the same as in **27**, with a trinuclear [VO−Cu−VO] metallic core chelated with two equatorially disposed $(L4)^{4-}$ ligands and with an axially bonded pyridine ligand (Cu). Another common feature is the *cis*-orientation of vanadyl cations in the same direction as the axial Cu−N bond (Figure 4.20).

The geometry around the vanadium(IV) centres reveals two sets of axial V=O bonds: one molecular form maintains the usual range observed in **23** and **27** (1.608(2)-1.610(3) Å: V3 and V4), while the other unveils slightly elongated $[V=O]^{2+}$ cations (1.612(2)-1.623(3) Å: V1 and V2). On the other hand, the equatorial V—O (average 1.927 Å) and V—N (average 2.082

Å) bonds are within the usual range (Table IV.A14). As expected, weaker bonding within $[V{=}O]^{2+}$ oxocation reduces the pyramidalisation of the coordination geometry around vanadium(IV) centres as can be seen from the metal-equatorial O_2N_2 plane distances of 0.519 Å (V1), 0.497 Å (V2), 0.535 Å (V3) and 0.550 Å (V4). The distorted geometry around the crystallographically inequivalent copper(II) centres reveals also two sets of axial Cu−N bond lengths (2.206(3) and 2.293(3) Å for Cu2 and Cu1, respectively). On the other hand, the equatorial Cu−N bond distances exhibit only minor differences with average lengths of 1.947 (Cu1) and 1.962 Å (Cu2). Like for the vanadyl centres, longer axial bonding on the Cu(II) sites results in smaller pyramidalisation of its coordination geometry as seen from the metal-equatorial O_2N_2 plane distances of 0.260 Å (Cu1) and 0.383 Å (Cu2). The differences described affect the linearity of the metallic core, which is nicely reflected with the V−Cu−V angles of 176.08(2)° (V1−Cu1−V2) and 178.74(2)° (V3−Cu2−V4). The molecular building blocks assemble within the crystal structure in a similar manner as in **27**. Apart from electrostatic attraction, the alternation of positively and negatively charged layers stabilises the structure with a plethora of hydrogen bonding contacts between the alkyl chain of the TBA^+ and the heteroatoms or the π-clouds of the complex anions. Interestingly, crystallisation pyridine and water molecules reside only in the vicinity of the *bis*-phenolato moieties belonging to the $[V3{-}Cu2{-}V4]^{2-}$ anion, while the periphery of remaining $[(VO)_2Cu(L4)_2(py)]^{2-}$ anion remains hydrogen bonded only with the TBA^+ cations.

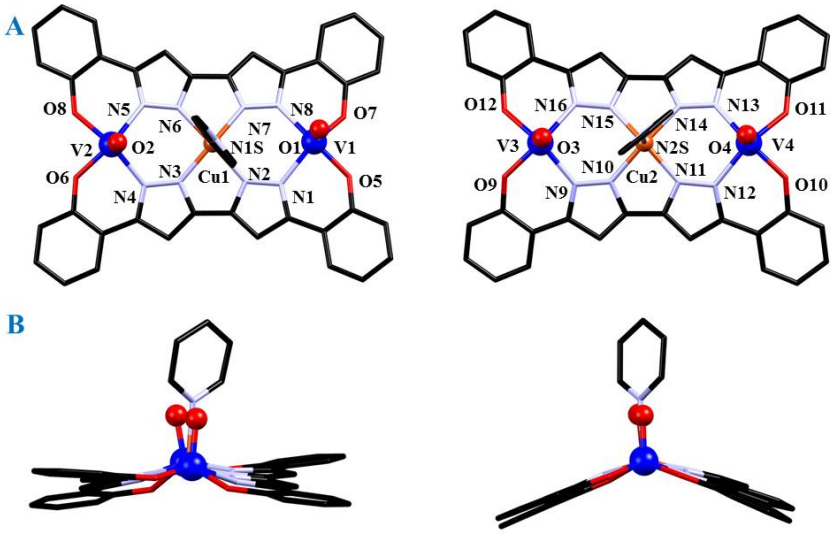

Figure 4.20: A) Molecular structure and labelling scheme of two crystallographically independent $[(VO)_2Cu(L4)_2]^{2-}$ anions. Vanadyl centres are shown as blue (V) and red (O) balls, while the copper(II)

ion is shown as orange ball. B) Side view of the $[(VO)_2Cu(L4)_2]^{2-}$ anions highlighting the *cis*-orientation of the axial ligands and the pyramidalisation of the metallic core.

Following the successful incorporation of the copper(II) ions within the vanadyl metalloligand, a similar reaction was tried out with nickel(II). Unfortunately, crystals of the targeted $(TBA)_2[(VO)_2Ni(L4)_2]$ compound could not be isolated, despite several synthetic attempts. In fact, the only crystals obtained from these reactions correspond to the starting reagent $(TBA)_2[(VO)_2(HL4)_2]$. This is likely because of the mismatch in size between the N_4 cavity and the Ni^{2+} ion. Unlike Cu^{2+}, nickel(II) ions favour coordination numbers four and six since those arrangements maximise the crystal field stabilisation energy of a $3d^8$ ion. In the former case, the N_4 chelating pocket of the metalloligand is slightly oversized for the square-planar Ni(II), while under the latter circumstances the octahedral Ni(II) doesn't fit inside the cavity.

Apart from the divalent 3*d* metals, one-pot synthesis has shown that the Co(III) ions are also easily nested within the almost identical *bis*-bipyrazole moiety as the one found in the vanadyl compound (Figure 4.17). Thus, the room temperature reaction involving the cobalt(II) salt (chloride or perchlorate) and compound **23** resulted with the one-electron oxidation of the metal centre, leading to the formation of orange crystals of the compound $(TBA)[(VO)_2Co(L4)_2(py)_2]$. Unfortunately, the size and the thickness of the needle-like crystals hampered the collection of good quality structural data. However, a detailed characterisation of the obtained compound (EA, EPR, mass spectrometry) confirmed undoubtedly the accuracy of the formula $(TBA)[(VO)_2Co(L4)_2(py)_2]$.

4.3.3. Heterometallic $[(VO)_2M(L4)_2]^{n-}$ assemblies: Solution studies

The stability of the clusters **27** and $(TBA)[(VO)_2Co(L4)_2(py)_2]$ in solution was investigated by electrospray ionization (ESI) mass spectrometry. Similarly to homometallic compounds **21**-**23**, the ESI(+) spectrogram of the solution of **27** in acetonitrile confirms the presence of the tetrabutylammonium cation (m/z=242.28; Figure IV.A12). On the other hand, negative ion electrospray ionization, ESI(−), confirms the integrity of the heterometallic $[(VO)_2Cu]$ cluster as witnessed by the peaks found at m/z=412.48 corresponding to $[(VO)_2Cu(L4)_2]^{2-}$ and m/z=825.98 (less intense) for $\{[(VO)_2Cu(L4)_2]^{2-}+H^+\}$ (Figure IV.A10). The isotopic distribution of these peaks coincides nicely with the theoretically expected, confirming the cluster

integrity and its heterometallic composition (Figure IV.A12). Similarly, the ESI(−) spectrogram of the acetonitrile solution containing the compound (TBA)[$(VO)_2Co(L4)_2(py)_2$] confirms the existence and the integrity of the $[(VO)_2Co(L4)_2]^-$ anion (m/z=820.97, Figure IV.A11). The isotopic distribution of this signal perfectly matches the theoretically predicted one for the heterometallic composition. The positive mode of the spectrogram reveals the expected TBA^+ counter ions (m/z=242.28), as well as the positively charged, protonated forms of the cluster identified as $\{[(VO)_2Co(L4)_2(py)]^-+2H^+\}^+$ (m/z=902.03) and $\{[(VO)_2Co(L4)_2(py)_2]^-+2H^+\}^+$ (m/z=981.07, Figure IV.A13). These findings collectively confirm the successful integration of the Co(III) ion within the metalloligand **23**.

Paramagnetic ^1H NMR spectroscopy of **27** confirmed additionally the integrity of this cluster in acetonitrile solution. Observed spectral window includes 15 detectable signals distributed in wide range from δ=-4.20 ppm to δ=25.95 ppm. Four diamagnetic peaks spread between 0.97 ppm and 3.09 ppm correspond to the tetrabutylammonium cations, judging by their intensity and chemical shift. Similarly, release of the lattice pyridine molecules gives rise to three diamagnetic signals found at δ=7.34, 7.75 and 8.59 ppm. In both cases, resolution of the representative spectral features is reduced to singlets, lacking any coupling pattern between the inequivalent protons due to paramagnetic nature of the solution.[53] Remaining signals belong to the chemically inequivalent protons from $\mathbf{L_4}^{4-}$ (five signals) and one pyridine molecule bonded to Cu^{II} (three signals). Those features, together with the detected large linebroadening of the peaks, indicate that the paramagnetic $[(VO)_2Cu]$ core of the cluster remains preserved in the solution.[53, 54] Fast nuclear relaxation and related low signal to noise ratio obstructed the correct assignment of these spectral features to corresponding protons, although extracted integrals hint that two broadest peripheral signals (δ=-4.20 and 25.95 ppm) arise from the axially bonded pyridine molecule at the Cu^{II} site.[55]

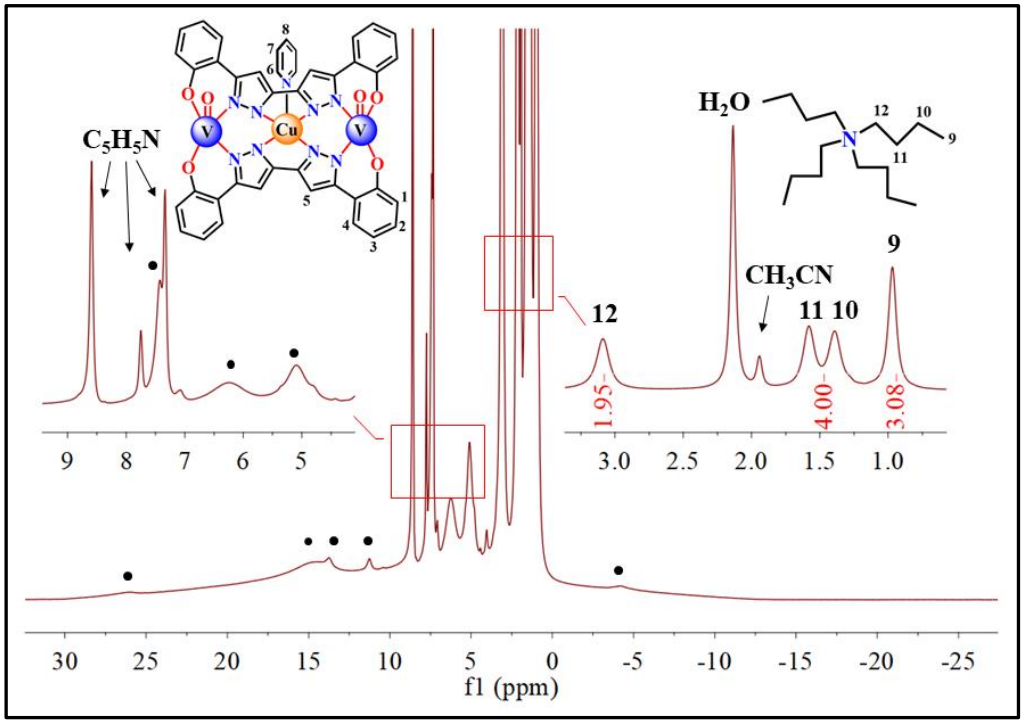

Figure 4.21: ^{1}H NMR of compound **27** in CD_3CN. Highlighted signals (●) represent the chemically inequivalent protons (1-8) of $[(VO)_2Cu(L4)_2]^{2-}$ anion in **27**. Numbered signals (9-12) correspond to the inequivalent protons from diamagnetic tetrabutylammonium cations while their integrals are shown in red.

4.3.4. Heterometallic $[(VO)_2M(L4)_2]^{n-}$ assemblies: Magnetic studies

The room temperature value of the $\chi_M T$ product of **27** (1.19 cm^3 K mol^{-1} at 300 K) is slightly higher than expected (1.125 cm^3 K mol^{-1}, g = 2.0) for three non-interacting S=1/2 centres. Upon lowering the temperature, the initial Curie behaviour (80-300 K) is succeeded by the rapid rise of $\chi_M T$ to a maximum of 1.76 cm^3 K mol^{-1}, reached at 5 K (Figure 4.21). This indicates the existence of moderate ferromagnetic interactions between the vanadyl and the copper ions. Below 3 K, a small drop of $\chi_M T$ is detectable, ending at 1.66 cm^3 K mol^{-1} (2 K), which likely arises from the zero-field splitting effects. Consistent with the ferromagnetic coupling, the highest value of the $M/N\mu_B$ *vs* H curve (2.93 μ_B at 5 T) lies very close to the expected 3 μ_B for the S=3/2 (g=2) ground state of the cluster.

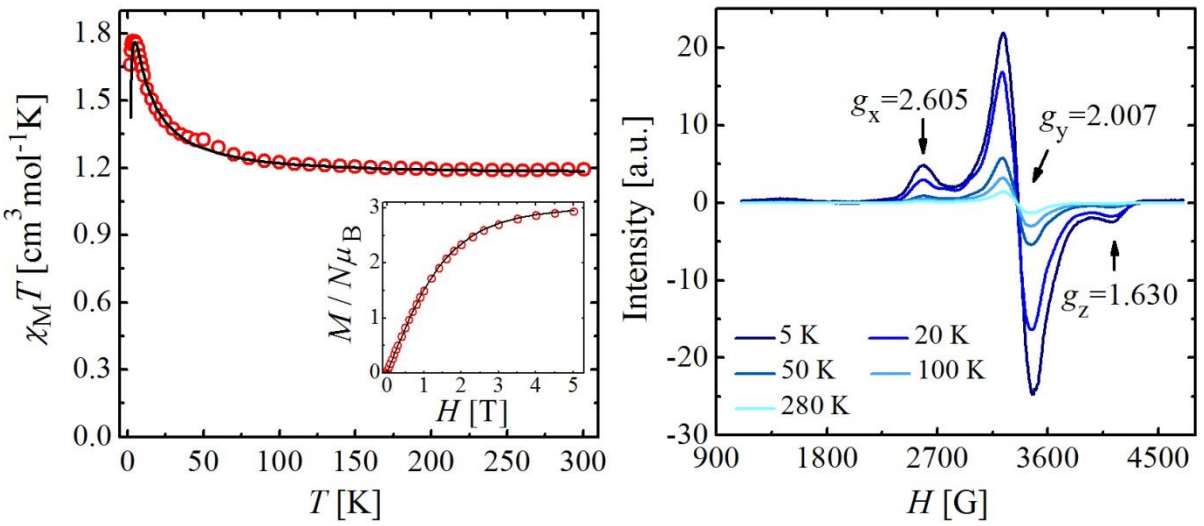

Figure 4.21: *Left:* $\chi_M T$ *vs T* and $M/N\mu_B$ *vs H* (inset) curves of compound **27** with the best fit (solid line). Measurement setup: warming mode (2→300 K), B = 1 T; T_{mag} = 2 K. *Right:* Variable temperature (4-280 K) X-band EPR spectra (f = 9.418 GHz) of a powdered sample of complex **27**.

Ferromagnetic interactions between the spin carriers were modelled by fitting the experimental data ($\chi_M T$ *vs T* and $M/N\mu_B$ *vs H*) to the isotropic Heisenberg-Dirac-Van Vleck spin Hamiltonian (PHI[25]):

$$\hat{H} = \mu_B B \sum_i g_i \hat{S}_i - 2J\left(\hat{S}_1\hat{S}_2 + \hat{S}_2\hat{S}_3\right) \quad (4.5)$$

The first term of this expression includes the Zeeman splitting, while the second one defines the interaction (J) between the peripheral vanadyl ions ($\hat{S}_1$ and $\hat{S}_3$) and the central Cu(II) ion ($\hat{S}_2$). Additional models involving the interaction between the peripheral vanadyl ions were also considered (see Eq 4.1.b) and discarded after giving unreasonable values for parameters J and J_1 (sign and magnitude). Thus, by fixing the g values of the individual ions to 2.00 (V^{4+}) and 2.05 (Cu^{2+}) the optimised model included the exchange constant J=6.54 cm^{-1} and small ferromagnetic intermolecular interaction of zJ=0.025 cm^{-1}. The latter interaction is probably established between the perpendicular layers of clusters assembled in a hydrogen bonding network via the crystallisation water molecules (*vide supra*). Interestingly, the existence of ferromagnetic interactions within the heterometallic $[(VO)_2Cu]$ core is in contrast with to the homometallic derivatives, in which antiferromagnetic interactions were detected, ranging from very weak (**23**, $[(VO)_2]$ to strong

(**21**, [Cu_3]). The antiferromagnetic interactions for homometallic compounds can be easily rationalised as the superexchange interaction where the molecular orbitals of ligands increase the overlap between the magnetic orbitals of the metal centres of the same symmetry (d_{x2-y2} for Cu(II) and d_{xy} for V(IV), respectively, Figure 4.21). On the other hand, the switch of the magnetic response for the heterometallic [$(VO)_2Cu$] complex arises from the fact that the molecular orbitals of ligands (sp^2 or 2*p* on N) cannot mediate an overlap between the orthogonal d_{xy} and d_{x2-y2} orbitals of the vanadyl and the Cu(II) centres, respectively (Figure 4.22). While the lobes of the d_{x2-y2} orbitals on the Cu(II) site coincide with the equatorial σ bonding, the lobes of the vanadyl d_{xy} orbitals are rotated by 45° with respect to d_{x2-y2} orbitals of Cu(II), meaning that they are localised exactly in between the equatorial bonds of the vanadyl centres. Therefore, the overlap integral between the two metallic sites is ≈0, thus the only contribution to this interaction can only be ferromagnetic. Evidently, the absolute values of the coupling constants for those compounds decrease in the order $|J_{CuCu}$, **21**$|>>|$ J_{CuVO}, **27**$|>|J_{VOVO}$, **23**$|\approx 0$. As mentioned earlier, the coupling strength for the *bis*-pyrazolato bridged Cu(II) dimers is correlated with the higher planarity of the [Cu(μ–*N*–*N*)$_2$Cu] core. On the other hand, magneto-structural correlations for ferromagnetically coupled Cu(II)-VO(IV) dimers are still unclear. In this context, the distance between the metals and the dihedral angle between their equatorial planes are the most commonly discussed factors.[56-60]

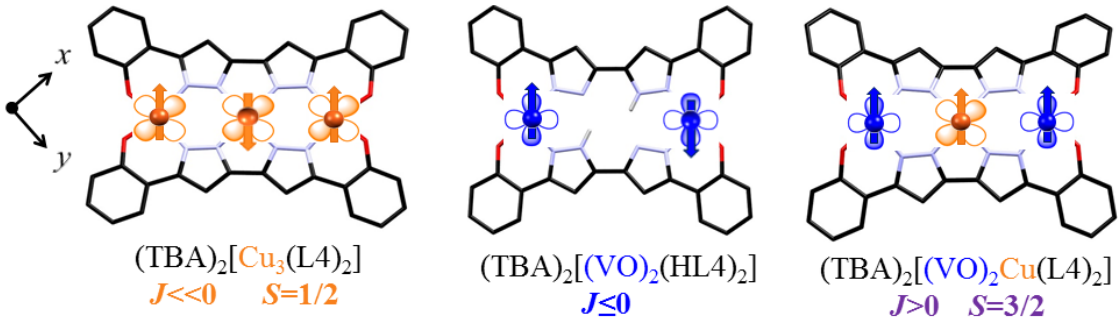

Figure 4.22: Rationalisation of the magnetic behaviour of compounds **21** (left), **23** (middle) and **27** (right) using the orbital symmetry model. Magnetic orbitals of the metal centres are highlighted with the schematic spin orientations emphasizing the nature of the coupling. Hydrogen atoms are omitted from the anionic clusters, except the ones affecting its charge and metal distribution. Axial ligands, counter ions and solvate molecules are omitted for clarity.

As emphasized in Chapter I, the principle of the strict orthogonality between magnetic orbitals was first employed by Olivier Kahn in a design of the first predictable ferromagnetic exchange in molecular magnets.[58, 59] These studies were focused on a tailored heterodinuclear Cu-VO compound incorporating the metallic core with edge sharing (O, O) square-pyramidal geometries. Strict orthogonality between the magnetic orbitals within the dimeric core allowed the observation of strong ferromagnetic interaction (J_{CuVO}=118 cm^{-1}; $\widehat{H} = -J\hat{S}_1\hat{S}_2$). Although Hatfield and Hodgson reported previously the ferromagnetism for the family of *bis*-hydroxo-bridged Cu(II) dimers (accidental orthogonality for Cu−O−Cu angles<97.5°)[61], the beauty of Kahn's approach comes from the fact that the strict orthogonality between the magnetic orbitals of two bridged metal centres implies the completely predictable ferromagnetism which cannot be hampered by the geometrical constraints of the molecule. The validity of this principle for the family of *bis*-oxo bridged Cu-VO compounds within the Schiff base scaffold was confirmed by the dimer published by Glaser[57] (J_{VOCu}=45.6 cm^{-1}; $\widehat{H} = -2J\hat{S}_1\hat{S}_2$) and by Cu-VO-Cu trimer studied by Bencini[56] (J_{VOCu1}=0 ± 5 cm^{-1} and J_{VOCu2}=42.5 ± 0.5 cm^{-1}; $\widehat{H} = -2J\hat{S}_1\hat{S}_2$). Similarly, Hoffman used the Schiff base−porphyrazine ligand holding two separate ligating sets of donors to promote the orthogonality between the Cu(II) and VO(IV) sites (J_{VOCu}=9.6 cm^{-1}; $\widehat{H} = -J\hat{S}_1\hat{S}_2$).[62] This idea was expanded in Glaser's work, where the judicious design of the β-diketimineamid ligand imposed the topological orthogonality between the magnetic orbitals in homometallic Cu(II) dimer (J_{CuCu}=4.8 cm^{-1}).[57] Nag *et al.* extended the family of the heterobimetallic VO-M to the late 3*d* metals (M=Cu^{2+}, Ni^{2+}, Co^{2+}, Fe^{2+} and Mn^{2+}), establishing the ferromagnetic exchange interactions for all dimers (J_{VOCu}=42.5 cm^{-1}> J_{VONi}=12.0 cm^{-1}> J_{VOCo}= J_{VOFe}= 4.4 cm^{-1} $\widehat{H} = -2J\hat{S}_1\hat{S}_2$), except the VO-Mn ($J_{VOMn}$=−14.2 cm^{-1}).[60]

As expected, comparison between the reported interactions and the values obtained here for J_{CuVO} indicates that the monoatomic *bis*-oxo bridges mediate a stronger coupling between the metal centres than the diatomic *N-N* moieties from the pyrazole ligands (smaller Cu-VO distances, stronger coupling). Similarly, ferromagnetic interactions in **27** are slightly reduced by the non-zero dihedral angles (6.90° and 9.35°) between the equatorial planes of the Cu(II) and VO(II) sites.

Variable temperature EPR spectroscopy (X-band) for the compound (TBA)[$(VO)_2Co(L4)_2(py)_2$] revealed an isotropic spectrum with one broad resonance centred at g=2.011 (Figure 4.24). Since the electronic structure of the octahedral Co(III) ions defines a diamagnetic ground state ($3d^6$ configuration), no significant coupling between the peripheral vanadyl centres should exist. Thus, the observed resonance corresponds to ΔM_s=1 transitions within the S=1/2 ground state of the peripheral vanadyl ions. The intensity of the spectra increases continuously upon lowering the temperature as expected from the Curie Law. Furthermore, the absence of any hyperfine structure arising from the interaction with ^{51}V nuclei (I=7/2) is likely the consequence of intermolecular dipole-dipole interactions, which causes a line broadening. The value of the $\chi_M T$ product at room temperature (0.79 cm^3 K mol^{-1} at 300 K) agrees with the presence of the two paramagnetic S=1/2 centres within the molecule, corroborating the diamagnetic nature of the integrated Co(III) ion.

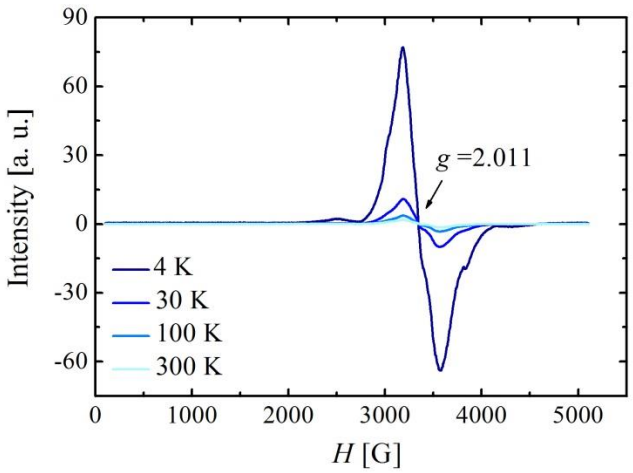

Figure 4.24: Variable temperature (4-300 K) X-band EPR spectra (f = 9.418 GHz) of a powdered sample of compound (TBA)[$(VO)_2Co(L4)_2(py)_2$].

4.3.5. Linking the heterometallic $[(VO)_2M(L4)_2]^{n-}$ assemblies using the vanadyl ions

Pursuit of the optimised synthetic procedures employing the metalloligand **23** in the base-free conditions produced another family of the heterometallic systems, generally formulated as $\{[(VO)_2M1(L4)_2]\text{-}M2\}_2$. Thus, the room temperature reaction in pyridine between one equivalent of **23** and two equivalents of the metal salt (perchlorate) resulted with clear solutions, from which the single-crystals were grown upon vapour-liquid diffusion

of Et_2O. Starting from the addition of the Cu(II) ions, the obtained compound was identified as $\{[(VO)_2Cu(L4)_2(py)_3]\text{-}\ M(py)_4\}_2$ (**28**):

$$4\ Cu(ClO_4)_2 + 2\ (TBA)_2[(VO)_2(HL4)_2] + 18\ py \longrightarrow \{[(VO)_2Cu(L4)_2(py)_3]\text{-}Cu(py)_4\}_2 + 4\ TBAClO_4 + 4\ (py\text{-}H^+)ClO_4$$

As it can be seen from this equation, basic pyridine medium allows the incorporation of the Cu(II) ions within the structure of the metalloligand by facilitating the removal of the acidic pyrazole protons. Structural analysis of the compound **28** (triclinic *P*-1 space group) revealed the unit cell composed of one discrete $\{[(VO)_2Cu(L4)_2(py)_3]\text{-}\ M(py)_4\}_2$ molecule accompanied by the twelve pyridine and two water molecules as the crystallisation solvents, while half of the content describes the asymmetric unit. Molecular structure of the octanuclear cluster can be visualised as two $[(VO)_2Cu(L4)_2(py)_3]$ platforms engaging its oxocation sites to sandwich two central $Cu(py)_4$ units in the heart of the structure. Therefore, the first equivalent of the Cu(II) ions fills the N_4 coordination pocket of the metalloligand delivering the $[(VO)_2Cu(L4)_2(py)_3]$ unit as the one seen in the compound **27**, while the second one serves as a linker which gathers two of these units into larger cluster. This structural expansion originates from the donor ability of the oxocation which allows the formation of the V=O−M structural synthons as the key connecting feature.

Structure and the topology of the $[(VO)_2Cu(L4)_2(py)_3]$ platforms differ from the compound **27** by the coordination geometry around the metals, since both vanadyl cations adopt the octahedral geometry upon coordination of additional pyridine molecule. Hence, each platform involves one square pyramidal Cu(II) ion residing in 'N_5' ligand field and two vanadyl ion positioned in the 'N_3O_3' ligand field. Bonding details of the Cu(II) site reveal the average Cu−N bond distance of 1.958 Å for the equatorial sites and the significantly elongated axial bond with the pyridine molecule of 2.361(3) Å. In comparison with the structure of the compound **27**, the equatorial bonds are perfectly maintained, while the axial Cu−N bonds have expanded for 0.134 Å, reducing the pyramidalisation of the coordination geometry (distance between the Cu(II) ion and the equatorial 'N_4' plane of 0.168 Å). Bonding details around the vanadyl centres reveal the average equatorial V−O bond distances of 1.933 Å and the V−N bond distances of 2.112 Å, while the axial $[VO]^{2+}$ moieties measure 1.631 Å. Similarly to the Cu(II) site, axial bonding with the pyridine molecule is significantly weaker averaging at 2.405 Å. In comparison with the free

metalloligand, slight elongation of the V=O bonds (average 0.03 Å) and the slight contraction of the equatorial V−O bonds (average −0.02 Å) are observed upon the formation of the V=O−Cu synthon. Additionally, reduced pyramidalisation of the coordination environment around the vanadium(IV) is reflected through the averaged distance from the equatorial donor plane of 0.29 Å. On the other hand, geometry around the connecting Cu(II) ions is axially elongated octahedral, shaped by the 'N_4O_2' ligand field involving the Cu2−O(=V) bonds at the axial sites and the four Cu2−N_{py} bonds in the equatorial plane. Strong Jahn-Teller distortion is mirrored in the existence of the long axial Cu2−O bond distances averaged at 2.521 Å, while the equatorial Cu2−N bond distances average at 2.032 Å. Square topology of the metallic core is reflected in almost linear V1−Cu1−V2 angles of 168.43(2)° at the platform edge and 175.00(2)° at the V1−Cu2−V2 linkage. Moreover, Cu···V distances in both directions are very similar, averaging at 4.015 Å within the platform and 4.141 Å for the axial linkage with the Cu(py)$_4$ fragment.

Molecular structure of the compound **28** is stabilised with three intramolecular C−H···O hydrogen bonding interactions between the pyridine molecules coordinated on Cu2 site and the *bis*-phenolato coordination pocket in the vicinity of the vanadium ions. Additionally, crystallisation water molecule takes part in six hydrogen bonding contacts, half as the hydrogen donor (two O−H···O and O−H···N) with the phenolic moiety of cluster and the solvate pyridine molecule and the other half as the hydrogen acceptor (three C−H···O) from the coordinated pyridine molecules on Cu2 site and the crystallisation pyridine molecule. Apart from this, C−H···π contacts established between the axially bonded pyridine ligands from the [$(VO)_2$Cu] platform and the phenolic or pyrazole aromatic cores of the neighbouring clusters organise the molecules into parallel layers. Similarly, twelve solvate pyridine molecules are engaged in numerous C−H···π and π···π contacts with the cluster components.

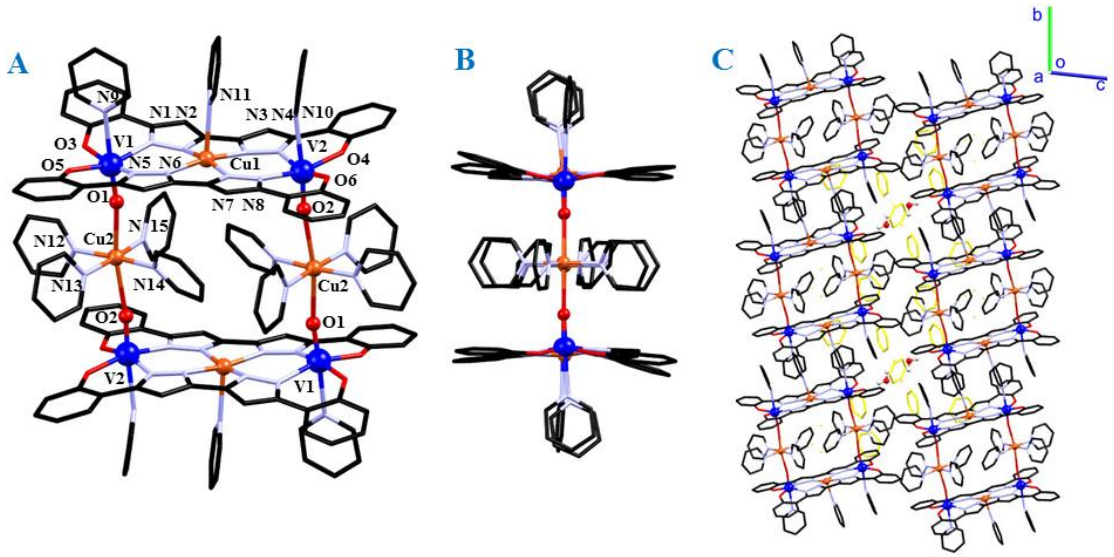

Figure 4.25: A) Molecular structure and labelling scheme of the compound **28**. Vanadyl centres are shown as blue (V) and red (O) balls, while the copper(II) ion is shown as orange ball. B) Side view of the cluster **28** highlighting the planarity of the metallic core. C) Crystal structure of the compound **28** emphasizing the formation of parallel layers of molecules with voids for the solvate pyridine (yellow) and water molecules. Hydrogen atoms (except from the water molecule) are omitted for clarity.

This linkage is commonly found in the the polyoxovanadate systems, where decoration with the metal ions through the V=O−M bonding reduces the negative charge of the system. However, similar bonding is very rarely present in coordination compounds involving the discrete vanadyl ions.

Application of the same synthetic procedure on the Ni(II) ions resulted with the formation of a slightly different compound, formulated as $\{[(VO)_2Ni(L4)_2(py)_2]\text{-}Ni(py)_3\}_2{-}C_4H_4N_2$ (**29**). However, the success of the initial reaction was limited by the low yield (<5%) and appearance of only few crystals. As the given formula of the compound **29** indicates, Ni(II) derivative incorporates in its structure one molecule of the pyrazine which appears in the reaction mixture as the small impurity in the commercially available pyridine solvent (<0.01%). Indeed, deliberate addition of the pyrazine (average 1 mg per 5 mg of the metalloligand) resulted with the formation of the same compound in the enormously incremented yield (56-59 %). Thus, optimised synthetic procedure describing the formation of the compound **29** can be written:

$$4\ Ni(ClO_4)_2 + 2\ (TBA)_2[(VO)_2(HL4)_2] + 14py + C_4H_4N_2 \longrightarrow \{[(VO)_2Ni(L4)_2(py)_2]\text{-}Ni(py)_3\}_2\text{-}C_4H_4N_2 + 4\ TBAClO_4 + 4\ (py\text{-}H^+)ClO_4$$

Crystallographic analysis of the obtained crystals (triclinic *P*-1 space group) disclosed the unit cell composed of one $\{[(VO)_2Cu(L4)_2(py)_2]\text{-}M(py)_3\}_2{-}C_4H_4N_2$ molecule and pyridine-Et_2O mixture of the crystallisation solvents in the non-integer ratio of 6.77:2.23 due to the occupational disorder. Molecular structure of the heterometallic cluster consists of two $[(VO)_2Ni(L4)_2(py)_2]$ platforms linked by two pyrazine bridged $Ni(py)_3$ units. Essentially, the structure of the compound **29** is identical to the previously seen **28** with the only major difference arising from the composition of linkages, where two $Cu(py)_4$ fragments are replaced with one $[Ni(py)_3]_2\text{-}(C_4H_4N_2)$.

Structure of the $[(VO)_2Ni(L4)_2(py)_2]$ platforms incorporates two octahedral vanadyl centres placed in the 'N_3O_3' ligand field and one square-planar Ni(II) centre in the *bis*-bipyrazole 'N_4' ligand field. Bonding details of the Ni(II) site reveal the average Ni1−N bond distance of 1.884 Å, similar to the homometallic Ni_3 compound **22** (1.843 Å) and significantly shorter in comparison with the Cu1 site in the structure of **28** (1.958 Å). Consequently, Ni(II) ion is perfectly incorporated in the ligand plane (metal to plane distance of 0.064 Å).

On the other hand, the coordination geometry of the vanadyl centres is similar to the one in compound **28**, with the average equatorial V−O bond distances of 1.933 Å and the V−N bond distances of 2.077 Å, while the axial $[VO]^{2+}$ moieties are slightly elongated to 1.642 Å. Consequently, the *trans* effect of the oxo group is reduced allowing the stronger axial bonding of the pyridine molecule (average 2.377 Å). Following the established tendency, formation of the V=O−Ni connectivity results with the slight elongation of the V=O bonds (average 0.04 Å), accompanied with the slight contraction of the equatorial V−O bonds (average −0.02 Å) and reduction of the pyramidalisation (0.314 Å). Octahedral geometry of the 'N_4O_2' ligand field around the connecting Ni2 ions outlines the average axial Ni2−O bond distances of 2.078 Å and the average equatorial Ni2−N bond distances average of 2.100 Å. Nonetheless, it should be mentioned that the Ni−N bond with the bridging pyrazine ligand is slightly weaker than those with the pyridine ligands (0.05 Å longer). Metallic $Ni_4(VO)_4$ core adopts the slightly distorted square topology in which the platform edge maintains the same geometry as in **28** defined with the V1−Ni1−V2 angles of 165.20(1)° while the

V1−Ni2−V2 linkage becomes slightly bent with the angle of 168.44(2)°. Average intermetallic distances for the V···Ni1 and the V···Ni2 edges are 3.928 Å and 3.683 Å, respectively.

Intramolecular stabilisation of the cluster **29** is achieved with six intramolecular C−H···O hydrogen bonding interactions between the pyridine molecules from the $[Ni(py)_3]_2$-$(C_4H_4N_2)$. and the *bis*-phenolato coordination pocket in the vicinity of the vanadium ions. Additionally, this unit is hydrogen bonded with the Et_2O molecule from the crystallisation solvent. Similarly to the compound **28**, C−H···π and π···π contacts between the pyridine ligands on the vanadyl sites of the neighbouring clusters organise the molecules into parallel chains. Such arrangement opens up the voids in the structure where pyridine and Et_2O molecules reside interacting with the aromatic scaffold of the cluster **29**.

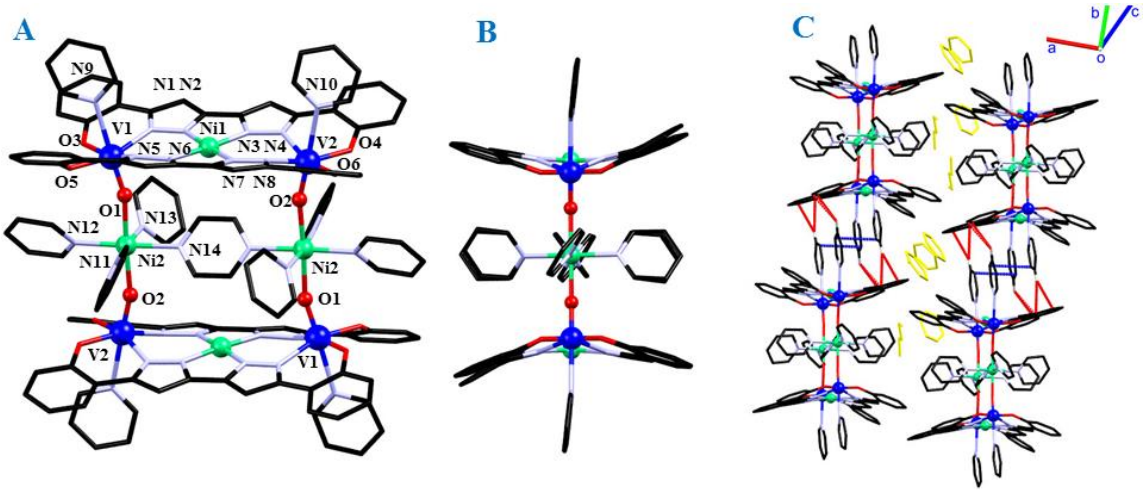

Figure 4.26: A) Molecular structure and labelling scheme of the compound **29**. Vanadyl centres are shown as blue (V) and red (O) balls, while the nickel(II) ions are shown as green balls. B) Side view of the cluster **29** highlighting the planarity of the metallic core. C) Crystal structure of the compound **29** emphasizing the formation of parallel chains via C−H···π (red) and π···π (blue) contacts between the pyridine molecules on vanadyl sites with the voids for the solvate pyridine and Et_2O molecules (yellow). Only hydrogen atoms taking part in the interactions are shown for clarity.

Similar synthetic efforts were carried out using the Co(II) ions, but the only isolable product was the $(TBA)[(VO)_2Co(L4)_2(py)_2]$ compound, as confirmed by the mass spectrometry and EPR. As mentioned earlier, structure of this compound includes the octahedral Co(III) ion holding two pyridine molecules in the axial positions which impose the steric encumbrance for the expansion of the trinuclear $[(VO)_2Co(L4)_2]^-$ anion across the vanadyl sites.

4.3.6. Heterotrimetallic $\{[(VO)_2M(L4)_2]\text{-}M1\}_2$ compounds- synthetic and structural insights

Following the structural analysis of the bimetallic octanuclear coordination compounds, next step was to test the possibility of incorporating two different secondary metal ions into the structure of the metalloligand **23** and to generate the octanuclear heterotrimetallic compounds. This idea was based on the fact that the vanadyl and the *bis*-bipyrazole binding sites offer two distinct ligand fields (O_2N_4 and N_4, respectively) and corresponding coordination geometries (octahedral and square pyramidal/square planar) which can provide the selective incorporation of two different metal ions. Looking at the previous findings, we have seen that the Cu(II) ions can be successfully integrated at both available coordination sites of the metalloligand since the formation of both trinuclear (**27**) and octanuclear compounds (**28**) was established. Interestingly, the attempts to chelate the Ni(II) ions exclusively within the *bis*-bipyrazole donor set were not successful, contradicting the reactivity observed in the formation of the octanuclear $\{[(VO)_2Ni(L4)_2]\text{-}Ni\}_2$ compounds where both functionalities of the metalloligand were occupied by the Ni(II) centres. These findings collectively indicate that the addition of 1:1 mixture of the Cu(II) and Ni(II) ions should result with the former being attached to the central N_4 ligand field within the metalloligand, while the Ni(II) ions should act as the more suitable linkers between the metallic platforms. In order to test that assumption, room temperature reactions in pyridine between the metalloligand and Cu^{2+}/Ni^{2+} mixture (1:1:1 stoichiometry) were carried out, in the presence and the absence of the pyrazine. The latter was varied only to avoid any directing of the reaction outcome since the pyrazine co-ligand binds only to the Ni(II) linkers while the pyridine solvent molecules are enough to complete the coordination environment around the Cu(II) linkers between the platforms. Surprisingly, both attempts yielded the same crystals which were identified as the $\{[(VO)_2Cu(L4)_2(py)_2]\text{-}Ni(py)_3\}_2\text{-}C_4H_4N_2$ (**30**), heterotrimetallic structural analogue of the compound **29**. Thus, the reaction taking place in the solution can be easily described as:

$$2Cu(ClO_4)_2 + 2Ni(ClO_4)_2 + 2(TBA)_2[(VO)_2(HL4)_2] + 14py + C_4H_4N_2 \longrightarrow \{[(VO)_2Cu(L4)_2(py)_2]\text{-}Ni(py)_3\}_2\text{-}C_4H_4N_2 + 4TBAClO_4 + 4\,(py\text{-}H^+)ClO_4$$

Crystal structure of this compound (triclinic *P*-1 space group) defines the unit cell containing one $\{[(VO)_2Cu(L4)_2(py)_2]\text{-}Ni(py)_3\}_2\text{-}C_4H_4N_2$ molecule and pyridine/Et_2O mixture of the crystallisation solvents (6:2 ratio). Unique molecular form of this compound reveals the expected distribution of the metals where the Cu(II) ions are integrated in the heart of the metalloligand structure, while pyrazine bridged $Ni(py)_3$ fragments act as the connectors between the symmetry equivalent $[(VO)_2Cu(L4)_2]$ platforms. Structure of the latter is very similar to the one in compound **29**, with two octahedrally coordinated vanadyl centres placed in the 'N_3O_3' ligand field and one square-planar Cu(II) centre nested within the *bis*-bipyrazole 'N_4' coordination pocket. However, the coordination geometry of the Cu(II) site exposes the longer Cu1−N bond distance (average 1.936 Å) than for the Ni(II) site in **29** Å (1.884 Å). On the other hand, in comparison with the Cu(II) site from the structures **27** and **28** (1.958 Å), observed distance is somewhat reduced. Reason for this comes from the different coordination geometry around the Cu(II) ion since the compound **30** incorporates the four-coordinated centre while the remaining heterometallic VO-Cu systems exhibit the pentacoordination at the Cu(II) site. Thus, longer Cu−N bond distances in the latter compounds are expected due to the fact that higher coordination number increases the ionic radii of the Cu(II) ion.[63] Additionally, while the pentacoordinated Cu(II) centres are positioned at least 0.17 Å above its coordination pocket, square-planar Cu(II) ion is almost perfectly merged with the ligand plane, taking into account the meaningless deviation of 0.013 Å. In contrast, the octahedral vanadyl centres are identical as their equivalents in the structure of the compound **29**, with the average bond distances of 1.643 Å/2.373 Å and 1.931 Å/2.090 Å for the axial V=O/V−N_{py} and equatorial V−O/V−N pairs of bonds. Likewise, average pyramidalisation of 0.299 Å is also maintained. Identity between the vanadyl sites is transmitted to the Ni(II) linking nodes, where the octahedral centres form the average axial Ni−O bonds of 2.077 Å and average equatorial Ni−N of 2.101 Å. Square topology of the $Ni_2(VO)_4Cu_2$ core is defined with the V1−Cu1−V2 angles of 166.10(2)° and with the V1−Ni2−V2 linkage angle of 168.70(2)°, while the averaged intermetallic distances for the V···Cu1 and the V···Ni2 edges are 3.932 Å and 3.687 Å, respectively.

Supramolecular arrangements of the cluster **30** are also similar to the compound **29** including eight intramolecular C−H···O hydrogen bonding interactions between the pyridine molecules of the $[Ni(py)_3]_2\text{-}(C_4H_4N_2)$ and the *bis*-phenolato coordination pocket of the

[$(VO)_2Cu$] platform. Additionally, C–H···π contacts between the pyridine ligands on the vanadyl sites and the phenolic rings from the neighbouring cluster arrange the molecules in the parallel chains which leave voids for the pyridine and Et_2O solvate molecules.

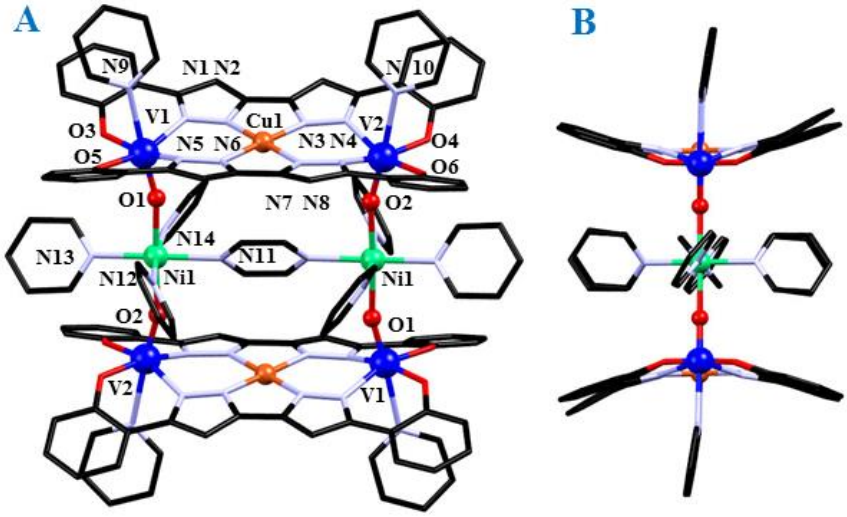

Figure 4.27: A) Molecular structure and labelling scheme of the compound **30**. Vanadyl centres are shown as blue (V) and red (O) balls, while the copper(II) and the nickel(II) ions are shown as orange and green balls, respectively. B) Side view of the cluster **30** highlighting the planarity of the metallic core. Hydrogen atoms are omitted for clarity.

Encouraged with the high selectivity in formation of the heterotrimetallic Cu(II)-Ni(II)-VO(IV) system, we decided to expand this family by varying the linker ions within the late divalent 3*d* metals (Mn(II) to Zn(II)). Thus, reproduction of the same synthetic procedure as for the compound **30** was immediately successful for the Mn^{2+}/Cu^{2+} and Zn^{2+}/Cu^{2+} pairs, while in the case of the Co^{2+}/Cu^{2} mixture, the obtained crystalline material was once again the (TBA)[$(VO)_2Co(L4)_2(py)_2$] compound. The latter results from the one-electron oxidation of the Co(II) to the Co(III) ions, which are then favourably integrated into the metalloligand structure over the Cu(II) ions, stopping the further expansion of the cluster. As mentioned earlier in the analysis of the homometallic structures, the cavity size of the central N_4 coordination pocket of the metalloligand **23** is almost perfectly tailored for the Co(III) ions (3.79 Å vs 3.76 Å, respectively) and marginally oversized for the Cu(II) ion (3.85Å). Thus, in order to overcome the thermodinamical stability of the (TBA)[$(VO)_2Co(L4)_2(py)_2$] over the heterotrimetallic {[$(VO)_2Cu(L4)_2$]-Co}$_2$ compound, the synthetic procedure was modified from the one-pot addition of the heterobimetallic mixture to the stepwise addition of the

metals, in Cu(II)→Co(II) order. This attempt was only partially successful since the formation of two types of the crystals was observed, first belonging to the aimed $\{[(VO)_2Cu(L4)_2]\text{-}Co\}_2$ compound and the second one to the thermodynamically more stable $(TBA)[(VO)_2Co(L4)_2(py)_2]$ compound. In fact, the appearance of the latter is delayed in the crystallisation process, indicating the possible oxidation and the rearrangement of the initially formed heterotrimetallic Cu(II)-Co(II)-VO(IV) system, as seen by the abrupt colour change of the reaction mixture (orange to dark red) over the course of the few days (see the solution studies). Hence, the only way to definitively direct the formation of the $\{[(VO)_2Cu(L4)_2]\text{-}Co\}_2$ compound was to change the metalloligand from the vanadyl dimer **23**, to the heterometallic $[(VO)_2Cu(L4)_2]$ trimer **27**. In this way, the central *bis*-bipyrazole chelating site is completely occupied by the Cu(II) ions so the only direction of the structural propagation can occur at the peripheral oxocation sites. As expected, addition of the Co(II) ions to the pyridine solution of the compound **27** produced successfully the expected heterotrimetallic system, enabling the complete crystallisation of the homogenous batch of crystals in a few days. Described synthetic procedures are summarised in the Figure 4.27.

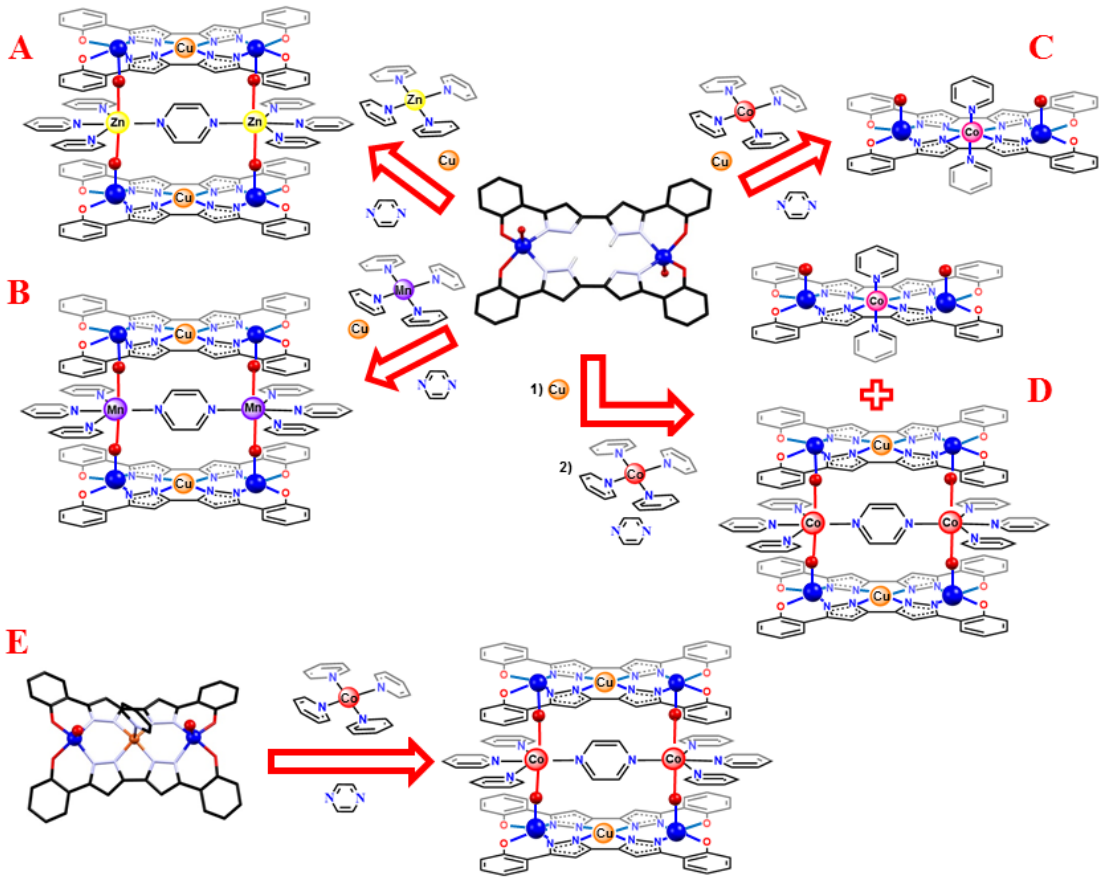

Figure 4.28: Summary of the synthetic procedures in the preparation of the heterotrimetallic $\{[(VO)_2Cu(L4)_2]\text{-}M\}_2$ compounds (M= Mn(II); Co(II); Zn(II)). A) and B) One-pot synthesis of the M(II)-Cu(II)-VO(IV) systems (M=Zn, Mn). C) Attempt of the one-pot synthesis of the Co(II)-Cu(II)-VO(IV) system resulting with the formation of $(TBA)[(VO)_2Co(III)(L4)_2(py)_2]$ compound. D) Stepwise synthesis of the Co(II)-Cu(II)-VO(IV) system resulting with the mixture of the compound. E) Directed synthesis of the heterotrimetallic $\{[(VO)_2Cu(L4)_2]\text{-}Co\}_2$ compound starting from the metalloligand **27**. Only relevant parts of the structures are shown for the simplicity.

Since the determination of the crystal structure for the M(II)-Cu(II)-VO(IV) systems (M=Mn(II), Co(II), Zn(II) proved their isostructural character (monoclinic $P2_1/n$ space group), for the sake of brevity, the common molecular features will be described together in the Mn/Co/Zn format. Crystallographic and bonding details are given in the Appendix (Table IV.A5 and IV.A18-A20, respectively).

Unit cell of these compounds includes two $\{[(VO)_2Cu(L4)_2(py)_2]\text{-}M(py)_3\}_2\text{-}C_4H_4N_2$ coordination compounds and 26 crystallisation pyridine molecules, while the asymmetric unit is defined by one quarter of the content. Thus, the centre of the inversion in the middle of the coordination cluster generates the other symmetry-related half. Molecular structure of the neutral $\{[(VO)_2Cu(L4)_2(py)_2]\text{-}M(py)_3\}_2\text{-}C_4H_4N_2$ clusters is very similar to the structure of the compound **30**, with two $[(VO)_2Cu(L4)_2(py)_2]$ platforms connected at the peripheral vanadyl sites by two pyrazine bridged $[M(py)_3]$ units (M=Mn, Co, Zn). However, the axial pyridine ligands of the $[(VO)_2Cu(L4)_2(py)_2]$ platforms are disposed differently than in the compound **30**, with one molecule bonded to the Cu(II) site and the other at one of the vandyl sites. Hence, each platform involves one square pyramidal Cu(II) ion in 'N_5' ligand field and two types of the vanadyl ions, one adopting the square-pyramidal geometry ('N_2O_3' ligand field) and the remaining one residing in the octahedral 'N_3O_3' ligand field. Donor atoms around the linker M(II) ions shape the octahedral 'N_4O_2' ligand field, involving the M−O(=V) bonds at the axial sites and M−N bond with the pyridine and pyrazine ligands in the equatorial plane.

Looking at the structural details within the $[(VO)_2Cu(L4)_2(py)_2]$ platforms, it's interesting to notice that the Cu(II) sites in all three compounds are essentially the same, having the average Cu−N bond distances of 1.954/1.954/1.959 Å at the equatorial sites and the axial bonds with the pyridine molecules of 2.362(3)/2.359(4)/2.354(4) Å, both given for

Mn/Co/Zn derivative, respectively. In comparison with the structure of the compound **27**, the equatorial bonds are perfectly maintained, while the axial Cu−N bonds have become elongated for more than 0.1 Å. Consequently, the pyramidalisation of the copper(II) sites is reduced in comparison with all molecular forms of the $[(VO)_2Cu(L4)_2(py)_2]^{2-}$, with the distances from the equatorial 'N_4' plane of 0.186/0.188/0.191 Å.

Structural parameters around the vanadyl centres reveal the similar tendency, where hexacoordinated site (V2) exhibits a slightly elongated bond distances than the pentacoordinate site (V1). The latter forms the average equatorial V1−O bond distances of 1.902/1.907/1.910 Å and the V1−N bond distances of 2.079/2.076/2.084 Å, while the axial $[VO]^{2+}$ moiety measures 1.648(3)/1.641(3)/1.633(4) Å (Mn/Co/Zn format). On the other hand, same parameters for the hexacoordinated site are 1.925/1.926/1.933 Å (equatorial V2−O bonds), 2.097/2.093/2.093 Å (equatorial V2−N bonds) and 1.653(3)/1.654(3)/1.647(3) Å (axial $[VO]^{2+}$moiety). Similarly, axial bonding with the pyridine molecule is defined with the long bond distances of 2.342(3)/2.339(4)/2.346(4) Å. Among all mentioned parameters, it is interesting to notice the correlation between the geometry of the vanadyl cation and the remaining bonds; shorter $[VO]^{2+}$ moiety produces the elongation in equatorial and axial bonding. In agreement with that, comparison of the coordinatively engaged pentacoordinate sites with their free counterparts from the compounds **23** and **27** reveals the slight elongation of the V=O bonds (average 0.03 Å) and the slight contraction of the equatorial V−O bonds (average −0.03 Å) upon coordination of the secondary metal ion. Consequently, pyramidalisation of the coordination environment around the vanadium(IV) ions is reduced in comparison with the structure of the free metalloligand. Corresponding distances from the equatorial ligating plane are 0.412/0.419/0.414 Å and 0.290/0.300/0.294 Å for the square-pyramidal and octahedral sites, respectively.

In contrast to the equivalence of the $[(VO)_2Cu(L4)_2(py)_2]^{2-}$platform for the compounds **31**-**33**, the coordination geometry of the connector sites is strongly determined by the nature of the residing metal, fingerprinting the unique topology of the heterotrimetallic structure. Average axial M−O bond distances measure 2.189/2.125/2.194 Å, while the average M−N bond distances at the equatorial sites are 2.274/2.177/2.175 Å for the Mn(II), Co(II) and Zn(II) sites, respectively. Additionally, these findings are confirmed by the geometry of the rectangular metallic core where V1−Cu−V2 bond angles at the platform edge are found to

be almost identical 160.05(2)/160.05(2)/159.96(2)°, while the V1−M−V2 connectors edges are aligned under the angles of 174.78(2)/172.70(3)/173.88(2)° (M=Mn(II), Co(II) and Zn(II), respectively). Average intermetallic V···Cu distances are 3.951 Å, 3.945 Å and 3.949 Å, while the V···M separations measure 3.803 Å, 3.747 Å and 3.804 Å for Mn(II), Co(II) and Zn(II), both respectively.

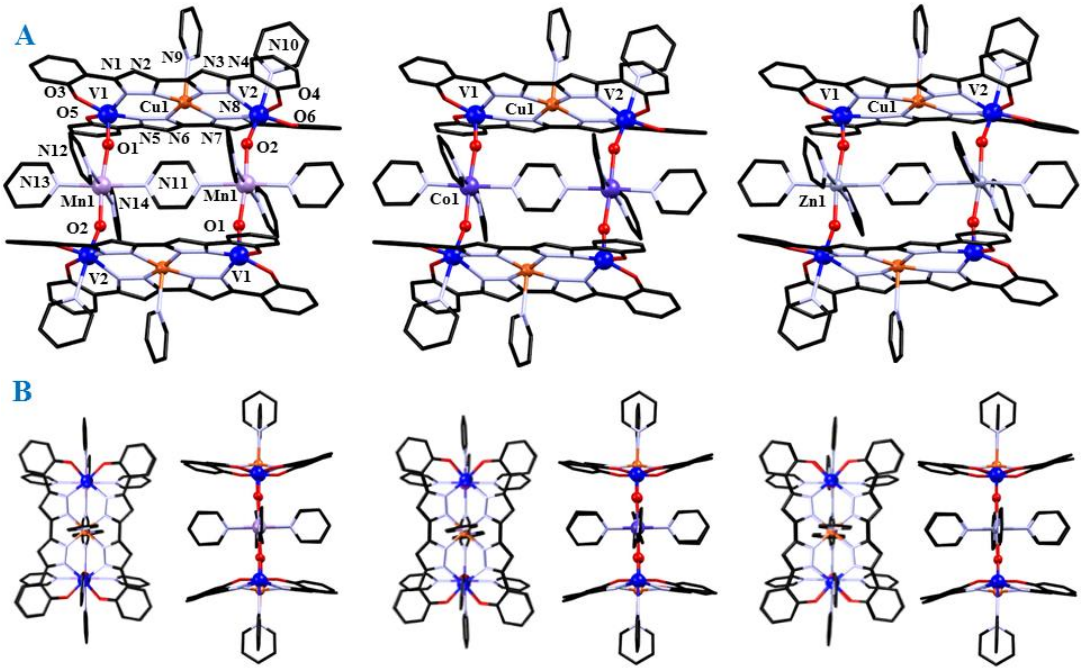

Figure 4.29: A) Molecular structure and labelling scheme of the compound **31**-**33** from left to right, respectively. Vanadyl centres are shown as blue (V) and red (O) balls, while the manganese(II), cobalt(II) and zinc(II) ions are shown as violet, purple and light-blue ball. B) Side and top view of the cluster **31**-**33** highlighting the planarity of the metallic core. Hydrogen atoms are omitted for clarity.

Intramolecular stabilisation of the structure is achieved through the several C−H···O hydrogen bonding interactions between the $M(py)_3$ connector and the *bis*-phenolato moieties. On the other hand, the same intermolecular interaction through the axial pyridine ligand on the Cu(II) site and the *bis*-phenolato pocket organises the molecules into supramolecular 1-D chain. Additionally, the rich network of 6 C−H···N contacts is established between the aromatic rings of the cluster (peripheral phenolato or pyrazolato core) and the assembly of six solvate pyridine molecules. Additionally, the clusters are connected *via* C−H···π interactions between the axial pyridine ligands on the VO(IV) and the Cu(II) sites and the $[M(py)_3]$ unit and the phenolate ring, respectively. The former contacts arrange the

parallel chains of the molecules into the zig-zag assembly, generating the voids in the crystal structure for the pyridine channels.

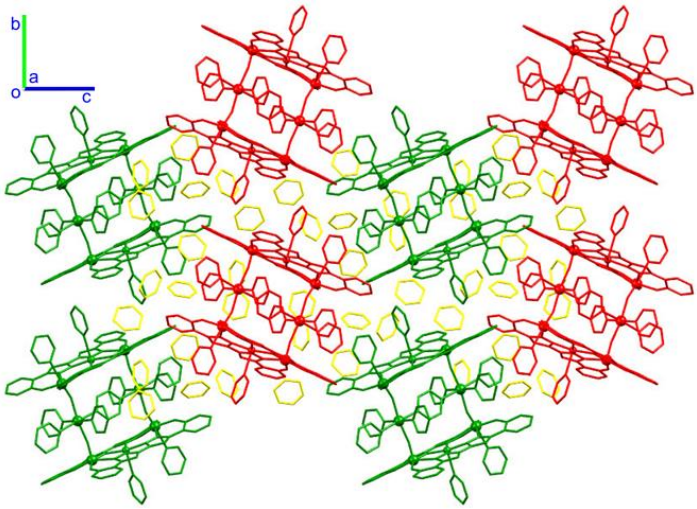

Figure 4.29: C) Crystal structure of the compound **31** emphasizing the zig-zag distribution (alternation of green and red molecules) of the parallel layers of molecules with voids for the solvate pyridine molecules (yellow). Same packing motif is found in the structures of the compounds **32** and **33.**

Compounds **31**-**33** join the very limited family of the multiheterometallic systems whose highlight was reached with the preparation of the tetrametallic systems reported by Winpenny[64] and Marvaud[65]. Winpenny *et al*. reported truly remarkable nanoscale assemblies (containing up to 60 3*d* metal ions) which were prepared using the simple Lewis acid-base concept. The role of the Lewis base had the bimetallic $[NH_2Pr_2][Cr^{III}_7Ni^{II}F_8(O_2CtBu)_{15}(O_2C\text{-}C_5H_4N)]$ ring which was connected through the pyridine-3-carboxylate (*N* donor) to the labile solvent site of selected Lewis acids: $[Fe^{III}_2Co^{II}(\mu_3\text{-}O)(O_2CtBu)_6(HO_2CtBu)_3]$, $[Mn^{II}_4Mn^{III}_2(\mu_4\text{-}O)_2(O_2CtBu)_{10}(THF)_4]_4$ and the $[Ni_{12}(chp)_{12}(O_2CMe)_{12}(H_2O)_6(THF)_6]$ (Hchp=6-chloro-2-hydroxypyridine). On the other hand, Marvoud used the co-crystallisation of the complex cation $[M3(tpy)_2]^{2+}$ (M3=Ni^{II}, Ru^{II}, Os^{II}) with the anionic cluster $[((valen)M1)Ln(OH_2)_2(M2(CN)_8)]_2^{2-}$ (M1=Cu^{II}, Ni^{II}; M2= Mo^{IV}, W^{IV}; Ln=Gd^{III}, Tb^{III}; valen- *N*,*N*′-*bis*(3-methoxy-salicylidene)-ethylenediamine). Similar concept is often employed in the preparation of the scarce 3*d*-4*f*-n*d*′ heterotrimetallic compounds, where hexa- or octacyanometallate or tris(oxalate) anions are attached to the positively charged $[M^{II}Ln^{III}]$ unit within the Schiff base or *bis*-β-diketone scaffold. [66-76] Alternatively, integration of the organic radicals such as verdazyl, nitronyl nitroxide, cyanocarbon radicals, *etc*. allowed the

preparation of the n*p*-n*f*-n*d*' and n*p*-n*d*-n*d*' heterospin systems.[77-79] Remarkably, heterotrimetallic 3*d*−3*d'*-3*d*'' remain scarcely explored, with the first examples being linear [$M1^{III}M2^{II}M3^{II}$] complexes (M1-Fe, Co; M2-Cu,Ni,Mn) reported by Chauhuri *et al*.[80, 81] Their synthesis involved three consecutive additions of different metal ions accompanied with the ligand transformation from mono-Schiff base to Schiff base-oxime. Similarly, embedded [$Mn^{II}Cu^{II}$][82-84] or [$Ni^{II}Ti^{IV}$][85] dimers within the compartmental Schiff base scaffold were used by Andruh/Jiang and Glaser, respectively, as the attachment block for additional M^{3+} centre (M=Fe^{3+}, Cr^{3+}]. Alternatively, Dunbar *et al.* used the terminal cyanide donors from iron(III) sites of the preformed $Co^{III}{}_3Fe^{III}{}_2$ metalloligand to bind six additional Ni^{II} ions, while Colacio *et al.* employed the similar strategy in a construction of the heterotrimetallic [Ni^{II}–Fe^{III}–Cu^{II}] chain.[86, 87] Worth of mention is also Winnpenny's idea of expanding the Lewis acid-base concept to connect the [Cr_7Ni] wheels through the central [$Cu^{II}{}_2$], [$Mn^{II}{}_4Mn^{III}{}_2$], [Ni_{12}] or M^{II} node (M=Co, Cu). [64, 88-90] A common feature in preparation of all those systems is the sequential synthesis in which metallic centres of preformed complex bind to mostly cyanide, pyridyl or carboxylate donors from the monometallic metalloligand or, alternatively, heteroatoms from the organic scaffold around the preformed complex bind the additional metal ions. On the other hand, here presented vanadyl metalloligand exploits simultaneously the chelating abilities of the functionalised organic backbone along with the donor properties of the oxocation to attach the metal ions in the topologically perpendicular positions. Such reactivity is unique and to the best of our knowledge still remains unreported. Similar topology of the vanadyl metalloligand was seen in already mentioned Schiff base-porphyrazine compound reported by Hoffman *et al.*[62] However, reactivity of that system towards 3*d* metals engages only the chelating ability of the empty N_4 coordination pocket of the porpyrazine moiety, leaving the pentacoordinated vanadyl ions chemically inert (embedded in the analogous O_3N_2 ligand field as in **23**). Cause for pronounced donor properties of the oxocations from the metalloligand **23** can be perhaps found in its negative charge and related increased electronic density around the vanadyl sites. The formation of unsupported V=O−M linkages is commonly encountered in the polyoxovanadate systems which reduce its large negative charge by decorating the periphery with the 3*d* metal ions.[91-98] In contrast, cation-cation connectivity is rarely present in the discrete vanadium(IV) coordination compounds. Most significant contribution to the latter involves the extensive work of Sommer *et al.* reporting the formation of linear V/Ti=O−M (M-Mn^{II}, Fe^{II}, Co^{II}, Ni^{II},

Cu^{II}),[99, 100] V/Ti=O−Cr−O=V/Ti and V=O−Cr−O=Ti synthons when mononuclear vanadyl metalloligand (N_4O ligand field) or its diamagnetic titanyl(IV) analogue are mixed with the chromium porphyrine[101, 102] or pentapyridyl chelated M^{II} compounds.

4.3.7. Formation of the heterometallic compounds – crystallographic insights

Summarising the analysis of the heterometallic structures, formation of the V=O−M2 structural synthons decreases the electronic density from the $[V=O]^{2+}$ cation causing its elongation. In contrast, the equatorial V−O bonds follow the opposite tendency and become shorter with reduction of the pyramidalisation of the vanadyl sites. When these structural changes are mutually compared for the compounds **28-33**, a metal-dependent tendency can be easily observed in reciprocal effect for both parameters (Figure 4.30). In addition, comparison of the structural parameters of the compound **23** and **27** indicate that integration of the Cu(II) ion in the chelating pocket of the metalloligand doesn't affect the vanadyl bonding geometry since both parameters are maintained.

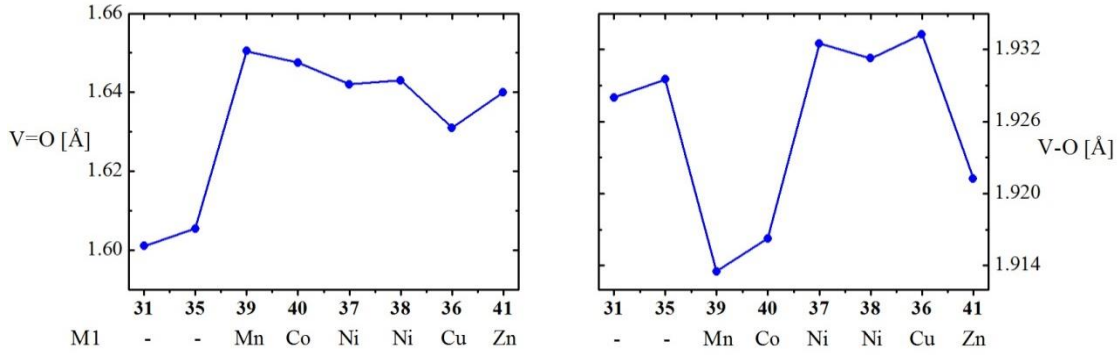

Figure 4.30: Bonding geometry of the vanadium(IV) sites in the structures of the compounds **23**-**27**.

Similar metal-dependent tendency can be easily detected in the bonding geometry of the octahedral M2 linkers, where axial M2−O(=V) distances decrease from the Mn(II) to the Ni(II) and then abruptly increase for the Cu(II) site as a consequence of the strong Jahn-Teller distortion. Interestingly, $3d^5$ Mn(II) and $3d^{10}$ Zn(II) ions exhibit almost the same bonding with the vanadyl centres. On the other hand, equatorial M2−N bond distances decrease systematically from Mn(II) to Cu(II) and increase for the Zn(II) site following the well-established Irving-Williams stability sequence. Averaging all bonds around the M2 centre, observed variation of the M2−X bond lengths correlates nicely with the ionic and the crystal radii of the divalent M2 cations.[63] Small discrepancy observed at Cu(II) site is again

conditioned with the strong Jahn-Teller elongation, since the axial bonds are > 0.5 Å longer from the equatorial ones. Interestingly, reciprocal correlation between the M2−O bond lengths and the V=O bonds can be established for the compounds **28**-**30**+**33** (M2=Ni, Cu, Zn), while the opposite trend is found for the Mn and Co derivative (compounds **31** and **32**) which exhibit the longest bonds within the [M2−O=V] fragment.

Geometry of the chelated M1 site remains essentially the same for all compounds holding the penta-coordinated Cu(II) site (**28**, **30**, **31**-**33**), while the small deviation seen for the compound **30** was already ascribed to the reduced ionic radii of the square-planar Cu(II) centre. In agreement with that explanation is the further reduction of the M1−N bond lengths for the four-coordinated Ni(II) site in the compound **29**.

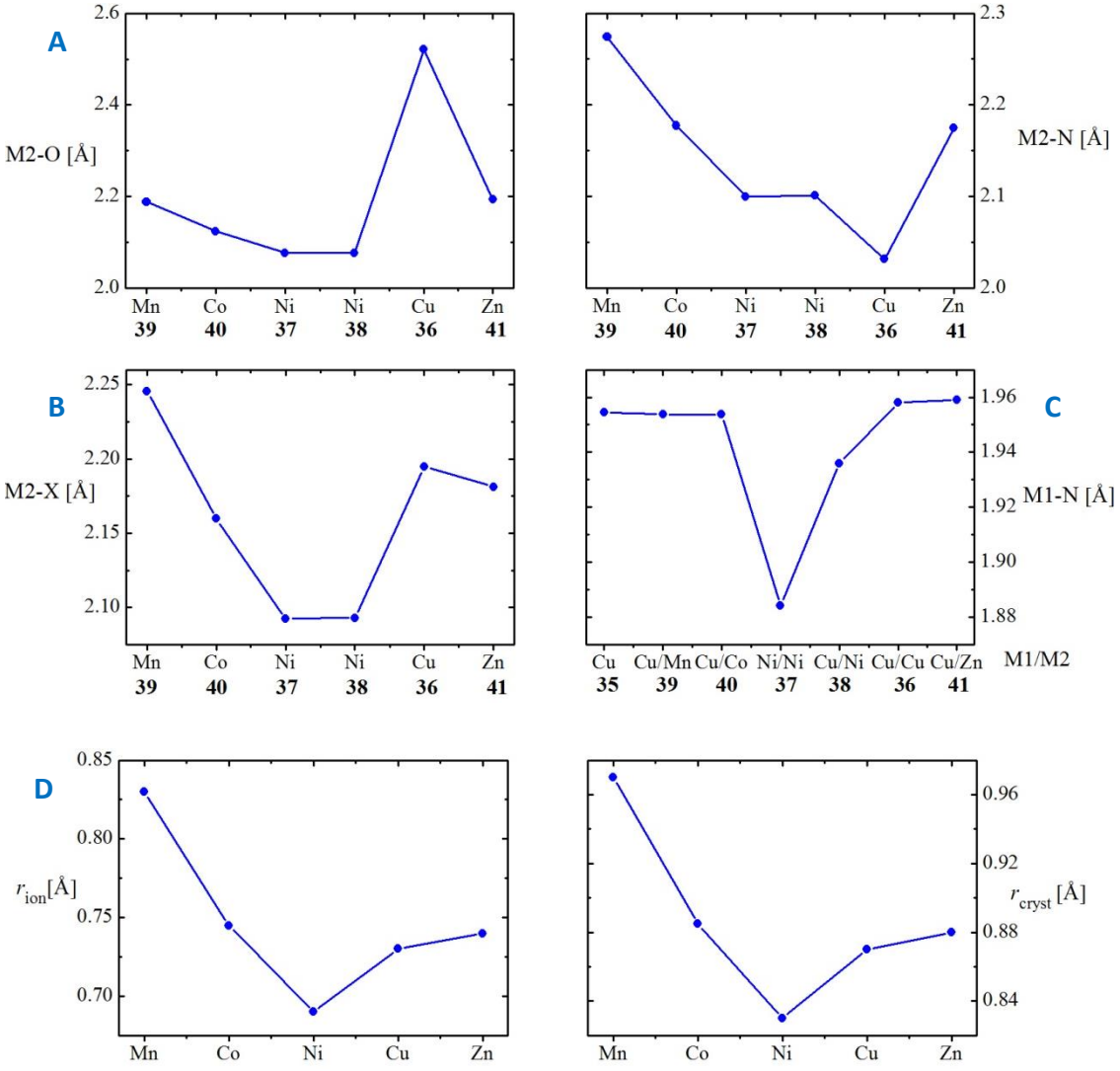

Figure 4.31: Bonding geometry of the M1 (A and B) and the M2 sites (C) in the structures of the compounds **28**-**33**. D) Shannon-Prewitt crystal and ionic radii of the elements.[63]

4.3.8. Formation of the heterometallic compounds – mechanistic insights

Summarising the previously elaborated results, bitopological metalloligand **23** has been successfully employed in the rational design of the trinuclear and octanuclear coordination entities. In that sense, the control of the reaction stoichiometry was dictating the metalloligand reactivity, which was later directly transmitted to the cluster nuclearity. Thus, addition of only one equivalent of the 3*d* metal ion activated only *bis*-bipyrazole chelating pocket of vanadyl compound, while doubling the quantity of the metal ions prompted additionally the donor abilities of the oxocation. Rigid orthogonality between the oxocation and the central N_4 chelating pocket extended the propagation of the metalloligand structure from 1-D to 2-D upon coordination of one or two secondary metal ions, respectively. Taking all this facts into account, the coordination driven self-assembly of the octanuclear $\{[(VO)_2M(L4)_2]\text{-}M1\}_2$ compounds can be rationalised with the initial formation of the trinuclear $[(VO)_2M(L4)_2]^{n-}$ assemblies which later become linked by the pyridine solvated M1 metal ions (B1 and B2). The strongest support to the proposed mechanism comes from the fact that the stepwise synthesis of the compound $\{[(VO)_2Cu(L4)_2]\text{-}Co\}_2$ (**32**) through the $[(VO)_2Cu(L4)_2]^{2-}$ intermediate resulted with the same outcome as the one-pot synthetic procedures starting from vanadyl metalloligand (**31** and **33**). Additionally, failed attempts to generate the hexanuclear $\{[(VO)_2(HL4)_2]\}_2$-M1 entities by engaging only the vanadyl binding sites and leaving the *bis*-bipyrazole cavity intact (A), resulted exclusively with the formation of $\{[(VO)_2M(L4)_2]\text{-}M1\}_2$ compounds (19-27 % yield).

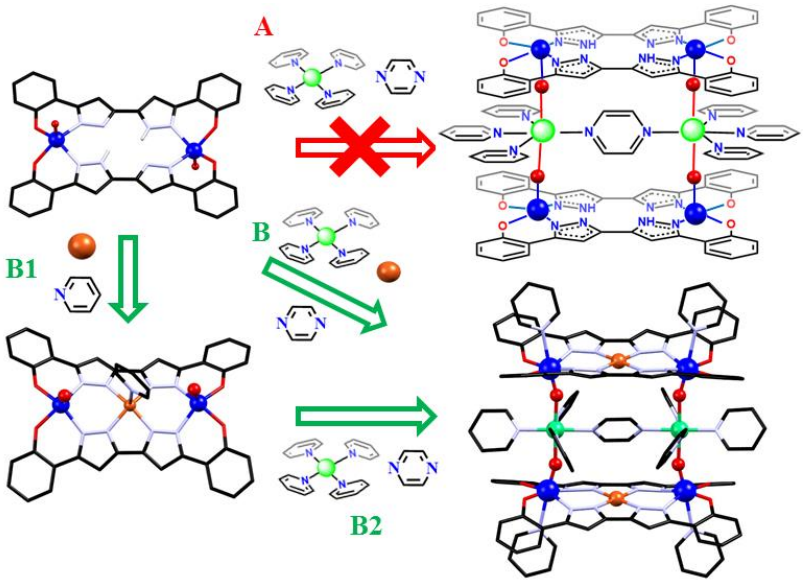

Figure 4.29: Summary of the mechanistic insights into the coordination driven self-assembly based on the metalloligand **23**. A) Failed attempts to generate the hexanuclear $\{[(VO)_2(HL4)_2]\}_2$-M1 compounds through the use of the vanadyl cation solely. B) Selective one-pot synthesis of the octanuclear heterobimetallic and heterotrimetallic compounds. B1) and B2) Stepwise synthesis as for the heterotrimetallic compound **32**.

However, taking into account the structural features of the free metalloligand, the formation of the discrete instead of polymeric compound is slightly surprising. As discussed above, coordination of the vanadyl ions by the two equatorially disposed $(HL4)^{3-}$ imposes the topological orthogonality between the two functional groups of the metalloligand, oxo donor from VO^{2+} and the chelating $(N\text{-}NH)_2$ pocket. Moreover, *trans* orientation of the vanadyl moieties seems to ensure the great degree of structural rigidity which favours the propagation into 1-D polymeric chain. Surprisingly, structural insights into derived heterometallic assemblies indicate the great degree of flexibility of the oxocation functionality. In fact, the common feature of all heterometallic compounds obtained from the metalloligand **23** is the *cis* orientation of the vanadyl moieties, meaning that upon integration of the secondary metal ion (Cu^{2+} or Ni^{2+}) into chelating *bis*-bipyrazole pocket one of the vanadyl moieties rotates 180° around its equatorial plane (Figure 4.30). Even more impressive is the structural transformation occurring when trinuclear compound **27** is converted into heterotrimetallic compound **32**. As seen earlier, structure of the compound **27** and of all its molecular forms revealed the *cis, cis* orientation of the vanadyl cations and the axial pyridine molecule on central Cu(II). However, upon addition of the cobalt(II) ions to

form the heterotrimetallic $\{[(VO)_2Cu(L4)_2]\text{-}Co\}_2$ compound, both vanadyl cations rearrange again around its equatorial plane (*cis* VO-VO) ending opposed to the axial pyridine molecule on the central Cu^{2+} site (*trans* VO-py). Identical features are also detected for the remaining octanuclear compounds (**28-33**). Besides this, additional degree of the oxocation flexibility is reflected in the possibility of adopting different coordination geometries, square-pyramidal (C.N. 5) and octahedral (C.N. 6). While the first is dominant in the structures with free vanadyl moieties (**23** and **27**), the formation of the V=O−M synthons in octanuclear compounds **28-33** decreases the electron density of the V=O bond and permits to the d_{z2} orbital of the vanadium(IV) to become available for coordination of another ligand (solvent pyridine molecules).

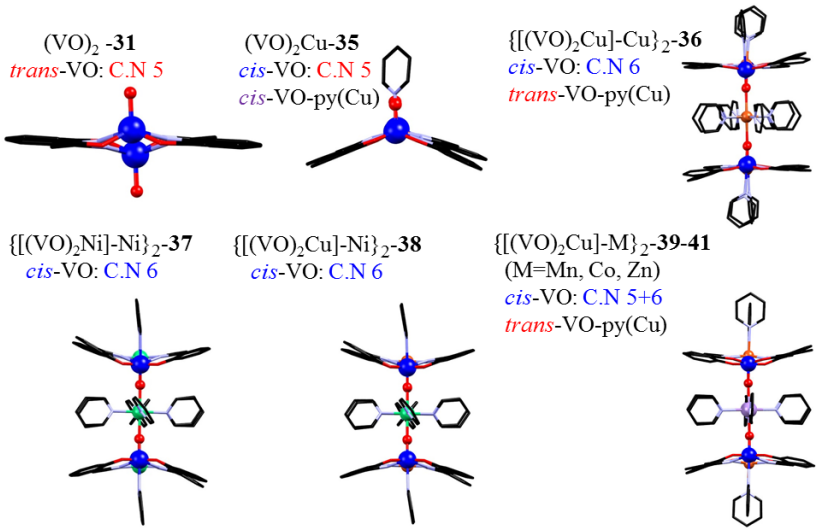

Figure 4.30: Flexibility of the vanadyl sites in the structures of the free metalloligand (**31**) and its heterometallic assemblies (**27**-**33**).

4.3.9. Heterometallic $\{[(VO)_2M(L4)_2]\}_2$-M1 compounds- solution studies

The stability of clusters **28-33** in solution was investigated by mass spectrometry, employing the techniques of electrospray ionization (ESI) and MALDI-TOF. In the case of heterobimetallic compounds **28** and **29**, the ESI(−) spectrogram of their THF solutions confirmed the existence of the heterometallic $[(VO)_2M]^{2-}$ platform as seen by the peaks found at m/z=412.48, 824.97 (the most intense peak) and 1651.94 corresponding to $[(VO)_2Cu(L4)_2]^{2-}$, $\{[(VO)_2Cu(L4)_2]^{2-}+H^+\}^-$ and $\{[(VO)_2Cu(L4)_2]^{2-}+H^+\}_2^-$ (Figure IV.A16) or m/z=409.99 and 820.98, indicative of $[(VO)_2Ni(L4)_2]^{2-}$ and $\{[(VO)_2Ni(L4)_2]^{2-}+H^+\}^-$ species, respectively. The experimentally detected isotopic distribution of these peaks coincides

nicely with the theoretically expected, confirming the integrity of platforms and its heterometallic composition (Figure IV.A16). Unfortunately, significant fragmentation of the linker M1 sites from the $[(VO)_2M(L4)_2]$ platform hindered the observation of molecular peaks corresponding to the entire octanuclear cluster $[M_4(VO)_4]$, even in ESI(+) mode. Hence, positive and negative ionization employing the milder MALDI-TOF technique were studied. Again, complete molecular peaks were not detected, but the resulting spectrograms provided much more information. The (+) MALDI-TOF spectrogram for both compounds revealed two common peaks: $\{[(VO)_2M(L4)_2]+DCTB\}^+$ (1140.1 and 1129.1) and the most intense $\{[(VO)_2M(L4)_2]_2+nM\}^+$ (n=1 1714.9 and n=2 1758.9) for copper(II) and nickel(II) derivatives, respectively. Additional molecular fragments were found for **28** at m/z=1777.8, identified as $\{[(VO)_2Cu(L4)_2]_2+Cu\}^+$, and for **29** at m/z=2637.8 corresponding to $\{[(VO)_2Cu(L4)_2]_3+3Ni\}^+$. On the other hand, negative mode MALDI-TOF technique confirmed the findings from ESI(-) with the dominant $[(VO)_2M(L4)_2]^-$ species (m/z =824.9 and 820.0; M=Cu, Ni). In the case of compound **28**, one additional peak of $\{[(VO)_2Cu(L4)_2]_2+Cu\}^-$ was found at m/z=1714.8, while in the case of compound **29**, molecular fragments $\{[(VO)_2Ni(L4)_2]_2+nNi\}^+$ were identified at m/z=1699.8 and 1758.8, for n=1, 2, respectively.

In the case of the heterotrimetallic compounds, results obtained from the mass spectrometry confirm undoubtedly the unique distribution of the metal ions within the cluster and its heterotrimetallic composition (Figures IV.A18-A21). The previous is easily detectable from the ESI(−) spectra of clusters **31**-**33** where only fragments corresponding to $[(VO)_2Cu(L4)_2]^{2-/-}$ (m/z=412.48; 825.98) were found, meaning that all four heterotrimetallic clusters contain exclusively Cu(II) centres chelated by the vanadyl metalloligand (Figures IV.A18-A21). Additional confirmation of this fact arises from the comparison of experimental and theoretical isotopic distributions of those peaks. On the other hand, (+) MALDI-TOF technique provided the evidence of the heterotrimetallic composition, with the most intense peak corresponding to protonated or proton-free metallic core $\{[(VO)_2Cu(L4)_2]_2+2M1\}^+$ of the clusters. Position of this peak is progressively shifted to higher m/z values (1761.8→1781.9) as the nature of M1 linker changes from the lighter Mn^{II} to the heavier Zn^{II}. Moreover, identical tendency can be found also in the (-) MALDI-TOF spectrograms where $\{[(VO)_2Cu(L4)_2]_2+M1\}^-$ shifts from m/z=1706.9 (M1=Mn) to m/z=1717.8 (M1=Zn). Detected sets of molecular fragments in the (+) MALDI-TOF spectrograms are unique for each compound, but in spite of that, general composition of found fragments can

be described with the formula $\{[(VO)_2Cu(L4)_2]_n+m\ M1\}^+$, where 1≤ n ≤3 and 1≤ m≤4. Almost identical molecular fragments are found in the (-) MALDI-TOF spectrograms, where the most dominant peak for all compounds corresponds to $[(VO)_2Cu(L4)_2]^-$ anion (m/z =824.9), confirming the results obtained from ESI(-).

Lastly, stepwise synthesis of the compound **32** including the consecutive additions of the metals in the Cu(II)→Co(II) order was also monitored by the mass spectrometry (Figure IV.A22). Negative mode spectrograms of ESI and MALDI-TOF techniques revealed the formation of heterogeneous systems composed of $[(VO)_2Cu(L4)_2]^{2-/-}$ (m/z=412.48; 824.97) and $[(VO)_2Co(L4)_2]^-$ (m/z=820.9) clusters. Hence, these findings confirm the pronounced competitivity for coordination between the Co^{III} and Cu^{II} ions, as it was expected from the analysis of size compatibility between the single ions and cavity of the vanadyl metalloligand.

4.3.10. Heterotrimetallic $\{[(VO)_2M(L4)_2]\}_2$-M1 compounds- magnetic properties

Magnetic properties of the compounds **28**-**33** were studied through variable temperature (2-300 K) magnetization measurements performed on their powdered microcrystalline samples under the constant magnetic field of 0.5 or 1 T. In addition, this study was complemented with magnetization measurements at 2 K in the field range of 0–5 T.

DC studies on compound **28** revealed the room temperature (300 K) $\chi_M T$ product of 3.37 cm^3Kmol^{-1} which is higher than the expected 3.00 cm^3Kmol^{-1} for a heterometallic system incorporating four uncoupled S=1/2 (VO^{2+}) and four S=1/2 (Cu^{2+}) spin centres (g=2.0, Figure 4.31). Upon cooling, the $\chi_M T$ product remains almost constant down to 25 K (3.28 cm^3Kmol^{-1}) and later starts to decrease reaching the minimum value of 2.66 cm^3Kmol^{-1} at 2 K. Such temperature dependence of the $\chi_M T$ product indicates that interactions between metal ions within the cluster are either negligible or there are competitive ferromagnetic and antiferromagnetic interactions (V=O−Cu−O=V) within the cluster. In agreement with this conclusion, field-dependent magnetization measurements at 2K yielded the highest measured value of 4.32 μ_B at 5 T which lies only slightly below the expected 8.00 μ_B for eight uncoupled S=1/2 (g=2, Figure 4.31). Estimation of the strength of magnetic coupling was done by fitting experimental data ($\chi_M T$ *vs* T and $M/N\mu_B$ *vs* H) using the matrix diagonalization of the spin Hamiltonian defined according to scheme 4.2:

$$\hat{H} = \mu_B B \sum_i g_i \hat{S}_i - 2J_1\left(\hat{S}_{V1}\hat{S}_{Cu1} + \hat{S}_{V2}\hat{S}_{Cu2} + \hat{S}_{V3}\hat{S}_{Cu2} + \hat{S}_{V4}\hat{S}_{Cu1}\right) - 2J_2\left(\hat{S}_{V1}\hat{S}_{Cu3} + \hat{S}_{V2}\hat{S}_{Cu3} + \hat{S}_{V3}\hat{S}_{Cu4} + \hat{S}_{V4}\hat{S}_{Cu4}\right)$$

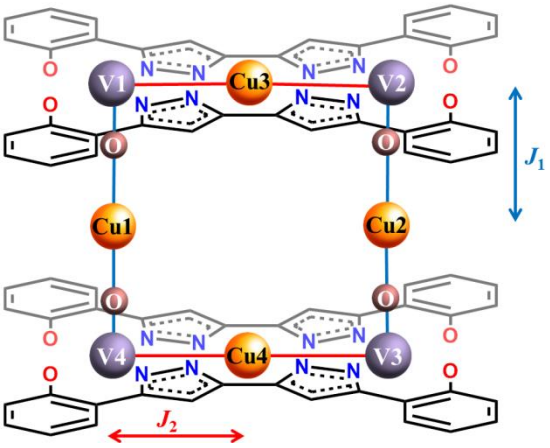

Scheme 4.2: Coupling scheme for the compound **28**. Atom numbering is not related with the crystallographic symmetry and serves only for purpose of simplifying the spin Hamiltonian.

Best model was acquired by fixing g_{Cu3}=g_{Cu4}=2.15, g_{Cu1}=g_{Cu2}=2.10 and g_V=2.05, yielding J_2=6.05 cm^{-1} and J_1=–4.32 cm^{-1} (Figure 4.31). Reason why proposed model is reasonable can be found in the crystal structure of this compound where magnetic d_{xy} and $d_{x^2-y^2}$ orbitals of vanadyl and copper sites, respectively, are orthogonal (Cu3 and Cu4 sites) and parallel (Cu1 and Cu2 sites). Similarly, oxygen bridge between two metallic sites is in fact perpendicular to d_{xy} and $d_{x^2-y^2}$ orbitals of vanadyl and copper along the linkages between the platforms, providing less efficient coupling.

Variable temperature EPR spectroscopy of powdered sample revealed that this compound is EPR active at room temperature, exhibiting one resonance centred at g=2.023 which gains on intensity as the temperature increases, as expected from the susceptibility measurements. At 4 K, energy of this transition shifts to g=1.995, which follows the appearance of a small plateau found in $\chi_M T$ *vs* T measurements at 4 K. Origin of this feature could be related with intermolecular interactions which could provide pathways for some small coupling between the molecules.

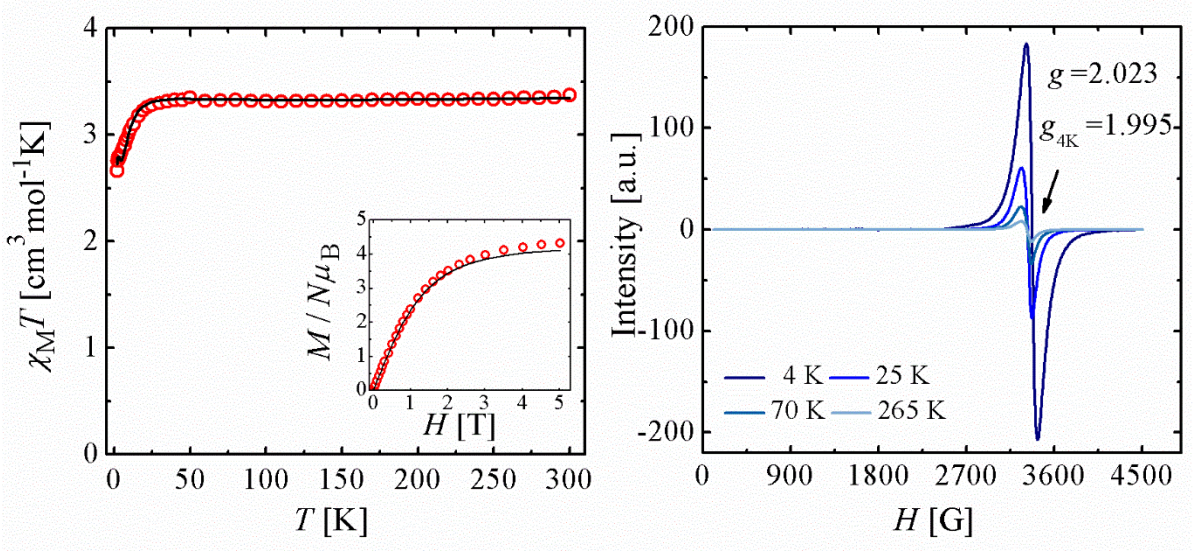

Figure 4.31: *Left:* $\chi_M T$ *vs* T and $M/N\mu_B$ *vs* H (inset) curves of compound **28** with the best fit (solid line). Measurement setup: warming mode (2→300 K), B = 1 T; T_{mag} = 2 K. *Right:* Variable temperature (4-265 K) X-band EPR spectra (f = 9.419 GHz) of a powdered sample of complex **28**.

SQUID magnetometry measurements on compound **29** revealed the room temperature (300 K) $\chi_M T$ product of 4.55 cm^{3}Kmol^{-1} which is higher than the expected 3.50 cm^{3}Kmol^{-1} for a heterometallic system incorporating four uncoupled S=1/2 (VO^{2+}) and two S=1 (Ni^{2+}) spin centres (g=2.0, Figure 4.32). Two additional Ni^{II} centres intercalated in the heart of metalloligand are expected to be diamagnetic because of their square-planar coordination geometry and 3d^8 electronic configuration. Upon cooling, the $\chi_M T$ product increases slowly down to 150 K and later more abruptly, reaching the maximum value of 6.09 cm^{3}Kmol^{-1} at 30 K. Further lowering of the temperature reveals sharp decline of the $\chi_M T$ values ending at 2.75 cm^{3}Kmol^{-1} at 2 K. Such temperature dependence of the $\chi_M T$ product indicates the competitive ferromagnetic (V=O−Ni−O=V, dominant) and antiferromagnetic interactions (Ni-pyrazine-Ni) within the cluster. In agreement with this conclusion, field-dependent magnetization measurements at 2K yielded the highest measured value of 7.70 μ_B at 5 T which lies only slightly below the expected 8.00 μ_B for two effective S=2 V=O−Ni−O=V fragments (g=2, Figure 4.32). To estimate the strength of magnetic coupling, experimental data ($\chi_M T$ *vs* T and $M/N\mu_B$ *vs* H) were modelled (PHI) using the matrix diagonalization of the spin Hamiltonian defined according to scheme 4.3:

$$\hat{H} = \mu_B B \sum_i g_i \hat{S}_i - 2J_1\left(\hat{S}_{V1}\hat{S}_{Ni1} + \hat{S}_{V2}\hat{S}_{Ni2} + \hat{S}_{V3}\hat{S}_{Ni2} + \hat{S}_{V4}\hat{S}_{Ni1}\right) - 2J_2\left(\hat{S}_{Ni1}\hat{S}_{Ni2}\right)$$

or

$$\hat{H} = \mu_B B \sum_i g_i \hat{S}_i - 2J_1\left(\hat{S}_{V1}\hat{S}_{Ni1} + \hat{S}_{V2}\hat{S}_{Ni2} + \hat{S}_{V3}\hat{S}_{Ni2} + \hat{S}_{V4}\hat{S}_{Ni1}\right) - zJ$$

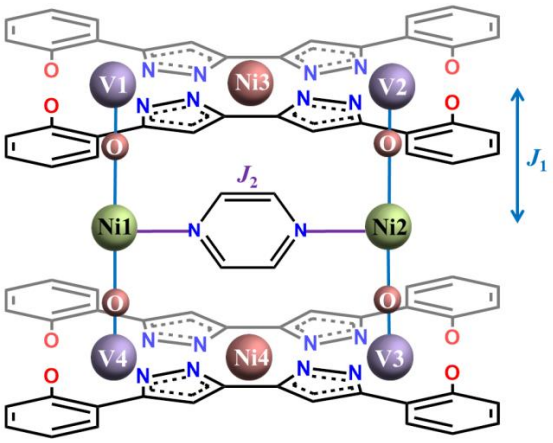

Scheme 4.3: Coupling scheme for the compound **29**. Diamagnetic square-planar Ni^{II} centres are shown in red, while paramagnetic octahedral Ni^{II} centres are shown as green balls. Atom numbering is not related with crystallographic symmetry and serves only for purpose of simplifying the spin Hamiltonian.

Successful models were created by fixing g_{VO}=2.00 and g_{Ni}=2.12, giving J_1=39.83 cm^{-1} and J_2=–0.98 cm^{-1} or J_1=40.47 cm^{-1} and zJ=–0.07 cm^{-1} (Figure 4.32). Possible interaction between peripheral vanadyl ions within the same platform were not considered since interactions of this type were not found to be relevant even in vanadyl precursor **23**. Unlike copper (II), magnetic orbitals of Ni(II) include $d_{x^2-y^2}$ and d_{z^2} where latter is strictly orthogonal to magnetic d_{xy} orbital of VO centre, leading to appearance of strong ferromagnetic coupling through oxygen bridge.

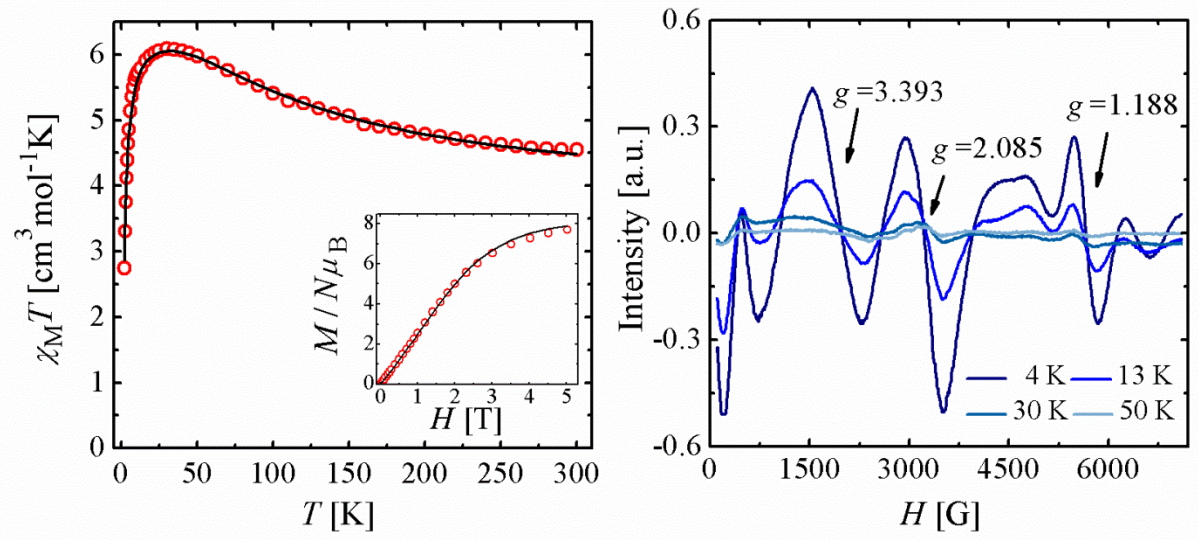

Figure 4.32: *Left:* $\chi_M T$ *vs* T and $M/N\mu_B$ *vs* H (inset) curves of compound **29** with the best fit (solid line). Measurement setup: warming mode (2→300 K), B = 0.5 T; T_{mag} = 2 K. *Right:* Variable temperature (4-50 K) X-band EPR spectra (f = 9.419 GHz) of a powdered sample of complex **29**.

These findings were consistent with temperature dependent EPR spectra of powdered sample. At room temperature, compound **29** is EPR silent, despite having EPR active S=1/2 vanadyl centres. Upon cooling below 50 K, complex pattern of resonances starts to intensify, following the rise of $\chi_M T$ product from dc measurements, indicating that those features are related with high spin states of the cluster.

SQUID magnetometry measurements on heterotrimetallic compound **30** revealed the room temperature (300 K) $\chi_M T$ product of 5.15 cm^{3}Kmol^{-1} which is higher than the expected 4.25 cm^{3}Kmol^{-1} for a heterometallic system incorporating four uncoupled S=1/2 (VO^{2+}), two uncoupled S=1/2 (Cu^{2+}) and two S=1 (Ni^{2+}) spin centres (g=2.0, Figure 4.33). This finding confirms the accuracy and uniqueness of assigned heterotrimetallic composition since any presence of diamagnetic Ni^{II} centres in the heart of metalloligand would diminish the total magnetic moment of this compound. Upon cooling, the $\chi_M T$ product increases slowly down to 50 K, followed by later abrupt increase up to the maximum value of 9.52 cm^{3}Kmol^{-1} at 6 K. In the lowest temperature range, small decline of the $\chi_M T$ values starts to happen ending at 7.17 cm^{3}Kmol^{-1} at 2 K. Such temperature dependence of the $\chi_M T$ product indicates the presence of very strong ferromagnetic (V=O−Ni−O=V, dominant) and (V=O−Cu−O=V, weaker) interactions within the cluster, while small drop might be related with ZFS effects on ground S=5 spin state. In agreement with this conclusion, field-dependent magnetization

measurements at 2K yielded the highest measured value of 9.69 μ_B at 5 T which lies only slightly below the expected 10.00 μ_B for strongly ferromagnetically coupled $[(VO)_4Cu_2Ni_2]$ cluster (g=2, Figure 4.33). To estimate the strength of magnetic coupling, experimental data ($\chi_M T$ *vs* T and $M/N\mu_B$ *vs* H) were modelled (PHI) using the matrix diagonalization of the spin Hamiltonian defined according to scheme 4.4:

$$\hat{H} = \mu_B B \sum_i g_i \hat{S}_i - 2J_1\left(\hat{S}_{V1}\hat{S}_{Ni1} + \hat{S}_{V2}\hat{S}_{Ni2} + \hat{S}_{V3}\hat{S}_{Ni2} + \hat{S}_{V4}\hat{S}_{Ni1}\right) - 2J_2\left(\hat{S}_{V1}\hat{S}_{Cu1} + \hat{S}_{V2}\hat{S}_{Cu1} + \hat{S}_{V3}\hat{S}_{Cu2} + \hat{S}_{V4}\hat{S}_{Cu2}\right) - 2J_3\left(\hat{S}_{Ni1}\hat{S}_{Ni2}\right)$$

or

$$\hat{H} = \mu_B B \sum_i g_i \hat{S}_i - 2J_1\left(\hat{S}_{V1}\hat{S}_{Ni1} + \hat{S}_{V2}\hat{S}_{Ni2} + \hat{S}_{V3}\hat{S}_{Ni2} + \hat{S}_{V4}\hat{S}_{Ni1}\right) - 2J_2\left(\hat{S}_{V1}\hat{S}_{Cu1} + \hat{S}_{V2}\hat{S}_{Cu1} + \hat{S}_{V3}\hat{S}_{Cu2} + \hat{S}_{V4}\hat{S}_{Cu2}\right) - zJ$$

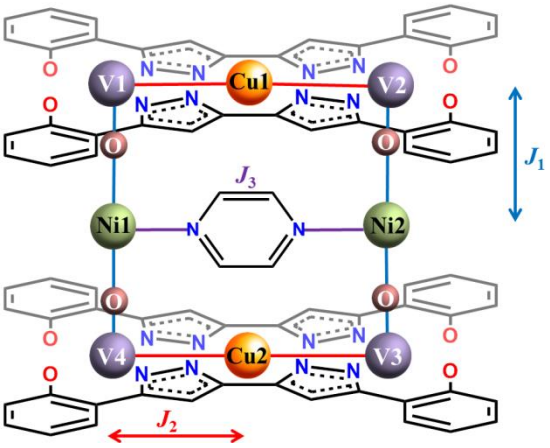

Scheme 4.4: Coupling scheme for the compound **38**. Atom numbering is not related with crystallographic symmetry and serves only for the purpose of simplifying the spin Hamiltonian.

The best models were created by fixing g_{VO}=g_{Cu}=2.00 and g_{Ni}=2.05, yielding J_1=42.80 cm^{-1}, J_2=4.29 cm^{-1} and zJ=0.03 cm^{-1} (Figure 4.32). Possible interaction between linker Ni^{II} spin carriers between the platforms was considered also, but refinement of that model reduced completely any contributions of J_3. Likewise, coupling between peripheral vanadyl ions within the same platform were not considered since interactions of this type were not found to be relevant even in vanadyl precursor **23**. Extracted J_1=42.80 cm^{-1} agrees nicely with previously described compound **29**, while J_2 is slightly reduced in comparison with compound **27** holding isolated [(VO)Cu(VO)] platforms (J_2 =6.54 cm^{-1}).

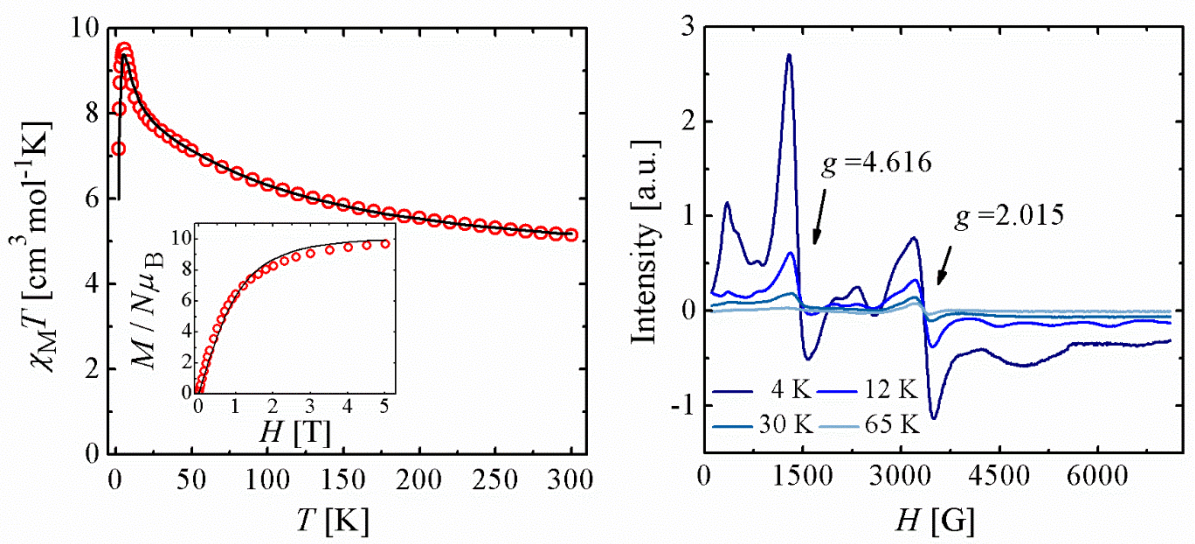

Figure 4.33: *Left:* $\chi_M T$ *vs T* and $M/N\mu_B$ *vs H* (inset) curves of compound **30** with the best fit (solid line). Measurement setup: warming mode (2→300 K), B = 1 T; T_{mag} = 2 K. *Right:* Variable temperature (4-65 K) X-band EPR spectra (f = 9.419 GHz) of a powdered sample of complex **30**.

Conclusions from susceptibility measurements were reinforced by variable-temperature EPR spectroscopy (4-300 K). Compound **30** was found to be EPR inactive at the room temperature, similarly as **29**, which is expected scenario bearing in mind strong ferromagnetic coupling within the cluster which diminished single-ion spin identities. Upon lowering the temperature below 60 K, half-field resonance centred at g=2.015 starts to appear, accompanied with down-field transitions at g=4.616 and g≈14 which collectively intensify upon cooling. Again, such temperature evolution of spectra is completely consistent with susceptibility studies, leading to conclusion that those transitions belong to coupled states of cluster.

SQUID magnetometry measurements on heterotrimetallic compound **31** revealed the room temperature (300 K) $\chi_M T$ product of 12.69 cm^{3}Kmol^{-1} which is higher than the expected 11.00 cm^{3}Kmol^{-1} for a heterometallic system incorporating four uncoupled S=1/2 (VO^{2+}), two uncoupled S=1/2 (Cu^{2+}) and two S=5/2 (Mn^{2+}) spin centres (g=2.0, Figure 4.34). This finding confirms the accuracy and uniqueness of assigned heterotrimetallic composition. Upon cooling, the $\chi_M T$ product increases steadily down to 30 K, followed by later abrupt increase up to the maximum value of 27.63 cm^{3}Kmol^{-1} at 3 K. In the lowest temperature range, small decline of the $\chi_M T$ values starts to happen ending at 26.27 cm^{3}Kmol^{-1} at 2 K. Such temperature dependence of the $\chi_M T$ product indicates the presence of very strong

ferromagnetic (V=O−Mn−O=V, dominant) and (V=O−Cu−O=V, weaker) interactions within the cluster, while small drop might be related with ZFS effects on ground S=8 spin state or nearby excited states. In agreement with this conclusion, field-dependent magnetization measurements at 2K yielded the highest measured value of 14.93 μ_B at 5 T which lies only slightly below the expected 16.00 μ_B for strongly ferromagnetically coupled $[(VO)_4Cu_2Mn_2]$ cluster (g=2, Figure 4.34). Due to high complexity of this system, no analytical expression was derived to estimate the strength of the coupling, although attempted simulations indicate J_1≈12 cm^{-1} and J_2≈6 cm^{-1}.

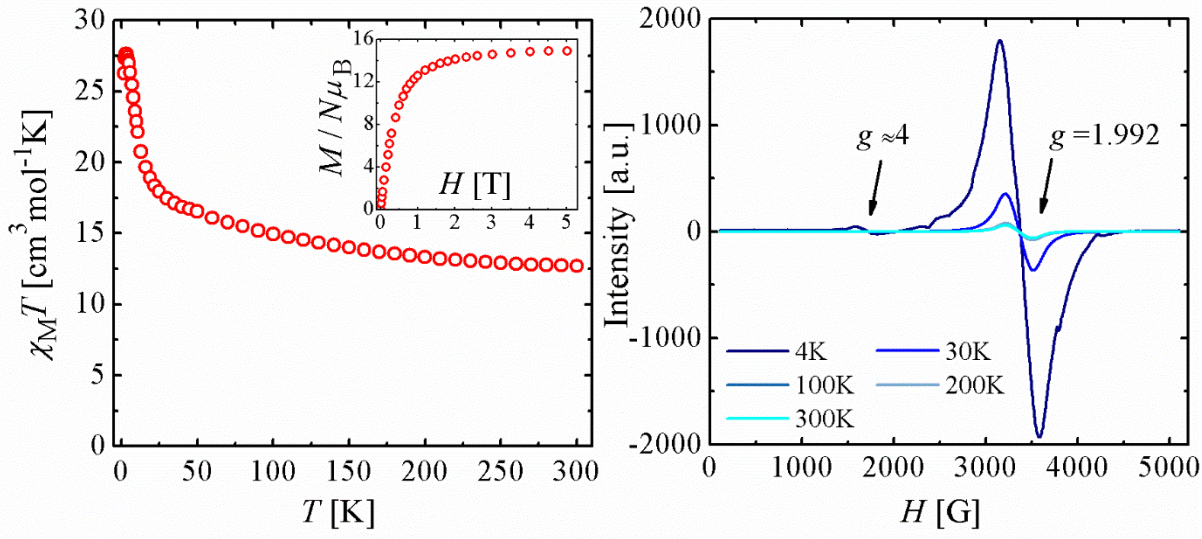

Figure 4.34: *Left:* $\chi_M T$ *vs* T and $M/N\mu_B$ *vs* H (inset) curves of compound **31**. Measurement setup: warming mode (2→300 K), B = 0.3 T; T_{mag} = 2 K. *Right:* Variable temperature (4-300 K) X-band EPR spectra (f = 9.419 GHz) of a powdered sample of complex **31**.

Variable temperature EPR studies showed that compound **31** is EPR active at the room temperature, exhibiting one resonance centred at g=1.992 which intensifies upon cooling. At 4 K, additional spectral feature centred at g≈4 becomes detectable.

SQUID magnetometry measurements on heterotrimetallic compound **32** revealed the room temperature (300 K) $\chi_M T$ product of 8.90 cm^3Kmol^{-1} which is higher than the expected 6.00 cm^3Kmol^{-1} for a heterometallic system incorporating four uncoupled S=1/2 (VO^{2+}), two uncoupled S=1/2 (Cu^{2+}) and two high-spin S=3/2 (Co^{2+}) spin centres (g=2.0, Figure 4.35). This finding confirms the accuracy and uniqueness of assigned heterotrimetallic composition. Upon cooling, the $\chi_M T$ product increases steadily down to 30 K, followed by later abrupt increase up to the maximum value of 16.77 cm^3Kmol^{-1} at 5 K. In the lowest temperature

range, small decline of the $\chi_M T$ values starts to happen ending at 11.29 cm^3Kmol^{-1} at 2 K. Such temperature dependence of the $\chi_M T$ product indicates the presence of very strong ferromagnetic (V=O−Co−O=V, dominant) and (V=O−Cu−O=V, weaker) interactions within the cluster, while small drop might be related with ZFS effects on ground S=6 spin state or nearby excited states. In agreement with this conclusion, field-dependent magnetization measurements at 2K revealed fast saturation of reduced magnetizations in the fields up to 1 T, which represents inflection point after which slower linear dependence happens, ending at 8.07 μ_B at 5 T which lies substantially below the expected 12.00 μ_B for strongly ferromagnetically coupled $[(VO)_4Cu_2Co_2]$ cluster (g=2, Figure 4.35). Due to high complexity of this system, no analytical expression was derived to estimate the strength of the coupling. Compound **32** is also found to be EPR silent in temperature range 4-300 K under X-band frequencies.

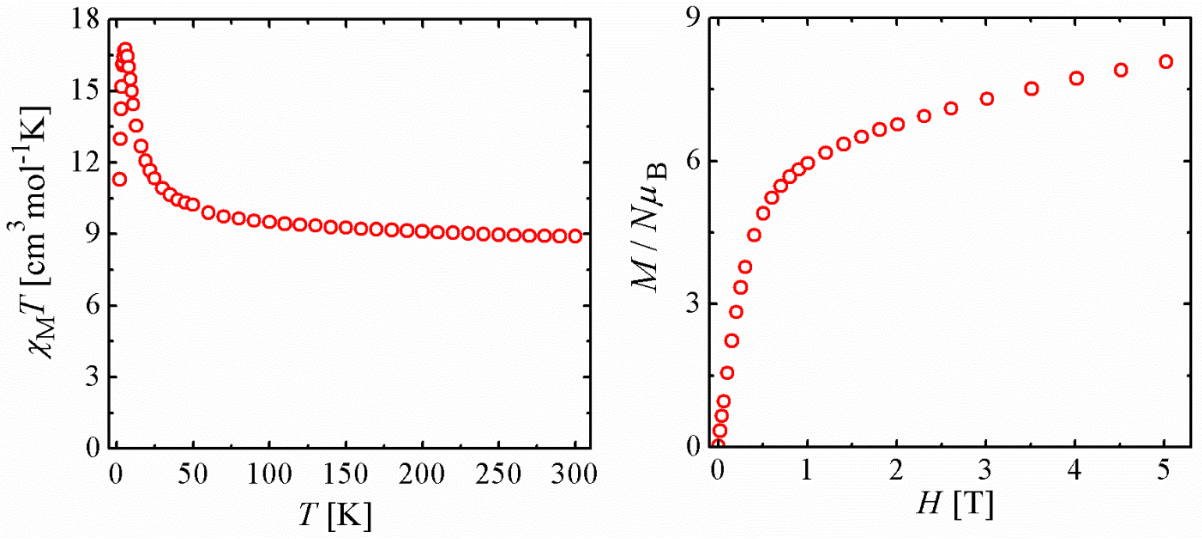

Figure 4.35: *Left:* $\chi_M T$ *vs* T and $M/N\mu_B$ *vs* H curves of compound **32**. Measurement setup: warming mode (2→300 K), B = 0.5 T; T_{mag} = 2 K.

SQUID magnetometry measurements on compound **33** revealed the room temperature (300 K) $\chi_M T$ product of 2.27 cm^3Kmol^{-1} which perfectly in agreement with the expected cm^3Kmol^{-1} for a heterometallic system incorporating four uncoupled S=1/2 (VO^{2+}) and two S=1/2 (Cu^{2+}) spin centres (g=2.0, Figure 4.36). Two additional Zn^{II} centres at linker positions between platforms are expected to be diamagnetic, hence magnetic studies confirmed heterotrimetallic nature of the compound. Upon cooling, the $\chi_M T$ product increases slowly down to 50 K and later more abruptly, reaching the maximum value of 3.35 cm^3Kmol^{-1} at 6

K. Further lowering of the temperature reveals small decline of the $\chi_M T$ values ending at 3.11 cm^3Kmol^{-1} at 2 K. Such temperature dependence of the $\chi_M T$ product indicates presence of ferromagnetic V−Cu−V interactions. In agreement with this conclusion, field-dependent magnetization measurements at 2K yielded the highest measured value of 5.63 μ_B at 5 T which lies only slightly below the expected 6.00 μ_B for two effective S=3/2 V=O−Cu−O=V clusters (g=2, Figure 4.36). To estimate the strength of magnetic coupling, experimental data ($\chi_M T$ *vs* T and $M/N\mu_B$ *vs* H) were modelled (PHI) using the matrix diagonalization of the spin Hamiltonian:

$$\hat{H} = \mu_B B \sum_i g_i \hat{S}_i - 2J\left(\hat{S}_{V1}\hat{S}_{Cu1} + \hat{S}_{V2}\hat{S}_{Cu1} + \hat{S}_{V3}\hat{S}_{Cu2} + \hat{S}_{V4}\hat{S}_{Cu2}\right) - zJ$$

The best models were created by fixing g_{VO}=g_{Cu}=2.00, yielding J=8.25 cm^{-1} and zJ=–0.02 cm^{-1} (Figure 4.36). Obtained J value is slightly increased in this case in comparison with compound **27** with isolated [(VO)Cu(VO)] platforms (J_2 =6.54 cm^{-1}).

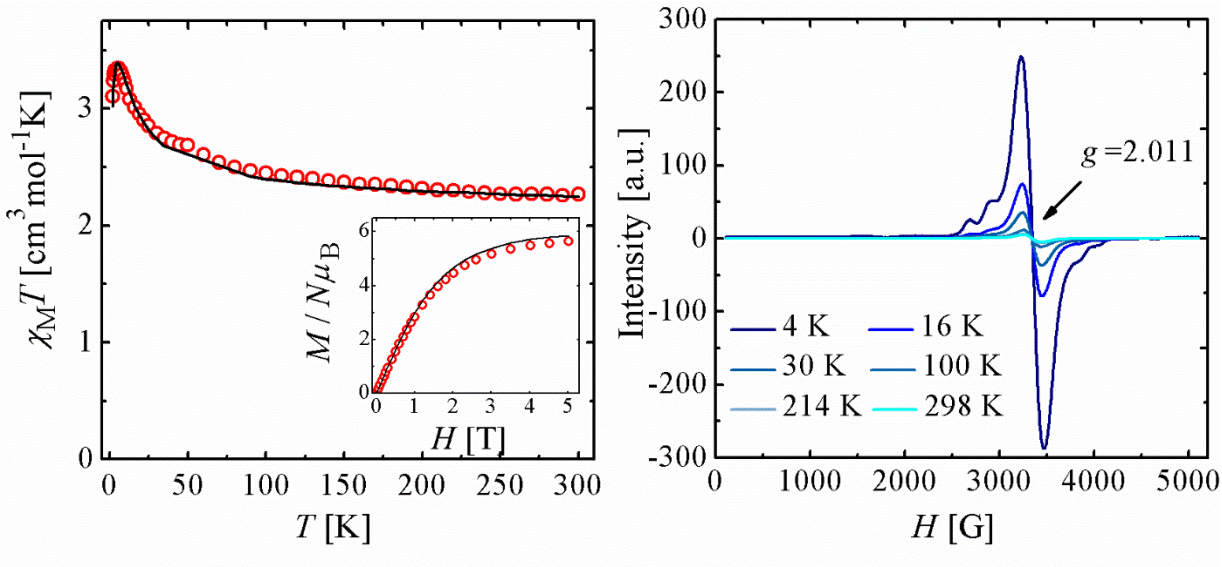

Figure 4.36: *Left:* $\chi_M T$ *vs* T and $M/N\mu_B$ *vs* H (inset) curves of compound **33** with the best fit (solid line). Measurement setup: warming mode (2→300 K), B = 1 T; T_{mag} = 2 K. *Right:* Variable temperature (4-298 K) X-band EPR spectra (f = 9.419 GHz) of a powdered sample of complex **33**.

Temperature variable EPR studies showed that sample is EPR active from the room temperature, as expected for molecule holding non-integer spin carriers, showing single resonance centred at g=2.011. Upon cooling, intensity of this ΔM_S transition increases, accompanied by appearance of broad resonance at g≈4, which probably originates from S=3/2 ground state of the cluster.

Encouraged with non-zero magnetic moment of heterometallic VO–M compounds **28**-**33**, we've decided to further test their magnetic properties using ac susceptibility measurements. Temperature and frequency dependence of the alternate-current (ac) magnetic susceptibility revealed that compounds **28**, **29** and **30** show none or very weak response of out-of-phase ac susceptibility (Figures IV.A23-25), even under applied field, while compounds **31**-**33** exhibit frequency dependent χ_M'' behaviour in applied magnetic fields (Figures A26-A28). The latter was particulary striking for $[(VO)_4Cu_2Mn_2]$ cluster **31**, so we have continued its study in a collaboration with Dr Olivier Roubeau. Studies were undertaken using PPMS SQUID magnetometer under applied, optimised dc field of 1000 Oe (Figure IV.A29) and range of frequencies (1-10 000 Hz) since he maximum in χ'' occurs above 1 kHz. The values of the maxima in χ'' are smaller than half those of χ' at low frequency, while χ' does not reach 0 at the highest frequency meaning that only fraction of spin exhibits slow relaxation. On the other hand, the values of the maxima in χ'' do agree with the decrease in χ' (about half of it). The maximum in the χ'' vs. frequency data shifts to above 10 kHz already around 4.5 K so measurements were thus done only up to 7 K (1.8-7 K range). Frequency dependent sets of the out-of-phase AC susceptibility (χ_M'') show that the maximum of the χ_M'' *vs* *ν* curves is shifted towards higher frequency value as the temperature is increased accompanied with the decaying intensity (Figure 4.37).

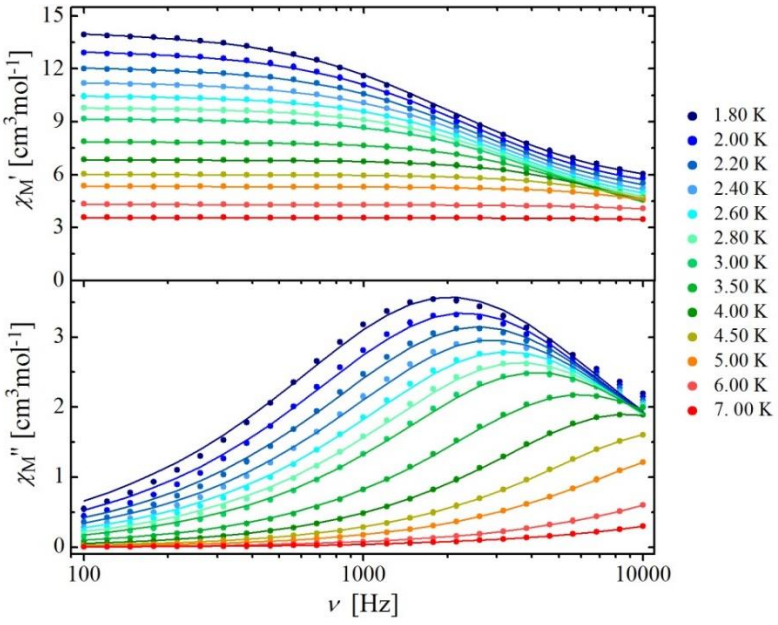

Figure IV.A10: Frequency dependence of the in- (χ_M') and out-of-phase (χ_M'') AC susceptibility for the compound **31** under an applied DC field of 1000 Oe. Solid lines are fits to the experimental data.

The latter is clearly visible from the temperature dependence of the AC susceptibility data (Figure IV.A30) which also indicates that the maximum for the χ_M'' at the lowest temperature appears between 1778.3 and 2154.4 Hz. A representation of the results in the complex χ-plane (Argand plot, Figure 4.38), reveals a set of semicircles (indicative of single relaxation process) which lose their intensity upon heating. In order to quantify the dynamics of the magnetization (relaxation time and the width of its distribution), the χ_M' and χ_M'' data were fitted simultaneously to the generalised Debye model[39]:

$$\chi_{AC}(\omega) = \chi_S + \frac{\chi_T - \chi_S}{1+(i\omega\tau)^{(1-\alpha)}}$$

As seen in Figure 4.38, the fitted parameters are in good agreement with the experimental data, yielding a narrow distribution of α values for the entire temperature range taken into consideration ($0.03<\alpha<0.16$).

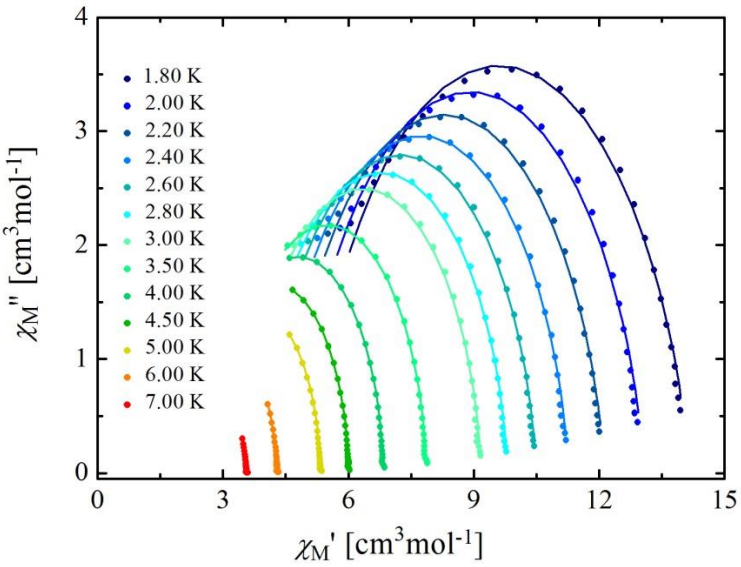

Figure 4.38: *Bottom:* Cole-Cole isotherms of the AC susceptibility for **31** under an applied DC field of 1000 Oe. Solid lines are fits of experimental data.

4.3.11. Experimental

Solvents and reagents were used as received from the commercial suppliers in preparation of ligand and compounds. Sodium hydride was applied as a suspension in mineral oil (60% w/w), while tetrabutylammonium hydroxide was used as a solution in methanol (*c*=1

mol/dm^3). Vanadyl sulfate was used as hydrated salt ($VOSO_4 \cdot xH_2O$), similarly as hexahydrated copper(II), nickel(II), cobalt(II), zinc(II) and manganese(II) perchlorates. Synthetic procedures involving $CuCl_2 \cdot 2H_2O$, $NiCl_2 \cdot 6H_2O$ and $CoCl_2 \cdot 6H_2O$ can be reproduced also by changing the metal source to perchlorate salts. In the synthesis of compounds **24a** and **24b**, manganese(II) chloride tetrahydrate and manganese(III) acetate dihydrate were used, respectively.

H_4L4: Ligand **H_4L1** (1.50 g, 4.60 mmol) was suspended in 50 mL of methanol (yellow suspension) followed by addition of hydrazine monohydrate (46.00 mmol, 2.23 mL) which caused immediate dissolution of solid and colour fading. Mixture was brought to reflux and maintained like this for 14 h. After approximately 1h, precipitation of white solid was observed. Upon completion of the reaction, mixture was cooled to room temperature triggering the extensive precipitation of ligand **H_4L4**. Average yield was 55 % (0.81 g). Additional crop of the product can be collected after reduction of solvent volume to half (average 8%, 0.12 g). Single crystals of the ligand **H_4L4** can be obtained directly from the reaction mixture or by recrystallization from acetone. ^{1}H NMR (400 MHz, d_6-Acetone), δ(ppm): 6.96 (d, 2H, -Ar-*H*), 7.24 (t, 2H, -Ar-*H*), 7.75 (s, 1H, -Ar-*H*), 10.85 (broad s, Ar-O*H*), 12.90 (broad s, Ar-N*H*); ^{1}H NMR (400 MHz, d_6-DMSO), δ(ppm): 6.91 (t, 1H, -Ar-*H*), 6.96 (d, 1H, -Ar-*H*), 7.16 (s, 1H, -Ar-*H*), 7.19 (t, 1H, -Ar-*H*), 7.73 (d, 1H, -Ar-*H*). ESI MS: *m*/*z* [H_4L4+H^+]= 319.12, [H_4L4+Na^+]= 341.10. IR (KBr pellet) ν/cm^{-1}: 3415 s, 3186 b, 3149 b, 3051 b, 2919 b, 1587 s, 1554 s, 1516 s, 1508 s, 1463 s, 1392 s, 1348 s, 1287 s, 1252 s, 1169 s, 1115 s, 1066 s, 1045 s, 1015 s, 969 s, 932 s, 825 s, 784 s, 741 s, 702 s, 679 s, 663 s, 647 s, 614 s, 564 s, 540 s, 478 s, 466 s. EA (%): Calc. (Found for **H_4L4**): C 67.92 (68.06); H 4.43 (4.37); N 17.60 (17.71).

$(TBA)_2[Cu_3(L4)_2(py)_{0.5}]$ (**21**): Tetrabutylammonium hydroxide (380 µL, 0.380 mmol) was added to the colourless pyridine solution of **H_4L4** (30.0 mg, 0.094 mmol in 10 mL) causing its immediate change of colour to light yellow. Obtained solution was stirred for 10 min and then was added dropwise to the pyridine solution of $CuCl_2 \cdot 2H_2O$ (24.1 mg, 0.141 mmol), changing its colour from green to dark brown. Resulting solution was stirred for 1h at room temperature, followed by filtration to remove small amount of formed precipitate (≈3 mg) and then layered with hexanes. Orange-brown needles appeared after several hours and were allowed to grow until the system was homogenous (approximately 20 days). Average yield was 67 % (41.0 mg). Faster crystallisation was achieved using Et_2O and toluene as antisolvents. IR (KBr pellet) ν/cm^{-1}: 3386 b, 3190 b, 3058 b, 2959 s, 2932 b, 2873 s 1594 s,

1559 s, 1492 s, 1458 s, 1380 s, 1363 s, 1314 s, 1297 s, 1269 s, 1216 s, 1152 s, 1121 s, 1061 s, 1037 s, 998 s, 929 s, 878 s, 850 s, 828 s, 785 s, 748 s, 692 s, 666 s, 606 s, 597 s, 575 s, 551 s, 443 s. EA (%): Calc. (Found for $C_{68}H_{92}N_{10}O_4Cu_3 \cdot 1.8H_2O$): C 61.11 (61.12); H 7.21 (7.23); N 10.48 (10.44).

$(TBA)_2[Ni_3(L4)_2]$ (**22**): Tetrabutylammonium hydroxide (380 µL, 0.380 mmol) was added to the colourless pyridine solution of **H_4L4** (30.0 mg, 0.094 mmol in 10 mL) causing its immediate change of colour to light yellow. Obtained solution was stirred for 10 min and then was added dropwise to the pyridine solution of $NiCl_2 \cdot 6H_2O$ (33.6 mg, 0.141 mmol) changing its colour from green to orange-red. Resulting solution was stirred for 1h at room temperature, with the noticeable appearance of the crystalline product after 30 min. Subsequent filtration and layering of the filtrate with Et_2O led to formation of brown-red needles after several hours which were allowed to grow until the system was homogenous (approximately 10 days). Average yield was 43 % (26.0 mg). ^{1}H NMR (400 MHz, d_6-DMSO), δ(ppm): 0.93 (t, 6H, -N-$CH_2CH_2CH_2CH_3$), 1.30 (sxt, 4H, -N-$CH_2CH_2CH_2CH_3$), 1.56 (quin, 4H, -N-$CH_2CH_2CH_2CH_3$), 3.16 (m, 4H, -N-$CH_2CH_2CH_2CH_3$), 6.33 (t, 1H, -Ar-*H*), 6.53 (d, 1H, -Ar-*H*), 6.65 (s, 1H, -Ar-*H*), 6.85 (t, 1H, -Ar-*H*), 7.28 (d, 1H, -Ar-*H*). IR (KBr pellet) ν/cm^{-1}: 3050 b, 2958 s, 2932 b, 2873 s, 1595 s, 1560 s, 1508 s, 1458 s, 1378 s, 1314 s, 1278 s, 1248 s, 1201 s, 1150 s, 1121 s, 1066 s, 1033 s, 1002 s, 927 s, 879 s, 857 s, 778 s, 738 s, 700 s, 678 s, 605 s, 682 s, 558 s, 450 s. EA (%): Calc. (Found for $C_{68}H_{92}N_{10}O_4Ni_3 \cdot 1.25py \cdot 1.3H_2O$): C 63.16 (63.20); H 7.20 (7.24); N 11.16 (11.20).

$(TBA)_2[(VO)_2(HL4)_2]$ (**23**): Tetrabutylammonium hydroxide (380 µL, 0.380 mmol) was added to the colourless pyridine solution of **H_4L4** (30.0 mg, 0.094 mmol in 10 mL) causing its immediate change of colour to light yellow. Obtained solution was stirred for 10 min and then was added dropwise to the hot pyridine solution of $VOSO_4 \cdot xH_2O$ (34.1 mg, 0.188 mmol) changing its colour from blue to violet. Resulting solution was stirred for 1h at room temperature, filtered and layered with Et_2O. Violet block appeared overnight and were allowed to grow until the system was homogenous (approximately 10 days). Average yield was 68 % (40.0 mg). IR (KBr pellet) ν/cm^{-1}: 3430 b, 3052 b, 2959 s, 2932 b, 2872 s, 1596 s, 1560 s, 1482 s, 1458 s, 1440 s, 1379 s, 1347 s, 1312 s, 1299 s, 1268 s, 1251 s, 1151 s, 1118 s, 1062 s, 1035 s, 975 s, 933 s, 878 s, 855 s, 785 s, 748 s, 697 s, 669 s, 635 s, 620 s, 576 s, 529 s, 504 s. EA (%): Calc. (Found for $C_{68}H_{94}N_{10}O_6V_2 \cdot 1.1\ H_2O$): C 64.35 (64.62); H 7.64 (7.92); N 11.04 (11.07).

[$Mn_2(HL4)_2$] (**24a**): Tetrabutylammonium hydroxide (285 µL, 0.285 mmol) was added to the colourless pyridine solution of **H_4L4** (30.0 mg, 0.094 mmol in 10 mL) causing its immediate change of colour to light yellow. Obtained solution was stirred for 10 min and then was added dropwise to the pyridine solution of $MnCl_2 \cdot 4H_2O$ (18.7 mg, 0.094 mmol) changing its colour from light pink to dark green. Resulting solution was stirred for 1h at room temperature, filtered and layered with Et_2O or hexanes. Green blocks appeared after 10 days and were allowed to grow until the system was homogenous (approximately 10 or 20 days for Et_2O and hexanes, respectively). Average yield was 26 % (16 mg).IR (KBr pellet) ν/cm^{-1}: 3044 b, 2959 s, 2933 b, 2872 b, 1595 s, 1559 s, 1508 s, 1485 s, 1458 s, 1438 s, 1383 s, 1351 s, 1295 s, 1255 s, 1244 s, 1216 s, 1154 s, 1125 s, 1070 s, 1034 s, 1003 s, 985 s, 856 s, 792 s, 748 s, 688 s, 671 s. EA (%): Calc. (Found for $C_{72}H_{78}N_{13}O_4Mn_2Cl \cdot 1.65H_2O$: C 63.38 (63.49); H 6.01 (6.13); N 13.34 (13.33).

[$Mn_2(HL4)_2$] (**24b**): Tetrabutylammonium hydroxide (285 µL, 0.285 mmol) was added to the colourless pyridine solution of **H_4L4** (30.0 mg, 0.094 mmol in 10 mL) causing its immediate change of colour to light yellow. Obtained solution was stirred for 10 min and then was added dropwise to the pyridine solution of $Mn(CH_3COO)_3 \cdot 2H_2O$ (25.3 mg, 0.094 mmol) changing its colour from orange to dark green. Resulting solution was stirred for 1h at room temperature, filtered and layered with hexanes. Dark green plates appeared after 7 days and were allowed to grow until the system was homogenous (approximately 3 weeks). Average yield was 60 % (30 mg).IR (KBr pellet) ν/cm^{-1}: 3040 b, 1596 s, 1560 s, 1486 s, 1458 s, 1442 s, 1349 s, 1309 s, 1296 s, 1256 s, 1243 s, 1215 s, 1154 s, 1121 s, 1068 s, 1035 s, 1003 s, 989 s, 925 s, 856 s, 775 s, 742 s, 689 s, 673 s. EA (%): Calc. (Found for $C_{56}H_{46}N_{12}O_4Mn_2 \cdot 0.7H_2O$: C 62.89 (63.09); H 4.09 (4.30); N 15.72 (15.58).

[$Co_3(L4)_2(py)_5(OMe)$] (**25**): Tetrabutylammonium hydroxide (380 µL, 0.380 mmol) was added to the colourless pyridine solution of **H_4L4** (30.0 mg, 0.094 mmol in 10 mL) causing its immediate change of colour to light yellow. Obtained solution was stirred for 10 min and then was added dropwise to the pyridine solution of $CoCl_2 \cdot 6H_2O$ (33.6 mg, 0.141 mmol) changing its colour from red to green-brown. Resulting solution was stirred for 1h at room temperature, filtered and layered with Et_2O. Dark green needles appeared after several days and were allowed to grow until the system was homogenous (approximately 10 days). Average yield was 48 % (28 mg). IR (KBr pellet) ν/cm^{-1}: 3419 b, 3116 b, 3053 b, 2958 s, 2933 b, 2873 s, 1594 s, 1560 s, 1508 s, 1458 s, 1379 s, 1315 s, 1278 s, 1246 s, 1198 s, 1150 s, 1120

s, 1065 s, 1031 s, 1001 s, 926 s, 856 s, 743 s, 700 s, 677 s, 650 s, 617 s, 587 s, 539 b, 471 b. EA (%): Calc. (Found for $C_{62}H_{48}N_{13}O_5Co_3 \cdot 1.35H_2O$): C 59.28 (59.27); H 4.07 (4.09); N 14.49 (14.51).

$(TBA)_2[Cu_2(HL4)_2]$ (**26**): Tetrabutylammonium hydroxide (380 µL, 0.380 mmol) was added to the colourless pyridine solution of **H_4L4** (30.0 mg, 0.094 mmol in 10 mL) causing its immediate change of colour to light yellow. Obtained solution was stirred for 10 min and then was added dropwise to the pyridine solution of $CuCl_2 \cdot 2H_2O$ (8.0 mg, 0.047 mmol) and $VOSO_4 \cdot xH_2O$ (17.1 mg, 0.094 mmol) changing its colour from marine blue to olive green. Resulting solution was stirred for 1h at room temperature, filtered and layered with Et_2O. Brown needles and block which appeared after 24h belong were characterised as compounds **21** (6%, 4 mg) and **23** (12%, 7 mg) respectively, and were allowed to grow until the system was homogenous (approximately 10 days). Addition of another crop of Et_2O to the remaining solution caused the crystallisation of compound **26** (17%, 10 mg). IR (KBr pellet) ν/cm^{-1}: 3436 b, 2960 s, 2931 b, 2873 s, 1597 s, 1556 s, 1504 s, 1482 s, 1464 s, 1410 b, 1380 s, 1349 s, 1318 s, 1304 s, 1282 s, 1267 s, 1189 b, 1150 s, 1121 s, 1063 s, 1034 s, 994 s, 975 s, 882 s, 856 s, 749 s, 664 s, 589 s, 563 s, 529 s.

$(TBA)_2[Cu(VO)_2(L4)_2]$ (**27**): To a pyridine solution of compound **23** (25 mg, 0.020 mmol in 18 mL) was added TBAOH (40 µL, 0.040 mmol) causing its change of colour from violet to light blue. Obtained solution was stirred for 10 min, followed by addition of pyridine solution of $CuCl_2 \cdot 2H_2O$ (1.7 mg, 0.010 mmol in 2 mL). Resulting olive green solution was stirred for 1h at room temperature, filtered and layered with Et_2O. Dark green blocks appeared after two weeks in an average yield of 29 % (8 mg). IR (KBr pellet) ν/cm^{-1}: 3051 b, 2958 s, 2932 b, 2872 s, 1594 s, 1560 s, 1481 s, 1456 s, 1378 s, 1361 s, 1313 s, 1297 s, 1272 s, 1246 s, 1198 s, 1151 s, 1120 s, 1061 s, 1034 s, 983 s, 859 s, 807 s, 781 s, 749 s, 698 s, 685 s, 671 s. EA (%): Calc. (Found for $C_{73}H_{97}N_{11}O_6V_2Cu \cdot 2.1H_2O$): C 61.40 (61.55); H 7.14 (7.05); N 10.79 (10.64).

$[Cu_4(VO)_4(L4)_4(py)_{14}]$ (**28**): To a violet pyridine solution of compound **23** (20 mg, 0.016 mmol in 15 mL) was added pyridine solution of $Cu(ClO_4)_2 \cdot 6H_2O$ (11.8 mg, 0.032 mmol in 5 mL). Resulting yellow-brown solution was stirred for 1h at room temperature and filtered. Vapour diffusion of Et_2O to the filtrate allowed growth of brown crystal blocks over the period of 10 days. Average yield was 33 % (). IR (KBr pellet) ν/cm^{-1}: 3430 b, 3050 b, 1597 s, 1561 s, 1508 s, 1491 s, 1458 s, 1445 s, 1379 s, 1314 s, 1296 s, 1267 s, 1242 s, 1154 s, 1122 s, 1062 s, 1036 s, 996 s, 929 s, 859 s, 783 s, 739 s, 696 s, 674 s, 641 s, 622 s, 577 s, 541 s, 440 s.

[$Ni_4(VO)_4(L4)_4(py)_{10}(C_4H_4N_2)$] (**29**): To a violet pyridine solution of compound **23** (20 mg, 0.016 mmol in 15 mL) was added pyridine solution of $Ni(ClO_4)_2{\cdot}6H_2O$ (11.7 mg, 0.032 mmol in 5 mL) and pyrazine (approximately 3-4 mg). Resulting orange solution was stirred for 1h at room temperature and filtered. Vapour diffusion of Et_2O to the filtrate allowed growth of orange-red crystal blocks over the period of 10 days. Average yield was 48 % (10 mg). IR (KBr pellet) ν/cm^{-1}: 3409 b, 3051 b, 1597 s, 1560 s, 1503 s, 1457 s, 1444 s, 1411 s, 1302 s, 1268 s, 1245 s, 1183 s, 1153 s, 1123 s, 1065 s, 1036 s, 998 s, 940 s, 904 s, 859 s, 811 s, 781 s, 742 s, 699 s, 674 s, 624 s, 579 s, 554 s, 477 s, 441 b. EA (%): Calc. (Found for $C_{126}H_{94}N_{28}O_{12}Ni_4V_4{\cdot}5.35H_2O$): C 55.49 (55.50); H 3.87 (3.47); N 14.38 (13.98).

[$Ni_2Cu_2(VO)_4(L4)_4(py)_{10}(C_4H_4N_2)$] (**30**): To a violet pyridine solution of compound **23** (20 mg, 0.016 mmol in 15 mL) was added pyridine solution (5 mL) of $Ni(ClO_4)_2{\cdot}6H_2O$ (5.8 mg, 0.016 mmol), $Cu(ClO_4)_2{\cdot}6H_2O$ (5.9 mg, 0.016 mmol) and pyrazine (approximately 3-4 mg). Resulting yellow-brown solution was stirred for 1h at room temperature and filtered. Vapour diffusion of Et_2O to the filtrate allowed growth of brown crystal blocks over the period of 10 days. Average yield was 43 % (9 mg). IR (KBr pellet) ν/cm^{-1}: 3423 b, 3053 b, 1600 s, 1561 s, 1508 s, 1489 s, 1458 s, 1445 s, 1363 s, 1314 s, 1297 s, 1267 s, 1246 s, 1189 s, 1153 s, 1123 s, 1064 s, 1036 s, 997 s, 940 s, 921 s, 900 s, 859 s, 815 s, 800 s, 742 s, 701 s, 673 s, 624 s, 576 s, 541 s, 436 s. EA (%): Calc. (Found for $C_{126}H_{94}N_{28}O_{12}V_4Cu_2Ni_2{\cdot}4.85H_2O{\cdot}2\ C_5H_5N$): C 56.60 (56.59); H 3.97 (3.99); N 14.56 (14.58).

[$Mn_2Cu_2(VO)_4(L4)_4(py)_{10}(C_4H_4N_2)$] (**31**): To a violet pyridine solution of compound **23** (20 mg, 0.016 mmol in 15 mL) was added pyridine solution (5 mL) of $Mn(ClO_4)_2{\cdot}6H_2O$ (5.8 mg, 0.016 mmol), $Cu(ClO_4)_2{\cdot}6H_2O$ (5.9 mg, 0.016 mmol) and pyrazine (approximately 3-4 mg). Resulting yellow-orange solution was stirred for 1h at room temperature and filtered. Vapour diffusion of Et_2O to the filtrate allowed growth of yellow crystal blocks over the period of 10 days. Average yield was 48 % (10 mg). IR (KBr pellet) ν/cm^{-1}: 3397 b, 3057 b, 1595 s, 1560 s, 1508 b, 1487 s, 1458 s, 1442 s, 1357 s, 1311 s, 1297 s, 1268 s, 1245 s, 1203 s, 1151 s, 1119 s, 1063 s, 1035 s, 1010 s, 996 s, 932 s, 901 s, 880 s, 859 s, 783 s, 745 s, 696 s, 672 s, 624 s, 574 s, 542 s, 448 s, 433 s. EA (%): Calc. (Found for $C_{126}H_{94}N_{28}O_{12}V_4Cu_2Mn_2{\cdot}2.2H_2O{\cdot}4.35\ C_5H_5N$): C 58.83 (58.79); H 4.01 (4.05); N 15.02 (15.06).

[$Co_2Cu_2(VO)_4(L4)_4(py)_{10}(C_4H_4N_2)$] (**32**): To a green pyridine solution of compound **23** (15 mg, 0.011 mmol in 15 mL) was added pyridine solution (5 mL) of $Co(ClO_4)_2{\cdot}6H_2O$ (3.9 mg, 0.011 mmol) and pyrazine (approximately 3 mg). Resulting orange solution was stirred for 1h at

room temperature and filtered. Vapour diffusion of Et_2O to the filtrate allowed growth of orange crystal blocks over the period of 10 days. Average yield was 56 % (8 mg). IR (KBr pellet) ν/cm^{-1}: 3426 b, 3051 b, 1598 s, 1561 s, 1507 s, 1491 s, 1458 s, 1444 s, 1378 s, 1314 s, 1297 s, 1267 s, 1245 s, 1201 s, 1151 s, 1121 s, 1063 s, 1035 s, 1012 s, 998 s, 942 s, 921 s, 902 s, 860 s, 786 s, 750 s, 699 s, 676 s, 622 s, 576 s, 541 s, 436 s. EA (%): Calc. (Found for $C_{126}H_{94}N_{28}O_{12}V_4Cu_2Co_2 \cdot 1.4C_5H_5N$): C 58.05 (58.18); H 3.70 (3.55); N 14.96 (14.94).

$[Zn_2Cu_2(VO)_4(L4)_4(py)_{10}(C_4H_4N_2)]$ (**33**): To a violet pyridine solution of compound **23** (20 mg, 0.016 mmol in 15 mL) was added pyridine solution (5 mL) of $Zn(ClO_4)_2 \cdot 6H_2O$ (6.0 mg, 0.016 mmol), $Cu(ClO_4)_2 \cdot 6H_2O$ (5.9 mg, 0.016 mmol) and pyrazine (approximately 3-4 mg). Resulting yellow-brown solution was stirred for 1h at room temperature and filtered. Vapour diffusion of Et_2O to the filtrate allowed growth of yellow-brown crystal blocks over the period of 10 days. Average yield was 42 % (9 mg). IR (KBr pellet) ν/cm^{-1}: 3420 b, 3052 b, 1596 s, 1560 s, 1488 s, 1458 s, 1444 s, 1364 s, 1313 s, 1298 s, 1268 s, 1245 s, 1204 s, 1151 s, 1120 s, 1063 s, 1035 s, 997 s, 942 s, 910 s, 890 s, 859 s, 786 s, 741 s, 697 s, 672 s, 625 s, 575 s, 543 s, 432 s. EA (%): Calc. (Found for $C_{126}H_{94}N_{28}O_{12}V_4Cu_2Zn_2 \cdot 3.2H_2O \cdot 3.7C_5H_5N$): C 57.77 (57.78); H 3.99 (4.00); N 14.78 (14.79).

4.3.12. Literature

1. O. Kahn and B. Briat, *Journal of the Chemical Society, Faraday Transactions 2: Molecular and Chemical Physics*, 1976, **72**, 268-281.
2. O. Kahn and B. Briat, *Journal of the Chemical Society, Faraday Transactions 2: Molecular and Chemical Physics*, 1976, **72**, 1441-1446.
3. S. Gomez-Coca, E. Cremades, N. Aliaga-Alcalde and E. Ruiz, *J. Am. Chem. Soc.*, 2013, **135**, 7010-7018.
4. J. D. Rinehart and J. R. Long, *Chemical Science*, 2011, **2**, 2078-2085.
5. K. S. Pedersen, J. Bendix and R. Clerac, *Chem. Commun.*, 2014, **50**, 4396-4415.
6. A. N. Kost and I. I. Grandberg, *Adv. Heterocycl. Chem.*, 1966, **6**, 347-429.
7. T. Jozak, D. Zabel, A. Schubert, Y. Sun and W. R. Thiel, *Eur. J. Inorg. Chem.*, 2010, **2010**, 5135-5145.
8. M. A. Monge, E. G. Pµebla, J. Elguero, C. Toiron, W. Meutermans and I. Sobrados, *Spectrochimica Acta Part A: Molecular Spectroscopy*, 1994, **50**, 727-734.
9. S. Terashima, G. N. Newton, T. Shiga and H. Oshio, *Inorganic Chemistry Frontiers*, 2015, **2**, 125-128.
10. A. W. Augustyniak, M. Fandzloch, M. Domingo, I. Lakomska and J. A. R. Navarro, *Chem. Commun.*, 2015, **51**, 14724-14727.
11. M. R. Bond, L. M. Mokry, T. Otieno, J. Thompson and C. J. Carrano, *Inorg. Chem.*, 1995, **34**, 1894-1905.
12. V. Chandrasekhar, A. Dey, T. Senapati and E. C. Sanudo, *Dalton Transactions*, 2012, **41**, 799-803.
13. D. Collison, D. R. Eardley, F. E. Mabbs, A. K. Powell and S. S. Turner, *Inorg. Chem.*, 1993, **32**, 664-671.
14. N. S. Dean, M. R. Bond, C. J. O'Connor and C. J. Carrano, *Inorg. Chem.*, 1996, **35**, 7643-7648.
15. E. Kime-Hunt, K. Spartalian, M. DeRusha, C. M. Nunn and C. J. Carrano, *Inorg. Chem.*, 1989, **28**, 4392-4399.
16. M. Kosugi, S. Hikichi, M. Akita and Y. Moro-oka, *Inorg. Chem.*, 1999, **38**, 2567-2578.
17. M. Mohan, M. R. Bond, T. Otieno and C. J. Carrano, *Inorg. Chem.*, 1995, **34**, 1233-1242.
18. L. M. Mokry, J. Thompson, M. R. Bond, T. Otieno, M. Mohan and C. J. Carrano, *Inorg. Chem.*, 1994, **33**, 2705-2706.
19. T. Otieno, L. M. Mokry, M. R. Bond, C. J. Carrano and N. S. Dean, *Inorg. Chem.*, 1996, **35**, 850-856.
20. Y. Xing, Y. Zhang, Y. Xu, B. Zhang, S. Niu and F. Bai, *Chin. Sci. Bull.*, 2006, **51**, 2189-2196.
21. Y. H. Xing, F. Y. Bai, K. Aoki, Z. Sun and M. F. Ge, *Synthesis and Reactivity in Inorganic, Metal-Organic, and Nano-Metal Chemistry*, 2007, **37**, 203-211.
22. C. W. Hahn, P. G. Rasmussen and J. C. Bayon, *Inorg. Chem.*, 1992, **31**, 1963-1965.
23. H. Chen, C. Ma, S. Xiang, M. Hu, Y. Si, C. Chen and Q. Liu, *J. Coord. Chem.*, 2008, **61**, 3556-3567.
24. H. Miyasaka, A. Saitoh and S. Abe, *Coord. Chem. Rev.*, 2007, **251**, 2622-2664.
25. N. F. Chilton, R. P. Anderson, L. D. Turner, A. Soncini and K. S. Murray, *J. Comput. Chem.*, 2013, **34**, 1164-1175.

26. P. King, R. Clerac, C. E. Anson and A. K. Powell, *Dalton Transactions*, 2004, DOI: 10.1039/B315067D, 852-861.
27. G. A. Craig, M. Schütze, D. Aguilà, O. Roubeau, J. Ribas-Ariño, S. Vela, S. J. Teat and G. Aromí, *Inorg. Chem.*, 2014, **53**, 3290-3297.
28. R. Belda, J. Pitarch-Jarque, C. Soriano, J. M. Llinares, S. Blasco, J. Ferrando-Soria and E. García-España, *Inorg. Chem.*, 2013, **52**, 10795-10803.
29. V. Mishra, F. Lloret and R. Mukherjee, *Eur. J. Inorg. Chem.*, 2007, **2007**, 2161-2170.
30. C. Miranda, F. Escartí, L. Lamarque, E. García-España, P. Navarro, J. Latorre, F. Lloret, Hermás R. Jiménez and María J. R. Yunta, *Eur. J. Inorg. Chem.*, 2005, **2005**, 189-208.
31. H. Matsushima, H. Hamada, K. Watanabe, M. Koikawa and T. Tokii, *J. Chem. Soc., Dalton Trans.*, 1999, DOI: 10.1039/A808074G, 971-978.
32. T. Kamiusuki, H. Okawa, N. Matsumoto and S. Kida, *J. Chem. Soc., Dalton Trans.*, 1990, DOI: 10.1039/DT9900000195, 195-198.
33. D. J. de Geest, A. Noble, B. Moubaraki, K. S. Murray, D. S. Larsen and S. Brooker, *Dalton Transactions*, 2007, DOI: 10.1039/B614637F, 467-475.
34. V. P. Hanot, T. D. Robert, J. Kolnaar, J. G. Haasnoot, J. Reedijk, H. Kooijman and A. L. Spek, *J. Chem. Soc., Dalton Trans.*, 1996, DOI: 10.1039/DT9960004275, 4275-4281.
35. T.-L. Hu, J.-R. Li, C.-S. Liu, X.-S. Shi, J.-N. Zhou, X.-H. Bu and J. Ribas, *Inorg. Chem.*, 2006, **45**, 162-173.
36. A. Noble, J. Olguín, R. Clérac and S. Brooker, *Inorg. Chem.*, 2010, **49**, 4560-4569.
37. D. Ajo, A. Bencini and F. Mani, *Inorg. Chem.*, 1988, **27**, 2437-2444.
38. L. K. Frensch, K. Pröpper, M. John, S. Demeshko, C. Brückner and F. Meyer, *Angew. Chem. Int. Ed.*, 2011, **50**, 1420-1424.
39. K. S. Cole and R. H. Cole, *The Journal of Chemical Physics*, 1941, **9**, 341-351.
40. L. Tesi, E. Lucaccini, I. Cimatti, M. Perfetti, M. Mannini, M. Atzori, E. Morra, M. Chiesa, A. Caneschi, L. Sorace and R. Sessoli, *Chemical Science*, 2016, **7**, 2074-2083.
41. J. H. Van Vleck, *Physical Review*, 1940, **57**, 426-447.
42. M. Atzori, L. Tesi, E. Morra, M. Chiesa, L. Sorace and R. Sessoli, *J. Am. Chem. Soc.*, 2016, **138**, 2154-2157.
43. M. Atzori, E. Morra, L. Tesi, A. Albino, M. Chiesa, L. Sorace and R. Sessoli, *J. Am. Chem. Soc.*, 2016, **138**, 11234-11244.
44. M. Atzori, L. Tesi, S. Benci, A. Lunghi, R. Righini, A. Taschin, R. Torre, L. Sorace and R. Sessoli, *J. Am. Chem. Soc.*, 2017, **139**, 4338-4341.
45. W. Lin, T. Bodenstein, V. Mereacre, K. Fink and A. Eichhöfer, *Inorg. Chem.*, 2016, **55**, 2091-2100.
46. R. C. Poulten, M. J. Page, A. G. Algarra, J. J. Le Roy, I. López, E. Carter, A. Llobet, S. A. Macgregor, M. F. Mahon, D. M. Murphy, M. Murugesu and M. K. Whittlesey, *J. Am. Chem. Soc.*, 2013, **135**, 13640-13643.
47. M. Ding, G. E. Cutsail Iii, D. Aravena, M. Amoza, M. Rouzieres, P. Dechambenoit, Y. Losovyj, M. Pink, E. Ruiz, R. Clerac and J. M. Smith, *Chemical Science*, 2016, **7**, 6132-6140.
48. R. Boča, C. Rajnák, J. Titiš and D. Valigura, *Inorg. Chem.*, 2017, **56**, 1478-1482.
49. S. Gómez-Coca, A. Urtizberea, E. Cremades, P. J. Alonso, A. Camón, E. Ruiz and F. Luis, *Nature Communications*, 2014, **5**, 4300.
50. J. Krzystek, G. J. Yeagle, J.-H. Park, R. D. Britt, M. W. Meisel, L.-C. Brunel and J. Telser, *Inorg. Chem.*, 2003, **42**, 4610-4618.

51. B. Nelly, R. Thayalan, T. S. M., B. E. K., R. Gopalan and J. L. F., *Chemistry – A European Journal*, 2012, **18**, 5906-5918.
52. Z.-Y. Zhang, C. Brouca-Cabarrecq, C. Hemmert, F. Dahan and J.-P. Tuchagues, *J. Chem. Soc., Dalton Trans.*, 1995, DOI: 10.1039/DT9950001453, 1453-1460.
53. F. H. Köhler, *Paramagnetic Complexes in Solution: The NMR Approach*, 2011.
54. I. Bertini, C. Luchinat, G. Parigi and E. Ravera, in *NMR of Paramagnetic Molecules (Second Edition)*, Elsevier, Boston, 2017, pp. 175-253.
55. I. Bertini, C. Luchinat, G. Parigi and E. Ravera, in *NMR of Paramagnetic Molecules (Second Edition)*, Elsevier, Boston, 2017, pp. 77-126.
56. A. Bencini, C. Benelli, A. Dei and D. Gatteschi, *Inorg. Chem.*, 1985, **24**, 695-699.
57. T. Glaser, H. Theil, I. Liratzis, T. Weyhermüller and E. Bill, *Inorg. Chem.*, 2006, **45**, 4889-4891.
58. O. Kahn, J. Galy, Y. Journaux, J. Jaud and I. Morgenstern-Badarau, *J. Am. Chem. Soc.*, 1982, **104**, 2165-2176.
59. O. Kahn, P. Tola, J. Galy and H. Coudanne, *J. Am. Chem. Soc.*, 1978, **100**, 3931-3933.
60. S. Mohanta, K. K. Nanda, L. K. Thompson, U. Flörke and K. Nag, *Inorg. Chem.*, 1998, **37**, 1465-1472.
61. V. H. Crawford, H. W. Richardson, J. R. Wasson, D. J. Hodgson and W. E. Hatfield, *Inorg. Chem.*, 1976, **15**, 2107-2110.
62. M. Zhao, C. Zhong, C. Stern, A. G. M. Barrett and B. M. Hoffman, *J. Am. Chem. Soc.*, 2005, **127**, 9769-9775.
63. R. Shannon, *Acta Crystallographica Section A*, 1976, **32**, 751-767.
64. G. F. S. Whitehead, F. Moro, G. A. Timco, W. Wernsdorfer, S. J. Teat and R. E. P. Winpenny, *Angew. Chem. Int. Ed.*, 2013, **52**, 9932-9935.
65. N. Bridonneau, L.-M. Chamoreau, P. P. Laine, W. Wernsdorfer and V. Marvaud, *Chem. Commun.*, 2013, **49**, 9476-9478.
66. K.-Q. Hu, X. Jiang, S.-Q. Wu, C.-M. Liu, A.-L. Cui and H.-Z. Kou, *Dalton Transactions*, 2015, **44**, 15413-15416.
67. C. Chen, Y. Liu, P. Li, H. Zhou and X. Shen, *Dalton Transactions*, 2015, **44**, 20193-20199.
68. D. Visinescu, M.-G. Alexandru, A. M. Madalan, I.-R. Jeon, C. Mathoniere, R. Clerac and M. Andruh, *Dalton Transactions*, 2016, **45**, 7642-7649.
69. N. Bridonneau, G. Gontard and V. Marvaud, *Dalton Transactions*, 2015, **44**, 5170-5178.
70. H. Zhou, C. Chen, K. Wu, Y. Liu and X. Shen, *Eur. J. Inorg. Chem.*, 2016, **2016**, 4921-4927.
71. V. Vieru, T. D. Pasatoiu, L. Ungur, E. Suturina, A. M. Madalan, C. Duhayon, J.-P. Sutter, M. Andruh and L. F. Chibotaru, *Inorg. Chem.*, 2016, **55**, 12158-12171.
72. T. Shiga, H. Ōkawa, S. Kitagawa and M. Ohba, *J. Am. Chem. Soc.*, 2006, **128**, 16426-16427.
73. D. Visinescu, A. M. Madalan, M. Andruh, C. Duhayon, J.-P. Sutter, L. Ungur, W. Van den Heuvel and L. F. Chibotaru, *Chemistry – A European Journal*, 2009, **15**, 11808-11814.
74. M.-J. Liu, K.-Q. Hu, C.-M. Liu, A.-L. Cui and H.-Z. Kou, *New J. Chem.*, 2016, **40**, 8643-8649.
75. H. Zhou, C. Chen, J. Lu, Y. Liu and X. Shen, *Inorg. Chim. Acta*, 2016, **453**, 482-487.

76. S. Dhers, H. L. C. Feltham, R. Clérac and S. Brooker, *Inorg. Chem.*, 2013, **52**, 13685-13691.
77. G. Novitchi, S. Shova, Y. Lan, W. Wernsdorfer and C. Train, *Inorg. Chem.*, 2016, **55**, 12122-12125.
78. H. O. Stumpf, Y. Pei, O. Kahn, L. Ouahab and D. Grandjean, *Science*, 1993, **261**, 447-449.
79. M. Zhu, L. Li and J.-P. Sutter, *Inorganic Chemistry Frontiers*, 2016, **3**, 994-1003.
80. C. Nazari Verani, T. Weyhermuller, E. Rentschler, E. Bill and P. Chaudhuri, *Chem. Commun.*, 1998, DOI: 10.1039/A806575F, 2475-2476.
81. C. N. Verani, E. Rentschler, T. Weyhermuller, E. Bill and P. Chaudhuri, *J. Chem. Soc., Dalton Trans.*, 2000, DOI: 10.1039/B005768L, 4263-4271.
82. D. Visinescu, J.-P. Sutter, C. Ruiz-Pérez and M. Andruh, *Inorg. Chim. Acta*, 2006, **359**, 433-440.
83. M.-G. Alexandru, D. Visinescu, S. Shova, M. Andruh, F. Lloret and M. Julve, *Inorg. Chem.*, 2017, **56**, 2258-2269.
84. H. Wang, L.-F. Zhang, Z.-H. Ni, W.-F. Zhong, L.-J. Tian and J. Jiang, *Crystal Growth & Design*, 2010, **10**, 4231-4234.
85. B. Sonnenburg, I. Liratzis, A. Stammler, H. Bögge and T. Glaser, *Eur. J. Inorg. Chem.*, 2015, **2015**, 912-915.
86. C. P. Berlinguette and K. R. Dunbar, *Chem. Commun.*, 2005, DOI: 10.1039/B418698B, 2451-2453.
87. A. Rodríguez-Diéguez, R. Kivekäs, R. Sillanpää, J. Cano, F. Lloret, V. McKee, H. Stoeckli-Evans and E. Colacio, *Inorg. Chem.*, 2006, **45**, 10537-10551.
88. J. Ferrando-Soria, E. Moreno Pineda, A. Chiesa, A. Fernandez, S. A. Magee, S. Carretta, P. Santini, I. J. Vitorica-Yrezabal, F. Tuna, G. A. Timco, E. J. L. McInnes and R. E. P. Winpenny, 2016, **7**, 11377.
89. G. F. S. Whitehead, B. Cross, L. Carthy, V. A. Milway, H. Rath, A. Fernandez, S. L. Heath, C. A. Muryn, R. G. Pritchard, S. J. Teat, G. A. Timco and R. E. P. Winpenny, *Chem. Commun.*, 2013, **49**, 7195-7197.
90. A. Fernandez, E. Moreno Pineda, C. A. Muryn, S. Sproules, F. Moro, G. A. Timco, E. J. L. McInnes and R. E. P. Winpenny, *Angew. Chem. Int. Ed.*, 2015, **54**, 10858-10861.
91. G.-C. Ou, L. Jiang, X.-L. Feng and T.-B. Lu, *Dalton Transactions*, 2009, DOI: 10.1039/B810802A, 71-76.
92. M. I. Khan, E. Yohannes and R. J. Doedens, *Angew. Chem. Int. Ed.*, 1999, **38**, 1292-1294.
93. X.-L. Wang, C.-H. Gong, J.-W. Zhang, L.-L. Hou, J. Luan and G.-C. Liu, *CrystEngComm*, 2014, **16**, 7745-7752.
94. Y.-Y. Zhou, S. Yao, J.-H. Yan, L. Chen, T.-T. Wang, C.-J. Wang and Z.-M. Zhang, *Dalton Transactions*, 2015, **44**, 20435-20440.
95. G.-C. Ou, X.-Y. Yuan, Z.-Z. Li, W.-Y. Li, F. Zeng, J.-H. Deng and D.-C. Zhong, *Eur. J. Inorg. Chem.*, 2016, **2016**, 3500-3505.
96. M. I. Khan, R. C. Nome, S. Deb, J. H. McNeely, B. Cage and R. J. Doedens, *Crystal Growth & Design*, 2009, **9**, 2848-2852.
97. M. Yuan, Y. Li, E. Wang, C. Tian, L. Wang, C. Hu, N. Hu and H. Jia, *Inorg. Chem.*, 2003, **42**, 3670-3676.
98. Q. Wu, X. Hao, X. Feng, Y. Wang, Y. Li, E. Wang, X. Zhu and X. Pan, *Inorg. Chem. Commun.*, 2012, **22**, 137-140.

99. X. Wu, T. Huang, T. T. Lekich, R. D. Sommer and W. W. Weare, *Inorg. Chem.*, 2015, **54**, 5322-5328.
100. E. M. Goggins, T. T. Lekich, W. W. Weare, R. D. Sommer, M. A. Ribeiro and C. B. Pinheiro, *Eur. J. Inorg. Chem.*, 2016, **2016**, 1054-1059.
101. T. Huang, X. Wu, W. W. Weare and R. D. Sommer, *Eur. J. Inorg. Chem.*, 2014, **2014**, 5662-5674.
102. T. Huang, X. Wu, X. Song, H. Xu, T. I. Smirnova, W. W. Weare and R. D. Sommer, *Dalton Transactions*, 2015, **44**, 18937-18944.

CHAPTER V

CONCLUSIONS AND FUTURE PERSPECTIVE

Research presented in this manuscript was based on implementation of sophisticatedly designed *bis*−β-diketone and polypyrazolyl scaffolds in controlled assembly of paramagnetic 3*d* coordination compounds. Synthetic control provided means for subtle modulation of corresponding magnetic properties of formed compounds, enabling evolution of molecules with great relevance in evolving field of molecular magnetism.

Chapter II presented new synthetic strategy of rational preparation of oxo-hydroxido coupled pair of homometallic and heterometallic dimers based on *bis*−β-diketone ligand H_4L1. Two fused phenol-β-diketone coordination pockets provided enough flexibility for selective manipulation of ligand conformation and coordination modes. Particularly, by imposing pair-impair metal-ligand ratio, with large excess of *3*d metal ions, controlled assembly of coupled pairs of dimers or monomers was achieved. Moreover, it was shown that only one ligand molecule in the backbone of the structure was enough to impose desired site selectivity which was successfully exploited to generate all possible heterometallic pairs of late 3*d* metals. Structural analysis of those coordination entities proved that bonding details correlated with the nature of metal ions can be used as a fingerprinting evidence for correct positional assignment of heterometallic topologies. Magnetic studies proved meaningful insight in strength of antiferromagnetic interactions between identical of diverse spin carries, providing some meaningful knowledge to be exploited. Oxalato core of the ligand ensured effective coupling between the dimers or monomers, giving rise to singlet ground state in all compounds. Additionally, it was clearly show that [NiCu] dimers from all possible combinations provide best isolated ground state doublet and thus should be exploited as potential qubit candidates. Gathered knowledge from this section inspired the evolution of Chapter III, where novel library of structurally related asymmetric and multidentate *bis*−β-diketone ligand was designed and exploited in construction of molecular prototypes of multiqubit quantum logic gates. Direct transfer of imposed asymmetry of the ligands to their coordination compounds enabled successful preparation of three new compounds which fulfil the basic requirement of asymmetry and ground state doublet to be considered as molecular prototypes of C-NOT quantum gates. In that aspect, structure of compound **18** represents the biggest achievement as a very first example of a coordination compound which features the triple asymmetry between the component qubits. However, despite of coherent spin dynamics in those systems, magnetic

studies and EPR spectroscopy have shown that degree of imposed asymmetry for now remains too small for having any possibility of addressing the qubits individually to perform basic quantum operations. One way to overcome this issue would be to increase the asymmetry of ligands with larger substituents and find ways how to predesign clusters of different nuclearity within the same molecule. This might be achieved by exploiting two new symmetric oxo-hydroxo-bridged $[CuNi]_2$ (compounds **19** and **20**) as potential metalloligands since they still retain free coordination pockets in their structure and could produce clusters with {[CuNi]···M···[CuNi]} topology. Similarly, conversion of methoxy substituent to phenol in asymmetric ligand H_4LA2 will create more nucleophilic coordination pocket which can be activated by deprotonation. In this way, clusters with {[M'MM']···[MM']} topology might be formed. Nevertheless, as one of the highlights of this research line, it was shown how rational ligand design can be exploited to tune the interaction between individual qubits, while control of reaction stoichiometry can provide means of changing their topology. Also, initial steps are undertaken in expanding the coordination chemistry of more complex *bis*−β-diketone ligand to vanadium(IV) based qubits. Obtained neutral clusters $[(V^{IV}O)_4(H_2L5)_4(py)_4]$ (**14**) and $[(V^{V}O)_4(V^{IV}O)_2\ (O)_4(L6)_2(py)_6]$ (**15**) exhibit very peculiar metal topologies and composition, differing significantly from structural patterns established in the related chemistry of divalent 3*d* metals which might be also related to supramolecular features inherent to the V=O moiety. This chemistry is yet to be expanded to other asymmetry and multidentate ligands in order construct operable vandyl molecular qugates.

Finally, Chapter IV expanded the ligand library to pyrazole derivatives of *bis*−β-diketone ligands and exposed extensive coordination chemistry of phenolic pyrazole ligand **H_4L4**. Initial idea behind its implementation was to selectively chelate different 3*d* metals into linear arrays based on their preference towards (-*N*,*N*) or (-*O*,*N*) coordination environment of the ligand. Homometallic series of obtained compounds indicated that only vanadyl cation (VO^{2+}) and Mn^{3+} ion discriminate two different ligating donor sets and reside exclusively in the (-*O,N*) coordination pocket, leaving central -N_4 chelating metal-free, inspired their further use as metalloligands. Great structural rigidity and excessive negative charge of metalloligand **23** enhanced nucleophilic nature of vanadyl ions, providing means for bitopic structural expansion in selective formation of derived heterobimetallic and heterotrimetallic clusters. Additionally, orthogonality in expansion of metalloligand

structure ensured double orthogonality between magnetic orbitals of vanadyl and heavier 3*d* ions resulting with purely ferromagnetically coupled clusters which even exhibit slow relaxation of magnetization when constructed from isotropic metal ions. This fundamental discovery seeks for further exploitation involving even more complex metalloligands and other *3*d and 4*f* ions. Alternatively, replacement of paramagnetic vanadyl ion for its diamagnetic titanyl analogue should exploit this reactivity patterns in a construction of molecular quantum gates with two inequivalent spin qubits. Additionally, anisotropic Mn(III) metalloligand can be also employed for encapsulation of different metal ions and formation of new families of heterobimetallic compounds with interesting magnetic properties. Overall, work presented along these lines exposed different ways of constructing heterometallic compounds providing good initial playground for many novel directions of research within coordination chemistry and molecular magnetism.

APPENDIX I

INTRODUCTION

Table I.A1: Single molecule magnets referenced at Figure 1.6.

Label	Formula	Refcode	Reference
$Mn^{III/IV}_{12}$	$[Mn_{12}(CH_3COO)_{16}(H_2O)_4O_{12}]$	AQACMN	33-35
$Mn^{III/IV}_4$	$[Mn_4(CH_3CH_2COO)_3O_3Cl_4(py)_3]_2$	KUCHIZ	38-39
Mn^{III}_{84}	$[Mn_{84}(CH_3COO)_{78}O_{72}(CH_3O)_{24}(CH_3OH)_{12}(H_2O)_{42}(OH)_6]$	BEQXEB	40
$Mn^{II/III}_{19}$	$[Mn_{19}(\mu_3,\eta^1\text{-}N_3)_8O_8(CH_3CN)_6(HL)_{12}]Cl_2$	XELCUN	42
Mn^{III}_6	$[Mn_6(C_6H_5COO)_2O_2(sao)_6(EtOH)_4]$	CEYMAV	37
Fe^{II}	$[K(DME)_4][(tpa^{Mes})Fe]$	JIWVER	93
Fe^{I}	$[K(crypt\text{-}222)][Fe(C(Si(CH_3)_3)_3)_2]$	BIJFIL	96
SCO-Fe^{II}	$[PhB(MesIm)_3Fe\text{-}N{=}PPh_3]$	EWOPUC	100
Co^{II}	[(sIPr)CoNDmp]	PAHWED	99
Cu_2Tb_2	$[CuL_ATb(hfac)_2]_2$	MUTKER	47
$Mn^{III}_{18}Mn^{IV}_3Dy$	$[Mn_{21}DyO_{20}(OH)_2(^t BuCOO)_{20}(HCOO)_4(NO_3)_3(H_2O)_7]$	ZASBAY	50
$Mn^{III}_6Tb_2$	$[Mn_6Tb_2O_3(sao)_6(CH_3O)_6(CH_3OH)_4(H_2O)_2]$	CUKDAP[1]	51
$Mn^{II}_6(UO_2)_{12}$	$[(UO_2)(salen)_2Mn(C_5H_5N)_3]_2$	FENJIT	61
$Co^{III}_2Dy_2$	$[Co_2Dy_2(CH_3O)_2(teaH)_2(piv)_6]$	SIRQAN	52
$Cr^{III}_4Dy_4$	$[Cr_4Dy_4F_4(OCH_3)_{1.25}(OH)_{2.75}(C_6H_5COO)_8(mdea)_4]$	EQIKEW	58
$[Pc_2Tb]$	$[TBA][Pc_2Tb]$	JERGAP	45
$[Tb]_2$	$[K(18\text{-}crown\text{-}6)(THF)_2]$ $[\{[(Me_3Si)_2N]_2(THF)Tb\}_2(\mu\text{-}\eta^2\text{:}\eta^2\text{-}N_2]$	CAJRIQ	72
$[Dy]_2$	$[(Cp^{pm}_2Ln)_2(\mu\text{-bpym}\cdot)](BPh_4)$	YEZBOW	75
$[Er(COT)_2]$	$[K(18\text{-}crown\text{-}6)][Er(COT)_2]$	YIWTUV01	78
$[Dy_4K_2]$	$[Dy_4K_2O(O^tBu)_{12}]$	SIBJUK	80
$[Dy(t\text{-}BuO)_2]$	$[Dy(O^tBu)_2(C_5H_5N)_5][B(C_6H_5)]$	RAPDUK	86
$[Dy(cpd)_2]$	$[(Cp^{ttt})_2DyC][B(C_6F_5)_4]$	BAWLOD MEKDOY	82 83

H_3L=2,6-bis(hydroxymethyl)-4-methylphenol; $saoH_2$=2-hydroxybenzaldehyde oxime; tpa^{Mes}= tris(5-mesityl-1H-pyrrol-2-ylmethyl)amine-*N*,*N*',*N*'',*N*'''; DME=1,2-dimethoxyethane; crypt-222=4,7,13,16,21,24-hexaoxa-1,10-diazabicyclo[8.8.8]hexacosane; $PhB(MesIm)_3$= tris(3-mesitylimidazolyl-2-ylidene)phenylborate; sIPr=1,3-bis(2',6'-diisopropylphenyl)-4,5-dihydro-imidazol-2-ylidene; Dmp= 2,6-dimesitylphenyl; hfac=hexafluoroacetylacetone; H_3L_A= 1-(2-hydroxybenzamido)-2-(2-hydroxy-3-methoxybenzylideneamino)ethane; $salenH_2$=*N*, *N*'-ethylenebis(salicylimine); $teaH_3$=triethanolamine; piv=trimethylacetate; $mdeaH_2$=*N*-methyldiethanolamine; TBA=tetrabutylammonium cation; Pc=phtalocyanine; Cp^{pm}=pentamethylcyclopentadienyl; bpym= 2,2'-bipyrimidine; COT^{2-}= cyclooctatetraene dianion; Cp^{ttt}= 1,2,4-tri(tert-butyl)cyclopentadienyl

[1]Only reported structural data in the CSD database can be found for the $[Mn^{III}_6Gd_2]$ analogue (G. Rigaux, F. White, E. Brechin, CSD Communication, 2015).

APPENDIX II

TOPOLOGY AND SITE SELECTIVITY IN HYDROXO-β-DIKETONATO COUPLED PAIRS OF 3*d* DIMERS

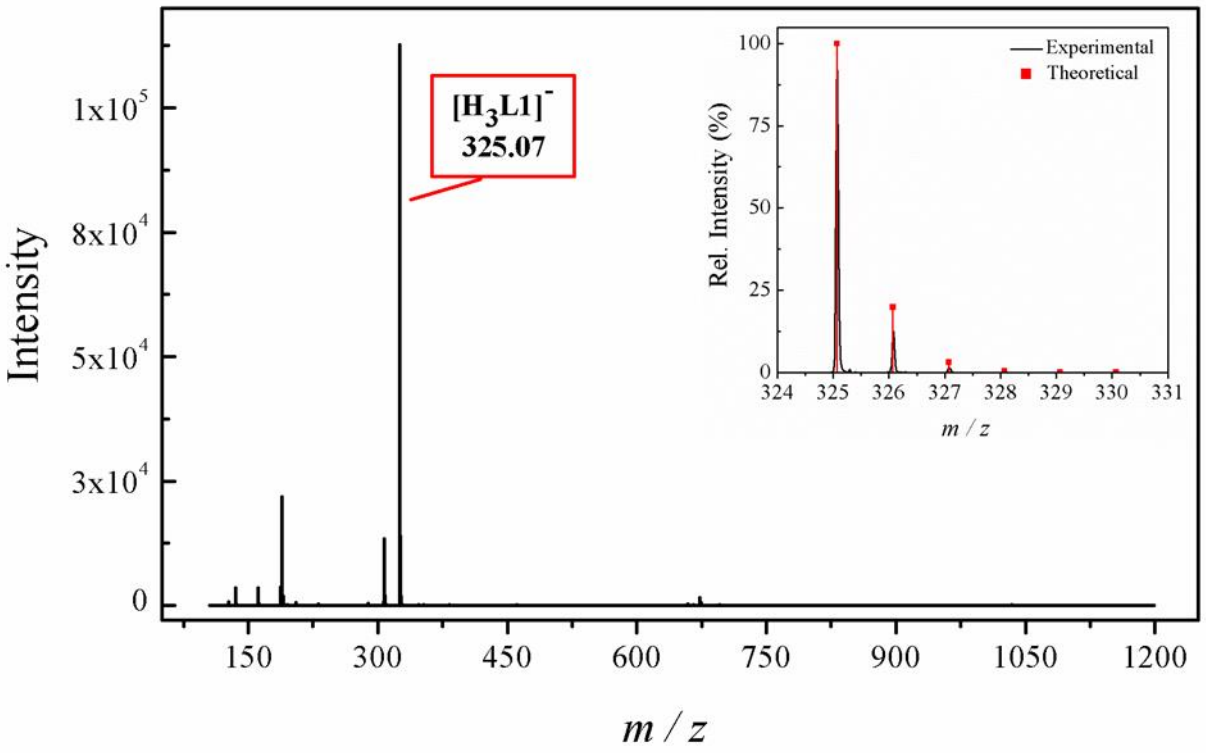

Figure II.A1: ESI(-) mass spectrogram of THF solution of ligand **H_4L1**. *Inset*: Isotopic distribution of the most abundant molecular peak.

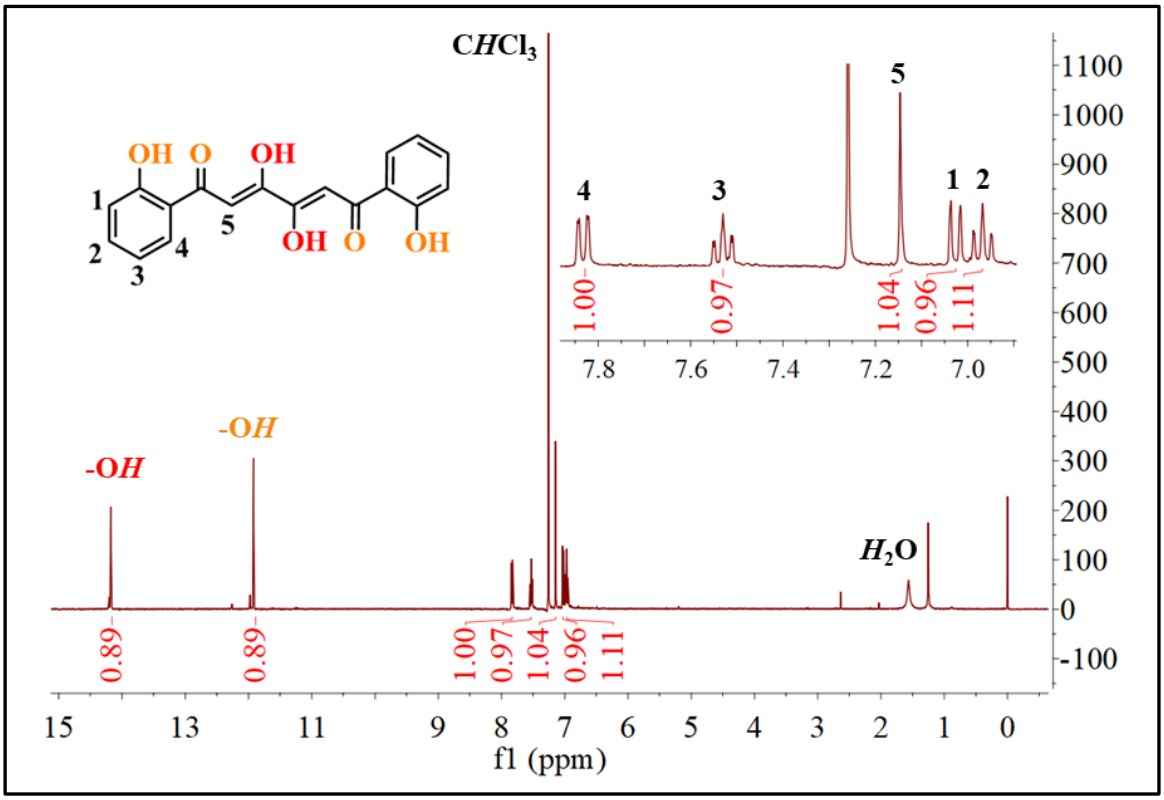

Figure II.A2: ^{1}H NMR spectrum of ligand **H_4L1** in deuterated chloroform.

Table II.A1: Crystallographic data for ligand **H_4L1**

	H_4L1
Formula	$C_{18}H_{14}O_6$
M_r	326.29
Crystal system	Monoclinic
Space group	$P2_1/c$
a (Å)	15.026(5)
b (Å)	3.7516(12)
c (Å)	12.998(4)
α (°)	90
β (°)	104.592(4)
γ (°)	90
V (Å^3)	709.1(4)
Z	2
ρ_{calc} (g/cm^3)	1.528
μ (cm^{-1})	0.116
Shape and colour	Colourless plate
Crystal size (mm^3)	0.01·0.13·0.21
λ (Å)	0.71073
T (K)	100(2)
Reflections	2127
Unique reflections	1674
Parameters	111
Restraints	0
R_1 (all data)[a]	0.0743
R_1 [$I>2\sigma(I)$][a]	0.0560
wR_2 (all data)[b]	0.1459
wR_2 [$I>2\sigma(I)$][b]	0.1401
S (all data)[c]	1.117
S [$I>2\sigma(I)$][c]	1.117
Largest residuals (e Å^3)	0.456/–0.269

[a] $R_1 = \Sigma||F_o| - |F_c|| / \Sigma|F_o|$;

[b] $wR_2 = \{\Sigma[w(F_o^2 - F_c^2)^2] / \Sigma[w(F_o^2)^2]\}^{1/2}$;[c] $S = \{\Sigma[w(F_o^2 - F_c^2)^2] / (n - p)\}^{1/2}$

Table II.A2: Bond distances [Å] within **H_4L1**

O3–C9	1.351(3)
C9–C8	1.401(3)
C8–C7	1.380(3)
C7–C6	1.397(3)
C6–C5	1.377(3)
C5–C4	1.410(3)
C4–C9	1.419(2)
C4–C3	1.472(2)
C3–O2	1.266(2)
C3–C2	1.445(2)
C2–C1	1.361(2)
C1–O1	1.331(2)
C1–C1#	1.480(2)

Symmetry operation:
= 2−x, 1 −y, 1−z

Table II.A3: Hydrogen bonding and π···π contacts in the structure of **H_4L1**

D–H···A	**D–H (Å)**	**H···A (Å)**	**D···A (Å)**	**D–H···A (°)**
O3–H3··O2	0.820	1.878	2.595(2)	145.2
O1–H1···O2	0.819	1.848	2.557(2)	144.0
O1–H1···O2#	0.819	2.891	3.003(2)	89.9
O1–H1···O2#1	0.819	2.537	2.884(2)	106.9

Symmetry operation: # = 2−x, 1/2 +y, 1/2−z; #1= 2−x, –1/2 +y, 1/2−z

π···π

Cg···Cg	**d (Å)**	**Cg···Cg**	**d (Å)**
phenol-phenol	4.423		

Symmetry operation: # = x, 1+y, z

Table II.A4: Crystallographic data for the compounds **1**-**5**

	1	**2**	**3**	**4**	**5**
Formula	$C_{68}H_{62}N_{10}O_{14}Co_2Cl_2$	$C_{68}H_{62}N_{10}O_{14}Ni_2Cl_2$	$C_{68}H_{62}N_{10}O_{14}Zn_2Cl_2$	$C_{88}H_{82}N_{14}O_{16}Co_4Cl_2$	$C_{83}H_{77}N_{13}O_{16}Ni_4Cl_2$
M_r	1432.03	1431.56	1444.91	1898.29	1818.31
Crystal system	Triclinic	Triclinic	Triclinic	Monoclinic	Monoclinic
Space group	*P*–1	*P*–1	*P*–1	*I*2/*a*	$P2_1/n$
a (Å)	15.3284(7)	9.2632(8)	15.3913(18)	29.108(2)	26.357(3)
b (Å)	15.7803(7)	13.2872(11)	15.8401(18)	10.3741(9)	9.9481(9)
c (Å)	16.5946(7)	14.6349(13)	16.6232(19)	31.141(4)	32.202(3)
α (°)	108.418(3)	67.048(5)	68.854(6)	90	90
β (°)	92.558(3)	78.703(5)	87.677(6)	112.727(4)	100.744(5)
γ (°)	118.959(2)	87.388(5)	60.736(6)	90	90
V (Å^3)	3236.4(3)	1625.6(2)	3251.2(7)	8673.5(15)	8295.6(13)
Z	2	1	2	4	4
ρ_{calc} (g/cm^3)	1.469	1.462	1.476	1.454	1.456
μ (cm^{-1})	0.670	0.736	0.895	0.888	1.033
Shape and colour	Red block	Orange block	Yellow block	Red block	Orange block
Crystal size (mm^3)	0.350·0.270·0.110	0.280·0.245·0.130	0.265·0.240·0.120	0.370·0.290·0.130	0.360·0.260·0.140
λ (Å)	0.71073	0.71073	0.71073	0.71073	0.71073
T (K)	100(2)	100(2)	100(2)	100(2)	100(2)
Reflections	10807	12313	10889	8831	13365
Unique reflections	7356	9625	7989	6514	9341
Parameters	895	895	895	624	1106
Restraints	38	45	31	211	272
R_1 (all data)[a]	0.0858	0.0890	0.0827	0.0763	0.1275
R_1 [$I>2\sigma(I)$][a]	0.0566	0.0678	0.0609	0.0541	0.0932
wR_2 (all data)[b]	0.1681	0.2003	0.1810	0.1390	0.2559
wR_2 [$I>2\sigma(I)$][b]	0.1469	0.1893	0.1649	0.1259	0.2323
S (all data)[c]	1.030	1.051	1.041	1.032	1.039
S [$I>2\sigma(I)$][c]	1.017	1.051	1.031	1.026	1.048
Largest residuals (e Å^3)	1.238/–0.740	1.393/–0.942	1.733/-1.217	0.729/-0.616	1.960/-1.013

[a] $R_1 = \Sigma||F_o| - |F_c|| / \Sigma|F_o|$; [b] $wR_2 = \{\Sigma[w(F_o^2 - F_c^2)^2] / \Sigma[w(F_o^2)^2]\}^{1/2}$; [c] $S = \{\Sigma[w(F_o^2 - F_c^2)^2] / (n - p)\}^{1/2}$

Table II.A5: Crystallographic data for the compounds **6**-**9**

	6	**7**	**8**	**9**
Formula	$C_{68}H_{64}N_{10}O_{17}Cu_4Cl_2$	$C_{68}H_{62}N_{10}O_{16}Zn_4Cl_2$	$C_{88}H_{82}N_{14}O_{16}Co_2Cu_2Cl_2$	$C_{78}H_{72}N_{12}O_{16}Ni_2Cu_2Cl_2$
M_r	1618.35	1607.74	1907.51	1748.87
Crystal system	Triclinic	Triclinic	Monoclinic	Monoclinic
Space group	*P*-1	*P*-1	$P2_1/n$	$P2_1/n$
a (Å)	10.656(3)	10.1124(4)	27.025(5)	25.6213(9)
b (Å)	17.146(5)	11.0811(4)	9.9214(19)	9.7380(3)
c (Å)	20.341(6)	16.3664(6)	32.136(6)	32.1177(10)
α (°)	105.205(14)	82.807(2)	90	90
β (°)	93.101(14)	75.865(2)	101.091(9)	97.032(2)
γ (°)	104.424(14)	73.385(2)	90	90
V (Å^3)	3445.0(17)	1701.15(11)	8455(3)	7953.1(4)
Z	2	1	4	4
ρ_{calc} (g/cm^3)	1.560	1.569	1.498	1.461
μ (cm^{-1})	1.373	1.952	1.022	1.431
Shape and colour	Yellow block	Yellow needle	Orange block	Orange needle
Crystal size (mm^3)	0.420·0.330·0.190	0.450·0.060·0.020	0.210·0.190·0.120	0.210·0.030·0.020
λ (Å)	0.71073	0.7749	0.71073	0.71073
T (K)	100(2)	100(2)	100(2)	100(2)
Reflections	15050	9811	13834	16247
Unique reflections	11592	8217	10429	12399
Parameters	941	454	1139	1013
Restraints	23	0	63	104
R_1 (all data)[a]	0.0665	0.0352	0.0804	0.0858
R_1 [$I>2\sigma(I)$][a]	0.0494	0.0265	0.0573	0.0617
wR_2 (all data)[b]	0.1488	0.0694	0.1437	0.1426
wR_2 [$I>2\sigma(I)$][b]	0.1360	0.0666	0.1317	0.1335
S (all data)[c]	1.027	1.073	1.037	1.089
S [$I>2\sigma(I)$][c]	1.024	1.073	1.028	1.077
Largest residuals (e Å^3)	1.567/–0.996	0.434/–0.416	1.230/–1.032	0.977/–0.784

[a] $R_1 = \Sigma||F_o| - |F_c|| / \Sigma|F_o|$; [b] $wR_2 = \{\Sigma[w(F_o^2 - F_c^2)^2] / \Sigma[w(F_o^2)^2]\}^{1/2}$; [c] $S = \{\Sigma[w(F_o^2 - F_c^2)^2] / (n - p)\}^{1/2}$

Table II.A6: Crystallographic data for the compounds **10**-**13**

	10	**11**	**12**	**13**
Formula	$C_{68}H_{64}N_{10}O_{17}Zn_2Cu_2Cl_2$	$C_{88}H_{82}N_{14}O_{16}Co_2Ni_2Cl_2$	$C_{88}H_{82}N_{14}O_{16}Ni_2Zn_2Cl_2$	$C_{83}H_{77}N_{13}O_{16}Co_2Zn_2Cl_2$
M_r	1622.01	1897.85	1910.73	1832.07
Crystal system	Triclinic	Monoclinic	Monoclinic	Monoclinic
Space group	*P*-1	$P2_1/n$	$P2_1/n$	$P2_1/n$
a (Å)	10.1178(8)	9.6988(6)	26.7952(12)	26.3136(11)
b (Å)	17.8332(13)	30.2633(18)	9.9122(4)	10.0179(4)
c (Å)	19.2342(14)	15.0258(9)	32.3981(13)	31.8064(13)
α (°)	88.781(5)	90	90	90
β (°)	81.541(5)	99.887(3)	101.384(2)	99.336(3)
γ (°)	86.654(5)	90	90	90
V (Å^3)	3426.6(4)	4344.8(5)	8435.6(6)	8273.3(6)
Z	2	2	4	4
ρ_{calc} (g/cm^3)	1.572	1.451	1.504	1.471
μ (cm^{-1})	1.842	0.938	1.438	1.392
Shape and colour	Brown needle	Orange block	Orange block	Red plate
Crystal size (mm^3)	0.210·0.010·0.010	0.490·0.120·0.100	0.320·0.110·0.050	0.320·0.080·0.040
λ (Å)	0.7749	0.71073	0.71073	0.71073
T (K)	100(2)	100(2)	100(2)	100(2)
Reflections	9449	10719	19423	17605
Unique reflections	6584	8363	15960	14177
Parameters	946	640	1123	1067
Restraints	219	327	2	152
R_1 (all data)[a]	0.1335	0.0810	0.0896	0.0974
R_1 [$I>2\sigma(I)$][a]	0.0970	0.0631	0.0738	0.0786
wR_2 (all data)[b]	0.2676	0.1694	0.1828	0.1862
wR_2 [$I>2\sigma(I)$][b]	0.2511	0.1585	0.1755	0.1773
S (all data)[c]	1.092	1.025	1.152	1.126
S [$I>2\sigma(I)$][c]	1.098	1.030	1.152	1.118
Largest residuals (e Å^3)	1.215/–1.079	1.274/–1.193	2.139/–1.658	1.902/–1.012

[a] $R_1 = \Sigma||F_o| - |F_c|| / \Sigma|F_o|$; [b] $wR_2 = \{\Sigma[w(F_o^2 - F_c^2)^2] / \Sigma[w(F_o^2)^2]\}^{1/2}$; [c] $S = \{\Sigma[w(F_o^2 - F_c^2)^2] / (n - p)\}^{1/2}$

Table II.A7: Interatomic distances [Å] and angles [°] for the compound **1**

Co1···Co2	7.217(1)	Co2–O5	2.098(3)	N1–Co1–O2	89.1(1)	N4–Co1–N1	93.3(1)	N5–Co2–N8	89.3(1)
Co1–O2	2.115(3)	Co2–N6	2.161(3)	N2–Co1–O2	88.6(1)	O4–Co2–O5	86.5(1)	N7–Co2–O4	88.2(1)
Co1–O3	2.020(3)	Co2–N8	2.181(3)	N2–Co1–O3	88.0(1)	O5–Co2–N6	88.1(1)	N7–Co2–O5	90.8(1)
Co1–N1	2.133(3)	Co2–N5	2.188(3)	N2–Co1–N3	95.2(1)	N6–Co2–N8	99.8(1)	N7–Co2–N6	89.7(1)
Co1–N3	2.173(3)	Co2–N7	2.182(3)	N2–Co1–N1	89.3(1)	N8–Co2–O4	85.7(1)	N7–Co2–N8	93.7(1)
Co1–N2	2.172(3)	O2–Co1–O3	86.5(1)	N4–Co1–O2	85.3(1)	N5–Co2–O4	87.6(1)		
Co1–N4	2.173(3)	O3–Co1–N3	85.5(1)	N4–Co1–O3	89.0(1)	N5–Co2–O5	85.6(1)		
Co2–O4	2.030(3)	N3–Co1–N1	99.0(1)	N4–Co1–N3	90.5(1)	N5–Co2–N6	94.2(1)		

Table II.A8: Interatomic distances [Å] and angles [°] for the compound **2**

Ni1···Ni2	7.154(1)	Ni2–O5	2.107(1)	N1–Ni1–O2	89.9(1)	N4–Ni1–N1	93.3(1)	N5–Ni2–N8	91.6(1)
Ni1–O2	2.045(1)	Ni2–N6	2.114(2)	N2–Ni1–O2	90.9(1)	O4–Ni2–O5	88.8(1)	N7–Ni2–O4	85.5(1)
Ni1–O3	1.968(1)	Ni2–N8	2.118(1)	N2–Ni1–O3	88.2(1)	O5–Ni2–N6	86.2(1)	N7–Ni2–O5	86.5(1)
Ni1–N1	2.148(2)	Ni2–N5	2.107(2)	N2–Ni1–N3	91.8(1)	N6–Ni2–N8	100.1(1)	N7–Ni2–N6	92.0(1)
Ni1–N3	2.108(2)	Ni2–N7	2.094(2)	N2–Ni1–N1	91.3(1)	N8–Ni2–O4	85.0(8)	N7–Ni2–N8	93.9(1)
Ni1–N2	2.140(2)	O2–Ni1–O3	86.9(1)	N4–Ni1–O2	86.2(1)	N5–Ni2–O4	88.6(1)		
Ni1–N4	2.101(2)	O3–Ni1–N3	84.0(1)	N4–Ni1–O3	87.0(1)	N5–Ni2–O5	87.3(1)		
Ni2–O4	2.043(1)	N3–Ni1–N1	99.1(1)	N4–Ni1–N3	90.3(1)	N5–Ni2–N6	93.4(1)		

Table II.A9: Interatomic distances [Å] and angles [°] for the compound **3**

Zn1···Zn2	7.254(1)	Zn2–O5	2.156(4)	N1–Zn1–O2	88.9(1)	N4–Zn1–N1	93.7(2)	N5–Zn2–N8	89.2(2)
Zn1–O2	2.177(4)	Zn2–N6	2.172(4)	N2–Zn1–O2	88.0(1)	O4–Zn2–O5	85.4(1)	N7–Zn2–O4	88.0(1)
Zn1–O3	2.047(3)	Zn2–N8	2.194(6)	N2–Zn1–O3	87.5(1)	O5–Zn2–N6	87.8(1)	N7–Zn2–O5	90.7(1)
Zn1–N1	2.132(4)	Zn2–N5	2.221(3)	N2–Zn1–N3	96.1(2)	N6–Zn2–N8	101.3(2)	N7–Zn2–N6	89.6(2)
Zn1–N3	2.186(6)	Zn2–N7	2.188(3)	N2–Zn1–N1	88.7(2)	N8–Zn2–O4	85.8(2)	N7–Zn2–N8	94.3(2)
Zn1–N2	2.185(3)	O2–Zn1–O3	85.1(1)	N4–Zn1–O2	84.5(1)	N5–Zn2–O4	88.1(1)		
Zn1–N4	2.199(3)	O3–Zn1–N3	86.0(1)	N4–Zn1–O3	89.3(1)	N5–Zn2–O5	85.2(1)		
Zn2–O4	2.061(3)	N3–Zn1–N1	100.2(2)	N4–Zn1–N3	90.9(2)	N5–Zn2–N6	93.8(2)		

Table II.A10: Interatomic distances [Å] and angles [°] for the compound **4**

Co1···Co2	3.1608(9)	Co1−N1	2.115(3)	O1–Co1–O2	84.0(1)	N1–Co1–N2	108.1(1)	N5–Co2–N4	90.3(1)
Co2···Co2#	7.266(1)	Co2–O2	2.098(2)	O2–Co1–O4	79.1(1)	O2–Co2–O3	86.4(1)	N5–Co2–O4	92.6(1)
Co1···Co1#	11.523(1)	Co2–O3	2.027(3)	O4–Co1–N2	95.3(1)	O3–Co2–N4	91.8(1)	N3–Co2–O2	88.1(1)
Co1–O1	1.921(4)	Co2–N4	2.140(3)	N2–Co1–O1	91.5(1)	N4–Co2–O4	102.7(1)	N3–Co2–O3	90.9(1)
Co1–O2	2.139(3)	Co2–O4	2.010(3)	N1–Co1–O1	120.3(1)	O4–Co2–O2	79.2(1)	N3–Co2–N4	88.6(1)
Co1–O4	1.971(3)	Co2–N5	2.178(3)	N1–Co1–O2	84.9(1)	N5–Co2–O2	92.9(1)	N3–Co2–O4	90.4(1)
Co1−N2	2.120(4)	Co2–N3	2.204(3)	N1–Co1–O4	100.9(1)	N5–Co2–O3	86.3(1)	#=1/2–x, 3/2–y, 1/2–z	

Table II.A11: Interatomic distances [Å] and angles [°] for the compound **5**

Ni1···Ni2	3.093(1)	Ni2−N5	2.148(8)	O4–Ni1–N2	93.5(3)	N5–Ni2–O3	90.7(2)	N8–Ni3–O8	90.6(3)
Ni3···Ni4	3.085(1)	Ni3−O5	2.020(5)	N2–Ni1–O1	91.8(3)	N5–Ni2–O2	90.1(2)	N8–Ni3–N7	90.1(3)
Ni2···Ni3	7.217(1)	Ni3−O6	2.061(5)	N1–Ni1–O1	102.1(3)	N5–Ni2–O4	89.9(3)	O6–Ni4–O7	86.6(2)
Ni1···Ni4	11.333(2)	Ni3−O8	2.052(6)	N1–Ni1–O2	101.2(3)	N5–Ni2–N4	85.8(3)	O7–Ni4–N10	88.9(3)
Ni1–O1	1.952(6)	Ni3−N7	2.078(7)	N1–Ni1–O4	104.2(3)	O5–Ni3–O6	89.7(2)	N10–Ni4–O8	95.7(3)
Ni1–O2	2.061(6)	Ni3−N6	2.145(8)	N1–Ni1–N2	95.1(3)	O6–Ni3–O8	80.1(2)	O8–Ni4–O6	82.1(2)
Ni1–O4	1.965(6)	Ni3−N8	2.121(8)	O3–Ni2–O2	88.5(2)	O8–Ni3–N7	98.8(3)	N9–Ni4–O6	104.8(3)
Ni1–N2	2.088(7)	Ni4−O7	1.924(6)	O2–Ni2–O4	79.8(2)	N7–Ni3–O5	91.4(2)	N9–Ni4–O7	96.7(3)
Ni1–N1	2.007(5)	Ni4−O6	2.031(5)	O4–Ni2–N4	99.3(2)	N6–Ni3–O5	91.5(2)	N9–Ni4–N10	95.3(3)
Ni2–O3	2.013(5)	Ni4−O8	2.000(6)	N4–Ni2–O3	92.4(3)	N6–Ni3–O6	87.8(2)	N9–Ni4–O8	103.1(3)
Ni2–O2	2.081(6)	Ni4−N10	2.069(6)	N3–Ni2–O3	88.1(3)	N6–Ni3–O8	88.5(3)		
Ni2–O4	2.006(6)	Ni4−N9	2.028(8)	N3–Ni2–O2	91.3(3)	N6–Ni3–N7	91.9(3)		
Ni2–N4	2.106(8)	O1–Ni1–O2	86.2(2)	N3–Ni2–O4	91.6(3)	N8–Ni3–O5	89.1(2)		
Ni2–N3	2.119(8)	O2–Ni1–O4	81.2(2)	N3–Ni2–N4	92.8(3)	N8–Ni3–O6	90.2(2)		

Table II.A12: Interatomic distances [Å] and angles [°] for the compound **6**

Cu1···Cu2	3.0198(9)	Cu2–N4	1.991(3)	O1–Cu1–O2	86.5(1)	N3–Cu2–O2	91.0(1)	O6–Cu4–O8	77.3(1)
Cu3···Cu4	3.0165(9)	Cu2–N3	2.323(3)	O2–Cu1–O4	78.0(1)	N3–Cu2–O3	89.4(1)	O8–Cu4–N7	99.1(1)
Cu2···Cu3	7.069(2)	Cu3–O5	1.926(3)	O4–Cu1–N2	100.4(1)	N3–Cu2–O4	91.4(1)	N7–Cu4–O7	91.9(1)
Cu1···Cu4	11.155(3)	Cu3–O6	1.991(2)	N2–Cu1–O1	90.5(1)	N3–Cu2–N4	101.1(1)	O7–Cu4–O6	86.5(1)
Cu1–O1	1.899(3)	Cu3–O8	1.907(2)	N1–Cu1–O1	96.3(1)	O5–Cu3–N5	90.5(1)	N8–Cu4–O6	108.4(1)
Cu1–O2	2.002(3)	Cu3–N5	1.999(3)	N1–Cu1–O2	105.5(1)	N5–Cu3–O8	99.9(1)	N8–Cu4–O8	97.1(1)
Cu1–O4	1.925(2)	Cu3–N6	2.265(3)	N1–Cu1–O4	94.6(1)	O8–Cu3–O6	77.6(1)	N8–Cu4–N7	98.3(1)
Cu1–N2	2.019(3)	Cu4–O8	1.920(2)	N1–Cu1–N2	100.1(1)	O6–Cu3–O5	89.6(1)	N8–Cu4–O7	95.3(1)
Cu1–N1	2.209(3)	Cu4–O6	1.992(3)	O2–Cu2–O3	90.4(1)	N6–Cu3–O5	89.6(1)		
Cu2–O3	1.936(3)	Cu4–O7	1.913(2)	O3–Cu2–N4	91.7(1)	N6–Cu3–N5	102.4(1)		
Cu2–O2	1.974(2)	Cu4–N7	1.994(3)	N4–Cu2–O4	98.8(1)	N6–Cu3–O8	94.9(1)		
Cu2–O4	1.923(3)	Cu4–N8	2.233(3)	O4–Cu2–O2	78.8(1)	N6–Cu3–O6	92.3(1)		

Table II.A13: Interatomic distances [Å] and angles [°] for the compound **7**

Zn1···Zn2	3.1763(4)	Zn1–N1	2.093(1)	O1–Zn1–O2	82.42(5)	N1–Zn1–N2	103.40(5)	N5–Zn2–N4	93.61(5)
Zn2···Zn2#	7.3534(5)	Zn2–O2	2.179(1)	O2–Zn1–O4	78.27(4)	O2–Zn2–O3	84.50(4)	N5–Zn2–O4	90.21(5)
Zn1···Zn1#	11.4984(5)	Zn2–O3	2.031(1)	O4–Zn1–N2	96.97(5)	O3–Zn2–N4	89.53(4)	N3–Zn2–O2	86.48(4)
Zn1–O1	1.967(1)	Zn2–N4	2.150(1)	N2–Zn1–O1	93.09(5)	N4–Zn2–O4	108.77(5)	N3–Zn2–O3	87.81(4)
Zn1–O2	2.146(1)	Zn2–O4	1.972(1)	N1–Zn1–O1	93.42(5)	O4–Zn2–O2	77.11(4)	N3–Zn2–N4	88.48(5)
Zn1–O4	1.955(1)	Zn2–N5	2.227(1)	N1–Zn1–O2	113.99(5)	N5–Zn2–O2	91.25(4)	N3–Zn2–O4	90.87(5)
Zn1–N2	2.117(1)	Zn2–N3	2.252(1)	N1–Zn1–O4	102.22(5)	N5–Zn2–O3	90.35(4)	#=1–x, –y, 2–z	

Table II.A14: Interatomic distances [Å] and angles [°] for the compound **8**

Cu1···Co1	3.0640(9)	Co1–N5	2.211(4)	O4–Cu1–N2	95.1(1)	N5–Co1–O3	92.0(1)	N8–Co2–O8	90.4(1)
Cu2···Co2	3.087(1)	Co2–O5	2.011(3)	N2–Cu1–O1	89.3(2)	N5–Co1–O2	87.1(1)	N8–Co2–N7	91.9(2)
Co1···Co2	7.274(2)	Co2–O6	2.133(3)	N1–Cu1–O1	90.9(2)	N5–Co1–O4	90.0(1)	O6–Cu2–O7	89.2(1)
Cu1···Cu2	11.215(2)	Co2–O8	1.984(3)	N1–Cu1–O2	107.4(1)	N5–Co1–N4	94.3(1)	O7–Cu2–N10	90.7(2)
Cu1–O1	1.886(4)	Co2–N7	2.145(4)	N1–Cu1–O4	101.4(1)	O5–Co2–O6	85.3(1)	N10–Cu2–O8	93.0(1)
Cu1–O2	1.995(3)	Co2–N6	2.203(4)	N1–Cu1–N2	94.0(2)	O6–Co2–O8	77.4(1)	O8–Cu2–O6	81.7(1)
Cu1–O4	1.929(3)	Co2–N8	2.166(4)	O3–Co1–O2	87.2(1)	O8–Co2–N7	103.3(1)	N9–Cu2–O6	99.5(1)
Cu1–N2	2.052(4)	Cu2–O7	1.881(4)	O2–Co1–O4	78.0(1)	N7–Co2–O5	94.3(1)	N9–Cu2–O7	98.3(2)
Cu1–N1	2.237(4)	Cu2–O6	2.013(3)	O4–Co1–N4	101.2(1)	N6–Co2–O5	92.4(1)	N9–Cu2–N10	95.1(2)
Co1–O3	2.020(3)	Cu2–O8	1.922(3)	N4–Co1–O3	93.5(1)	N6–Co2–O6	88.4(1)	N9–Cu2–O8	103.2(1)
Co1–O2	2.093(3)	Cu2–N10	2.039(4)	N3–Co1–O3	87.7(1)	N6–Co2–O8	90.2(1)		
Co1–O4	2.024(3)	Cu2–N9	2.241(4)	N3–Co1–O2	90.2(1)	N6–Co2–N7	85.3(1)		
Co1–N4	2.098(4)	O1–Cu1–O2	88.7(1)	N3–Co1–O4	89.7(1)	N8–Co2–O5	87.8(1)		

Table II.A15: Interatomic distances [Å] and angles [°] for the compound **9**

Cu1···Ni1	3.0544(7)	Ni1–N5	2.159(4)	O4–Cu1–N2	95.4(1)	N5–Ni1–O3	89.8(1)	N8–Ni2–O8	93.0(1)
Cu2···Ni2	3.0471(7)	Ni2–O5	1.991(3)	N2–Cu1–O1	90.9(1)	N5–Ni1–O2	89.5(1)	N8–Ni2–N7	93.7(1)
Ni1···Ni2	7.1466(9)	Ni2–O6	2.065(3)	N1–Cu1–O1	88.7(1)	N5–Ni1–O4	89.1(1)	O6–Cu2–O7	88.0(1)
Cu1···Cu2	11.1608(8)	Ni2–O8	2.004(3)	N1–Cu1–O2	113.6(1)	N5–Ni1–N4	91.1(1)	O7–Cu2–N10	91.1(1)
Cu1–O1	1.886(3)	Ni2–N7	2.071(4)	N1–Cu1–O4	100.4(1)	O5–Ni2–O6	88.9(1)	N10–Cu2–O8	93.9(1)
Cu1–O2	1.994(3)	Ni2–N6	2.164(4)	N1–Cu1–N2	92.8(1)	O6–Ni2–O8	79.2(1)	O8–Cu2–O6	82.4(1)
Cu1–O4	1.933(3)	Ni2–N8	2.139(4)	O3–Ni1–O2	89.2(1)	O8–Ni2–N7	99.9(1)	N9–Cu2–O6	102.1(1)
Cu1–N2	2.063(4)	Cu2–O7	1.901(3)	O2–Ni1–O4	78.0(1)	N7–Ni2–O5	91.9(1)	N9–Cu2–O7	97.9(1)
Cu1–N1	2.238(4)	Cu2–O6	2.010(3)	O4–Ni1–N4	102.4(1)	N6–Ni2–O5	89.0(1)	N9–Cu2–N10	95.8(1)
Ni1–O3	2.002(3)	Cu2–O8	1.927(3)	N4–Ni1–O3	90.5(1)	N6–Ni2–O6	91.7(1)	N9–Cu2–O8	97.5(1)
Ni1–O2	2.058(3)	Cu2–N10	2.049(4)	N3–Ni1–O3	91.0(1)	N6–Ni2–O8	88.7(1)		
Ni1–O4	2.035(3)	Cu2–N9	2.216(4)	N3–Ni1–O2	89.2(1)	N6–Ni2–N7	87.2(1)		
Ni1–N4	2.071(4)	O1–Cu1–O2	88.2(1)	N3–Ni1–O4	89.9(1)	N8–Ni2–O5	89.1(1)		
Ni1–N3	2.115(4)	O2–Cu1–O4	81.9(1)	N3–Ni1–N4	90.1(1)	N8–Ni2–O6	87.4(1)		

Table II.A16: Interatomic distances [Å] and angles [°] for the compound **10**

Cu1···Zn1	3.098(2)	Zn1–N5	2.20(1)	O4–Cu1–N2	92.4(4)	N5–Zn1–O3	90.2(4)	N8–Zn2–O8	91.5(4)
Cu2···Zn2	3.116(2)	Zn2–O5	2.040(9)	N2–Cu1–O1	90.3(4)	N5–Zn1–O2	93.6(4)	N8–Zn2–N7	94.8(4)
Zn1···Zn2	7.180(2)	Zn2–O6	2.16(1)	N1–Cu1–O1	98.2(4)	N5–Zn1–O4	96.1(4)	O6–Cu2–O7	86.9(4)
Cu1···Cu2	11.089(2)	Zn2–O8	2.005(9)	N1–Cu1–O2	104.1(4)	N5–Zn1–N4	90.3(4)	O7–Cu2–N10	92.8(4)
Cu1–O1	1.90(1)	Zn2–N7	2.11(1)	N1–Cu1–O4	104.0(4)	O5–Zn2–O6	85.3(4)	N10–Cu2–O8	95.5(4)
Cu1–O2	2.052(9)	Zn2–N6	2.24(1)	N1–Cu1–N2	96.7(5)	O6–Zn2–O8	75.8(4)	O8–Cu2–O6	81.4(4)
Cu1–O4	1.90(1)	Zn2–N8	2.22(1)	O3–Zn1–O2	85.9(4)	O8–Zn2–N7	103.9(4)	N9–Cu2–O6	111.2(4)
Cu1–N2	2.09(1)	Cu2–O7	1.91(1)	O2–Zn1–O4	77.1(4)	N7–Zn2–O5	94.8(4)	N9–Cu2–O7	89.3(4)
Cu1–N1	2.21(1)	Cu2–O6	2.000(9)	O4–Zn1–N4	106.0(4)	N6–Zn2–O5	87.0(4)	N9–Cu2–N10	97.5(4)
Zn1–O3	1.994(9)	Cu2–O8	1.92(1)	N4–Zn1–O3	90.7(4)	N6–Zn2–O6	87.4(4)	N9–Cu2–O8	98.7(4)
Zn1–O2	2.13(1)	Cu2–N10	2.07(1)	N3–Zn1–O3	85.8(4)	N6–Zn2–O8	90.5(4)		
Zn1–O4	1.95(1)	Cu2–N9	2.24(1)	N3–Zn1–O2	90.3(4)	N6–Zn2–N7	88.1(4)		
Zn1–N4	2.12(1)	O1–Cu1–O2	89.5(4)	N3–Zn1–O4	88.9(4)	N8–Zn2–O5	90.0(4)		

Table II.A17: Interatomic distances [Å] and angles [°] for the compound **11**

Co1···Ni1	3.1633(8)	Co1–N1	2.072(3)	O1–Co1–O2	83.4(1)	N1–Co1–N2	95.3(1)	N5–Ni1–N4	92.9(1)
Ni1···Ni1#	7.2037(7)	Ni1–O2	2.051(2)	O2–Co1–O4	78.3(1)	O2–Ni1–O3	88.5(1)	N5–Ni1–O4	93.9(1)
Co1···Co1#	11.5656(9)	Ni1–O3	2.018(2)	O4–Co1–N2	103.2(1)	O3–Ni1–N4	90.6(1)	N3–Ni1–O2	88.6(1)
Co1–O1	1.928(3)	Ni1–N4	2.108(3)	N2–Co1–O1	90.0(1)	N4–Ni1–O4	101.8(1)	N3–Ni1–O3	87.0(1)
Co1–O2	2.150(2)	Ni1–O4	2.031(2)	N1–Co1–O1	112.2(1)	O4–Ni1–O2	79.1(1)	N3–Ni1–N4	90.0(1)
Co1–O4	1.962(2)	Ni1–N5	2.165(4)	N1–Co1–O2	92.0(1)	N5–Ni1–O2	88.4(1)	N3–Ni1–O4	90.8(1)
Co1–N2	2.124(3)	Ni1–N3	2.127(3)	N1–Co1–O4	109.3(1)	N5–Ni1–O3	87.6(1)	#=–x, –y, 1–z	

Table II.A18: Interatomic distances [Å] and angles [°] for the compound **12**

Zn1···Ni1	3.1507(7)	Ni1–N5	2.150(4)	O4–Zn1–N2	96.4(1)	N5–Ni1–O3	90.6(1)	N8–Ni2–O8	89.0(1)
Zn2···Ni2	3.1231(7)	Ni2–O5	2.027(3)	N2–Zn1–O1	90.8(1)	N5–Ni1–O2	91.0(1)	N8–Ni2–N7	92.6(1)
Ni1···Ni2	7.2191(9)	Ni2–O6	2.029(3)	N1–Zn1–O1	106.6(2)	N5–Ni1–O4	89.4(1)	O6–Zn2–O7	82.3(1)
Zn1···Zn2	11.5427(9)	Ni2–O8	2.048(3)	N1–Zn1–O2	99.6(1)	N5–Ni1–N4	85.5(1)	O7–Zn2–N10	88.8(2)
Zn1–O1	1.940(3)	Ni2–N7	2.079(4)	N1–Zn1–O4	110.2(2)	O5–Ni2–O6	90.2(1)	N10–Zn2–O8	97.7(1)
Zn1–O2	2.200(3)	Ni2–N6	2.126(4)	N1–Zn1–N2	99.7(2)	O6–Ni2–O8	79.8(1)	O8–Zn2–O6	78.9(1)
Zn1–O4	1.941(3)	Ni2–N8	2.156(4)	O3–Ni1–O2	87.9(1)	O8–Ni2–N7	98.1(1)	N9–Zn2–O6	110.1(1)
Zn1–N2	2.129(4)	Zn2–O7	1.943(4)	O2–Ni1–O4	80.4(1)	N7–Ni2–O5	91.9(1)	N9–Zn2–O7	95.7(2)
Zn1–N1	2.071(4)	Zn2–O6	2.152(3)	O4–Ni1–N4	99.1(1)	N6–Ni2–O5	89.4(1)	N9–Zn2–N10	99.1(2)
Ni1–O3	2.012(3)	Zn2–O8	1.959(3)	N4–Ni1–O3	92.6(1)	N6–Ni2–O6	90.2(1)	N9–Zn2–O8	109.5(1)
Ni1–O2	2.045(3)	Zn2–N10	2.128(4)	N3–Ni1–O3	88.9(1)	N6–Ni2–O8	89.3(1)		
Ni1–O4	2.014(3)	Zn2–N9	2.069(5)	N3–Ni1–O2	90.8(1)	N6–Ni2–N7	88.9(1)		
Ni1–N4	2.094(4)	O1–Zn1–O2	82.4(1)	N3–Ni1–O4	91.4(1)	N8–Ni2–O5	92.1(1)		

Table II.A19: Interatomic distances [Å] and angles [°] for the compound **13**

Zn1···Co1	3.1423(8)	Co1–N5	2.200(4)	O4–Zn1–N2	96.8(2)	N5–Co1–O3	91.8(1)	N8–Co2–O8	91.4(2)
Zn2···Co1	3.1631(9)	Co2–O5	2.016(3)	N2–Zn1–O1	89.8(2)	N5–Co1–O2	88.0(1)	N8–Co2–N7	89.9(2)
Co1···Co2	7.2082(9)	Co2–O6	2.102(4)	N1–Zn1–O1	93.2(2)	N5–Co1–O4	90.2(1)	O6–Zn2–O7	83.2(2)
Zn1··Zn2	11.4455(9)	Co2–O8	2.003(3)	N1–Zn1–O2	112.4(2)	N5–Co1–N4	93.9(2)	O7–Zn2–N10	91.9(2)
Zn1–O1	1.945(4)	Co2–N7	2.135(4)	N1–Zn1–O4	107.8(2)	O5–Co2–O6	85.1(1)	N10–Zn2–O8	94.9(2)
Zn1–O2	2.136(3)	Co2–N6	2.218(5)	N1–Zn1–N2	101.5(2)	O6–Co2–O8	80.0(1)	O8–Zn2–O6	78.9(1)
Zn1–O4	1.974(3)	Co2–N8	2.175(4)	O3–Co1–O2	87.8(1)	O8–Co2–N7	100.9(2)	N9–Zn2–O6	96.2(2)
Zn1–N2	2.124(4)	Zn2–O7	1.928(4)	O2–Co1–O4	78.9(1)	N7–Co2–O5	94.0(1)	N9–Zn2–O7	108.0(2)
Zn1–N1	2.081(5)	Zn2–O6	2.195(3)	O4–Co1–N4	101.2(1)	N6–Co2–O5	90.5(1)	N9–Zn2–N10	99.8(2)
Co1–O3	2.033(3)	Zn2–O8	1.951(3)	N4–Co1–O3	92.1(1)	N6–Co2–O6	90.9(2)	N9–Zn2–O8	112.3(2)
Co1–O2	2.086(3)	Zn2–N9	2.073(4)	N3–Co1–O3	88.8(1)	N6–Co2–O8	90.3(2)		
Co1–O4	2.027(3)	Zn2–N10	2.115(5)	N3–Co1–O2	90.3(1)	N6–Co2–N7	87.1(2)		
Co1–N4	2.127(4)	O1–Zn1–O2	82.8(2)	N3–Co1–O4	88.9(1)	N8–Co2–O5	88.5(2)		
Co1–N3	2.200(4)	O2–Zn1–O4	78.9(1)	N3–Co1–N4	87.8(2)	N8–Co2–O6	92.1(2)		

Table II.A20: Bonding details for homometallic and heterometallic compounds **4**-**13**.

Compound $[M1M2]_2$	<M1–L1> [Å][a]	<M1–O_3N_{eq}> [Å][b]	<M1–N_{ax}> [Å][c]	τ (M1)[d]	d(M1–O_3N_{plane}) [Å][e]	<M2–L1> [Å][f]	<M2– O_3N_{eq}> [Å][g]	<M2–N_{ax}> [Å][h]	d(M2–O_3N_{plane}) [Å][i]	$\Theta(M1M2)_{eq}$ °[j]	$\Theta(M2M2)_{eq}$ °[k]
4 $[CoCo]_2$	2.053	2.038	2.115(3)	0.550	0.492	2.109	2.069	2.191	0.019	20.80	0.00
5 $[NiNi]_2$	2.012	2.011	2.017	0.183 0.012	0.366 0.344	2.079	2.052	2.133	0.037 0.000	19.14 4.61	17.70
6 $[CuCu]_2$	2.011	1.958	2.221	0.145 0.142	0.325 0.308	2.023	1.956	2.294	0.207 0.119	22.13 20.20	0.49
7 $[ZnZn]_2$	2.056	2.046	2.093(1)	0.272	0.466	2.135	2.083	2.239	0.054	12.18	0.00
8 $[CuCo]_2$	2.019	1.965	2.239	0.127 0.133	0.303 0.285	2.107	2.063	2.193	0.041 0.038	19.69 4.00	17.46
9 $[CuNi]_2$	2.022	1.970	2.227	0.253 0.022	0.297 0.283	2.073	2.037	2.144	0.003 0.035	8.49 12.03	19.02
10 $[CuZn]_2$	2.029	1.980	2.225	0.275 0.032	0.311 0.364	2.129	2.064	2.260	0.062 0.088	10.49 21.48	22.21
11 $[CoNi]_2$	2.047	2.041	2.072(3)	0.613	0.414	2.083	2.052	2.146	0.031	16.81	0.00
12 $[ZnNi]_2$	2.053	2.049	2.070	0.335 0.040	0.487 0.479	2.074	2.043	2.134	0.036 0.021	18.55 3.57	20.60
13 $[ZnCo]_2$	2.052	2.046	2.077	0.448 0.175	0.487 0.485	2.110	2.066	2.198	0.016 0.041	19.38 6.38	24.21

a-average metal-ligand bond distance for pentacoordinate M1 site; *b*-average equatorial metal-ligand bond distance for pentacoordinate M1 site; *c*-average axial metal-ligand bond distance for pentacoordinate M1 site; *d*-angular parameter $\tau=(\alpha-\beta)/60°$ indexing the degree of trigonality for pentacoordinate complexes; *e*-distance of pentacoordinate M1 centre from the corresponding equatorial O_3N plane; *f*-average metal-ligand bond distance for hexacoordinate M2 site; *g*-average equatorial metal-ligand bond distance for hexacoordinate M2 site; *h*-average axial metal-ligand bond distance for hexacoordinate M2 site; *i*- distance of hexacoordinate M2 centre from the corresponding equatorial O_3N plane; *j*-angle between O_3N equatorial planes of adjacent M1 and M2 sites; *k*- angle between O_3N equatorial planes of adjacent M2 sites.

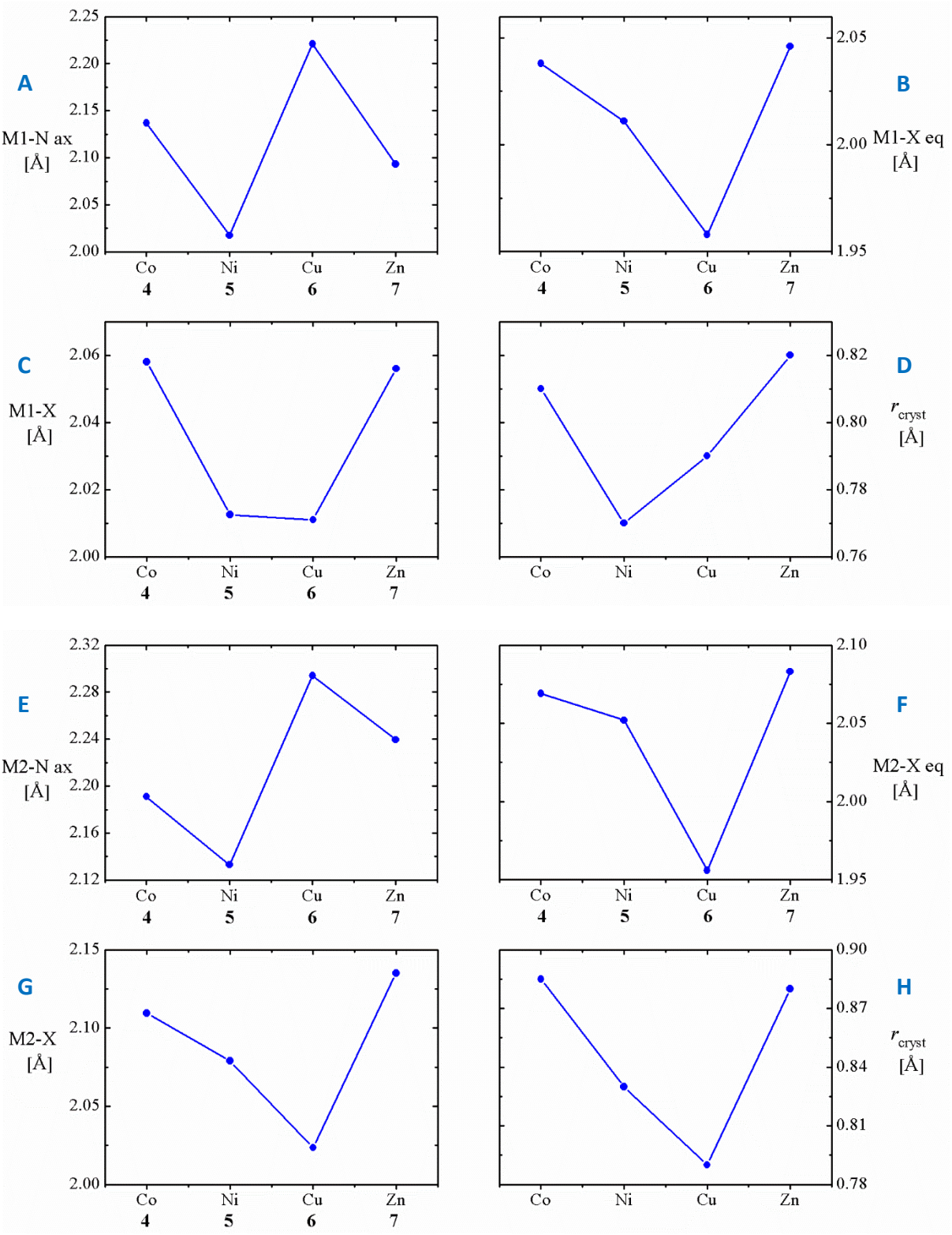

Figure II.A3: Bonding geometry of pentacoordinate M1 and hexacoordinate M2 centres in compounds **4**-**7**. Average axial M–N bond distances (A and E), average equatorial M–X bond distances (B and F), average distance of all M–X bonds (C and G) and Shannon-Prewitt crystal and ionic radii of the elements (D and H).

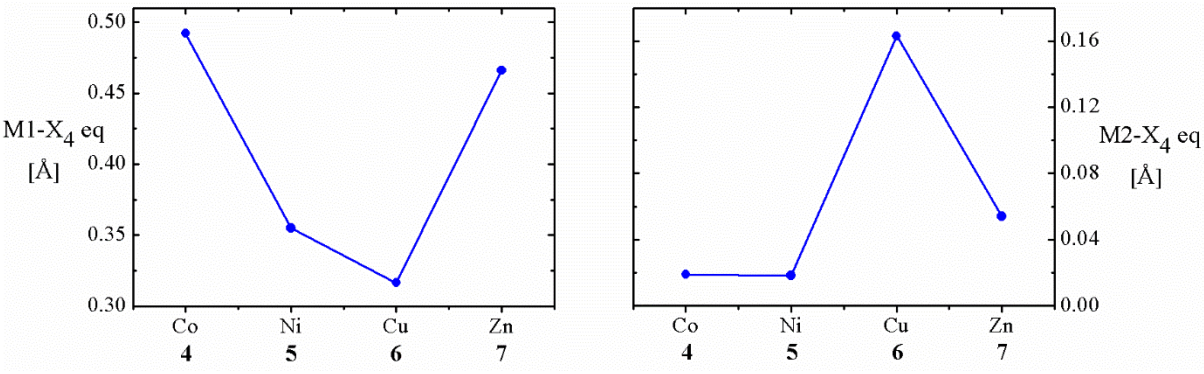

Figure II.A4: Distance from equatorial plane for pentacoordinate M1 and hexacoordinate M2 centres in compounds **4**-**7**.

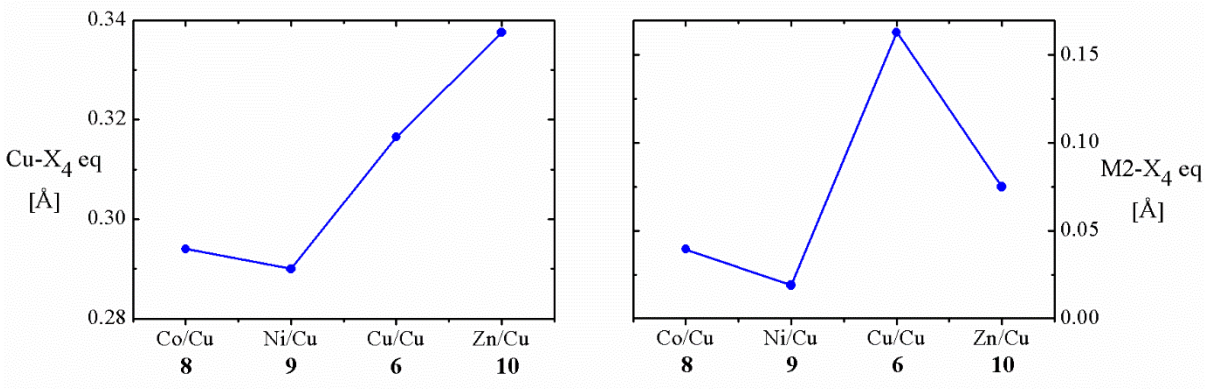

Figure II.A5: Distance from equatorial plane for pentacoordinate Cu and hexacoordinate M2 centres in compounds **6**, **8**-**10**.

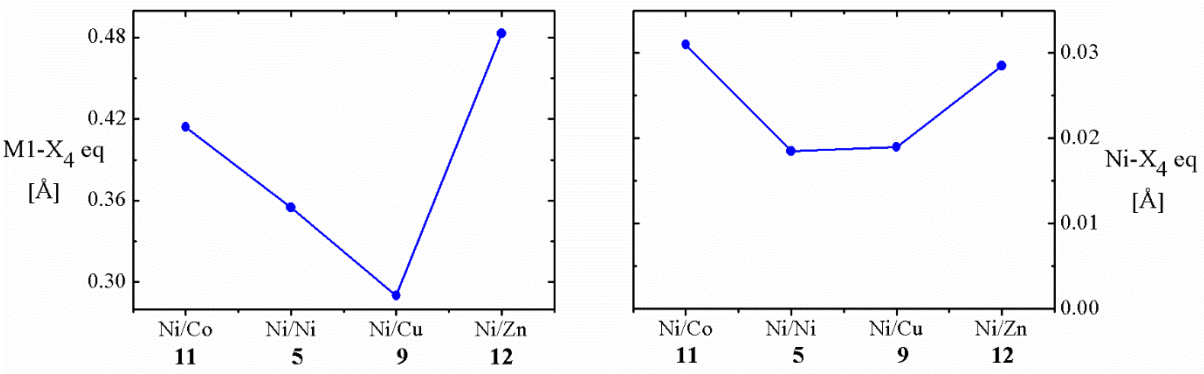

Figure II.A6: Distance from equatorial plane for pentacoordinate M1 and hexacoordinate Ni centres in compounds **5**, **11**-**12**.

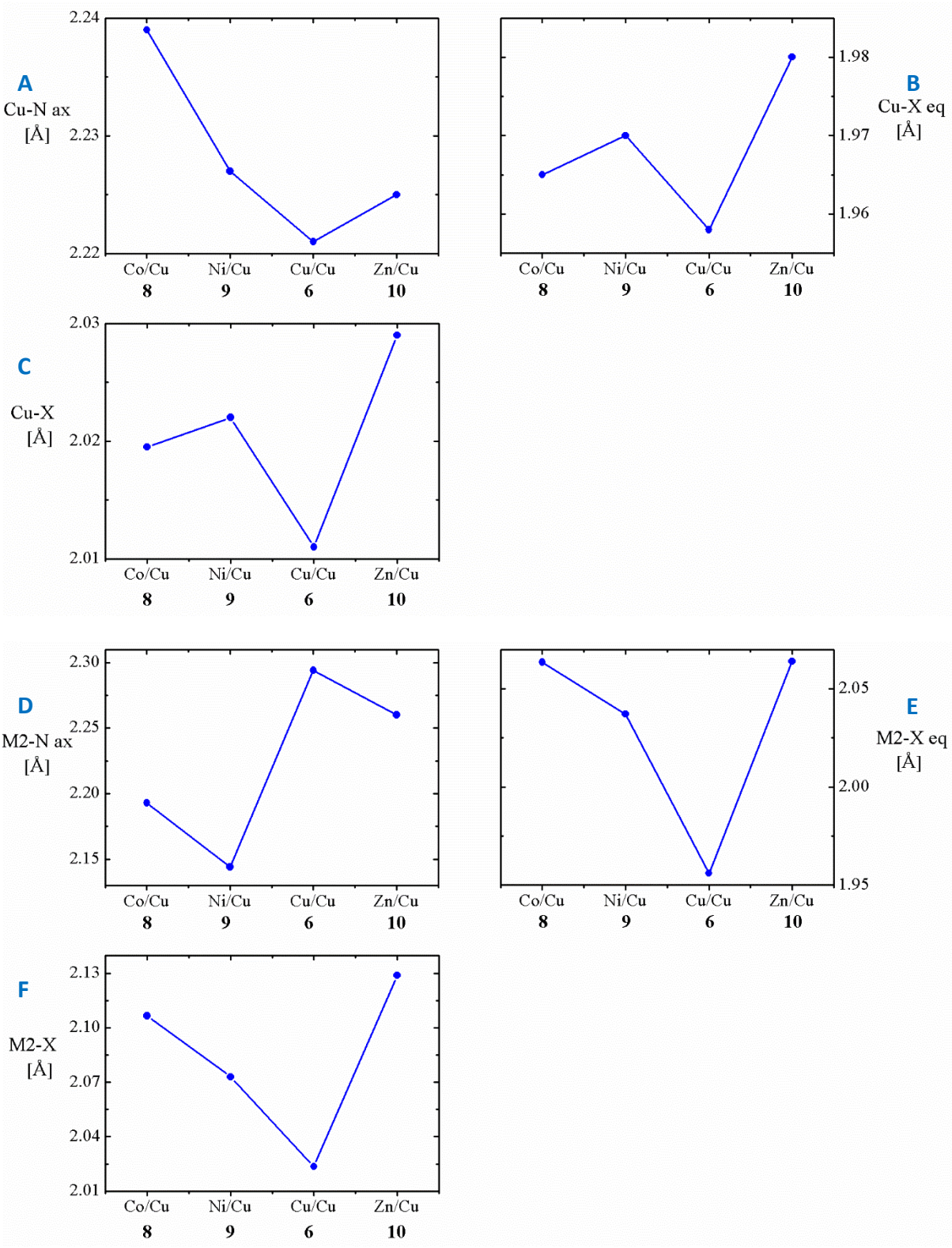

Figure II.A7: Bonding geometry of pentacoordinate Cu and hexacoordinate M2 centres in compounds **6**, **8**-**10**. Average axial M–N bond distances (A and D), average equatorial M–X bond distances (B and E), average distance of all M–X bonds (C and F).

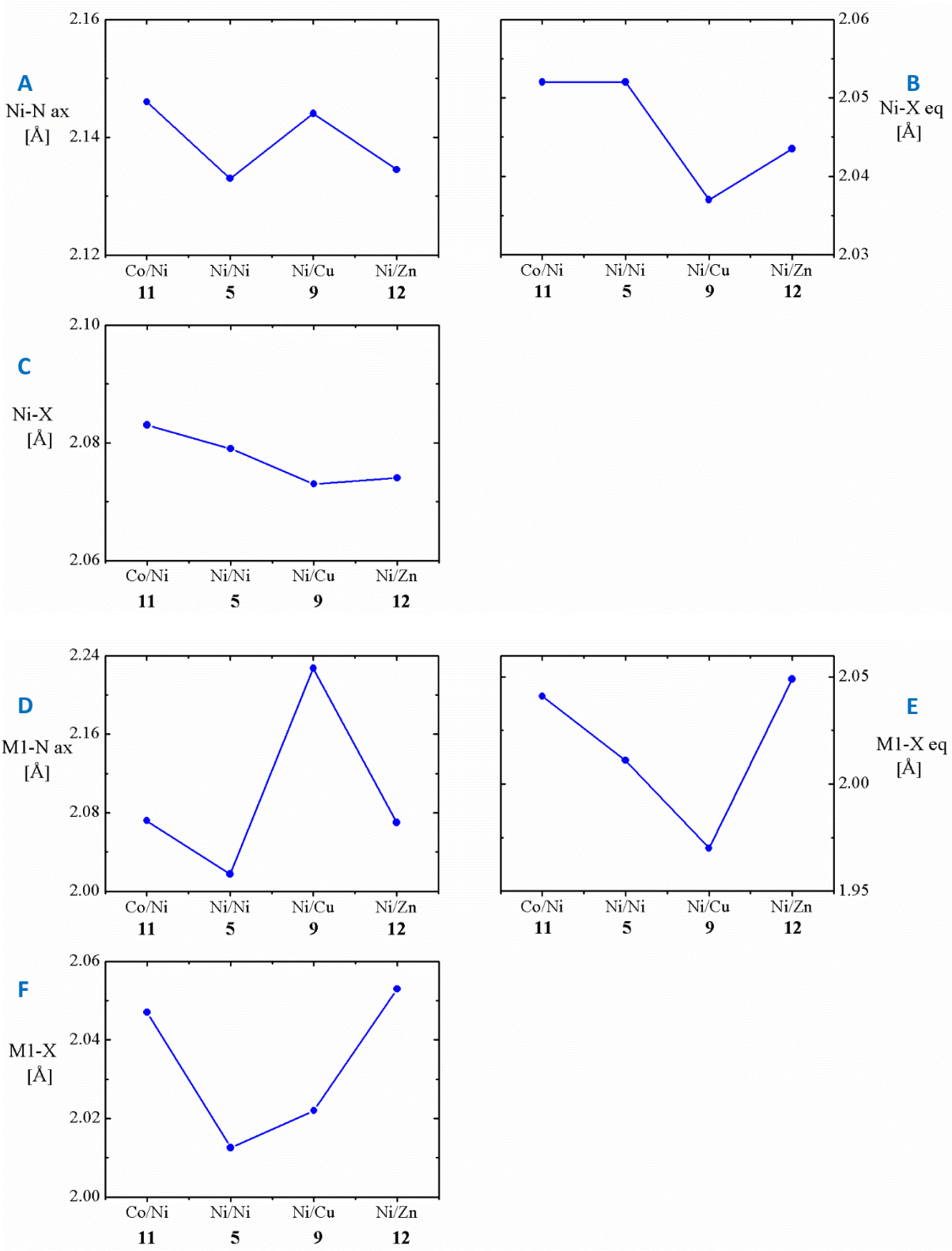

Figure II.A8: Bonding geometry of pentacoordinate M1 and hexacoordinate Ni centres in compounds **5**, **9**, **11**-**12**. Average axial M–N bond distances (A and D), average equatorial M–X bond distances (B and E), average distance of all M–X bonds (C and F).

APPENDIX III

DESIGN AND PREPARATION OF COORDINATION COMPOUNDS AS MOLECULAR PROTOTYPES OF QUANTUM GATES

Table III.A1: Crystallographic data for the compounds **14** and **15**

	14	**15**
Formula	$C_{146}H_{114}N_{10}O_{28}V_4$	$C_{93.20}H_{73.20}N_{11.44}O_{22}V_6$
M_r	2660.23	2011.03
Crystal system	Monoclinic	Triclinic
Space group	$P2_1/c$	P-1
a (Å)	16.642(5)	10.8898(7)
b (Å)	14.680(4)	14.0346(9)
c (Å)	26.887(8)	15.3322(10)
α (°)	90	103.967(4)
β (°)	104.060(4)	104.004(4)
γ (°)	90	92.234(5)
V (Å^3)	6372(3)	2194.6(3)
Z	2	1
ρ_{calc} (g/cm^3)	1.387	1.522
μ (cm^{-1})	0.458	0.695
Shape and colour	Yellow plate	Orange plate
Crystal size (mm^3)	0.140·0.040·0.008	0.130·0.130·0.050
λ (Å)	0.7749	0.71073
T (K)	100(2)	100(2)
Reflections	6444	5893
Unique reflections	4254	4365
Parameters	727	631
Restraints	286	186
R_1 (all data)[a]	0.1591	0.0810
R_1 [$I>2\sigma(I)$][a]	0.1177	0.0538
wR_2 (all data)[b]	0.2986	0.1427
wR_2 [$I>2\sigma(I)$][b]	0.2742	0.1287
S (all data)[c]	1.137	1.024
S [$I>2\sigma(I)$][c]	1.059	1.017
Largest residuals (e Å^3)	0.597/–0.368	1.448/–0.561

[a] $R_1 = \Sigma||F_o| - |F_c|| / \Sigma|F_o|$; [b] $wR_2 = \{\Sigma[w(F_o^2 - F_c^2)^2] / \Sigma[w(F_o^2)^2]\}^{1/2}$; [c] $S = \{\Sigma[w(F_o^2 - F_c^2)^2] / (n - p)\}^{1/2}$

Table III.A2: V═O···C and V═O···H—C close contacts in the structure of compound **14**

V═O···C	**V═O (Å)**	**O···C (Å)**	**V···C (Å)**	**V═O···C (°)**
V1═O13···C51	1.584(9)	3.12(2)	4.70(1)	173.5(5)
V1═O13···C52	1.584(9)	4.13(2)	5.67(2)	163.4(5)
C–H···O (=V)	**C–H (Å)**	**O···H (Å)**	**O···C (Å)**	**C–H···O (°)**
C30–H30A···O14(V2)	0.95	2.668	3.51(1)	148.3
C33–H33A···O14(V2)	0.95	2.532	3.46(1)	166.7
C40–H40A···O14(V2)	0.95	2.678	3.29(1)	122.5
C42–H42A···O14(V2)	0.95	2.706	3.36(2)	126.2
C45–H45A···O14(V2)	0.95	2.431	3.31(2)	154.1
C13–H13A···O13(V1)	0.95	2.585	3.38(1)	141.9

Table III.A3: Interatomic distances [Å] and angles [°] for the compound **14**

V1–V2	7.514(3)	V2=O14	1.606(8)	N1–V1–O3	162.4(4)	O8–V1–O2	81.7(3)	O14–V2–O4	97.4(4)
V1–V1#	17.546(5)	V2–O4	1.944(9)	O2–V1–O9	163.3(4)	N2–V2–O10	89.3(4)	O14–V2–N2	94.4(4)
V2–V2#	6.508(3)	V2–O5	2.154(8)	O13–V1–O8	176.3(4)	O10–V2–O11	88.2(3)	O5–V2–O4	82.1(3)
V1–V2#	10.892(4)	V2–O10	1.959(9)	O13–V1–N1	95.5(4)	O11–V2–O4	88.8(3)	O5–V2–O11	82.2(3)
V1–O2	2.011(8)	V2–O11	1.996(8)	O13–V1–O9	97.9(4)	O4–V2–N2	88.7(4)	O5–V2–O10	80.7(3)
V1–O3	1.972(8)	V2–N2	2.142(10)	O13–V1–O3	102.1(4)	O4–V2–O10	162.7(4)	O5–V2–N2	80.9(4)
V1=O13	1.584(9)	O2–V1–O3	87.4(3)	O13–V1–O2	98.7(4)	O11–V2–N2	163.1(4)		
V1–O8	2.129(9)	O3–V1–O9	87.5(3)	O8–V1–N1	80.8(4)	O14–V2–O5	175.2(4)		
V1–O9	1.992(9)	O9–V1–N1	90.4(4)	O8–V1–O9	81.8(3)	O14–V2–O11	102.5(4)	Symmetry operation:	
V1–N1	2.149(10)	N1–V1–O2	89.6(4)	O8–V1–O3	81.6(3)	O14–V2–O10	99.9(4)	# = 1−x, 1−y, 1−z	

Table III.A4: Interatomic distances [Å] and angles [°] for the compound **15**

V1–V2	3.125(1)	V1–N4	2.195(4)	O2–V1–O10	74.3(1)	O4–V1–O12	100.4(2)	O6–V3–N2	91.1(1)
V2–V3	3.560(1)	V1–O4	1.875(3)	O10–V1–O12	103.6(2)	O4–V1–O10	99.1(1)	O6–V3–N3	164.4(2)
V1–V3	5.644(1)	V2=O9	1.602(3)	O12–V1–O3	100.0(1)	O11–V2–O1	93.9(1)	N2–V3–O11	169.9(2)
V1–V1#	8.894(1)	V2–O1	1.894(4)	O3–V1–O2	80.7(1)	O1–V2–O2	82.2(1)	O7–V3–O5	172.8(1)
V1–V2#	8.999(1)	V2–O2	2.064(3)	O12–V1–O2	171.8(1)	O2–V2–O10	74.7(1)	O5–V3–N2	84.0(1)
V1–V3#	10.744(1)	V2–O10	1.923(4)	O10–V1–O3	153.9(2)	O10–V2–O11	95.7(1)	O5–V3–N3	81.2(1)
V2–V2#	10.118(1)	V2–O11	1.689(3)	O4–V1–N4	167.1(2)	O9–V2–O11	107.6(2)	O5–V3–O6	83.3(1)
V2–V3#	12.094(1)	V3=O7	1.595(3)	N4–V1–O10	86.1(2)	O9–V2–O10	101.3(1)	O5–V3–O11	85.9(1)
V3–V3#	14.679(1)	V3–O6	1.987(3)	N4–V1–O12	89.8(2)	O9–V2–O1	103.6(1)	O7–V3–O6	100.7(1)
V1–O2	2.221(4)	V3–O11	1.964(3)	N4–V1–O3	83.0(1)	O9–V2–O2	102.9(1)	O7–V3–N2	89.9(2)
V1=O12	1.594(4)	V3–O5	2.124(3)	N4–V1–O2	82.2(1)	N2–V3–N3	88.5(2)	O7–V3–N3	94.8(2)
V1–O10	1.735(3)	V3–N3	2.121(5)	O4–V1–O2	87.8(1)	N3–V3–O11	89.0(2)	O7–V3–O11	100.1(1)
V1–O3	1.992(3)	V3–N2	2.167(4)	O4–V1–O3	87.3(1)	O11–V3–O6	88.7(1)	Symmetry: # = −x, −y, −z	

Table III.A5: Hydrogen bonding in the structure of compound **14**

D–H···A	D–H (Å)	H···A (Å)	D···A (Å)	D–H···A (°)
O1–H1···O2	0.840	1.790	2.53(1)	145.5
O7–H7···O2	0.841	2.708	3.40(1)	141.1
O7–H7···O8	0.841	1.754	2.50(1)	146.1
O12–H12···O11	0.840	1.810	2.52(1)	141.2
O6–H6···O5	0.840	1.779	2.50(1)	143.4
C58–H58A···O7	0.95	2.640	3.28(2)	125.7
C28–H28A···O1	0.95	2.470	3.19(2)	133
C11–H11A···O12	0.95	2.31	3.22(2)	161.1
C5–H5A···O12	0.95	2.632	3.57(2)	167
C2–H2A···N1S	0.95	2.67	3.42(2)	136

Table III.A6: V═O···C and (V═)O···H—C close contacts in the structure of compound **15**

V═O···C	V═O (Å)	O···C (Å)	V···C (Å)	V═O···C (°)
V3═O7···C29	1.595(3)	3.039(6)	3.932(6)	112.3(2)
C–H···O(=V)	**C–H (Å)**	**O···H (Å)**	**O···C (Å)**	**C–H···O (°)**
C30–H30···O9(V2)	0.950	2.355	3.297(5)	171.1
C37–H37···O9(V2)	0.950	2.574	3.510(7)	168.5
C35–H35···O12(V1)	0.950	2.594	3.523(7)	166.0
C33–H33···O12(V1)	0.949	2.646	3.303(7)	126.8
C17–H17···O9(V2)	0.950	2.614	3.342(7)	133.7
C24–H24···O7(V3)	0.951	2.596	3.210(2)	122.6
C19–H19···O7(V3)	0.950	2.656	3.519(5)	151.4

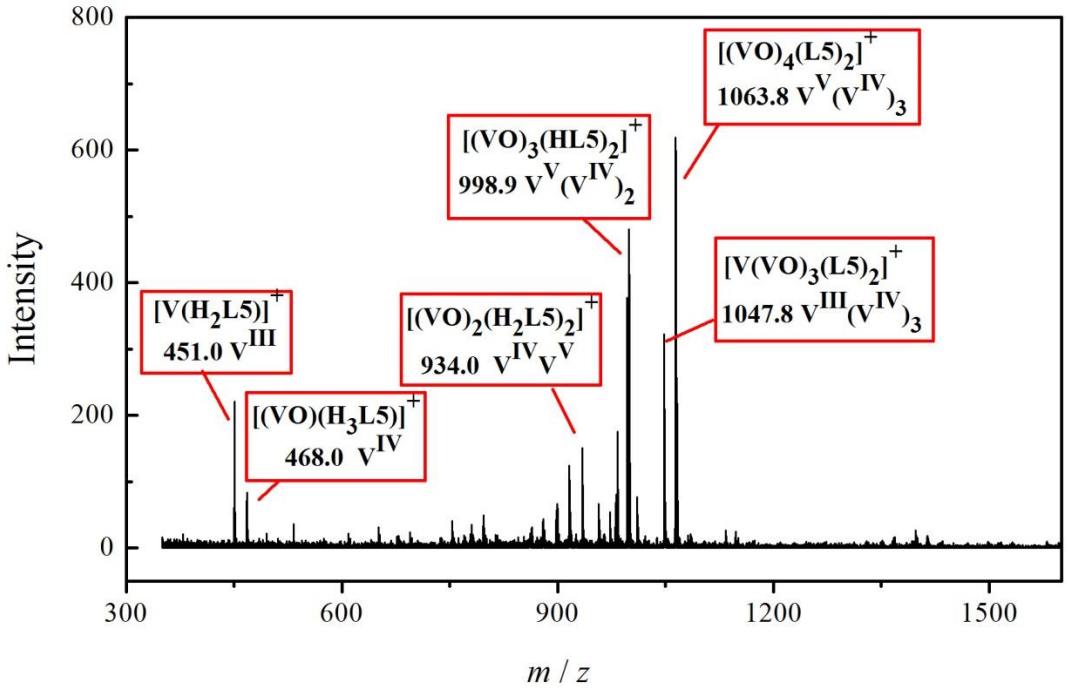

Figure III.A1: (+) MALDI-TOF of THF solution of compound **14**. Oxidation states of vanadium ions are indicated as the superscripts.

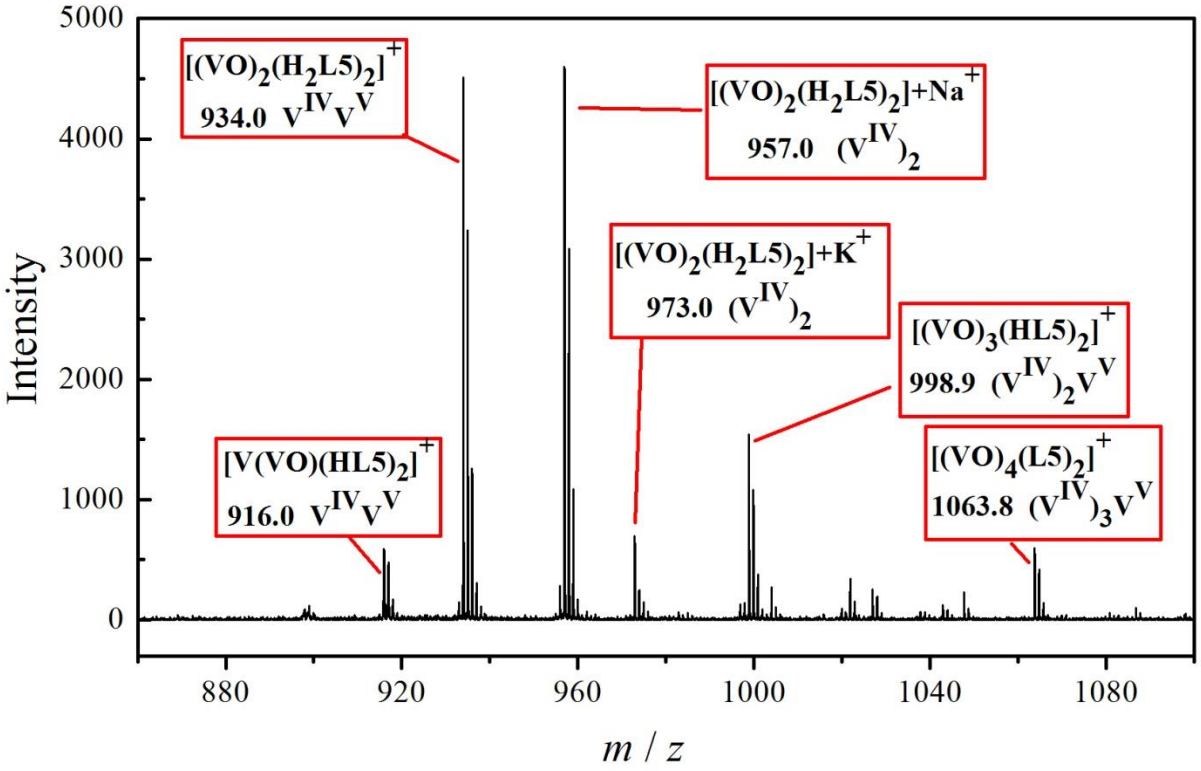

Figure III.A2: (+) MALDI-TOF of THF solution of compound **14** with the DCTB matrix (1:1 volume ratio). Oxidation states of vanadium ions are indicated as the superscripts.

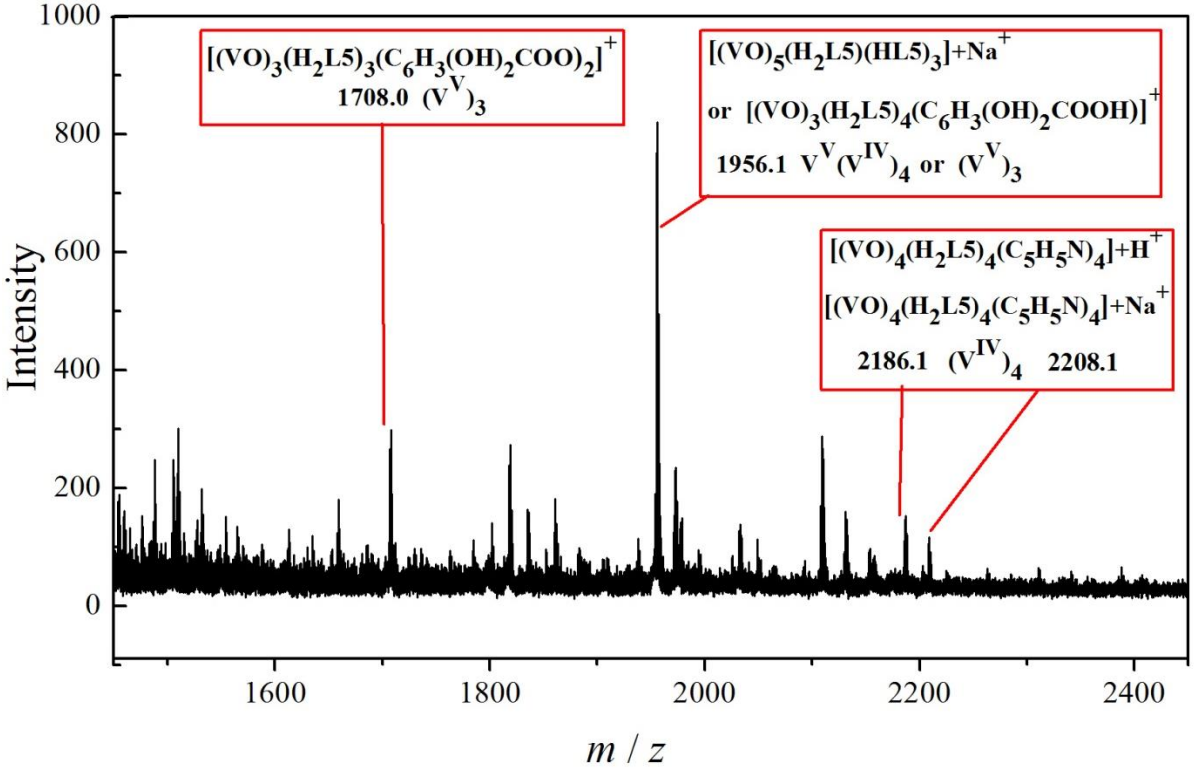

Figure III.A3: (+) MALDI-TOF of MeOH solution of compound **14** containing saturated solution of DHB in CH_3CN (1:1 volume ratio). Oxidation states of vanadium ions are indicated as the superscripts.

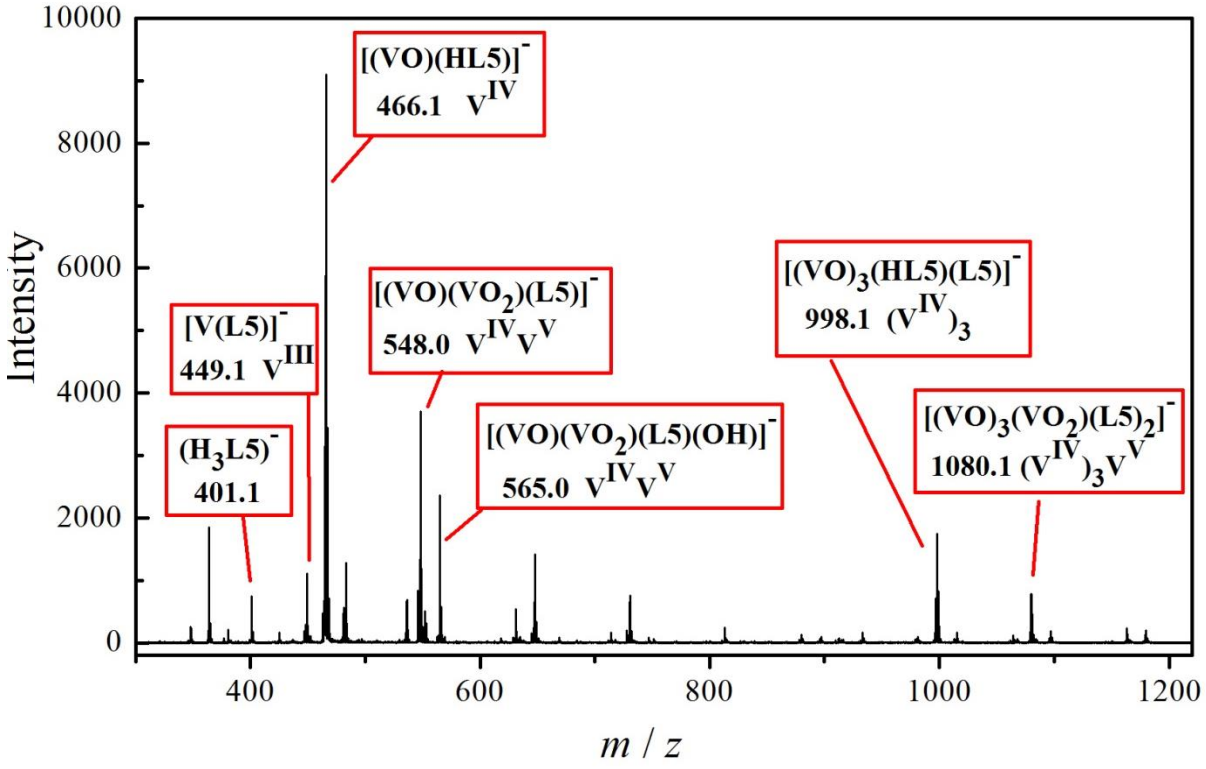

Figure III.A4: (-) MALDI-TOF of THF solution of compound **14**. Oxidation states of vanadium ions are indicated as the superscripts.

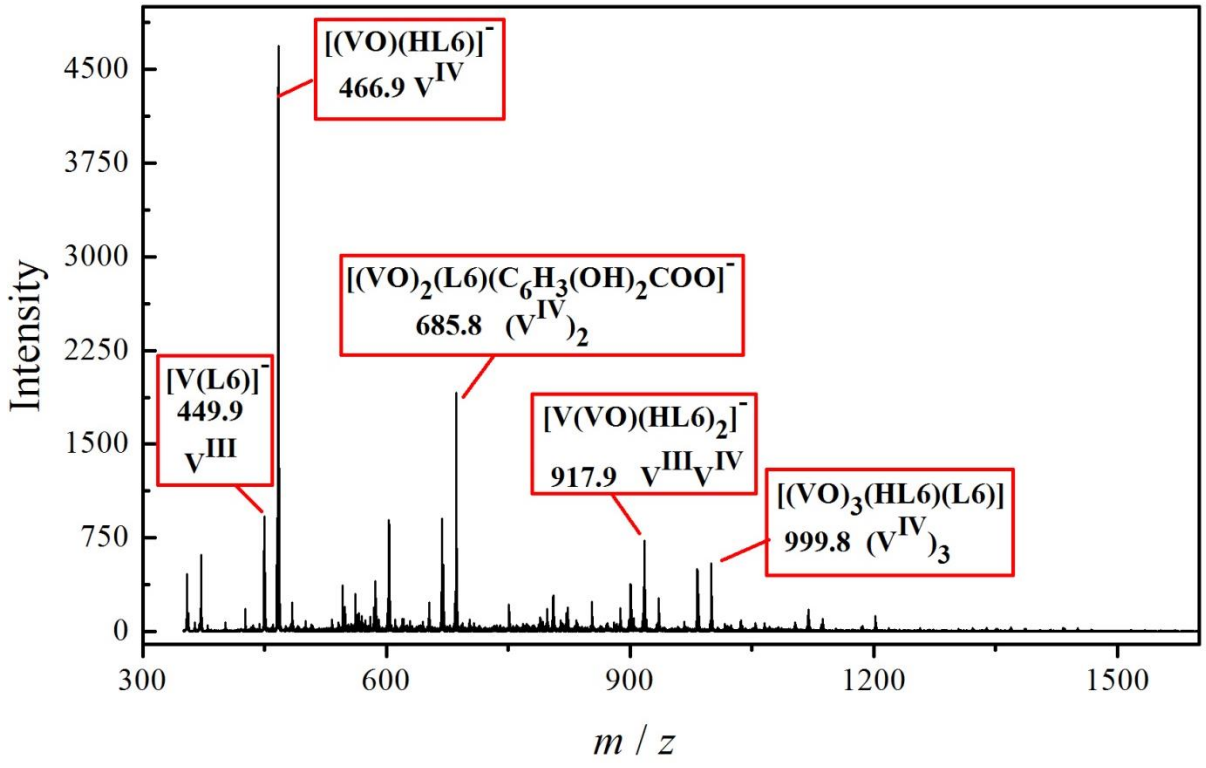

Figure III.A5: (-) MALDI-TOF of MeOH solution of compound **15** containing saturated solution of DHB in CH_3CN (1:1 volume ratio). Oxidation states of vanadium ions are indicated as the superscripts.

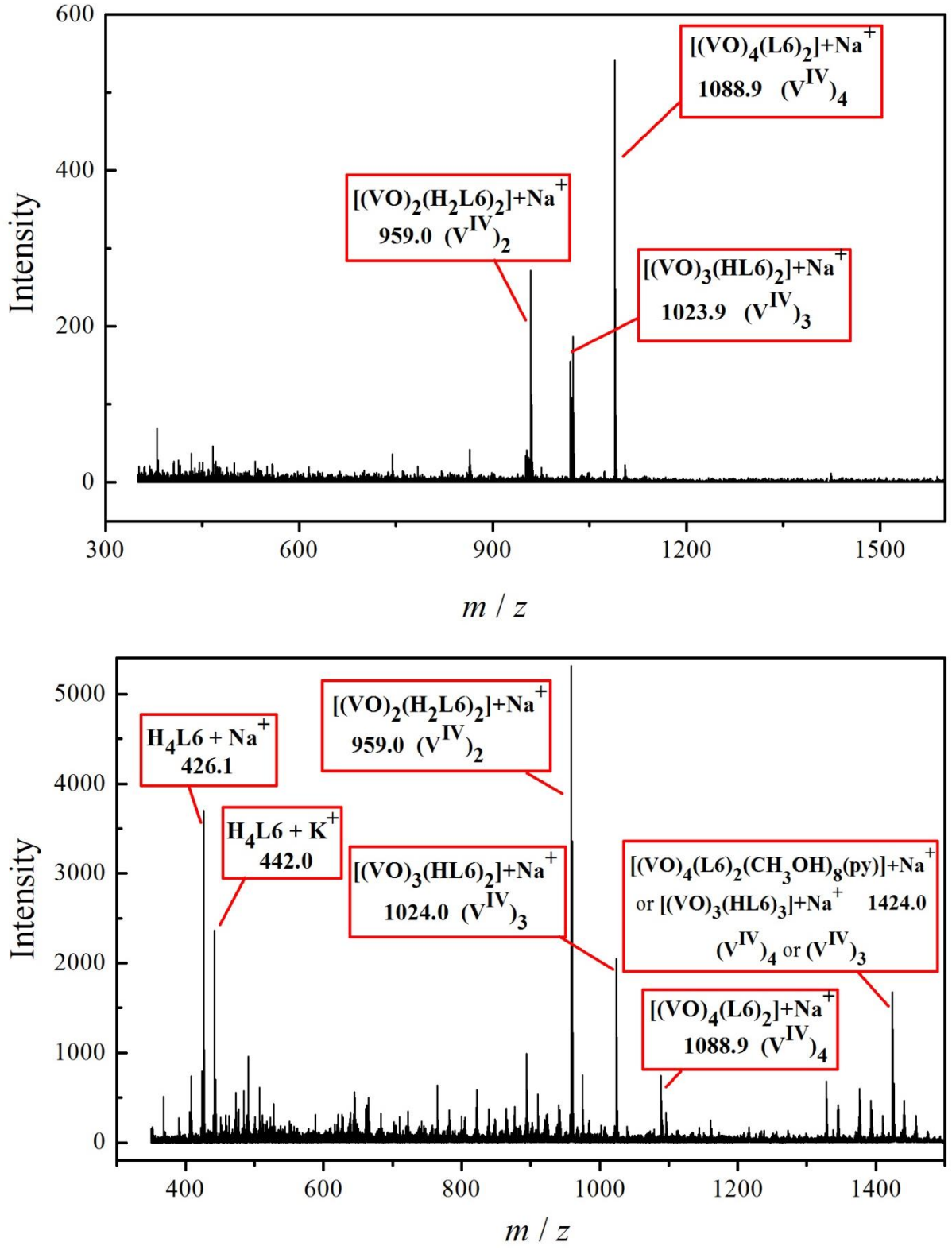

Figure III.A6: (+) MALDI-TOF of MeOH solution of compound **15**. Oxidation states of vanadium ions are indicated as the superscripts. *Top*: solution without matrix. *Bottom*: solution with matrix containing saturated solution of DHB in CH_3CN (1:1 volume ratio).

Table III.A7: Crystallographic data for the ligands **H_4LA1**, **H_4LA2**, **H_4L7**, **H_2L8a** and **H_2L8b**

	H_4LA1	**H_4LA2**	**H_4L7**	**H_2L8a**	**H_2L8b**
Formula	$C_{23}H_{17}NO_6$	$C_{25}H_{20}O_7$	$C_{28}H_{20}N_2O_6$	$C_{30}H_{18}N_2O_5$	$C_{30}H_{18}N_2O_5$
M_r	403.38	432.41	480.46	486.46	486.46
Crystal system	Monoclinic	Orthorhombic	Monoclinic	Monoclinic	Monoclinic
Space group	$P2_1/c$	$Fdd2$	$P2_1/n$	$P2_1/n$	$P2_1/c$
a (Å)	5.0822(2)	22.347(8)	3.692(8)	6.4072(3)	12.8188(9)
b (Å)	9.6261(4)	67.02(2)	12.36(3)	17.0201(7)	24.454(2)
c (Å)	18.1734(7)	5.194(2)	25.87(6)	20.2346(8)	7.1006(5)
α (°)	90	90	90	90	90
β (°)	97.810(2)	90	91.59(3)	97.569(3)	102.702(5)
γ (°)	90	90	90	90	90
V (Å^3)	880.83(6)	7779(5)	1180(4)	2187.38(16)	2171.4(3)
Z	2	16	2	4	4
ρ_{calc} (g/cm^3)	1.521	1.477	1.352	1.477	1.488
μ (cm^{-1})	0.134	0.131	0.1116	0.085	0.085
Shape and colour	Yellow lozange	Yellow plate	Yellow needle	Yellow plate	Yellow needle
Crystal size (mm^3)	0.090·0.090·0.030	0.170·0.050·0.020	0.640·0.020·0.020	0.060·0.060·0.020	0.150·0.010·0.005
λ (Å)	0.7749	0.7749	0.7749	0.7749	0.7749
T (K)	100(2)	100(2)	100(2)	100(2)	100(2)
Reflections	2571	4437	1678	2832	2566
Unique reflections	2163	3839	1202	1966	1958
Parameters	145	302	166	340	340
Restraints	0	1	0	0	0
R_1 (all data)[a]	0.0620	0.0484	0.1427	0.1182	0.0789
R_1 [$I>2\sigma(I)$][a]	0.0523	0.0389	0.1128	0.0866	0.0566
wR_2 (all data)[b]	0.1449	0.0938	0.2810	0.2521	0.1535
wR_2 [$I>2\sigma(I)$][b]	0.1396	0.0891	0.2666	0.2287	0.1397
S (all data)[c]	1.132	1.042	1.104	1.076	1.047
S [$I>2\sigma(I)$][c]	1.132	1.042	1.104	1.076	1.047
Largest residuals (e Å^3)	0.521/–0.273	0.244/–0.216	0.424/–0.348	0.717/–0.263	0.845/–0.265

[a] $R_1 = \Sigma||F_o| - |F_c|| / \Sigma|F_o|$; [b] $wR_2 = \{\Sigma[w(F_o^2 - F_c^2)^2] / \Sigma[w(F_o^2)^2]\}^{1/2}$; [c] $S = \{\Sigma[w(F_o^2 - F_c^2)^2] / (n - p)\}^{1/2}$

Table III.A8: Bond distances [Å] within **H_4LA1**

O1–C1	1.341(2)	C1–C2	1.408(2)
C2–C3	1.368(2)	C3–C4	1.393(2)
C4–C5	1.379(2)	C5–C6	1.404(2)
C6–C1	1.408(2)	C6–C7	1.478(2)
C7–O2	1.263(2)	C7–C8	1.439(2)
C8–C9	1.366(2)	C9–O3	1.327(2)
C9–C10	1.477(2)	C10–N1	1.29(2)
N1–C12	1.39(2)	C12–C10	1.398(2)
C10–C11	1.44(2)	C11–C12	1.33(2)
C12–C10	1.398(2)		

Table III.A9: Hydrogen bonding and π···π contacts in the structure of **H_4LA1**

D–H···A	D–H (Å)	H···A (Å)	D···A (Å)	D–H···A (°)
O1–H1···O2	0.90(3)	1.76(3)	2.568(1)	148(2)
O3–H3···O2	0.84(3)	1.83(2)	2.569(1)	146(2)
O3–H3···O1#	0.84(3)	2.55(3)	3.142(2)	128(2)
O1–H1···O2#	0.90(3)	2.46(3)	2.921(2)	112(2)

Symmetry operation: # = 2−x, −y, 1−z; #1 = −1+x, y, z

π···π

C···C	d (Å)	C···C	d (Å)
phenol-β-diketone (C1#1···C8)	3.325(2)	pyridine-β-diketone (C7#1···C10)	3.381(2)

Table III.A10: Bond distances [Å] within **H_4LA2**

O1–C1	1.350(3)	C7–C8	1.433(3)	C13–C12	1.391(3)	C20–C21	1.407(3)
C1–C2	1.394(4)	C8–C9	1.370(3)	C12–C11	1.388(3)	C21–C22	1.378(3)
C2–C3	1.373(4)	C9–O3	1.336(3)	C11–C10	1.408(3)	C22–C23	1.396(3)
C3–C4	1.400(4)	C9–C10	1.478(3)	C13–C17	1.484(3)	C23–C24	1.379(3)
C4–C5	1.374(4)	C10–C15	1.416(3)	C17–O5	1.327(3)	C24–C25	1.392(3)
C5–C6	1.408(4)	C15–O4	1.356(3)	C17–C18	1.364(3)	C25–C20	1.417(3)
C6–C1	1.418(3)	O4–C16	1.436(3)	C18–C19	1.440(3)	C25–O7	1.348(3)
C6–C7	1.479(3)	C15–C14	1.391(2)	C19–O6	1.271(3)		
C7–O2	1.274(3)	C14–C13	1.393(3)	C19–C20	1.469(3)		

Table III.A11: Hydrogen bonding and π···π contacts in the structure of **H_4LA2**

D–H···A	D–H (Å)	H···A (Å)	D···A (Å)	D–H···A (°)
O1–H1···O2	0.88(3)	1.77(3)	2.567(2)	149(3)
O3–H3···O2	0.97(3)	1.64(3)	2.518(2)	150(3)
C8–H8···O4	0.950	2.134	2.791(3)	125.2
O5–H5···O6	0.91(3)	1.66(3)	2.494(2)	152(3)
O7–H7···O6	0.87(3)	1.80(3)	2.572(2)	147(3)
O1#–H1#···O5	0.88(3)	2.43(4)	3.064(3)	129(3)
O7–H7···O3#	0.87(3)	2.53(3)	3.181(3)	132(3)
C24#1–H24#1···O7	0.950(3)	2.537	3.284(3)	135.6

Symmetry operation: # = 1/2+x, y, 1/2+z; #1 = 3/2−x, 1−y, 1/2+z; #2 = −1/2+x, y, 1/2+z

π···π

C···C	d (Å)	C···C	d (Å)
phenol-β-diketone (O1···C17#2)	3.206(3)	β-diketone -β-diketone (C7···O6#2; O2···C19#2)	3.111(3) 3.104(3)

Table III.A12: Bond distances [Å] within **H_4L7**

O1–C1	1.364(9)	C5–C6	1.41(1)	C8–C9	1.36(1)	C12–C13	1.40(1)
C1–C2	1.38(1)	C6–C1	1.39(1)	C9–O3	1.339(9)	C13–C13#	1.448(9)
C2–C3	1.36(1)	C6–C7	1.46(1)	C9–C10	1.46(1)	C13–N1	1.353(8)
C3–C4	1.39(1)	C7–O2	1.262(9)	C10–C11	1.39(1)	N1–C14	1.329(8)
C4–C5	1.37(1)	C7–C8	1.44(1)	C11–C12	1.37(1)	C14–C10	1.399(9)

Symmetry operation: # = 2−x, 1−y, 1−z

Table III.A13: Hydrogen bonding and π···π contacts in the structure of **H_4L7**

D–H···A	**D–H (Å)**	**H···A (Å)**	**D···A (Å)**	**D–H···A (°)**
O1–H1···O2	0.840	1.803	2.543(8)	145.9
O3–H3···O2	0.841	1.758	2.502(9)	146.3
C2#–H2#···N1	0.949	2.641	3.55(1)	159.5

Symmetry operation: # = 1/2−x, −1/2+y, 3/2−z; #1 = −1+x, y, z

π···π

Cg···Cg	**d (Å)**	**Cg···Cg**	**d (Å)**
bipy-bipy	3.692	phenol-phenol	3.692
(C10···C11#1)	3.36(1)		

Table III.A14: Bond distances [Å] within **H_2L8a**

O1–C1	1.341(8)	C9–O3	1.319(6)	C15–C14	1.362(9)	C24–C25	1.451(8)
C1–C2	1.393(9)	C9–C10	1.464(8)	C14–C13	1.415(9)	C25–C30	1.397(9)
C2–C3	1.363(9)	C10–C11	1.387(9)	C16–C17	1.388(8)	C30–O4	1.375(7)
C3–C4	1.387(9)	C11–C12	1.387(9)	C17–C18	1.349(9)	O4–C22	1.369(6)
C4–C5	1.359(9)	C12–C13	1.412(8)	C18–C19	1.386(8)	C25–C26	1.406(8)
C5–C6	1.424(7)	C13–C21	1.411(9)	C19–N2	1.339(7)	C26–C27	1.362(8)
C6–C1	1.413(8)	C21–N1	1.357(8)	N2–C20	1.331(7)	C27–C28	1.360(10)
C6–C7	1.448(8)	C10–N1	1.340(7)	C19–C22	1.475(8)	C28–C29	1.360(10)
C7–O2	1.308(6)	C21–C20	1.462(7)	C22–C23	1.345(8)	C29–C30	1.405(8)
C7–C8	1.404(8)	C20–C16	1.409(8)	C23–C24	1.430(9)		
C8–C9	1.396(8)	C16–C15	1.449(9)	C24–O5	1.243(8)		

Table III.A15: Bond distances [Å] within **H_2L8b**

O1–C1	1.356(4)	C9–O3	1.274(4)	C15–C14	1.356(6)	C24–C25	1.468(5)
C1–C2	1.393(5)	C9–C10	1.494(5)	C14–C13	1.425(5)	C25–C30	1.394(5)
C2–C3	1.363(5)	C10–C11	1.402(5)	C16–C17	1.406(5)	C30–O4	1.380(4)
C3–C4	1.380(6)	C11–C12	1.369(5)	C17–C18	1.376(5)	O4–C22	1.358(4)
C4–C5	1.390(5)	C12–C13	1.408(6)	C18–C19	1.400(5)	C25–C26	1.401(5)
C5–C6	1.389(5)	C13–C21	1.419(5)	C19–N2	1.331(5)	C26–C27	1.369(6)
C6–C1	1.406(5)	C21–N1	1.349(4)	N2–C20	1.345(4)	C27–C28	1.402(5)
C6–C7	1.484(5)	C10–N1	1.331(5)	C19–C22	1.475(5)	C28–C29	1.376(5)
C7–O2	1.335(5)	C21–C20	1.450(5)	C22–C23	1.343(5)	C29–C30	1.383(5)
C7–C8	1.371(5)	C20–C16	1.410(5)	C23–C24	1.432(5)		
C8–C9	1.421(5)	C16–C15	1.434(5)	C24–O5	1.248(4)		

Table III.A16: Hydrogen bonding and π···π contacts in the structure of **H_2L8a**

D–H···A	D–H (Å)	H···A (Å)	D···A (Å)	D–H···A (º)
O1–H1···O2	1.07(8)	1.58(8)	2.590(6)	156(7)
O3–H3···O2	1.14(7)	1.50(7)	2.542(6)	148(6)
C4–H4···O5	0.950	2.381	3.221(8)	147.2
C14#–H14#···O5	0.950	2.682	3.577(8)	157.2
O1–H1···O3#1	1.07(8)	2.44(8)	3.065(6)	116(5)
O3–H3···O2#1	1.14(7)	2.29(7)	2.802(6)	105(4)

Symmetry operation: #=−1/2+x, 3/2−y, 1/2+z; #1=−x, 2−y, 1−z; #2=−1+x, y, z; #3=2−x, 1−y, 1−z

π···π

C···C	d (Å)	Cg···Cg	d (Å)
C3···C23#2	3.309(8)	C9···C15#2	3.385(8)
C3···C24#2	3.307(8)	C10···C15#2	3.319(8)
C4···C22#2	3.343(8)	C18···C30#3	3.400(8)
C8···C16#2	3.377(8)		

flavone-phenol, phenanthroline-β-diketone, phenanthroline-flavone

Table III.A17: Hydrogen bonding and π···π contacts in the structure of **H_2L8b**

D–H···A	D–H (Å)	H···A (Å)	D···A (Å)	D–H···A (º)
O2–H2···O3	1.07(5)	1.49(4)	2.479(3)	152(4)
O1–H1···O5	1.06(4)	1.66(4)	2.700(4)	166(4)
C2–H2A···O5	0.949	2.694	3.380(5)	129.7
C23–H23···O1	0.951	2.535	3.222(5)	129.3
C8–H8A···O1	0.950	2.256	2.881(4)	122.6
C29#–H29#···O3	0.950	2.471	3.413(4)	171.3
C18#–H18#···O2	0.950	2.678	3.481(5)	142.6

Symmetry operation: # = 1−x, 1/2+y, 1/2−z; #1 = 1−x, 1− y, −z; #2 = 1−x, 1− y, 1−z

π···π

C···C	d (Å)	C···C	d (Å)
C12···C30#1	3.336(5)	C1···C17#2	3.246(6)
C14···C24#1	3.290(5)	C10···C30#2	3.315(6)
C21···C22#1	3.378(5)	C21···C24#2	3.370(6)

flavone-phenanthroline + phenol-phenanthroline

Table III.A18: Crystallographic data for the compounds **16**-**20**

	16	**17**	**18**	**19**	**20**
Formula	$C_{103}H_{95}N_{17}O_{16}Ni_2Cu_2Cl_2$	$C_{100}H_{92}N_{15}O_{17}Ni_2Cu_2Cl_2$	$C_{155}H_{128}N_{16}O_{21}Ni_3Cu_3$	$C_{85}H_{82}N_{12}O_{17}Ni_2Cu_2Cl_2$	$C_{185}H_{161}N_{29}O_{32}Ni_4Cu_4Cl_4$
M_r	2142.35	2091.28	2917.47	1863.27	3933.22
Crystal system	Monoclinic	Monoclinic	Triclinic	Monoclinic	Triclinic
Space group	$P2_1/c$	$P2_1/c$	$P\bar{1}$	$P2_1/c$	$P\bar{1}$
a (Å)	18.189(2)	18.415(4)	17.429(5)	11.7527(8)	9.3977(6)
b (Å)	9.9763(12)	9.950(2)	22.792(7)	10.2517(8)	19.5175(12)
c (Å)	27.950(3)	27.958(6)	23.211(6)	35.693(2)	25.0771(15)
α (°)	90	90	119.151(4)	90	102.312(3)
β (°)	99.792(3)	100.144(4)	92.989(4)	91.294(2)	97.017(3)
γ (°)	90	90	108.934(4)	90	92.808(3)
V (Å^3)	4997.8(10)	5043(2)	7366(4)	4299.4(5)	4446.8(5)
Z	2	2	2	2	1
ρ_{calc} (g/cm^3)	1.424	1.377	1.316	1.439	1.469
μ (cm^{-1})	0.919	0.909	1.220	1.055	1.024
Shape and colour	Yellow stick	Yellow block	Orange block	Orange block	Yellow block
Crystal size (mm^3)	0.487·0.104·0.099	0.470·0.150·0.080	0.080·0.040·0.040	0.366·0.100·0.093	0.643·0.360·0.211
λ (Å)	0.71073	0.71073	0.7749	0.71073	0.71073
T (K)	100(2)	100(2)	100(2)	100(2)	100(2)
Reflections	10202	10314	27132	8781	21076
Unique reflections	8120	7823	17689	6957	15840
Parameters	610	650	166	598	1288
Restraints	144	68	0	209	594
R_1 (all data)[a]	0.0784	0.0774	0.1427	0.0638	0.1010
R_1 [$I>2\sigma(I)$][a]	0.0624	0.0570	0.1128	0.0484	0.0776
wR_2 (all data)[b]	0.1850	0.1690	0.2810	0.1298	0.2210
wR_2 [$I>2\sigma(I)$][b]	0.1733	0.1552	0.2666	0.1212	0.2019
S (all data)[c]	1.090	1.051	1.104	1.026	1.028
S [$I>2\sigma(I)$][c]	1.053	1.049	1.104	1.021	1.025
Largest residuals (e Å^3)	1.204/–0.916	1.574/–0.582	3.459/–1.169	1.014/–0.789	3.897/–2.486

[a] $R_1 = \Sigma||F_o| - |F_c|| / \Sigma|F_o|$; [b] $wR_2 = \{\Sigma[w(F_o^2 - F_c^2)^2] / \Sigma[w(F_o^2)^2]\}^{1/2}$; [c] $S = \{\Sigma[w(F_o^2 - F_c^2)^2] / (n - p)\}^{1/2}$

Table III.A19: Interatomic distances [Å] and angles [°] for the compound **16**

Ni1–N4	2.088(4)	Cu1−N1	2.076(3)	N3–Ni1–N4	89.4(1)	O3–Ni1–N4	91.4(1)	O2–Cu1–O4	82.7(1)
Ni1–O3	2.007(3)	Cu1−O1	1.901(3)	N3–Ni1–O2	90.6(1)	N4–Ni1–O4	100.9(1)	N2–Cu1–O1	91.8(1)
Ni1–O2	2.065(3)	Cu1–O2	1.985(3)	N3–Ni1–O4	90.5(1)	O4–Ni1–O2	78.6(1)	N2–Cu1–N1	95.7(1)
Ni1–O4	2.029(3)	Cu1–O4	1.943(3)	N5–Ni1–N4	88.4(1)	O2–Ni1–O3	89.1(1)	N2–Cu1–O2	110.7(1)
Ni1–N3	2.122(3)	Cu1–Ni1	3.0482(8)	N5–Ni1–O3	91.5(1)	O4–Cu1–N1	94.5(1)	N2–Cu1–O4	95.9(1)
Ni1–N5	2.107(3)	Ni1–Ni1#	11.122(1)	N5–Ni1–O4	89.3(1)	N1–Cu1–O1	90.6(1)	Symmetry operation:	
Cu1−N2	2.229(4)	N3–Ni1–O3	89.2(1)	N5–Ni1–O2	91.6(1)	O1–Cu1–O2	89.1(1)	# = −x, 2−y, −z	

Table III.A20: Interatomic distances [Å] and angles [°] for the compound **17**

Ni1–N5	2.089(3)	Cu1−N1	2.075(3)	N3–Ni1–N5	89.6(1)	O3–Ni1–N5	91.5(1)	O2–Cu1–O4	82.5(1)
Ni1–O3	2.010(2)	Cu1−O1	1.900(3)	N3–Ni1–O2	90.8(1)	N5–Ni1–O4	100.8(1)	N2–Cu1–O1	91.0(1)
Ni1–O2	2.058(3)	Cu1–O2	1.990(2)	N3–Ni1–O4	90.2(1)	O4–Ni1–O2	78.5(1)	N2–Cu1–N1	95.5(1)
Ni1–O4	2.039(3)	Cu1–O4	1.944(3)	N4–Ni1–N5	88.3(1)	O2–Ni1–O3	89.2(1)	N2–Cu1–O2	112.2(1)
Ni1–N4	2.119(4)	Cu1–Ni1	3.0520(8)	N4–Ni1–O3	91.4(1)	O4–Cu1–N1	94.6(1)	N2–Cu1–O4	96.3(1)
Ni1–N3	2.116(3)	Ni1–Ni1#	11.199(2)	N4–Ni1–O4	89.6(1)	N1–Cu1–O1	90.9(1)	Symmetry operation:	
Cu1−N2	2.218(3)	N3–Ni1–O3	89.2(1)	N4–Ni1–O2	91.4(1)	O1–Cu1–O2	89.0(1)	# = −x, −y, −z	

Table III.A21: Interatomic distances [Å] and angles [°] for the compound **19**

Ni1–N4	2.095(3)	Cu1−N1	2.020(3)	N3–Ni1–N4	90.2(1)	O3–Ni1–N4	93.8(1)	O2–Cu1–O4	81.09(9)
Ni1–O3	2.020(2)	Cu1−O1	1.900(2)	N3–Ni1–O2	93.62(9)	N4–Ni1–O4	100.9(1)	N2–Cu1–O1	97.3(1)
Ni1–O2	2.095(2)	Cu1–O2	2.003(2)	N3–Ni1–O4	92.4(1)	O4–Ni1–O2	77.07(9)	N2–Cu1–N1	95.5(1)
Ni1–O4	2.009(2)	Cu1–O4	1.931(2)	N5–Ni1–N4	87.8(1)	O2–Ni1–O3	88.28(9)	N2–Cu1–O2	91.40(9)
Ni1–N3	2.106(3)	Cu1–Ni1	3.0972(6)	N5–Ni1–O3	89.28(9)	O4–Cu1–N1	95.6(1)	N2–Cu1–O4	107.9(1)
Ni1–N5	2.137(3)	Ni1–Ni1#	15.278(1)	N5–Ni1–O4	91.4(1)	N1–Cu1–O1	90.2(1)	Symmetry operation:	
Cu1−N2	2.308(4)	N3–Ni1–O3	87.3(1)	N5–Ni1–O2	88.54(9)	O1–Cu1–O2	90.09(9)	# = −1−x, −y, −z	

Table III.A22: Interatomic distances [Å] and angles [°] for the compound **18**

Ni1–Cu1	3.032(1)	Ni2−N5	2.130(7)	N1–Cu1–O9	95.6(2)	O15–Cu2–O7	96.1(2)	O21–Cu3–O20	89.7(2)
Ni2–Cu2	3.054(1)	Ni2−N6	2.136(7)	O8–Cu1–O1	91.7(2)	O7–Cu2–O6	88.9(2)	O20–Cu3–O13	81.0(2)
Ni3–Cu3	3.041(1)	Cu2–O16	1.983(3)	O1–Cu1–O2	89.7(1)	O6–Cu2–O16	80.3(2)	O13–Cu3–O14	90.1(2)
Ni1···Ni2	10.226(2)	Cu2–O6	1.982(5)	O2–Cu1–O9	81.9(2)	O16–Cu2–O15	89.2(2)	N8–Ni3–O20	88.3(4)
Ni2···Ni3	10.157(2)	Cu2–O15	1.908(4)	O9–Cu1–O8	90.5(2)	N5–Ni2–O6	90.9(2)	N8–Ni3–O13	89.3(4)
Ni3···Ni1	10.325(3)	Cu2–N4	2.219(7)	N3–Ni1–O9	93.0(2)	N5–Ni2–O16	92.0(2)	N8–Ni3–O19	92.6(4)
Ni1−N3	2.136(7)	Cu2–O7	1.909(3)	N3–Ni1–O2	89.7(2)	N5–Ni2–O5	88.6(2)	N8–Ni3–O12	92.3(4)
Ni1–N2	2.086(7)	Cu3−N7	2.239(7)	N3–Ni1–O10	88.6(2)	N5–Ni2–O17	88.7(2)	N9–Ni3–O13	89.7(2)
Ni1–O10	1.981(4)	Cu3−O13	2.017(4)	N3–Ni1–O3	87.2(2)	N6–Ni2–O16	92.8(2)	N9–Ni3–O20	92.6(2)
Ni1–O3	1.962(4)	Cu3–O20	1.970(3)	N2–Ni1–O2	92.0(2)	N6–Ni2–O6	91.7(2)	N9–Ni3–O19	88.6(2)
Ni1–O2	2.022(4)	Cu3–O21	1.891(5)	N2–Ni1–O9	92.8(2)	N6–Ni2–O5	87.0(2)	N9–Ni3–O12	86.6(2)
Ni1–O9	2.009(4)	Cu3–O14	1.889(4)	N2–Ni1–O10	90.5(2)	N6–Ni2–O17	89.5(2)	O12–Ni3–O13	90.8(1)
Cu1–O9	1.973(4)	Ni3–N8	2.23(2)	N2–Ni1–O3	87.1(2)	O17–Ni2–O16	91.0(2)	O13–Ni3–O20	80.2(2)
Cu1−O2	1.987(4)	Ni3–N9	2.164(9)	O3–Ni1–O2	91.1(2)	O16–Ni2–O6	79.1(2)	O20–Ni3–O19	91.8(2)
Cu1–O1	1.885(4)	Ni3−O12	1.976(6)	O2–Ni1–O9	80.2(2)	O6–Ni2–O5	91.5(2)	O19–Ni3–O12	97.1(2)
Cu1–O8	1.884(5)	Ni3−O13	2.025(3)	O9–Ni1–O10	91.5(2)	O5–Ni2–O17	98.3(2)	Ni2···Ni1···Ni3	59.24(1)
Cu1–N1	2.194(7)	Ni3–O19	1.978(4)	O10–Ni1–O3	97.3(2)	N7–Cu3–O21	106.4(2)	Ni1···Ni3···Ni2	59.90(1)
Ni2–O16	2.013(5)	Ni3–O20	1.998(4)	N4–Cu2–O7	97.8(2)	N7–Cu3–O14	100.8(2)	Ni3···Ni2···Ni1	60.87(1)
Ni2–O6	2.002(3)	N1–Cu1–O8	103.0(2)	N4–Cu2–O15	99.1(2)	N7–Cu3–O20	95.8(2)		
Ni2–O5	1.966(5)	N1–Cu1–O1	103.8(2)	N4–Cu2–O6	96.6(2)	N7–Cu3–O13	93.8(2)		
Ni2−O17	1.970(3)	N1–Cu1–O2	94.6(2)	N4–Cu2–O16	102.1(2)	O21–Cu3–O14	93.0(2)		

Table III.A23: Interatomic distances [Å] and angles [°] for the compound **20**

Ni1–Cu1	3.0502(8)	Cu1–N3	2.220(4)	N3–Cu1–O2	101.1(1)	N6–Ni1–N7	90.9(1)	O5–Ni2–N9	95.6(1)
Ni2–Cu2	3.0703(9)	Cu2–N12	2.014(4)	N3–Cu1–O4	99.1(1)	N6–Ni1–O3	84.3(1)	N9–Ni2–O8	98.3(1)
Ni1···Ni2	11.477(1)	Cu2–N11	2.275(7)	O4–Cu1–O2	81.8(1)	N6–Ni1–O2	90.6(1)	N8–Ni2–O8	88.8(2)
Cu1···Cu2	10.637(1)	Cu2–O7	1.900(5)	O2–Cu1–O1	88.8(1)	N6–Ni1–O4	91.0(1)	N8–Ni2–O6	92.1(4)
Ni1–N7	2.057(3)	Cu2–O6	1.991(3)	O1–Cu1–N4	90.3(2)	O7–Cu2–N12	88.7(2)	N8–Ni2–O5	87.4(4)
Ni1–N5	2.096(4)	Cu2–O8	1.907(4)	N4–Cu1–O4	93.3(1)	N12–Cu2–O8	95.5(2)	N8–Ni2–N9	88.5(2)
Ni1–N6	2.142(4)	Ni2–O6	2.063(4)	O4–Ni1–O2	78.5(1)	O8–Cu2–O6	81.5(1)	N10–Ni2–O5	90.4(1)
Ni1–O3	2.018(4)	Ni2–O8	2.019(3)	N2–Ni1–O3	91.5(1)	O6–Cu2–O7	89.6(2)	N10–Ni2–O6	89.6(1)
Ni1–O2	2.044(3)	Ni2–N9	2.066(4)	O3–Ni1–N7	94.4(1)	N11–Cu2–N12	99.4(2)	N10–Ni2–O8	93.7(1)
Ni1–O4	2.011(3)	Ni2–O5	2.034(3)	N7–Ni1–O4	95.6(1)	N11–Cu2–O8	94.1(2)	N10–Ni2–N9	90.0(1)
Cu1–O1	1.889(4)	Ni2–N8	2.163(5)	N5–Ni1–O4	94.2(1)	N11–Cu2–O6	101.3(2)		
Cu1–O2	2.010(3)	Ni2–N10	2.146(4)	N5–Ni1–O2	86.6(1)	N11–Cu2–O7	99.2(2)		
Cu1–O4	1.910(3)	N3–Cu1–N4	100.6(1)	N5–Ni1–O3	89.9(1)	O8–Ni2–O6	77.1(1)		
Cu1–N4	2.057(4)	N3–Cu1–O1	96.5(2)	N5–Ni1–N7	92.6(1)	O6–Ni2–O5	89.1(1)		

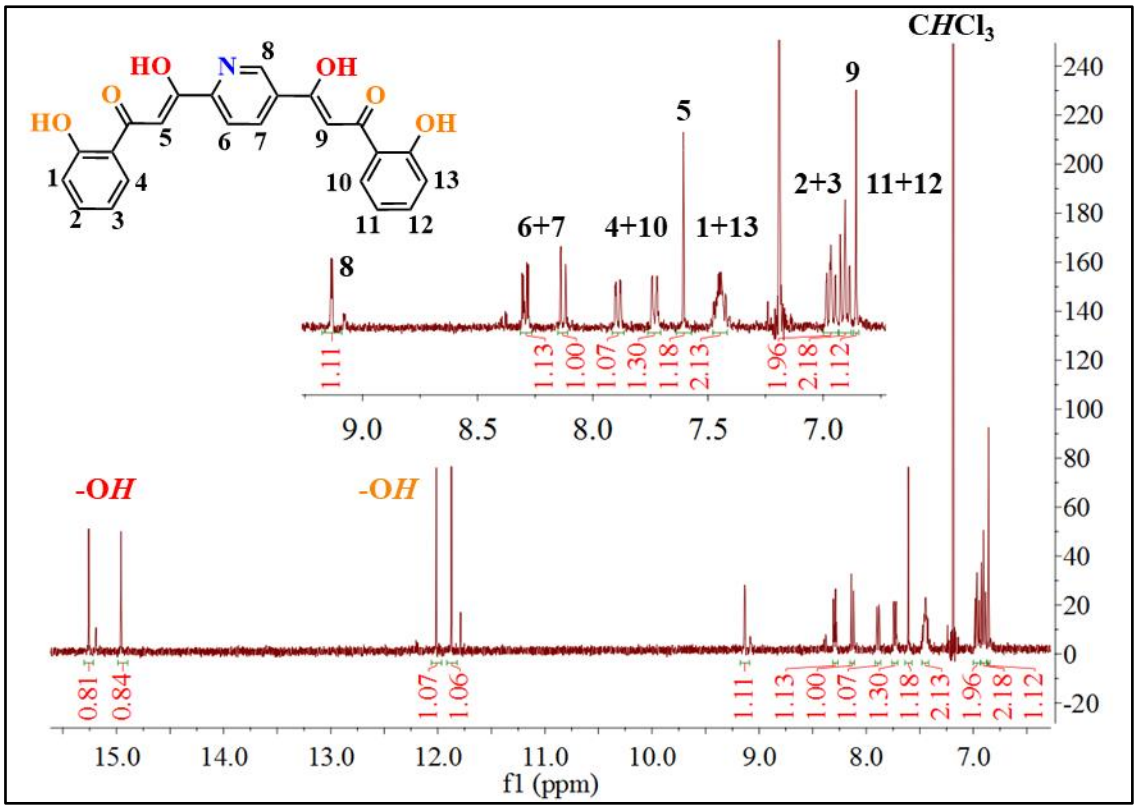

Figure III.A7: ^{1}H NMR spectrum of ligand **H_4LA1** in $CDCl_3$.

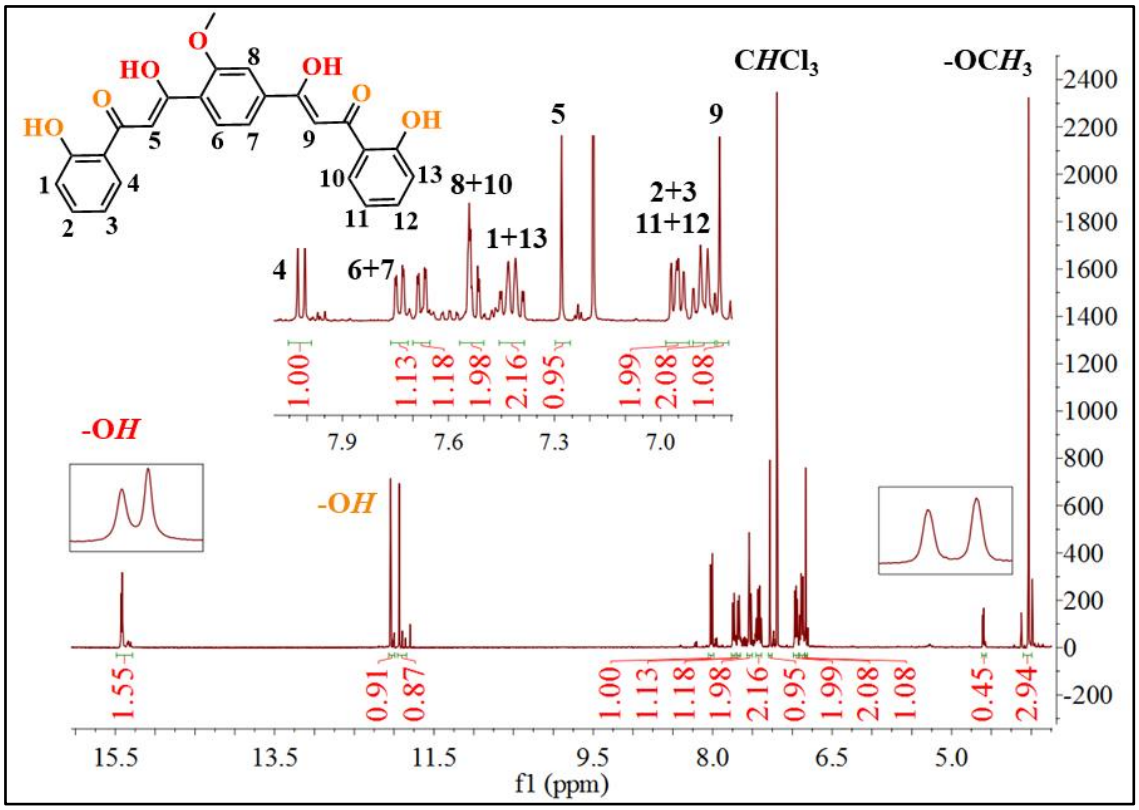

Figure III.A8: ^{1}H NMR spectrum of ligand **H_4LA2** in $CDCl_3$.

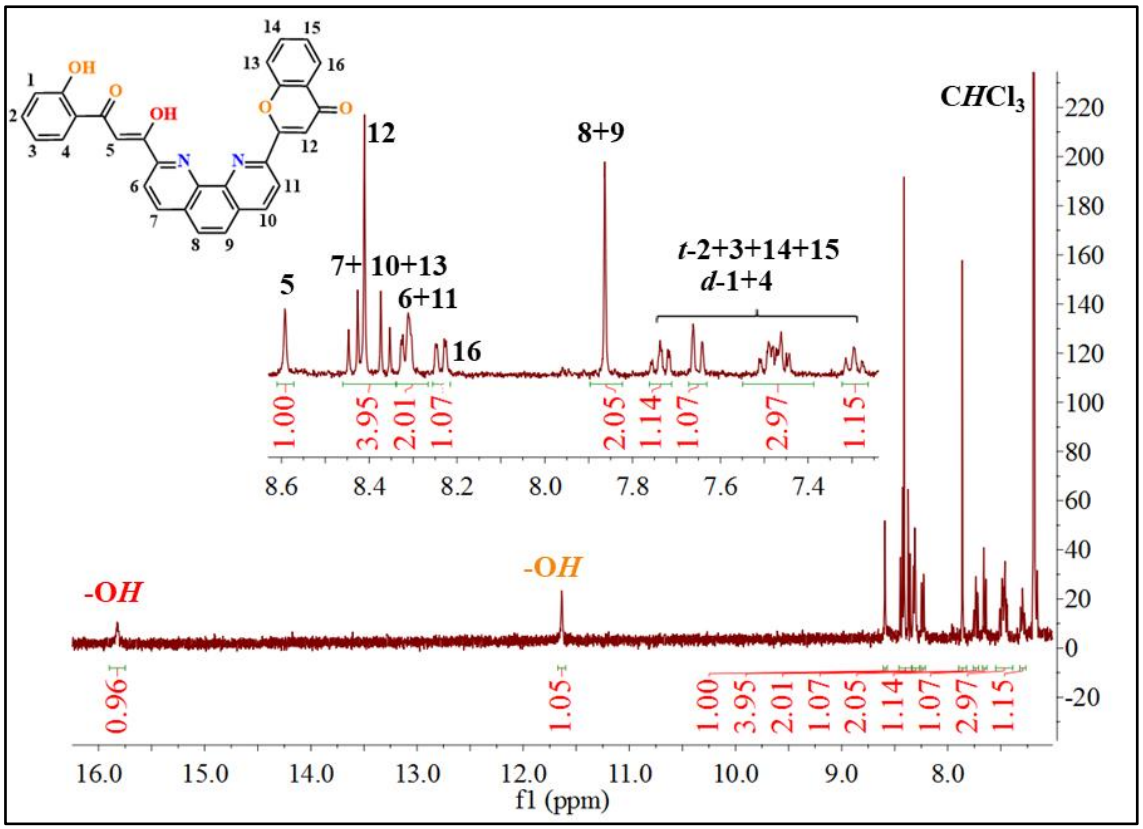

Figure III.A9: ^{1}H NMR spectrum of ligand **H_2L8** in $CDCl_3$.

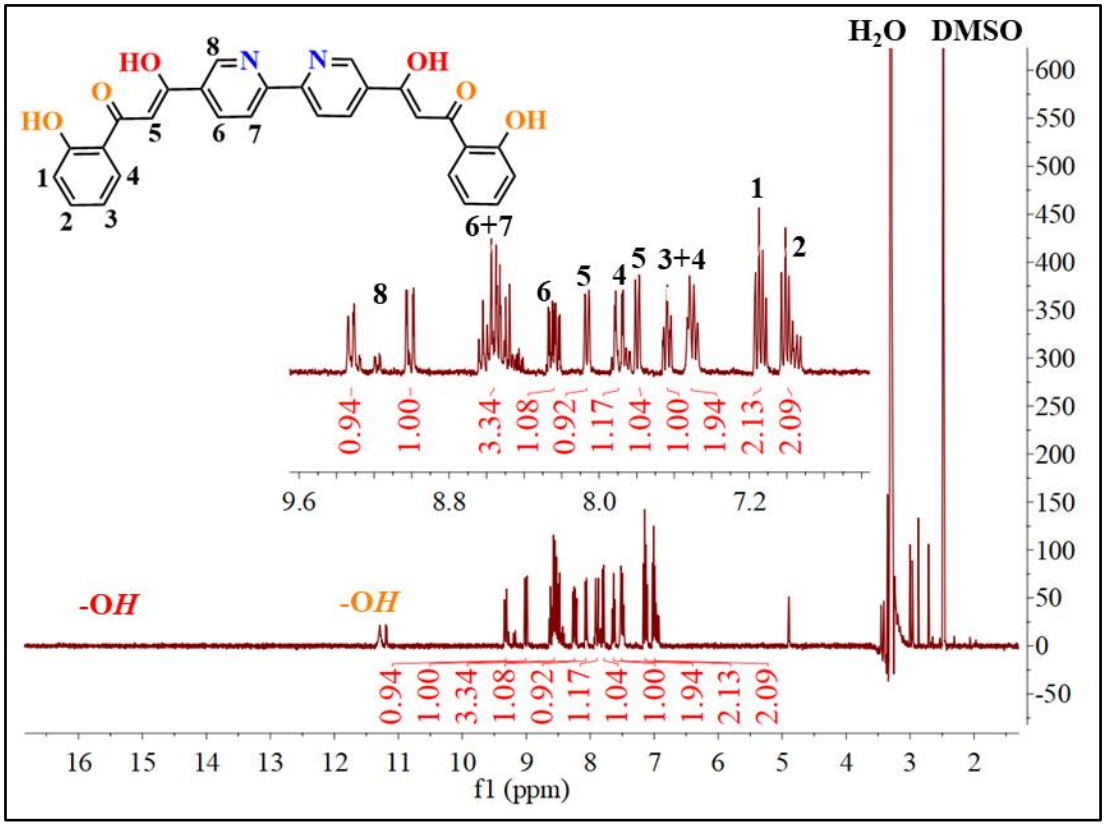

Figure III.A10: ^{1}H NMR spectrum of ligand **H_4L7** in d_6-DMSO.

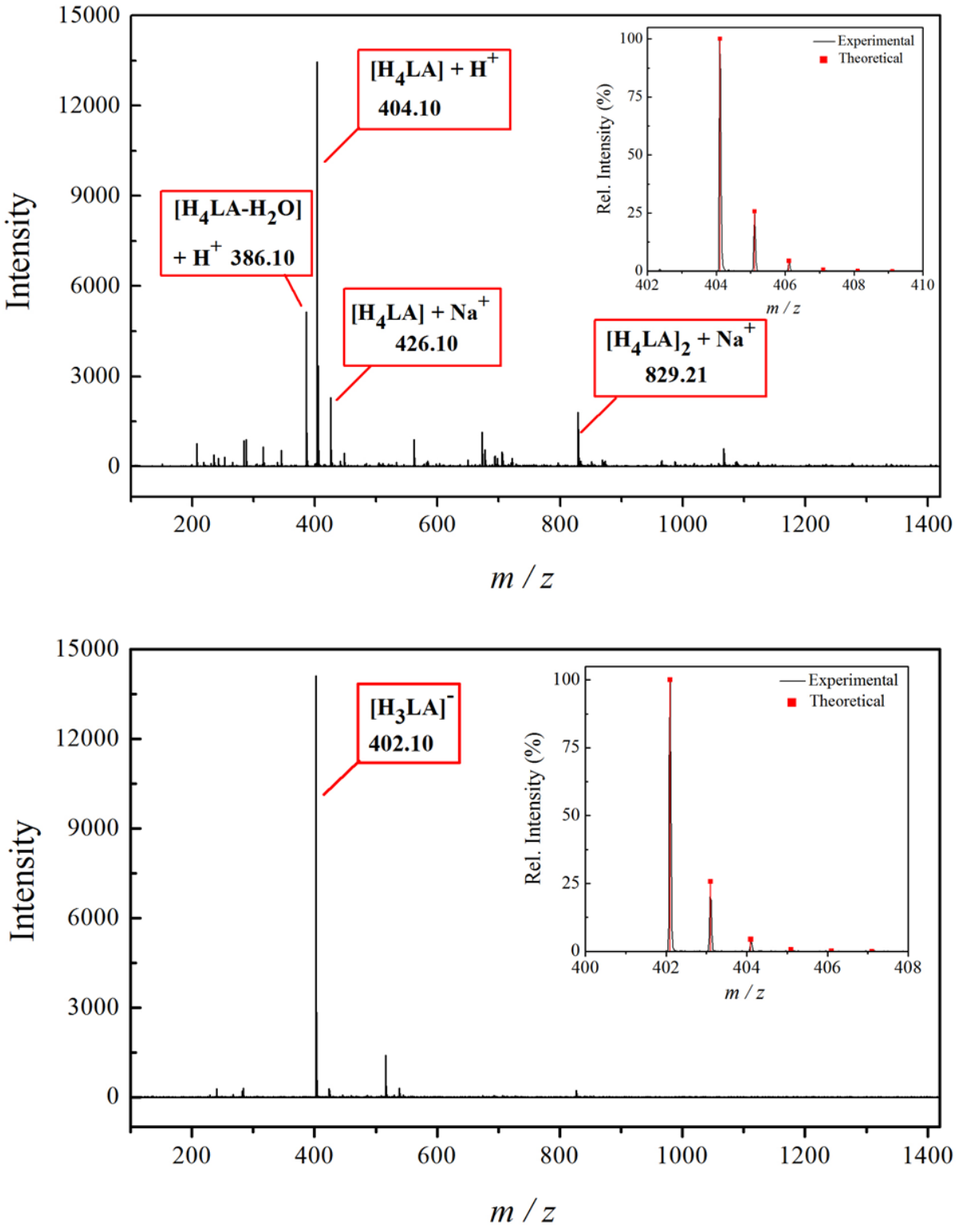

Figure III.A11: ESI mass spectrogram of the THF solution of ligand **H_4LA1** in positive (*top*) and negative (bottom) mode. *Insets*: Experimental and theoretical isotopic distribution of the most abundant molecular peak.

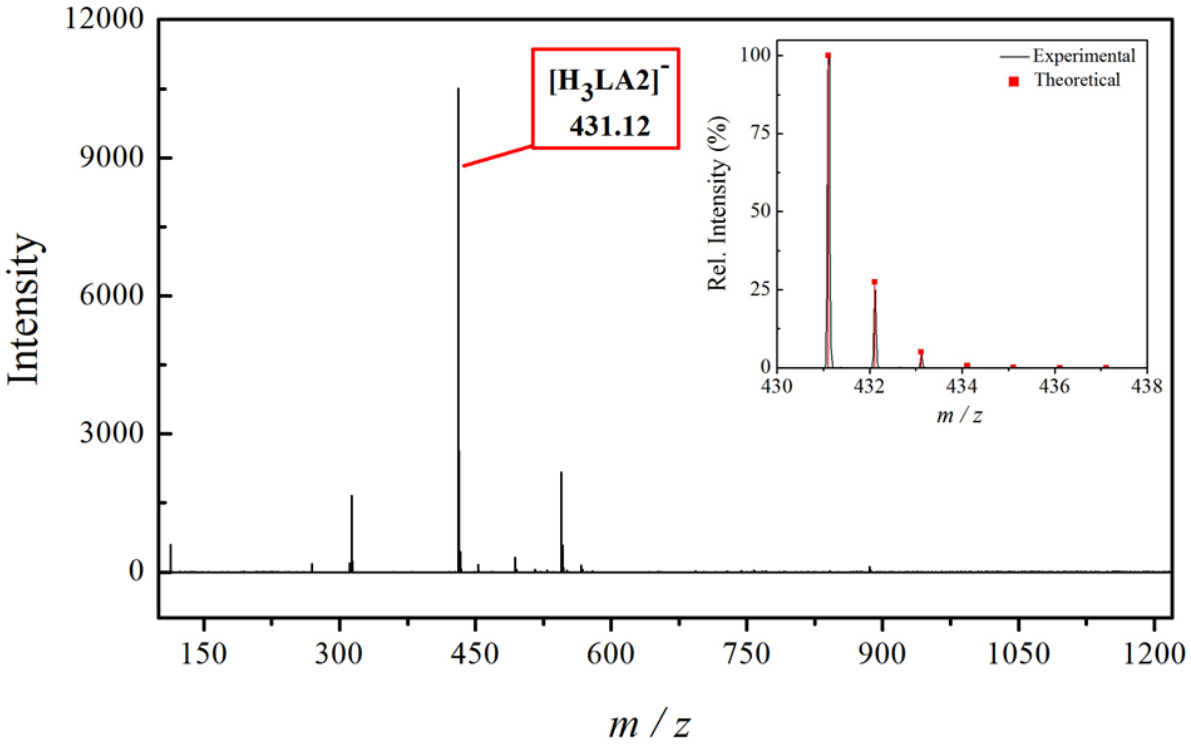

Figure III.A12: ESI(-) mass spectrogram of the THF solution of ligand **H_4LA2** in the negative mode. *Inset*: Experimental and theoretical isotopic distribution of the most abundant molecular peak.

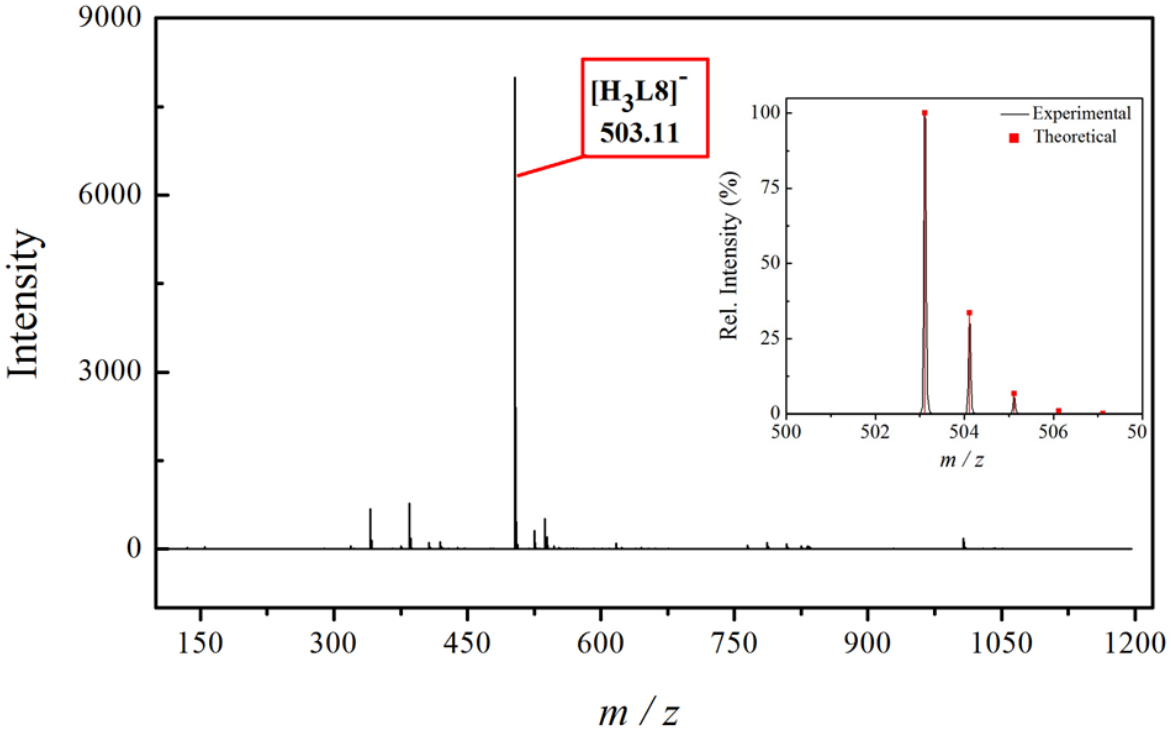

Figure III.A13: ESI mass spectrogram of the $CHCl_3$ solution of ligand **H_4L8** in the negative mode. *Inset*: Experimental and theoretical isotopic distribution of the most abundant molecular peak.

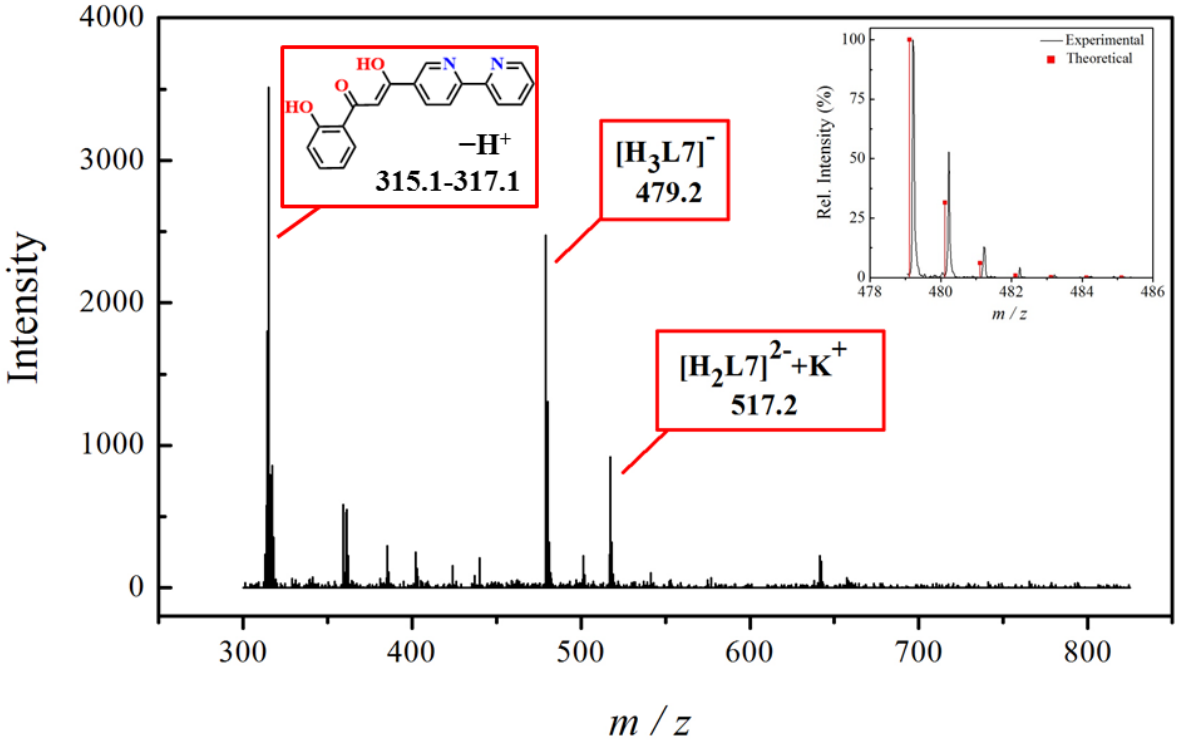

Figure III.A14: MALDI-TOF spectrogram of the THF solution of ligand **H_4L7** in the negative mode. *Inset*: Experimental and theoretical isotopic distribution of the molecular peak. Slight offset (Δ(*m*/*z*)=0.1) between the theoretically expected and observed signal is within the experimental error of the MALDI-TOF technique.

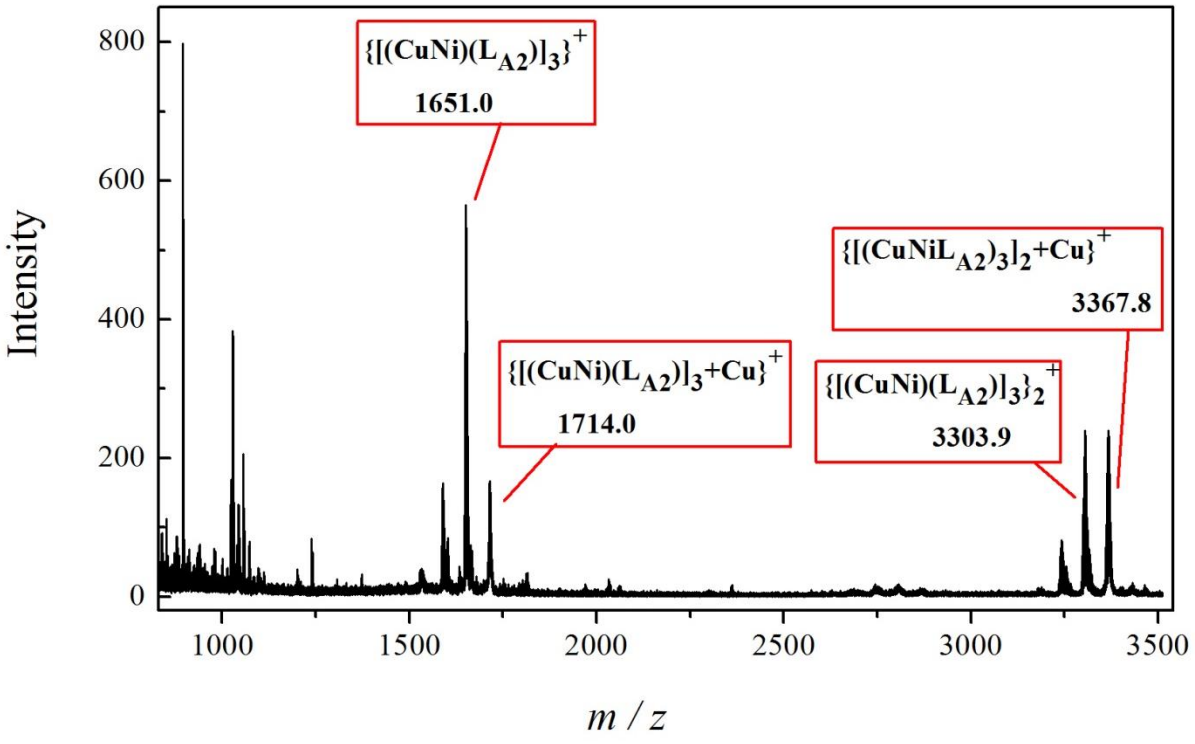

Figure III.A15: MALDI(+) mass spectrogram of the THF solution of compound **18**.

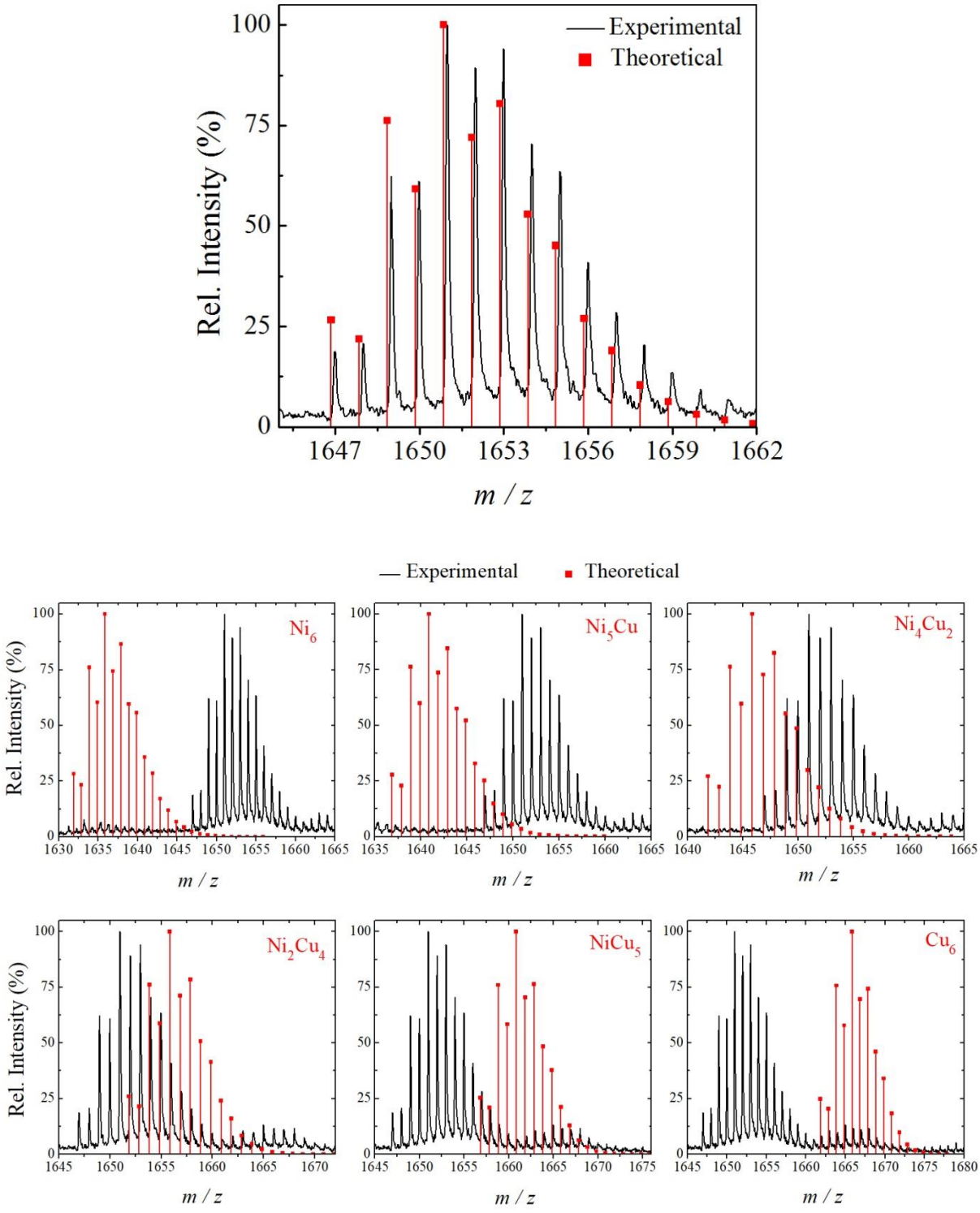

Figure III.A16: *Top*: Isotopic distribution for the most abundant molecular peak $[Ni_3Cu_3(LA2)_3]^+$ from the experimental mass spectrogram of compound **18**. *Bottom*: Comparison between the observed isotopic distribution for the most abundant molecular peak in the experimental MALDI-TOF data of **46** (black lines) and simulated isotopic pattern for any possible metallic composition of $[Ni_xCu_y(LA2)_3]^+$ ion (x,y = 0…6, red lines).

Table III.A24: Magneto-structural data of reported compounds containing {Ni(μ_2-O)$_2$Cu} core

Molecular Formula CSD refcode	Ni–O Cu–O (Å)	Cu–O–Ni (°)	O_a –Ni– O_b O_a –Cu– O_b (°)	Ni···Cu (Å)	Magnetic data
		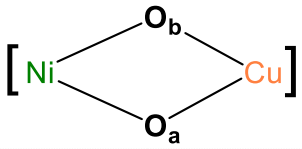			
[(CuNi)$_2$L$_2$(py)$_6$] **LEHCEJ**[a] **[12]**	2.034(4) 2.030(4) 1.988(4) 1.975(4)	99.4(2) 99.2(2)	79.1(1) 81.5(1)	3.060(1)	J= -65.8 cm^{-1}; g_{Cu}=2.16; g_{Ni}=2.27; zJ= −0.3 cm^{-1}; TIP=1.7·10^{-4} cm^{3}mol^{-1} X-band powder EPR: g = 2.22[b]
Ni(MeOH)(HL1) Cu(MeOH)]$_2$ [Ln(dbm)$_4$]$_2$ QEKGOF[c] **[56]**	2.048(7) 1.994(7) 1.956(7) 1.927(7)	97.6(3) 98.4(3)	79.9(3) 84.0(3)	2.991(2)	J_{intra} = -84.1 cm^{-1} g=1.98; J_{inter} = -6.0 cm^{-1} $\hat{H} = -2(J_{\mathrm{intra}}(\hat{S}_{\mathrm{Cu}}\hat{S}_{\mathrm{Ni}}) + J_{\mathrm{inter}}(\hat{S}_{\mathrm{Cu}}\hat{S}_{\mathrm{Ni}}))$
[CuNi(fsa)$_2$(en) (H$_2$O)$_2$] BIHZEX[d] **[52]**	2.021(2) 1.895(2)	98.8(1)	78.0(1) 84.3(1)	2.975(1)	J= -71.0 cm^{-1} g=2.35 X-band powder EPR: $g_{\parallel}$= 2.20, $g_{\perp}$ =2.28; g_{av}=2.27
[Cu(salen)Ni(hfa)$_2$] DEWPAW[e] **[51]**	2.063(2) 2.107(2) 1.908(2) 1.892(2)	94.10(8) 92.23(7)	75.08(7) 83.93(8)	2.897(1)	J= -11.8 cm^{-1} g=2.30
[{Cu(HL1)Ni (N$_3$)}$_2$] KAHVAQ[c] **[54]**	2.037(1) 2.037(1) 1.953(1) 1.957(1)	101.13(4) 101.25(4)	76.72(4) 80.59(4)	3.085(1)	J_{intra} = -114.9 cm^{-1} g_{Cu}=2.12; g_{Ni}=2.16; J_{inter} = 1.0 cm^{-1}; TIP=1.3·10^{-4} cm^{3}mol^{-1} $\hat{H} = -2(J_{\mathrm{intra}}(\hat{S}_{\mathrm{Cu}}\hat{S}_{\mathrm{Ni}}) + J_{\mathrm{inter}}(\hat{S}_{\mathrm{Cu}}\hat{S}_{\mathrm{Ni}}))$ X-band powder EPR: g_{av}=2.21
[(tmtacn)Co(μ-OH) Cu(L1)Ni(OH$_2$)$_2$] [ClO$_4$]$_2$ KAJFEG[c,f] **[54]**	2.013(5) 2.036(4) 1.966(5) 1.958(4)	101.8(2) 100.7(2)	77.2(2) 80.1(2)	3.081(1)	J= -130.0 cm^{-1} g_{Cu}=2.24; g_{Ni}=2.27; TIP=3.6·10^{-4} cm^{3}mol^{-1} X-band powder EPR: g_{av}=2.20
[Cu(L2)NiCl$_2$] LINWIO[g] **[55]**	2.03(1) 2.00(1) 1.98(1) 1.96(1)	101.3(5) 101.9(5)	74.5(4) 76.7(4)	3.089(3)	J= -47.0 cm^{-1} g_{Cu}=2.10; g_{Ni}=2.16; TIP=2.8·10^{-4} cm^{3}mol^{-1}

Molecular Formula **CSD refcode**	Ni–O Cu–O (Å)	Cu–O–Ni (°)	O_a –Ni– O_b O_a –Cu– O_b (°)	Ni···Cu (Å)	Magnetic data
$[(CuNi)_2(L3)_2(py)_6]$ **MUKJEI**[h] **[50]**	2.019(4) 2.020(4) 1.984(4) 1.979(4)	99.1(2) 98.9(2)	80.0(2) 81.8(2)	3.043(1)	J= -72.9 cm^{-1} g_{Cu}=2.3; g_{Ni}=2.4; zJ= −0.4 cm^{-1}
$[Cu((prp)_2en)$ **$Ni(hfa)_2]$** **NIPFCU**[e,i] **[53]**	-	-	-	3.097(1)	J= -48.0 cm^{-1} g_{Cu}=2.05; g_{Ni}=2.27; TIP=2.8·10^{-4} cm^3mol^{-1}
$[Cu(L4)Ni(bipy)_2]$ **QADWOH**[j] **[59]**	2.069(8) 2.141(7) 1.921(8) 1.927(7)	98.3(3) 96.1(3)	73.6(3) 81.9(3)	3.025(2)	J= -118.0 cm^{-1} g_{Cu}=1.99; g_{Ni}=2.35; TIP=2.2·10^{-4} cm^3mol^{-1} X-band solution EPR: $g_{\|}$= 2.09, $g_{\perp}$ =2.18
$[Cu(L2)Ni](ClO_4)_2$ **UDUWEV**[g] **[60]**	2.044(3) 2.177(4) 1.908(4) 1.925(3)	92.1(1) 96.9(1)	78.2(1) 88.0(1)	2.959(1)	J= -12.0 cm^{-1} g_{Cu}=2.08; g_{Ni}=2.18; TIP=2.8·10^{-4} cm^3mol^{-1} X-band solution EPR: $g_{\|}$= 2.09, $g_{\perp}$ =2.24
$[Cu(L5)Ni(DMF)_2]$ **$(ClO_4)_2$** **UKIPOT**[k] **[58]**	2.072(3) 2.084(4) 1.929(3) 1.963(3)	100.1(3) 101.7(3)	75.6(3) 81.8(3)	3.103(1)	J= -67.0 cm^{-1} g =2.29; zJ= −0.17 cm^{-1} TIP=2.8·10^{-4} cm^3mol^{-1} X-band solution EPR: $g_{\|}$= 2.15, $g_{\perp}$ =2.26
$[Cu(L6)Ni](ClO_4)_2$ **ZOJFEJ**[l] **[57]**	2.062(8) 2.073(7) 1.890(8) 1.908(7)	99.9(3) 99.8(3)	75.7(3) 83.8(3)	3.037(3)	J= -90.0 cm^{-1} g_{Cu}=2.09; g_{Ni}=2.15; zJ= 0.49 cm^{-1} TIP=2.8·10^{-4} cm^3mol^{-1} X-band solution EPR: $g_{\|}$= 2.16, $g_{\perp}$ =2.27

$$\hat{H} = \mu_B(g_{\mathrm{Cu}}\hat{S}_{\mathrm{Cu}} + g_{\mathrm{Ni}}\hat{S}_{\mathrm{Ni}})B - 2J_{\mathrm{Cu-Ni}}(\hat{S}_{\mathrm{Cu}}\hat{S}_{\mathrm{Ni}})$$

[a] H_4L= 1,2-bis{5-[3-oxo-3-(2-hydroxyphenyl)propanoyl]-2-methyl-thio-phen-3-yl}cyclopentene;

[b] Alternative fits:

$$\hat{H} = D_{\mathrm{Ni}}\left(\hat{S}_{z_2}^2 - \frac{\hat{S}_2^2}{3} + \hat{S}_{z_3}^2 - \frac{\hat{S}_3^2}{3}\right) + \mu_B\left(g_{\mathrm{Cu}}(\hat{S}_{\mathrm{Cu1}} + \hat{S}_{\mathrm{Cu2}}) + g_{\mathrm{Ni}}(\hat{S}_{\mathrm{Ni1}} + \hat{S}_{\mathrm{Ni2}})\right)B$$
$$- 2(J_{\mathrm{Cu-Ni}}(\hat{S}_{\mathrm{Cu1}}\hat{S}_{\mathrm{Ni1}} + \hat{S}_{\mathrm{Cu2}}\hat{S}_{\mathrm{Ni2}}) + J_{\mathrm{Ni-Ni}}(\hat{S}_{\mathrm{Ni1}}\hat{S}_{\mathrm{Ni2}}))$$

g_{Ni}=2.23, D_{Ni}=4.56 cm^{-1}, g_{Cu}=2.20, $J_{Ni\text{-}Cu}$=−60.0 cm^{-1}; $J_{Ni\text{-}Ni}$=−0.2 cm^{-1}

g_{Ni}=2.27, D_{Ni}=−9.95 cm^{-1}, g_{Cu}=2.20, $J_{Ni\text{-}Cu}$=−64.0 cm^{-1}; $J_{Ni\text{-}Ni}$=−0.2 cm^{-1}

[c] H_4L1=*N*,*N*'-bis(2-hydroxy-3-hydroxyiminomethyl-5-methylphenylmethylene)-1,3-propanediamine, Hdbm=1,3-diphenyl-propane-1,3-dione; [d] $H_4(fsa)_2en$= *N*,*N*'-(1 -hydroxy-2-carboxybenzylidene)- 1,2-diaminoethane; [e] H_2salen=*N*,*N*'-ethylenebis(oxosalicyldiimine);

Hhfa=hexafluoroacetylacetone; [f] tmtacn=1,4,7-trimethyl-1,4,7-triazacyclononane; [g] H_2L2= *N*,*N*’-(*N*,*N*'-dimethyl-*N*,*N*'-ethylenedi(5-bromo-2-hydroxy-3-methylenebenzylamine)-1,3-propanediamine; [h] H_4L3=1,3-bis[3-oxo-3-(2-hydroxyphenyl)propionyl]benzene; [i] $(Hprp)_2$en= *N*,*N*’-ethylenebis(2-hydroxypropiophenone imine); [j] H_4L4= 1,2-bis(2-hydroxybenzamido)benzene; [k] H_2L5= *N*,*N*’-(*N*,*N*'-dimethyl-*N*,*N*'-1,8-naphthyldi(5-methyl-2-hydroxy-3-methylenebenzylamine)-1,3-propanediamine; [l] H_2L6= *N*,*N*’-(*N*,*N*'-ethylenedi(5-methyl-2-hydroxy-3-methylenebenzylimine)-1,4-butanediamine

APPENDIX IV

PYRAZOLE BASED COORDINATION COMPOUNDS: SERENDIPITOUS VERSUS TAILORED-METALLOLIGAND SYNTHETIC APPROACH

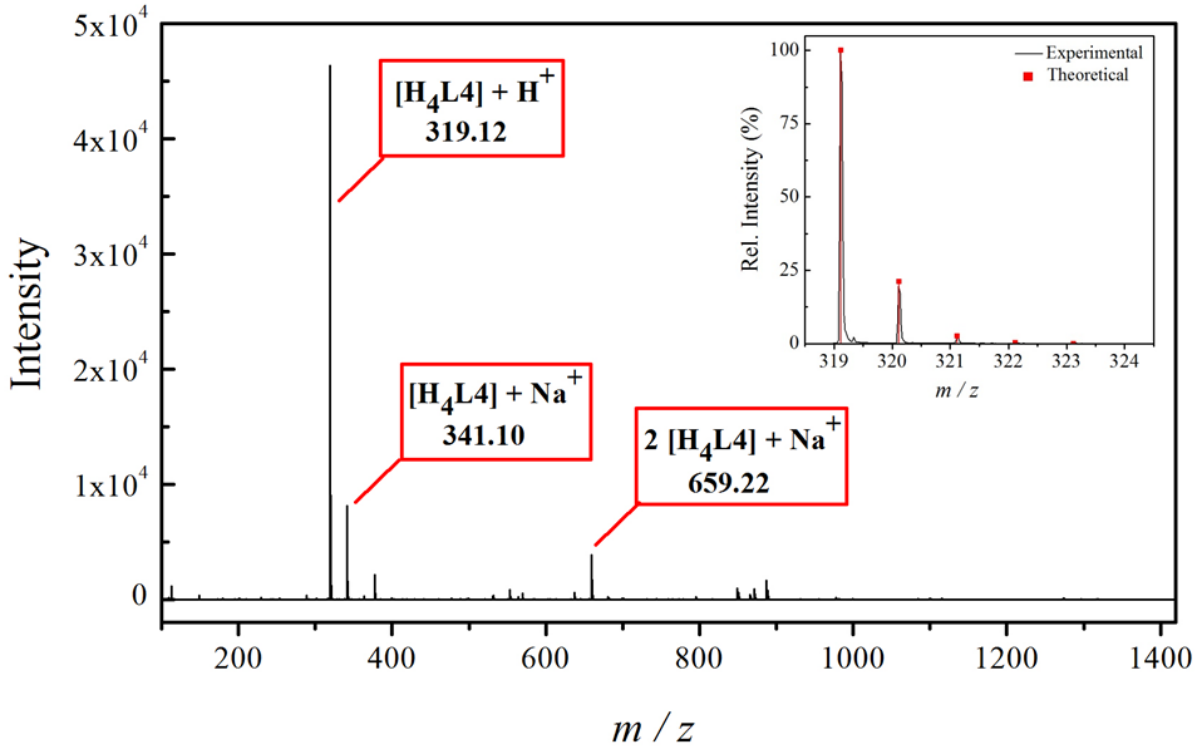

Figure IV.A1: ESI (+) mass spectrogram of acetone solution of ligand **H_4L4**. *Inset*: Isotopic distribution of the most abundant molecular peak.

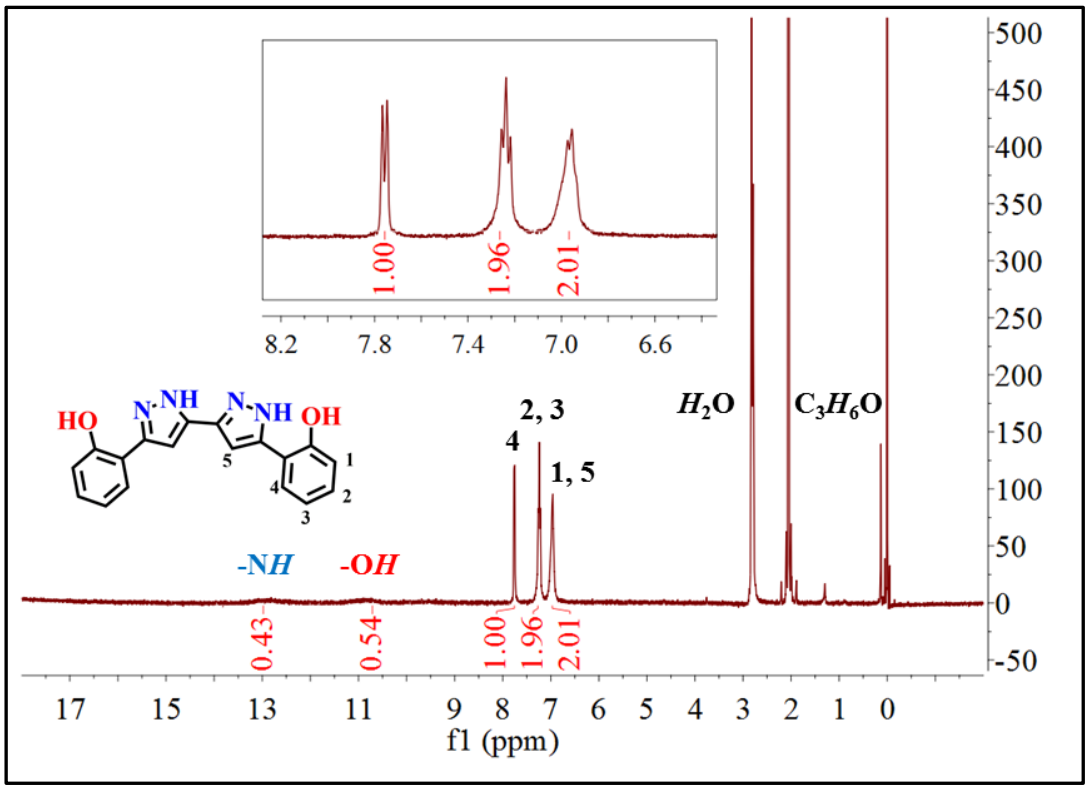

Figure IV.A2: ^{1}H NMR spectrum of ligand **H_4L4** in deuterated acetone.

Table IV.A1: Crystallographic data for ligand **H_4L4**

	H_4L4
Formula	$C_{18}H_{14}N_4O_2 \cdot H_2O$
M_r	336.35
Crystal system	Monoclinic
Space group	*C*2/*c*
a (Å)	28.460(7)
b (Å)	4.9320(11)
c (Å)	24.318(6)
α (°)	90
β (°)	112.810(9)
γ (°)	90
V (Å^3)	3146.4(13)
Z	8
ρ_{calc} (g/cm^3)	1.420
μ (cm^{-1})	0.120
Shape and colour	Colourless needle
Crystal size (mm^3)	0.02·0.03·0.180
λ (Å)	0.7749
T (K)	100(2)
Reflections	4283
Unique reflections	3514
Parameters	259
Restraints	13
R_1 (all data)[a]	0.0659
R_1 [*I*>2σ(*I*)][a]	0.0552
wR_2 (all data)[b]	0.1598
wR_2 [*I*>2σ(*I*)][b]	0.1508
S (all data)[c]	1.043
S [*I*>2σ(*I*)][c]	1.042
Largest residuals (e Å^3)	0.369/–0.427

[a] $R_1 = \Sigma||F_o| - |F_c|| / \Sigma|F_o|$;

[b] $wR_2 = \{\Sigma[w(F_o^2 - F_c^2)^2] / \Sigma[w(F_o^2)^2]\}^{1/2}$;[c] $S = \{\Sigma[w(F_o^2 - F_c^2)^2] / (n - p)\}^{1/2}$

Table IV.A2: Bond distances [Å] within **H_4L4**

O1–C1	1.367(2)
O2–C18	1.362(2)
N1–C7	1.359(2)
N2–C9	1.346(2)
N3–C10	1.352(2)
N4–C12	1.349(2)
N1–N2	1.355(2)
N3–N4	1.351(2)
C1–C2	1.402(3)
C1–C6	1.407(2)
C2–C3	1.381(3)
C3–C4	1.393(2)
C4–C5	1.390(3)
C5–C6	1.404(2)
C6–C7	1.467(2)
C7–C8	1.394(2)
C8–C9	1.399(2)
C9–C10	1.457(2)
C10–C11	1.388(2)
C11–C12	1.408(2)
C12–C13	1.466(2)
C13–C14	1.402(2)
C13–C18	1.411(2)
C14–C15	1.388(2)
C15–C16	1.390(2)
C16–C17	1.383(2)
C17–C18	1.393(2)

Table IV.A3: Hydrogen bonding and π···π contacts in the structure of **H_4L4**

D–H···A	**D–H (Å)**	**H···A (Å)**	**D–A (Å)**	**D–H···A (°)**
O2–H2··N4	0.95(2)	1.80(2)	2.6293(17)	144(2)
N3–H3N···N2#	0.89(2)	*2.06(2)	2.8994(18)	157.3(18)
N1–H1N···O1	0.88(2)	2.18(2)	2.6820(17)	115.8(16)
O1–H1···O1W	1.07(3)	1.77(2)	2.781(4)	155(2)
O1–H1···O2W	1.07(3)	1.62(3)	2.689(4)	178(2)
O1W–H2W···O2#	0.949(19)	1.84(2)	2.762(3)	164(5)
O1W–H1W···O1#2	0.97(2)	2.13(3)	3.072(4)	165(5)
O2W–H4W···O2#3	1.005(18)	2.04(2)	3.007(5)	162(4)
O2W–H3W···O1#2	0.99(2)	2.39(2)	3.352(4)	164(4)

Symmetry operation: # = −x, 1 −y, 1−z; #2= x, 1+y, z; #3=x, 1−y, −1/2+z

π···π

Cg···Cg	**d (Å)**	**Cg···Cg**	**d (Å)**
phenol-pyrazole	3.484	pyrazole-pyrazole	3.557
phenol-pyrazole	4.423		

Table IV.A4: Crystallographic data for the compounds **21-26**

	21	**22**	**23**	**24**	**25**	**26**
Formula	$C_{78}H_{102}N_{12}O_4Cu_3$	$C_{78}H_{102}N_{12}O_4Ni_3$	$C_{181}H_{233}N_{29}O_{12}V_4$	$C_{72}H_{78}N_{13}O_4ClMn_2$	$C_{143}H_{131}N_{31}O_{11}Co_6$	$C_{68}H_{94}N_{10}O_4Cu_2$
M_r	1462.33	1447.84	3210.71	1334.8	2933.46	1242.61
Crystal system	Monoclinic	Monoclinic	Triclinic	Triclinic	Monoclinic	Monoclinic
Space group	$P2_1/n$	$P2_1/n$	$P-1$	$P-1$	$P2_1/c$	$P2_1/c$
a (Å)	8.568(3)	8.482(3)	12.8070(10)	8.3710(19)	23.345(2)	7.8198(5)
b (Å)	28.957(11)	28.896(10)	18.384(2)	15.460(4)	17.7746(17)	27.4395(14)
c (Å)	14.668(6)	14.743(5)	20.411(2)	26.037(6)	33.987(3)	14.7093(9)
α (°)	90	90	73.022(10)	98.380(13)	90	90
β (°)	98.270(6)	97.908(5)	72.779(2)	95.823(14)	103.765(4)	97.987(4)
γ (°)	90	90	70.673(2)	103.734(13)	90	90
V (Å^3)	3601(2)	3579(2)	4230.0(7)	3205.7(13)	13698(2)	3125.6(3)
Z	2	2	1	2	4	2
ρ_{calc} (g/cm^3)	1.349	1.343	1.260	1.383	1.422	1.320
μ (cm^{-1})	1.181	1.057	0.354	0.498	0.812	0.738
Shape and colour	Light brown needle	Brown needle	Violet block	Orange plate	Dark red needle	Light brown block
Crystal size (mm^3)	0.320·0.020·0.010	0.46·0.03·0.01	0.260·0.200·0.07	0.190·0.092·0.060	0.474·0.083·0.048	0.220·0.090·0.065
λ (Å)	0.7749	0.7749	0.7749	0.71073	0.71073	0.71073
T (K)	100(2)	100(2)	100(2)	100(2)	100(2)	100(2)
Reflections	7362	8169	19250	12135	21014	5946
Unique reflections	5092	6014	14566	8311	13411	4439
Parameters	511	543	1105	822	1741	384
Restraints	416	447	136	31	192	0
R_1 (all data)[a]	0.1102	0.1070	0.1006	0.0967	0.1269	0.0764
R_1 [$I>2\sigma(I)$][a]	0.0786	0.0799	0.0851	0.0629	0.0847	0.0517
wR_2 (all data)[b]	0.2355	0.2409	0.2677	0.1858	0.2635	0.1281
wR_2 [$I>2\sigma(I)$][b]	0.2100	0.2187	0.2501	0.1633	0.2302	0.1176
S (all data)[c]	1.022	1.098	1.043	1.063	1.038	1.043
S [$I>2\sigma(I)$][c]	1.031	1.032	1.033	1.057	1.037	1.043
Largest residuals (e Å^3)	1.165/–1.096	2.247/–1.062	0.971/-0.598	1.240/-1.060	2.835/-1.145	0.520/–0.545

[a] $R_1 = \Sigma||F_o| - |F_c|| / \Sigma|F_o|$; [b] $wR_2 = \{\Sigma[w(F_o^2 - F_c^2)^2] / \Sigma[w(F_o^2)^2]\}^{1/2}$; [c] $S = \{\Sigma[w(F_o^2 - F_c^2)^2] / (n - p)\}^{1/2}$

Table IV.A5: Crystallographic data for the compounds **27-30**

	27	**27A**	**28**	**29**	**30**
Formula	$C_{151}H_{203}N_{23}O_{14}Cu_2V_4$	$C_{156}H_{206}N_{24}O_{13}Cu_2V_4$	$C_{192}H_{164}N_{40}O_{14}Cu_4V_4$	$C_{169}H_{149}N_{35}O_{14}Ni_4V_4$	$C_{169}H_{149}N_{35}O_{14}Ni_2Cu_2V_4$
M_r	2895.19	2956.28	3713.54	3332.78	3342.48
Crystal system	Monoclinic	Orthorhombic	Triclinic	Triclinic	Triclinic
Space group	$P2_1/c$	*Pbca*	*P*-1	*P*-1	*P*-1
a (Å)	16.1841(7)	23.5352(14)	15.9229(7)	13.2215(8)	13.2395(6)
b (Å)	19.9484(9)	33.596(2)	17.5939(8)	16.8111(10)	16.9075(8)
c (Å)	22.8742(10)	37.473(2)	17.7122(8)	19.0631(11)	19.1609(9)
α (°)	90	90	86.862(3)	65.410(3)	64.679(2)
β (°)	106.294(3)	90	68.446(2)	80.733(3)	80.668(2)
γ (°)	90	90	66.112(2)	87.404(3)	87.134(2)
V (Å^3)	7088.2(5)	29630(3)	4193.8(3)	3801.5(4)	3824.8(3)
Z	2	8	1	1	1
ρ_{calc} (g/cm^3)	1.356	1.325	1.470	1.462	1.451
μ (cm^{-1})	0.619	0.593	0.789	0.797	0.823
Shape and colour	Olive green block	Green block	Yellow plate	Orange-red plate	Yellow-brown plate
Crystal size (mm^3)	0.150·0.100·0.080	0.225·0.175·0.105	0.138·0.093·0.061	0.350·0.140·0.085	0.200·0.100·0.100
λ (Å)	0.71073	0.71073	0.71073	0.71073	0.71073
T (K)	100(2)	100(2)	100(2)	100(2)	100(2)
Reflections	11605	25270	19173	18006	18961
Unique reflections	7661	17402	12401	13560	14266
Parameters	986	1876	1156	1087	1077
Restraints	228	106	88	189	223
R_1 (all data)[a]	0.0976	0.0856	0.1047	0.0731	0.0813
R_1 [$I>2\sigma(I)$][a]	0.0585	0.0479	0.0626	0.0517	0.0608
wR_2 (all data)[b]	0.1602	0.1261	0.1864	0.1492	0.1755
wR_2 [$I>2\sigma(I)$][b]	0.1387	0.1069	0.1611	0.1352	0.1616
S (all data)[c]	1.058	1.031	1.090	1.045	1.076
S [$I>2\sigma(I)$][c]	1.055	1.025	1.083	1.036	1.054
Largest residuals (e Å^3)	0.729/–0.661	1.496/–0.757	1.133/–1.103	1.144/–0.831	1.792/–0.941

[a] $R_1 = \Sigma||F_o| - |F_c|| / \Sigma|F_o|$; [b] $wR_2 = \{\Sigma[w(F_o^2 - F_c^2)^2] / \Sigma[w(F_o^2)^2]\}^{1/2}$; [c] $S = \{\Sigma[w(F_o^2 - F_c^2)^2] / (n - p)\}^{1/2}$

Table IV.A6: Crystallographic data for the compounds **31-33**

	31	**32**	**33**
Formula	$C_{191}H_{159}N_{41}O_{12}Mn_2Cu_2V_4$	$C_{191}H_{159}N_{41}O_{12}Co_2Cu_2V_4$	$C_{191}H_{159}N_{41}O_{12}Zn_2Cu_2V_4$
M_r	3661.30	3669.28	3682.16
Crystal system	Monoclinic	Monoclinic	Monoclinic
Space group	$P2_1/n$	$P2_1/n$	$P2_1/n$
a (Å)	15.8901(14)	15.8291(10)	16.0476(5)
b (Å)	18.0563(16)	17.9114(10)	17.9623(6)
c (Å)	29.163(3)	29.2315(16)	28.9935(9)
α (°)	90	90	90
β (°)	96.693(5)	96.901(3)	96.5057(12)
γ (°)	90	90	90
V (Å^3)	8310.2(13)	8227.7(8)	8303.6(5)
Z	2	2	2
ρ_{calc} (g/cm^3)	1.463	1.481	1.473
μ (cm^{-1})	0.690	0.746	0.828
Shape and colour	Orange-yellow plate	Orange-red plate	Yellow plate
Crystal size (mm^3)	0.120·0.120·0.055	0.127·0.090·0.056	0.345·0.125·0.100
λ (Å)	0.71073	0.71073	0.71073
T (K)	100(2)	100(2)	100(2)
Reflections	14619	15074	17508
Unique reflections	9448	10203	12340
Parameters	1172	1201	1114
Restraints	134	708	336
R_1 (all data)[a]	0.1047	0.1059	0.0993
R_1 [$I>2\sigma(I)$][a]	0.0616	0.0694	0.0677
wR_2 (all data)[b]	0.1782	0.2037	0.2085
wR_2 [$I>2\sigma(I)$][b]	0.1550	0.1801	0.1855
S (all data)[c]	1.074	1.044	1.044
S [$I>2\sigma(I)$][c]	1.070	1.044	1.030
Largest residuals (e Å^3)	0.845/–0.623	0.843/–0.936	1.199/–0.893

[a] $R_1 = \Sigma||F_o| - |F_c|| / \Sigma|F_o|$; [b] $wR_2 = \{\Sigma[w(F_o^2 - F_c^2)^2] / \Sigma[w(F_o^2)^2]\}^{1/2}$; [c] $S = \{\Sigma[w(F_o^2 - F_c^2)^2] / (n - p)\}^{1/2}$

Table IV.A7: Interatomic distances [Å] and angles [°] for compound **21**

Cu1–Cu2A	3.87(6)	N1–Cu1–O1	90.0(2)
Cu1#–Cu2A	3.87(6)	O1–Cu1–O2#	84.9(1)
Cu1–Cu1#	7.704(2)	O2#–Cu1–N4#	88.8(2)
Cu1–Cu2B	3.87(6)	N4#–Cu1–N1	101.9(2)
Cu1#–Cu2B	3.87(6)	N1S–Cu2A–N2	90(2)
Cu1-O1	1.909(3)	N1S–Cu2A–N3	94(2)
Cu1-N1	1.963(4)	N1S–Cu2A–N2#	109(2)
Cu1-N4#	1.971(5)	N1S–Cu2A–N3#	106(2)
Cu1-O2#	1.923(4)	N2–Cu2A–N3#	95(3)
Cu2A-N1S	2.45(6)	N3#–Cu2A–N2#	78(2)
Cu2A-N2	1.89(6)	N2#–Cu2A–N3	95(3)
Cu2A-N3	1.89(6)	N3–Cu2A–N2	85(2)
Cu2A-N2#	2.02(6)	N3–Cu2B–N2	78(2)
Cu2A-N3#	2.01(6)	N2–Cu2B–N3#	95(3)
Cu2B-N2#	1.89(6)	N3#–Cu2B–N2#	85(2)
Cu2B-N2	2.02(6)	N2#–Cu2B–N3	95(3)
Cu2B-N3#	1.89(6)	Cu1–Cu2A–Cu1#	170(2)
Cu2B-N3	2.01(6)	Cu1–Cu2B–Cu1#	170(2)

Symmetry operation: # = 1−x, 1−y, −z

Table IV.A8: Interatomic distances [Å] and angles [°] for compound **22**

Ni1–Ni2	3.843	Ni1–Ni2–Ni1	180.0
Ni1#–Ni2	3.843	O1–Ni1–N1	89.9(2)
Ni1–O1	1.862(4)	N1–Ni1–N4#	99.2(2)
Ni1–N1	1.898(5)	N4#–Ni1–O2#	91.6(2)
Ni1–O2#	1.863(3)	O2#–Ni1–O1	81.2(1)
Ni1–N4#	1.907(4)	N2–Ni2–N3	86.1(2)
Ni2–N2	1.835(4)	N3–Ni2–N2#	93.9(2)
Ni2–N3	1.851(4)	N2#–Ni2–N3#	86.1(2)
Ni2–N3#	1.851(4)	N3#–Ni2–N2	93.9(2)
Ni2–N2#	1.835(4)	Symmetry operation: # = 1−x, 1−y, 1−z	

Table IV.A9: Interatomic distances [Å] and angles [°] for compound **23**

V1–V1#1	8.2549(7)	O2–V1–O3#1	83.44(8)
V2-V2#1	8.2790(7)	O3#1–V1–N4#1	82.72(8)
V1=O1	1.602(2)	N1–V1–N4#1	92.18(8)
V1-O2	1.917(2)	N1–V1–O2	84.96(8)
V1-O3#1	1.933(2)	O4–V2–O5	107.8(1)
V1–N4#1	2.087(2)	O4–V2–O6#2	107.8(1)
V1–N1	2.087(2)	O4–V2–N5	102.6(1)
V2=O4	1.600(2)	O4–V2–N8#2	103.3(1)
V2–O5	1.913(2)	O5–V2–O6#2	84.47(9)
V2–O6#2	1.950(2)	O6#2–V2–N8#2	82.61(9)
V2–N5	2.088(2)	N8#2–V2–N5	91.94(8)
V2–N8#2	2.095(2)	N5–V2–O5	84.97(8)
V1B–V1B#1	8.0899(8)	O1B–V1B–O2	100(1)
V2B-V2B#2	8.0361(8)	O1B–V1B–O3#1	99(1)
V1B=O1B	1.54(3)	O1B–V1B–N4#1	102(1)
V1B-O2	1.859(6)	O1B–V1B–N1	103(1)
V1B-O3#1	1.917(5)	O2–V1B–O3#1	85.5(3)
V1B–N4#1	2.071(7)	O3#1–V1B–N4#1	83.5(2)
V1B–N1	2.025(5)	N4#1–V1B–N1	94.5(3)
V2B=O4B	1.54(3)	N1–V1B–O2	88.3(3)
V2B–O5	1.912(6)	O4B–V2B–O6#2	99(1)
V2B–O6#2	1.916(5)	O4B–V2B–O5	100(1)
V2B–N5	2.044(5)	O4B–V2B–N5	101(1)
V2B–N8#2	2.007(7)	O4B–V2B–N8#2	100(1)
O1–V1–O2	108.47(9)	N8#2–V2B–O6#2	85.8(3)
O1–V1–O3#1	108.2(1)	O6#2–V2B–O5	85.4(3)
O1–V1–N1	103.25(9)	O5–V2B–N5	86.2(3)
O1–V1–N4#1	103.02(9)	N5–V2B–N8#2	95.9(3)

Symmetry operation: #1 = −x, 1−y, 2−z; #2 = −x, 1−y, 1−z

Table IV.A.10: Interatomic distances [Å] and angles [°] for **24**

Mn1–Mn1#1	8.101(2)	O2#1–Mn1–N4#1	86.0(1)
Mn2–Mn2#2	8.120(2)	N4#1–Mn1–N1	96.7(1)
Mn1–N1S	2.340(3)	N1–Mn1–O1	87.5(1)
Mn1–N2S	2.345(3)	N2S–Mn1–N1	89.3(1)
Mn1–O2#1	1.877(3)	N2S–Mn1–N4#1	89.7(1)
Mn1–O1	1.869(3)	N2S–Mn1–O2#1	92.8(1)
Mn1–N4#1	2.026(3)	N2S–Mn1–O1	93.0(1)
Mn1–N1	2.007(3)	N3S–Mn2–O3	92.1(1)
Mn2–N4S	2.322(4)	N3S–Mn2–O4#2	92.3(1)
Mn2–N3S	2.316(3)	N3S–Mn2–N8#2	84.8(1)
Mn2–O4#2	1.868(3)	N3S–Mn2–N5	86.2(1)
Mn2–O3	1.877(2)	N5–Mn2–O3	86.2(1)
Mn2–N8#2	2.020(3)	O3–Mn2–O4#2	88.5(1)
Mn2–N5	2.035(3)	O4#2–Mn2–N8#2	88.0(1)
N1S–Mn1–O1	90.1(1)	N8#2–Mn2–N5	97.1(1)
N1S–Mn1–N1	84.0(1)	N4S–Mn2–N8#2	90.0(1)
N1S–Mn1–N4#1	87.7(1)	N4S–Mn2–N5	88.3(1)
N1S–Mn1–O2#1	94.1(1)	N4S–Mn2–O3	93.4(1)
O2#1–Mn1–O1	89.7(1)	N4S–Mn2–O4#2	93.7(1)

Symmetry operation: #1 = 1−x, 1−y, −z; #2 = −x, −y, 1−z

Table IV.A11: Distances [Å] and angles [°] for **25**

Co1–Co2	3.824(1)	Co1–O1	1.897(5)
Co2–Co3	3.822(1)	Co1–O4	1.879(5)
Co1–Co3	7.646(1)	Co1–N1	1.926(5)
Co4–Co5	3.837(1)	Co1–N8	1.925(5)
Co5–Co6	3.834(1)	Co1–N5S	1.939(6)
Co4–Co6	7.671(2)	Co1–N1S	1.958(6)
Co1–Co2–Co3	179.75(3)	Co2–N7	1.896(5)
Co4–Co5–Co6	179.06(4)	Co2–N6	1.886(5)

Table IV.A11: Interatomic distances [Å] and angles [°] for compound **25**

Co2–N3	1.882(5)	N8–Co1–N1	98.7(2)	N3S–Co3–O2	85.9(2)
Co2–N2	1.876(5)	N1–Co1–O1	87.7(2)	N3S–Co3–N4	92.9(2)
Co2–O5	1.891(5)	N1S–Co1–N1	93.1(2)	N3S–Co3–N5	90.7(2)
Co2–N2S	1.996(6)	N1S–Co1–O1	86.3(2)	N3S–Co3–O3	88.6(2)
Co3–N4	1.919(5)	N1S–Co1–O4	87.6(2)	O7–Co4–O10	84.1(2)
Co3–N5	1.939(5)	N1S–Co1–N8	90.9(2)	O10–Co4–N16	89.8(2)
Co3–O3	1.887(5)	N5S–Co1–O4	90.5(2)	N16–Co4–N9	97.9(2)
Co3–O2	1.897(4)	N5S–Co1–N8	91.3(2)	N9–Co4–O7	88.1(2)
Co3–N4S	1.938(6)	N5S–Co1–N1	88.4(2)	N6S–Co4–O10	88.4(2)
Co3–N3S	1.955(6)	N5S–Co1–O1	91.2(2)	N6S–Co4–N16	89.9(3)
Co4–O7	1.875(5)	O5–Co2–N7	91.0(2)	N6S–Co4–N9	91.4(2)
Co4–O10	1.887(5)	O5–Co2–N6	91.0(2)	N6S–Co4–O7	87.3(2)
Co4–N9	1.927(6)	O5–Co2–N3	85.4(2)	N10–Co5–N11	83.4(2)
Co4–N16	1.931(6)	O5–Co2–N2	84.9(2)	N11–Co5–N14	96.5(2)
Co4–N6S	1.966(7)	N7–Co2–N6	83.2(2)	N14–Co5–N15	83.5(2)
Co4–N9S	1.937(5)	N6–Co2–N3	96.7(2)	N15–Co5–N10	96.3(2)
Co5–N15	1.876(6)	N3–Co2–N2	82.6(2)	O11–Co5–N15	90.4(2)
Co5–N10	1.880(6)	N2–Co2–N7	97.2(2)	O11–Co5–N10	84.8(2)
Co5–N11	1.880(6)	N2S–Co2–N3	91.2(2)	O11–Co5–N11	85.0(2)
Co5–N14	1.880(6)	N2S–Co2–N2	90.8(2)	O11–Co5–N14	91.5(2)
Co5–O11	1.910(5)	N2S–Co2–N7	92.4(2)	N12–Co6–O8	88.8(2)
Co5–N7S	1.994(7)	N2S–Co2–N6	93.3(2)	O8–Co6–O9	84.0(2)
Co6–N12	1.941(6)	N4S–Co3–N5	92.2(2)	O9–Co6–N13	89.3(2)
Co6–N13	1.953(6)	N4S–Co3–N4	88.4(2)	N13–Co6–N12	97.9(2)
Co6–O9	1.879(6)	N4S–Co3–O2	91.1(2)	N10S–Co6–O8	92.2(3)
Co6–O8	1.882(5)	N4S–Co3–O3	89.8(2)	N10S–Co6–N12	90.9(3)
Co6–N8S	1.970(5)	O3–Co3–O2	83.7(2)	N10S–Co6–N13	89.0(3)
Co6–N10S	1.939(7)	O2–Co3–N4	87.5(2)	N10S–Co6–O9	89.6(3)
O1–Co1–O4	82.9(2)	N4–Co3–N5	98.5(2)		
O4–Co1–N8	90.8(2)	N5–Co3–O3	90.5(2)		

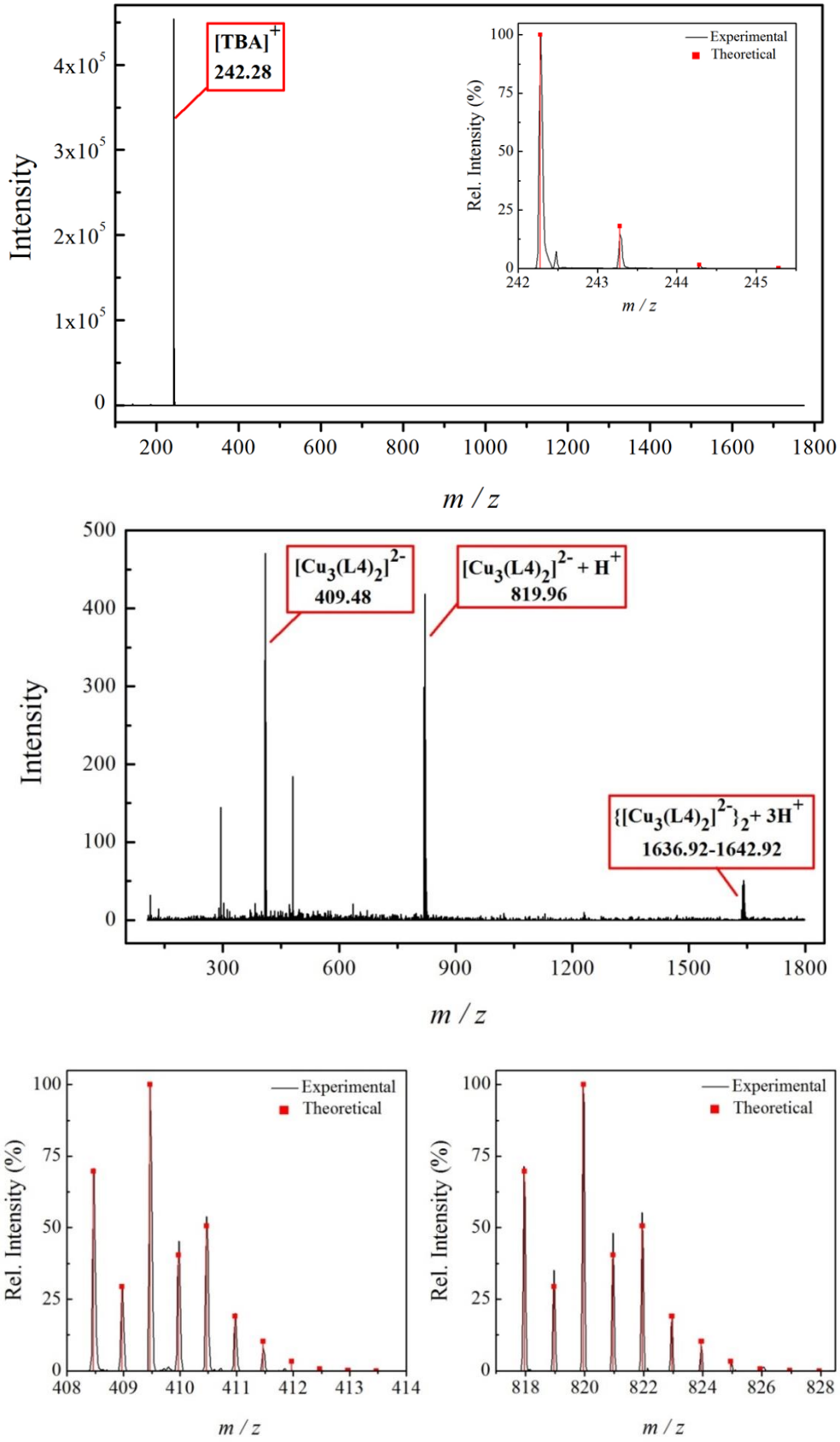

Figure IV.A3: ESI mass spectrogram of acetonitrile solution of compound **21**. *Top*: (+) mode with the isotopic distribution for TBA^+. *Bottom*: (-) mode with the isotopic distribution for two most abundant molecular peaks.

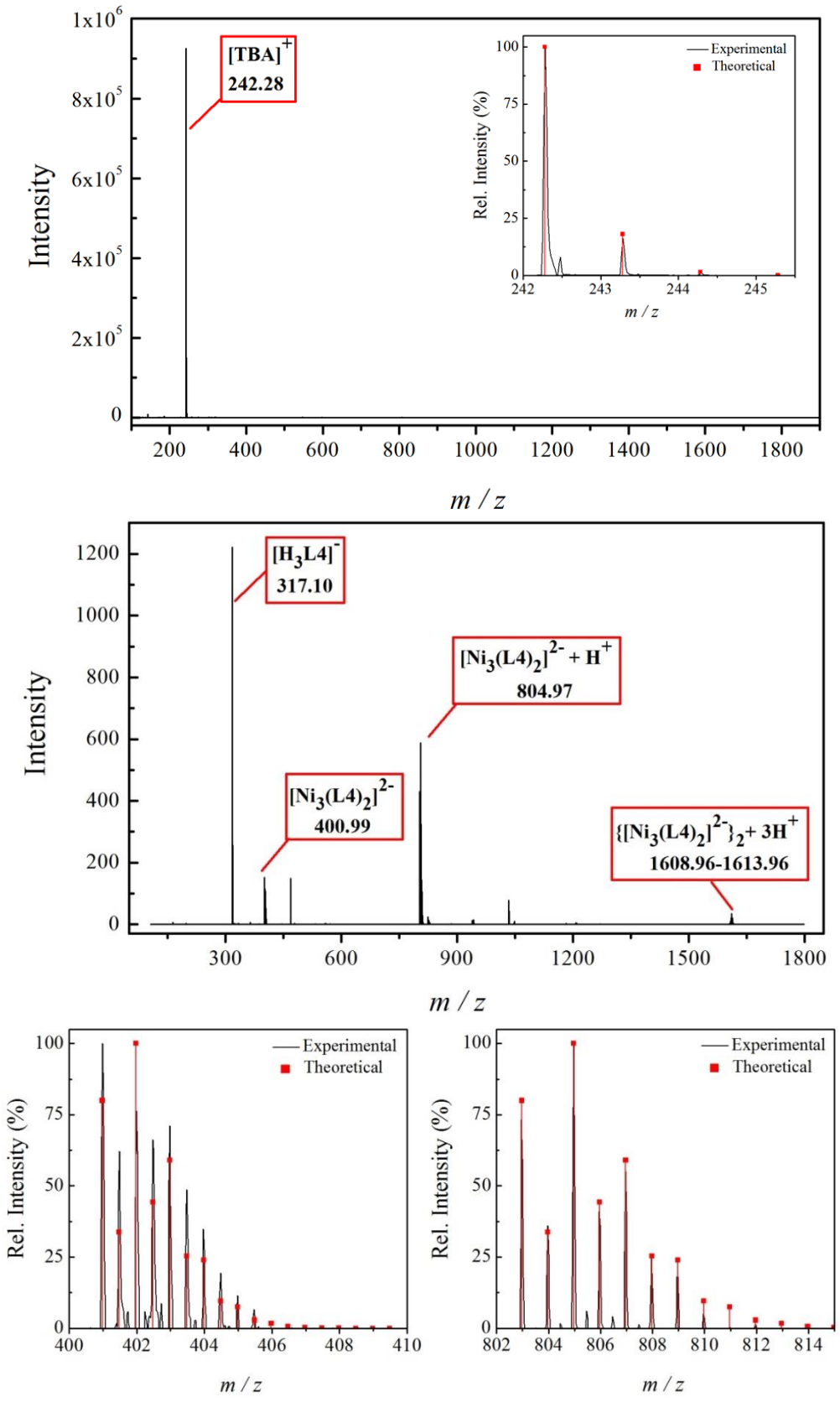

Figure IV.A4: ESI mass spectrogram of acetonitrile solution of compound **22**. *Top*: (+) mode with the isotopic distribution for TBA^+. *Bottom*: (-) mode with the isotopic distribution for two most abundant molecular peaks.

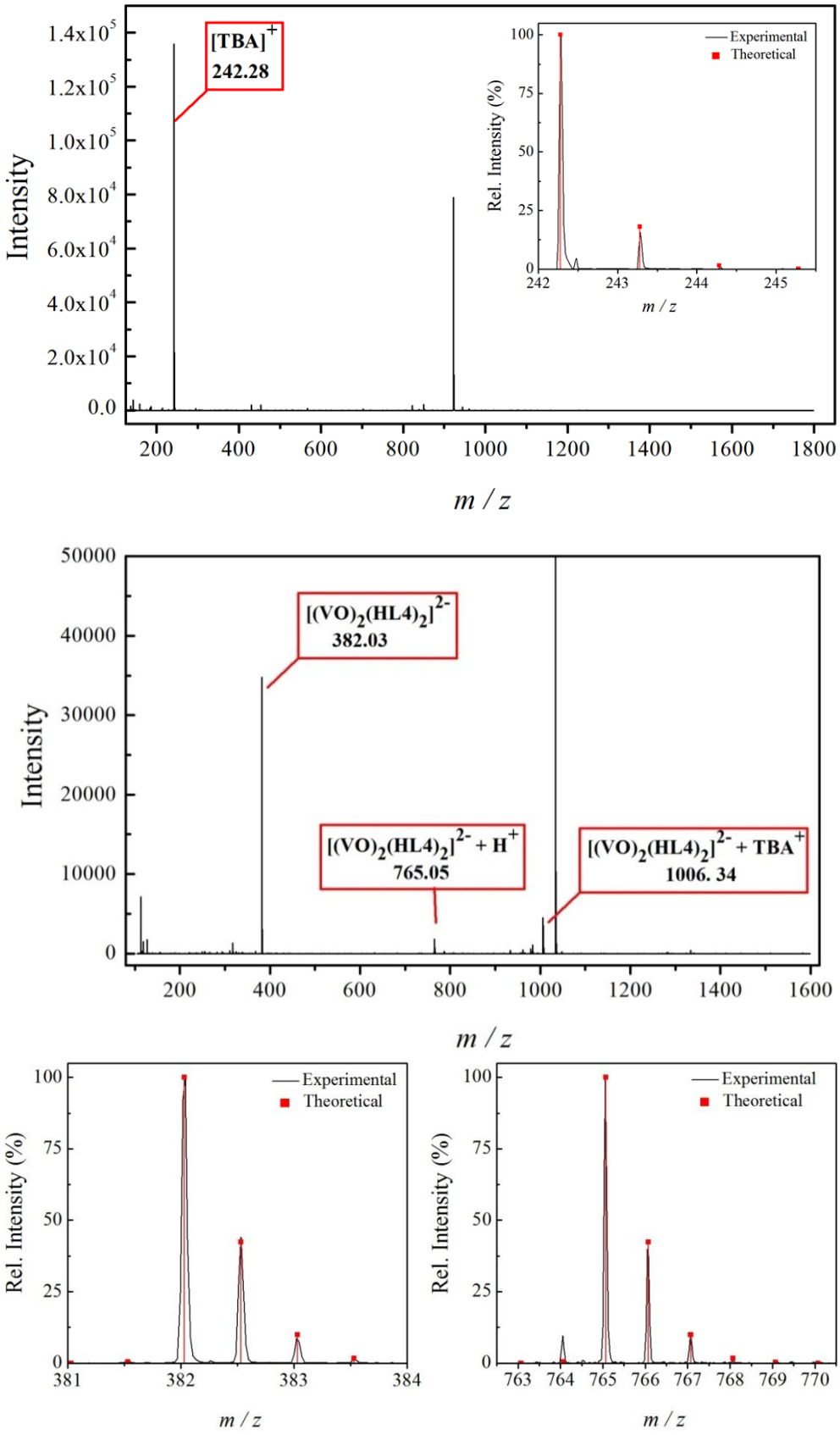

Figure IV.A5: ESI mass spectrogram of methanol solution of compound **23**. *Top*: (+) mode with the isotopic distribution for TBA^+. *Bottom*: (-) mode with the isotopic distribution for two most abundant molecular peaks.

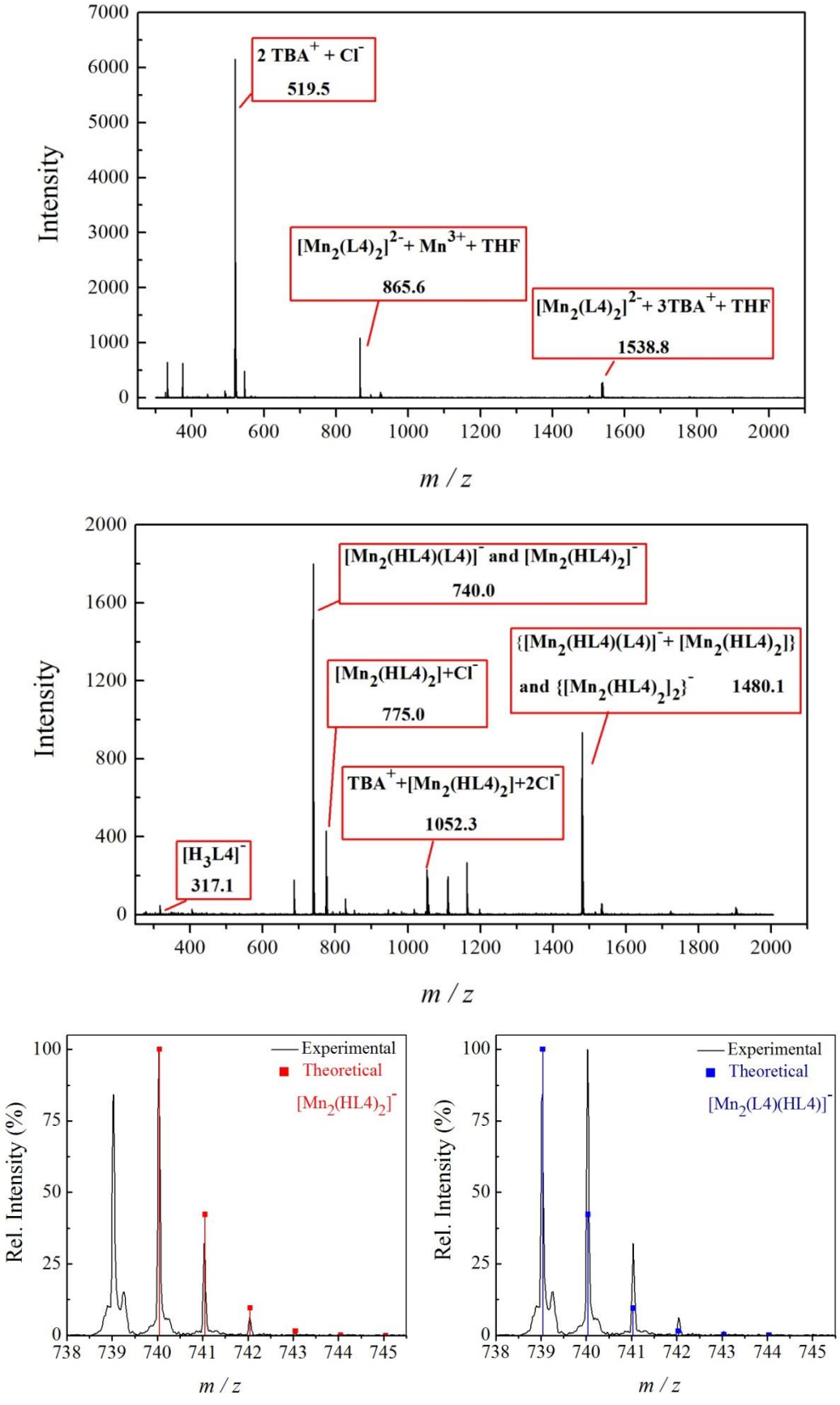

Figure IV.A6: MALDI-TOF mass spectrogram of THF solution of compound **24** in (+) (*top*) and (-) mode (*bottom*) with isotopic distribution of main molecular peak as mixture of two species.

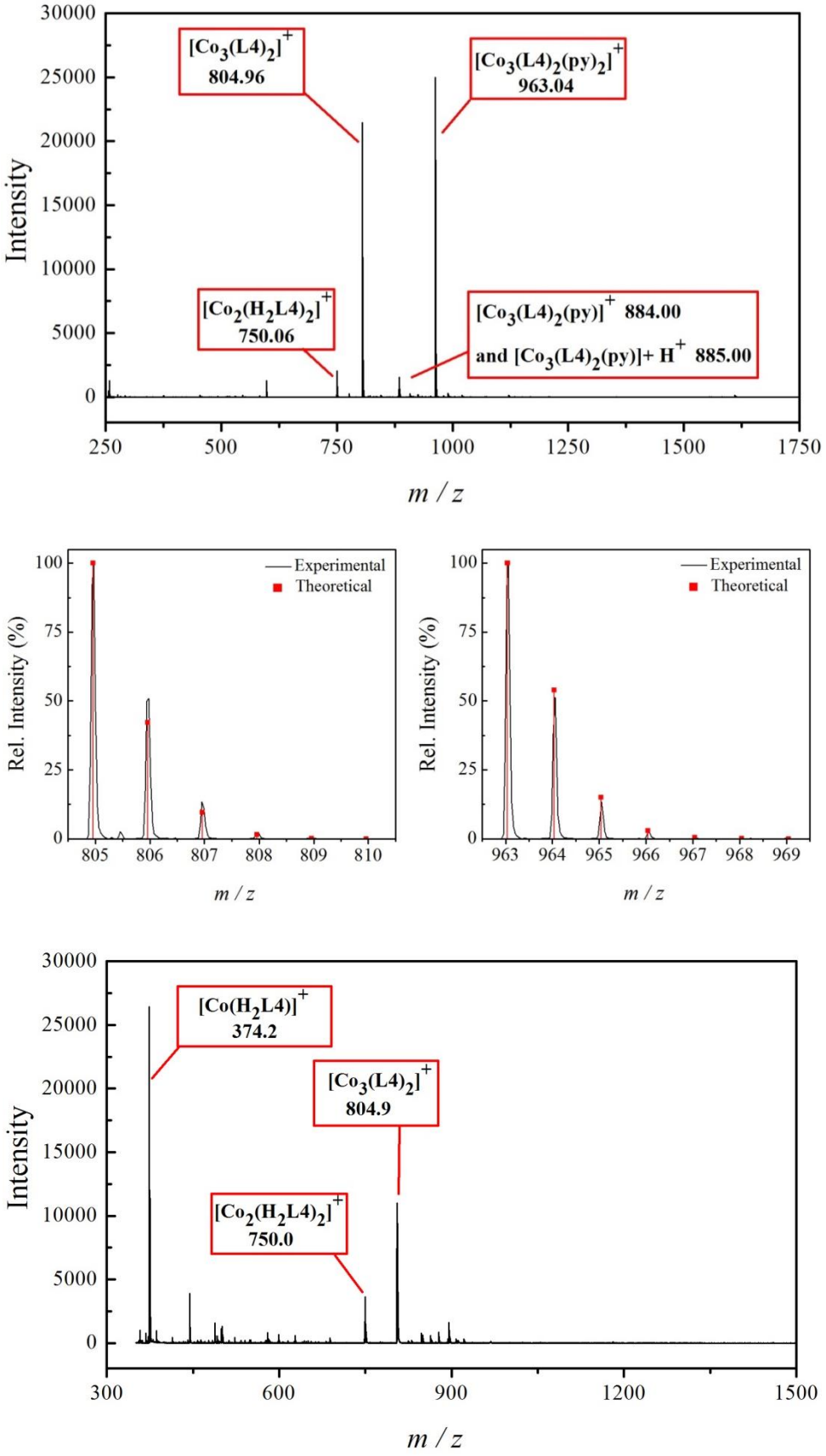

Figure IV.A7: *Top*: ESI(+) mass spectrogram of methanol solution of compound **25** with the isotopic distribution for two most abundant molecular peaks. *Bottom*: MALDI-TOF (+) mass spectrogram.

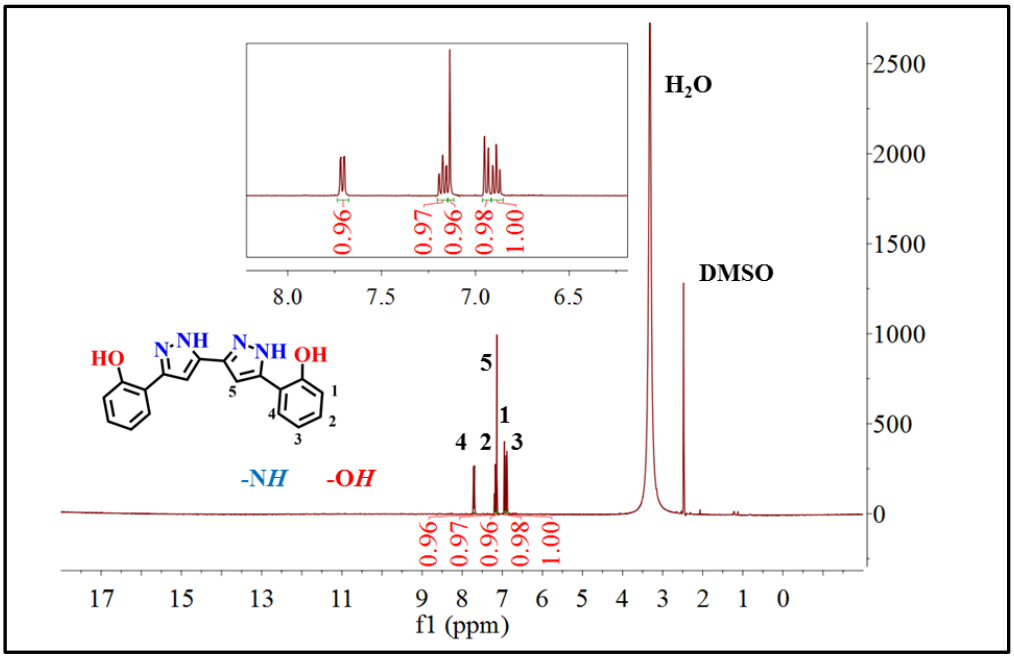

Figure IV.A8: ^{1}H NMR spectrum of ligand **H_4L4** in deuterated DMSO.

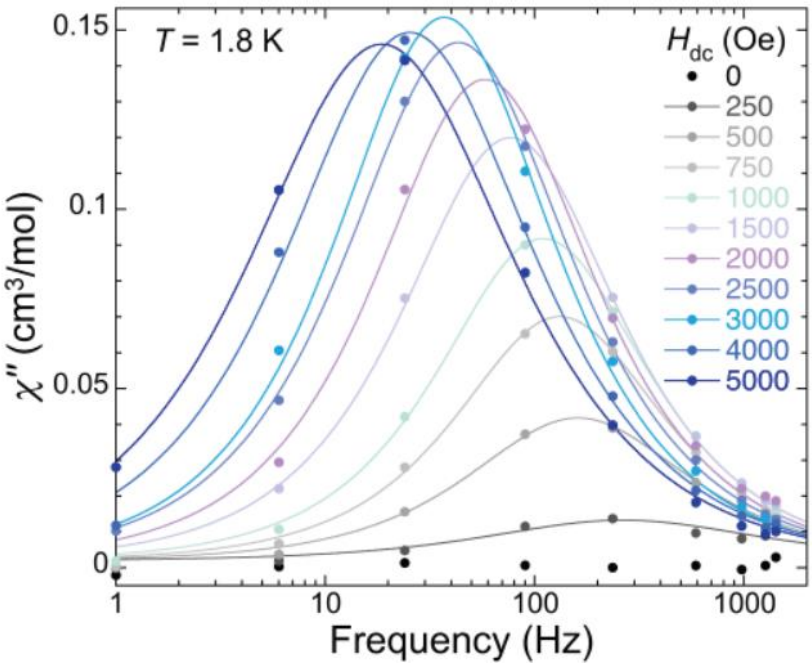

Figure IV.A9: Field dependence of the χ''_M signal of **23** at 1.8 K.

Table IV.A12: Interatomic distances [Å] and angles [°] for **26**

Cu1–Cu1#	3.9145(7)	N1–Cu1–O1	92.4(1)
Cu1–O1	1.894(2)	O1–Cu1–N3#	88.8(1)
Cu1–N1	1.914(3)	N3#–Cu1–N2#	80.9(1)
Cu1–N3#	1.965(3)	N2#–Cu1–N1	98.3(1)
Cu1–N2#	1.990(3)		
Symmetry operation: # = 1−x, 2−y, 1−z			

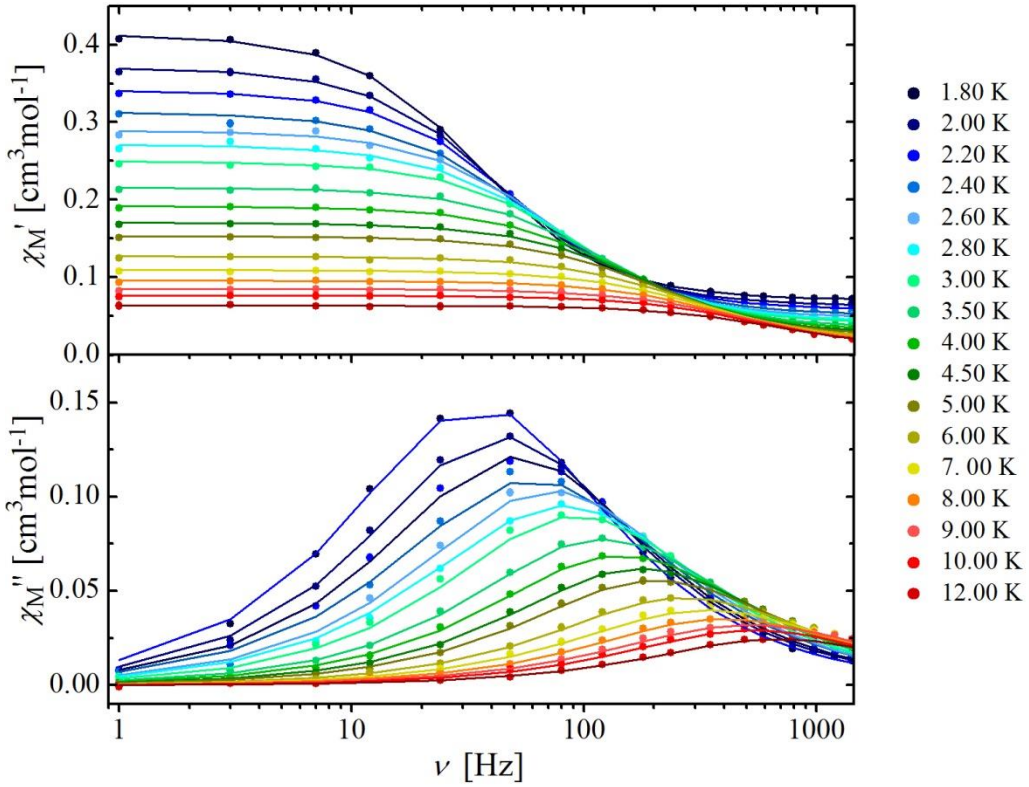

Figure IV.A10: Frequency dependence of the in- (χ_M') and out-of-phase (χ_M'') AC susceptibility for the compound **23** under an applied DC field of 3000 Oe. The solid lines are fits to the experimental data.

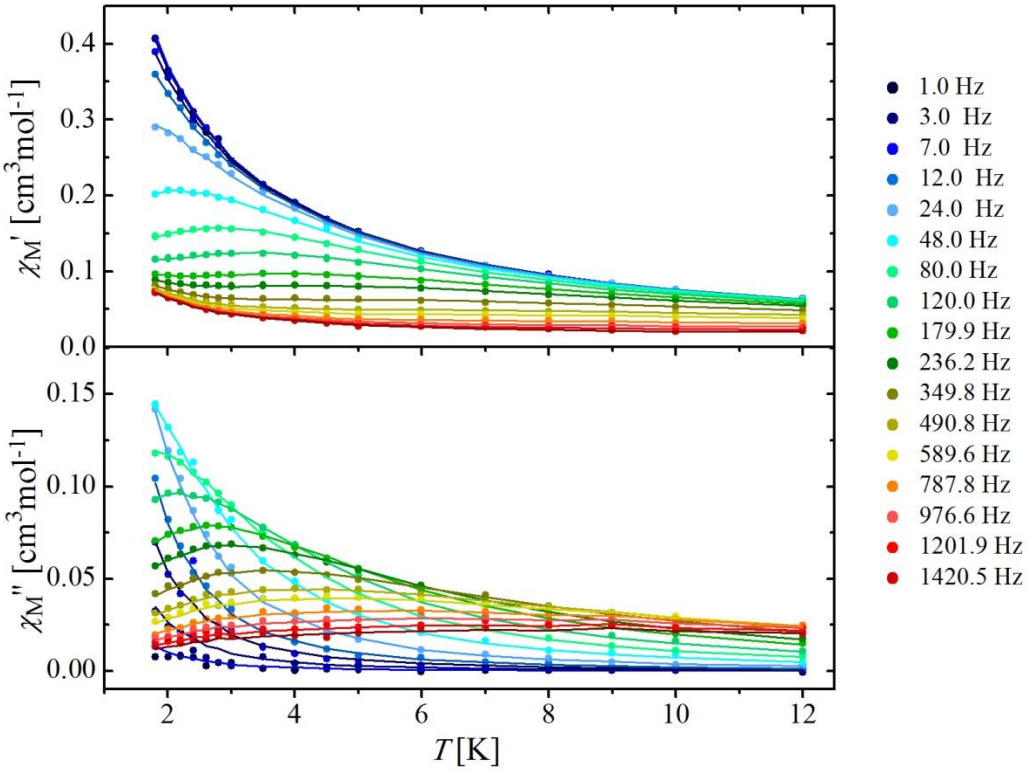

Figure IV.A11: Temperature dependence of the in- (χ_M') and out-of-phase (χ_M'') AC susceptibility for the compound **23** under an applied DC field of 3000 Oe. The solid lines are fits to the experimental data.

Table IV.A13: Interatomic distances [Å] and angles [°] for the compound **27**

V1–V2	7.763(1)	Cu1–N3	1.946(3)	V1–Cu1–V2	175.10(2)	N1S–Cu1–N2	101.3(2)	O6–V2–O2	107.5(1)
V1–Cu1	3.9089(8)	Cu1–N6	1.954(4)	O5–V1–O1	110.0(1)	N1S–Cu1–N3	99.2(2)	O6–V2–O3	108.4(1)
V2–Cu1	3.8609(8)	Cu1–N7	1.958(3)	O5–V1–O4	107.0(1)	N1S–Cu1–N6	106.0(2)	O6–V2–N5	102.8(1)
V1–O1	1.935(4)	Cu1–N1S	2.227(3)	O5–V1–N1	101.2(1)	N1S–Cu1–N7	102.4(2)	N4–V2–O2	83.8(1)
V1–O4	1.936(3)	V2=O6	1.609(3)	O5–V1–N8	105.7(1)	N2–Cu1–N3	81.3(1)	O2–V2–O3	82.0(1)
V1–N1	2.082(3)	V2–O2	1.929(3)	O4–V1–O1	80.9(1)	N3–Cu1–N6	93.1(1)	O3–V2–N5	84.2(1)
V1–N8	2.079(4)	V2–O3	1.918(3)	O1–V1–N1	83.8(1)	N6–Cu1–N7	81.5(1)	N5–V2–N4	94.2(1)
V1=O5	1.602(3)	V2–N4	2.070(4)	N1–V1–N8	95.0(1)	N7–Cu1–N2	93.9(1)		
Cu1–N2	1.960(4)	V2–N5	2.061(3)	N8–V1–O4	83.5(1)	O6–V2–N4	102.8(2)		

Table IV.A14: Interatomic distances [Å] and angles [°] for the compound **27A**

V1–V2	7.884(1)	Cu1–N3	1.946(3)	V1–Cu1–V2	176.08(2)	N1S–Cu1–N2	96.1(1)	O2–V2–O6	110.0(1)
V1–Cu1	3.9470(9)	Cu1–N6	1.946(3)	O1–V1–O7	112.2(1)	N1S–Cu1–N3	94.0(1)	O2–V2–O8	105.8(1)
V2–Cu1	3.9419(9)	Cu1–N7	1.941(3)	O1–V1–O5	104.5(1)	N1S–Cu1–N6	98.8(1)	O2–V2–N5	102.1(1)
V1–O1	1.612(2)	Cu1–N1S	2.293(3)	O1–V1–N1	105.6(1)	N1S–Cu1–N7	101.7(1)	N4–V2–O6	83.3(1)
V1–O5	1.933(2)	V2–O2	1.623(3)	O1–V1–N8	98.8(1)	N2–Cu1–N3	82.1(1)	O6–V2–O8	81.2(1)
V1–N1	2.081(2)	V2–O6	1.927(2)	O5–V1–O7	80.96(9)	N3–Cu1–N6	95.8(1)	O8–V2–N5	84.3(1)
V1–N8	2.077(2)	V2–O8	1.918(2)	O5–V1–N1	83.8(1)	N6–Cu1–N7	81.8(1)	N5–V2–N4	97.2(1)
V1–O7	1.922(2)	V2–N4	2.087(3)	N1–V1–N8	97.1(1)	N7–Cu1–N2	96.1(1)		
Cu1–N2	1.953(2)	V2–N5	2.084(3)	N8–V1–O7	83.5(1)	O2–V2–N4	100.3(1)		
V3–V4	7.877(1)	Cu2–N11	1.968(2)	V3–Cu2–V4	178.74(2)	N2S–Cu2–N10	101.8(1)	O4–V4–O10	107.4(1)
V3–Cu2	3.923(1)	Cu2–N14	1.962(2)	O3–V3–O9	109.0(1)	N2S–Cu2–N11	99.7(1)	O4–V4–O11	107.8(1)
V4–Cu2	3.954(1)	Cu2–N15	1.964(2)	O3–V3–O12	107.5(1)	N2S–Cu2–N14	100.2(1)	O4–V4–N13	103.1(1)
V3–O3	1.608(2)	Cu2–N2S	2.206(3)	O3–V3–N9	102.7(1)	N2S–Cu2–N15	103.3(1)	N12–V4–O10	84.1(1)
V3–O9	1.915(2)	V4–O4	1.610(3)	O3–V3–N16	103.3(1)	N10–Cu2–N11	81.8(1)	O10–V4–O11	80.0(1)
V3–N9	2.079(2)	V4–O10	1.925(2)	O9–V3–O12	81.5(1)	N11–Cu2–N14	94.1(1)	O11–V4–N13	83.9(1)
V3–N16	2.077(2)	V4–O11	1.937(2)	O12–V3–N16	83.6(1)	N14–Cu2–N15	81.9(1)	N12–V4–N13	94.8(1)
V3–O12	1.937(2)	V4–N12	2.082(2)	N16–V3–N9	94.5(1)	N15–Cu2–N10	93.4(1)		
Cu2–N10	1.954(2)	V4–N13	2.086(2)	N9–V3–O9	84.0(1)	O4–V4–N12	105.6(1)		

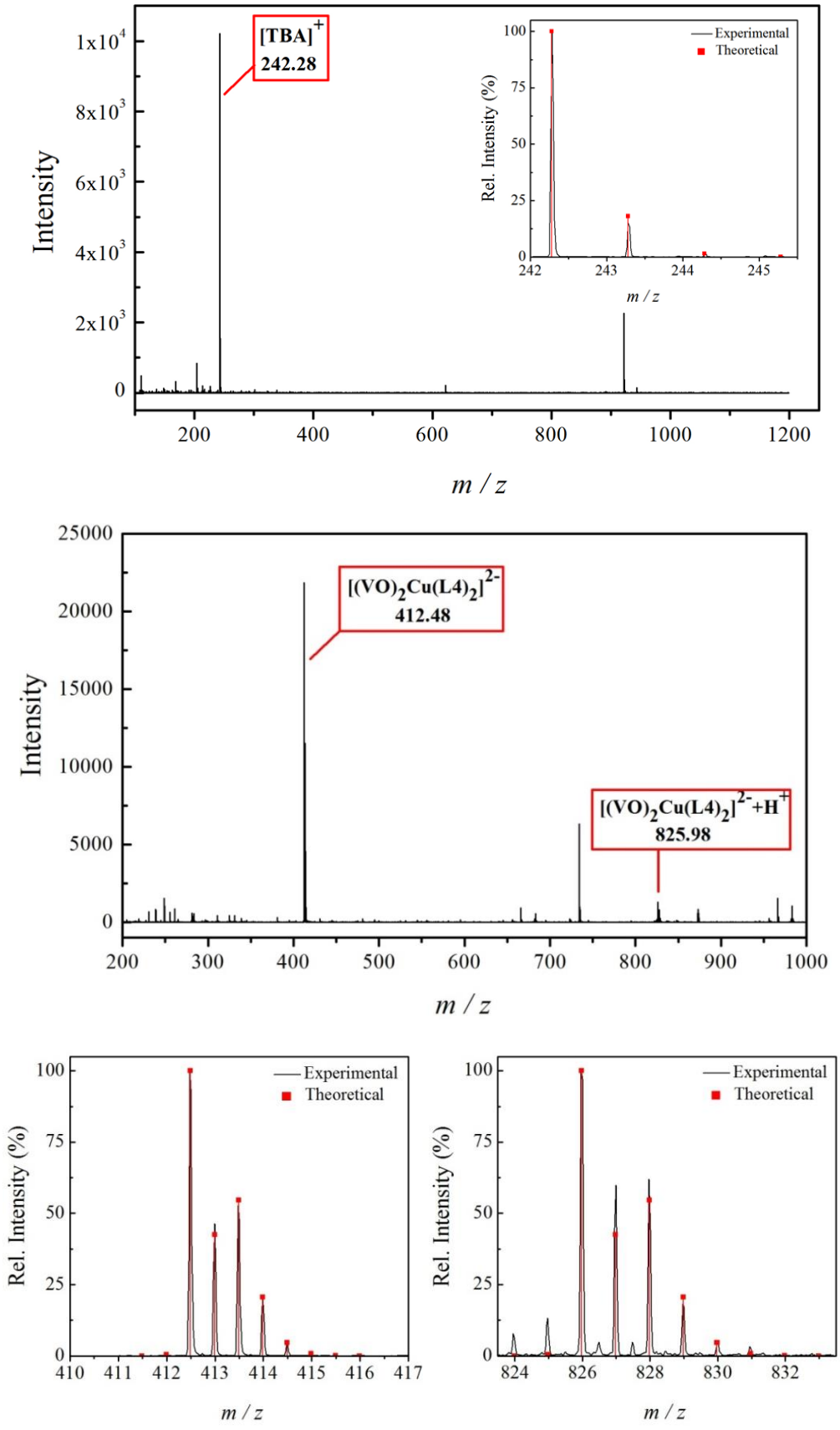

Figure IV.A12: ESI mass spectrogram of acetonitrile solution of compound **27**. *Top*: (+) mode with the isotopic distribution for TBA^+. *Bottom*: (-) mode with the isotopic distribution for two most abundant molecular peaks.

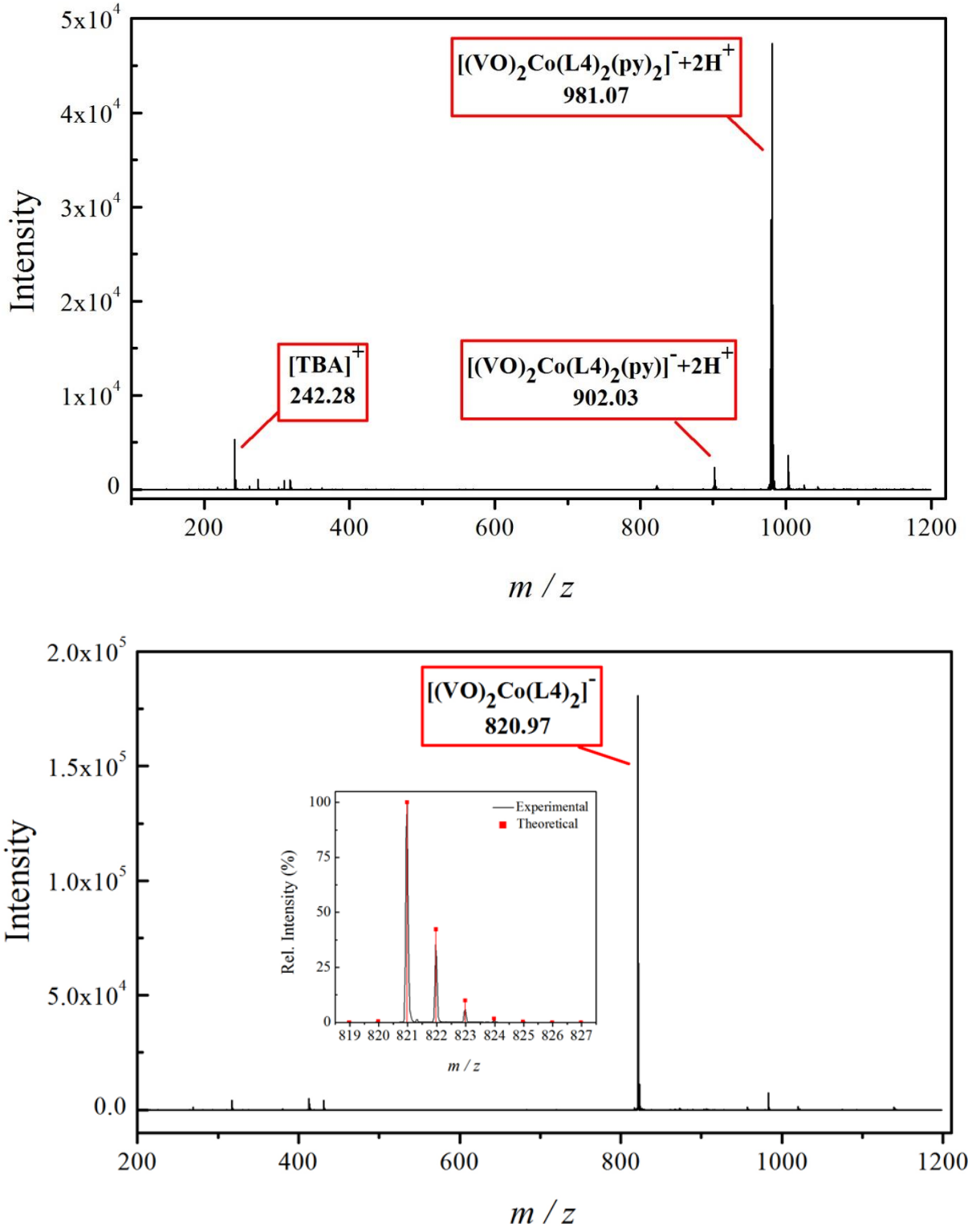

Figure IV.A13: ESI mass spectrogram of acetonitrile solution of compound (TBA)[$(VO)_2Co(L4)_2(py)_2$]. *Top*: (+) mode spectrogram. *Bottom*: (-) mode with the isotopic distribution for the most abundant molecular peak.

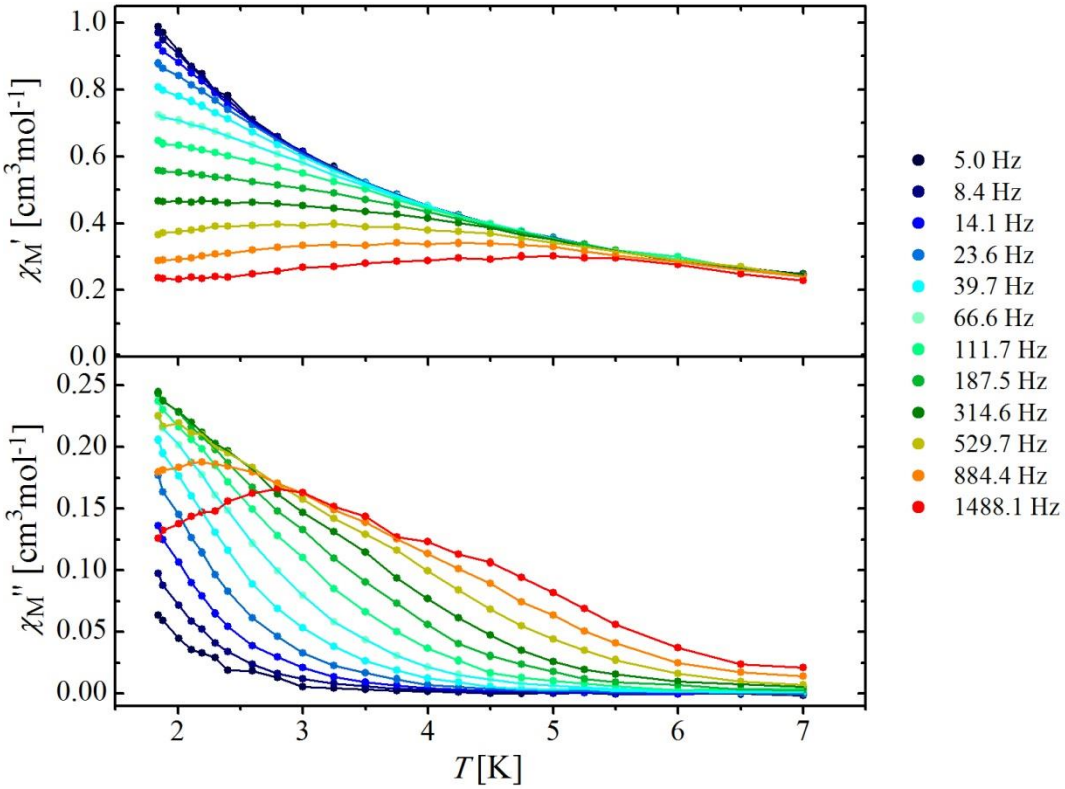

Figure IV.A14: Temperature dependence of the in- (χ_M') and out-of-phase (χ_M'') AC susceptibility for the compound **27** under an applied DC field of 1000 Oe. The solid lines are guides for the eye.

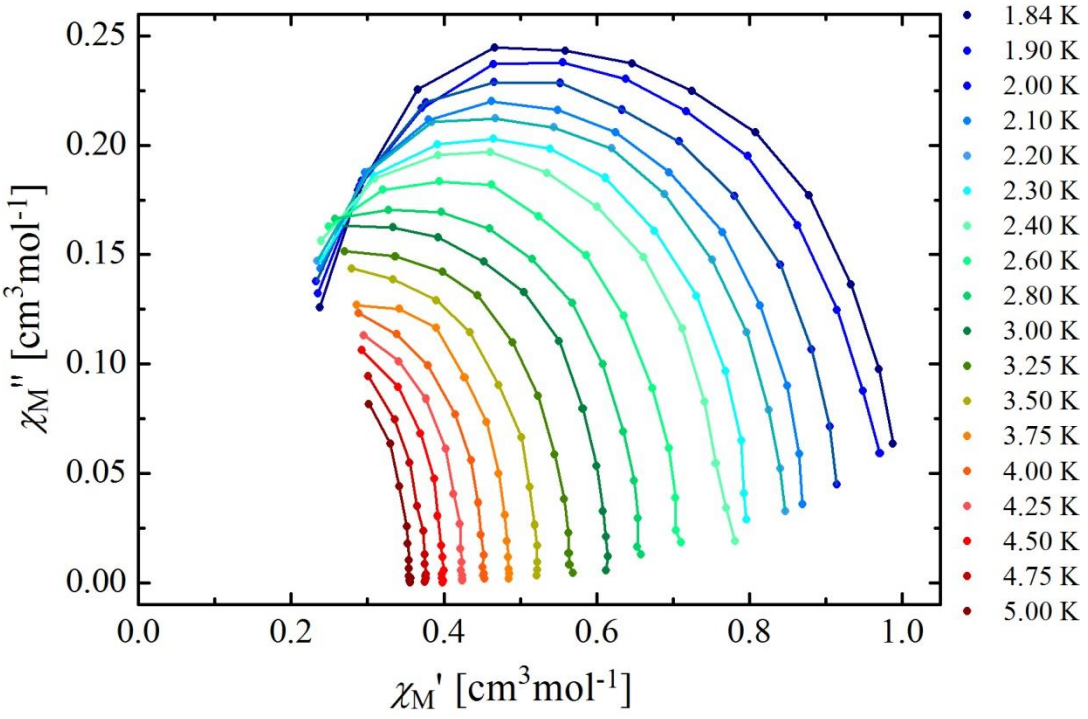

Figure IV.A15: Cole-Cole isotherms of the AC susceptibility for **27** under an applied DC field of 1000 Oe. The solid lines are guides for the eye.

Table IV.A15: Interatomic distances [Å] and angles [°] for the compound **28**

V1–V2	8.2747(9)	Cu1–N11	2.361(3)	O1–V1–N5	96.7(1)	N11–Cu1–N7	93.8(1)	O4–V2–N4	85.4(1)
V1–Cu1	4.0239(9)	V2=O2	1.629(2)	O1–V1–O3	99.4(1)	N7–Cu1–N3	97.4(1)	N4–V2–N8	98.6(1)
V2–Cu1	4.0060(9)	V2–O4	1.927(3)	O1–V1–O5	100.9(1)	N3–Cu1–N2	82.4(1)	O2–Cu2–N12	90.9(1)
V1–Cu2	4.0889(8)	V2–O6	1.944(4)	O1–V1–N1	96.4(1)	N2–Cu1–N6	96.1(1)	O2–Cu2–N13	94.1(1)
V2–Cu2	4.1937(8)	V2–N4	2.113(4)	O5–V1–O3	85.0(1)	N6–Cu1–N7	82.4(1)	O2–Cu2–N14	88.9(1)
V1=O1	1.633(2)	V2–N8	2.114(3)	O3–V1–N1	86.4(1)	O2–V2–O6	99.3(1)	O2–Cu2–N15	84.1(1)
V1–N1	2.102(3)	V2–N10	2.433(3)	N1–V1–N5	97.3(1)	O2–V2–O4	102.4(1)	N12–Cu2–N13	86.0(1)
V1–N5	2.120(4)	Cu2–O1	2.470(2)	N5–V1–O5	86.6(1)	O2–V2–N8	95.9(1)	N13–Cu2–N14	88.0(1)
V1–O5	1.930(2)	Cu2–O2	2.572(2)	N9–V1–O5	80.6(1)	O2–V2–N4	95.6(1)	N14–Cu2–N15	96.0(1)
V1–O3	1.932(4)	Cu2–N12	2.024(3)	N9–V1–N5	80.6(1)	N10– V2–N4	82.0(1)	N15–Cu2–N12	90.0(1)
V1–N9	2.376(3)	Cu2–N13	2.032(4)	N9–V1–N1	82.4(1)	N10– V2–N8	81.1(1)	O1–Cu2–N12	91.5(1)
Cu1–N2	1.959(4)	Cu2–N14	2.037(3)	N9–V1–O3	83.4(1)	N10– V2–O4	80.9(1)	O1–Cu2–N13	96.7(1)
Cu1–N7	1.951(4)	Cu2–N15	2.033(4)	N11–Cu1–N3	90.0(1)	N10– V2–O6	83.5(1)	O1–Cu2–N14	89.9(1)
Cu1–N6	1.967(3)	V1–Cu1–V2#	168.43(2)	N11–Cu1–N2	95.7(1)	N8–V2–O6	85.6(1)	O1–Cu2–N15	85.3(1)
Cu1–N3	1.955(3)	V1–Cu2–V2#	175.00(2)	N11–Cu1–N6	100.1(1)	O6–V2–O4	85.4(1)	# = −x, 2−y, 2−z	

Table IV.A16: Interatomic distances [Å] and angles [°] for the compound **29**

V1–V2	7.3278(9)	Ni1–N7	1.885(2)	V1–Ni2–V2	168.44(2)	N2–Ni1–N3	82.8(1)	O6–V2–O4	87.11(9)
V1–Ni1	3.9260(6)	V2=O2	1.642(2)	O1–V1–O3	101.18(9)	N3–Ni1–N7	96.9(1)	O2–Ni2–N11	88.82(9)
V2–Ni1	3.9290(7)	V2–O4	1.928(2)	O1–V1–O5	100.9(1)	N7–Ni1–N6	83.1(1)	O2–Ni2–N12	91.96(9)
V1–Ni2	3.6856(7)	V2–O6	1.932(2)	O1–V1–N1	97.5(1)	O2–V2–N4	97.2(1)	O2–Ni2–N13	91.15(9)
V2–Ni2	3.6797(7)	V2–N4	2.084(2)	O1–V1–N5	96.6(1)	O2–V2–N8	96.7(1)	O2–Ni2–N14	89.25(9)
V1=O1	1.642(2)	V2–N8	2.075(2)	O5–V1–O3	87.71(9)	O2–V2–O4	101.7(1)	N11–Ni2–N12	92.9(1)
V1–N1	2.077(3)	V2–N10	2.378(3)	O3–V1–N1	86.11(9)	O2–V2–O6	100.8(1)	N12–Ni2–N13	93.6(1)
V1–N5	2.071(3)	Ni2–O1	2.082(2)	N1–V1–N5	93.4(1)	N10– V2–N4	81.3(1)	N13–Ni2–N14	88.2(1)
V1–O5	1.932(2)	Ni2–O2	2.073(2)	N5–V1–O5	87.14(9)	N10– V2–N8	82.3(1)	N14–Ni2–N11	85.2(1)
V1–O3	1.938(2)	Ni2–N11	2.100(2)	N9–V1–O5	81.42(9)	N10– V2–O4	79.32(9)	O1–Ni2–N11	90.11(9)
V1–N9	2.376(3)	Ni2–N12	2.079(3)	N9–V1–O3	79.96(9)	N10– V2–O6	80.77(9)	O1–Ni2–N12	90.87(9)
Ni1–N2	1.884(2)	Ni2–N13	2.084(3)	N9–V1–N5	82.37(9)	O4–V2–N4	86.17(9)	O1–Ni2–N13	89.60(9)
Ni1–N6	1.890(2)	Ni2–N14	2.136(2)	N9–V1–N1	80.27(9)	N4–V2–N8	93.6(1)	O1–Ni2–N14	87.89(9)
Ni1–N3	1.878(2)	V1–Ni1–V2#	165.20(1)	N6–Ni1–N2	96.9(1)	N8–V2–O6	87.43(9)	# = 2−x, −y, 1−z	

Table IV.A17: Interatomic distances [Å] and angles [°] for the compound **30**

V1–V2	7.3374(9)	Cu1–N6	1.937(3)	V1–Ni1–V2	168.70(2)	N2–Cu1–N3	82.1(1)	O6–V2–O4	87.7(1)
V1–Cu1	3.9308(7)	V2=O2	1.644(3)	O1–V1–O3	101.9(1)	N3–Cu1–N7	97.8(1)	O2–Ni1–N11	88.2(1)
V2–Cu1	3.9327(7)	V2–O4	1.936(2)	O1–V1–O5	101.5(1)	N7–Cu1–N6	82.0(1)	O2–Ni1–N12	89.7(1)
V1–Ni1	3.6824(7)	V2–O6	1.936(2)	O1–V1–N1	96.1(1)	O2–V2–N4	96.6(1)	O2–Ni1–N13	90.5(1)
V2–Ni1	3.6908(7)	V2–N4	2.092(3)	O1–V1–N5	95.2(1)	O2–V2–N8	95.2(1)	O2–Ni1–N14	90.3(1)
V1=O1	1.642(3)	V2–N8	2.084(3)	O5–V1–O3	86.8(1)	O2–V2–O4	101.1(1)	N11–Ni1–N12	87.8(1)
V1–N1	2.092(2)	V2–N10	2.368(3)	O3–V1–N1	85.3(1)	O2–V2–O6	101.7(1)	N12–Ni1–N13	93.8(1)
V1–N5	2.093(3)	Ni1–O1	2.073(3)	N1–V1–N5	96.7(1)	N10– V2–N4	80.1(1)	N13–Ni1–N14	93.0(1)
V1–N9	2.377(4)	Ni1–O2	2.081(3)	N5–V1–O5	86.1(1)	N10– V2–N8	83.6(1)	N14–Ni1–N11	85.4(1)
V1–O5	1.932(2)	Ni1–N11	2.148(3)	N9–V1–N1	81.2(1)	N10– V2–O4	80.4(1)	O1–Ni1–N11	89.4(1)
V1–O3	1.921(2)	Ni1–N12	2.087(3)	N9–V1–N5	83.5(1)	N10– V2–O6	81.8(1)	O1–Ni1–N12	91.1(1)
Cu1–N2	1.932(3)	Ni1–N13	2.076(3)	N9–V1–O3	79.6(1)	O4–V2–N4	85.0(1)	O1–Ni1–N13	91.9(1)
Cu1–N7	1.942(3)	Ni1–N14	2.093(3)	N9–V1–O5	81.3(1)	N4–V2–N8	96.4(1)	O1–Ni1–N14	88.7(1)
Cu1–N3	1.933(3)	V1–Cu1–V2#	166.10(2)	N6–Cu1–N2	98.1(1)	N8–V2–O6	85.9(1)	# = 2−x, 1−y, 2−z	

Table IV.A18: Interatomic distances [Å] and angles [°] for the compound **31**

V1–V2	7.598(1)	Cu1–N9	2.362(3)	V1–Mn1–V2	174.78(2)	N2–Cu1–N3	81.1(1)	O6–V2–O4	86.4(1)
V1–Cu1	3.945(1)	V2=O2	1.653(3)	O1–V1–O3	106.0(1)	N3–Cu1–N7	97.3(1)	O2–Mn1–N11	86.3(1)
V2–Cu1	3.9575(9)	V2–O4	1.925(3)	O1–V1–O5	104.7(1)	N7–Cu1–N6	81.3(1)	O2–Mn1–N12	90.4(1)
V1–Mn1	3.830(1)	V2–O6	1.925(3)	O1–V1–N1	99.3(1)	O2–V2–N4	95.2(1)	O2–Mn1–N13	97.0(1)
V2–Mn1	3.776(1)	V2–N4	2.098(3)	O1–V1–N5	98.6(1)	O2–V2–N8	96.0(1)	O2–Mn1–N14	88.9(1)
V1=O1	1.648(3)	V2–N8	2.095(4)	O5–V1–O3	82.1(1)	O2–V2–O4	100.9(1)	N11–Mn1–N12	90.1(1)
V1–N1	2.081(4)	V2–N10	2.342(3)	O3–V1–N1	84.2(1)	O2–V2–O6	101.7(1)	N12–Mn1–N13	88.4(1)
V1–N5	2.076(3)	Mn1–O1	2.198(3)	N1–V1–N5	99.3(1)	N10– V2–N4	81.0(1)	N13–Mn1–N14	90.2(1)
V1–O5	1.904(3)	Mn1–O2	2.179(3)	N5–V1–O5	84.5(1)	N10– V2–N8	81.2(1)	N14–Mn1–N11	91.4(1)
V1–O3	1.900(3)	Mn1–N11	2.321(4)	N9–Cu1–N2	95.5(1)	N10– V2–O4	82.3(1)	O1–Mn1–N11	85.6(1)
Cu1–N6	1.955(4)	Mn1–N12	2.257(4)	N9–Cu1–N3	96.1(1)	N10– V2–O6	82.5(1)	O1–Mn1–N12	92.4(1)
Cu1–N2	1.953(3)	Mn1–N13	2.266(4)	N9–Cu1–N6	94.4(1)	O4–V2–N4	86.0(1)	O1–Mn1–N13	91.2(1)
Cu1–N7	1.950(3)	Mn1–N14	2.252(4)	N9–Cu1–N7	95.9(1)	N4–V2–N8	97.4(1)	O1–Mn1–N14	88.5(1)
Cu1–N3	1.957(4)	V1–Cu1–V2#	160.05(2)	N6–Cu1–N2	98.1(1)	N8–V2–O6	85.4(1)	# = 1−x, 2−y, 2−z	

Table IV.A19: Interatomic distances [Å] and angles [°] for the compound **32**

V1–V2	7.478(1)	Cu1–N9	2.359(4)	V1–Co1–V2	172.70(3)	N2–Cu1–N3	81.4(2)	O6–V2–O4	86.0(1)
V1–Cu1	3.938(1)	V2=O2	1.654(3)	O1–V1–O3	105.9(2)	N3–Cu1–N7	97.2(2)	O2–Co1–N11	88.7(1)
V2–Cu1	3.951(1)	V2–O4	1.928(3)	O1–V1–O5	105.4(2)	N7–Cu1–N6	81.4(2)	O2–Co1–N12	90.3(1)
V1–Co1	3.757(1)	V2–O6	1.924(3)	O1–V1–N1	99.8(2)	O2–V2–N4	95.7(2)	O2–Co1–N13	94.0(1)
V2–Co1	3.737(1)	V2–N4	2.088(5)	O1–V1–N5	98.4(2)	O2–V2–N8	96.1(2)	O2–Co1–N14	89.0(1)
V1=O1	1.641(3)	V2–N8	2.097(4)	O5–V1–O3	81.9(1)	O2–V2–O4	101.3(2)	N11–Co1–N12	90.6(2)
V1–N1	2.084(4)	V2–N10	2.339(4)	O3–V1–N1	84.0(2)	O2–V2–O6	102.0(2)	N12–Co1–N13	88.5(2)
V1–N5	2.067(5)	Co1–O1	2.128(3)	N1–V1–N5	99.5(2)	N10– V2–N4	80.4(2)	N13–Co1–N14	90.6(2)
V1–O5	1.910(3)	Co1–O2	2.121(3)	N5–V1–O5	84.4(2)	N10– V2–N8	81.3(2)	N14–Co1–N11	90.3(2)
V1–O3	1.903(3)	Co1–N11	2.251(4)	N9–Cu1–N2	95.0(2)	N10– V2–O4	81.9(1)	O1–Co1–N11	87.2(1)
Cu1–N6	1.957(4)	Co1–N12	2.139(5)	N9–Cu1–N3	96.9(2)	N10– V2–O6	82.2(1)	O1–Co1–N12	91.7(1)
Cu1–N2	1.954(5)	Co1–N13	2.191(4)	N9–Cu1–N6	94.2(2)	O4–V2–N4	86.1(2)	O1–Co1–N13	90.1(1)
Cu1–N7	1.946(5)	Co1–N14	2.128(5)	N9–Cu1–N7	96.0(2)	N4–V2–N8	97.6(2)	O1–Co1–N14	89.1(1)
Cu1–N3	1.958(4)	V1–Cu1–V2#	160.02(3)	N6–Cu1–N2	97.9(2)	N8–V2–O6	85.2(2)	# = −x, 2−y, −z	

Table IV.A20: Interatomic distances [Å] and angles [°] for the compound **33**

V1–V2	7.597(1)	Cu1–N9	2.354(4)	V1–Zn1–V2	173.88(2)	N2–Cu1–N3	81.3(1)	O6–V2–O4	86.2(1)
V1–Cu1	3.9484(8)	V2=O2	1.647(3)	O1–V1–O3	104.8(1)	N3–Cu1–N7	97.4(1)	O2–Zn1–N11	88.4(1)
V2–Cu1	3.9505(8)	V2–O4	1.933(3)	O1–V1–O5	106.2(1)	N7–Cu1–N6	81.3(1)	O2–Zn1–N12	88.9(1)
V1–Zn1	3.8255(9)	V2–O6	1.933(3)	O1–V1–N1	98.4(1)	O2–V2–N4	96.0(1)	O2–Zn1–N13	95.4(1)
V2–Zn1	3.7824(9)	V2–N4	2.091(4)	O1–V1–N5	99.4(1)	O2–V2–N8	95.1(1)	O2–Zn1–N14	90.3(1)
V1=O1	1.633(3)	V2–N8	2.095(3)	O5–V1–O3	82.2(1)	O2–V2–O4	101.7(1)	N11–Zn1–N12	89.8(1)
V1–N1	2.083(3)	V2–N10	2.346(4)	O3–V1–N1	84.2(1)	O2–V2–O6	101.3(1)	N12–Zn1–N13	91.7(1)
V1–N5	2.085(4)	Zn1–O1	2.208(3)	N1–V1–N5	99.3(1)	N10– V2–N4	80.7(1)	N13–Zn1–N14	89.2(1)
V1–O5	1.908(3)	Zn1–O2	2.180(3)	N5–V1–O5	84.4(1)	N10– V2–N8	81.1(1)	N14–Zn1–N11	89.4(1)
V1–O3	1.911(3)	Zn1–N11	2.282(3)	N9–Cu1–N2	94.3(1)	N10– V2–O4	82.4(1)	O1–Zn1–N11	85.3(1)
Cu1–N6	1.958(3)	Zn1–N12	2.112(5)	N9–Cu1–N3	96.4(1)	N10– V2–O6	82.4(1)	O1–Zn1–N12	89.1(1)
Cu1–N2	1.956(4)	Zn1–N13	2.177(3)	N9–Cu1–N6	95.1(1)	O4–V2–N4	85.3(1)	O1–Zn1–N13	90.9(1)
Cu1–N7	1.964(4)	Zn1–N14	2.128(4)	N9–Cu1–N7	96.5(1)	N4–V2–N8	97.7(1)	O1–Zn1–N14	91.6(1)
Cu1–N3	1.958(3)	V1–Cu1–V2#	159.96(2)	N6–Cu1–N2	97.8(1)	N8–V2–O6	85.9(1)	# = −x, 1−y, −z	

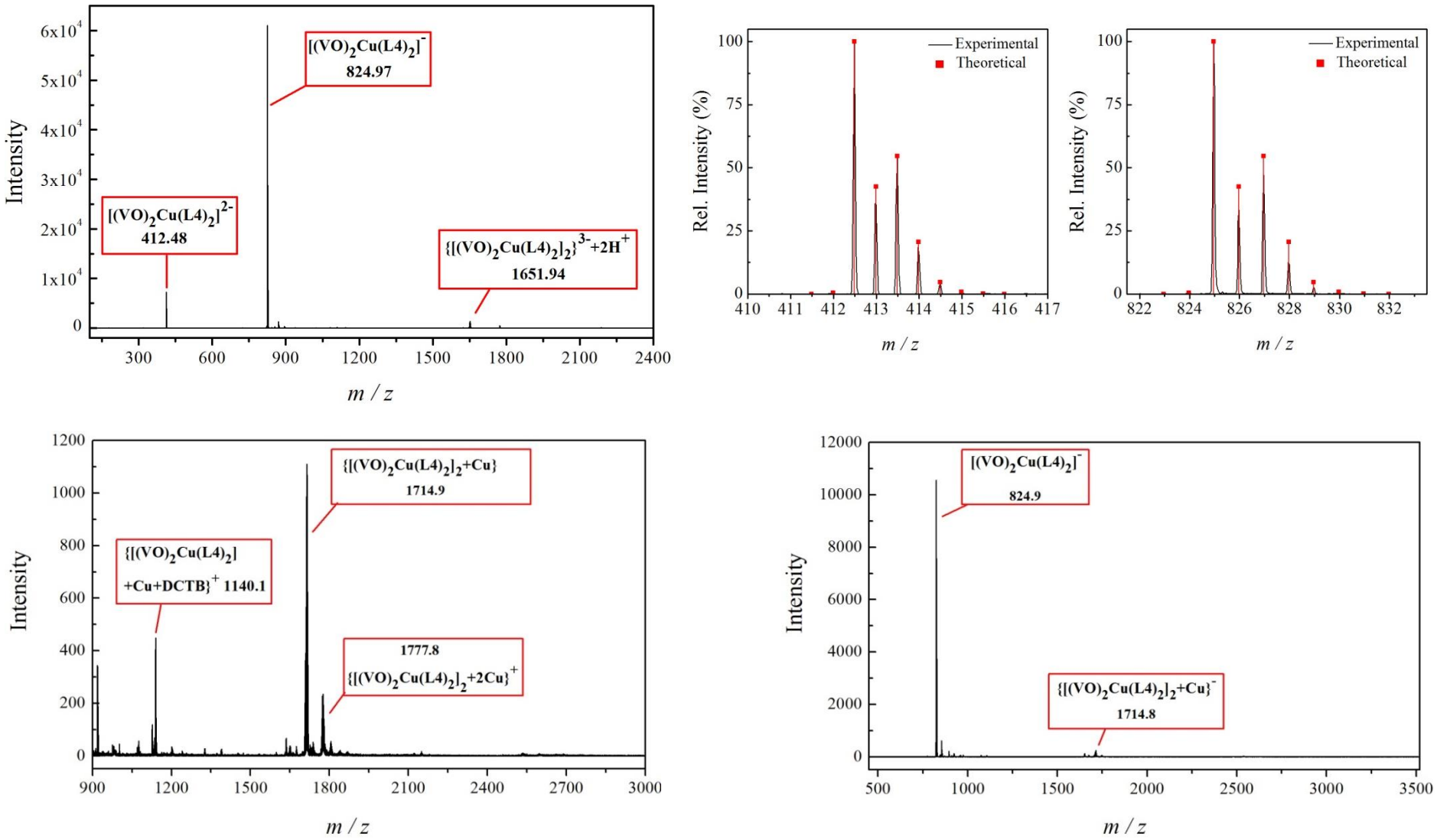

Figure IV.A16: *Top*: ESI(-) mass spectrogram of THF solution of compound **28** (*left*) with the isotopic distribution for two most abundant molecular peaks (*right*). *Bottom*: MALDI-TOF (+) (*left*) and (-) (*right*) mass spectrogram.

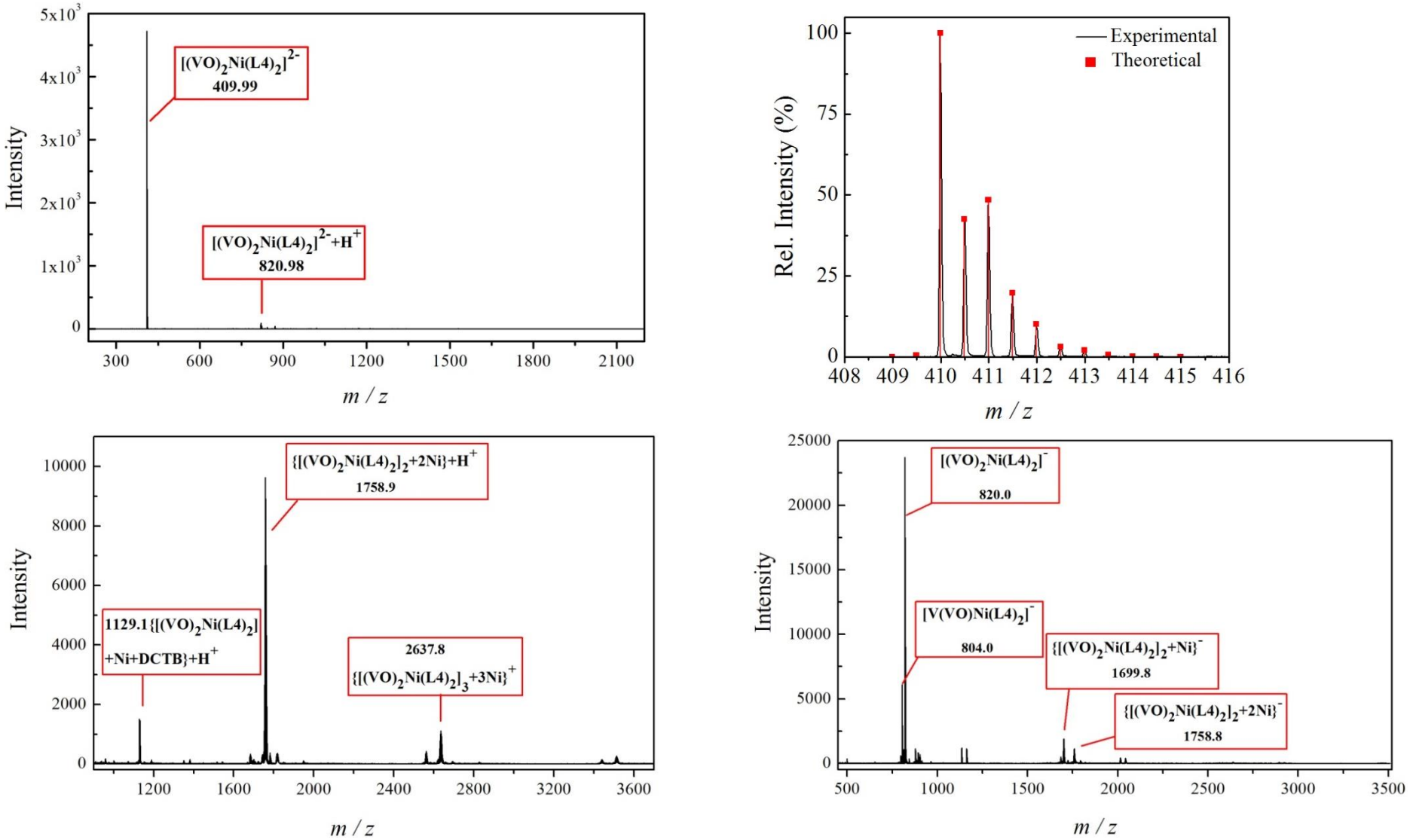

Figure IV.A17: *Top*: ESI(-) mass spectrogram of THF solution of compound **29** (*left*) with the isotopic distribution for two most abundant molecular peaks (*right*). *Bottom*: MALDI-TOF (+) (*left*) and (-) (*right*) mass spectrogram.

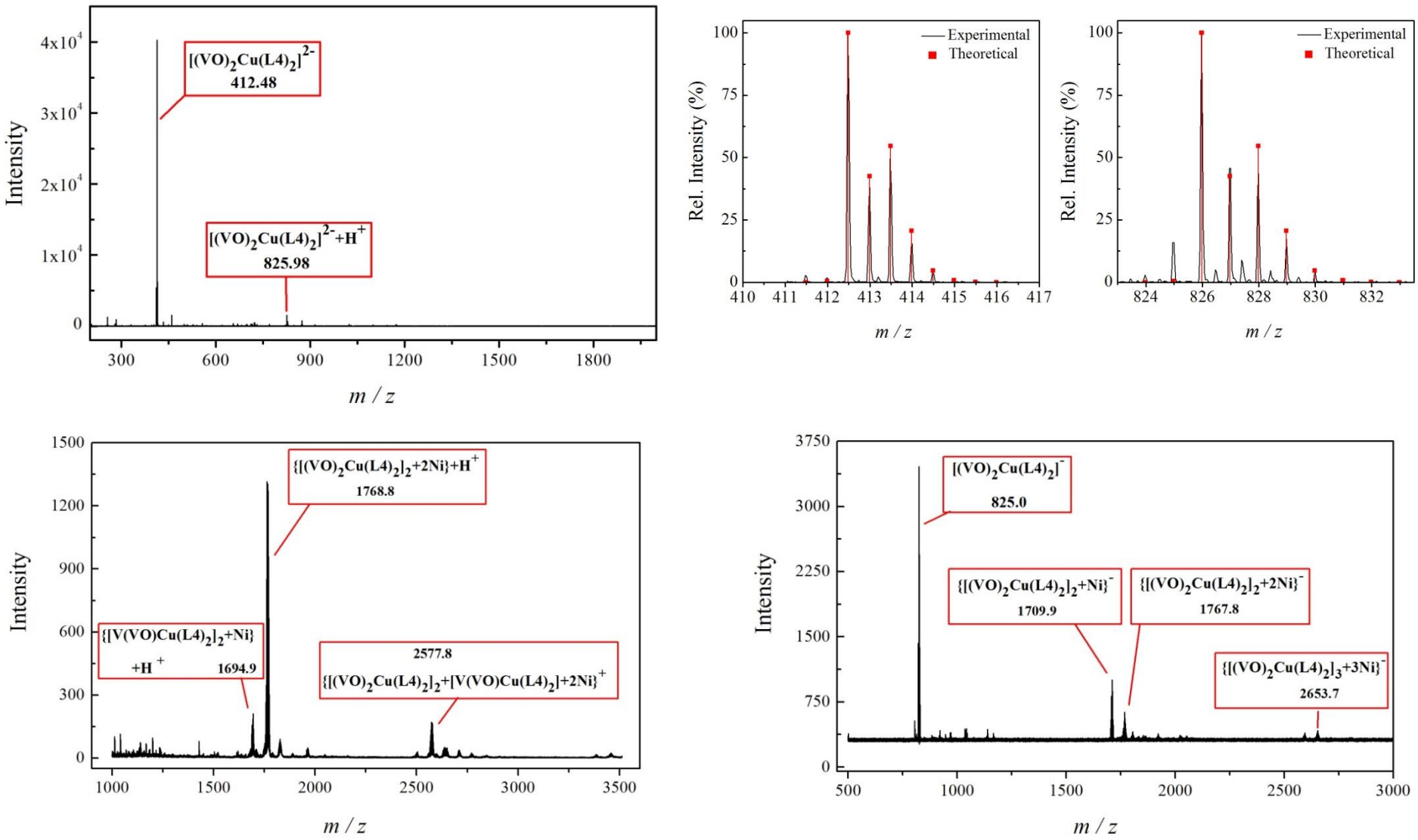

Figure IV.A18: *Top*: ESI(-) mass spectrogram of THF solution of compound **30** (*left*) with the isotopic distribution for two most abundant molecular peaks (*right*). *Bottom*: MALDI-TOF (+) (*left*) and (-) (*right*) mass spectrogram.

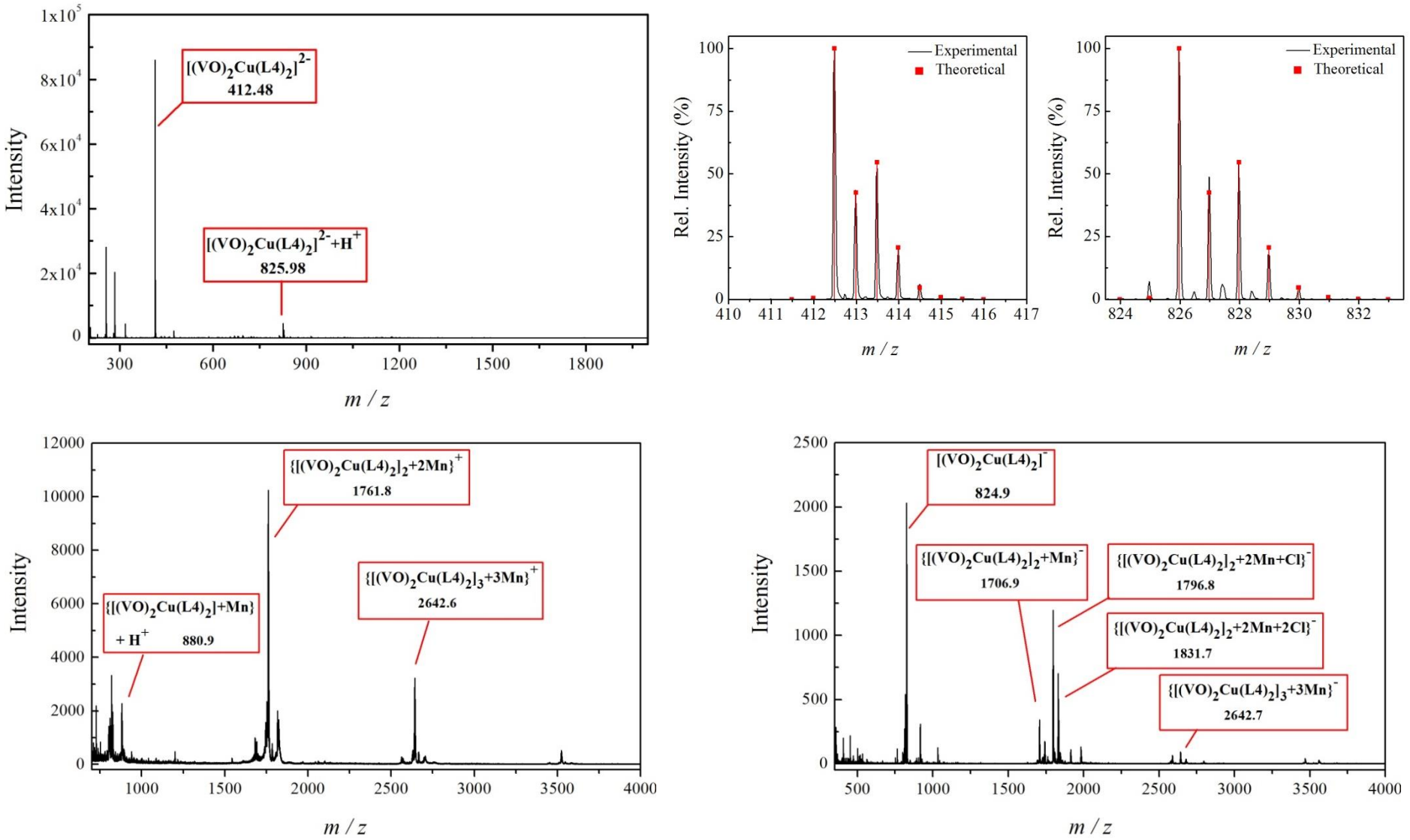

Figure IV.A19: *Top*: ESI(-) mass spectrogram of THF solution of compound **31** (*left*) with the isotopic distribution for two most abundant molecular peaks (*right*). *Bottom*: MALDI-TOF (+) (*left*) and (-) (*right*) mass spectrogram.

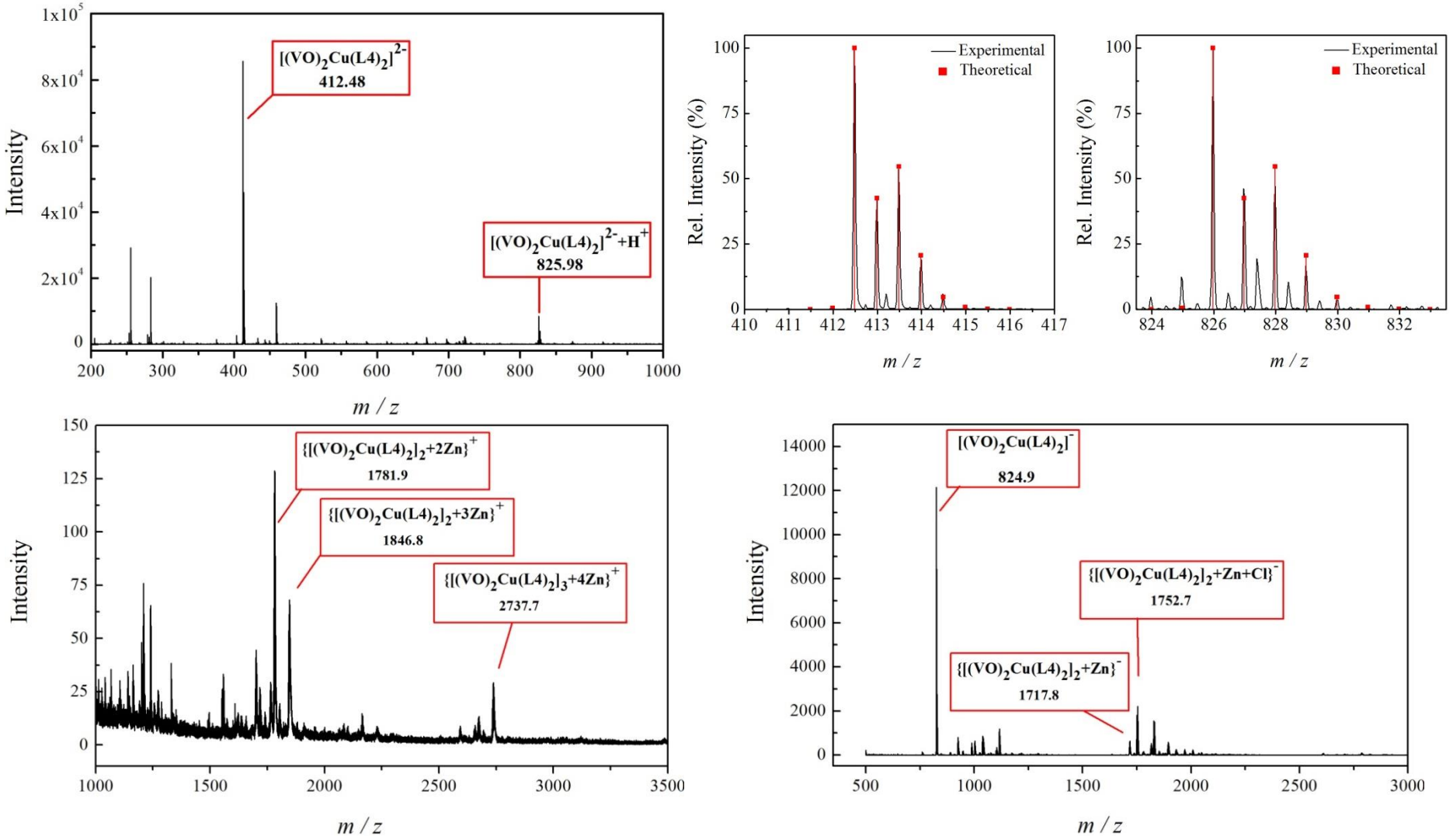

Figure IV.A20: *Top*: ESI(-) mass spectrogram of THF solution of compound **33** (*left*) with the isotopic distribution for two most abundant molecular peaks (*right*). *Bottom*: MALDI-TOF (+) (*left*) and (-) (*right*) mass spectrogram.

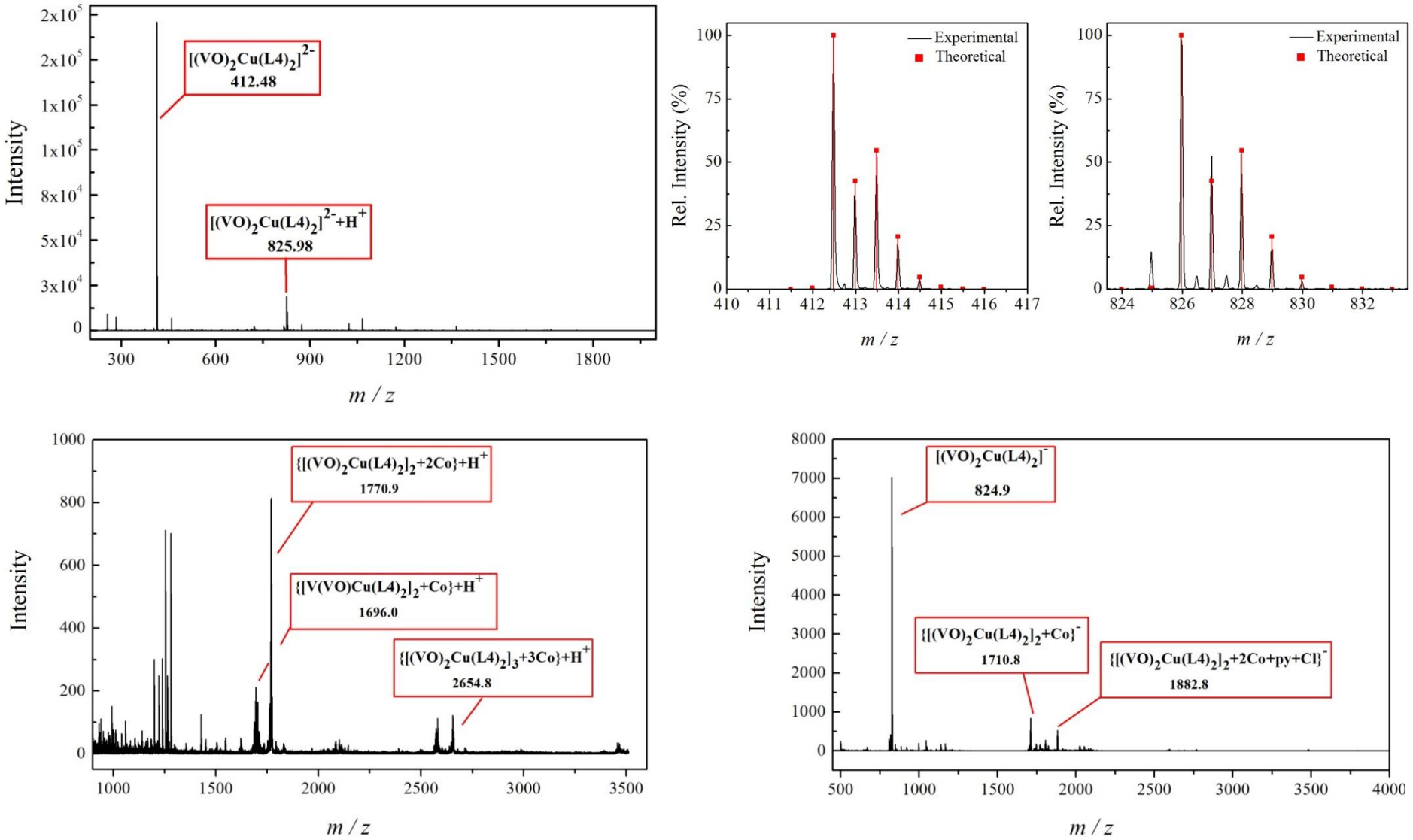

Figure IV.A21: *Top*: ESI(-) mass spectrogram of THF solution of compound **32** (*left*) with the isotopic distribution for two most abundant molecular peaks (*right*). *Bottom*: MALDI-TOF (+) (*left*) and (-) (*right*) mass spectrogram.

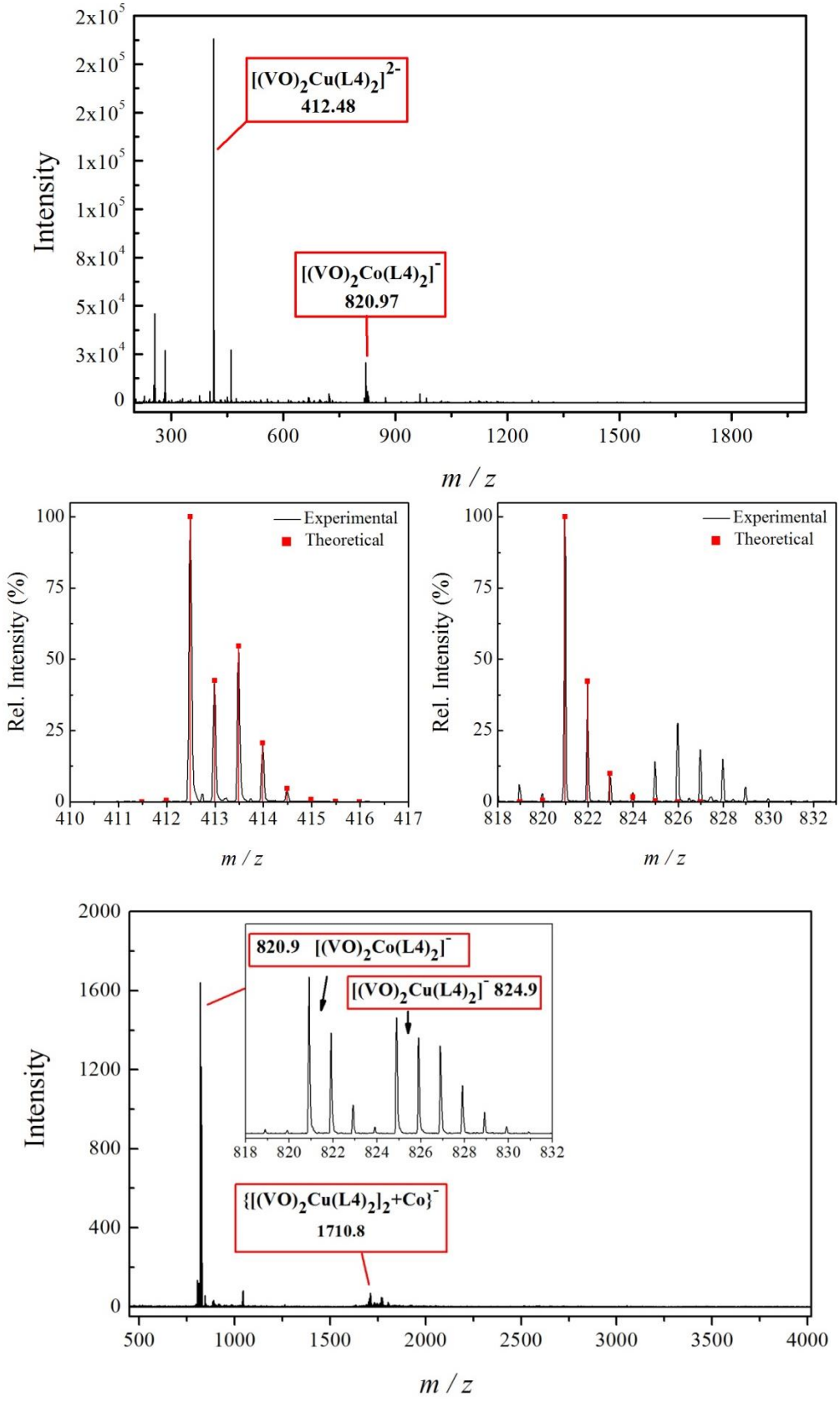

Figure IV.A22: *Top*: ESI(-) mass spectrogram of THF solution of *in situ* prepared compound **32** with the isotopic distribution for two most abundant molecular peaks. *Bottom*: MALDI-TOF (-) mass spectrogram of the same solution.

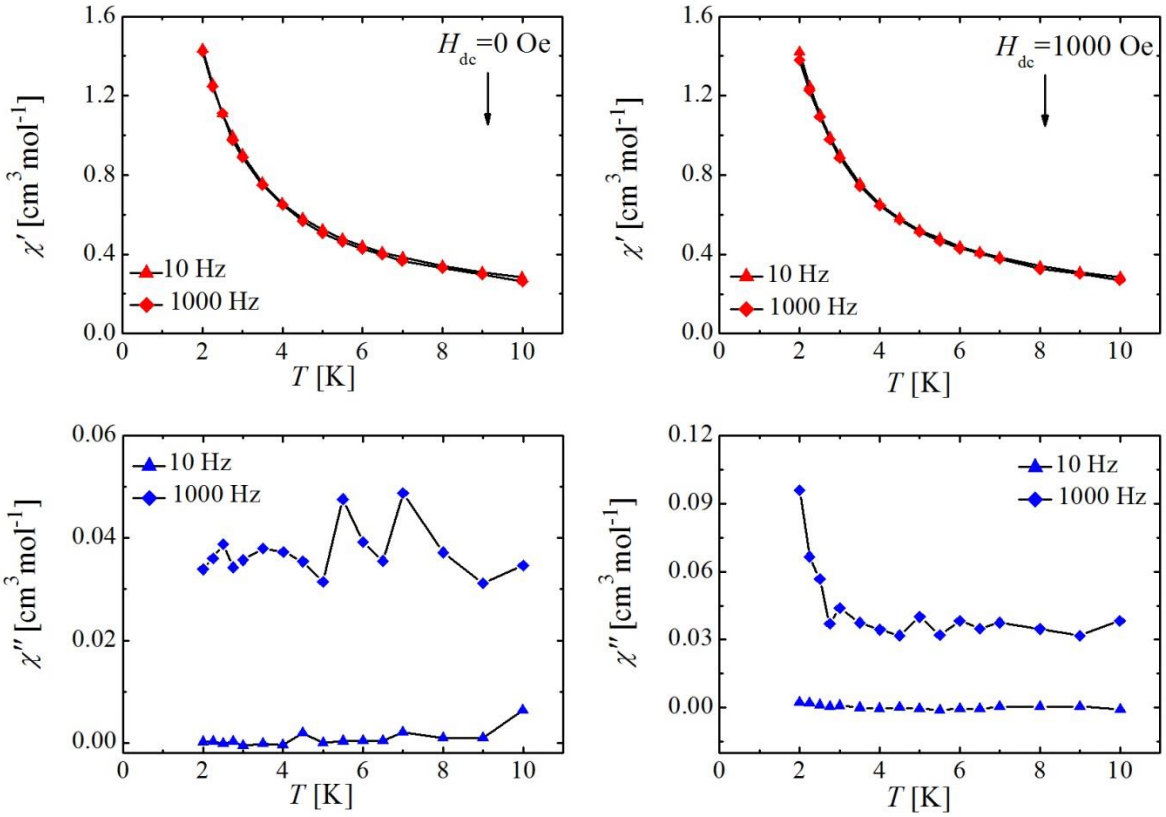

Figure IV.A23: Temperature dependence of the in- (χ'_M) and out-of-phase (χ''_M) AC susceptibility for the compound **28** under zero or 1000 Oe applied DC field. The solid lines are guides for the eye.

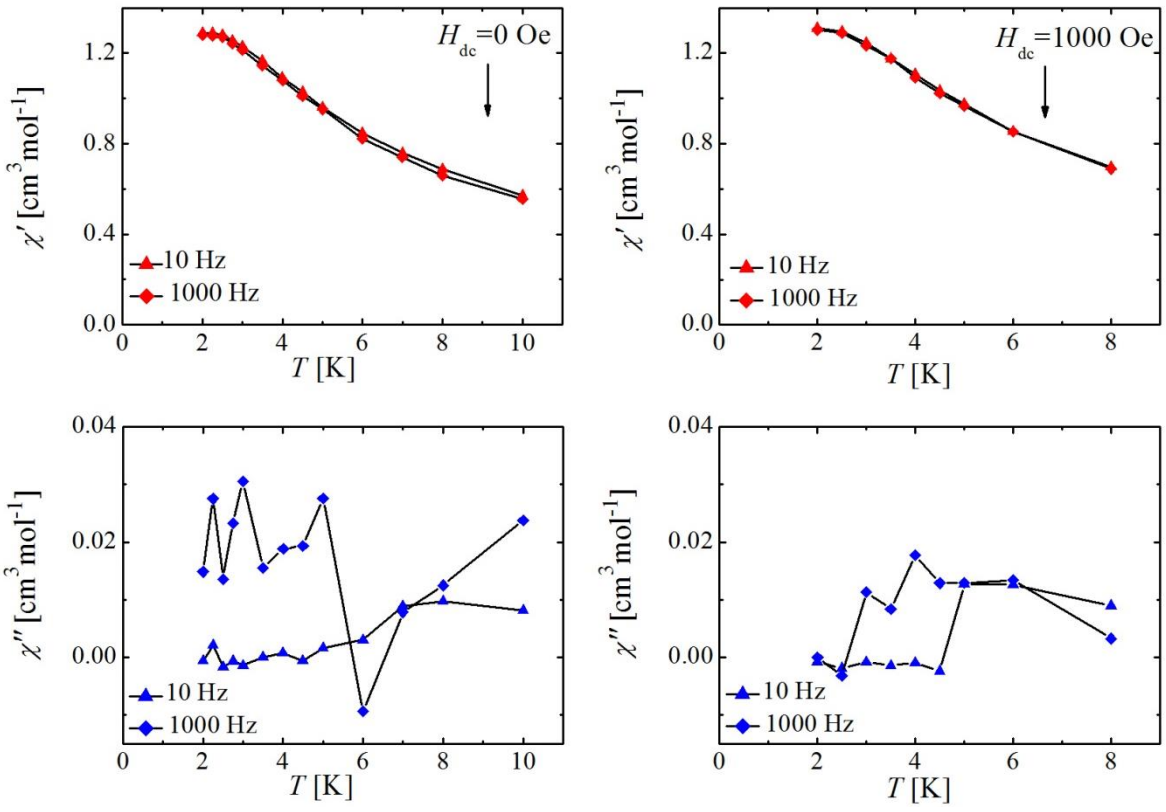

Figure IV.A24: Temperature dependence of the in- (χ'_M) and out-of-phase (χ''_M) AC susceptibility for the compound **29** under zero or 1000 Oe applied DC field. The solid lines are guides for the eye.

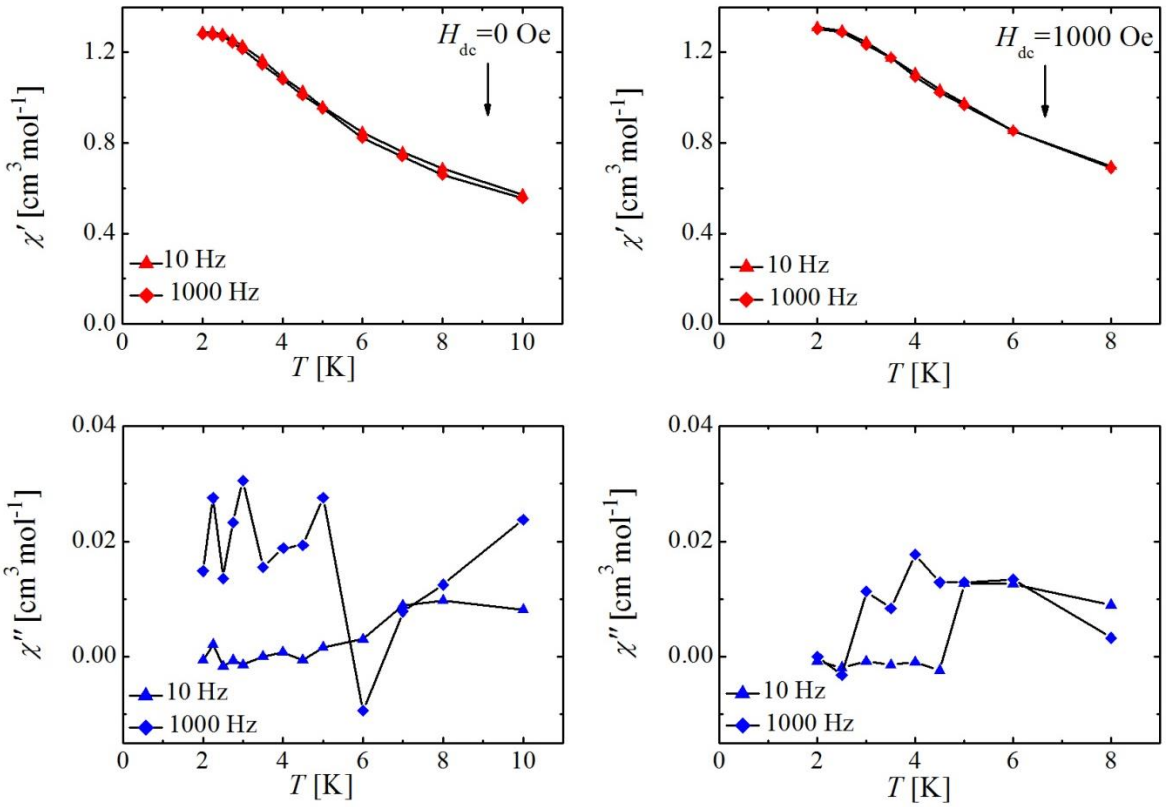

Figure IV.A25: Temperature dependence of the in- (χ'_M) and out-of-phase (χ''_M) AC susceptibility for the compound **30** under zero or 1000 Oe applied DC field. The solid lines are guides for the eye.

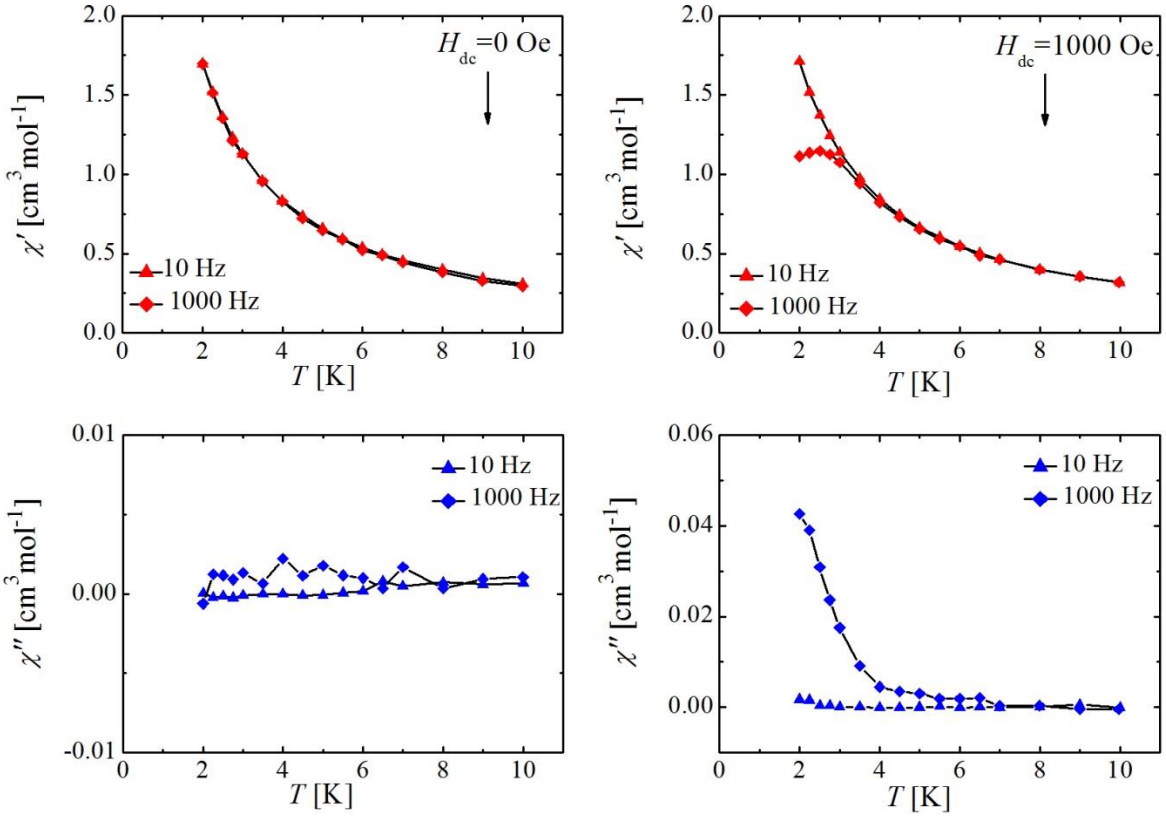

Figure IV.A26: Temperature dependence of the in- (χ'_M) and out-of-phase (χ''_M) AC susceptibility for the compound **31** under zero or 1000 Oe applied DC field. The solid lines are guides for the eye.

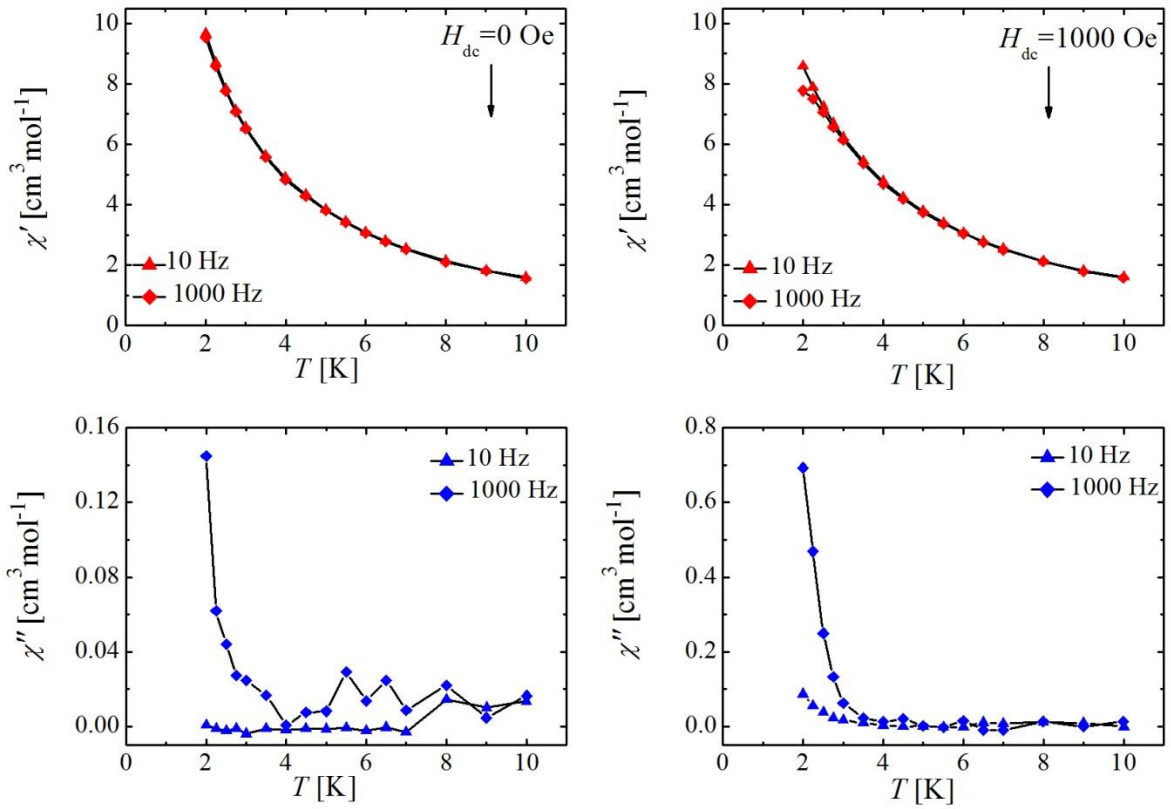

Figure IV.A27: Temperature dependence of the in- (χ'_M) and out-of-phase (χ''_M) AC susceptibility for the compound **32** under zero or 1000 Oe applied DC field. The solid lines are guides for the eye.

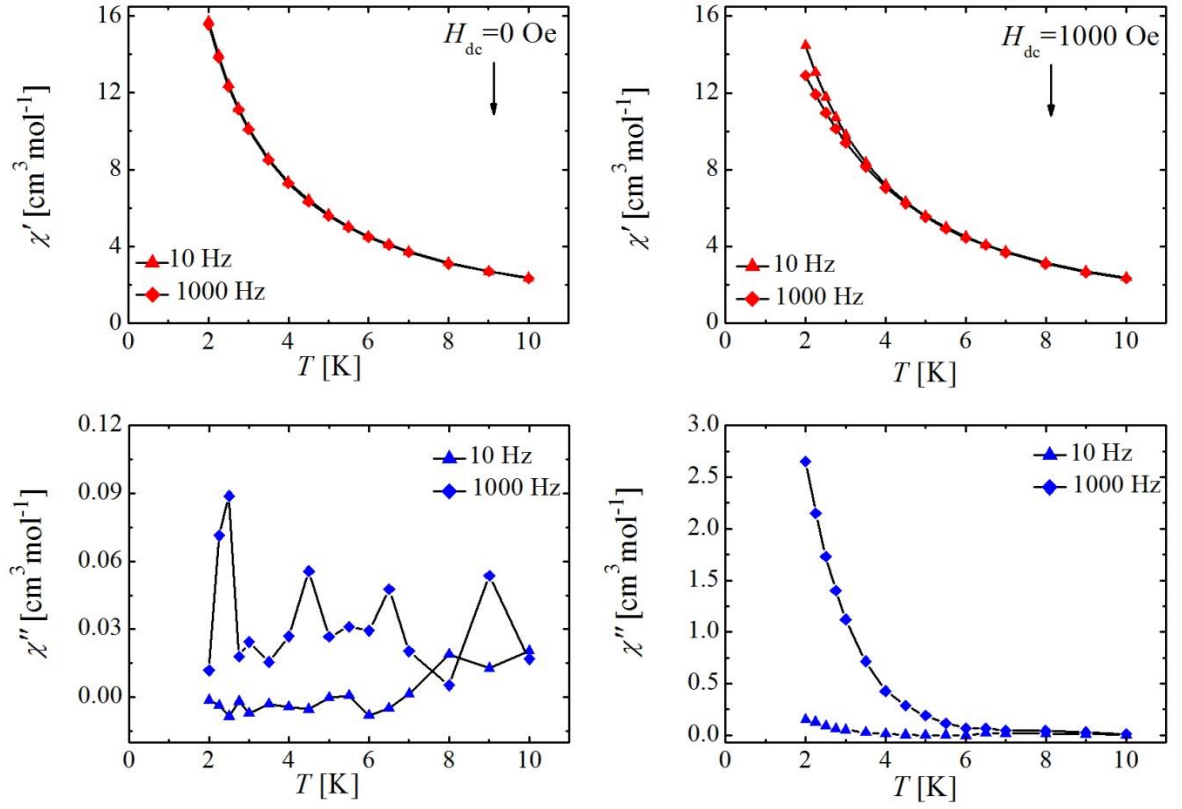

Figure IV.A28: Temperature dependence of the in- (χ'_M) and out-of-phase (χ''_M) AC susceptibility for the compound **31** under zero or 1000 Oe applied DC field. The solid lines are guides for the eye.

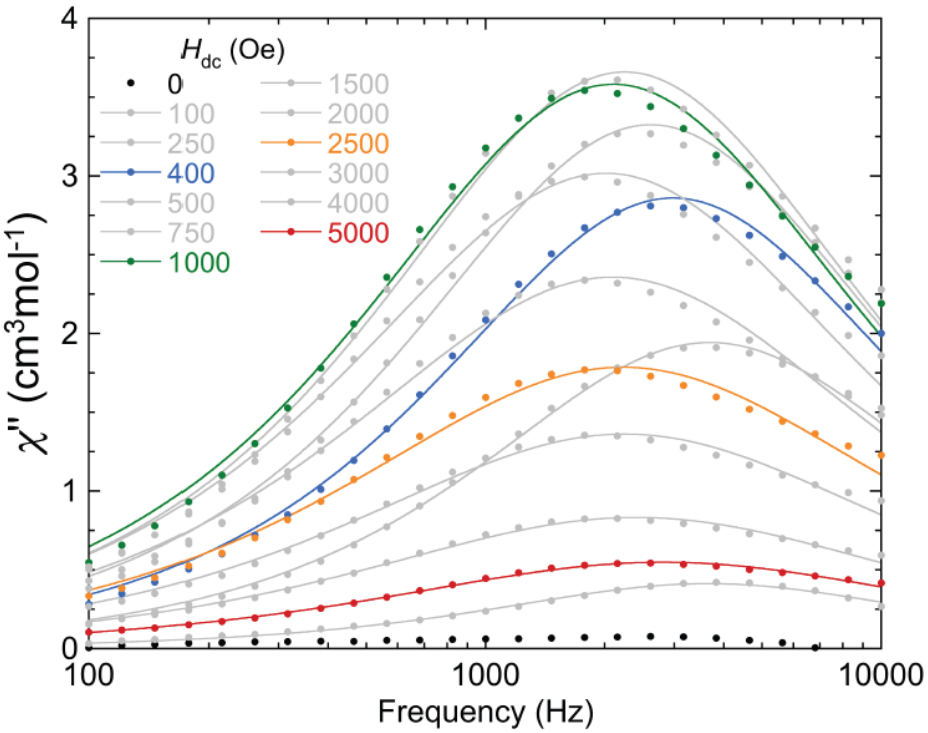

Figure IV.A29: Field dependence of the out-of-phase (χ_M'') AC susceptibility for the compound **31**. The solid lines are fits of the experimental data.

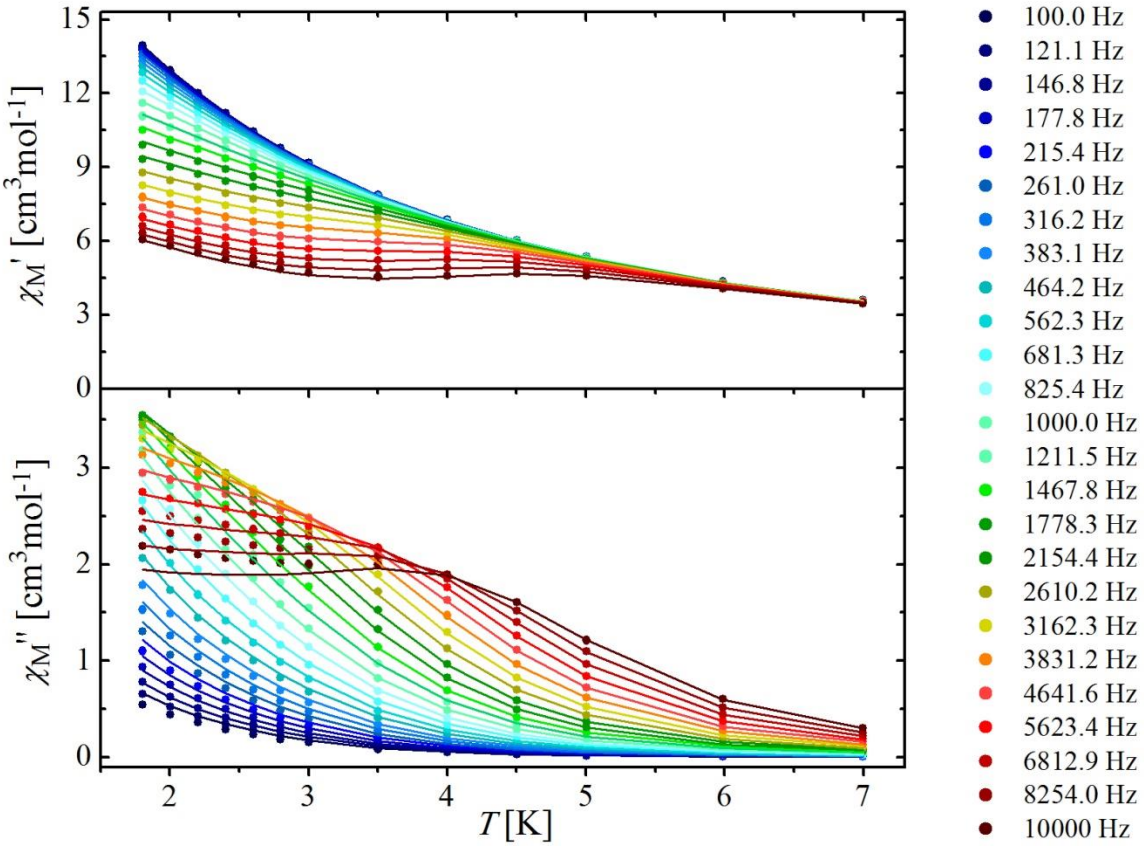

Figure IV.A30: Temperature dependence of the in- (χ_M') and out-of-phase (χ_M'') AC susceptibility for the compound **31** under an applied DC field of 1000 Oe. The solid lines are fits of experimental data.

Physical Measurements

X-Ray Crystallography

Crystallographic data were collected at 100 K on a Bruker APEX II CCD diffractometer equipped with a 111 monochromator (λ = 0.7749 Å) on the Advanced Light Source beamline 11.3.1 at Lawrence Berkeley National Laboratory or on a Bruker APEX II QUAZAR diffractometer equipped with a microfocus multilayer monochromator with Mo Kα radiation (λ = 0.71073 Å) at Universitat de Barcelona (GMMF lab). Data reduction and absorption corrections in both cases were performed with SAINT and SADABS, respectively.[1,2] The structures were solved with direct or Patterson methods and refined on F^2 with SHELX-TL suite.[3,4]

Magnetic measurements

Variable-temperature magnetic susceptibility data were obtained on polycrystalline samples with a Quantum Design MPMS5 SQUID magnetometer at the "Unitat de Mesures Magnètiques" of the Universitat de Barcelona or with a Quantum Design MPMS-XL SQUID magnetometer at the Physical Measurements Service at Universidad de Zaragoza. Pascal's constants were used to estimate diamagnetic corrections to the molar paramagnetic susceptibility and a correction was applied for the sample holder. Results of SQUID measurements ($\chi_M T$ vs T curve and $M/N_{\mu B}$ vs H) were fitted simultaneously using the program PHI.[5]

Elemental Analyses

Elemental analyses were performed at Scientific and Technological Centers of the University of Barcelona using an elemental organic analyzer Thermo EA Flash 2000 working in standard conditions recommended by the supplier of the instrument (helium flow 140 ml/min, combustion furnace at 950ºC, chromatografic column oven at 65ºC).

EPR Spectroscopy

X-Band EPR spectra (9.42 GHz) of powdered samples were collected on a Bruker ESP300E spectrometer with a liquid helium cryostat in the temperature range between 4 K and 300 K. Obtained spectra were processed with WINEPR Bruker software (version 2.11.0.0).

Pulsed EPR

Q-band measurements were performed in a collaboration with Dr Joris van Slageren at Universitat Stuttgart with a custom-built spectrometer. The pulse sequences used were

π/2–τ–π–τ-echo (Hahn echo) for determination of echo-detected EPR spectra and phase memory time and π–T–π/2–τ_{fix}–π–τ_{fix}–echo (inversion recovery) for determination of spin–lattice relaxation time.

Mass spectrometry

Mass spectra of the compounds and ligands were obtained analyzing their solutions with the MALDI—TOF and/or ESI technique in both positive and negative modes. MALDI-TOF spectrograms were collected in the reflector mode on the 4800 *Plus* MALDI TOF/TOF (ABSciex-2010) instrument equipped with Nd:YAG solid state laser (355 nm, frequency 200 Hz, pulse 3-7 ns). Analyses were carried out using different conditions: solution of the compound without any matrix, solution of the compound and the saturated matrix of the DHB (2,5-dihydroxybenzoic acid) in acetonitrile (1:1 volume ratio) or solution of the compound with the matrix containing dichloromethane solution of DCTB (10 mg/mL; *trans*-2-[3-(4-*tert*-butylphenyl)-2-methyl-2-propenylidene]malononitrile (1:1 volume ratio). In the last two cases, a mixture of sample and matrix solution was spotted on the sample plate and left to dry before the analysis by MALDI-TOF. ESI mass spectrograms were determined using a LC/MSD-TOF (Agilent Technologies) with a dual source equipped with a lock spray for internal reference introduction.

^{1}H NMR spectroscopy

^{1}H NMR spectra were recorded at room temperature with a Varian Unity 400 MHz spectrometer (University of Barcelona).

IR Spectroscopy

IR spectra were recorded as KBr pellets, in the range 4000−400 cm^{-1}, with a Nicolet 5700 FT-IR spectrometer.

1. *SAINT*, version V8.32B; Bruker AXS Inc.: Madison, WI, USA, 2005.

2. *SADABS*, version 2012/1; Bruker AXS Inc.: Madison, WI, USA, 2005.

3. G. M. Sheldrick, *Acta Crystallogr. Sect* A, 2008, **64**, 112-122.

4. G.M. Sheldrick, *Acta Crystallogr. Sect. A*, 2015, **71**, 3–8.

5. N. F. Chilton, R. P. Anderson, L. D. Turner, A. Soncini and K. S. Murray, *J. Comput. Chem.*, 2013, **34**, 1164-1175.

6. I. Tkach, A. Baldansuren, E. Kalabukhova, S. Lukin, A.Sitnikov, A. Tsvir, M. Ischenko, Y.Rosentzweig, E. Roduner, *Appl. Magn. Reson.*, 2008, **35**, 95–112.

List of publications

1. L. A. Barrios, **I. Borilovic**, J. Salinas Uber, D. Aguilà, O. Roubeau, G. Aromí, *Dalton Trans.,* 2013, **42**, 12185-12192. (DOI: 10.1039/c3dt51232k)
2. V. Velasco, D. Aguilà, L. A. Barrios, **I. Borilovic**, O. Roubeau, J. Ribas-Ariño, M. Fumanal, S. J. Teat, G. Aromí, *Chem. Sci.*, 2015, **6**, 123-131. (DOI: 10.1039/C4SC02491E)
3. A. Presa, R. F. Brissos, A. B. Caballero, **I. Borilovic**, L. Korrodi-Gregório, R. Pérez-Tomás, O. Roubeau, P. Gamez, *Angew. Chem. Int Ed.* 2015, **54**, 4561-4565. (DOI: 10.1002/anie.201412157)
4. A. Hernán-Gómez, E. Herd, M. Uzelac, T. Cadenbach, A. R. Kennedy, **I. Borilovic**, G. Aromí, E. Hevia, *Organometallics*, 2015, **34**, 2614-2623. (DOI: 10.1021/om501251q)
5. L. C. H. Maddock, T. Cadenbach, A. R. Kennedy, **I. Borilovic**, G. Aromí, E. Hevia, *Inorg. Chem.*, 2015, **54**, 9201-9210. (DOI: 10.1021/acs.inorgchem.5b01638)
6. **I. Borilovic**, O. Roubeau, I. Fernández Vidal, S. Teat, G. Aromí, *Magnetochemistry*, 2015, **1**, 45-61. (DOI: 10.3390/magnetochemistry1010045)
7. M. Uzelac, **I. Borilovic**, M. Amores, T. Cadenbach, A. R. Kennedy, G. Aromí, E. Hevia, *Chem. Eur. J*., 2016, **22**, 4843-4854. (DOI:10.1002/chem.201504956)
8. L. C. H. Maddock, **I. Borilovic**, Jamie McIntyre, Alan R. Kennedy, Guillem Aromí , Eva Hevia, *Dalton Trans.,* 2017,**46**, 6683-6691. (DOI:10.1039/C7DT01319A)
9. J. Požar, I. Nikšić-Franjić, M. Cvetnić, K. Leko, N. Cindro, K. Pičuljan, **I. Borilović**, L. Frkanec, V. Tomišić, *J. Phys. Chem. B,* 2017*,* **121**, 8539–8550. (DOI:10.1021/acs.jpcb.7b05093)

Conference contributions:

Oral communications:

1. September 2015- 5th European Conference on Molecular Magnetism (ICMM-2015), Zaragoza, Spain

   Flash presentation: *Topology and site selectivity in hydroxo-diketonato based molecular clusters: magnetostructural correlations*

   I. Borilovic, O. Roubeau, G. Aromí

2. May 2016-2nd Bordeaux Olivier Kahn Discussions (BOOK-D), Bordeaux, France
   Flash presentation: Heterometallic Cu-VO molecular clusters: Serendipitous versus tailored-metalloligand synthetic approach
   I. Borilovic, O. Roubeau, G. Aromí

3. July 2018-43nd International Conference on Coordination Chemistry, Sendai, Japan
   Oral communication: Designing Molecules With Inequivalent Spin Qubits
   I. Borilovic, O. Roubeau, G. Aromí

Poster presentations:

1. February 2012- IXth Meeting of Young Chemist and Chemical Engeeinners, Zagreb, Croatia
   N. Bregović, **I. Borilović**, D. Božić, L. Frkanec, V. Tomišić
   Triptophane calix[4]arene derivate as fluoride receptor – cooperative ion pair binding

2. July 2014*:* 14th International Conference on Molecule-Based Magnets (ICMM-2014), St. Petersburg, Russia
   I. Borilovic, D. Aguilà, L. Barrios, O. Roubeau, G. Aromí
   Site selective 3d heterometallic molecular strings based on bis-β-diketone ligand

3. September 2015: 5th European Conference on Molecular Magnetism (ICMM-2015), Zaragoza, Spain

   I. Borilovic, O. Roubeau, G. Aromí
   Topology and site selectivity in hydroxo-diketonato based molecular clusters: magnetostructural correlations

4. September 2015: 5th European Conference on Molecular Magnetism (ICMM-2015), Zaragoza, Spain
   I. Borilovic, O. Roubeau, G. Aromí
   Carbonate windmills - effective fixation of CO_2 into novel discrete coordination entities
5. May 2016: 2nd Bordeaux Olivier Kahn Discussions (BOOK-D), Bordeaux, France
   I. Borilovic, O. Roubeau, G. Aromí

Magnetic molecular architectures: Serendipitous versus tailored-metalloligand synthetic approach

6. September 2016: 15th International Conference on Molecular Magnetism (ICMM-2016), Sendai, Japan

   I. Borilovic, O. Roubeau, G. Aromí

   Magnetic molecular architectures: Serendipitous versus tailored-metalloligand synthetic approach

Acknowledgemets

If I have seen further it is by standing on the shoulders of Giants.

Isaac Newton

The first giant who stood up his back and shoulders for me is Guillem. He deserves a huge THANK YOU for taking the risk with me and for giving me the opportunity of a lifetime: to live in this incredible city and to work in a dream lab on the most amazing chemistry. I will never forget to appreciate that because I remember well who I was as a person and a researcher when we first met at airport and who I am today. Everything in between happened thank to his support, enthusiasm, trust and a constant encouragement to seek for something more. Apart from that, he showed me how to be critical with the research and how to get the most out of it, by investing his constant efforts to give another dimension to the chemistry we were creating along the way. From the personal viewpoint he gave me even more and made me feel as at home from the very first moment here.

Right after him, I'm immensely indebted to Olivier, who taught me the most things during my time as a PhD, by resolving patiently all my doubts along the way, especially with the crystallography. Thank you for many weekend/vacation replies to emails, measurements and fruitful discussion. It was a true privilege to know you and to learn from you!

My love for chemistry arised from the very first moment our paths have crossed. Two dearest teachers, mentors and friends, Vlatka Miličević and Margareta Vargek accepted generously my interest and dedicated many of their free mornings, afternoons and Saturdays to educate me a bit more and to give me the joy of doing my first experiments. I know both will laugh when they read these lines and say that those things were insignificant, but to a kid of 13+ years, they've opened up a brave new world of imagination and gave the confidence of being good at something. From today's perspective, I appreciate that even more because I realise the greatness of their dedication and sacrifice, driven simply by the fact that you saw some potential in me. I consider myself incredibly lucky to be surrounded with such amazing people and will do my best to continue this legacy with every student that crosses my way. Likewise, I must acknowledge all my teachers and professors, starting from the elementary school to university, who shaped my life by giving

me the foundation of knowledge which I can generously exploit now. In particularly, I must acknowledge Dr Srećko Kirin, Prof Marina Cindrić and Prof Vladislav Tomišić who allowed me to work on their diverse scientific projects while I was an undergraduate student. The experiences I've collected with them help me greatly to develop my scientific skills. During the PhD adventure, I was lucky enough to meet many great scientific role models for any young researcher. In that sense, I must point out Prof Eva Hevia and Prof Patrick Gamez, who gave me the amazing opportunity to participate in their science and capture a small glimpse of their wisdom. Besides learning from them, the greatest pleasure of knowing them is the fact that both are amazing people who encouraged me a lot during this path. Same goes for Dr Carolina Sañudo, for being a real friend when I needed it the most and for being a first class scientist with whom I had the pleasure of sharing many great discussion and moments.

One of the greatest pleasures of doing the PhD here was to work with many great people who helped me grow as a person and as a scientist. All past and present members of GMMF have become like my family and I will never find enough ways to thank them for accepting me so well and giving me so many beautiful memories in and out of the lab. I must point out Gavin and David who were my role models from the first moment since I've walked in the group and who showed me how to be a proper PhD student by setting the bar high with the work they carried out in the group. Jorge and Leo are kindly acknowledged for helping me out in my baby steps with this chemistry and life in Spain. Same goes for Raul and Santi with whom I've shared many great moments during my stay in BCN and became good friends. Good spirit and top-notch science from all the other past and present members of GMMF, MJ, Lidia, Mariona, Vero, Jose, Nuria, Marta, Albert, Rosa, Carlos, will live with me forever. Same goes for excellent technicians working at UB, whose expertise and human approach always went beyond their job and allowed me to carry out the research on a high level. In that sense, I must acknowledge Nuria Clos, for many magnetic measurements, for fighting with me patiently to capture the proper way of measuring the air-sensitive samples and for all the enjoyable moments spent in conversation. Deeply appreciated is also help, support and fantastic work of Irene Fernandez and Laura Ortiz in the mass spectrometry, as well as Regina Roca and Francisco Cardenas for their valuable contributions in EA and NMR studies.

Thanks to all the ‘ordinary people in the shadow’ who made my life here easier and enjoyable: to Cesar, for many pleasant conversations about Barça and for finding a solution for every crazy idea I had. To Ana, Teresa and Cristina, who always did their best to help me out and to Maribel for many kind words of encouragement, genuine happiness and for saving for me one cup of coffee at any time.

Immense thank you to my parents for the incredible amount of hard work they endured just to provide me a better life. I’m sorry I never took the time to say this to you earlier, now I can only hope you both knew that you are my true heroes, embracing me every step of the way with your support, understanding and encouragement. Same goes for the rest of my huge family and my dear friend Duška for making me feel unconditionally loved and appreciated.

And finally, the most heartfelt thank you goes to Marina. The greatest privilege, honour and luck of my life is to have you as my best friend and as a part of my family. No words will ever be good enough to acknowledge you for believing in me often beyond my own hesitations, for being the best possible co-worker, my voice of reason and my rock since the earliest student days. From all the giants mentioned here, I have no doubt you are the one who will amaze and brighten up the world in the most spectacular way. Can’t wait to see it!

Ivana